Transactions of the ASME®

Technical Editor, LEON M. KEER (1993)

The Technological Institute
Northwestern University
Evanston, IL 60201

APPLIED MECHANICS DIVISION

Chairman, MICHAEL J. FORRESTAL
Secretary, L. B. FREUND
Associate Technical Editors,
S. K. DATTA (1993)
G. J. DVORAK (1993)
C. O. HORGAN (1992)
R. L. HUSTON (1991)
D. J. INMAN (1992)
W. G. KNAUSS (1991)
J. T. C. LIU (1993)
R. M. McMEEKING (1991)
A. K. NOOR (1991)
J. W. RUDNICKI (1992)
C. F. SHIH (1993)
J. G. SIMMONDS (1992)
P. D. SPANOS (1992)
K. R. SREENIVASAN (1992)
Z. WARHAFT (1992)
L. T. WHEELER (1991)

BOARD ON COMMUNICATIONS
Chairman and Vice-President
R. E. NICKELL
Members-at-Large
W. BEGELL, T. F. CONRY, M. FRANKE,
R. L. KASTOR, M. KUTZ, R. MATES,
T. C. MIN, R. E. REDER,
R. D. ROCKE, W. O. WINER,
A. J. WENNERSTROM, B. ZIELS

President, C. O. VELZY
Exec. Dir.
D. L. BELDEN
Treasurer, ROBERT A. BENNETT

PUBLISHING STAFF
Mng. Dir., Publ.,
CHARLES W. BEARDSLEY
Managing Editor,
CORNELIA MONAHAN
Production Editor, JUDY SIERANT
Prod. Asst., MARISOL ANDINO

Transactions of the ASME, Journal of Applied Mechanics (ISSN 0021-8936) is published quarterly (Mar., June, Sept., Dec.) for $120 per year by The American Society of Mechanical Engineers, 345 East 47th Street, New York, NY 10017. Second class postage paid at New York, NY and additional mailing offices. POSTMASTER: Send address changes to Transactions of the ASME, Journal of Applied Mechanics, c/o THE AMERICAN SOCIETY OF MECHANICAL ENGINEERS, 22 Law Drive, Box 2300, Fairfield, NJ 07007-2300.

CHANGES OF ADDRESS must be received at Society headquarters seven weeks before they are to be effective. Please send old label and new address.

PRICES: To members, $29.00, annually; to nonmembers, $120.00. Add $15.00 for postage to countries outside the United States and Canada.

STATEMENT from By-Laws. The Society shall not be responsible for statements or opinions advanced in papers or . . . printed in its publications (B7.1, Par. 3).

COPYRIGHT © 1990 by the American Society of Mechanical Engineers. Reprints from this publication may be made on condition that full credit be given the TRANSACTIONS OF THE ASME, JOURNAL OF APPLIED MECHANICS, and the author, and date of publication be stated.

INDEXED by Applied Mechanics Reviews and Engineering Information, Inc.

Journal of Applied Mechanics

Published Quarterly by The American Society of Mechanical Engineers

VOLUME 57 • NUMBER 2 • JUNE 1990

257 In Memoriam

TECHNICAL PAPERS

259 Elastic-Plastic Analysis of Combined Mode II and III Crack-Tip Fields Under Small-Scale Yielding Conditions (90-WA/APM-6)
J. Pan and C. F. Shih

268 Internal Stress Arising From a Spherically Symmetric, Finite Plastic Strain and Yielding of a Hollow Sphere
T. Sakaki, K. Sugimoto, and T. Kuroki

276 Creep of a Hollow Sphere
T. Sakaki, T. Kuroki, and K. Sugimoto

282 Viscoplastic Constitutive Modeling of High Strain-Rate Deformation, Material Damage, and Spall Fracture
J. A. Nemes, J. Eftis, and P. W. Randles

292 A Dynamic Measuring Technique for Bulk Stiffness Constants as a Function of a Temperature and Microstructure for U-6 wt pct Nb
D. R. Lowry, A. Wolfenden, and G. M. Ludtka

298 Analytical Solutions for Circular Bars Subjected to Large Strain Plastic Torsion
K. W. Neale and S. C. Shrivastava

307 A Rudimentary Analysis of Improving Fatigue Life Metals by Shot-Peening (90-WA/APM-8)
Y. F. Al-Obaid

313 Effects of State Recovery on Creep Buckling Under Variable Loading
D. N. Robinson and S. M. Arnold

321 Kinematics for Bodies Undergoing Residual Stress and its Applications to the Left Ventricle
K. Takamizawa and T. Matsuda

330 The Effect of Contact Generation on the Elastic Properties of a Granular Medium
A. L. Endres

337 A Method for Identifying Parameters of Mechanical Joints
J. Wang and P. Sas

343 The Dynamic Energy Release Rate for a Steadily Propagating Mode I Crack in an Infinite, Linearly Viscoplastic Body
J. R. Walton

354 Effects of Crack Surface Heat Conductance on Stress Intensity Factors
A.-Y. Kuo

359 Interface Crack Between Two Dissimilar Half Spaces Subjected to a Uniform Heat Flow at Infinity—Open Crack
A.-Y. Kuo

365 Effect of Material Properties on the Stability of Static Thermoelastic Contact
R. Zhang and J. R. Barber

370 Cross-Approximation Method for Solving Dynamics Problems of Arbitrarily Shaped Plates
K. Poltorak

376 Analysis of Simply-Supported Orthotropic Cylindrical Shells Subject to Lateral Impact Loads
A. P. Christoforou and S. R. Swanson

383 Torsional Response of Rectangular Composite Laminates (90-WA/APM-3)
C.-L. Tsai, I. M. Daniel, and G. Yaniv

388 A High-Order Mixture Homogenization of Bi-laminated Composites
H. Murakami and A. Toledano

398 Rayleigh and Love Waves in Cladded Anisotropic Medium (90-WA/APM-4)
M. Bouden and S. K. Datta

404 Hypersingular Boundary Integral Equations: Some Applications in Acoustic and Elastic Wave Scattering (90-WA/APM-7)
G. Krishnasamy, L. W. Schmerr, T. J. Rudolphi, and F. J. Rizzo

415 Analysis of Surface Wave Generation by Laser Interferences
K. J. Faran, R. J. D. Miller, and S. M. Gracewski

419 On the Free Vibrations of Suspended Cables With Frictional End Restraint
H. M. Irvine

423 Nonclassically Damped Dynamic Systems: An Iterative Approach (90-WA/APM-5)
F. E. Udwadia and R. S. Esfandiari

(Contents continued on Inside Back Cover)

We are saddened to inform you that

J. W. NUNZIATO

Associate Editor for the Journal of Applied Mechanics, died on May 26, 1990.

Downloaded 04 May 2010 to 171.66.16.49. Redistribution subject to ASME license or copyright; see http://www.asme.org/terms/Terms_Use.cfm

CONTENTS (CONTINUED)

434 **Modal Sensors/Actuators**
C.-K. Lee and F. C. Moon

442 **On Randomly Excited Hysteretic Structures**
G. Q. Cai and Y. K. Lin

449 **Nonlinear Finite Deformation Response of Open Cell Polyurethane Sponge to Fluid Filtration**
Y. Lanir, S. Sauob, and P. Maretsky

455 **Analysis of Inclined Wall Plume by the k-ϵ Turbulence Model**
Y. Fukushima and N. Hayakawa

BRIEF NOTES

Flow Along a Cylinder With Periodic Suction **C. Y. Wang** 466

Orthogonal Curvilinear Coordinates and Angular Velocity **T. R. Kane and D. A. Levinson** 468

Unified Iso-Deflection Curves for Orthotropic Plates Under Lateral Pressure Pulse **J. Ari-Gur and M. J. Kenig** 470

472 Axisymmetric Upheaval Buckling of a Heavy Sheet
R. E. Hobbs

474 Some Remarks on Three Micromechanical Models in Composite Media
Y. Benveniste

476 Dynamic Stiffness of Cracked Interfaces
D. A. Sotiropoulos

DISCUSSION

479 **Discussion of a previously published paper by M. Ojalvo**

BOOK REVIEWS

481 ***Material Instabilities in Continuum Mechanics and Related Mathematical Problems,* edited by J. M. Ball . . .** Reviewed by **D. D. Joseph**

482 Books Received by the Office of the Technical Editor

483, 484 Worldwide Mechanics Meetings List

448 I.U.T.A.M. 18th International Congress of Theoretical and Applied Mechanics

375 Call for Papers—Joint ICF/FEFG International Conference on Fracture of Engineering Materials and Structures

480 Change of Address Form

Downloaded 04 May 2010 to 171.66.16.49. Redistribution subject to ASME license or copyright; see http://www.asme.org/terms/Terms_Use.cfm

In Memoriam

Jacob Pieter Den Hartog

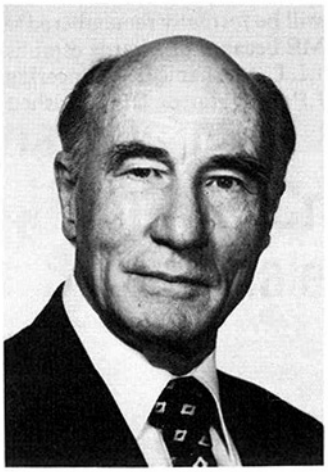
Jacob Pieter Den Hartog, internationally famous vibration consultant, author, and teacher, died on Mar. 17, 1989 after a long illness. He was the author of the best known textbook on vibrations and was widely acclaimed for his skill in identifying the underlying mechanisms responsible for unexpected vibration problems in machines and structures.

Den Hartog had been active in the Applied Mechanics Division of The ASME since its inception in 1927. Volume 50 (1927–1928) of The ASME Transactions was the first volume to contain papers contributed by the fledgling division. Three of Den Hartog's papers appear in this volume. When the Journal of Applied Mechanics began separate publication in 1933, it contained at least one Den Hartog contribution each year for the first seven years. Den Hartog served as Chairman of the Division in 1940 and 1941 and was honored with the Timoshenko medal in 1972. He returned to address the Division as the featured speaker during the celebration of the 50th anniversary of the founding of the Division in 1977.

Den Hartog was born on July 23, 1901 in The Netherlands East Indies (now Indonesia) where he lived until the family returned to Holland in 1916. He received his engineering training at Delft Polytechnical Institute in Holland, graduating with an E.E. degree in 1924. Because of poor economic conditions in Holland at that time, he emigrated immediately to the United States. Through a series of fortunate accidents he soon found himself in Pittsburgh working for Westinghouse as the assistant to a Russian emigré, Stephen P. Timoshenko, 20 years his senior. At that time American industry was growing rapidly and there were many opportunities to apply the more sophisticated techniques of European engineers. Timoshenko assigned the young Den Hartog a variety of vibration problems associated with electric motors and generators. Den Hartog worked at Westinghouse during the day and studied mathematics at the University of Pittsburgh in the evenings. He completed a Ph.D. program in 1929, with a thesis on nonlinear vibration. In 1931 he spent a sabbatical year in Gottingen, in the laboratory of Professor Prandtl. On his return in 1932 he joined the faculty of Harvard University and began his teaching career. He started lecturing on vibrations and assembling an extensive collection of vibration demonstration models. His lectures had such a reputation that professors from nearby M.I.T. would take the trolley across town to sit in with the Harvard students. Here he published the first edition of his famous text *Mechanical Vibrations* in 1934.

When the storm clouds of impending war began to gather, Den Hartog decided he could serve his adopted country better in the military than as a civilian. He was called to active duty in the Navy in 1941 and spent the war working on ship vibration problems for the Bureau of Ships. When the war was over, in 1945, Captain Den Hartog returned to civilian life and to a new post as Professor of Mechanical Engineering at M.I.T.

At M.I.T. he enthusiastically took up his teaching and consulting work. He was endowed with great energy. In addition to revised editions of *Mechanical Vibrations*, he published three distinctive textbooks (*Mechanics* in 1948, *Strength of Materials* in 1949, and *Advanced Strength of Materials* in 1952) which are still maintained in print by Dover Publications. He spent four months in 1955 as a Fulbright Visiting Lecturer in Japan and was invited to give the Thomas Hawksley Lecture in London in 1957, the first American to be so honored. Den Hartog served briefly as Department Head (1954–1958), but administration was not his strong suit. He



J. P. Den Hartog

loved to lecture and he loved to tackle challenging consulting problems. He loved music, was a good amateur violinist and a marvelous raconteur. He and his wife Beppie also loved to act as unofficial ambassadors to foreign students and scientists. They owned an island in the middle of Lake Winnipesaukee which they used to entertain visitors. For many foreign scientists their most vivid memory of America is of being bundled into a car, driven up to New Hampshire, seated in a canoe and paddled across the lake to spend an idyllic weekend on the island. In 1967 Den Hartog became Emeritus Professor but he continued consulting and part-time teaching until 1980 when arthritic joints finally deprived him of his mobility.

In his research publications Den Hartog made major contributions to the problems of nonlinear vibrations, Coulomb friction damping, galloping of electrical transmission lines, vibrations of electrical machinery, dynamic vibration absorbers, and torsional vibration dampers. The essential ideas and practical results of many of these investigations were incorporated in subsequent editions of *Mechanical Vibrations*. There were four editions in English: 1934, 1940, 1947, and 1956. There were also 15 foreign editions in 11 different languages. The style is simple and direct. The reader is skillfully led to the essential heart of each problem by means of simplified models. Sketches and diagrams are used in place of mathematical equations wherever possible.

Den Hartog's talents were widely recognized and he received many honors from his fellow engineers, from universities, and from prestigious academies. From The ASME, in addition to the Timoshenko medal, he received the Richards medal, the Worcester Reed Warner medal, and The ASME medal. The American Society of Engineering Education awarded him the Lamme medal and the Acoustical Society of America awarded him the Trent-Crede medal. He was an Honorary Member of The ASME and the Japan Society of Mechanical Engineers, and a Fellow of the British Institution of Mechanical Engineers. He was awarded honorary doctorates from Carnegie Institute of Technology, the University of Ghent, the Technical University of Delft, Salford University, and the University of Newcastle-Upon-Tyne. He was elected to both the U.S. National Academy of Science and the U.S. National Academy of Engineering, and to the American

Copyright © 1990 by ASME
Downloaded 03 May 2010 to 171.66.16.244. Redistribution subject to ASME license or copyright; see http://www.asme.org/terms/Terms_Use.cfm

Academy of Arts and Sciences and the Royal Dutch Academy of Arts and Sciences. At the end of his career he received three major awards during his 80th year: the James Watt medal from the British Institution of Mechanical Engineers, the Founders medal from the U.S. National Academy of Engineers, and the Order of the Rising Sun from the Emperor of Japan.

Den Hartog will be formally remembered within M.I.T. and within The ASME because of awards established in his name. In 1981, the M.I.T. Mechanical Engineering Department inaugurated the J.P. Den Hartog Distinguished Educator award to recognize "excellence . . .in the tradition of Den Hartog." In 1987 The ASME Design Engineering Division established the Jacob P. Den Hartog award for "sustained meritorious contributions to vibration engineering" and presented the first medal to Den Hartog. Those of us who were fortunate enough to know him in his active days will always remember his uncanny physical insight and the energetic enthusiasm with which he made it all seem so simple.

Stephen H. Crandall
Massachusetts Institute of Technology

Downloaded 03 May 2010 to 171.66.16.244. Redistribution subject to ASME license or copyright; see http://www.asme.org/terms/Terms_Use.cfm

Elastic-Plastic Analysis of Combined Mode II and III Crack-Tip Fields Under Small-Scale Yielding Conditions

J. Pan
Mechanical Engineering and Applied Mechanics, The University of Michigan, Ann Arbor, MI 48109

C. F. Shih
Division of Engineering, Brown University, Providence, RI 02912
Mem. ASME

Within the context of the small-strain approach, combined mode II and III small-scale yielding solutions of a stationary crack are obtained by finite element analysis. To investigate the behavior of the near-tip fields, the normalized stresses ahead of the crack tip are plotted as functions of the normalized radial distance to the tip for several combinations of prescribed mode II and III elastic K fields. The angular variations of the normalized stresses at a fixed radial distance deep within the plastic zone are also plotted for several combinations of remote mode II and III elastic K fields. These plots show an interesting pattern: Well within the plastic zone, the in-plane stresses can be said to be slightly less singular than $r^{-1/(n+1)}$ *while the out-of-plane shear stresses are slightly more singular than* $r^{-1/(n+1)}$*, where n is the strain-hardening exponent of the material. However, over physically relevant distances ahead of the tip and for the full range of combined mode II and III loadings, the ratio of the in-plane shear stress to the out-of-plane shear stress agrees well with the ratio estimated by linear elastic crack-tip fields.*

1 Introduction

Asymptotic plane-strain and plane-stress crack-tip stress and strain fields for power-law materials and perfectly plastic materials have been obtained under pure mode I and pure mode II conditions (Hutchinson, 1968a,b; Rice and Rosengren, 1968; and Rice, 1968a) and under pure mode III conditions (Rice, 1968b). However, cracks in typical engineering structures are generally subject to combined mode I, II, and III loading. Thus, asymptotic crack-tip fields for combined mode loadings are essential to the fracture analysis of flawed structures. For example, for safety consideration under postulated accidental conditions, circumferential surface cracks due to stress corrosion cracking in nuclear piping systems experience combined mode I, II, and III conditions along the crack front when the cracked pipes are subjected to remote bending and torsional loads. The mode I conditions along the crack front are due to the bending loads while the combined mode II and III conditions are due to the torsional loads.

The asymptotic crack-tip stress and strain fields for power-law materials and perfectly plastic materials under combined mode I and II conditions have been presented by Shih (1973, 1974). Further investigations of the combined mode I and II crack-tip fields for perfectly plastic materials can be found in Nemat-Nasser and Obata (1984), Saka et al. (1986), and Dong and Pan (1990a,b). Within the small-scale yielding formulation, Pan and Shih (1989) have obtained the near-tip fields by finite element methods for a complete range of remotely applied combined mode I and III elastic K fields. Their computational results show that within the plastic zone, the in-plane stresses are more singular than the out-of-plane shear stresses. The qualitative nature and quantitative results for the angular and radial variations of both the in-plane stresses and the out-of-plane shear stresses agree well with the results from the perturbation analysis of Pan (1989). The perturbation approach was adopted because the highly nonlinear governing differential equations (due to the coupling of the in-plane and out-of-plane fields) did not appear amenable to the usual separable solutions. In Pan's analysis, the perturbed asymptotic crack-tip fields were obtained under the assumption that either the in-plane mode or the out-of-plane shear mode is small compared to the other.

Under combined in-plane and out-of-plane shear loading conditions, the in-plane and out-of-plane shear stresses near a crack tip are coupled through the effective stress in the plastic stress-strain relations. The out-of-plane shear stresses therefore affect the in-plane stresses in the plastically deforming region and vice versa. The purpose of our study is to examine the effect of this coupling on near-tip fields

Contributed by the Applied Mechanics Division of THE AMERICAN SOCIETY OF MECHANICAL ENGINEERS for presentation at the Winter Annual Meeting, Dallas, Texas, November 25-30, 1990.

Discussion on this paper should be addressed to the Technical Editor, Leon M. Keer, The Technological Institute, Northwestern University, Evanston, IL 60208, and will be accepted until two months after final publication of the paper itself in the JOURNAL OF APPLIED MECHANICS. Manuscript received by The ASME Applied Mechanics Division, January 23, 1989; final revision, June 16, 1989.

Paper No. 90-WA/APM-6.

Copyright © 1990 by ASME
Downloaded 03 May 2010 to 171.66.16.244. Redistribution subject to ASME license or copyright; see http://www.asme.org/terms/Terms_Use.cfm

systematically. To eludicate the rather complicated nature of the near-tip fields for a complete range of combined-mode loadings, many numerical solutions must be presented in an appropriately normalized form. Therefore, solutions for combined mode I and III problems are discussed in Pan and Shih (1989), and solutions for combined mode II and III problems are presented in this paper. For combined mode I, II, and III problems, the results will be presented in subsequent papers. It may be noted that for cases where perturbation solutions for the crack-tip fields have been obtained (Pan, 1989), the perturbation solutions and the finite element solutions are in good agreement. The current combined mode II and III solutions may have some implications on the nonplanar segmentation of a crack front subject to mode III loading (Rice, 1985; Meade and Keer, 1984; and Palaniswamy and Knauss, 1978). As suggested by Rice (1985) and Palaniswamy and Knauss (1978), the segmentation of the crack front may be due to the crack front perturbation in a wavy form which induces different signs of mode II contributions on opposite sides of the protrusion.

2 Hutchinson-Rice-Rosengren (HRR) Crack-Tip Fields

To describe the elastic-plastic behavior of the materials we consider here, we use the Ramberg-Osgood law, which is widely employed for fitting uniaxial tensile stress-strain relations:

$$\frac{\epsilon}{\epsilon_o} = \frac{\sigma}{\sigma_o} + \alpha\left(\frac{\sigma}{\sigma_o}\right)^n \tag{1}$$

where ϵ is the tensile strain, σ is the tensile stress, ϵ_o and σ_o are the reference strain and reference stress (we take $\epsilon_o = \sigma_o/\mathrm{E}$ where E is Young's modulus), α is a material constant, and n is the hardening exponent. A generalization of equation (1) can be written as the sum of an elastic part, ϵ_{ij}^e, and a volume-preserving plastic part, ϵ_{ij}^p:

$$\epsilon_{ij} = \epsilon_{ij}^e + \epsilon_{ij}^p. \tag{2}$$

The terms in (2) are given by

$$\epsilon_{ij}^e = \frac{(1+\nu)}{\mathrm{E}} s_{ij} + \frac{(1-2\nu)}{3\mathrm{E}} \sigma_{kk}\delta_{ij}$$
$$\epsilon_{ij}^p = \frac{3}{2}\alpha\left(\frac{\sigma_e}{\sigma_o}\right)^{n-1}\frac{s_{ij}}{\sigma_o} \tag{3}$$

where ν is Poisson's ratio, s_{ij} the deviatoric stress, and $\sigma_e\,(=(3s_{ij}s_{ij}/2)^{1/2})$ the effective stress.

We consider a crack in a Ramberg-Osgood solid, as shown in Fig. 1, where r and θ are the polar coordinates centered at the crack tip. As r approaches 0, the linear elastic part of the strain is negligible compared to the plastic part. The asymptotic crack-tip stress, strain, and displacement fields can then be expressed as (Hutchinson, 1968a,b; Rice and Rosengren, 1968; Rice, 1968b; Shih, 1973, 1974)

$$\sigma_{ij} = \sigma_o\left(\frac{J}{\alpha\sigma_o\epsilon_o Ir}\right)^{1/(n+1)}\tilde{\sigma}_{ij}(\theta;n,M)$$
$$\epsilon_{ij} = \alpha\epsilon_o\left(\frac{J}{\alpha\sigma_o\epsilon_o Ir}\right)^{n/(n+1)}\tilde{\epsilon}_{ij}(\theta;n,M) \tag{4}$$
$$u_i - \hat{u}_i = \sigma\epsilon_o r\left(\frac{J}{\alpha\sigma_o\epsilon_o Ir}\right)^{n/(n+1)}\tilde{u}_{ij}(\theta;n,M)$$

where the dimensionless constant, I, and the dimensionless angular functions $\tilde{\sigma}_{ij}$, $\tilde{\epsilon}_{ij}$, and $\tilde{u}_i$ depend upon the hardening exponent n; the state of plane-strain, plane-stress, or antiplane deformation; and the mode parameter M (mode I, mode II, mixed-mode I and II, or mode III). The constants $\hat{u}_i$ allow for a possible rigid body motion of the crack tip itself. The J integral (Rice, 1968a) in equation (4) represents the amplitude of the singular crack-tip stress and strain fields. Recent studies of the asymptotic crack-tip fields for power-law hardening orthotropic materials and for power-law hardening pressure-sensitive dilatant materials show the same type of functional forms as equation (4) for the asymptotic crack-tip fields (Pan and Shih, 1986, 1988; Li and Pan, 1989, 1990).

3 Computational Model

We consider the small-scale yielding problem depicted in Fig. 1, where the top half of a circular domain is shown. We select the upper half of the domain due to the nature of antisymmetry for in-plane mode II and out-of-plane mode III deformation. Along the remote circular boundary, displacement fields based on the mode II and mode III asymptotic crack-tip solutions for linear elastic materials are applied. The in-plane displacements u_i $(i=1, 2)$ and the out-of-plane displacement u_3 are prescribed as

$$u_i = \frac{K_{II}}{2G}\left(\frac{r}{2\pi}\right)^{1/2}\tilde{u}_i^{II}(\theta,\nu) \tag{5}$$

and

$$u_3 = \frac{K_{III}}{2G}\left(\frac{r}{2\pi}\right)^{1/2}\tilde{u}_3^{III}(\theta) \tag{6}$$

where G represents the shear modulus, and K_{II} and K_{III} represent the far-field mode II and mode III stress intensity factors. The dimensionless functions $\tilde{u}_i^{II}(\theta,\nu)$ and $\tilde{u}_3^{III}(\theta)$ are the well-known linear elastic asymptotic displacement solutions (for example, see Kanninen and Popelar, 1985).

The finite element model of the half circular domain is constructed using 9-node quadrilateral Lagrangian elements. Wedge-shaped 9-node elements are used in the immediate crack-tip region. The size of the wedge-shaped elements in the radial direction is denoted as r_i. These elements are surrounded by semi-circular strips of elements; four strips of elements span each decade of r_i/r_o, where r_o denotes the radius of the half circle as shown in Fig. 1. We take $r_i/r_o = 10^{-15}$ in this investigation. Therefore, 60 strips of elements, which are generated by a logarithmic scale, span the domain between $r/r_o = 10^{-15}$ and $r/r_o = 1$. Within each strip, the angular distance from 0 to π is spanned by 9 elements of equal size. Therefore, the total number of elements is 549.

The finite element formulation for this work will be discussed only briefly here. We used the *B-bar* method (Hughes, 1980) to construct the strain-displacement matrix of our 9-node quadrilateral Lagrangian elements. This method alleviates the poor performance of our quadrilateral Lagrangian elements in the fully-plastic range (Nagtegaal et al., 1974). In this study, we employed the parameter tracking

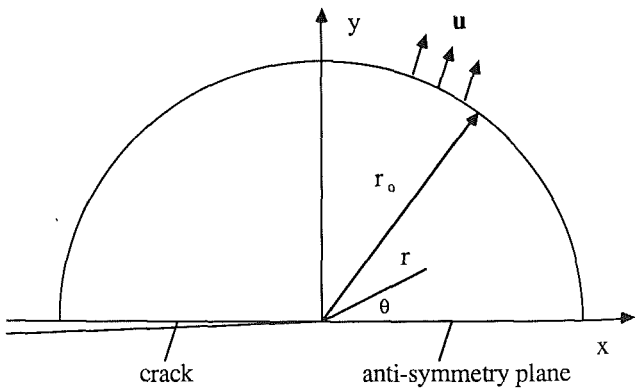


Fig. 1 A crack subjected to combined mode II and III elastic *K* fields along the circumferential boundary

Downloaded 03 May 2010 to 171.66.16.244. Redistribution subject to ASME license or copyright; see http://www.asme.org/terms/Terms_Use.cfm

method (Shih and Needleman, 1984). We begin by obtaining the linear elastic solution at a load. This solution is then used as the initial estimate in the iteration for a mildly nonlinear problem with, say, $n=2$. We then use the convergent solution for the mildly nonlinear problem as the initial estimate for a more nonlinear problem. In this manner, solutions can be obtained for high-hardening to low-hardening materials. Generally speaking, after four to five iterations, a convergent solution with a Euclidean error norm of about 10^{-6} will be obtained for a slightly lower hardening solution from a slightly higher one.

4 Mode Mixity

The far-field is completely specified by the two stress intensity factors, K_{II} and K_{III} (recall that the angular functions $\tilde{u}_i^{II}(\theta, \nu)$ and $\tilde{u}_3^{III}(\theta)$ are known). Alternatively, we can use another set of two parameters, the J integral and an elastic mixity factor, to specify the elastic far-field. The J integral is related to K_{II} and K_{III} by

$$J=\frac{1-\nu^2}{E}K_{II}^2+\frac{1}{2G}K_{III}^2. \tag{7}$$

The elastic mixity factor M_{23}^e for the small-scale yielding formulation is defined as

$$M_{23}^e=\frac{2}{\pi}\tan^{-1}\left[\lim_{r\to\infty}\frac{\sigma_{r\theta}(\theta=0)}{\sigma_{\theta z}(\theta=0)}\right]=\frac{2}{\pi}\tan^{-1}\left[\frac{K_{II}}{K_{III}}\right]. \tag{8}$$

According to equation (8), M_{23}^e equals 1 for pure mode II and 0 for pure mode III. The value of M_{23}^e lies between 1 and 0 for any combination of mode II and III loadings.

Within the plastic zone, the relative strength of the two modes at a distance r directly ahead of the crack tip can be expressed by the plastic mixity factor $M_{23}^p(r)$, defined as

$$M_{23}^p(r)=\frac{2}{\pi}\tan^{-1}\left[\frac{\sigma_{r\theta}(r,\theta=0)}{\sigma_{\theta z}(r,\theta=0)}\right] \tag{9}$$

Here, r is smaller than the smallest radial extent of the plastic zone. Thus, M_{23}^p equals 1 for pure mode II crack-tip fields and 0 for pure mode III crack-tip fields. The value of M_{23}^p ranges between 1 and 0 for combined mode near-tip fields. The plastic mixity factor M_{23}^p is a measure of the mixture of the two modes whereas the J integral is a measure of the amplitude of the near-tip fields. Important features of the combined mode II and III near-tip fields at the radial distance r can be conveniently expressed by the mixity parameter and the J integral.

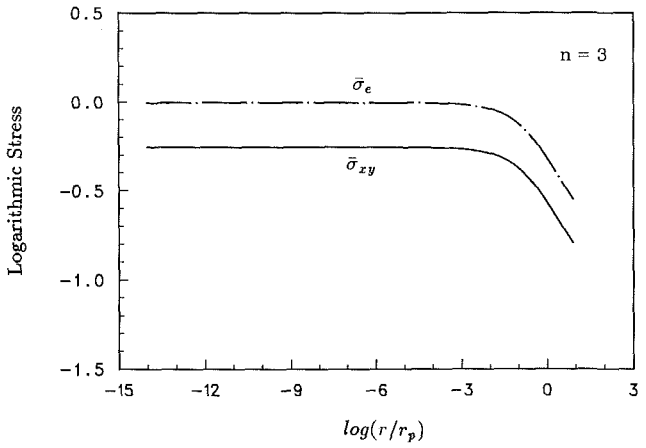


Fig. 2(a)

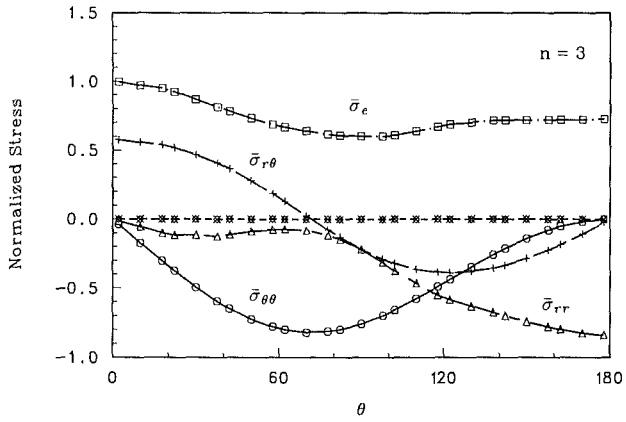


Fig. 2(c)

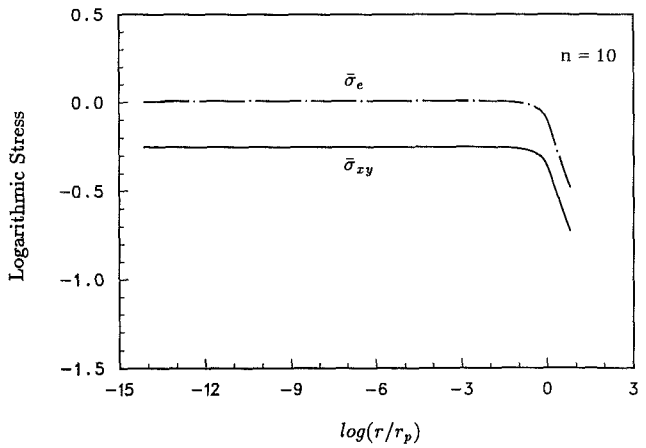


Fig. 2(b)

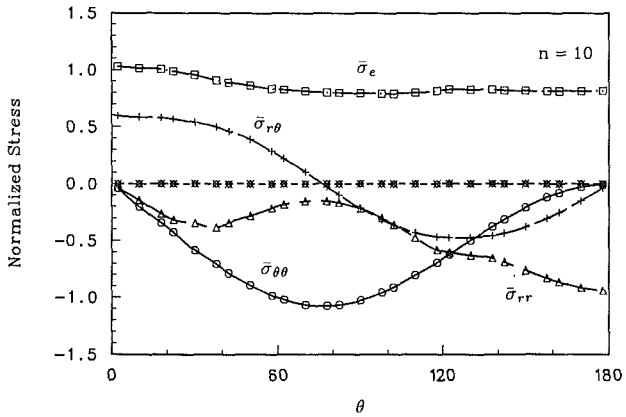


Fig. 2(d)

Fig. 2 Case 1 ($M_{23}^e=1$, pure mode II): the normalized stresses $\bar{\sigma}_{ij}$ at $\theta=10^o$ as functions of r/r_p plotted in a log-log scale for (a) $n=3$ and (b) $n=10$; the normalized stresses $\bar{\sigma}_{ij}$ at $r/r_p=10^{-3}$ plotted as functions of θ for (c) $n=3$ and (d) $n=10$

Downloaded 03 May 2010 to 171.66.16.244. Redistribution subject to ASME license or copyright; see http://www.asme.org/terms/Terms_Use.cfm

5 Numerical Results

The deformation plasticity solutions for combinations ranging from pure mode II to pure mode III and for hardening exponents n ranging from 1 to 10 are obtained. In these computations, we set $\nu = 0.3$ and $\alpha = 0.1$. Our finite element solutions produced the correct HRR singularities, namely $r^{-1/(n+1)}$, for the special cases of pure mode II and pure mode III remote loadings. For the elastic problem (a test case), the numerical solutions produced the precise elastic $1/\sqrt{r}$ singularity and the associated angular functions for various combinations of mode II and III loadings. Furthermore, for each of the convergent solutions, our J values, as calculated by the domain integral method (Li et al., 1985; Shih et al., 1986; Moran and Shih, 1987) for each of the semi-circular strips, differed by less than one percent from the prescribed value as determined by (7). The path-independence of the computed J values and the excellent agreement with (7) attest to the quality of our finite element solutions.

By the process of parameter tracking, we have obtained solutions for the full range of n values ($1 \le n \le 10$) and mixtures of mode II and III. To keep the paper within a resonable length, only solutions for $n = 3$ and 10 for remote displacement boundary conditions corresponding to five mixities, namely, $M^e_{23} = 1$, 0.83, 0.5, 0.17, and 0, are presented. These five cases represent the pure mode II, $K_{III}/K_{II} = 0.27$, $K_{III}/K_{II} = 1$, $K_{II}/K_{III} = 0.27$, and the pure mode III cases.

To examine the dependence of the near-tip stresses on the radial distance r (at fixed θ), we plot the normalized stresses (in the x, y, and z coordinates) ahead of the crack tip as functions of the normalized radial distance to the tip using a log-log scale. The numerically determined stresses are divided by the HRR singularity such that $\tilde{\sigma}_{ij} = \sigma_{ij}/[\sigma_o (J/\alpha\sigma_o\epsilon_o r)^{1/(n+1)}]$. The radial distance is divided by the length of the plastic zone, r_p, ahead of the crack tip. The normalized stresses plotted in the figures are based on the actual computed values in the x, y, and z coordinates along the central column (at $\theta = 10^o$) of the Gauss points in the first wedge strip of the elements immediately above the antisymmetry plane. Comparisons of the solutions at different θ's as functions of the normalized radial distance deep within the plastic zone indicate that the nature of the singularity is virtually the same. In order to investigate the mathematical structure of the near-tip fields and to reveal the similarities (if any) between the combined-mode near-tip fields and the pure mode II and mode III HRR fields, it is necessary to examine fields that are well below those that are physically relevant. For example, we have plotted the radial variations of the normalized stresses for distances as small as $r/r_p \approx 10^{-14}$. In applying these solutions to fracture analysis under combined-mode loading, fields within such distances would obviously be disregarded.

To examine the angular variations of the near-tip stress fields, we plot the normalized stresses $\tilde{\sigma}_{ij}$ (in the r, θ, and z coordinates) as functions of θ at a radial distance of $r/r_p \approx 10^{-3}$. The normalized stresses plotted in the figures are

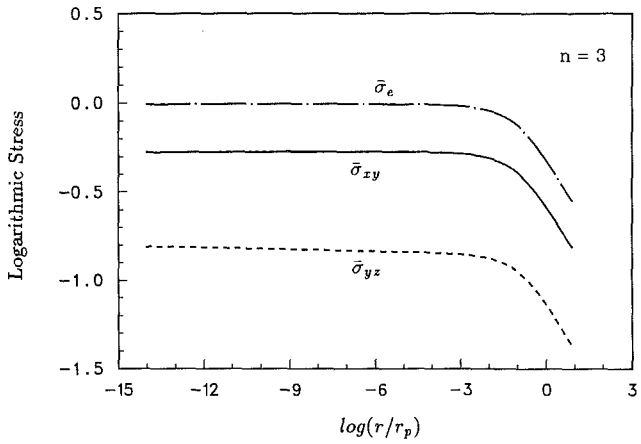


Fig. 3(a)

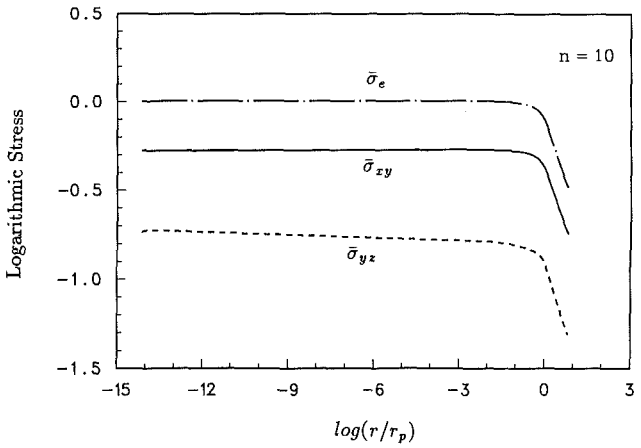


Fig. 3(b)

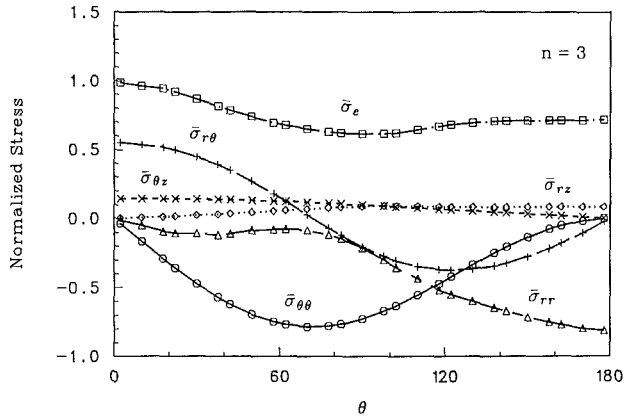


Fig. 3(c)

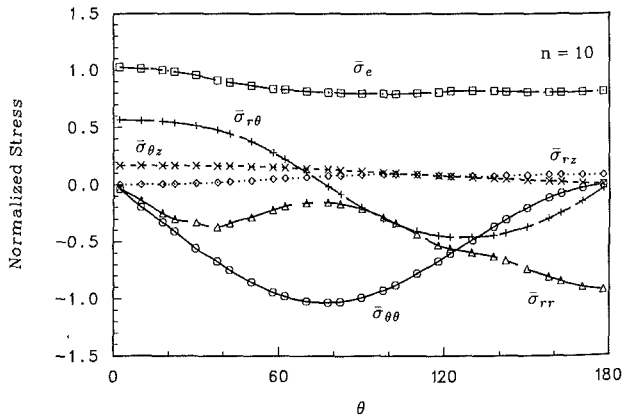


Fig. 3(d)

Fig. 3 Case 2 ($M^e_{23} = 0.83$, $K_{III}/K_{II} = 0.27$): the normalized stresses $\tilde{\sigma}_{ij}$ at $\theta = 10^o$ as functions of r/r_p plotted in a log-log scale for (a) $n = 3$ and (b) $n = 10$; the normalized stresses $\tilde{\sigma}_{ij}$ at $r/r_p \approx 10^{-3}$ plotted as functions of θ for (c) $n = 3$ and (d) $n = 10$

Downloaded 03 May 2010 to 171.66.16.244. Redistribution subject to ASME license or copyright; see http://www.asme.org/terms/Terms_Use.cfm

based on the computed values in the x, y, and z coordinates along the central row of the Gauss points in the semi-circular strip of the elements at about $r/r_p \approx 10^{-3}$.

For each problem analyzed, the magnitude of the far-field displacement field is chosen so that the maximum extent of the plastic zone (as a function of θ) is about at most ten percent of r_o. Thus the stresses deep within the plastic zone can be investigated under the small-scale yielding conditions. Our computations have resulted in values of r_p/r_o ranging from 0.1 to 0.001. These computational results reveal the same qualitative and quantitative trends for the near-tip fields.

Solutions for each of the five cases in the order of departure from mode II are presented as follows:

Case 1: $M^e_{23} = 1$ (Pure Mode II). Figures 2(a) and 2(b) show the normalized in-plane shear stress $\tilde{\sigma}_{xy}$ and the normalized effective stress $\tilde{\sigma}_e$ at $\theta = 10^o$ as functions of the normalized radial distance r/r_p in a log-log scale for $n = 3$ and 10, respectively. For cases 1–5 shown in Figs. 2–6, outside of the plastic zone ($\log(r/r_p) > 0$), the variation of the stresses with the radial distance is in agreement with the elastic singularity. Within the plastic zone, the stresses begin to level off at about $r/r_p \approx 10^{-2}$ for $n = 3$ and at about $r/r_p \approx 10^{-1}$ for $n = 10$. Since the numerically-determined stresses are normalized by the HRR singularity, the leveling off means the radial variation of the stresses is in accord with the HRR singularity. Indeed, the magnitudes of the computed stresses are equal to those of the HRR singularity; furthermore, these computed magnitudes appropriate to the HRR singularity are achieved much more rapidly for the lower-hardening ($n = 10$) material. Although we have plotted only the stresses $\tilde{\sigma}_{xy}$ and $\tilde{\sigma}_e$, the other three stresses $\tilde{\sigma}_{yy}$, $\tilde{\sigma}_{xx}$, and $\tilde{\sigma}_{zz}$ show the same trends. In the case of the $n = 10$ material, which is representative of the hardening characteristics of typical structural steels, the HRR fields are good approximations of the actual stresses and strains for $r/r_p \leq 10^{-1}$ (note that $r/r_p = 10^{-1}$ is a physically relevant distance).

Figures 2(c) and 2(d) show the normalized stresses $\tilde{\sigma}_{ij}$ at about $r/r_p \approx 10^{-3}$ as functions of θ for $n = 3$ and $n = 10$, respectively. The angular functions of the normalized stresses closely resemble the HRR asymptotic solutions (for example, see the solutions plotted in Pan (1989)). The solutions for this case provide an additional measure of the accuracy of our finite element solutions.

Case 2: $M^e_{23} = 0.83$ ($K_{III}/K_{II} = 0.27$). Figures 3(a) and 3(b) show the normalized in-plane shear stress $\tilde{\sigma}_{xy}$, the normalized effective stress $\tilde{\sigma}_e$, and the normalized out-of-plane shear stress $\tilde{\sigma}_{yz}$ at $\theta = 10^o$ as functions of r/r_p in a log-log scale for $n = 3$ and 10, respectively. Well within the plastic zone $\tilde{\sigma}_{xy}$ and $\tilde{\sigma}_e$ level off quickly to reach the HRR singularity, whereas $\tilde{\sigma}_{yz}$ continuously increases as the normalized distance r/r_p decreases.

Note that for this case (and for cases 3 and 4) the two other

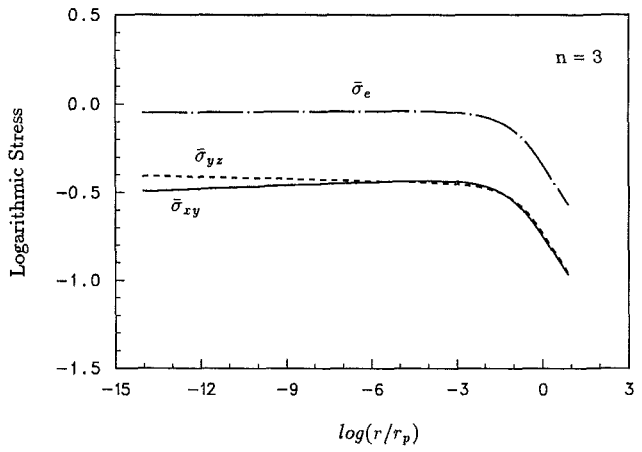


Fig. 4(a)

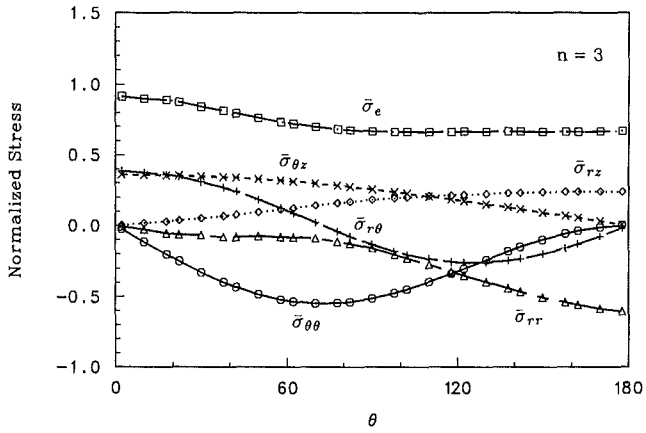


Fig. 4(c)

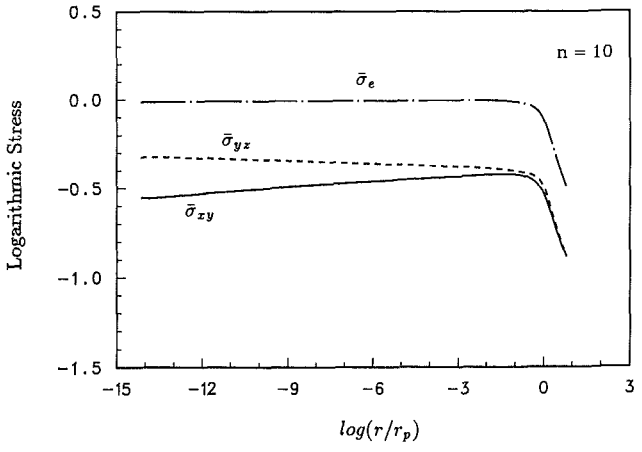


Fig. 4(b)

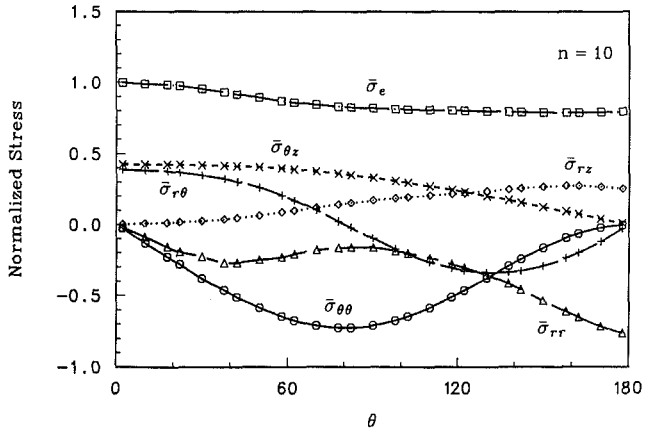


Fig. 4(d)

Fig. 4 Case 3 ($M^e_{23} = 0.5$, $K_{III}/K_{II} = 1$): the normalized stresses $\tilde{\sigma}_{ij}$ at $\theta = 10^o$ as functions of r/r_p plotted in a log-log scale for (a) $n = 3$ and (b) $n = 10$; the normalized stresses $\tilde{\sigma}_{ij}$ at $r/r_p \approx 10^{-3}$ plotted as functions of θ for (c) $n = 3$ and (d) $n = 10$

Downloaded 03 May 2010 to 171.66.16.244. Redistribution subject to ASME license or copyright; see http://www.asme.org/terms/Terms_Use.cfm

in-plane stresses, $\tilde{\sigma}_{yy}$ and the $\tilde{\sigma}_{xx}$, show the same trend as that of $\tilde{\sigma}_{xy}$, and the other out-of-plane shear stress $\tilde{\sigma}_{xz}$ shows the same trend as that of $\tilde{\sigma}_{yz}$. This suggests that well within the plastic zone and within the range of r/r_p indicated in the figures, the out-of-plane shear stresses are slightly more singular than the in-plane shear stresses. As shown in the figures, the strengthening of the out-of-plane shear stresses as r/r_p decreases is more pronounced for low-hardening materials (with large n). The differences of the singularity of $\tilde{\sigma}_{yz}$ in r from the HRR singularity are estimated from the figures as 0.004 for $n=3$ and 0.005 for $n=10$ averaged over ten decades of r/r_p. The results agree well with the value of 0.003 for $n=3$ and 0.005 for $n=10$ from the perturbation analysis of the asymptotic behavior of the crack-tip fields (Pan, 1989).

Figures 3(c) and 3(d) show the normalized stresses $\tilde{\sigma}_{ij}$ at about $r/r_p \approx 10^{-3}$ as functions of θ for $n=3$ and 10, respectively. The in-plane stresses shown in the figures nearly preserve the angular functional forms of the pure mode II HRR fields (Figs. 2(c) and 2(d)). The angular variations of the out-of-plane stresses $\tilde{\sigma}_{rz}$ and $\tilde{\sigma}_{\theta z}$, however, differ from those of the pure mode III case (Figs. 6(c) and 6(d)). The characteristics of these out-of-plane stress functions plotted in a magnified scale are shown to agree well with those of the asymptotic analysis of Pan (1989).

The elastic mixity factor M^e_{23} is about 0.83 ($\sigma_{\theta z}(\theta=0)/\sigma_{r\theta}(\theta=0)=0.27$). As r/r_p decreases from unity, the plastic mixity factor M^p_{23} changes only slightly. Actually, as r/r_p decreases, M^p_{23} increases slightly and then decreases for high-hardening materials, whereas M^p_{23} monotonically decreases for low-hardening materials. At about $r/r_p \approx 10^{-3}$, the plastic mixity factor M^p_{23} is 0.84 for $n=3$ and 0.82 for $n=10$ ($\sigma_{\theta z}(\theta=0)/\sigma_{\theta\theta}(\theta=0)=0.26$ for $n=3$ and 0.30 for $n=10$). At a very small distance, $r/r_p \approx 10^{-14}$, the plastic mixity factor M^p_{23} decreases to 0.83 for $n=3$ and 0.79 for $n=10$ ($\sigma_{\theta z}(\theta=0)/\sigma_{r\theta}(\theta=0)=0.27$ for $n=3$ and 0.34 for $n=10$). This demonstrates that well within the plastic zone the out-of-plane shear stresses relative to the in-plane shear stresses increase slightly as r/r_p decreases. This behavior is more pronounced for low-hardening materials (with large n).

Case 3: $M^e_{23}=0.5$ ($K_{III}/K_{II}=1$). Figures 4(a) and 4(b) show $\tilde{\sigma}_{xy}$, $\tilde{\sigma}_e$, and $\tilde{\sigma}_{yz}$ at $\theta=10^o$ as functions of r/r_p in a log-log scale for $n=3$ and 10, respectively. Within the plastic zone, $\tilde{\sigma}_e$ quickly levels off whereas $\tilde{\sigma}_{yz}$ continues to increase slightly and $\tilde{\sigma}_{xy}$ levels off and decreases slightly as r/r_p decreases.

These stress plots indicate that well within the plastic zone, the singularity of the in-plane stresses is slightly weaker than that of the out-of-plane shear stresses. A comparison of Figs. 4(a) and 4(b) shows that the strengthening of the out-of-plane shear stress and the weakening of the in-plane shear stress as r/r_p decreases are more pronounced for low-hardening materials (with large n).

Figures 4(c) and 4(d) show the normalized stresses $\tilde{\sigma}_{ij}$ at

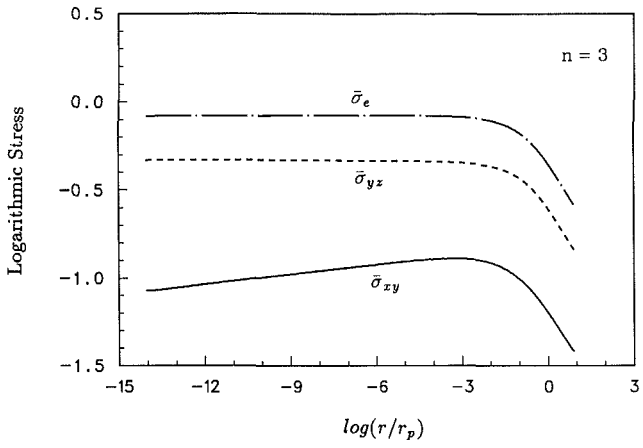


Fig. 5(a)

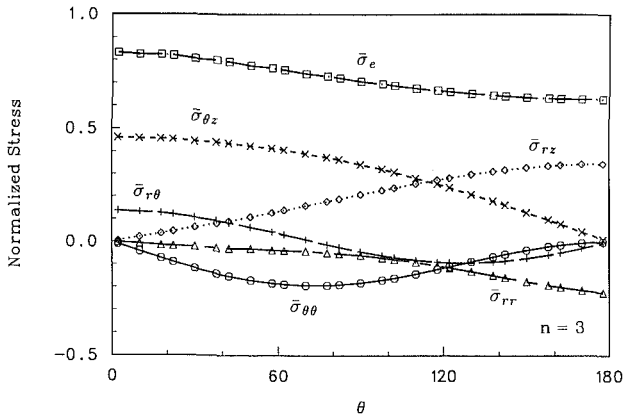


Fig. 5(c)

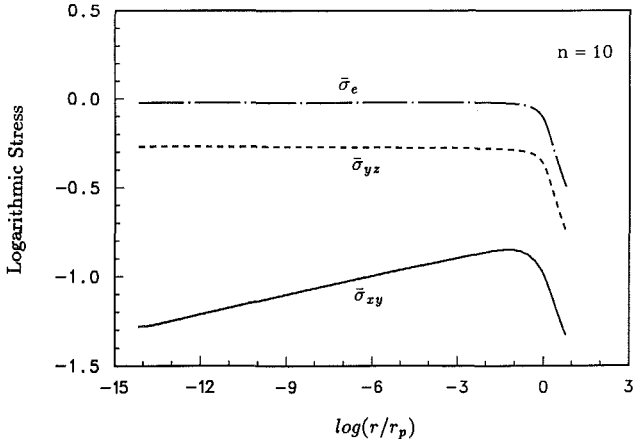


Fig. 5(b)

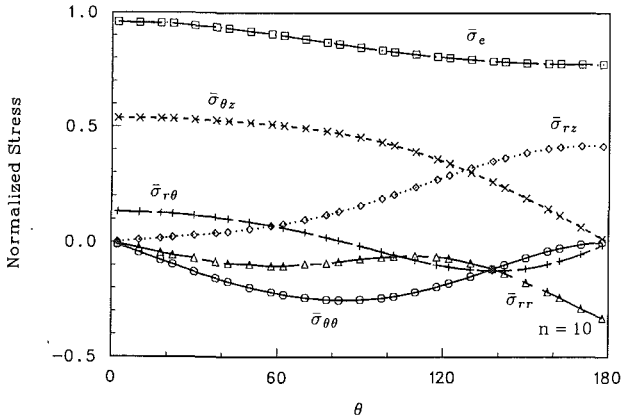


Fig. 5(d)

Fig. 5 Case 4 ($M^e_{23}=0.17$, $K_{II}/K_{III}=0.27$): the normalized stresses $\tilde{\sigma}_{ij}$ at $\theta=10^o$ as functions of r/r_p plotted in a log-log scale for (a) $n=3$ and (b) $n=10$; the normalized stresses $\tilde{\sigma}_{ij}$ at $r/r_p \approx 10^{-3}$ plotted as functions of θ for (c) $n=3$ and (d) $n=10$

Downloaded 03 May 2010 to 171.66.16.244. Redistribution subject to ASME license or copyright; see http://www.asme.org/terms/Terms_Use.cfm

about $r/r_p \approx 10^{-3}$ as functions of θ for $n=3$ and 10, respectively. The angular functions of the out-of-plane shear stresses $\tilde{\sigma}_{rz}$ and $\tilde{\sigma}_{\theta z}$ for $n=3$ and 10 resemble those of the pure mode III case (Figs. 6(*c*) and 6(*d*)). The angular functions of the in-plane stresses shown in Figs. 4(*c*) and 4(*d*) possess some of the characteristics of the perturbed mode II solutions (Pan, 1989).

The elastic mixity factor M^e_{23} is 0.5 ($\sigma_{r\theta}(\theta=0)/\sigma_{\theta z}(\theta=0)=1$). As r/r_p decreases from unity, the plastic mixity factor M^p_{23} increases slightly and then decreases for high-hardening materials, whereas M^p_{23} monotonically decreases for low-hardening materials. At about $r/r_p \approx 10^{-3}$, the plastic mixity factor M^p_{23} is 0.53 for $n=3$ and 0.47 for $n=10$ ($\sigma_{r\theta}(\theta=0)/\sigma_{\theta z}(\theta=0)=1.08$ for $n=3$ and 0.91 for $n=10$). At a very small distance, $r/r_p \approx 10^{-14}$, the plastic mixity factor M^p_{23} decreases to 0.45 for $n=3$ and 0.35 for $n=10$ ($\sigma_{r\theta}(\theta=0)/\sigma_{\theta z}(\theta=0)=0.85$ for $n=3$ and 0.61 for $n=10$). This demonstrates again that the near-tip fields gradually approach the pure mode III field as r/r_p decreases. This effect is more pronounced for low-hardening materials (with large n).

Case 4: $M^e_{23}=0.17$ ($K_{II}/K_{III}=0.27$). Figures 5(*a*) and 5(*b*) show $\tilde{\sigma}_{xy}$, $\tilde{\sigma}_e$, and $\tilde{\sigma}_{yz}$ at $\theta=10^o$ as functions of r/r_p in a log-log scale for $n=3$ and 10, respectively. Within the plastic zone, $\tilde{\sigma}_{yz}$ and $\tilde{\sigma}_e$ level off rather quickly, and the in-plane shear stress $\tilde{\sigma}_{xy}$ levels off and then decreases as r/r_p decreases.

The numerical solutions support the observation made in connection with the preceding cases: Well within the plastic zone the in-plane stresses are less singular than the out-of-plane shear stresses. This tendency is more pronounced for low-hardening materials, as shown in Fig. 5(*b*) for $n=10$. This trend suggests that as $r/r_p \to 0$, the relative contribution of the in-plane shear stresses to the effective stress vanishes, and the out-of-plane shear stresses and $\tilde{\sigma}_e$ must approach the HRR singularity asymptotically. The differences of the singularity of $\tilde{\sigma}_{xy}$ in r from the HRR singularity are estimated from the figures as 0.017 for $n=3$ and 0.035 for $n=10$ averaged over ten decades of r/r_p. For $n=3$, the value agrees with the value of 0.020 from the perturbation analysis of the asymptotic crack-tip fields (Pan, 1989). However, for $n=10$, the value does not match well with the value of 0.088 from Pan (1989).

The results that have been presented show that well within the plastic zone the near-tip plasticity has the effect of decreasing the magnitude of the in-plane stresses and of increasing the magnitude of the out-of-plane shear stresses. This effect is clearly revealed by the curves in Figs. 3–5.

Figures 5(*c*) and 5(*d*) show the normalized stresses $\tilde{\sigma}_{ij}$ at about $r/r_p \approx 10^{-3}$ as functions of θ for $n=3$ and 10, respectively. In these figures, the contribution of the in-plane stresses to the effective stress is small compared to that of the out-of-plane shear stresses. The angular functions of the in-plane stresses, therefore, agree well with the perturbed mode II solutions of Pan (1989). The angular functions of the out-

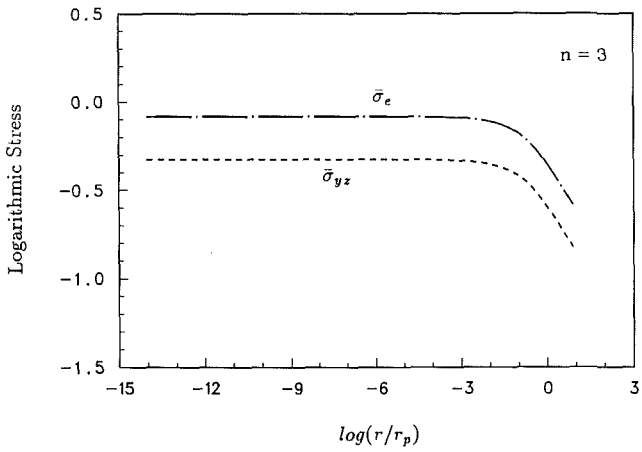


Fig. 6(*a*)

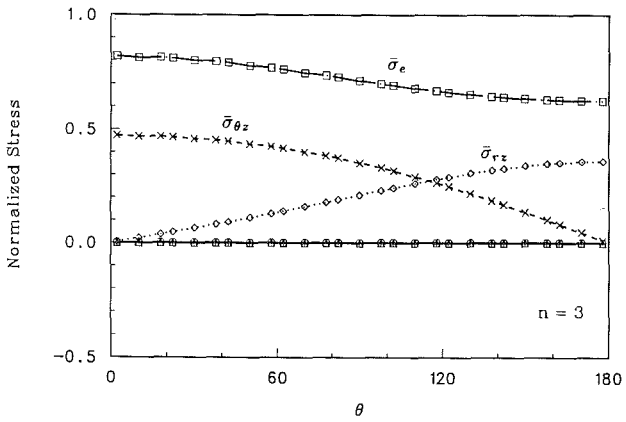


Fig. 6(*c*)

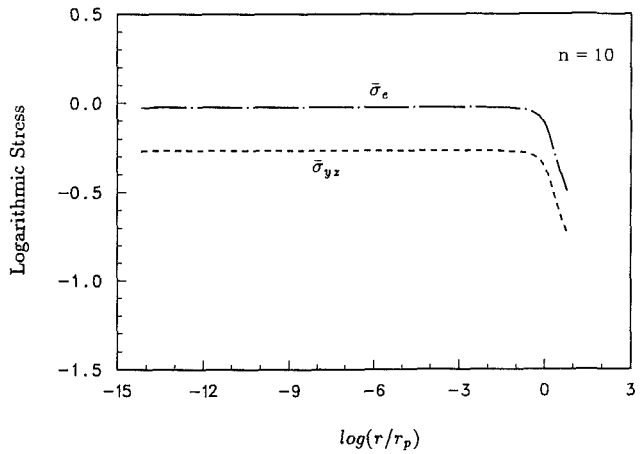


Fig. 6(*b*)

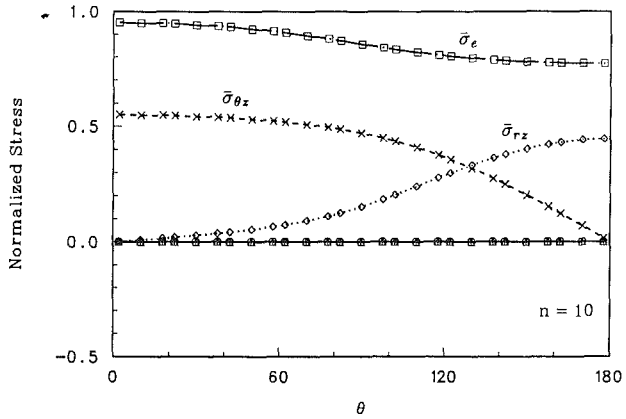


Fig. 6(*d*)

Fig. 6 Case 5 ($M^e_{23}=0$, pure mode III): the normalized stresses $\tilde{\sigma}_{ij}$ at $\theta=10^o$ as functions of r/r_p plotted in a log-log scale for (*a*) $n=3$ and (*b*) $n=10$; the normalized stresses $\tilde{\sigma}_{ij}$ at $r/r_p \approx 10^{-3}$ plotted as functions of θ for (c) $n=3$ and (*d*) $n=10$

Downloaded 03 May 2010 to 171.66.16.244. Redistribution subject to ASME license or copyright; see http://www.asme.org/terms/Terms_Use.cfm

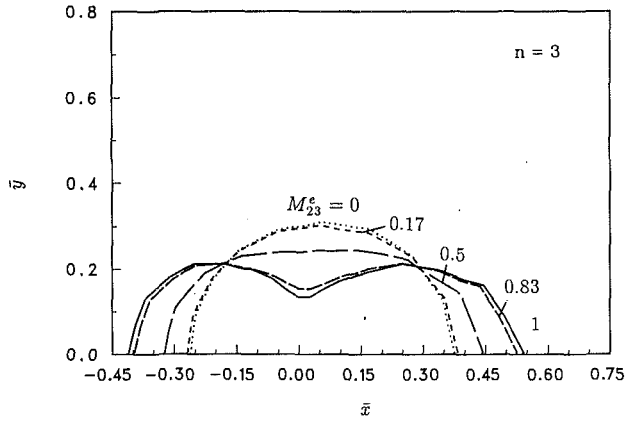


Fig. 7(a)

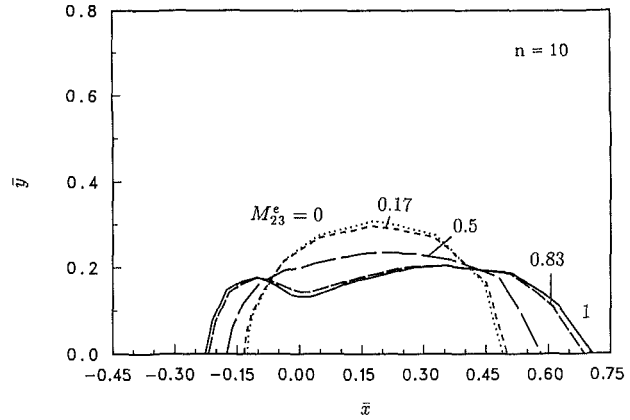


Fig. 7(b)

Fig. 7 The plastic zones for Cases 1-5 plotted in the normalized coordinates $\bar{x}$ ($= x\sigma_o^2/JE$) and $\bar{y}$ ($= y\sigma_o^2/JE$) for (a) $n = 3$ and (b) $n = 10$

of-plane shear stresses $\tilde{\sigma}_{rz}$ and $\tilde{\sigma}_{\theta z}$ resemble those of the pure mode III case (Figs. 6(*c*) and 6(*d*)).

The mixity factor M^e_{23} is about 0.17 ($\sigma_{r\theta}(\theta=0)/\sigma_{\theta z}(\theta=0)=0.27$) at the remote elastic far-field. As in the preceding cases, when r/r_p decreases from unity, the plastic mixity factor M^p_{23} increases slightly and then decreases for high-hardening materials, whereas M^p_{23} monotonically decreases for low-hardening materials. At about $r/r_p \approx 10^{-3}$, the plastic mixity factor M^p_{23} is 0.19 for $n=3$ and 0.16 for $n=10$ ($\sigma_{r\theta}(\theta=0)/\sigma_{\theta z}(\theta=0)=0.30$ for $n=3$ and 0.25 for $n=10$). At a very small distance, $r/r_p \approx 10^{-14}$, the plastic mixity factor M^p_{23} decreases to 0.12 for $n=3$ and 0.06 for $n=10$ ($\sigma_{r\theta}(\theta=0)/\sigma_{\theta z}(\theta=0)=0.19$ for $n=3$ and 0.10 for $n=10$). This demonstrates that the near-tip fields approach the pure mode III field as r/r_p decreases. This effect is more pronounced for low-hardening materials (with large n).

Case 5: $M^e_{23}=0$ (Pure Mode III). Figures 6(*a*) and 6(*b*) show $\tilde{\sigma}_{yz}$ and $\tilde{\sigma}_e$ at $\theta = 10^o$ as functions of r/r_p in a log-log scale for $n=3$ and 10, respectively. Within the plastic zone, the stresses begin to level off at $r/r_p \approx 10^{-2}$ for $n=3$ and at about $r/r_p \approx 10^{-1}$ for $n=10$. In other words, the HRR singularity dominates over these distances. Although we have only plotted the behavior of two representative stresses, the trend of the other shear stress $\tilde{\sigma}_{xz}$ is identical. It may be noted that for low-hardening materials (with large n), the HRR singularity is approached much more rapidly.

Figures 6(*c*) and 6(*d*) show the normalized stresses $\tilde{\sigma}_{ij}$ at about $r/r_p \approx 10^{-3}$ as functions of θ for $n=3$ and $n=10$, respectively. The angular functions of the normalized stresses closely resemble the HRR asymptotic solutions (for example, see the solutions plotted in Pan (1989)). Actually, the numerically-determined stresses reach magnitudes appropriate to the HRR singularity at about $r/r_p \approx 10^{-2}$ for $n=3$ and at about $r/r_p \approx 10^{-1}$ for $n=10$. The solutions for this case demonstrate again the accuracy of our finite element solutions.

Plastic Zones. Figures 7(*a*) and 7(*b*) show the plastic zone size and shape for Cases 1-5 in the normalized coordinates $\bar{x}$ ($= x\sigma_o^2/JE$) and $\bar{y}$ ($= y\sigma_o^2/JE$) for $n=3$ and $n=10$, respectively. The results of the plastic zone sizes and shapes for the pure mode II case ($M^e_{23}=1$) agree with the results of Shih (1973, 1974). The plastic zone sizes and shapes for $M^e_{23}=1$ and 0.83 and for $M^e_{23}=0$ and 0.17 are close to each other. As shown in the figures, when the mode III contribution increases, the plastic zone shape changes. In addition, as the hardening exponent increases, the plastic zone shifts to the front of the tip. This trend agrees well with those of the pure mode II and the pure mode III cases.

6 Conclusions

We have obtained numerical solutions for a crack in a power-law hardening material under small-scale yielding conditions and for a rather complete range of loadings between pure mode II and pure mode III. Our computational results show that deep within the plastic zone, the in-plane stresses are less singular than the out-of-plane shear stresses. The qualitative nature and quantitative results for the angular functions and the deviation of the radial variations of the out-of-plane shear stresses (or the in-plane stresses) from the HRR singularity under predominantly mode II conditions (or predominantly mode III conditions) are in agreement with the results obtained from the perturbation analysis of Pan (1989).

Based on the path-independence of the J integral, Rice and Rosengren (1968) argued that for circular paths centered at the tip, the angular average of the integrand of the J integral, which has order of stress times strain, should vary inversely with r. For single mode problems (either the in-plane modes or the out-of-plane shear mode), since all the stress components have the same singularity as $r\to 0$, the stress components must possess the $r^{-1/(n+1)}$ singularity for power-law materials. However, under combined in-plane and out-of-plane shear mode conditions, since the in-plane stresses and the out-of-plane shear stresses do not have the same singular behavior for ranges of r well within the plastic zone, as revealed by finite element computations of Pan and Shih (1989) and this paper, the argument leading to the HRR singularity by Rice and Rosengren (1968) no longer applies unless the stresses with the weaker singularity become vanishingly small. However, along concentric circular paths, the angular average of the integrand of the J integral still has to vary inversely with r as $r\to 0$. The validity of this argument does not require the out-of-plane shear stresses and the in-plane stresses to exhibit the same dependence on the radial distance r. In fact, the magnitude of the out-of-plane shear stresses increases slightly faster than $r^{-1/(n+1)}$ as $r\to 0$ for $r \ll r_p$, whereas the magnitude of the in-plane stresses increases slightly slower than $r^{-1/(n+1)}$ (see Figs. 3-5).

Within the plastic zone, the plots of the normalized in-plane shear stress or the normalized out-of-plane shear stress as functions of r/r_p in a log-log scale in Figs. 3-5 resemble straight lines when one or the other is more dominant. But when the contributions of the in-plane stresses and the out-of-plane shear stresses to the effective stress are comparable, these lines are curved. In the interval where the in-plane and out-of-plane shear stresses are comparable, the stresses cannot be expressed in separable forms of r and θ, as can those of the HRR fields under either pure in-plane or pure out-of-plane shear loading conditions.

In this paper, we have investigated the stress fields at

Downloaded 03 May 2010 to 171.66.16.244. Redistribution subject to ASME license or copyright; see http://www.asme.org/terms/Terms_Use.cfm

distances ranging from $r/r_p = 1$ to $r/r_p \approx 10^{-14}$. For typical structural steels, finite deformation effects should be taken into consideration at radial distances to the crack tip smaller than $r/r_p \approx 10^{-3}$. As mentioned previously, we investigated fields over distances that are well below those physically relevant in order to study the mathematical structure of the plastic near-tip fields and to reveal any similarities between the combined-mode near-tip fields and those for pure mode II and mode III. Of course, in applying these solutions to fracture analysis under combined-mode loading, fields within such physically irrelevant distances would be disregarded.

Within the small-scale yielding formulation, our numerical solutions suggest that the out-of-plane shear stresses are more singular than the in-plane stresses well within the plastic zone. However, over length scales that are physically relevant, shown in Figs. 3–5, the ratio of the in-plane shear stress to the out-of-plane shear stress ahead of the crack tip remains approximately the same as that predicted by the linear elastic far-fields. We conclude that under combined mode II and III loadings, linear elastic fracture mechanics analysis gives a good estimate of the ratio of the near-tip in-plane shear stress to the out-of-plane shear stress ahead of the crack tip as long as small-scale yielding conditions prevail. This conclusion is in contrast to that of the combined mode I and III case, where the ratio of the near-tip in-plane opening stress to the out-of-plane shear stress ahead of the crack tip increases quite substantially as r/r_p decreases within the plastic zone. Note that the ratio of the in-plane shear stress to the out-of-plane shear stress ahead of the crack tip is a convenient measure of the mode mixity. When we consider the critical conditions for crack growth, mode I types of growth may possibly be more reasonable in light of accumulated experimental observations. Therefore, a combined mode II and III crack may grow in a manner that the crack front may tilt and twist to seek the maximum principal opening stress (for example, see Lawn and Wilshaw (1975)).

Acknowledgment

J. P. acknowledges the support of this work by the National Science Foundation under grant no. MSM-8613544 at The University of Michigan. C. F. S. acknowledges the support of this work by the Material Research Group, funded by the National Science Foundation at Brown University. Helpful discussions on this subject with Prof. J. R. Rice of Harvard University are greatly appreciated.

References

Dong, P., and Pan, J., 1990, "Plane-Strain Mixed-Mode Near-Tip Fields in Elastic Perfectly Plastic Solids under Small-Scale Yielding Conditions," *Int. J. Fract*, in press.

Dong, P., and Pan, J., 1990, "Asymptotic Crack-Tip Fields for Perfectly Plastic Solids under Plane-Stress and Mixed-Mode Loading Conditions," ASME JOURNAL OF APPLIED MECHANICS, in press.

Hughes, T. J. R., 1980, "Generalization of Selective Integration Procedure to Anisotropic and Nonlinear Materials," *International Journal for Numerical Methods in Engineering*, Vol. 9, pp. 187–207.

Hutchinson, J. W., 1968a, "Singular Behavior at the End of a Tensile Crack in a Hardening Material," *J. Mech. Phys. Solids*, Vol. 16, pp. 13–31.

Hutchinson, J. W., 1968b, "Plastic Stress and Strain Fields at a Crack Tip," *J. Mech. Phys. Solids*, Vol. 16, pp. 337–347.

Kanninen, M. F., and Popelar, C. H., 1985, *Advanced Fracture Mechanics*, Oxford University Press, Oxford, U.K.

Lawn, B. R., and Wilshaw, T. R., 1975, *Fracture of Brittle Solids*, Cambridge University Press, Cambridge, U.K.

Li, F. Z., and Pan, J., 1989, "Plane-Stress Crack-Tip Fields for Pressure-Sensitive Dilatant Materials, *Eng. Fract. Mech.*, in press.

Li, F. Z., and Pan, J., 1990, "Plane-Strain Crack-Tip Fields for Pressure-Sensitive Dilatant Materials," ASME JOURNAL OF APPLIED MECHANICS, Vol. 57, pp. XX.

Li, F. Z., Shih, C. F., and Needleman, A., 1985, "A Comparison of Methods for Calculating Energy Release Rates," *Eng. Fract. Mech.*, Vol. 21, pp. 405–421.

Meade, K. P., and Keer, L. M., 1984, "Stress Intensity Factors for Semi-infinite Plane Crack with a Wavy Front," *Journal of Elasticity*, Vol. 14, pp. 79–92.

Moran, B., and Shih, C. F., 1987, "Crack Tip and Associated Domain Integrals from Momentum and Energy Balance," *Eng. Fract. Mech.*, Vol. 27, pp. 615–642.

Nagtegaal, J. C., Parks, D. M., and Rice, J. R., 1974, "On Numerical Accurate Finite Element Solutions in the Fully Plastic Range," *Computer Methods in Applied Mechanics and Engineering*, Vol. 4, pp. 153–178.

Nemat-Nasser, S., and Obata, M., 1984, "On Stress Field Near a Stationary Crack Tip," *Mechanics of Materials*, Vol. 3, pp. 235–243.

Palaniswamy, K., and Knauss, W. G., 1978, "On the Problem of Crack Extension in Brittle Solids under General Loading," *Mechanics Today*, Vol. 4, S. Nemat-Nasser, ed., pp. 87–148.

Pan, J., 1989, "Asymptotic Analysis of a Crack in a Power-Law Material under Combined In-Plane and Out-of-Plane Shear Loading Conditions," *J. Mech. Phys. Solids*, in press.

Pan, J., and Shih, C. F., 1986, "Plane-Strain Crack-Tip Fields for Power-Law Hardening Orthotropic Materials," *Mechanics of Materials*, Vol. 5, pp. 299–316.

Pan, J., and Shih, C. F., 1988, "Plane-Stress Crack-Tip Fields for Power-Law Hardening Orthotropic Materials," *Int. J. Fract.*, Vol. 37, pp. 171–195.

Pan, J., and Shih, C. F., 1989, "Elastic-Plastic Analysis of Combined Mode I and III Crack-Tip Fields under Small-Scale Yielding Conditions," *J. Mech. Phys. Solids*, in press.

Rice, J. R., and Rosengren, G. F., 1968, "Plane Strain Deformation Near a Crack Tip in a Power Law Hardening Material," *J. Mech. Phys. Solids*, Vol. 16, pp. 1–12.

Rice, J. R., 1968a, "A Path Independent Integral and the Approximate Analysis of Strain Concentration by Notches and Cracks," ASME JOURNAL OF APPLIED MECHANICS, Vol. 35, pp. 379–386.

Rice, J. R., 1968b, "Mathematical Analysis in the Mechanics of Fracture," *Fracture*, Vol. 2, H. Liebowitz, ed., Academic Press, New York, pp. 191–311.

Rice, J. R., 1985, "First-Order Variation in Elastic Fields Due to Variation in Location of a Planar Crack Front," ASME JOURNAL OF APPLIED MECHANICS, Vol. 52, pp. 571–579.

Saka, M., Abe, H., and Tanaka, S., 1986, "Numerical Analysis of Blunting of a Crack Tip in a Ductile Material under Small-Scale Yielding and Mixed Mode Loading," *Computational Mechanics*, Vol. 1, pp. 11–19.

Shih, C. F., 1973, "Elastic-Plastic Analysis of Combined Mode Crack Problems," Ph.D. Thesis, Harvard University, Cambridge, Mass.

Shih, C. F., 1974, "Small-Scale Yielding Analysis of Mixed Mode Plane-Strain Crack Problems, *Fracture Analysis*, ASTM STP 560, pp. 187–210.

Shih, C. F., and Needleman, A., 1984, "Fully Plastic Crack Problems, Parts I and II," ASME JOURNAL OF APPLIED MECHANICS, Vol. 51, pp. 48–64.

Shih, C. F., Moran, B., and Nakamura, T., 1986, "Energy Release Rate along a Three-Dimensional Crack Front in a Thermally Stressed Body," *Int. J. Fract.*, Vol. 30, pp. 79–102.

Downloaded 03 May 2010 to 171.66.16.244. Redistribution subject to ASME license or copyright; see http://www.asme.org/terms/Terms_Use.cfm

T. Sakaki
Professor,
Department of Mechanical Engineering,
Faculty of Technology.

K. Sugimoto[1]
Research Associate,
Department of Mechanical Engineering,
Faculty of Technology.

T. Kuroki[2]
Graduate Student.

Tokyo Metropolitan University,
Fukazawa 2-1-1, Setagayu-ku,
Tokyo 158, Japan

Internal Stress Arising From a Spherically Symmetric, Finite Plastic Strain and Yielding of a Hollow Sphere

Internal stress arising from a spherically symmetric, finite plastic strain is obtained on the basis of the Eshelby's theory on inclusions with stress-free strain. Using the internal stress, yielding of a thick-walled hollow sphere is discussed. From the present analysis, distribution of plastic strain in a yield zone and stress distribution are easily obtained, even if a hollow sphere has any type of flow curve. The present analysis is also applicable to forward and reverse loading.

1 Introduction

Yielding of a hollow sphere subjected to inner pressure has been discussed by Hill (1950), where the stress state after partial or general yielding was derived from the yield criterion and the equilibrium of stress. In his analysis, plastic strain was obtained by subtracting the elastic strain derived from actual stress by the Hooke's law from total strain. Thus, the equation representing the yield criterion was somewhat complicated, and it was rather difficult to obtain the plastic strain.

If the internal stress arising from a spherically symmetric plastic strain can be obtained directly from the plastic strain distribution, the analysis of yielding of a hollow sphere will be simplified, and the plastic strain in the yield zone will be more easily obtained. The calculation method of internal stress due to a spherically symmetric plastic strain has been developed to explain the transformation-induced yielding of the ferrite phase around a spherical martensite island in a ferrite-martensite dual-phase steel (Sakaki et al., 1983), where the plastic strain was restricted within an infinitesimal value and the ferrite was assumed to strain harden linearly with plastic strain. By another way, Boyle and Spence (1983) have derived the internal stress arising from a spherically symmetric, small plastic strain.

In the present study, plastic strain is extended to a finite strain, and the internal stress arising from a spherically symmetric, finite plastic strain is obtained. Using the internal stress, yielding of a thick-walled hollow sphere with an arbitrary flow curve is discussed.

2 Internal Stress Arising From a Spherically Symmetric, Finite Plastic Strain

Let us consider an infinite body containing a spherical hollow in it, (see Fig. 1). The body is assumed to be elastically and plastically isotropic. Let us introduce coordinates r and θ, the radial and the tangential directions, respectively, where the origin is located at the center of the spherical hollow. Let stress components be denoted by σ_{rr} and $\sigma_{\theta\theta}$, deviatoric stress components by s_{rr} and $s_{\theta\theta}$, and mean normal stress by σ_m. In the present study, only spherically symmetric problems are dealt with.

2.1 Eigenstrain and Internal Stress. Let the radius of the spherical hollow be a_0 under an initial state free from stress and plastic strain. Let us push a spherical core into the hollow, where the core is assumed to have an infinitesimal isotropic eigenstrain (Mura and Mori, 1976) or stress-free strain (Eshelby, 1957) of e_m^*, i.e., the radius of the core is $(1+e_m^*)a_0$ without constraint by the body. The core is assumed to have the same elastic constants as the body. The stress acting on the core and the body is expressed as follows, if the body does not yield (Eshelby, 1957, 1959; Mura and Mori, 1976).

In the core $(0 \leqq r < a_0)$,

$$s_{rr}^*(r) = s_{\theta\theta}^*(r) = 0 \tag{1}$$

$$\sigma_m^*(r) = \frac{-2E}{3(1-\nu)} e_m^*. \tag{2}$$

In the body $(r > a_0)$,

$$s_{rr}^*(r) = -2s_{\theta\theta}^*(r) = \frac{-2E}{3(1-\nu)} \frac{a_0^3}{r^3} e_m^* \tag{3}$$

[1]Presently, Associate Professor, Department of Functional Machinery and Mechanics, Faculty of Textile Science and Technology, Shinshu University, Tokida 3-15-1, Ueda, Nagano 386, Japan.

[2]Presently at Nippon Steel Corporation, Ltd., Research and Development Laboratory-III, Material Forming Process Research Laboratory, Edamitsu 1-1-1, Yawata-Higashi-ku, Kitakyushu-city, Fukuoka 805, Japan.

Contributed by the Applied Mechanics Division of THE AMERICAN SOCIETY OF MECHANICAL ENGINEERS for publication in the JOURNAL OF APPLIED MECHANICS.

Discussion on this paper should be addressed to the Technical Editor, Leon M. Keer, The Technological Institute, Northwestern University, Evanston, IL 60208, and will be accepted until two months after final publication of the paper itself in the JOURNAL OF APPLIED MECHANICS. Manuscript received by the ASME Applied Mechanics Division, March 18, 1988; final revision, April 10, 1989.

Copyright © 1990 by ASME
Downloaded 03 May 2010 to 171.66.16.244. Redistribution subject to ASME license or copyright; see http://www.asme.org/terms/Terms_Use.cfm

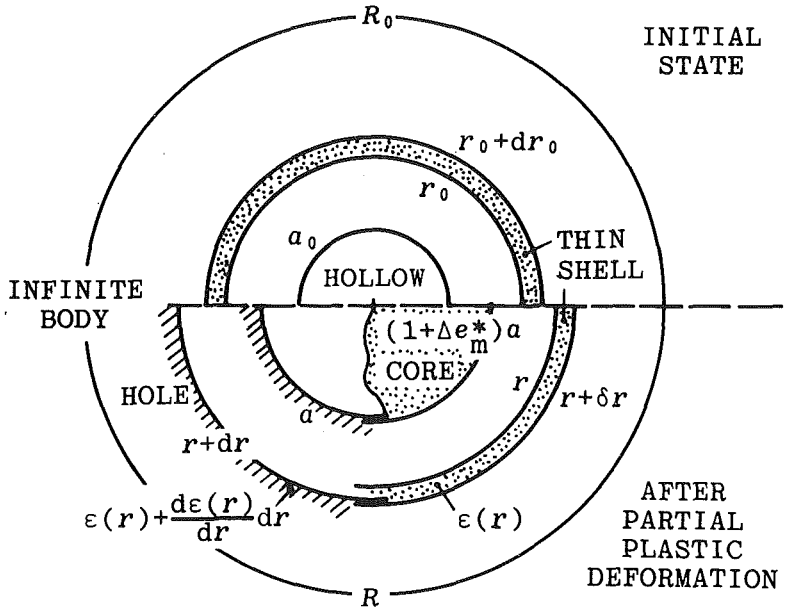


Fig. 1 Misfit between a thin shell and surrounding hole, and misfit between core and hollow

$$\sigma^*_m(r)=0, \tag{4}$$

where E and ν are, respectively, the Young's modulus and Poisson's ratio of the body and the core. Equations (1)–(4) are the basis of the following calculations.

2.2 Plastic Strain and Increment of Misfit Strain. Let us consider a region of $a_0 \leqq r_0 \leqq R_0$ in the initial state which is free from plastic strain and stress. Let us consider a thin shell in this region (Fig. 1), where its inner and outer radii are r_0 and r_0+dr_0, respectively. Let us assume that a spherically symmetric, finite plastic strain has taken place in the previously considered region, and that the radius of the hollow has varied from a_0 to a. The inner and the outer radii of the thin shell are assumed to have varied from r_0 to r and r_0+dr_0 to $r+\delta r$, respectively. a, r, and δr are assumed to be concerned only with the plastic deformation but not with the elastic one. Let the finite plastic strain component in the θ directions be denoted by $\epsilon(r)$, where the coordinate r is that after the plastic deformation. Then, the plastic strain component in the r direction becomes $-2\epsilon(r)$ because of constant volume. In this state, the following relations are obtained:

$$a=e^{\epsilon(a)}a_0,$$

$$r=e^{\epsilon(r)}r_0,$$

$$\delta r=e^{-2\epsilon(r)}dr_0.$$

If the radius of the hole surrounding the thin shell has varied from r_0+dr_0 to $r+dr$ and a plastic strain $\epsilon(r)+\{d\epsilon(r)/dr\}dr$ has taken place, the following relation is obtained:

$$r+dr=(r_0+dr_0)\exp\left\{\epsilon(r)+\frac{d\epsilon(r)}{dr}dr\right\}.$$

Consequently, the thin shell has an increment of isotropic misfit strain, de^*_m, which is

$$de^*_m=\frac{(r+\delta r)-(r+dr)}{r+dr}=\frac{-1}{3r^3}\frac{d}{dr}[r^3\{1-e^{-3\epsilon(r)}\}]dr, \tag{5}$$

where de^*_m is defined based on the plastic strain state of the surrounding hole.

Further, let us push a core with a radius of $(1+\Delta e^*_m)a$ into the hollow with the radius of a after the plastic deformation, where Δe^*_m is an increment of misfit strain. The internal stress due to Δe^*_m and de^*_m can be calculated as will be shown in Appendix A. This calculation is valid for infinitesimal Δe^*_m and de^*_m because of the nature of the Eshelby's theory (Eshelby, 1957, 1959).

2.3 Internal Stress Due to Finite Plastic Strain in an Infinite Body. If an finite plastic strain $\epsilon(r)$ takes place in the yield zone $(a \leqq r \leqq R)$ of an infinite body and the core has a Δe^*_m, the resultant internal stress is expressed as follows using equations (5) and (A9)–(A14).

In the core $(0 \leqq r < a)$,

$$s^*_{rr}(r)=s^*_{\theta\theta}(r)=0 \tag{6}$$

$$\sigma^*_m(r)=\frac{-2E}{3(1-\nu)}\left[\Delta e^*_m+\frac{1-e^{-3\epsilon(a)}}{3}-I(a,R)\right]. \tag{7}$$

In the yield zone $(a<r \leqq R)$,

$$s^*_{rr}(r)=-2s^*_{\theta\theta}(r)$$

$$=\frac{-2E}{3(1-\nu)}\left[\frac{a^3}{r^3}\Delta e^*_m+\frac{a^3}{r^3}\frac{1-e^{-3\epsilon(a)}}{3}-\frac{1-e^{-3\epsilon(r)}}{3}\right] \tag{8}$$

$$\sigma^*_m(r)=\frac{-2E}{3(1-\nu)}\left[\frac{1-e^{-3\epsilon(r)}}{3}-I(r,R)\right]. \tag{9}$$

In the elastic zone $(r \geqq R)$,

$$s^*_{rr}(r)=-2s^*_{\theta\theta}(r)$$

$$=\frac{-2E}{3(1-\nu)}\left[\frac{a^3}{r^3}\Delta e^*_m+\frac{a^3}{r^3}\frac{1-e^{-3\epsilon(a)}}{3}\right] \tag{10}$$

$$\sigma^*_m(r)=0, \tag{11}$$

where

$$I(x,y)\equiv\int_x^y\frac{1-e^{-3\epsilon(r)}}{r}dr. \tag{12}$$

2.4 Internal Stress Due to a Finite Plastic Strain in a Hollow Sphere. Let us consider a hollow sphere in which a finite plastic strain of $\epsilon(r)$ has taken place. The inner and the outer radii of the hollow sphere are a and b, respectively, after

Downloaded 03 May 2010 to 171.66.16.244. Redistribution subject to ASME license or copyright; see http://www.asme.org/terms/Terms_Use.cfm

the plastic deformation. At first, let us consider the finite body dealt with in the previous section. The condition for the outer surface being a free surface is to add an isotropic image stress $\sigma_{m,\text{image}}$ on the hollow sphere and the core, where

$$\sigma_{m,\text{image}} = -\sigma^*_{rr}(b) = -s^*_{rr}(b) - \sigma^*_m(b), \tag{13}$$

where $s^*_{rr}(b)$ and $\sigma^*_m(b)$ are given by (8)-(9) or (10)-(11). Consequently, the isotropic stress in the core is given by the sum of the image stress and σ^*_m given by (7). Thus, the condition for the inner surface being a free surface is expressed as

$$\sigma^*_m(r) + \sigma_{m,\text{image}} = 0, \ (0 \leqq r < a). \tag{14}$$

From equations (7)-(14), Δe^*_m is determined as

$$\Delta e^*_m = -\frac{1-e^{-3\epsilon(a)}}{3} + \frac{b^3}{b^3-a^3} I(a,b), \tag{15}$$

where $I(a,b)$ is replaced by $I(a,R)$ if $R<b$.

As a conclusion, the following formulas for the internal stress are obtained:

(1) In case of partial yielding, $(a \leqq R \leqq b)$.

In the yield zone $(a \leqq r \leqq R)$,

$$s^P_{rr}(r) = -2s^P_{\theta\theta}(r) = \frac{2E}{3(1-\nu)}\left[\frac{1-e^{-3\epsilon(r)}}{3} - \frac{b^3}{b^3-a^3}\frac{a^3}{r^3} I(a,R)\right] \tag{16}$$

$$\sigma^P_m(r) = \frac{-2E}{3(1-\nu)}\left[\frac{1-e^{-3\epsilon(r)}}{3} - \frac{a^3}{b^3-a^3} I(a,R) - I(r,R)\right]. \tag{17}$$

In the elastic zone $(R \leqq r \leqq b)$,

$$s^P_{rr}(r) = -2s^P_{\theta\theta}(r) = \frac{-2E}{3(1-\nu)}\frac{b^3}{b^3-a^3}\frac{a^3}{r^3} I(a,R) \tag{18}$$

$$\sigma^P_m(r) = \frac{2E}{3(1-\nu)}\frac{a^3}{b^3-a^3} I(a,R). \tag{19}$$

(2) After general yielding $(R>b)$,

$$s^P_{rr}(r) = -2s^P_{\theta\theta}(r) = \frac{2E}{3(1-\nu)}\left[\frac{1-e^{-3\epsilon(r)}}{3} - \frac{b^3}{b^3-a^3}\frac{a^3}{r^3} I(a,b)\right] \tag{20}$$

$$\sigma^P_m(r) = \frac{-2E}{3(1-\nu)}\left[\frac{1-e^{-3\epsilon(r)}}{3} - \frac{a^3}{b^3-a^3} I(a,b) - I(r,b)\right]. \tag{21}$$

2.5 Plastic Strain Causing No Internal Stress. There is a spherically symmetric plastic strain $\epsilon_0(r)$ causing no internal stress. The plastic strain is obtained by taking de^*_m given by (5) to be identically zero. If $\epsilon_0(a)$ at the inner surface takes an arbitrary finite value, $\epsilon_0(r)$ is expressed as follows,

$$r^3\{1-e^{-3\epsilon_0(r)}\} = a^3\{1-e^{-3\epsilon_0(a)}\}. \tag{22}$$

or

$$\epsilon_0(r) = -\frac{1}{3}\ln\left[1-\frac{a^3}{r^3}\{1-e^{-3\epsilon_0(a)}\}\right]. \tag{23}$$

Similar expression as (23) has appeared in Hellan's study on spherical void growth assuming incompressibility (Hellan, 1975).

Let us assume that an arbitrary finite plastic strain, $\epsilon(r)$, is composed of a finite plastic strain, $\epsilon_0(r)$, and an infinitesimal plastic strain, $\Delta\epsilon(r)$, causing an internal stress, i.e.,

$$\epsilon(r) = \epsilon_0(r) + \Delta\epsilon(r). \tag{24}$$

The meaning of $\Delta\epsilon(r)$ will be explained in Appendix B. The assumption is convenient to analyze yielding and creeping of a hollow sphere. The internal stress expressed by equations (16)-(21) is rewritten as follows bearing the previous assumption in mind:

(1) In the case of partial yielding, $(a \leqq R \leqq b)$.

In the yield zone $(a \leqq r \leqq R)$,

$$s^P_{rr}(r) = -2s^P_{\theta\theta}(r) = \frac{2E}{3(1-\nu)}\left[\frac{1-e^{-3\epsilon_0(R)}}{3}\frac{b^3-R^3}{b^3-a^3}\frac{a^3}{r^3} + e^{-3\epsilon_0(r)}\Delta\epsilon(r) - \frac{3b^3}{b^3-a^3}\frac{a^3}{r^3}\Delta I(a,R)\right] \tag{25}$$

$$\sigma^P_m(r) = \frac{-2E}{3(1-\nu)}\left[\frac{1-e^{-3\epsilon_0(R)}}{3}\frac{b^3-R^3}{b^3-a^3} + e^{-3\epsilon_0(r)}\Delta\epsilon(r) - \frac{3a^3}{b^3-a^3}\Delta I(a,R) - 3\Delta I(r,R)\right]. \tag{26}$$

In the elastic zone $(R \leqq r \leqq b)$,

$$s^P_{rr}(r) = -2s^P_{\theta\theta}(r) = \frac{-2E}{3(1-\nu)}\left[\frac{1-e^{-3\epsilon_0(R)}}{3}\frac{R^3-a^3}{b^3-a^3}\frac{b^3}{r^3} + \frac{3b^3}{b^3-a^3}\frac{a^3}{r^3}\Delta I(a,R)\right] \tag{27}$$

$$\sigma^P_m(r) = \frac{2E}{3(1-\nu)}\left[\frac{1-e^{-3\epsilon_0(R)}}{3}\frac{R^3-a^3}{b^3-a^3} + \frac{3a^3}{b^3-a^3}\Delta I(a,R)\right] \tag{28}$$

where

$$\Delta I(x,y) \equiv \int_x^y \frac{e^{-3\epsilon_0(r)}\Delta\epsilon(r)}{r} dr. \tag{29}$$

(2) After general yielding $(R>b)$,

$$s^P_{rr}(r) = -2s^P_{\theta\theta}(r) = \frac{2E}{3(1-\nu)}\left[e^{-3\epsilon_0(r)}\Delta\epsilon(r) - \frac{3b^3}{b^3-a^3}\frac{a^3}{r^3}\Delta I(a,b)\right] \tag{30}$$

$$\sigma^P_m(r) = \frac{-2E}{3(1-\nu)}\left[e^{-3\epsilon_0(r)}\Delta\epsilon(r) - \frac{3a^3}{b^3-a^3}\Delta I(a,b) - 3\Delta I(r,b)\right]. \tag{31}$$

If $e^{-3\epsilon_0(r)}\Delta\epsilon(r)$ is inversely proportional to r^3 in the range of $a \leqq r \leqq b$, $\Delta\epsilon(r)$ does not cause any internal stress.

The internal stress due to the plastic strain $\epsilon(r)$ tends to restore the $\epsilon(r)$, but it tends to plastically deform the other parts in the same mode as at $r=r$.

2.6 Internal Stress Due to an Infinitesimal Plastic Strain. If a plastic strain $\epsilon(r)$ is infinitesimal,

$$1-e^{-3\epsilon(r)} \fallingdotseq 3\epsilon(r). \tag{32}$$

Thus, equations (16)-(21) are reduced to

Downloaded 03 May 2010 to 171.66.16.244. Redistribution subject to ASME license or copyright; see http://www.asme.org/terms/Terms_Use.cfm

$$s_{rr}^P(r) = -2s_{\theta\theta}^P(r)$$

$$= \frac{2E}{3(1-\nu)}\left[\epsilon(r) - \frac{3b^3}{b^3-a^3}\frac{a^3}{r^3}\int_a^b \frac{\epsilon(r)}{r}dr\right] \tag{33}$$

$$\sigma_m^P(r) = \frac{-2E}{3(1-\nu)}\left[\epsilon(r) - \frac{3a^3}{b^3-a^3}\int_a^b \frac{\epsilon(r)}{r}dr - 3\int_r^b \frac{\epsilon(r)}{r}dr\right]. \tag{34}$$

If $a \leqq R \leqq b$, $\epsilon(r)$ is taken to be zero in the range of $R \leqq r \leqq b$. Equations (33) and (34) are identical with the solution for the residual stress derived by Boyle and Spence (1983).

An infinitesimal plastic strain, $\epsilon_0(r)$, causing no internal stress is expressed as a function of $\epsilon_0(a)$ as,

$$\epsilon_0(r) = (a^3/r^3)\epsilon_0(a). \tag{35}$$

When an infinitesimal plastic strain, $\epsilon(r)$, is divided into $\epsilon_0(r)$ and an infinitesimal $\Delta\epsilon(r)$ causing an internal stress, $\epsilon(r)$ in (33) and (34) may be replaced by $\Delta\epsilon(r)$ in a case of general yielding. If an elastic zone is involved, $\Delta\epsilon(r)$ is taken to be $-\epsilon_0(r)$ to make $\epsilon(r) = 0$ in the elastic zone.

2.7 Presence of Some Isolated Yield Zones. Cowper (1960) and Johnson and Mellor (1962) have analyzed the elastic-plastic behavior of a thick-walled hollow sphere subjected to a thermal stress due to radial steady heat flow, and pointed out as follows. If the temperature gradient is increased sufficiently, a second yield zone appears around the outer surface or in an intermediate region in addition to the first yield zone around the inner surface. In such a case or, more generally, if a hollow sphere consists of isolated yield zones and isolated elastic zones, the internal stress is given by (20), (21), and (12) or (33) and (34) by putting $\epsilon(r) = 0$ in the elastic zones, or given by (30), (31), and (29) by taking $\Delta\epsilon(r) = -\epsilon_0(r)$ in the elastic zones.

3 Yielding of a Hollow Sphere

When a hollow sphere is subjected to inner and outer pressures of P_a and P_b, respectively, the applied stress is expressed as follows (Timoshenko and Goodier, 1951):

$$s_{rr}^A(r) = -2s_{\theta\theta}^A(r) = -\frac{b^3}{b^3-a^3}\frac{a^3}{r^3}(P_a - P_b) \tag{36}$$

$$\sigma_m^A(r) = \frac{a^3}{b^3-a^3}(P_a - P_b) - P_b. \tag{37}$$

Let us deal with the following two cases in a lump.

(1) The hollow sphere expands gradually under a condition of $P_a - P_b > 0$ and $\epsilon(r) \geqq 0$. Let us define a variable k as $+1$.

(2) The hollow sphere shrinks continually since $P_a - P_b < 0$, where $\epsilon(r) \leqq 0$ and k is taken to be -1.

Let us assume that a part or the whole of the hollow sphere has yielded and a finite plastic strain has taken place. In this state, the total stress becomes the sum of the applied stress and the internal stress given by equations (16)–(21) or (25)–(31). Let us define a stress, $\sigma(r)$, as

$$\sigma(r) = s_{\theta\theta}^A(r) - s_{rr}^A(r) + s_{\theta\theta}^P(r) - s_{rr}^P(r). \tag{38}$$

Then, the Mises' equivalent stress is expressed by $k\sigma(r)$. In the present spherically symmetric problem, the equivalent plastic strain $\bar{\epsilon}(r)$ is given by the following equation using the plastic strain component in the tangential directions,

$$\bar{\epsilon}(r) = 2k\epsilon(r) = 2k\{\epsilon_0(r) + \Delta\epsilon(r)\}. \tag{39}$$

3.1 Partial Yielding. If flow stress is denoted by $S(\bar{\epsilon})$ and the strain-hardening rate by $H(\bar{\epsilon})$ in uniaxial tension, the yield criterion in the yield zone of $a \leqq r \leqq R$ $(R \leqq b)$ is represented as follows using equations (16), (25), (36), and (38).

$$\sigma(r) = \frac{3}{2}\frac{b^3}{b^3-a^3}\frac{a^3}{r^3}(P_a - P_b)$$

$$-\frac{E}{1-\nu}\left[\frac{1-e^{-3\epsilon(r)}}{3} - \frac{b^3}{b^3-a^3}\frac{a^3}{r^3}I(a,R)\right]$$

$$= kS\{2k\epsilon(r)\}, \qquad (a \leqq r \leqq R) \tag{40}$$

or

$$\sigma(r) = \frac{3}{2}\frac{b^3}{b^3-a^3}\frac{a^3}{r^3}(P_a - P_b)$$

$$-\frac{E}{1-\nu}\left[\frac{1-e^{-3\epsilon_0(R)}}{3}\frac{b^3-R^3}{b^3-a^3}\frac{a^3}{r^3}\right.$$

$$\left. + e^{-3\epsilon_0(r)}\Delta\epsilon(r) - \frac{3b^3}{b^3-a^3}\frac{a^3}{r^3}\Delta I(a,R)\right]$$

$$= kS\{2k\epsilon_0(r)\} + 2H\{2k\epsilon_0(r)\}k\Delta\epsilon(r), \quad (a \leqq r \leqq R). \tag{41}$$

Let us assume here that

$$\Delta\epsilon(a) = \epsilon(a) - \epsilon_0(a) = 0 \tag{42}$$

as a matter of convenience in calculation. This assumption is reasonable since specifying the value of $\Delta\epsilon(a)$ to a certain value means that some small part of $\epsilon_0(r)$ belongs to $\Delta\epsilon(r)$ or to $\epsilon_0(r)$ itself (Sakaki et al., 1990).

From three equations (40) at $r = R$, $r = r$, and $r = a$, the following two relations are obtained in the yield zone:

$$\frac{R^3}{a^3} = \left[\frac{E}{1-\nu}\frac{1-e^{-3\epsilon(a)}}{3} + kS\{2k\epsilon(a)\}\right] \Big/ kS(0), \tag{43}$$

and

$$r^3\left[\frac{1-e^{-3\epsilon(r)}}{3} + \frac{1-\nu}{E}kS\{2k\epsilon(r)\}\right]$$

$$= a^3\left[\frac{1-e^{-3\epsilon(a)}}{3} + \frac{1-\nu}{E}kS\{2k\epsilon(a)\}\right] = R^3\frac{1-\nu}{E}kS(0) \tag{44}$$

where $S(0)$ is the yield stress. From equation (43), the radius of yield zone R is specified as a function of $\epsilon(a)$. If $a \leqq R \leqq b$ (partial yielding), R represents the actual radius of yield zone. If $R > b$ (general yielding), R becomes a hypothetical radius. The plastic strain $\epsilon(r)$ is obtained as a function of $\epsilon(a)$ or R by solving equation (44) numerically.

The plastic strain is obtained in another way. Using two equations (41) at $r = a$ and $r = r$ and equation (42), $\Delta\epsilon(r)$ is obtained as

$$\left.\begin{aligned} \Delta\epsilon(r) &= \frac{kS\{2k\epsilon_0(a)\}(a^3/r^3) - kS\{2k\epsilon_0(r)\}}{(E/(1-\nu))e^{-3\epsilon_0(r)} + 2kH\{2k\epsilon_0(r)\}}, && (a \leqq r \leqq R) \\ \Delta\epsilon(r) &= -\epsilon_0(r), && (R \leqq r \leqq b) \end{aligned}\right\} \tag{45}$$

where $\epsilon_0(r)$ is given by (23). The $\Delta\epsilon(r)$ satisfies the two conditions that $\Delta\epsilon(a) = 0$ and $\epsilon(R) = \epsilon_0(R) + \Delta\epsilon(R) = 0$.

In Section 2.5, $\Delta\epsilon(r)$ has been assumed to be infinitesimal.

On expanding a hollow sphere, $\Delta\epsilon(r)$ depends significantly on $\epsilon_0(a)$ and the strain-hardening rate compared with the yield stress. If $\epsilon_0(a) \leqq 1.5$ and $H/E \leqq 2.5 \times 10^{-3}$, $|\Delta\epsilon(r)|$ is less than 0.03. If the value of $\epsilon_0(a)$ exceeds 1.5, however, a steep gradient of plastic strain occurs around the inner surface. Further, if H/E is larger than 2.5×10^{-3}, a steep gra-

Downloaded 03 May 2010 to 171.66.16.244. Redistribution subject to ASME license or copyright; see http://www.asme.org/terms/Terms_Use.cfm

dient of internal stress is required. In such a case, $\Delta\epsilon(r)$ cannot be treated as infinitesimal, thus equation (44) must be solved numerically. On the other hand, on shrinking a hollow sphere, a steep gradient of plastic strain does not occur, thus $\Delta\epsilon(r)$ is always kept within an infinitesimal value.

The pressure difference corresponding to R or $\epsilon_0(a)$ is obtained by the following manner. Using $\sigma(r)$ given by equation (40), one relation is obtained through the following integration:

$$\int_a^R \frac{\sigma(r)}{r}dr. \tag{46}$$

This integration corresponds to solving the equation of equilibrium of stress in usual analysis. Using the integration and equation (40) at $r=a$, $I(a,R)$ in both the relations can be eliminated, and P_a-P_b is expressed as a function of R and the yield and flow stresses, i.e.,

$$k(P_a-P_b)=\frac{2}{3}\frac{b^3-R^3}{b^3}S(0)+2\int_a^R \frac{S\{2k\epsilon(r)\}}{r}dr. \tag{47}$$

This relation is identical to the Hill's solution (Hill, 1950) if the Poisson's ratio is taken to be 1/2 in his theory.

When the hollow sphere has partially yielded in the range of $a\leqq r\leqq R$, the total stress on the hollow sphere becomes the sum of the applied stress in equations (36)–(37) and the internal stress in equations (16)–(19) or (25)–(28), and is given as follows.

In the yield zone $(a\leqq r\leqq R)$,

$$s_{rr}(r)=-2s_{\theta\theta}(r)=-\frac{2}{3}kS\{2k\epsilon(r)\} \tag{48}$$

$$\sigma_m(r)=-\frac{2}{3}\frac{b^3-R^3}{b^3}kS(0)+\frac{2}{3}kS\{2k\epsilon(r)\}-2k\int_r^R \frac{S\{2k\epsilon(r)\}}{r}dr-P_b. \tag{49}$$

In the elastic zone $(R\leqq r\leqq b)$,

$$s_{rr}(r)=-2s_{\theta\theta}(r)=-\frac{2}{3}\frac{R^3}{r^3}kS(0) \tag{50}$$

$$\sigma_m(r)=\frac{2}{3}\frac{R^3}{b^3}kS(0)-P_b. \tag{51}$$

The internal stress due to $\epsilon(r)$ or $\Delta\epsilon(r)$ is given by subtracting the applied stress from the total stress. The internal stress becomes the residual stress if additional plastic deformation has not occurred during unloading.

3.2 After General Yielding. After general yielding of the hollow sphere $(R\geqq b)$, $\epsilon(r)$ and $\Delta\epsilon(r)$ for a specified $\epsilon(a)$ $(=\epsilon_0(a))$ are still given by (44) and (45), respectively. The pressure difference and the total stress corresponding to $\epsilon(a)$ are obtained from (47)–(49) by replacing R by b.

3.3 Discussion. In the foregoing calculations elastic strain has not appeared, since the internal stress is directly obtained from a plastic strain. This is one of the advantages of the Eshelby's theory. If elastic strain is needed, it will be easily obtained from stress and the Hooke's law. Hill (1950) has analyzed yielding of a thick-walled hollow sphere. In his analysis, elastic strain is related to stress by the Hooke's law and equivalent stress is to plastic equivalent strain by the Mises' yield criterion. Therefore, the internal stress due to plastic strain distribution is taken into account, and the same plastic strain as that obtained in the present study will be obtained in his analysis. But, as elastic strain is included in equations, it is difficult to obtain plastic strain. If yielding of a hollow sphere is analyzed, assuming rigid plastic material and excluding small plastic strain causing internal stress, plastic strain deviates from that obtained in the present study only by a small amount, which is influenced by $(1-\nu)S/\mathrm{E}$ in equation (44) or by $\Delta\epsilon(r)$ in (45).

4 Special Case

Let us consider a special case where plastic strain is restricted within a small one and a hollow sphere strain hardens linearly with respect to the plastic strain. Let the yield stress and the strain-hardening rate be denoted by Y_0 and H_0, respectively. The results are obtained as follows in the same manner as described in Section 3 using equations (33) and (34) (Sakaki, 1984).

The pressure difference is related to R as,

$$k(P_a-P_b)=\frac{2}{3}Y_0\left[h\left\{1+\frac{2(1-\nu)H_0}{E}\frac{R^3}{a^3}+\ln\frac{R^3}{a^3}\right\}-\frac{R^3}{b^3}\right] \tag{52}$$

where

$$h=1/\{1+2(1-\nu)H_0/\mathrm{E}\}\fallingdotseq 1. \tag{53}$$

The approximation is true for usual values of H_0 and E. The relations between R, $\epsilon(a)$, and $\epsilon(r)$ are as follows in the range of $a\leqq r\leqq R$:

$$\epsilon(a)=\frac{k(1-\nu)Y_0h}{\mathrm{E}}\left(\frac{R^3}{a^3}-1\right) \tag{54}$$

$$\epsilon(r)=\frac{k(1-\nu)Y_0h}{\mathrm{E}}\left(\frac{R^3}{r^3}-1\right)=\epsilon(a)\frac{a^3}{r^3}-\frac{k(1-\nu)Y_0h}{\mathrm{E}}\left(1-\frac{a^3}{r^3}\right). \tag{55}$$

Equations (52), (54), and (55) are valid for R smaller and also larger than b. If $R\leqq b$, R is an actual radius of the yield zone, but if $R\geqq b$, R becomes a hypothetical radius. From equation (55), it is found that the plastic strain causing the internal stress takes a constant value of $-k(1-\nu)Y_0h/\mathrm{E}$.

P_a-P_b for the inner surface yielding is obtained from (52) as,

$$k(P_a-P_b)=\frac{2}{3}Y_0\left(1-\frac{a^3}{b^3}\right). \tag{56}$$

This relation is well known (Hill, 1950).

If the hollow sphere has partially yielded $(a\leqq R\leqq b)$, the stress on it is as follows.

In the yield zone $(a\leqq r\leqq R)$,

$$s_{rr}(r)=-2s_{\theta\theta}(r)=-\frac{2}{3}k\{Y_0+2H_0k\epsilon(r)\} \tag{57}$$

$$\sigma_m(r)=-\frac{2}{3}kY_0\left[h\ln\frac{R^3}{r^3}-\frac{R^3}{b^3}\right]-P_b. \tag{58}$$

In the elastic zone $(R\leqq r\leqq b)$,

$$s_{rr}(r)=-2s_{\theta\theta}(r)=-\frac{2}{3}kY_0\frac{R^3}{r^3} \tag{59}$$

$$\sigma_m(r)=\frac{2}{3}kY_0\frac{R^3}{b^3}-P_b. \tag{60}$$

Downloaded 03 May 2010 to 171.66.16.244. Redistribution subject to ASME license or copyright; see http://www.asme.org/terms/Terms_Use.cfm

At yielding of the outer surface, the pressure difference and the plastic strain at the inner surface are given as follows using (52) and (54):

$$k(P_a^*-P_b^*)=\frac{2}{3}Y_0\left[h\left\{1+\frac{2(1-\nu)H_0}{\mathrm{E}}\frac{b^3}{a^3}+\ln\frac{b^3}{a^3}\right\}-1\right] \tag{61}$$

$$\epsilon^*(a)=\frac{k(1-\nu)Y_0h}{\mathrm{E}}\left(\frac{b^3}{a^3}-1\right). \tag{62}$$

After general yield, P_a-P_b is conveniently related to $\epsilon(a)$ as,

$$k(P_a-P_b)=k(P_a^*-P_b^*)+\frac{4}{3}kH_0\{\epsilon(a)-\epsilon^*(a)\}\left(1-\frac{a^3}{b^3}\right). \tag{63}$$

The total stress on the hollow sphere is

$$s_{rr}(r)=-2s_{\theta\theta}(r)=-\frac{2}{3}k\{Y_0+2H_0k\epsilon(r)\} \tag{64}$$

$$\sigma_m(r)=\frac{2}{3}k\{Y_0+2H_0k\epsilon(b)\}-\frac{2}{3}kY_0h\frac{b^3}{r^3}-P_b. \tag{65}$$

5 Expanding and Subsequent Shrinking

In this section expanding of a hollow sphere by inner pressure, and subsequent shrinking by outer pressure, is discussed.

5.1 Expanding by Inner Pressure. A hollow sphere is assumed to have been partially or generally yielded by an inner pressure, P_a, and the initial inner, outer, and an arbitral radii a_0, b_0, and r_0 have varied to a_1, b_1, and r_1, respectively, by yielding. Let the plastic strain in the θ directions be denoted as

$$\epsilon_1(r_1)=\ln(r_1/r_0), \tag{66}$$

where, if $\epsilon_1(r_1)=0$, $r_1=r_0$. Since $2\epsilon_1(r_1)$ corresponds to a uniaxial strain, let flow stress be represented by $S_1\{2\epsilon_1(r_1)\}$ ($\geqq 0$) (Fig. 2). Then, the following condition is satisfied:

$$\sigma(r_1)=\frac{3}{2}\frac{b_1^3}{b_1^3-a_1^3}\frac{a_1^3}{r_1^3}P_a-\frac{\mathrm{E}}{1-\nu}\left[\frac{1-e^{-3\epsilon_1(r_1)}}{3}-\frac{b_1^3}{b_1^3-a_1^3}\frac{a_1^3}{r_1^3}I_1(a_1,b_1)\right]$$

$$=\begin{cases}S_1\{2\epsilon_1(r_1)\}, & (a_1\leqq r_1\leqq R_1,\ \text{yield zone}) \quad (67a)\\ (R_1^3/r_1^3)S_1(0), & (R_1\leqq r_1\leqq b_1,\ \text{elastic zone}), \quad (67b)\end{cases}$$

where $I_1(a_1,b_1)$ is the integral (12) with respect to $\epsilon_1(r_1)$.

Then, in view of (43) and (44), the following relation in the yield zone is obtained:

$$a_1^3\left[\frac{1-e^{-3\epsilon_1(a_1)}}{3}+\frac{1-\nu}{\mathrm{E}}S_1\{2\epsilon_1(a_1)\}\right]=r_1^3\left[\frac{1-e^{-3\epsilon_1(r_1)}}{3}+\frac{1-\nu}{\mathrm{E}}S_1\{2\epsilon_1(r_1)\}\right]$$

$$=R_1^3\frac{1-\nu}{\mathrm{E}}S_1(0), \quad (a_1\leqq r_1\leqq R_1). \tag{68}$$

In the elastic zone of $R_1\leqq r_1\leqq b_1$, $\epsilon_1(r_1)=0$ and $r_1=r_0$.

In the inner pressure, P_a, corresponding to the condition of (67a,b) is obtained as

$$P_a=\frac{2}{3}\frac{b_1^3-R_1^3}{b_1^3}S_1(0)+2\int_{a_1}^{R_1}\frac{S_1\{2\epsilon_1(r_1)\}}{r_1}dr_1. \tag{69}$$

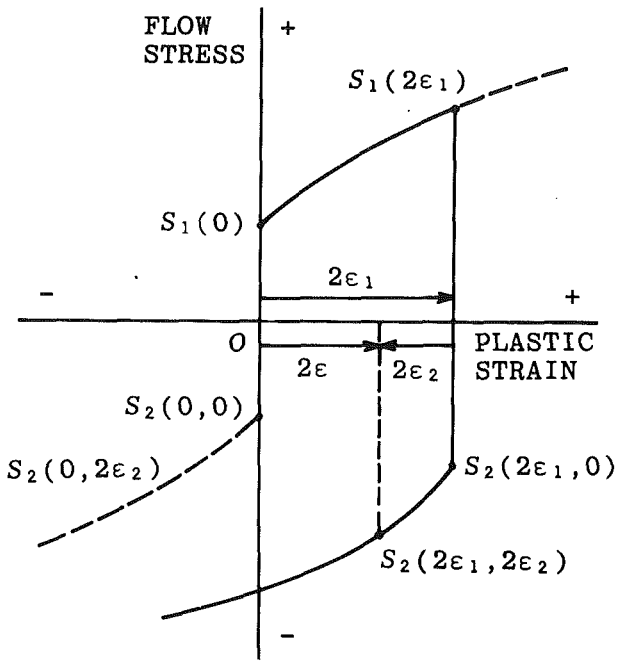


Fig. 2 Stress-strain curve

If, in general yielding ($R_1\geqq b_1$), R_1 in (69) must be replaced by b_1.

5.2 Shrinking by Outer Pressure. When unloading the inner pressure and then applying an outer pressure, let the hollow sphere deform in the inverse direction. In the inverse deformation usually the Bauschinger effect due to metallurgical factors occurs, and the reyield stress becomes a function of previous plastic strain of $\epsilon_1(r_1)$. Thus, let the reyield stress be represented by $S_2\{2\epsilon_1(r_1),0\}$ (including its sign, Fig. 2). If $\epsilon_1(r_1)=0$, $S_2(0,0)=-S_1(0)$.

Then, let us seek the place where the reyield takes place at first. The criterion of reyielding under an outer pressure P_b and the internal stress due to $\epsilon_1(r_1)$ is as follows:

$$\sigma(r_1)=-\frac{3}{2}\frac{b_1^3}{b_1^3-a_1^3}\frac{a_1^3}{r_1^3}P_b-\frac{E}{1-\nu}\left[\frac{1-e^{-3\epsilon_1(r_1)}}{3}-\frac{b_1^3}{b_1^3-a_1^3}\frac{a_1^3}{r_1^3}I_1(a_1,b_1)\right]$$

$$=S_2\{2\epsilon_1(r_1),0\}, \quad (\text{in } a_1\leqq r_1\leqq b_1). \tag{70}$$

After eliminating the terms of internal stress from (67a) or (67b) and (70), P_b is obtained as

$$P_b=-P_a+\frac{2}{3}\frac{b_1^3-a_1^3}{b_1^3}\frac{r_1^3}{a_1^3}[S_1\{2\epsilon_1(r_1)\}-S_2\{2\epsilon_1(r_1),0\}] \quad (\text{in } a_1\leqq r_1\leqq R_1) \tag{71a}$$

$$P_b=-P_a+\frac{2}{3}\frac{b_1^3-a_1^3}{b_1^3}\frac{R_1^3+r_1^3}{a_1^3}S_1(0), \quad (\text{in } R_1\leqq r_1\leqq b_1). \tag{71b}$$

If the hollow sphere has generally yielded ($R_1\geqq b_1$), only (71a) is employed. On increasing the outer pressure P_b from zero, reyield onsets at the place where P_b is minimum in (71a,b). The place is represented by r_1^*, and the minimum P_b by P_b^*. If $P_b^*<0$, it means that reyield onsets during unloading at the first inner pressure. When P_b exceeds P_b^*, reyield in the inverse direction takes place, and radii a_1, r_1, and b_1 vary to a_2, r_2, and b_2, respectively. Let us represent the plastic strain oc-

Downloaded 03 May 2010 to 171.66.16.244. Redistribution subject to ASME license or copyright; see http://www.asme.org/terms/Terms_Use.cfm

curred in the inverse direction by $\epsilon_2(r_2)$, and the entire plastic strain by $\epsilon(r_2)$, i.e.,

$$\epsilon_2(r_2)=\ln(r_2/r_1) \tag{72}$$

$$\epsilon(r_2)=\ln(r_2/r_0)=\epsilon_1(r_1)+\epsilon_2(r_2). \tag{73}$$

If $\epsilon_2(r_2)=0$, $r_2=r_1$.

Since flow stress S_2 in the reverse direction becomes a function of $\epsilon_1(r_1)$ and $\epsilon_2(r_2)$, the flow stress is denoted by $S_2\{2\epsilon_1(r_1),2\epsilon_2(r_2)\}$ including its sign (Fig. 2). If $\epsilon_1(r_1)=0$, S_2 is assumed to be

$$S_2\{0,2\epsilon_2(r_2)\}=-S_1\{-2\epsilon_2(r_2)\}. \tag{74}$$

Let us assume that reyielding onsets at an intermediate radius r_1^* ($a_1\leqq r_1^*\leqq b_1$), and a reyield zone spreads over a range of $R_2^*\leqq r_2\leqq R_2^{**}$ where R_2^* and R_2^{**} are inner and outer boundaries of the reyield zone, respectively. The criterion of reyielding is expressed as

$$\sigma(r_2)=-\frac{3}{2}\frac{b_2^3}{b_2^3-a_2^3}\frac{a_2^3}{r_2^3}P_b$$
$$-\frac{E}{1-\nu}\left[\frac{1-e^{-3\epsilon_1(r_1)-3\epsilon_2(r_2)}}{3}-\frac{b_2^3}{b_2^3-a_2^3}\frac{a_2^3}{r_2^3}I_2(a_2,b_2)\right]$$
$$=S_2\{2\epsilon_1(r_1),2\epsilon_2(r_2)\},\quad (R_2^*\leqq r_2\leqq R_2^{**}), \tag{75}$$

where

$$I_2(a_2,b_2)\equiv\int_{a_2}^{b_2}\frac{1-e^{-3\epsilon_1(r_1)-3\epsilon_2(r_2)}}{r_2}dr_2. \tag{76}$$

As a result, the boundary radii R_2^* and R_2^{**} and the plastic strain in the reyield zone are related to each other as follows:

$$R_2^{*3}\left[\frac{1-e^{-3\epsilon_1(R_2^*)}}{3}+\frac{1-\nu}{E}S_2\{2\epsilon_1(R_2^*),0\}\right]$$
$$=r_2^3\left[\frac{1-e^{-3\epsilon_1(r_1)-3\epsilon_2(r_2)}}{3}+\frac{1-\nu}{E}S_2\{2\epsilon_1(r_1),2\epsilon_2(r_2)\}\right]$$
$$=R_2^{**3}\left[\frac{1-e^{-3\epsilon_1(R_2^{**})}}{3}+\frac{1-\nu}{E}S_2\{2\epsilon_1(R_2^{**}),0\}\right]. \tag{77}$$

If R_2^{**} (or R_2^*) is specified to a value, the corresponding R_2^* (or R_2^{**}) and $\epsilon_2(r_2)$ in the reyield zone are obtained from (77). The corresponding outer pressure is as follows:

$$P_b=\frac{2}{3}\frac{R_2^{*3}-a_2^3}{a_2^3}\left[\frac{E}{1-\nu}\frac{1-e^{-3\epsilon_1(R_2^*)}}{3}+S_2\{2\epsilon_1(R_2^*),0\}\right]$$
$$-\frac{2}{3}\frac{E}{1-\nu}\int_{a_2}^{R_2^*}\frac{1-e^{-3\epsilon_1(r_2)}}{r_2}dr_2+\int_{R_2^*}^{R_2^{**}}\frac{S_2\{2\epsilon_1(r_1),2\epsilon_2(r_2)\}}{r_2}dr_2$$
$$+\frac{2}{3}\frac{b_2^3-R_2^{**3}}{b_2^3}\left[\frac{E}{1-\nu}\frac{1-e^{-3\epsilon_1(R_2^{**})}}{3}+S_2\{2\epsilon_1(R_2^{**}),0\}\right]$$
$$-\frac{2}{3}\frac{E}{1-\nu}\int_{R_2^{**}}^{b_2}\frac{1-e^{-3\epsilon_1(r_2)}}{r_2}dr_2. \tag{78}$$

If $R_2^*\leqq a_2$, or if reyielding onsets at the inner surface ($r_1^*=a_1$), the first side in (77) is replaced by

$$a_2^3\left[\frac{1-e^{-3\epsilon_1(a_1)-3\epsilon_2(a_2)}}{3}+\frac{1-\nu}{E}S_2\{2\epsilon_1(a_1),2\epsilon_2(a_2)\}\right],$$

and also R_2^* in (78) is taken to be a_2.

If $R_2^{**}\geqq b_2$, the third side in (77) is replaced by

$$b_2^3\left[\frac{1-e^{-3\epsilon_1(b_1)-3\epsilon_2(b_2)}}{3}+\frac{1-\nu}{E}S_2\{2\epsilon_1(b_1),2\epsilon_2(b_2)\}\right],$$

and also R_2^{**} in (78) is taken to be b_2.

For a case where two or more isolated reyield zones takes place, similar analysis is available.

6 Conclusions

Internal stress arising from a spherically symmetric finite plastic strain has been obtained on the basis of the Eshelby's theory on inclusions with stress-free strain. A spherically symmetric finite plastic strain consists of a finite plastic strain free from internal stress and an infinitesimal plastic strain causing an internal stress. When a hollow sphere is subjected to inner and outer pressures, if plastic strain is divided into a finite plastic strain free from internal stress and an infinitesimal one causing internal stress, the distribution of plastic strain in yield zone and stress distribution are directly obtained for arbitrary flow curve. But, if not divided, numerical calculation is needed to know plastic strain and stress. The present analysis is also applicable to foward and reverse loading.

References

Boyle, J. T., and Spence, J., 1983, *Stress Analysis for Creep*, Butterworth and Co. Ltd., London.

Cowper, G. R., 1960, "The Elastoplastic Thick-Walled Sphere Subjected to a Radial Temperature Gradient," ASME JOURNAL OF APPLIED MECHANICS, Vol. 27, pp. 496-500.

Eshelby, J. D., 1957, "The Determination of the Elastic Field of an Ellipsoidal Inclusion, and Related Problems," *Proceedings of the Royal Society*, Vol. 241A, pp. 376-396.

Eshelby, J. D., 1959, "The Elastic Field Outside an Ellipsoidal Inclusion," *Proceedings of the Royal Society*, Vol. 252A, pp. 561-569.

Hellan, K., 1975, "An Approximate Study of Void Expansion by Ductility or Creep," *International Journal of Mechanical Sciences*, Vol. 17, pp. 369-374.

Hill, R., 1950, *The Mathematical Theory of Plasticity*, The Clarendon Press, Oxford, U.K.

Johnson, W., and Mellor, P. B., 1962, "Elastic-Plastic Behavior of Thick-Walled Spheres of Non-Work-Hardening Material Subjected to a Steady-State Radial Temperature Gradient," *International Journal of Mechanical Sciences*, Vol. 4, pp. 147-158.

Mura, T., and Mori, T., 1976, *Micro Mechanics*, Baifukan, Tokyo.

Sakaki, T., Sugimoto, K., and Fukuzato, T., 1983, "Role of Internal Stress for Continuous Yielding of Dual-Phase Steels," *Acta Metallurgica*, Vol. 31, pp. 1737-1746.

Sakaki, T., 1984, "Yielding and Stress and Plastic Strain Distributions in a Hollow Sphere Subjected Internal and External Pressures," *Transactions of the Japan Society of Mechanical Engineers*, Series A, Vol. 50, pp. 661-668.

Sakaki, T., Kuroki, T., and Sugimoto, K., 1990, "Creep of a Hollow Sphere," ASME JOURNAL OF APPLIED MECHANICS, Vol. 57, pp. 276-281.

Timoshenko, S., and Goodier, J. N., 1951, *Theory of Elasticity*, 2nd ed., McGraw-Hill, New York.

APPENDIX A

Internal Stress Arising From Continuously Distributing Misfit Strains

Let us consider an infinite body with a spherical hollow in it. As assumed in Section 2.2, a finite plastic strain, $\epsilon(r)$, has taken place in the yield zone of $a\leqq r\leqq R$, and a core has been pushed into the hollow. The thin shell introduced in Section 2.2 has inner and outer radii of r' and $r'+\delta r'$, respectively, and the radius of the surrounding hole is $r'+dr'$, where r', $r'+\delta r'$, and $r'+dr'$ were called r, $r+\delta r$, and $r+dr$, respectively, in Section 2.2. In this state, the thin shell has the increment of misfit strain de_m^* given by equation (5). The increment of internal stress due to de_m^* is identical with the internal stress in the state where only spherical region of $0\leqq r<r'+dr'$ has a uniform isotropic eigenstrain de_m^* in an infinite body. Thus, the increment of internal stress, ds_{rr}^*, etc., is obtained as follows in view of equations (1)-(4).

In the region of $0\leqq r<r'+dr'$,

Downloaded 03 May 2010 to 171.66.16.244. Redistribution subject to ASME license or copyright; see http://www.asme.org/terms/Terms_Use.cfm

$$ds^*_{rr}(r) = ds^*_{\theta\theta}(r) = 0 \tag{A1}$$

$$d\sigma^*_m(r) = \frac{-2E}{3(1-\nu)} de^*_m. \tag{A2}$$

In the region of $r > r' + dr'$,

$$ds^*_{rr}(r) = -2ds^*_{\theta\theta}(r) = \frac{-2E}{3(1-\nu)} \frac{r'^3}{r^3} de^*_m \tag{A3}$$

$$d\sigma^*_m(r) = 0. \tag{A4}$$

The increment of internal stress, Δs^*_{rr}, etc., due to the increment of misfit strain, Δe^*_m, in the core region is also obtained as follows.

In the core ($0 \leqq r < a$),

$$\Delta s^*_{rr}(r) = \Delta s^*_{\theta\theta}(r) = 0 \tag{A5}$$

$$\Delta\sigma^*_m(r) = \frac{-2E}{3(1-\nu)} \Delta e^*_m. \tag{A6}$$

In the body ($r > a$),

$$\Delta s^*_{rr}(r) = -2\Delta s^*_{\theta\theta}(r) = \frac{-2E}{3(1-\nu)} \frac{a^3}{r^3} \Delta e^*_m \tag{A7}$$

$$\Delta\sigma^*_m(r) = 0. \tag{A8}$$

Since de^*_m ranges continuously over the yield zone, the internal stress s^*_{rr}, etc., arising from de^*_m and Δe^*_m becomes the sum of the previously described increments; i.e., in the core ($0 \leqq r < a$),

$$s^*_{rr}(r) = s^*_{\theta\theta}(r) = 0 \tag{A9}$$

$$\sigma^*_m(r) = \Delta\sigma^*_m + \int_{r'=a}^{R} d\sigma^*_m = \frac{-2E}{3(1-\nu)} \left[\Delta e^*_m + \int_{r'=a}^{R} de^*_m \right]. \tag{A10}$$

In the yield zone of the body ($a < r \leqq R$),

$$s^*_{rr}(r) = -2s^*_{\theta\theta}(r) = \Delta s^*_{rr} + \int_{r'=a}^{r} ds^*_{rr} + \frac{-2E}{3(1-\nu)} \frac{1}{r^3} \left[a^3 \Delta e^*_m + \int_{r'=a}^{r} r'^3 de^*_m \right]. \tag{A11}$$

$$\sigma^*_m(r) = \int_{r'=r}^{R} d\sigma^*_m = \frac{-2E}{3(1-\nu)} \int_{r'=r}^{R} de^*_m \tag{A12}$$

In the elastic zone of the body ($r \geqq R$),

$$s^*_{rr}(r) = -2s^*_{\theta\theta}(r) = \Delta s^*_{rr} + \int_{r'=a}^{R} ds^*_{rr} = \frac{-2E}{3(1-\nu)} \frac{1}{r^3} \left[a^3 \Delta e^*_m + \int_{r'=a}^{R} r'^3 de^*_m \right]. \tag{A13}$$

$$\sigma^*_m(r) = 0. \tag{A14}$$

APPENDIX B

The Meaning of $\Delta\epsilon(r)$

Let us consider a hollow sphere with initial inner and outer radii of a_0 and b_0, respectively, where the hollow sphere is free from plastic strain and internal stress. Let an initial radius be denoted by r_0, where $a_0 \leqq r_0 \leqq b_0$. Let us introduce a spherically symmetric, finite plastic strain, $\epsilon_0(r_1)$, causing no internal stress, where r_1 is the radius after the deformation. Further, let us add a spherically symmetric, infinitesimal plastic strain, $\Delta\epsilon_1(r)$, where r is a final radius and $r = r_1 + \Delta r$. In the final state, the total plastic strain, $\epsilon(r)$, is expressed as

$$\epsilon(r) = \ln(r/r_0) = \epsilon_0(r_1) + \Delta\epsilon_1(r), \tag{B1}$$

where $\epsilon_0(r_1) = \ln(r_1/r_0)$ and $\Delta\epsilon_1(r) = \ln(1 + \Delta r/r_1) \fallingdotseq \Delta r/r_1$. When $\epsilon(r)$ is divided into $\epsilon_0(r_1)$ and $\Delta\epsilon_1(r)$, $\epsilon_0(r_1)$ and $\Delta\epsilon_1(r)$ have clear physical meaning. $\epsilon_0(r_1)$ and $\Delta\epsilon_1(r)$, however, are not convenient for the calculations in Sections 2.5, 3.1, and 3.2. Therefore, $\epsilon(r)$ was divided into a finite $\epsilon_0(r)$ and an infinitesimal $\Delta\epsilon(r)$, as a matter of convenience, in equation (24) in Section 2.5, i.e.,

$$\epsilon(r) = \epsilon_0(r) + \Delta\epsilon(r). \tag{B2}$$

As $\epsilon_0(r)$ satisfies equation (22),

$$\epsilon_0(r_1) = \epsilon_0(r) - \left\{ \frac{d\epsilon_0(r)}{dr} \right\}_{r=r} \Delta r = \epsilon_0(r) - \{1 - e^{+3\epsilon_0(r)}\} \Delta\epsilon_1(r). \tag{B3}$$

Combining (B1)–(B3), the following relations are obtained:

$$\Delta\epsilon_1(r) = e^{-3\epsilon_0(r)} \Delta\epsilon(r) \tag{B4}$$

$$\epsilon_0(r_1) = \epsilon_0(r) + \{1 - e^{-3\epsilon_0(r)}\} \Delta\epsilon(r). \tag{B5}$$

When equation (B4) is substituted into equations (25)–(31), these equations, with respect to $\Delta\epsilon_1(r)$, become identical with equations (33) and (34) dealing with an infinitesimal $\epsilon(r)$. This is easily understood if the state where $\epsilon_0(r_1)$ has occurred is considered anew as the initial state. In Section 3.1, $\Delta\epsilon(a)$ has been assumed to be zero as a matter of convenience. In such a case, $\Delta\epsilon_1(a)$ also becomes zero.

Downloaded 03 May 2010 to 171.66.16.244. Redistribution subject to ASME license or copyright; see http://www.asme.org/terms/Terms_Use.cfm

T. Sakaki
Professor,
Department of Mechanical Engineering,
Faculty of Technology.

T. Kuroki[1]
Graduate Student.

K. Sugimoto[1]
Research Associate,
Department of Mechanical Engineering,
Faculty of Technology.

Tokyo Metropolitan University,
Fukazawa 2-1-1, Setagaya-ku
Tokyo 158, Japan

Creep of a Hollow Sphere

Using internal stress arising from a spherically symmetric, finite plastic strain, creep of a hollow sphere subjected to inner and outer pressures, and also thermal stress, is discussed. If computer-aided numerical calculation method is used, creep is easily followed up to a finite plastic strain range including initial transient creep, whatever type of creep law is employed. If assumed in a steady state, creep rate, stress, small plastic strain leading to a stress state in steady creep, and another small plastic strain relaxing thermal stress are analytically obtained. Numerical method is also applicable to creep relaxation. Further, the origin of residual stress after unloading is clarified.

1 Introduction

Creep of a thick-walled hollow sphere subjected to a constant inner pressure has been discussed by Von Rimrott (1959b) in a finite plastic strain range. Assuming the power-law creep and a uniform temperature, he has analytically derived the fracture time at which the plastic strain at the inner surface becomes infinity, and has also shown that the fracture time is finite for the power-law creep.

Johnson and Khan (1963) have precisely analyzed creep of a thick-walled hollow sphere subjected to inner and outer pressures and a thermal stress due to radial steady heat flow in a small plastic strain range. They have analytically derived creep rate and stress state of a hollow sphere in a steady-state creep, and further proposed a calculation method of creep rate and stress state at an arbitrary time including transient creep which appears during transition from initial elastic stress state to plastic stress-state or steady-state. Their analytical method of transient creep, however, is rather complicated. Boyle and Spence (1983) have shown the general calculation method of creep of arbitrary structures under multiaxial stress state and its application to transient creep of hollow spheres in a small strain range. Creep relaxation of hollow spheres has been discussed by Spence and Hult (1973) on the assumption that the sum of elastic and plastic strains is held constant during relaxing. In the previous studies introduced, internal stress arising from distribution of plastic strain has been taken into account. But, the internal stress has not been clearly explained as internal stress, except for the residual stress derived by Boyle and Spence for spherically symmetric, small plastic strain.

If the internal stress arising from a spherically symmetric, finite plastic strain (Sakaki et al., 1990) is used, creep of a hollow sphere subjected to inner and outer pressures, and also radially symmetric thermal stress is easily followed by computer-aided numerical calculation method up to a finite plastic strain range including initial transient creep, whatever type of creep law is employed. The quantities in a steady state, such as creep rate, stress, small plastic strain leading to plastic stress state, and another small plastic strain relaxing the thermal stress, are also analytically obtained. Creep relaxation can be followed by numerical method. Further, the origin of residual stress after unloading is clarified, and residual stress is revealed to depend on the temperature dependence of elastic constants.

2 Fundamentals

Let us consider a hollow sphere with current inner and outer radii of a and b, respectively. The hollow sphere is assumed to be elastically, plastically, and also thermally isotropic. Let us introduce spherically symmetric coordinates r and θ, the radial and the tangential directions, respectively, where the origin is located at the center of the hollow sphere. Let stress components be denoted by σ_{rr} and $\sigma_{\theta\theta}$, deviatoric stress components by s_{rr} and $s_{\theta\theta}$, and mean normal stress by σ_m. Stress, plastic strain, and temperature are expressed with respect to a current radius r after plastic deformation.

2.1 Applied Stress. If the hollow sphere is subjected to inner and outer pressures of P_a and P_b, respectively, the applied stress is expressed as follows (Timoshenko and Goodier, 1951):

[1]Presently at Nippon Steel Corporation, Ltd., Research and Development Laboratory, Material Forming Process Research Laboratory, Edamitsu 1-1-1, Yawata-Higashi-ku, Kitakyushu-city, Fukuoka 805, Japan.

[2]Presently Associate Professor, Department of Functional Machinery and Mechanics, Faculty of Textile Science and Technology, Shinshu University, Tokida 3-15-1, Ueda, Nagano 386, Japan.

Contributed by the Applied Mechanics Division of THE AMERICAN SOCIETY OF MECHANICAL ENGINEERS for publication in the JOURNAL OF APPLIED MECHANICS.

Discussion on this paper should be addressed to the Technical Editor, Prof. Leon M. Keer, The Technological Institute, Northwestern University, Evanston, IL 60208, and will be accepted until two months after final publication of the paper itself in the JOURNAL OF APPLIED MECHANICS. Manuscript received by the ASME Applied Mechanics Division, March 18, 1988; final revision, April 10, 1989.

Copyright © 1990 by ASME
Downloaded 03 May 2010 to 171.66.16.244. Redistribution subject to ASME license or copyright; see http://www.asme.org/terms/Terms_Use.cfm

$$s_{rr}^{A}(r) = -2s_{\theta\theta}^{A}(r) = -\frac{b^3}{b^3-a^3}\frac{a^3}{r^3}(P_a - P_b) \tag{1}$$

$$\sigma_m^{A}(r) = \frac{a^3}{b^3-a^3}(P_a - P_b) - P_b. \tag{2}$$

2.2 Thermal Stress. When the inner and outer surfaces are held at constant temperatures of T_a and T_b, respectively, and the hollow sphere is in a radial steady heat flow, the temperature $T(r)$ and the corresponding thermal stress are expressed as follows (Timoshenko and Goodier, 1951),

$$T(r) = T_a - \frac{(r-a)b}{(b-a)r}(T_a - T_b) \tag{3}$$

$$s_{rr}^{T}(r) = -2s_{\theta\theta}^{T}(r)$$

$$= \frac{-2\mathrm{E}}{3(1-\nu)}\alpha(T_a - T_b)\frac{ba}{b^3-a^3}\left[\frac{b^2+ba+a^2}{2r} - \frac{3b^2a^2}{2r^3}\right] \tag{4}$$

$$\sigma_m^{T}(r) = \frac{\mathrm{E}}{1-\nu}\alpha(T_b - T_a)\frac{ba}{b^3-a^3}\left[b + a - \frac{2(b^2+ba+a^2)}{3r}\right] \tag{5}$$

where E is the Young's modulus, ν is the Poisson's ratio, and α is the coefficient of linear thermal expansion. Equations (4) and (5) have been derived on the assumption that E, ν, and α are independent of temperature. Thus, (4) and (5) are valid for a small temperature difference of $T_a - T_b$. If the hollow sphere is in an arbitrary radial heat flow and $T(r)$ is time-dependent, the corresponding thermal stress is expressed by (A10) and (A11) in Appendix.

2.3 Internal Stress Arising From a Finite Plastic Strain. When a hollow sphere has a spherically symmetric plastic strain, let us represent the plastic strain component in the tangential (θ) directions by $\epsilon(r)$. Then, the component in the radial (r) direction becomes $-2\epsilon(r)$ by the law of constant volume. The internal stress due to an arbitrary finite plastic strain, $\epsilon(r)$, is expressed as follows as derived in another paper (Sakaki et al., 1990).

$$s_{rr}^{P}(r) = -2s_{\theta\theta}^{P}(r) = \frac{2\mathrm{E}}{3(1-\nu)}\left[\frac{1-e^{-3\epsilon(r)}}{3} - \frac{b^3}{b^3-a^3}\frac{a^3}{r^3}I(a,b)\right] \tag{6}$$

$$\sigma_m^{P}(r) = \frac{-2\mathrm{E}}{3(1-\nu)}\left[\frac{1-e^{-3\epsilon(r)}}{3} - \frac{a^3}{b^3-a^3}I(a,b) - I(r,b)\right] \tag{7}$$

where

$$I(r,b) \equiv \int_r^b \frac{1-e^{-3\epsilon(r)}}{r}dr, \quad (a \leqq r \leqq b). \tag{8}$$

Let us divide a finite plastic strain, $\epsilon(r)$, into a finite plastic strain, $\epsilon_0(r)$, free from internal stress and an infinitesimal plastic strain, $\Delta\epsilon(r)$, causing an internal stress, i.e.,

$$\epsilon(r) = \epsilon_0(r) + \Delta\epsilon(r). \tag{9}$$

If $\epsilon_0(a)$ is specific to an arbitrary value, $\epsilon_0(r)$ is given as

$$r^3\{1 - e^{-3\epsilon_0(r)}\} = a^3\{1 - e^{-3\epsilon_0(a)}\} \tag{10}$$

or

$$\epsilon_0(r) = -\frac{1}{3}\ln\left[1 - \frac{a^3}{r^3}\{1 - e^{-3\epsilon_0(a)}\}\right]. \tag{11}$$

Equations (6) and (7) are rewritten using $\epsilon_0(r)$ and $\Delta\epsilon(r)$ as

$$s_{rr}^{P}(r) = -2s_{\theta\theta}^{P}(r)$$

$$= \frac{2\mathrm{E}}{3(1-\nu)}\left[e^{-3\epsilon_0(r)}\Delta\epsilon(r) - \frac{3b^3}{b^3-a^3}\frac{a_3}{r^3}\Delta I(a,b)\right] \tag{12}$$

$$\sigma_m^{P}(r) = \frac{-2\mathrm{E}}{3(1-\nu)}\left[e^{-3\epsilon_0(r)}\Delta\epsilon(r) - \frac{3a^3}{b^3-a^3}\Delta I(a,b) - 3\Delta I(r,b)\right] \tag{13}$$

where

$$\Delta I(r,b) \equiv \int_r^b \frac{e^{-3\epsilon_0(r)}\Delta\epsilon(r)}{r}dr, \quad (a \leqq r \leqq b). \tag{14}$$

Assuming an infinitesimal $\epsilon(r)$, equations (6) and (7) are reduced to

$$s_{rr}^{P}(r) = -2s_{\theta\theta}^{P}(r)$$

$$= \frac{2\mathrm{E}}{3(1-\nu)}\left[\epsilon(r) - \frac{3b^3}{b^3-a^3}\frac{a^3}{r^3}\int_a^b \frac{\epsilon(r)}{r}dr\right] \tag{15}$$

$$\sigma_m^{P}(r) = \frac{-2\mathrm{E}}{3(1-\nu)}\left[\epsilon(r) - \frac{3a^3}{b^3-a^3}\int_a^b \frac{\epsilon(r)}{r}dr - 3\int_r^b \frac{\epsilon(r)}{r}dr\right]. \tag{16}$$

Equations (15) and (16) are identical with those derived by Boyle and Spence (1983). If an infinitesimal $\epsilon(r)$ is divided into $\epsilon_0(r)$ free from internal stress and $\Delta\epsilon(r)$ causing an internal stress, where

$$\epsilon_0(r) = (a^3/r^3)\epsilon_0(a), \tag{17}$$

$\epsilon(r)$ in equations (15) and (16) may be replaced by $\Delta\epsilon(r)$.

If elastic zone (s) are involved, $\Delta\epsilon(r)$ in equations (12)–(14) or (15), (16) is taken to be $-\epsilon_0(r)$ in the elastic zone (s).

3 Creep of a Hollow Sphere

3.1 General Case. Let us consider a general case where pressures and temperature may be time-dependent. At a current time of t, the total stress acting on the hollow sphere is given by the sum of the applied stress, equations (1) and (2), the thermal stress, (A10) and (A11) in the Appendix in the general case or (4) and (5) if in a steady heat flow, and the internal stress due to a current plastic strain—equations (6)–(7), (12)–(13), or (15)–(16). Let us represent the deviatoric components of the total stress by $s_{rr}(r,t)$ and $s_{\theta\theta}(r,t)$ and its mean normal stress by $\sigma_m(r,t)$. Then the Mises' equivalent stress becomes

$$\bar{\sigma}(r,t) = |s_{\theta\theta}(r,t) - s_{rr}(r,t)| = 3|s_{\theta\theta}(r,t)|. \tag{18}$$

The increment of equivalent plastic strain, $\overline{d\epsilon}$ during an infinitesimal time interval, dt, is decided by a creep law, i.e.,

$$\overline{d\epsilon}(r,t) = f\{\bar{\sigma}(r,t), \bar{\epsilon}(r,t), T(r,t), \ldots\}dt, \tag{19}$$

where f may be an arbitrary function of equivalent stress $\bar{\sigma}$, the equivalent plastic strain $\bar{\epsilon}$, the temperature T, deformation and thermal history, and so on. The increment of the plastic strain component $d\epsilon(r,t)$ in the tangential (θ) directions is given as follows, bearing the Prandtl-Reuss' law in mind (Boyle and Spence, 1983):

$$d\epsilon(r,t) = \frac{3s_{\theta\theta}(r,t)}{2\bar{\sigma}(r,t)}\overline{d\epsilon}(r,t). \tag{20}$$

From the nature of spherical symmetry, the plastic strain-increment in the radial (r) direction is given by $-2\epsilon(r,t)$, and thus

$$\overline{d\epsilon}(r,t) = 2|d\epsilon(r,t)|. \tag{21}$$

Downloaded 03 May 2010 to 171.66.16.244. Redistribution subject to ASME license or copyright; see http://www.asme.org/terms/Terms_Use.cfm

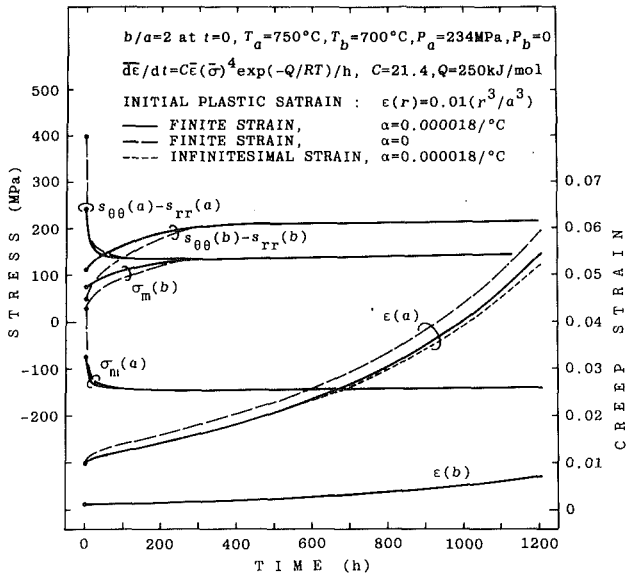


Fig. 1 An example of creep of a hollow sphere, where creep rate depends on current creep strain and current equivalent stress

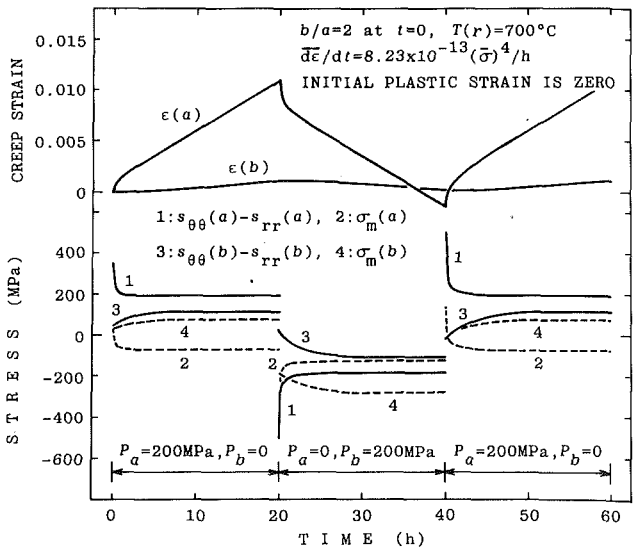


Fig. 2 An example of cyclic deformation of a hollow sphere, where creep rate depends only on current equivalent stress

Current equivalent plastic strain, $\bar{\epsilon}(r,t)$, is given by the following integration through a strain path:

$$\bar{\epsilon}(r,t)=\int \overline{d\epsilon}\,(r,t). \tag{22}$$

Johnson and Khan (1963) have shown an analytical method to follow creep of a hollow sphere including transient creep arising from initial stress redistribution. But, if the computer-aided numerical technique is used, the present method just described is simpler than their method, and also easily applicable to any type of creep laws. Boyle and Spence (1983) have derived the general method for analyzing transient creep due to initial stress redistribution in arbitrary structures under a multiaxial stress state, and shown its application to a hollow sphere. In their analysis, applied stress, thermal stress and internal stress due to plastic or creep strain distribution are taken into account. They have also derived a stress arising from spherically symmetric small plastic strain, which is identical with equations (15) and (16), and called the residual stress. If an internal stress due to plastic strain distribution has been obtained, creep analysis can be most easily performed by the method described in this section.

3.2 Relaxation of Thermal Stress. The process of relaxation of thermal stress can be followed by the strain-increment method described in the previous section. Here, however, let us derive the plastic strain needed to relax perfectly the thermal stress in the steady heat flow. Let us assume that an infinitesimal plastic strain $\Delta\epsilon^T(r)$ causing an internal stress $s^P_{\theta\theta}(r)$, etc., is superposed on a finite plastic strain, $\epsilon_0(r)$, free from internal stress in the state where the thermal stress is perfectly relaxed. The conditions are

$$s^T_{\theta\theta}(r)+s^P_{\theta\theta}(r)=0 \tag{23}$$

$$\sigma^T_m(r)+\sigma^P_m(r)=0. \tag{24}$$

From equations (4), (12), and (23), the following relation is obtained:

$$e^{-3\epsilon_0(r)}\Delta\epsilon^T(r)=\frac{3b^3}{b^3-a^3}\frac{a^3}{r^3}\Delta I^T(a,b)$$

$$+\alpha(T_a-T_b)\frac{ba}{b^3-a^3}\left[\frac{b^2+ba+a^2}{2r}-\frac{3b^2a^2}{2r^3}\right], \tag{25}$$

where

$$\Delta I^T(a,b)\equiv\int_a^b\frac{e^{-3\epsilon_0(r)}\Delta\epsilon^T(r)}{r}dr. \tag{26}$$

Dividing both the sides of equation (25) by r and then integrating from $r=a$ to b, $\Delta I^T(a,b)$ in both the sides are eliminated and the integral of the second term becomes zero. Thus, the value of $\Delta I^T(a,b)$ may take an arbitrary value. The reason is that $\Delta\epsilon^T(r)$ does not cause any internal stress, if $e^{-3\epsilon_0(r)}\Delta\epsilon^T(r)$ is inversely proportional to r^3. Let us take the value of $\Delta I^T(a,b)$ so that $\Delta\epsilon^T(a)=0$, as a matter of convenience. Then,

$$e^{-3\epsilon_0(r)}\Delta\epsilon^T(r)=\frac{\alpha(T_a-T_b)}{2}\frac{b}{b-a}\frac{a}{r}\left(1-\frac{a^2}{r^2}\right)$$

$$=\frac{3(1-\nu)}{E}s^T_{\theta\theta}(r)+\frac{\alpha(T_a-T_b)}{2}\frac{(2b^2-ba-a^2)b}{b^3-a^3}\frac{a^3}{r^3}. \tag{27}$$

The $\Delta\epsilon^T(r)$ also satisfies equation (24). Consequently, the plastic strain required to relax the thermal stress in radial steady heat flow is given by the sum of $\Delta\epsilon^T(r)$ and an arbitrary $\epsilon_0(r)$. If $\epsilon_0(r)$ is restricted within an infinitesimal value, $e^{-3\epsilon_0(r)}$ in (27) may be taken to be unity.

When the process of relaxation of thermal stress is followed by the strain-increment method the plastic strain in the final state, where the thermal stress is perfectly relaxed, becomes the sum of the $\Delta\epsilon^T(r)$ and some $\epsilon_0(r)$ because of preferential creep around the inner or the outer surface.

3.3 Examples of Calculation by Strain-Increment Method. Some examples of computer-aided numerical calculation by the strain-increment method (the Euler method) described in Section 3.1 will be shown, where the creep law is assumed as

$$\frac{\overline{d\epsilon}\,(r,t)}{dt}=C\{\bar{\sigma}(r,t)\}^n\{\bar{\epsilon}(r,t)\}^m\exp\left\{\frac{-Q}{RT(r,t)}\right\} \tag{28}$$

where C is a constant, n and m are exponents representing stress and strain dependence of creep rate, respectively, Q is an activation energy, R is the gas constant, and $T(r,t)$ is the absolute temperature. C, n, m, and Q are assumed to be independent of temperature. The Young's modulus E is assumed to be 150 GPa and the Poisson's ratio $\nu=0.4$. In the following three examples, extreme pressures are applied to reveal transient phenomena.

Downloaded 03 May 2010 to 171.66.16.244. Redistribution subject to ASME license or copyright; see http://www.asme.org/terms/Terms_Use.cfm

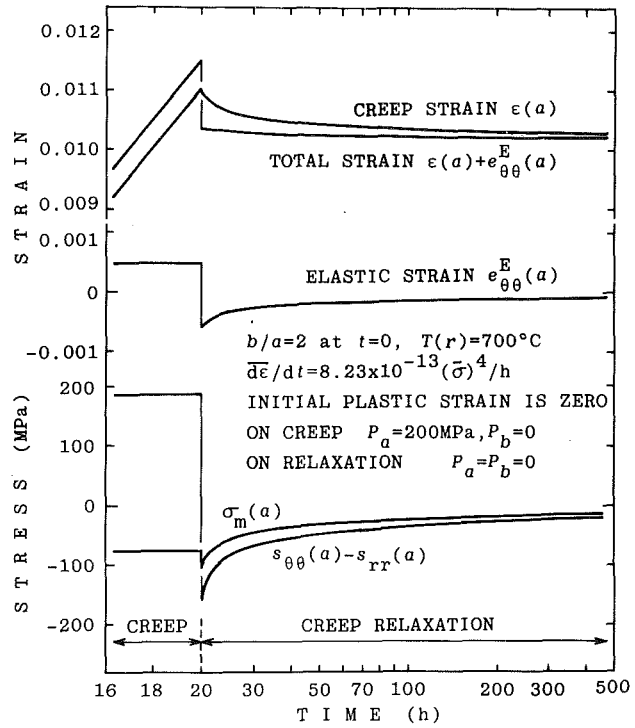


Fig. 3 An example of stress relaxation by creep after usual creep

An example is shown in Fig. 1, where P_a, P_b, T_a, and T_b are held constant during creeping. At the beginning of $t=0$, it is assumed that a hollow sphere has an initial small plastic strain free from internal stress and is left in a steady heat flow and combined applied and thermal stresses. When $\epsilon(r,t)$ is treated as a finite creep strain and the thermal stress is taken into account (the solid lines), the stress state varies up to about 500 h and a transient creep appears. Such a transient creep due to stress redistribution has been reported by Johnson and Khan (1963) and by Boyle and Spence (1983). Then, it comes into an approximate steady state, or so-called plastic stress state, and the stress state varies very slowly. Comparing the solid lines and the dashed lines representing the stress components, the influence of the thermal stress is found to vanish after the transient creep. The creep strains in the two previous cases differ by some amount, since in the latter case larger initial creep strain is needed to relax the higher initial total stress. If the creep strain is treated as infinitesimal (the dotted line), the creep strain is estimated as a rather smaller value than that treated as finite.

Another example is shown in Fig. 2, in which temperature is uniform, initial plstic strain is zero, and the outer and the inner pressures are exchanged every 20 hours. The transient creep after exchanging the pressures is easily obtained by the strain-increment method.

Third is a stress relaxation after creeping. In the example shown in Fig. 2, if the inner pressure is unloading at $t=20$ h, the hollow sphere is left in a residual stress state arising from the plastic strain leading to the plastic stress state. The residual stress begins to relax just after unloading, as shown in Fig. 3, and the creep strain, the elastic strain, and the total strain, which is the sum of them in the tangential (θ) directions, vary with time. Spence and Hult (1973) have analyzed such a stress relaxation assuming the total strain being held constant during relaxing. Strictly speaking, however, the total strain varies by a small amount.

3.4 Creep in the Plastic Stress State. As explained in the previous section, the thermal stress has already been relaxed in the plastic stress state or the (nearly) stationary state in a steady heat flow. In this state, let us assume that the total creep strain, $\epsilon(r,t)$, is composed of a finite plastic strain, $\epsilon_0(r,t)$, free from internal stress, an infinitesimal $\Delta\epsilon^T(r)$, (27) relaxing the thermal stress and another infinitesimal $\Delta\epsilon^P(r)$ leading to the plastic stress state. Further, let us assume that variations of $\Delta\epsilon^T(r)$ and $\Delta\epsilon^P(r)$ are far less than that of $\epsilon_0(r,t)$ during a short time of dt, and also that variation of $T(r)$ due to slight change of b/a is also very small. These assumptions will be found to be true later.

When $\epsilon_0(a,t)$ at the inner surface takes some value, $\epsilon_0(r,t)$ is given by (11). Thus, the following relation on the creep rate is derived, since the radius r represents that after plastic deformation.

$$\dot{\epsilon}_0(r,t)=(a^3/r^3)\dot{\epsilon}_0(a,t), \tag{29}$$

where the dots on the variables indicate the time derivative. Let us discuss the following two cases in a lump.

(1) $P_a-P_b>0$, and thus the hollow sphere in the plastic stress state expands gradually and both $\epsilon_0(r,t)$ and $\dot{\epsilon}_0(r,t)$ are positive. In this case, let k be $+1$.

(2) On the other hand, $P_a-P_b<0$, and the hollow sphere shrinks gradually and $\epsilon_0(r,t)$ and $\dot{\epsilon}_0(r,t)$ are negative. In this case, k is taken to be -1.

In both the cases it is assumed that P_a, P_b, T_a, and T_b are held constant during creeping and the hollow sphere is in a steady heat flow.

Here, the creep law is assumed, as follows, instead of equation (28)

$$2k\dot{\epsilon}_0(r,t)=2k(a^3/r^3)\dot{\epsilon}_0(a,t)$$
$$=C\{\bar{\sigma}(r,t)\}^n\{2k\epsilon_0(r,t)\}^m\exp\left\{\frac{-Q}{RT(r)}\right\}, \tag{30}$$

where the meanings of C, n, m, Q, and R are the same as those in (28). Using (1), (12), and (18), equation (30) is transformed to

$$\bar{\sigma}(r,t)=k\left[\frac{3}{2}\frac{b^3}{b^3-a^3}\frac{a^3}{r^3}(P_a-P_b)\right.$$
$$\left.-\frac{\mathrm{E}}{1-\nu}\left\{e^{-3\epsilon_0(r,t)}\Delta\epsilon^P(r)-\frac{3b^3}{b^3-a^3}\frac{a^3}{r^3}\Delta I^P(a,b)\right\}\right]$$
$$=\left\{\frac{2k\dot{\epsilon}_0(a,t)}{C}\right\}^{1/n}\{2k\epsilon_0(r,t)\}^{-m/n}\frac{a^{3/n}}{r^{3/n}}\exp\left\{\frac{Q}{nRT(r)}\right\} \tag{31}$$

where

$$\Delta I^P(r,b)\equiv\int_r^b\frac{e^{-3\epsilon_0(r,t)}\Delta\epsilon^P(r)}{r}dr,\quad(a\leqq r\leqq b). \tag{32}$$

Dividing the second and the third sides of (31) by r and integrating them from $r=a$ to b, two $\Delta I^P(a,b)$ in the second side are eliminated and the creep rate $\dot{\epsilon}_0(a,t)$ at the inner surface is obtained as a function of P_a-P_b, i.e.,

$$\dot{\epsilon}_0(a,t)=\frac{kC}{2}\left[\frac{k(P_a-P_b)}{2I'(a,b)}\right]^n \tag{33}$$

where

$$I'(r,b)\equiv\int_r^b\{2k\epsilon_0(r,t)\}^{-m/n}\frac{1}{r}\frac{a^{3/n}}{r^{3/n}}\exp\left\{\frac{Q}{nRT(r)}\right\}dr,$$
$$(a\leqq r\leqq b). \tag{34}$$

Since two $\Delta I^P(a,b)$ have been eliminated by the aforementioned integration, $\Delta I^P(a,b)$ can take arbitrary value. Let us determine the value of $\Delta I^P(a,b)$ so that $\Delta\epsilon^P(a)$ at the inner surface becomes zero as a matter of convenience in calculation. As a result, $\Delta\epsilon^P(r)$ is obtained as

Downloaded 03 May 2010 to 171.66.16.244. Redistribution subject to ASME license or copyright; see http://www.asme.org/terms/Terms_Use.cfm

$$e^{-3\epsilon_0(r,t)}\Delta\epsilon^P(r)$$
$$=\frac{1-\nu}{2E}\frac{P_a-P_b}{I'(a,b)}\left[\{2k\epsilon_0(a,t)\}^{-m/n}\frac{a^3}{r^3}\right.$$
$$\left.\times\exp\left\{\frac{Q}{nRT_a}\right\}-\{2k\epsilon_0(r,t)\}^{-m/n}\frac{a^{3/n}}{r^{3/n}}\exp\left\{\frac{Q}{nRT(r)}\right\}\right]. \quad (35)$$

Using equations (12), (13), and (35), the internal stress due to $\Delta\epsilon^P(r)$ is expressed as

$$s^P_{rr}(r,t)=-2s^P_{\theta\theta}(r,t)=(P_a-P_b)\left[\frac{b^3}{b^3-a^3}\frac{a_3}{r^3}\right.$$
$$\left.-\frac{\{2k\epsilon_0(r,t)\}^{-m/n}}{3I'(a,b)}\frac{a^{3/n}}{r^{3/n}}\exp\left\{\frac{Q}{nRT(r)}\right\}\right] \quad (36)$$

$$\sigma^P_m(r,t)=-(P_a-P_b)\left[\frac{a^3}{b^3-a^3}+\frac{I'(r,b)}{I'(a,b)}\right.$$
$$\left.-\frac{\{2k\epsilon_0(r,t)\}^{-m/n}}{3I'(a,b)}\frac{a^{3/n}}{r^{3/n}}\exp\left\{\frac{Q}{nRT(r)}\right\}\right]. \quad (37)$$

The total stress s_{rr}, $s_{\theta\theta}$, and σ_m, controlling the creep in the plastic stress state, is given by the sum of the internal stress (36) and (37) and the applied stress (1) and (2), i.e.,

$$s_{rr}(r)=-2s_{\theta\theta}(r)=$$
$$-(P_a-P_b)\frac{\{2k\epsilon_0(r,t)\}^{-\frac{m}{n}}}{3I'(a,b)}\frac{a^{3/n}}{r^{3/n}}\exp\left\{\frac{Q}{nRT(r)}\right\} \quad (38)$$

$$\sigma_m(r)=-(P_a-P_b)\left[\frac{I'(r,b)}{I'(a,b)}\right.$$
$$\left.-\frac{\{2k\epsilon_0(r,t)\}^{-\frac{m}{n}}}{3I'(a,b)}\frac{a^{3/n}}{r^{3/n}}\exp\left\{\frac{Q}{nRT(r)}\right\}\right]-P_b. \quad (39)$$

If $\epsilon(r)$ may be treated as infinitesimal, (35) becomes equal to $\Delta\epsilon^P(r)$.

The total stress given by (38) and (39) and the creep rate expressed by (33) and (29) include some amount of error compared with those values obtained by the strain-increment method described in Sections 3.1 and 3.3. For example, in the case of Fig. 2, the total stress ((38) and (39)) coincides with that calculated by the strain-increment method within a small relative error of 0.1 percent in the steady state ($t=15$ to 20, 35 to 40 and 55 to 60 h). The creep rate ((33) and (29)) is associated with a relative error within 0.5 percent. These small relative errors arise from the simple creep law, i.e., the creep rate depends only on the current equivalent stress, and a very slow variation of total stress due to the variation of b/a during creeping. On the other hand, in the approximate steady-state in Fig. 1 ($t>500$ h), the relative errors in the total stress and in the creep rate are within 0.3 percent and 1.8 percent, respectively. These large relative errors arise from the creep law in which the creep rate depends on the current creep strain.

Johnson and Khan (1963) have analyzed creep of a hollow sphere in a steady state within a small strain range. If creep law is expressed by equation (30) with $m=0$ and temperature is uniform, the total stress and the creep rate in their analysis are identical with (38) and (39) and (33) and (29), respectively. When a radial temperature gradient is present, they have employed a creep law with a different temperature dependence from (30). Thus, (38) and (39) and (33) and (29) cannot be directly compared with their solution. But, if their creep law is employed in the present study, the same results will be obtained.

Von Rimrott (1959b) has analyzed creep of a thick-walled hollow sphere subjected to a constant inner pressure in a finite plastic strain range, assuming the creep law (equation (30)) with $m=0$ and a uniform temperature.

The advantage of his theory is that loading time is analytically evaluated as a function of a finite plastic strain at the inner surface without recourse to the strain-increment method, and the corresponding distributions of stress and plastic strain are also obtained. The plastic strain obtained in his theory differs from that obtained in the present study only by a small amount of $\Delta\epsilon^P(r)$ given by (35). He has also shown that the failure time at which the plastic strain at the inner surface becomes infinity remains within a finite time. Rimrott (1959a) and Rimrott et al. (1960) have also treated the creep and creep failure of a thick-walled and closed-end cylinder subjected to an inner pressure on the basis of the similar method for a hollow sphere.

3.5 Elastic Strain and Thermal Strain. In the previous sections, elastic and thermal strains have not appeared. If elastic strain components e^E_{rr} and $e^E_{\theta\theta}$ are needed, they are easily obtained from total stress componenets using the Hooke's law. If thermal strain is expressed using temperature difference from T_a, thermal strain components are expressed as

$$e^T_{rr}(r)=e^T_{\theta\theta}(r)=\alpha\{T(r)-T_a\}. \quad (40)$$

In the previous sections (and also in the Appendix), current radius r has been associated only with plastic strain $\epsilon(r)$. If elastic and thermal strains are taken into account, precise current radius becomes r^*, where

$$r^*=\{1+e^E_{\theta\theta}(r)+e^T_{\theta\theta}(r)\}r. \quad (41)$$

3.6 Residual Stress. In general, if a hollow sphere has been unloaded and cooled to room temperature after creeping and has a resultant plastic strain $\epsilon(r)$, the residual stress is expressed by equations (6)–(8) or (15)–(16) where the elastic constants must take values at room temperature.

When the creep law is represented by equation (30), and a hollow sphere has been crept into a plastic stress state as discussed in Section 3.4, and then ideally cooled to room temperature without any additional creep deformation, the creep strain is composed of $\epsilon_0(r)$, $\Delta\epsilon^T(r)$, and $\Delta\epsilon^P(r)$ as explained in Section 3.4. In this state, the components of residual stress, s^R_{rr}, etc., are represented as

$$s^R_{rr}(r)=-2s^R_{\theta\theta}(r)=K\{s^P_{rr}(r)-s^T_{rr}(r)\} \quad (42)$$
$$\sigma^R_m(r)=K\{\sigma^P_m(r)-\sigma^T_m(r)\} \quad (43)$$

where the stress components in the right hands of (42) and (43) are those given by (4), (5), (36), and (37), and

$$K=\frac{E_0}{1-\nu_0}\frac{1-\nu}{E} \quad (44)$$

where E_0 and ν_0 are the elastic constants at room temperature and E and ν are those at creep temperature.

4 Conclusions

Using internal stress arising from a spherically symmetric finite plastic strain, creep of a hollow sphere subjected to inner and outer pressures, and also thermal stress, has been discussed. If computer-aided numerical calculation method is used, creep is easily followed up to a finite plastic strain range including initial transient creep, whatever type of creep law is employed. If assumed in a steady state, creep rate, stress,

Downloaded 03 May 2010 to 171.66.16.244. Redistribution subject to ASME license or copyright; see http://www.asme.org/terms/Terms_Use.cfm

small plastic strain leading to a stress state in steady creep, and another small plastic strain relaxing thermal stress are analytically obtained. Numerical method is also applicable to creep relaxation. Further, the origin of residual stress after unloading is clarified.

References

Boyle, J. T., and Spence, J., 1983, *Stress Analysis for Creep*, Butterworth and Co. Ltd., London.

Johnson, A. E., and Khan, B., 1963, "Creep of Metallic Thick-Walled Spherical Vessels Subject to Pressure and Radial Thermal Gradient at Elevated Temperatures," *International Journal of Mechanical Sciences*, Vol. 5, pp. 507–532.

Rimrott, F. P. J., 1959a, "Creep of Thick-Walled Tubes Under Internal Pressure Considering Large Strains," ASME JOURNAL OF APPLIED MECHANICS, Vol. 26, pp. 271–275.

Von Rimrott, F., 1959b, "Versagenszeit beim Kriechen," *Ingenieur-Archiv*, Vol. 27, pp. 169–178.

Rimrott, F. P. J., Mills, E. J., and Marin, J., 1960, "Prediction of Creep Failure Time for Pressure Vessels," ASME JOURNAL OF APPLIED MECHANICS, Vol. 27, pp. 303–308.

Sakaki, T., Sugimoto, K., and Kuroki, T., 1990, "Internal Stress Arising from a Spherically Symmetric Finite Plastic Strain and Yielding of a Hollow Sphere," ASME JOURNAL OF APPLIED MECHANICS, Vol. 57, pp. 268–275.

Spence, J., and Hult, J., 1973, "Simple Approximations for Creep Relaxation," *International Journal of Mechanical Sciences*, Vol. 15, pp. 741–755.

Timoshenko, S., and Goodier, J. N., 1951, *Theory of Elasticity*, 2nd ed., McGraw-Hill, New York.

APPENDIX

Internal Stress Arising From Spherically Symmetric, Finite Plastic Strain, and Small Thermal Strain

When a hollow sphere has a spherically symmetric finite plastic strain and also a thermal strain under a radial heat flow, the internal stress arising from the strains is obtained as follows: At first let us consider a finite body containing a spherical hollow with an initial radius of a_0. Referring to the method described in another paper (Sakaki et al., 1990, Section 2, Appendix A, and Fig. 1), let us consider a spherical thin shell in the body. In the initial state free from any strain, let the inner and the outer radii of the thin shell be r_0 and r_0+dr_0, respectively, and the radius of the surrounding hole also be r_0+dr_0. Let us introduce a spherically symmetric finite plastic strain $\epsilon(r)$ defined in Section 2.3, where r represents the radius after plastic deformation. Subsequently, we introduce an isotropic thermal strain $\alpha\{T(r)-T_a\}$ defined based on the temperature T_a at the surface of the hollow, where α is a linear thermal expansion coefficient and $T(r)$ is the temperature at r. Then, the radius of the hollow, the inner and the outer radii of the thin shell, and the radius of the surrounding hole vary to a, r, $r+\delta r$, and $r+dr$, respectively, where

$$a=a_0\exp\{\epsilon(a)\} \tag{A1}$$

$$r=r_0\exp\{\epsilon(r)+\alpha\Delta T(r)\} \tag{A2}$$

$$r+\delta r=r_0\exp\{\epsilon(r)+\alpha\Delta T(r)\}+dr_0\exp\{-2\epsilon(r)+\alpha\Delta T(r)\} \tag{A3}$$

$$r+dr=(r_0+dr_0)\exp\left[\epsilon(r)+\frac{d\epsilon(r)}{dr}dr+\alpha\Delta T(r)+\alpha\frac{d\Delta T(r)}{dr}dr\right], \tag{A4}$$

and where

$$\alpha\Delta T(r)=\alpha\{T(r)-T_a\}. \tag{A5}$$

In such a combined strain state, the thin shell has an isotropic misfit strain of de_m^* referred to the radius of the surrounding hole, where

$$de_m^*=\frac{(r+\delta r)-(r+dr)}{r+dr}=de_m^{*P}+de_m^{*T}. \tag{A6}$$

Since the thermal strain is usually infinitesimal, the de_m^* becomes the sum of de_m^{*P} due to the plastic strain and de_m^{*T} due to the thermal strain as shown previously, where

$$de_m^{*P}=\frac{-1}{3r^3}\frac{d}{dr}[r^3\{1-e^{-3\epsilon(r)}\}]dr \tag{A7}$$

$$de_m^{*T}=-\alpha\frac{d\Delta T(r)}{dr}dr. \tag{A8}$$

Further, a spherical core with a radius of $(1+\Delta e_m^*)a$ is pushed into the hollow, where Δe_m^* is a small isotropic misfit strain. The internal stress due to Δe_m^* and the continuously distributing de_m^* is obtained by the method developed in another paper (Sakaki et al., 1990, Section 2, and Appendix A). If the body is a hollow sphere with inner and outer radii of a and b, respectively, the boundary conditions are taken into account to lead the inner and the outer surfaces to be traction-free. Then, the total internal stress becomes the sum of the internal stress (equations (6)–(8)) due to de_m^{*P} and the following thermal stress due to de_m^{*T}.

$$s_{rr}^T(r)=-2s_{\theta\theta}^T(r)$$

$$=\frac{2E\alpha}{3(1-\nu)}\left[T(r)-T_a-\frac{3}{r^3}\int_a^r\{T(r)-T_a\}r^2dr-\frac{3}{b^3-a^3}\frac{a^3}{r^3}\int_a^b\{T(r)-T_a\}r^2dr\right] \tag{A10}$$

$$\sigma_m^T(r)=\frac{-2E\alpha}{3(1-\nu)}\left[T(r)-T_a-\frac{3}{b^3-a^3}\int_a^b\{T(r)-T_a\}r^2dr\right] \tag{A11}$$

This thermal stress is identical with the solution derived by Timoshenko and Goodier (1951). If the hollow sphere is in a steady heat flow (equation (3)), the thermal stress above reduces to (4) and (5).

Downloaded 03 May 2010 to 171.66.16.244. Redistribution subject to ASME license or copyright; see http://www.asme.org/terms/Terms_Use.cfm

Viscoplastic Constitutive Modeling of High Strain-Rate Deformation, Material Damage, and Spall Fracture[1]

J. A. Nemes
Material Science and Technology Division,
Naval Research Laboratory,
Washington, DC

J. Eftis
Department of Civil, Mechanical, and
Environmental Engineering,
George Washington University,
Washington, DC

P. W. Randles
Material Science and Technology Division,
Naval Research Laboratory,
Washington, DC

The Perzyna viscoplastic constitutive theory, which contains a scalar variable for description of material damage, is used to study material behavior at high strain rates. The damage parameter for materials which undergo ductile fracture by nucleation, growth, and coalescence of microvoids, is taken to be the void volume fraction. The linear hardening law in both the constitutive equation and the derivation of the void growth rate equation has been replaced by a nonlinear hardening law that allows for the saturation of the hardening with increase of strain. The modified constitutive equations are then specialized to uniaxial deformation with multiaxial stress, which is typical of that occurring in flyer plate impact experiments. Calculations are performed showing the rate dependence of the material response and the effects of the growth of the void volume (damage). The change in the predicted response due to the modification of the hardening law is illustrated. Ductile spall fracture is modeled by considering the response to a simulated compressive-tensile wave using a critical value of the void volume as the local criteria for fracture.

1 Introduction

The term spall-fracture (or spallation) as used in shock wave research is defined as planar separation of the impacted material along the direction parallel to the incident and reflected plane wave fronts generated by the impact. The separation or fracture process itself is due, in essence, to the tensile stress wave pulse that is carried by the reflected plane waves (Butcher et al., 1964; Tuler and Butcher, 1968; Gilman and Tuler, 1970). By means of post shot photomicrographic observations, spall separation has been shown to represent the end result of an accumulation of microdamage events that occur during the passage of the shock wave reflection. For spall fracture in ductile materials, the microdamage is observed to consist of localized elastoplastic deformation surrounding the microvoids which are nucleated, and which subsequently grow and coalesce to form the spall plane. (A comprehensive discussion of the physical features associated with dynamic fracture of solids may be found in the review articles by Curran, Seaman and Shockey (1987) and Meyers and Aimone (1983).)

In keeping with the photomicrographic observations of the physical characteristics associated with spall fracture, Perzyna (1986) has proposed a viscoplastic constitutive theory for a solid with microvoids as a means for modeling deformation at high strain rates coupled with material damage.[2] A scalar variable, ξ, representing the void volume fraction (porosity) of the voided solid, is introduced directly into the viscoplastic constitutive equations for an elastic-plastic solid that is rate sensitive and that strain hardens. In addition, an evolution equation for the porosity parameter, that serves to describe the nucleation, growth, and interaction of the microvoids, is postulated.

In this paper we report on our efforts to determine the feasibility of employing such a constitutive theory for shock wave-spall fracture studies. However, prior to incorporating the constitutive theory into a general wave propagation computer code, it was considered advisable first to examine the predictive capability of the theory. Toward this end a technique was employed for simulating the uniaxial strain-time history that accompanies passage of multiaxial stress waves typical of flyer plate-target plate impact. In experiments of this kind, impact is produced by flyer plates travelling at velocities of several hundred meters per second. For thin target plates the initial compressive and reflected tensile stress/displacement pulses travel across the plate thickness in about 10^{-7}–10^{-6} s, producing strain rates of the order of 10^{4}–10^{6} s^{-1} in the target plate material.

[1] This paper is based on work submitted by the lead author in partial fulfillment of the requirements for a D.Sc. from George Washington University.

Contributed by the Applied Mechanics Division of THE AMERICAN SOCIETY OF MECHANICAL ENGINEERS for publication in the JOURNAL OF APPLIED MECHANICS.

Discussion on this paper should be addressed to the Technical Editor, Leon M. Keer, The Technological Institute, Northwestern University, Evanston, IL 60208, and will be accepted until two months after final publication of the paper itself in the JOURNAL OF APPLIED MECHANICS. Manuscript received by the ASME Applied Mechanics Division, October 4, 1988; final revision, July 1, 1989.

[2] The terms "voids" and "microvoids," here used indiscriminately, are meant to describe microstructural features on the scale of 10^{-2}–10^{-4} cm, several orders of magnitude greater than the scale of dislocation phenomena.

Copyright © 1990 by ASME
Downloaded 03 May 2010 to 171.66.16.244. Redistribution subject to ASME license or copyright; see http://www.asme.org/terms/Terms_Use.cfm

The constitutive theory in its present form presumes isothermal and adiabatic deformation. Its applicability is therefore limited to moderate shocks where deformation-induced temperature changes are negligible. Here "moderate shock" is meant to imply circumstances where the peak mean stress levels are in the low shock stress range, (5-50 kbar). With a characteristic time of the order of microseconds, the assumption of adiabatic deformation of the target plate material is considered to be a realistic approximation.

In the course of our study we have found it necessary to replace the linear isotropic hardening rule originally proposed by Perzyna, with a nonlinear hardening rule that admits saturation of the hardening as the strain progresses. As a consequence of this revision, the equations that serve to describe the growth rate of the microvoids had to be rederived. The reasons that compel such modification of the originally proposed constitutive equations are discussed in the following section.

2 Elastic-Viscoplastic Solid With Voids

2.1 Constitutive Equations. The rate of deformation tensor $\mathbf{D}$ is assumed to be linearly separable into elastic and viscoplastic components

$$\mathbf{D} = \mathbf{D}^e + \mathbf{D}^p. \tag{1}$$

The constitutive equation for the elastic rate of deformation presumes small-order recoverable deformation and has, therefore, the linear form

$$\mathbf{D}^e = \frac{1}{2\bar{\mu}}\left[\overset{\nabla}{\mathbf{T}} - \frac{\bar{\nu}}{1+\bar{\nu}}\left(tr\overset{\nabla}{\mathbf{T}}\right)\mathbf{1}\right], \tag{2}$$

where $\overset{\nabla}{\mathbf{T}}$ designates the Jaumann rate of change of the Cauchy stress tensor, $\mathbf{T}$, and $\mathbf{1}$ denotes the identity tensor. Because of the presence of voids, the elastic shear and bulk moduli $\bar{\mu}$ and $\bar{K}$, respectively, are assumed to be degraded according to the model proposed by MacKenzie (1950) (cf. also Johnson, 1981) whereby

$$\bar{\mu} = \mu(1-\xi)\left(1 - \frac{6K+12\mu}{9K+8\mu}\xi\right) \tag{3}$$

$$\bar{K} = \frac{4\mu K(1-\xi)}{4\mu+3K\xi}.$$

As a result, the Poisson ratio $\bar{\nu}$ for the voided solid is determined by the relation

$$\bar{\nu} = \frac{1}{2}\,\frac{3\bar{K}-2\bar{\mu}}{3\bar{K}+\bar{\mu}}. \tag{4}$$

In these expressions, ξ is the void volume fraction $\xi = (V - V_s)/V$ of the material, where V is the volume of a material element and V_s is the volume of the solid constituent of that material element. K and μ are the value of the moduli for the nonvoided solid. Actually, the solid with zero-void volume fraction, i.e., $\xi = 0$, represents an idealization of the polycrystalline material that contains some volume of voids, although small, with typical average initial void volume fraction ξ_0 of the order 10^{-3}-10^{-4}.

The inelastic rate of deformation has the form (Perzyna (1986))

$$\mathbf{D}^p = \frac{\gamma}{\phi}\Phi(\hat{F})\frac{\partial f}{\partial \mathbf{T}} \qquad \text{for } \hat{F} > 0,$$

$$\mathbf{D}^p = 0 \qquad \text{for } \hat{F} \le 0, \tag{5}$$

where Φ is a material functional of the yield function

$$\hat{F} = \frac{f}{\kappa} - 1, \tag{6}$$

and ϕ is the rate of deformation control function that depends upon the argument $(I_2/I_2^s - 1)$, and is defined to be such that $\phi(0) = 0$ and $\phi(\ldots) \equiv 0$ for $I_2 < I_2^s$. The invariant

$$I_2 = \|(II_{\mathbf{D}})^{\frac{1}{2}}\| = \left\|\left\{\frac{1}{2}(tr\mathbf{D})^2 - \frac{1}{2}tr(\mathbf{D}\cdot\mathbf{D})\right\}^{\frac{1}{2}}\right\|, \tag{7}$$

and I_2^s is the value of I_2 at the quasi-static rate of deformation.[3] Also,

$$\gamma = \frac{\gamma_0}{\kappa_0}, \tag{8}$$

where γ_0 is the material viscosity constant and κ_0 is a material parameter related to the rate-independent (quasi-static) initial yield stress. Because of the compressibility of the voids, the plastic deformation of the voided solid will also be compressible. Consequently, the yield function f is taken to have the form (cf., Shima and Oyane, 1976; Hancock, 1983; Doraivelu et al., 1984)

$$f = f(J_1, J_2', \xi) = J_2' + n\xi J_1^2. \tag{9}$$

The stress invariants

$$J_1 = tr\mathbf{T}$$

$$J_2' = -II_{\mathbf{T}}' = -\frac{1}{2}tr(\mathbf{T}'\cdot\mathbf{T}'), \tag{10}$$

where

$$\mathbf{T}' = \mathbf{T} - \frac{1}{3}(tr\mathbf{T})\mathbf{1}, \tag{11}$$

is the stress deviator. The coefficient n is a material parameter.

The function κ represents the material isotropic work hardening-softening behavior and is assumed to have the form

$$\kappa = \kappa(\epsilon^p, \xi) = [\kappa_0 + H\epsilon^p]^2\left[1 - n_1\xi^{\frac{1}{2}}\right]^2, \tag{12}$$

in which ϵ^p is the equivalent plastic strain invariant

$$\epsilon^p = \int_0^t \frac{2}{\sqrt{3}}\|(II_{\mathbf{D}^p})^{\frac{1}{2}}\|dt'. \tag{13}$$

H is a work-hardening coefficient and n_1 is a material parameter. We note that the isotropic hardening of the material constituent of the voided solid has a monotonically increasing linear hardening form $(\kappa_0 + H\epsilon^p)$.

In the course of developing ductile spall fractures of polycrystalline metals, metallographic observations have shown that the void volume fraction will increase, typically, by approximately two orders of magnitude, e.g., $\xi_0 \cong 0.001 \rightarrow \xi_F \cong 0.100$ (cf., Curran et al., 1987). At the microvoid scale this order of change of the void volume fraction is associated with relatively large strains that occur around and between the perimeters of the microvoids. A linear monotonically increasing hardening rule will, under such circumstances, predict intense hardening, leading to a situation where the void growth threshold mean stress becomes overwhelmingly large, thereby preventing further void growth and the concomitant stress relaxation at the larger strains. (This result is discussed and demonstrated in more detail in the following section.) Consequently, the linear hardening rule is replaced by a more realistic nonlinear hardening rule, one that allows for the saturation of the hardening of the material con-

[3] Quasi-static rate of deformation is meant here to signify the strain rate below which no significant rate effect of the viscoplastic material response can be observed by the usual means of laboratory testing.

Downloaded 03 May 2010 to 171.66.16.244. Redistribution subject to ASME license or copyright; see http://www.asme.org/terms/Terms_Use.cfm

stituent as the strain progresses. Thus, in place of (12), we introduce the isotropic hardening-softening relation

$$\kappa = [q + (\kappa_0 - q)e^{-\beta\epsilon^p}]^2\left[1 - n_1\xi^{\frac{1}{2}}\right]^2, \tag{14}$$

where q is the saturation hardening stress and β is a material hardening parameter.

The material functional, Φ, and the rate of deformation control function, ϕ, are taken as simple power functions of their arguments:

$$\Phi(\hat{F}) = \left(\frac{f(J_1, J_2', \xi)}{\kappa(\epsilon^p, \xi)} - 1\right)^{m_1} \tag{15}$$

$$\phi\left(\frac{I_2}{I_2^s} - 1\right) = \left(\frac{I_2}{I_2^s} - 1\right)^m. \tag{16}$$

These forms, together with expressions (9) and (14), upon insertion into $(5)_1$, yield the following constitutive equation for the nonlinear hardening viscoplastic solid with microvoids

$$\mathbf{D}^p = \frac{\gamma_0}{\left(\frac{I_2}{I_2^s} - 1\right)^m} \times \left[\frac{J_2' + n\xi J_1^2}{[q + (\kappa_0 - q)e^{-\beta\epsilon^p}]^2\left[1 - n_1\xi^{\frac{1}{2}}\right]^2} - 1\right]^{m_1} \times \frac{1}{\kappa_0}(2n\xi J_1\mathbf{1} + \mathbf{T}'). \tag{17}$$

Forming the trace of $\mathbf{D}^p$ as expressed by $(5)_1$ leads to the relation

$$\Phi(\hat{F}) = \frac{\{tr(\mathbf{D}^p \cdot \mathbf{D}^p)\}^{\frac{1}{2}}}{\gamma} \phi\left\{tr\left(\frac{\partial f}{\partial \mathbf{T}} \cdot \frac{\partial f}{\partial \mathbf{T}}\right)\right\}^{-\frac{1}{2}}. \tag{18}$$

Inserting expressions (15) and (16) and making use of the relation

$$\frac{\partial f}{\partial \mathbf{T}} = 2n\xi J_1\mathbf{1} + \mathbf{T}' \tag{19}$$

results in the following expression for f in (9)

$$J_2' + n\xi J_1^2 = [q + (\kappa_0 - q)e^{-\beta\epsilon^p}]^2\left[1 - n_1\xi^{\frac{1}{2}}\right]^2 \times \left\{1 + \left[\frac{\{tr(\mathbf{D}^p \cdot \mathbf{D}^p)\}^{\frac{1}{2}}}{\gamma_0}\left(\frac{I_2}{I_2^s} - 1\right)^m \times \kappa_0(12n^2\xi^2 J_1^2 + 2J_2')^{-\frac{1}{2}}\right]^{\frac{1}{m_1}}\right\}, \tag{20}$$

which is interpreted as the dynamical yield condition for the voided solid. It describes the continuous change of the yield surface as a consequence of the isotropic hardening, the rate sensitivity of the inelastic deformation, and the material degradation or damage caused by the nucleation and growth of the microvoids.

2.2 Void Growth Relations. The void volume fraction ξ of the solid with microvoids constitutes the material damage, and is considered to consist of distinct stages characterized by three different micromechanisms, namely, void diffusion, void nucleation, and void growth. Thus the porosity growth rate $\dot{\xi}$ for the material is the sum of growth rates

$$\dot{\xi} = \dot{\xi}_{\text{diff}} + \dot{\xi}_{\text{nucl}} + \dot{\xi}_{\text{grow}}. \tag{21}$$

At nonelevated temperatures, diffusional microprocesses creating void growth are not significant. Therefore, the accumulation of damage can be defined as consisting of nucleation and growth of microvoids.

Nucleation occurs as the creation of new voids, adding to the voids already existing, in the polycrystalline solid. For dynamical processes the thermally-activated mechanism of void nucleation is considered most important and is taken to have the form (cf. Curran et al., 1987, 1977; Seaman et al., 1976)

$$\dot{\xi}_{\text{nucl}} = \frac{h(\xi)}{1 - \xi}\left[\exp\left(\frac{m_2|\sigma - \sigma_N|}{k\theta}\right) - 1\right], \quad \sigma < \sigma_N \tag{22}$$

where $\sigma = (1/3)J_1$ is the mean stress,[4] σ_N is the threshold mean stress for void nucleation, θ is the temperature, k is the Botzmann constant, and m_2 is a material constant. The function $h(\xi)$ represents a void nucleation material function that is introduced to take account of the effect of microvoid interaction (due to the appearance of new voids and growth of the existing ones).

The rate of void growth is determined from an analysis of the collapse of voids in porous ductile solids, developed originally by Carroll and Holt (1972). The model for the porous solid considers a random distribution of microvoids, idealized as spherical holes of arbitrary size (on the microscale), in an elastic-perfectly plastic material. The nonrecoverable (plastic) volume change of the porous solid is taken to be caused entirely by the plastic deformation of the material. Rate dependence for the inelastic deformation was subsequently introduced into the model by Johnson (1981), followed by the inclusion of linear isotropic work hardening by Perzyna (1986). As indicated previously, the linear isotropic hardening rule gives predictive behavior that is physically unsatisfactory, and consequently was replaced by the nonlinear hardening rule that saturates with increasing strain. Thus, for the porous work-hardening viscoplastic solid, the rate of void growth can be expressed by the set of relations

$$\dot{\xi}_{\text{grow}} = \frac{1}{\eta} g(\xi)F(\xi, \xi_0)(\sigma - \sigma_G), \text{ for } \sigma < \sigma_G \tag{23}$$

where

$$F(\xi, \xi_0) = \frac{\sqrt{3}}{2}\xi\left(\frac{1 - \xi}{1 - \xi_0}\right)^{\frac{2}{3}}\left[\xi - \left(\frac{\xi}{\xi_0}\right)^{\frac{2}{3}}\right]^{-1} \tag{24}$$

$$\sigma_G = -\frac{k_1}{\sqrt{3}}(1 - \xi)\ln\left(\frac{1}{\xi}\right)[2q + (\kappa_0 - q)F_1(\xi, \xi_0)] \tag{25}$$

and

$$F_1(\xi, \xi_0) = \exp\left[\frac{2}{3}\beta\frac{(\xi_0 - \xi)}{\xi(1 - \xi_0)}\left(\frac{1 - \xi}{1 - \xi_0}\right)^{-\frac{2}{3}}\left(\frac{\xi_0}{\xi}\right)^{-\frac{2}{3}}\right] + \exp\left[\frac{2}{3}\beta\frac{(\xi_0 - \xi)}{(1 - \xi_0)}\left(\frac{1 - \xi}{1 - \xi_0}\right)^{-\frac{2}{3}}\right]. \tag{26}$$

In these expressions ξ_0 is the initial average void volume frac-

[4] Tensile stresses are taken as negative.

Downloaded 03 May 2010 to 171.66.16.244. Redistribution subject to ASME license or copyright; see http://www.asme.org/terms/Terms_Use.cfm

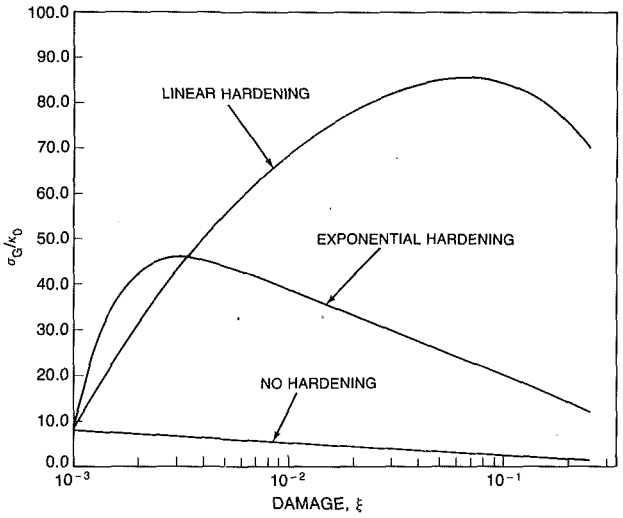


Fig. 1 Void growth threshold stress for three hardening assumptions

tion, σ_G is the void growth threshold mean stress, η and k_1 are material parameters, $g(\xi)$ is a material function. As with the material function $h(\xi)$, it is included to account for void interaction. Both functions serve to hasten the void nucleation and growth process and, therefore, are associated with the void coalescence that subsequently develops and that leads to material separation.

The rate of evolution of the void volume fraction that appears in the constitutive equations is thus determined from the combined rates

$$\dot{\xi} = \frac{h(\xi)}{1-\xi}\left[\exp\left(\frac{m_2\,|\sigma-\sigma_N|}{k\theta}\right)-1\right] + \frac{1}{\eta}g(\xi)F(\xi,\xi_0)(\sigma-\sigma_G). \tag{27}$$

For a linear isotropic hardening assumption (cf. equation 12)) the void growth rate is also given by equations (23) and (24). However, the expression for the threshold mean stress (25) will now have the form (Perzyna, 1986)

$$\sigma_G = -k_1\left[\frac{2}{3}\kappa_0(1-\xi)\ln\left(\frac{1}{\xi}\right) + \frac{2}{3}H(1-\xi)F_2(\xi,\xi_0)\right], \tag{28}$$

where

$$F_2(\xi,\xi_0) = 3\left(\frac{1-\xi}{1-\xi_0}\right)^{\frac{1}{3}}\left[1-\left(\frac{\xi_0}{\xi}\right)^{\frac{1}{3}}\right]. \tag{29}$$

Figure 1 shows a comparison of the variation of the void growth threshold stress σ_G with increase of porosity for no hardening, and for nonlinear (exponential) and linear isotropic hardening. The linear hardening causes a peak value of approximately twice the peak value for σ_G obtained for the nonlinear hardening. Furthermore, the peak value for σ_G for the linear hardening occurs at approximately 20 times the value for ξ that it does for the nonlinear hardening. The effect of monotonically increasing linear hardening at advanced strains, or at the large void volume fractions, is to provide for an unrealistic excess of hardening, so great as to cause cessation of the void growth process after sufficient strain. This is discussed further in 3.2.2.

2.3 Criterion for Ductile Spall Fracture. Shock-induced ductile fracture at high strain rates is a cooperative phenomena between inelastic deformation and the corresponding micro-damage that is generated by high mean stress pulses of sufficient amplitude and duration to cause local nucleation, growth, and coalescence of microvoids. Micrographic examination of spall fractured plates show the greatest concentration of microvoids at the surfaces of separation. Consequently, a local spall fracture criterion can be based upon the attainment of a critical microvoid volume fraction ξ_F (cf. Perzyna, 1984, 1986). Thus any point of the body will experience spall fracture when $\xi = \xi_F$. As material separation occurs, the material relinquishes its stress carrying capacity, with corresponding catastrophic increase of the rate of inelastic deformation. It follows from (15) and (5) that

$$\kappa = \kappa(\epsilon^p,\xi)_{\xi=\xi_F} = 0 \tag{30}$$

which leads to the condition

$$[q+(\kappa_0-q)e^{-\beta\epsilon^p}]^2\left[1-n_1\xi_F^{\frac{1}{2}}\right]^2 = 0. \tag{31}$$

from which the material constant n_1 can be identified as

$$n_1 = \frac{1}{(\xi_F)^{\frac{1}{2}}}. \tag{32}$$

Thus, the condition for spall fracture, which is determined by a critical value of the damage parameter, or void volume fraction, is incorporated directly into the material constitutive relation.

3 High Strain Rate Application

3.1 Determination of Material Parameters. The parameters required to complete the specification of the elasto-viscoplastic material response are ten in number: $\{\mu, K, q, \beta, I_2^s, \kappa_0, \gamma_0, m, m_1, n\}$. The microvoid volume fraction growth rate equation (27) requires determination of the parameters $\{m_2, \sigma_N, \eta, k_1, \xi_0\}$ and the material functions $g(\xi)$ and $h(\xi)$. Also needed is the void volume fraction at fracture ξ_F. Since temperature sensitivity has not been included in the constitutive equations, evaluation of the material parameters must be at the temperature of interest.

The test program for material parameter evaluation can limit strains to small order, and stress levels to values that are well below the microvoid nucleation and growth thresholds. Thus, the rate of deformation tensor can be approximated by the infinitesimal strain rate tensor, $\mathbf{D} = \dot{\mathbf{E}}$, while with the absence of void growth, $\dot{\xi} = 0$. The very small initial average porosity of the polycrystalline laboratory specimens, $\xi_0 \approx 10^{-3}$–10^{-4}, will remain the same throughout the test program and, consequently, one may consider the laboratory specimens as nonvoided solids, i.e., $\xi = \xi_0 \cong 0$.

The general dynamical yield condition (20), specialized to specific test situations, provides the means enabling direct determination as well as interpretation of several of the viscoplastic material constants. Consider loading at a rate of deformation such that $I_2 = I_2^s$ (i.e., at the quasi-static strain rate). With $\xi = 0$ and $\phi = 0$, equation (20) reduces to

$$J_2' = [q+(\kappa_0-q)e^{-\beta\epsilon^p}]^2 = \kappa(\epsilon^p,0), \tag{33}$$

which represents the quasi-static rate-independent yield condition that allows isotropic strain hardening. In particular if we consider a uniaxial tensile test performed at the quasi-static strain rate, $J_2' = 1/3\ T_{33}^2 \equiv 1/3\ T^2$, $D_{33} = \dot{E}_{33} \equiv \dot{E} = \dot{E}_s$, and at the onset of initial yield $T = T_Y$, $\epsilon^p = 0$. Then, from (33)

$$\kappa_0 = \frac{1}{\sqrt{3}}\,T_Y \text{ at strain rate } \dot{E}_s. \tag{34}$$

The material constant κ_0 represents the rate-independent or quasi-static initial yield stress. Next consider the onset of initial yield approached from the plastic side of the elasto-plastic

Downloaded 03 May 2010 to 171.66.16.244. Redistribution subject to ASME license or copyright; see http://www.asme.org/terms/Terms_Use.cfm

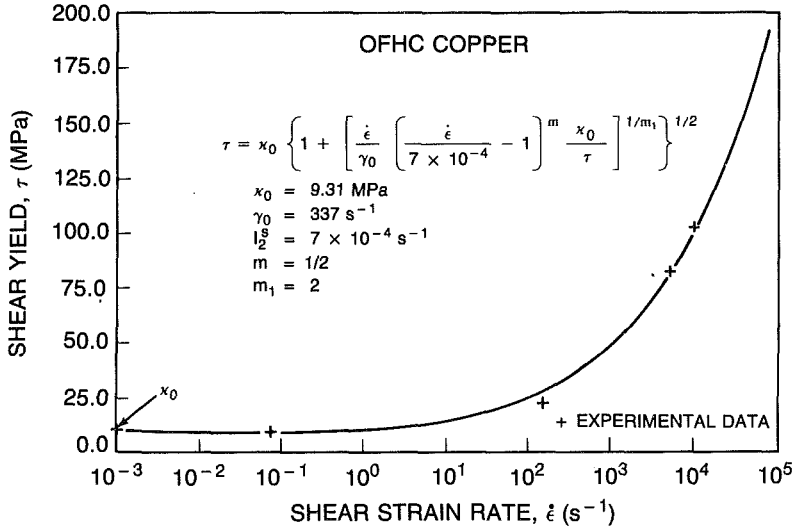


Fig. 2 Dynamical yield expression for pure shear condition compared with data from Dowling et al. (1970)

range of deformation for rates of loading $I_2 > I_2^s$. It follows from (20) that in the limit as $\epsilon^p \to 0$,

$$J_2' = \kappa_0^2 \left\{1 + \left[\frac{\kappa_0}{\gamma_0}\{tr(\mathbf{D}^p \cdot \mathbf{D}^p)\}^{\frac{1}{2}}\left(\frac{I_2}{I_2^s} - 1\right)^m \frac{1}{\sqrt{2J_2'}}\right]^{\frac{1}{m_1}}\right\} \tag{35}$$

which represents the rate dependence of the onset of yield. Further specialized, to uniaxial stress it is easily shown that (35) reduces to the form

$$T_Y = \sqrt{3}\kappa_0 \left\{1 + \left[\frac{3}{2}\frac{\kappa_0}{\gamma_0}\dot E^p \left(\frac{I_2}{I_2^s} - 1\right)^m \frac{1}{T_Y}\right]^{\frac{1}{m_1}}\right\}^{\frac{1}{2}} \tag{36}$$

which illustrates the rate dependence of the uniaxial tensile yield stress for strain rates $I_2 > I_2^s$. As the rate of deformation is reduced to the quasi-static strain rate, that is, as $I_2 \to I_2^s$, T_Y reduces to its lower bound rate-independent value $\sqrt{3}\,\kappa_0$.

Routine uniaxial tensile tests conducted at any strain rate that fall within the range of strain rates of the intended application are sufficient to determine the elastic modulii μ and K. Values for these constants were determined for OFHC copper from test data found in the literature. Uniaxial tensile tests, or simple shear tests, performed over a sufficiently wide range of strain enables determination of the variation of the initial yield stress with change of strain rate, from which values for κ_0 and I_2^s may be determined. The isotropic strain-hardening parameters q and β are determined at the quasi-static strain rate using (33).

In this regard we note that for strain rates below 10^{-1} s^{-1}, standard uniaxial test methods can be used. For the intermediate strain rate range 10^{-1}–10^2 s^{-1}, specialized uniaxial pneumatic/mechanical test machines are available. At the high strain rates beyond 10^2 s^{-1} up to 10^4 s^{-1}, specialized high strain rate test methods such as drop weight punch tests and Hopinkson bar tests have been employed (cf. Nicholas, 1982).

The same set of test data can also be used to determine the parameters γ_0, m, and m_1. Using data for OFHC copper from simple shear punch tests reports by Dowling, Harding, and Campbell (1970), values $\kappa_0 = 9.31$ MP_a and $I_2^s = 7 \times 10^{-4}$ s^{-1} were obtained. A plot of the variation of the initial shear yield stress versus the shear strain rate over the range of strain rates 10^{-3}–10^4 s^{-1} is shown in Fig. 2. For simple shear τ and shear strain rate $\dot\epsilon$, expression (35) for the onset of initial yield reduces to

$$\tau_Y = 9.31\left\{1 + \left[\frac{9.31}{\gamma_0}\dot\epsilon\left(\frac{\dot\epsilon}{7\times10^{-4}} - 1\right)^m \frac{1}{\tau_Y}\right]^{\frac{1}{m_1}}\right\}^{\frac{1}{2}}. \tag{37}$$

Curve fitting equation (37) to the experimental data shown in Fig. 2 determines that $\gamma_0 = 337$ s^{-1}, $m = 1/2$, and $m_1 = 2$.

The parameter n appearing in the yield function (9) serves essentially as a weighting between the deviatoric component, J_2', and the dilatational component, ξJ_1^2, of the stress. Biaxial stress tests to completely determine the yield condition of the voided solid, that is for $\xi_0 < \xi < \xi_F$, are required to evaluate the parameter n. Assuming that such tests are performed at the quasi-static strain rate I_2^s, then with $\epsilon^p = 0$, the condition for onset of initial yield follows from the reduced form of (20) as

$$J_2' + n\xi J_1^2 = \kappa_0^2\left[1 - n_1\xi^{\frac{1}{2}}\right]^2, \quad I_2 = I_2^s. \tag{38}$$

The parameter $n_1 = 1/(\xi_F)^{1/2}$. The void volume fraction at fracture ξ_F can be obtained from microscopic observation of post impact specimens. For ductile dynamic fracture of OFHC copper, ξ_F was determined to be 0.32 (cf. Seaman et al., 1971), so that $n_1 = 1.77$.

The yield condition represented by (38) is shown plotted in Figs. 3(*a*) and 3(*b*) for different values of n, and varying amounts of porosity. As may be seen from the figures, the effect of having a larger value of n is to reduce the dilatational component required to cause yield for the same degree of porosity. The values of n shown in the figures, and used in subsequent calculations, were chosen to illustrate the effect that the parameter has on the yield condition. Actual parameter determination requires multiaxial testing of the material having a porosity ξ higher than the average initial void volume fraction ξ_0 found in polycrystalline metals. For example, for a material porosity of $\xi = 0.10$, a series of tension-torsion yield tests will provide data that can be plotted along $\sqrt{J_2'}/\kappa_0$ and J_1/κ_0 axes. The value of n is determined so as to enable (38) to provide the best curve fit of this data. Using specimens fabricated from powder metallurgy techniques, Shima and Oyanne (1976) and Doraivelu et al. (1984) have performed uniaxial compression and tension tests, which provide data at one particular combination of distortional and dilatational stresses.

Downloaded 03 May 2010 to 171.66.16.244. Redistribution subject to ASME license or copyright; see http://www.asme.org/terms/Terms_Use.cfm

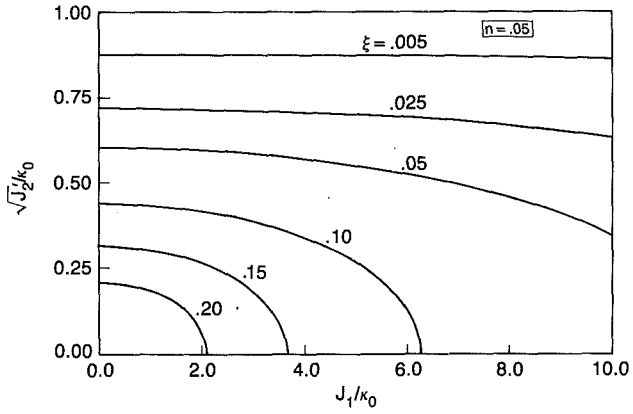


Fig. 3(a)

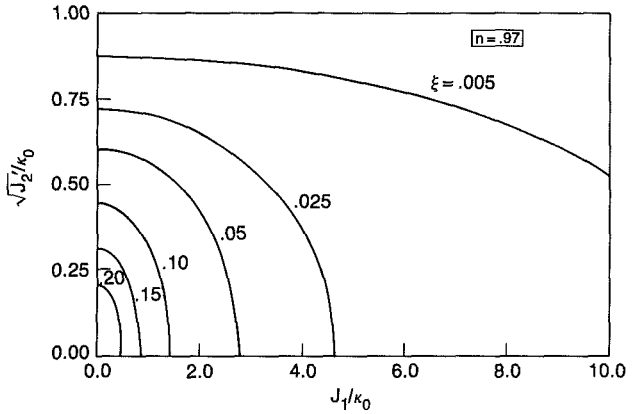


Fig. 3(b)

Fig. 3 Initial yield condition for varying amounts of porosity for (*a*) $n = .05$ and (*b*) $n = .97$

The material parameters and functions, which appear in the microvoid equations, namely σ_N, m_2, k_1, η, $h(\xi)$, and $g(\xi)$, are much more difficult to ascertain than the parameters appearing in the constitutive equations, since for the former, micrographic evaluation is required. Even with this capability, the myriad of phenomena occurring on the microscale makes the development of appropriate experiments that can isolate a single parameter itself a formidable task. Curran et al., (1987), using microscopic observations of materials under various stages of the damage process, have had some success in identifying microscopic parameters. Defining nucleation as the appearance of a void observable on micrographs at a scale of 100x, they found the threshold nucleation stress, σ_N, for OFHC copper to be 500 MPa. At mean stresses below this value, microvoid nucleation is not expected to occur. Also from their data, the nucleation material parameter, m_2 in (22) is found to be 2.025×10^{-23} cm^3. The function $h(\xi)$ is included in (22) to account for enhanced void nucleation that may occur due to microvoid interaction at the later stages of void development. Determination of such a function is difficult. In the calculations presented here, $h(\xi)$ is taken to have a constant value, which was obtained from the nucleation rate and nucleation size parameters identified by Curran et al., (1987). A value of 70.37 is utilized. The function $g(\xi)$ has been included in (23) to account for enhanced void growth during the coalescence stage of void development. Because of a lack of information, $g(\xi)$ is here taken to have a constant value at unity. For similar reasons, the coefficient, k_1, that serves as a proportionality factor in expression (25) for the void growth threshold stress, is also taken to have the value unity. The void growth material parameter appearing in (23) was given the value $\eta = 10$ Poise, suggested by Johnson (1981) for OFHC copper.

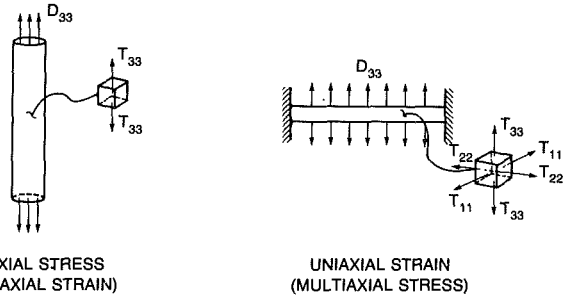


Fig. 4 Schematic of the idealized uniaxial stress and uniaxial strain conditions

A summary of the material parameters used in the calculations is presented in Table 1.

3.2 Uniaxial Stress and Strain.

3.2.1 Uniaxial Stress Without Void Growth. Consider uniaxial stress, say T_{33} with corresponding rate of deformation D_{33} (cf. Fig. 4), where the deformation proceeds without void growth, that is, for $\dot{\xi} = 0$ and $\xi = \xi_0 \cong 0$. For these circumstances constitutive equations (1), (2), and (17) reduce to

$$\dot{T}_{33} = \frac{1}{E} D_{33}, \text{ for } \hat{F} \leq 0$$

$$\dot{T}_{33} = \frac{1}{E}\left\{D_{33} - \frac{\gamma_0}{\left(\frac{I_2}{I_2^s} - 1\right)^m} \times \left[\frac{\frac{1}{3}T_{33}^2}{[q + (\kappa_0 - q)e^{-\beta\epsilon^p}]^2} - 1\right]^{m_1} \frac{2}{3}\frac{T_{33}}{\kappa_0}\right\}, \text{ for } \hat{F} > 0. \tag{39}$$

Since the deformation is without rotation, $\overset{\nabla}{T}_{33} = \dot{T}_{33}$, where the dot here signifies material time differentiation, and $E = 2(1+\nu)\mu$ is Young's elastic modulus. Without void volume change the plastic deformation is volume preserving and, because of the symmetry of the deformation, $D_{11}^p = D_{22}^p = -1/2\ D_{33}^p$. The equivalent plastic strain (13) accordingly simplifies to

$$\epsilon^p = \int_0^t D_{33}^p dt'. \tag{40}$$

Without shear it follows from (7) that

$$I_2 = \left\| (D_{11}D_{22} + D_{11}D_{33} + D_{22}D_{33})^{\frac{1}{2}} \right\|. \tag{41}$$

Once yield has taken place, however, the elastic rate of deformation becomes a relatively small part of the overall rate of deformation and $\mathbf{D} \cong \mathbf{D}^P$. Thus, in view of the symmetry equation, (41) is well approximated by

$$I_2 \cong \frac{\sqrt{3}}{2} D_{33}^p \cong \frac{\sqrt{3}}{2} D_{33}, \tag{42}$$

which is a convenient approximation, since it is D_{33} that is actually measured in a laboratory test.

Using the material parameter values listed in Table 1, equations (39)–(42) can be solved numerically, yielding the stress-strain curves shown in Fig. 5. The strain measure, E_{33}, is one of the axial components of the Eulerian strain tensor, $\mathbf{E}$, determined by time integration of the Eulerian strain rate tensor.

Downloaded 03 May 2010 to 171.66.16.244. Redistribution subject to ASME license or copyright; see http://www.asme.org/terms/Terms_Use.cfm

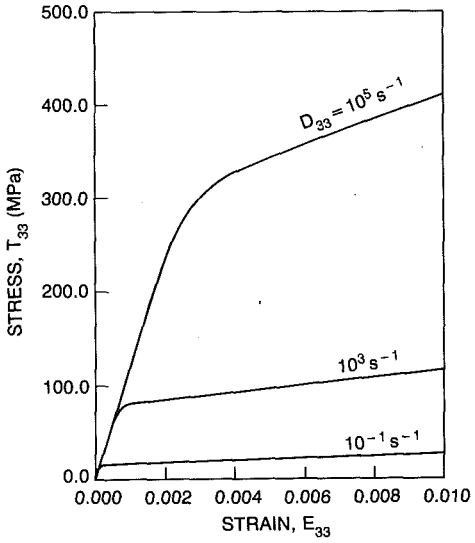


Fig. 5 Predicted uniaxial stress versus strain response for uniaxial stress condition at different strain rates

For the small strains indicated in Fig. 5, the rate of deformation is approximated by the strain rate and, therefore, $D_{33}=\dot{E}_{33}$. (The dot here denotes ordinary time derivative). The sensitivity of the yield stress to strain rate is shown to be pronounced at the high strain rates, qualitatively similar to the experimental data for copper reported by Nicholas (1982); and Dowling et al., (1970). Because of the small range of strain shown in Fig. 5, saturation of the hardening does not as yet begin to mainifest itself in these curves for the soft copper material.

3.2.2. Uniaxial Strain. The physical possibility of having a state of one-dimensional deformation may be observed, for example, in nonoblique plate impact experiments where a high velocity flyer plate collides with a thin target plate, making planar contact over an area that is very large compared to the target plate thickness. Orienting the X_3-rectangular coordinate direction parallel to the thickness direction of the rectangular target plate, the motion associated with uniaxial strain (shown schematically in Fig. 4) is given by the equations of motion

$$x_1=X_1$$
$$x_2=X_2$$
$$x_3=f(X_3,t) \quad , \tag{43}$$

where x_k, X_k are the rectangular spatial and referential coordinates, respectively. The function f is assumed to be positive valued, continuous, and differentiable. With $v_3=\partial f/\partial t$ as the only nonzero component of the velocity vector, the velocity gradient $\mathbf{L}$ has only one nonzero component $L_{33}=\partial v_3/\partial x_3$, and the spin tensor $\mathbf{W}=1/2(\mathbf{L}-\mathbf{L}^T)=\mathbf{0}$. The deformation produces no rotation and $\mathbf{D}=\mathbf{L}$. Thus, $D_{33}=L_{33}$ and all of the other components D_{jk} of $\mathbf{D}$ have the value zero. It follows, as may be easily shown, that $II_{\mathbf{D}}=0$ and, therefore, that the invariant $I_2=0$. This result causes the control function ϕ to assume the value $\phi=0$, since $\phi(\ldots)=0$ for $I_2\le I_2^S$. From expressions (20), (14), and (9), it follows that $f=\kappa$ and the yield becomes rate independent, which is clearly undesirable. In order to avoid this outcome, in the argument for ϕ, shown by (16), I_2 is replaced by I_2', which is the norm of the second invariant of the deviator of the rate of deformation $\mathbf{D}'=\mathbf{D}-1/3(tr\mathbf{D})\mathbf{1}$, i.e.,

$$I_2'=\left\|II_{\mathbf{D}'}^{\frac{1}{2}}\right\|=\left\|\left\{-\frac{1}{2}tr(\mathbf{D}'\cdot\mathbf{D}')\right\}^{\frac{1}{2}}\right\| \tag{44}$$

which is nonzero.

The uniaxial strain produces no rotation and no shear stress with respect to the coordinate directions. Therefore, the Cauchy stress tensor has only its principal values T_{kk} $k=1,2,3$, $T_{jk}=0$, $j\neq k$, with $T_{11}=T_{22}$ because of in-plane symmetry. In addition, since $\mathbf{W}=\mathbf{0}$, the Jaumann stress rate reduces to the material time derivative $\overset{\nabla}{\mathbf{T}}=\dot{\mathbf{T}}$. With these results the constitutive equations appropriate for uniaxial strain follow from (1), (2) and (17) as

$$\frac{1}{2\tilde{\mu}}\left[\dot{T}_{11}-\frac{\tilde{\nu}}{1+\tilde{\nu}}(2\dot{T}_{11}+\dot{T}_{33})\right]=0 \tag{45}$$

for $\hat{F}\le 0$

$$\frac{1}{2\tilde{\mu}}\left[\dot{T}_{33}-\frac{\tilde{\nu}}{1+\tilde{\nu}}(2\dot{T}_{11}+\dot{T}_{33})\right]=D_{33} \tag{46}$$

and

$$\frac{1}{2\tilde{\mu}}\left[\dot{T}_{11}-\frac{\tilde{\nu}}{1+\tilde{\nu}}(2\dot{T}_{11}+\dot{T}_{33})\right]=$$

$$-\frac{\gamma_0}{\left(\frac{I_2'}{I_2'^s}-1\right)^m}\left[\frac{J_2'+n\xi J_1^2}{[q+(\kappa_0-q)e^{-\beta\epsilon^p}]^2\left[1-n_1\xi^{\frac{1}{2}}\right]^2}-1\right]^{m_1}$$

$$\times\frac{1}{\kappa_0}(2n\xi J_1+T_{11}') \tag{47}$$

$$\frac{1}{2\tilde{\mu}}\left[\dot{T}_{33}-\frac{\tilde{\nu}}{1+\tilde{\nu}}(2\dot{T}_{11}+\dot{T}_{33})\right]=D_{33}-\frac{\gamma_0}{\left(\frac{I'^2}{I_2'^s}-1\right)^m}$$

$$\times\left[\frac{J_2'+n\xi J_1^2}{[q+(\kappa_0-q)e^{-\beta\epsilon^p}]^2\left[1-n_1\xi^{\frac{1}{2}}\right]^2}-1\right]^{m_1}$$

$$\times\frac{1}{\kappa_0}(2n\xi J_1+T_{33}') \tag{48}$$

for $\hat{F}>0$. The void volume fraction ξ appearing in (47) and (48) is determined concurrently from (27), whereas

$$J_1=2T_{11}+T_{33}$$
$$J_2'=\frac{1}{3}[T_{11}^2-2T_{11}T_{33}+T_{33}^2] \tag{49}$$
$$I_2'=\frac{1}{\sqrt{3}}D_{33}$$
$$\epsilon^p=\int_0^t\frac{2}{\sqrt{3}}\left\|((D_{11}^p)^2+2D_{11}^pD_{33}^p)^{\frac{1}{2}}\right\|dt'.$$

We consider first the stress-uniaxial strain response without void growth. Uniaxial strain without void growth arises, for example, when the impact-induced compressive wave pulses are traveling across the target plate thickness. Setting $\xi=\xi_0\cong 0$ and $\tilde{\mu}=\mu$, $\tilde{\nu}=\nu$ in equations (45)–(48), for a given rate of deformation D_{33}, the resulting set of coupled nonlinear differential equations can be solved incrementally for the stress variables T_{33} and T_{11}. Figure 6 illustrates the predicted stress-uniaxial strain response for the OFHC copper. The general features of these curves are qualitatively similar to the experimentally constructed stress-uniaxial strain curves for aluminum 1060 reported by Karnes (1968). As with the

Downloaded 03 May 2010 to 171.66.16.244. Redistribution subject to ASME license or copyright; see http://www.asme.org/terms/Terms_Use.cfm

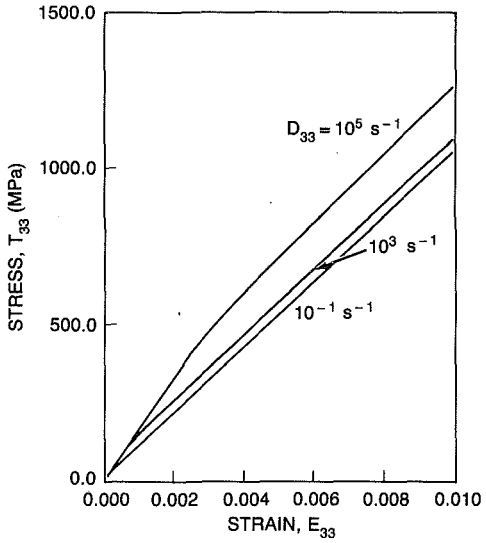


Fig. 6 Predicted stress versus uniaxial strain response for uniaxial strain condition at different strain rates

predicted uniaxial stress-strain response, they also demonstrate the strong increase of the yield stress (in this situation the Hugoniot elastic limit) as high strain rates are approached, as well as the relative softness of copper.

The predicted response of the material for uniaxial strain with void volume increase requires calculation of equations (24)–(27) in conjunction with equations (47) and (48). The results for OFHC copper are shown in Figs. 7(*a*)–7(*c*) for three rates of deformation. In Fig. 7(*a*), and in the following figures, the negative designations signify tensile stress and tensile strains. The stress-strain curves again illustrate the strong strain rate hardening, and when contrasted with Fig. 6, show the dramatic softening effect (relaxation of stress) caused by the growing microvoid volume as the strain develops. The softening continues until the stress is reduced to the smaller of the void nucleation and growth threshold stress values σ_N and σ_G. This may be seen also from the curves of damage versus strain of Fig. 7(*b*). The leveling off of the damage as the strain is increased is an indication that the stress has relaxed to the threshold stress level. This figure also shows that at a given value of the void volume fraction there will be larger strains as the strain rate is increased. In other words at the very high strain rates the rate of deformation out races, so to speak, the rate of damage increase with strain. This effect can also be observed in Fig. 7(*a*) where with increase of strain rate the strain, and thus the stress, becomes greater at the point where the pronounced softening begins. Figure 7(*c*) gives an indication of the strong influence of the rate of deformation on the time rate of damage accumulation. The leveling off of the damage with time again indicates relaxation of the stress to the threshold stress values.

The microvoid growth threshold stress given by equation (25) includes a nonlinear exponential contribution that saturates with increasing void volume, stemming from the exponential isotropic strain hardening shown in (14). This is a modification of the linear strain hardening in (12), employed by Perzyna (1986), which leads to the threshold stress given by (18), and of the perfectly plastic (no hardening) material behavior considered by Johnson (1981). The void growth threshold stress for Johnson's calculation is obtained from (28) by setting $H=0$. The effect that these strain hardening assumptions have on the threshold stress σ_G was discussed previously and shown in Fig. 1. The effect that the different isotropic hardening assumptions have on the predicted stress-strain response at strain rate $4\times10^5 s^{-1}$ is shown in Fig. 8. As expected, the linear strain hardening assumption gives the

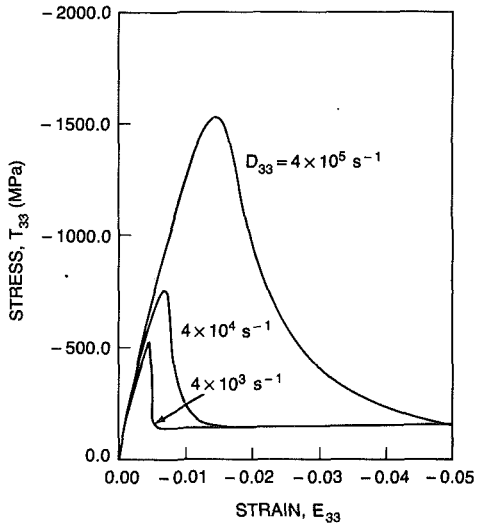


Fig. 7(*a*)

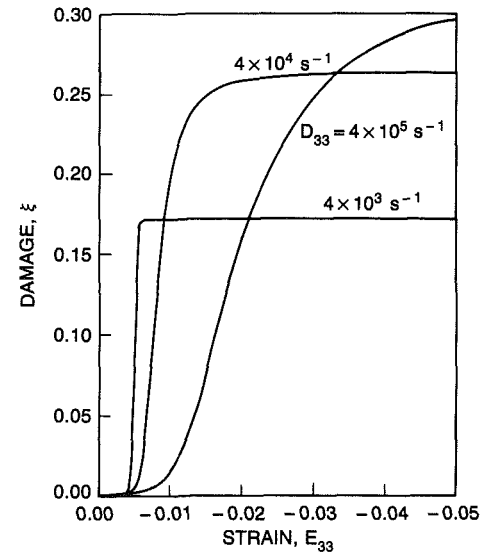


Fig. 7(*b*)

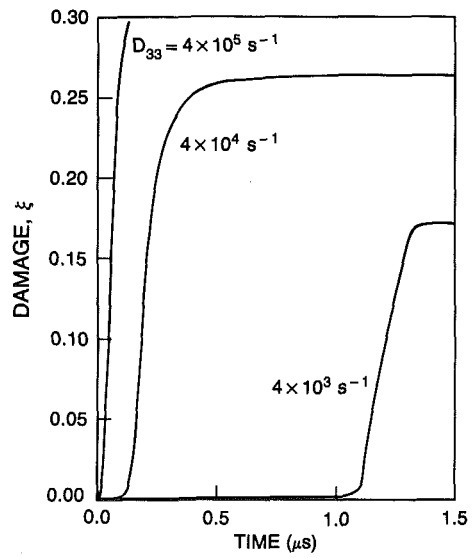


Fig. 7(*c*)

Fig. 7 Predicted response under uniaxial strain conditions with damage at different strain rates (*a*) stress versus strain, (*b*) damage versus strain, (*c*) damage versus time

Downloaded 03 May 2010 to 171.66.16.244. Redistribution subject to ASME license or copyright; see http://www.asme.org/terms/Terms_Use.cfm

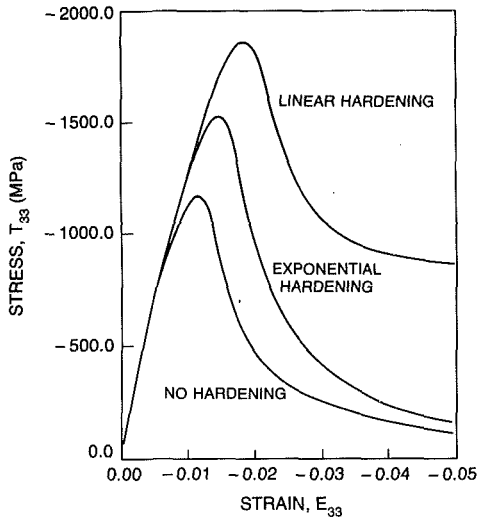


Fig. 8 Effect of hardening assumption on the stress versus uniaxial strain response for uniaxial strain conditions at $D_{33} = 4 \times 10^5\ s^{-1}$

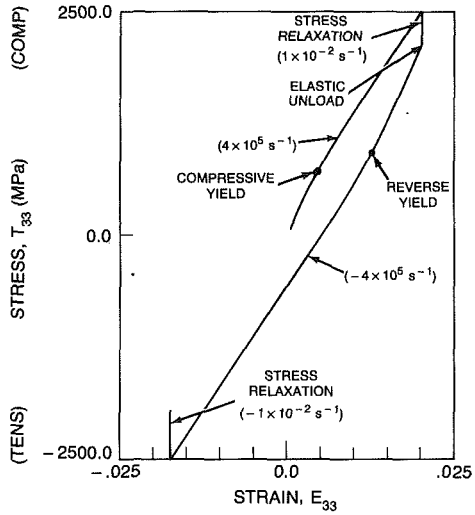


Fig. 9 Predicted stress versus uniaxial strain response to a simulated compressive-tensile wave deformation cycle

highest maximum stress while no hardening results in the lowest maximum stress. The linear strain hardening, however, causes the stress reduction due to void volume increase to virtually cease at a high stress level, rather than continuing on with further increase of strain as would be expected on physical grounds. Thus, the exponential strain hardening assumption gives a more realistic prediction of the softening associated with the microvoid growth.

3.2.3 Simulation of Spall Fracture. As mentioned previously, in plate impact experiments conducted to study spallation, propagation of longitudinal waves occurs within the target plate. The central portion of the target plate will experience a compressive wave followed by a tensile wave with mean stress levels sufficient to cause material damage and spallation. Therefore, material points within this region are subjected to a single compressive-tensile uniaxial strain cycle. The response of the material to such a cycle can be predicted using (27) and (45)–(49). The specified rates of deformation selected to simulate the passage of a compressive-tensile wave are:

$$D_{33} = \begin{cases} 4.0 \times 10^5\ s^{-1} & 0 < t \le 5.0 \times 10^{-8}\ s \\ 1.0 \times 10^{-2}\ s^{-1} & 5.0 \times 10^{-8} < t \le 5.0 \times 10^{-7}\ s \\ -4.0 \times 10^5\ s^{-1} & 5.0 \times 10^{-7} < t \le 5.95 \times 10^{-7}\ s \\ -1.0 \times 10^{-2}\ s^{-1} & 5.95 \times 10^{-7} < t \le 1.0 \times 10^{-6}\ s \end{cases}. \tag{50}$$

The response of the material with no void growth ($\dot{\xi} = 0$, $\xi = \xi_0 \cong 0$) is considered first. The predicted response to the rate of deformation history is shown in Fig. 9. The material behaves elastically until the compressive yield stress is reached. Thereafter, plastic deformation takes place at strain rate $4 \times 10^5\ s^{-1}$ until at .020 strain, the strain rate is reduced to $1 \times 10^{-2}\ s^{-1}$. At this point a significant amount of stress relaxation takes place as a result of the drop in the strain rate. Thereafter, the direction of strain is reversed and the material unloads elastically until reversed yield is reached. Since the constitutive equation considers only isotropic hardening, the reverse yield takes place after a stress difference that is equal to the sum of the value of the yield stress when reversed deformation began and the yield at the higher rate of deformation. It is interesting to note that for uniaxial strain, the reversed yield takes place while the stress is still compressive. The plastic deformation continues at strain rate $-4 \times 10^5\ s^{-1}$ into the tensile region until the deformation rate is reduced to $-1 \times 10^{-2}\ s^{-1}$ and stress relaxation again takes place.

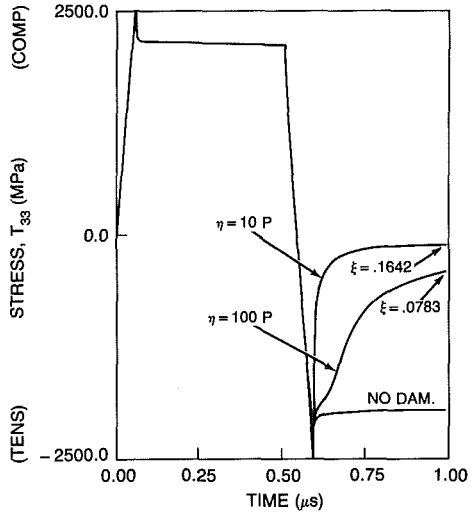


Fig. 10 Predicted stress history to a simulated compressive-tensile wave deformation cycle (no damage, damage with $\eta = 10P$, and damage with $\eta = 100P$). Porosity at the end of the cycle is shown.

The response of the material with voids is identical to that in Fig. 9 in the compressive region, since increase in the void volume fraction does not occur until either the nucleation or growth threshold stress is exceeded in tension. At tensile stresses greater than the threshold the response will be different. The effect of the increased void volume can be illustrated best by showing the stress versus time response. This is given in Fig. 10 for the case of no voids, and for void growth for two different values of the material parameter η, which appears in the void growth expression (23). All other parameters are as given in Table 1. The peak tensile stress attained in the cases where void growth takes place is not as great as that for no damage. In addition, the stress relaxation is now due to both the reduction in the specified deformation rate and to the accumulation of damage. The figure also gives the calculated void volume at the end of the cycle. As expected, the higher value of η results in a lower void volume and less stress relaxation. The stress relaxation shown with increase in void volume or damage is characteristic of conditions that occur in spallation. In fact, the shape of the stress reduction shown in Fig. 10

Downloaded 03 May 2010 to 171.66.16.244. Redistribution subject to ASME license or copyright; see http://www.asme.org/terms/Terms_Use.cfm

Table 1 OFHC copper material parameters

$\mu = 4.84 \times 10^4$ MPa	$n = .05$
$K = 10.49 \times 10^4$ MPa	$\xi_0 = .001$
$q = 125$ MPa	$\xi_F = 0.32$
$\beta = 6.14$	$n_1 = 1.77$
$H = 900$ MPa	$\sigma_N = -500$ MPa (tension)
$I_2^S = 7 \times 10^{-4}\ s^{-1}$	$m_2 = 2.025 \times 10^{-23}$ cm^3
$\kappa_0 = 9.31$ MPa	$h = 70.37$
$\gamma_0 = 337\ s^{-1}$	$g = 1$
$m = 1/2$	$k_1 = 1$
$m_1 = 2$	$\eta = 10$ Poise
$k\theta = 4.05 \times 10^{-21}$ J	

is similar to the "spall signal" measurements at the back of the target plate in impact experiments.

4 Summary

A viscoplastic constitutive theory that includes the possibility of describing material degradation has recently been developed by Perzyna. The material damage is described in terms of the rate of change of a scalar variable that represents the microvoid volume fraction, or porosity, of the solid, and is intended to describe materials that experience ductile degradation and fracture at high rates of strain. The porosity variable is introduced into the constitutive equations for a viscoplastic solid through the yield function and the hardening rule that expresses the isotropic hardening (or softening) of the material. An evolution equation that describes the change in void volume fraction as a consequence of nucleation, growth, and coalescence of microvoids is also postulated.

In this paper the linear hardening law proposed by Perzyna for both the constitutive equation and the derivation of the void growth rate expression has been replaced by a nonlinear strain-hardening law that allows for saturation with increasing inelastic deformation. The effect that the hardening law has on the void growth threshold stress is clearly significant. A comparison of the calculated macroscopic response for the different hardening assumptions shows that the nonlinear hardening provides the more realistic model of the physical behavior. In addition, it has also been found necessary to modify the argument of the rate of deformation control function under uniaxial strain conditions in order to preserve the intended rate-dependence of yield. The resulting constitutive theory for the voided solid is thus able to model rate-dependent, compressible, inelastic behavior that also includes isotropic strain hardening and material degradation.

A proposed test program has been presented for determination of the ten material parameters appearing in the constitutive equation. The more difficult of the tests requires performance of uniaxial tension or compression tests or pure shear tests at strain rates approaching 10^4–$10^5\ s^{-1}$. Also needed is the determination of the yield function of the voided solid, which requires quasi-static biaxial testing of a material of known porosity. Such tests, although not of the ordinary variety, do appear feasible. The material functions and parameters appearing in the void evolution equation, however, are much more complex and difficult to evaluate, and present a formidable challenge.

The elastic-viscoplastic constitutive model discussed here and applied to OFHC copper, gives predicted behavior at very high strain rates without material degradation under conditions of uniaxial stress and strain that are qualitatively correct. The ability of the constitutive model to predict stress-strain response with material damage accumulation and simulated plate impact-spall fracture also appears to be satisfactory. The results that we have described indicate that it would be highly desirable to incorporate the constitutive model into a general wave propagation computer code, that would allow for interesting numerical-experimental studies of shock-induced material damage and spall fracture.

Acknowledgment

The second named author wishes to acknowledge the support made possible through the ASEE-Navy Summer Faculty Research Program at the Naval Research Laboratory.

References

Butcher, B. M., Barker, L. M., Munson, D. E., and Lundergan, C. D., 1964, "Influence of Stress History on Time-Dependent Spall in Metals," *AIAA Journal*, Vol. 2, pp. 977–990.

Carroll, M. M., and Holt, A. C., 1972, "Static and Dynamic Pore-Collapse Relations for Ductile Solids," *J. Appl. Phys.*, Vol. 43, pp. 1626–1636.

Curran, D. R., Seaman, L., and Shockey, D. A., 1977, "Dynamic Failure in Solids," *Physics Today*, pp. 46–55.

Curran, D. R., Seaman, L., and Shockey, D. A., 1987, "Dynamic Failure of Solids," *Physics Reports*, Vol. 147, pp. 253–388.

Doraivelu, S. M., Gegel, H. L., Gunasekera, J. S., Malas, J. C., Morgan, J. T., and Thomas, Jr., J. F., 1984, "A New Yield Function for Compressible P/M Materials," *Int. J. Mech. Sci.*, Vol. 26, pp. 527–535.

Dowling, A. R., Harding, J., and Campbell, J. D., 1970, "The Dynamic Punching of Metals," *J. Inst. of Metals*, Vol. 98, pp. 215–224.

Gilman, J. J., and Tuler, F. R., 1970, "Dynamic Fracture by Spallation in Metals," *Int. J. of Fract. Mech.*, Vol. 6, pp. 169–182.

Hancock, J. W., 1983, "Plasticity of Porous Metals," *Yield, Flow and Fracture of Polycrystals*, T. N. Baker, ed., Applied Science Pub., Essex, U.K.

Johnson, J. N., 1981, "Dynamic Fracture and Spallation in Ductile Solids," *J. Appl. Phys.*, Vol. 53, pp. 2812–2825.

Karnes, C. H., 1968, "The Plate Impact Configuration for Determining Mechanical Properties of Materials at High Strain Rates," *Mechanical Properties of Materials Under Dynamic Loads*, U. S. Lindholm, ed., Springer-Verlag, New York.

MacKenzie, J. H., 1950, "The Elastic Constants of a Solid Containing Spherical Holes," *Proc. Phys. Soc.*, Vol. 63B, pp. 2–11.

Meyers, M. A., and Aimone, C. T., 1983, "Dynamic Fracture (Spalling) of Metals," *Prog. in Mater. Sci.*, Vol. 28, pp. 1–96.

Nicholas, T., 1982, "Material Behavior at High Strain Rates," *Impact Dynamics*, J. Zukas et al., eds., John Wiley and Sons, New York.

Perzyna, P., 1984, "Constitutive Modeling of Dissipative Solids for Postcritical Behavior and Fracture," *ASME Journal of Engineering Materials Technology*, Vol. 106, pp. 410–419.

Perzyna, P., 1986, "Internal State Variable Description of Dynamic Fracture of Ductile Solids," *Int. J. Solids Structures*, Vol. 22, pp. 797–818.

Seaman, L., Barbee, T. W., and Curran, D. R., 1971, "Dynamic Fracture Criteria for Homogeneous Materials," Stanford Res. Inst. Tech. Rep., No. AFWL-TR-71-156.

Seaman, L., Curran, D. R., and Shockey, D. A., 1976, "Computational Models for Ductile and Brittle Fracture," *J. Appl. Phys.*, Vol. 47, pp. 4814–4826.

Shima, S., and Oyane, M., 1976, "Plasticity Theory for Porous Solids," *Int. J. Mech. Sci.*, Vol. 18, pp. 285–291.

Tuler, F. R., and Butcher, B. M., 1968, "A Criterion for the Time Dependence of Dynamic Fracture," *Int. J. of Fract. Mech.*, Vol. 4., pp. 431–437.

Downloaded 03 May 2010 to 171.66.16.244. Redistribution subject to ASME license or copyright; see http://www.asme.org/terms/Terms_Use.cfm

A Dynamic Measuring Technique for Bulk Stiffness Constants as a Function of Temperature and Microstructure for U-6 wt pct Nb[1]

D. R. Lowry
Mem. ASME

A. Wolfenden[2]

G. M. Ludtka[3]

Mechanical Engineering Department,
Texas A&M University,
College Station, TX 77843-3123

Measurements of dynamic Young's modulus (E) and shear modulus (G) have been made with the piezoelectric ultrasonic composite oscillator technique (PUCOT) on gamma solution heat treated specimens of U-6 wt pct Nb at 80 and 40 kHz, respectively. Three aging conditions were employed to permit measurements for four different microstructures from ambient to 647°C. Values of Poisson's ratio (ν) were calculated from the measured values of E and G. The extreme ranges for E, G and ν extended from 171 to 55 GPa, from 66 to 17 GPa, and from 0.09 to 0.70, respectively.

Introduction

Uranium is used in a variety of applications, especially those requiring high density at low cost. Alloying in small quantities (to maintain high density) with materials such as titanium, molybdenum, or niobium permits improved mechanical properties and greater corrosion resistance when heat treatment is employed to maintain a solid solution (Snyder, 1978; Eckelmeyer, 1984). For accurate computer modeling of material behavior such as flow, fatigue, structural deflection, and fracture, precise input of parameters such as ultimate and yield strengths, fracture toughness, and modulus of elasticity is required. The focus of this research is to supply accurate stiffness data for depleted U-6 wt pct Nb. In particular, Young's (E) and shear (G) moduli are measured as a function of temperature and subsequent microstructure using the piezoelectric ultrasonic composite oscillator technique (PUCOT). Values of E and G are employed for estimates of Poisson's ratio according to Hooke (1678).

The PUCOT is ideal for obtaining the moduli of uranium alloys since it is a dynamic technique, employing ultrasonic stress waves generated by piezoelectric transducers attached to small specimens. It is amenable to a small enclosed environment with electronic controls outside of the enclosure for containment of any hazardous uranium oxide particles which may be produced at elevated temperatures.

The introduction of the PUCOT can be traced to the theory of Butterworth (1915) that a combination of electrical circuits could be employed to model accurately a longitudinal mechanical vibrator driven by a condenser coupled emf. Quimby (1925) employed this theory to analyze thoroughly the vibrations in solid bars of arbitrary length, driven by stress waves excited in a piezoelectric crystal. Balamuth (1934) applied the theory to bars with a fundamental frequency which matched that of the crystal driver. Rose (1936) made the first measurement of elastic constants in polycrystalline metals employing a two-component resonator. The two piezoelectric crystals were rearranged by Marx (1951) to create a composite oscillator. Robinson and Edgar (1974) found the equations for the circuit model proposed by Marx to be of the correct form but in need of some refinement. The equations which they suggested remain current, along with adjustments to allow for a fused quartz spacer rod between the crystals and the specimen for extension into a furnace (four component system). That same year Robinson et al. (1974) published a similar set of equations, altered for torsional wave propagation. Tallon and Wolfenden (1979) applied this to torsional crystals to obtain the shear modulus for single crystals of aluminum. The PUCOT was first applied to radioactive materials by Keene et al. (1986). The authors successfully obtained Young's and shear moduli at temperatures up to 800°C for depleted U-0.75 wt pct Ti.

The equivalent circuit for Young's modulus is given by Robinson and Edgar (1974) at the first harmonic ($n=0$ and $L_s/2$) as

$$\mathrm{E} = 4 L_s^2 \rho / \tau(s)^2. \tag{1}$$

Where: L_s = length of specimen

ρ = specimen density

$\tau(s)$ = period of specimen

Thus, Young's modulus may be determined at room

[1]Research sponsored by Martin Marietta Energy Systems, Inc. Oak Ridge Y-12 Plant, under contract number DE-AC05-840R21400 for the U. S. Department of Energy.

[2]Presently at CSIRO Australia, Division of Materials Science and Technology, Clayton VIC 3168, Australia.

[3]Presently at Oak Ridge Y-12 Plant, Oak Ridge, TN 37831.

Contributed by the Applied Mechanics Division of THE AMERICAN SOCIETY OF MECHANICAL ENGINEERS for publication in the JOURNAL OF APPLIED MECHANICS.

Discussion on this paper should be addressed to the Technical Editor, Leon M. Keer, The Technological Institute, Northwestern University, Evanston, IL 60208, and will be accepted until two months after final publication of the paper itself in the JOURNAL OF APPLIED MECHANICS. Manuscript received by the ASME Applied Mechanics Division, April 25, 1988; final revision, July 1, 1989.

Copyright © 1990 by ASME
Downloaded 03 May 2010 to 171.66.16.244. Redistribution subject to ASME license or copyright; see http://www.asme.org/terms/Terms_Use.cfm

temperature by measurements of the specimen density, the period, and the specimen length at resonance.

The same equivalent circuit used for Young's modulus applies for the shear modulus. The corresponding equation for resonance is given as

$$G = 8L_s^2\rho/\tau(s)^2. \tag{2}$$

Hartman (1986), however, has shown evidence that this equation is in error in that it differs from experiment by a factor of 2. Making this adjustment,

$$G = 4L_s^2\rho/\tau(s)^2. \tag{3}$$

Thus, the equation for the shear modulus is equivalent to that for Young's modulus. For high temperature measurements, considerations must be made to include the period of a quartz spacer rod (also at resonance with the system) as follows:

$$\tau(s) = m(S)^{1/2}\tau(DGQ)\tau(DGQS)/\{B\}, \tag{4}$$

where: $B = \{\tau(DGQ)^2 m(DGQS) - \tau(DGQS)^2 m(DGQ)\}^{1/2}$.

$m(D)$ = mass of drive crystal

$m(G)$ = mass of gage crystal

$m(Q)$ = mass of quartz spacer rod

$m(S)$ = mass of specimen

$m(QS)$ = mass of quartz spacer rod and specimen

$m(DGQ) = m(D) + m(G) + m(Q)$

$m(DGQS) = m(D) + m(G) + m(Q) + m(S)$

$\tau(DGQ)$ = period of drive and gage crystals and quartz spacer rod

$\tau(DGQS)$ = period of drive and gage crystals, quartz spacer rod, and specimen.

Materials and Methods

Materials. The material examined in this research project is depleted uranium-6 wt pct niobium. An equilibrium uranium-niobium phase diagram with superimposed nonequilibrium phases is portrayed in Fig. 1 (Vandermeer, 1981). The equilibrium phases for the 6 wt pct alloy to 647°C are α (orthorhombic) + γ_2 (body centered cubic). Above this temperature, the equilibrium phase is the γ_1 (body centered cubic). As seen in the phase diagram, several nonequilibrium martensitic phases for this alloy may exist below the solidus line: the α'' phase (monoclinic) can exist up to 160°C, and the γ^o phase (tetragonal) can exist from 180°C to about 400°C. However, this γ^o phase is very unstable and rapidly decomposes into the α''. Since the uranium-6 wt pct niobium alloy is not quench rate-sensitive, these martensitic microstructures may be obtained fully upon quenching from the γ_1 phase at rates as slow as 10°C per second.

From the time-temperature-transformation (TTT) diagram depicted in Fig. 2 (Vandermeer, 1981), it is seen that another nonequilibrium phase may be obtained upon subsequent heat treating. Aging a gamma solution heat treated (GSHT) specimen at an elevated temperature (between 400 and 647°C) allows the decomposition of the γ^o phase into the γ_{12} (body centered cubic) phase. The composition of this γ_{12} phase is defined by the extension of the $\alpha+\gamma_1/\gamma_1$ solvus below the solidus line to the critical invariant temperature (about 400°C). With further aging, the γ_{12} phase will return to the equilibrium microstructure of the γ_2. Because of the slow diffusing characteristics of niobium in uranium, this reaction is very sluggish.

Two dash numbers (−14 and −15) were used to distinguish two variations of a gamma solution heat treatment during which the specimens were heated to 800°C (γ_1 phase) for two

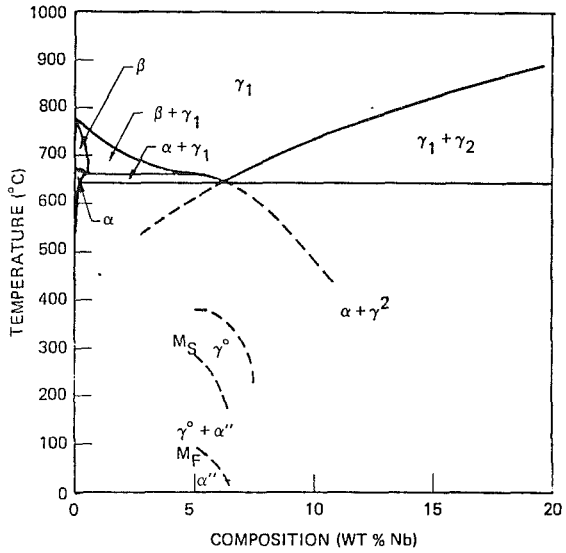


Fig. 1 Depleted uranium-niobium phase diagram with superimposed nonequilibrium phases

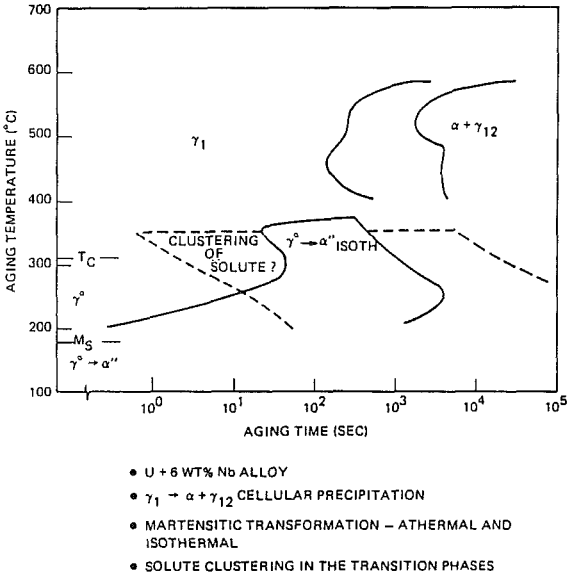


Fig. 2 Depleted U-6 percent Nb time-temperature-transformation diagram

hours. The former dash number indicated a water quench to room temperature while the latter represented a water quench with a subsequent age at 550°C for six hours. Some of the −14 specimens were aged at 325°C for ten hours to decompose the $\alpha'' + \gamma^o$ to the α''. These have been called −14b specimens. Thus three different heat treatments were employed for PUCOT measurements (−14, −14b, and −15) to represent different possible microstructures of gamma solution heat treated and water quenched (WQ) U-6 wt pct Nb.

The existence of twins in the martensitic states of this alloy was considered since their movement would have an adverse effect upon stiffness measurements. These stresses, applied at resonance for the PUCOT, were calculated to extend to 0.1 percent of the yield stress. This was assumed to be less than the stress required to move a twin through the material and was therefore thought to be of no consequence to measurements of E and G with a dynamic technique such as the PUCOT.

Apparatus. A schematic of the PUCOT system for measurements on depleted uranium alloys at high

Downloaded 03 May 2010 to 171.66.16.244. Redistribution subject to ASME license or copyright; see http://www.asme.org/terms/Terms_Use.cfm

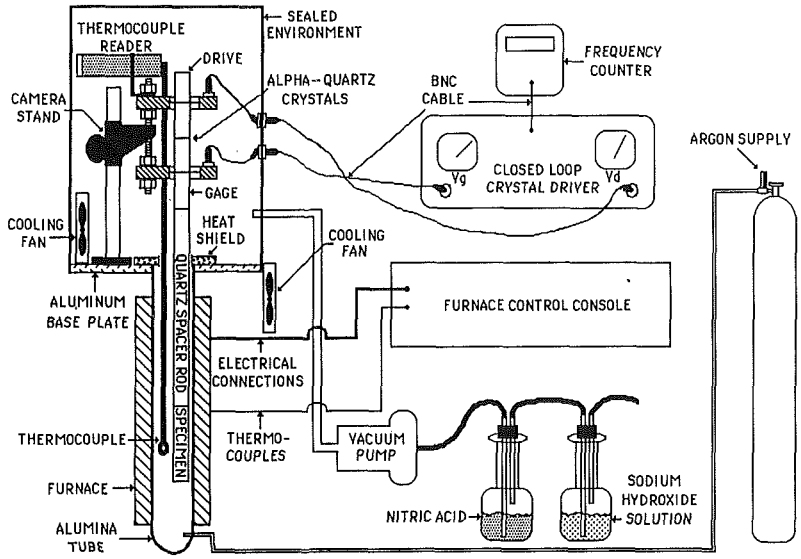


Fig. 3 Schematic of high temperature test setup

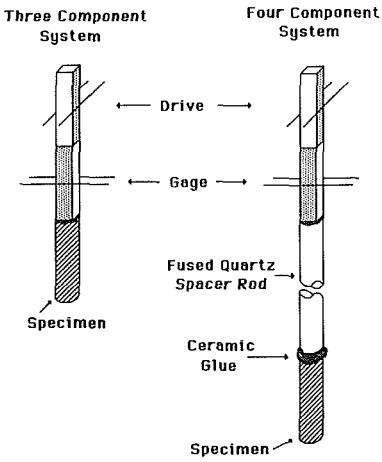


Fig. 4 Longitudinal piezoelectric composite oscillator—three and four component systems

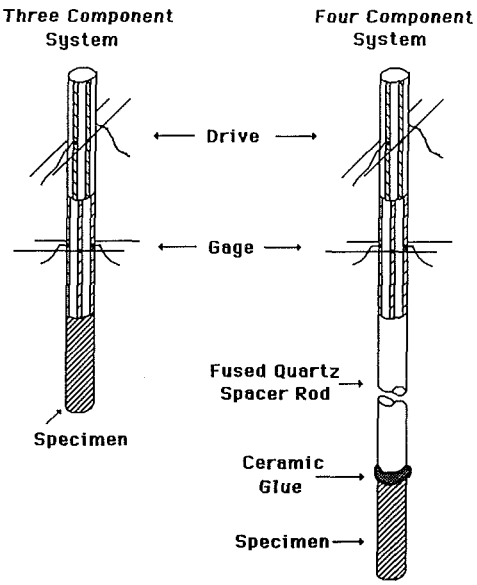


Fig. 5 Torsional piezoelectric composite oscillator—three and four component systems

temperatures (depicted in Fig. 3) is comprised of: a pair of longitudinal or torsional alpha-quartz crystals held by a pair of brass fixtures (jigs), a closed-loop crystal driver, a frequency counter, a Pt- (Pt- Rh) thermocouple with digital readout, a camera stand, an airtight enclosure, an electronically controlled furnace, an argon supply, and a particle filter system.

Two transducer-specimen configurations were employed in this experiment. The three component system (drive, gage, and specimen) was used at room temperature while the four component system (drive, gage, quartz spacer rod, and specimen) was used at higher temperatures. These are depicted in Figs. 4 and 5, respectively. The quartz rod was tuned to a multiple of the half wavelength of the transducer so that the specimen could be placed in the center of the furnace while the piezoelectric crystals remained near room temperature. The components were conjoined with a Loctite® glue except at the spacer rod-specimen interface where a ceramic glue was applied to withstand the elevated temperatures.

Experimental Methods. All specimen preparation such as the cutting of the ends to make them mutually perpendicular to the centerline of the specimen and mutually parallel was performed in a glove box. The treatment of the ends was done to define accurately the specimen length. The mass of each specimen was found to 0.1 mg with a Sartorius balance and the density determined according to Archimedes' principle.

Performing the PUCOT measurements is an iterative process. From equation (1) or (3) for longitudinal or torsional measurements,

$$\text{E or } G = 4L_s^2\rho/\tau(s)^2,$$

it is seen that both the modulus and the specimen length for resonance are initially unknown. Thus, the modulus was first estimated and the foregoing equation is solved in terms of the specimen length:

$$L_s = (\tau(s)/2)\{(\text{E or } G)/\rho\}^{1/2}.$$

From this estimate of resonant length, the specimen was cut to the nearest 0.02 mm and the PUCOT measurement was performed.

The specimen was concentrically attached to the gage crystal at ambient temperature, the period of the crystals set to 80 kHz (longitudinal) or 40 kHz (torsional) on the coarse setting of the driver, and the gage voltage (Vg) set at 0.1 volts (an intermediate setting employed for consistency). The drive voltage (Vd) was varied and the phase setting adjusted until the gage voltmeter indicated a maximum and the drive

Downloaded 03 May 2010 to 171.66.16.244. Redistribution subject to ASME license or copyright; see http://www.asme.org/terms/Terms_Use.cfm

voltmeter indicated a minimum. The period of the composite ($\tau(DGS)$) was then recorded and compared to the reference period ($\tau(DG)$—the period without the specimen) to verify resonance. If $\tau(S)$ and $\tau(DG)$ were equivalent within five percent, the modulus was recorded. If the ratio was greater than ± 5 percent from unity, an adjustment was made in the estimate of the modulus, a new length was cut, and the measurement was performed again until this criterion for resonance was met.

For elevated temperatures (above ambient) the specimen length had to be cut at room temperature to allow for the coefficient of thermal expansion. Thus, the length at room temperature was slightly less than that required for resonance at higher temperatures. Since the thermal expansion was neither constant nor linear with increasing temperature, a program was written to account for incremental amounts of expansion for different temperature intervals. At the higher temperatures, the reference period included the quartz spacer rod ($\tau(DGQ)$) as used in equation (4). The lengths of these spacer rods were obtained previously by Harmouche (1984) for the 80-kHz longitudinal transducers as

$$L = 358.9 + 0.022\mathrm{T} - 8.1 \times 10^{-6} T^2$$

and by Hartman (1986) for the 40-kHz torsional transducers as

$$L = 326.29 + 0.018\ T - 6.85 \times 10^{-6} T^2$$

where the length is in millimeters and the temperature is in degree Celsius. These 3-mm diameter spacer rods were trimmed with mutually parallel ends in a similar fashion as the specimens to the nearest quarter of a millimeter. Each spacer rod was concentrically attached to a specimen with a high temperature ceramic glue which was allowed to cure overnight. The spacer rod with specimen was then similarly attached to the gage crystal with a Loctite® glue which dried in 15 minutes.

The environmental controls (cooling fans, vacuum pump, and thermocouple reader) were timed to switch on and remain so as long as the furnace temperature was above 100°C. The argon supply was introduced at 700 liters per hour just prior to the lowering of the specimen into the furnace and adjusted to a lower setting (for measurements below 500°C) once the specimen reached the furnace temperature. For test temperatures above 300°C, the specimen was lowered into the furnace at a temperature less than or equal to 300°C and was heated subsequently at a rate of no greater than 100°C per hour. The argon supply was maintained until the enclosure could be reentered at furnace temperatures below 100°C.

With the exception of the inclusion of the spacer rod (Q) in the reference period and the PUCOT equations (four component system), the remainder of the experiment was conducted in conformance with the room temperature PUCOT (three component system). Experimentally, the longitudinal and torsional measurements were identical, with the exception of an emphasis on the centering of the three and four component systems for the latter to avoid disproportionate torques from the torsional wave form. Poisson's ratio was calculated from the measured values of E and G assuming conditions of isotropy and elastic homogeneity.

Results

The Young's and shear moduli and the corresponding Poisson's ratio, obtained by the PUCOT, are presented in graphical forms in Figs. 6 to 8 for three different heat treatments and four microstructures as a function of temperature. The particular heat treatments and phases are noted on each plot. Referring to Figs. 6 and 7 it is seen that the -15 specimens have the highest moduli from ambient to 647°C. The -14 specimens with the unstable γ^o phase (found slightly above ambient) have the lowest values and experience the sharpest decline with increasing temperature. Because the γ^o phase decomposes rapidly, PUCOT measurements for this heat treatment could not be obtained above 180°C. The instability from the high rate of diffusion yielded a rapidly decaying period ($\tau(DGQS)$) which produced uncertainty in the determination of the specimen length for resonance at higher temperatures. Therefore, the -14 specimens were aged at 325°C for ten hours (below the 400°C temperature for transformation to $\alpha+\gamma_{12}$ and for a sufficient time to stabilize the period $\tau(DGQS)$ to four places past the decimal point for 15 minutes, e.g., 12.4835 μs). The $-14b$ specimens yielded an intermediate range of moduli, close to that of the -14 specimens. Though effort was made to decompose totally the γ^o phase, it is interesting to note that an increase in the slope of the α'' curve occurs for both E and G curves slightly past 200°C where the dominance and rapid diffusion of this γ^o phase occurs (see Fig. 1).

For these experiments, Young's modulus ranged from 171 to 55 GPa, while the shear modulus went from 66 to 17 GPa and Poisson's ratio varied from 0.09 to 0.70 below the monoeutectoid.

Discussion

Phase Stability. In a comparison of the temperature dependence of the modulus data of U-6 wt pct Nb to that of other engineering materials, the -15 specimens ($GSHT+WQ$ and aged at 550°C for six hours) are typical. Apart from an abrupt drop in the shear modulus near ambient, the Young's and shear moduli decreased steadily with increasing temperature, and the Poisson's ratio remained around 0.3 until the phases changed from $\alpha+\gamma_{12}$ to $\alpha+\gamma_2$, where it dropped below 0.2 (see Figs. 6 to 8). However, after reheating this material into the γ_1 phase, other phases precipitated with different microstructures where the Young's and shear moduli could decrease by more than 50 percent while the Poisson's ratio could increase up to about 0.65. Two different values of the moduli were obtained in the $\alpha+\gamma_2$ phases for two different heat treatments as seen in Figs. 6 and 7. A good indication that other microstructures were not as stable as the $\alpha+\gamma_{12}/\alpha+\gamma_2$ phases of the -15 specimens is the fluctuation in the values obtained for Poisson's ratio in Fig. 8. Thus it is critical to know the metallurgical history and the intended use of this alloy prior to an engineering application.

Another indication that the $\alpha+\gamma_{12}/\alpha+\gamma_2$ phases of the -15 heat treatment were more stable can be found in the diffusion rates upon change of phase. The highest rate was experienced by the metastable γ^o phase and was too rapid to be monitored by PUCOT measurements with the present system. Over a 100°C range, the Poisson's ratio for the $\alpha''+\gamma^o$ microstructure increased from 0.1 to 0.6. The transformation from α'' to $\alpha+\gamma_2$ ($-14b$) was also faster than that from $\alpha+\gamma_{12}$ (-15). Referring to Fig. 6 or 7 the change of phase for the former occurred approximately 100°C earlier. The latter experienced a change during which a stable period could not be obtained as required for a PUCOT measurement. This discontinuity at the phase transformation may be explained by a clustering of solute shown in the T-T-T curves (see Fig. 2). Thus, the -15 heat treatment was the most sluggish to change and the most stable of those examined.

Stiffness Constants-Phase Sensitivity. The shear modulus was much more sensitive to the changes in microstructure than Young's modulus. Referring again to Figs. 6 and 7, this was demonstrated in the -14 specimens by the change from the α'' to the $\alpha''+\gamma^o$ near ambient, in the $-14b$ specimens by the change in slope at 200°C where the dominance of the γ^o phase occurred, and in both the -14 and -15 heat treatments in the change to the $\alpha+\gamma_2$ phases between 400 and 500°C. In each

Downloaded 03 May 2010 to 171.66.16.244. Redistribution subject to ASME license or copyright; see http://www.asme.org/terms/Terms_Use.cfm

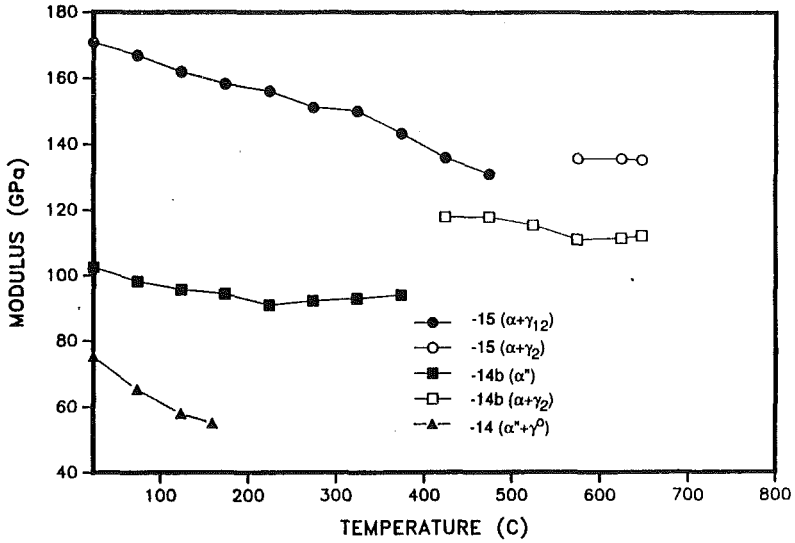


Fig. 6 Temperature dependence of modulus (E); depleted uranium—six percent niobium alloy

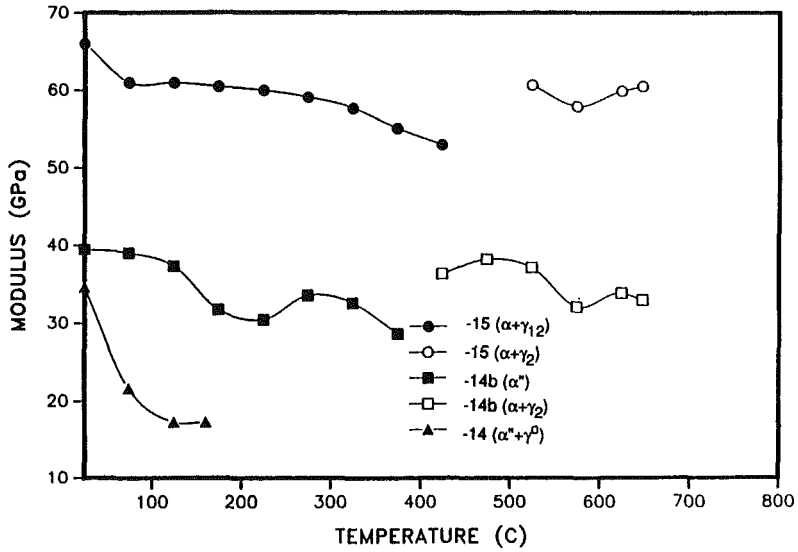


Fig. 7 Temperature dependence of modulus (G); depleted uranium—six percent niobium alloy

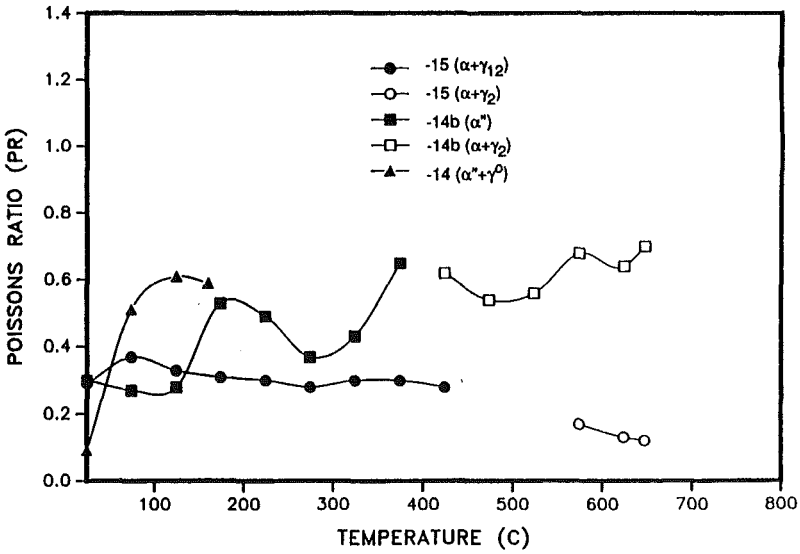


Fig. 8 Temperature dependence of Poissons ratio; depleted uranium—six percent niobium alloy

Downloaded 03 May 2010 to 171.66.16.244. Redistribution subject to ASME license or copyright; see http://www.asme.org/terms/Terms_Use.cfm

case, the change in the shear modulus was more pronounced than the change in Young's modulus for both direct and percent change comparisons. For the −15 specimens, the effect near room temperature was also seen in the shear modulus (similar to that in the −14 specimens) but was not distinguishable in Young's modulus.

This same behavior was also verified in the Poisson's ratio (Fig. 8), which was accentuated by relative changes between E and G, where obvious and abrupt changes occurred at the aforementioned temperatures. In the −15 heat treatment, there was a distinct rise in Poisson's ratio from room temperature to 50°C and a slight dip or change in slope between 200 and 300°C. This change just above ambient was even greater in the −14 specimens. The drop at 200°C in the −14b heat treatment was somewhat overshadowed by a sharp rise and subsequent drop in G compared to the flat, stepwise increase in E where the phases changed to $\alpha+\gamma_2$. Another anomaly, also more pronounced in the torsional measurements, was a drop in modulus at around 550°C.

This greater sensitivity of the shear modulus to microstructural changes can be explained qualitatively in terms of the number of defects excited by the torsional wave form as compared to the longitudinal wave form. Because of an induced shear strain in the x and y-directions (cross-sectional plane) by the torsional crystals, defects are excited in two directions during the shear modulus measurements, while the excursion of the longitudinal wave form occurs only in one direction—namely the z (axial). Thus, there exist more opportunities for the shear wave to interact with the lattice defects in the specimens.

Stiffness Constants-Texture Effects. The calculation of the Poisson's ratio in this research was performed with the assumptions of linear, homogeneous elasticity from Hooke's laws. These assumptions include the state of isotropy or random orientation of the grains within the material. This was not the case below the monoeutectoid line (650°C) for this material. The specimens were heated into the γ_1 regime, where the microstructure is most random, to minimize the texture from prior casting and swaging operations. However, the subsequent water quench to obtain martensite again introduced a preferred orientation to the microstructure. A survey of the literature failed to reveal the extent of the texture in U-6 wt pct Nb. Some information is available for the texture resultant from forming operations in U-2.4 wt pct Nb (Kollie, 1981) but this alloy can have different microstructures (see Fig. 1). An indication of the existence of texture was noticed when a single specimen was heated to 800°C and dropped into a container of water. The specimen hit the water at an oblique angle and consequently bent from the asymmetrical quench. Due to the texture in the specimens, the values of Poisson's ratio obtained in this research should be regarded as approximate only.

Conclusions

From the results of this research on the elastic moduli of U-6 wt pct Nb with the PUCOT, the following conclusions can be made:

(1) The stiffness constants (E and G) have been determined for four different microstructures of the U-6 wt pct Nb alloy from ambient to 647°C. Young's and shear moduli were found to vary from 171 to 55 and from 66 to 17 GPa, respectively. Estimations of Poisson's ratio varied from 0.09 to 0.70

(2) The moduli of this alloy (especially the shear) proved to be sensitive to the microstructure.

(3) The values of Young's modulus for the $\alpha+\gamma_{12}$ microstructure were the only data for which a linear curve fit proved adequate. This was the slowest to diffuse upon aging.

(4) The decomposition of the γ^o phase was so rapid that a stable resonant period could not be established for PUCOT measurements.

(5) The fact that different heat treatments could be employed to obtain common phases with different moduli verified a sensitivity to thermal history.

References

Balamuth, L., 1934, "Elastic Moduli and Temperature Variation of the Principal Young's Modulus of Rock Salt," *Phys. Rev.*, Vol. 45, p. 715.

Butterworth, S., 1915, *Proc. Phys. Soc.*, Vol. 27, London, U.K., p. 410.

Ecklemeyer, K. H., Romig, Jr., A. D., and Weirick, L. J., 1984, "The Effect of Quench Rate on the Microstructure, Mechanical Properties, and Corrosion Behavior of U-6 Pct Nb," *Metallurg. Trans. A*, Vol. 15A, pp. 1319–1330.

Harmouche, M. R., 1984, "The PUCOT for Measuring Dynamic Young's Modulus for the B2-CoAl, FeAl and NiAl Alloys," Master's Thesis, Texas A&M University, p. 82.

Hartman, J. T., 1986, "The Use of Ultrasonics in the Measurement and Analysis of Properties and Defects in Various Advanced Materials," Master's Report, Texas A&M University, pp. 46–66.

Hooke, Robert, 1678, *"De Potentia restitutiva"*, London, U.K.

Keene, K. H., 1986, "Determination of Young's Modulus and Mechanical Damping as a Function of Temperature for Depleted Uranium- 0.75 wt% Titanium using the PUCOT," Master's Thesis, Texas A&M University, pp. 11–17, 65–73.

Kollie, T. G., 1981, "Texture-Property Relationships in the Uranium- 2.4 Weight Percent Niobium Alloy," *Metallurgical Technology of Uranium and Uranium Alloys*, Vol. 1, American Society for Metals, Metals Park, Ohio, pp. 231–249.

Marx, J., 1951, "Use of Piezoelectric Gauge for Internal Friction Measurements," *Rev. Sci. Instr.*, Vol. 22, pp. 503–509.

Quimby, S. L., 1925, "On the Experimental Determination of the Viscosity of Vibrating Solids," *Phys. Rev.*, Vol. 25, pp. 558–573.

Robinson, W. H., and Edgar, A., 1974, "The Piezoelectric Method of Determining Mechanical Damping at Frequencies of 30 to 200 kHz," *IEEE Trans. Son. Ultrason.*, Vol. SU-21, pp. 98–105.

Robinson, W. H., Carpenter, S. H., and Tallon, J. L., 1974, "Piezoelectric Method of Determining Torsional Mechanical Damping Between 40 and 120 kHz," *J. Appl. Phys.*, Vol. 45, pp. 1975–1981.

Rose, C. F., 1936, "Variation of Adiabatic Elastic Moduli of Rock Salt with Temperature Between 80 and 270 K," *Phys. Rev.*, Vol. 49, p. 50.

Snyder, W. B., 1978, "Effects of Heat Treatment on the Microstructure and Mechanical Properties of Uranium-6 Nioibium Alloy," prepared for the U.S. Dept. of Energy under U.S. Contract W-7405 Eng 26, Oak Ridge Y-12 Plant, Oak Ridge, Tenn.

Tallon, J. L., and Wolfenden, A., 1979, "Temperature Dependence of Elastic Constants of Aluminum," *J. Phys. Chem. Sol.*, Vol. 40, pp. 831–837.

Vandermeer, R. A., 1981, "Martensitic Transformation, Shape Memory Effects, and Other Curious Mechanical Effects," *Metallurgical Technology of Uranium and Uranium Alloys*, Vol. 1, Amerian Society for Metals, Metals Park, Ohio, pp. 281–284.

Downloaded 03 May 2010 to 171.66.16.244. Redistribution subject to ASME license or copyright; see http://www.asme.org/terms/Terms_Use.cfm

Analytical Solutions for Circular Bars Subjected to Large Strain Plastic Torsion

K. W. Neale
Faculty of Applied Science,
Université de Sherbrooke,
Sherbrooke, QC, Canada
Assoc. Mem. ASME

S. C. Shrivastava
Department of Civil Engineering and Applied Mechanics,
McGill University,
Montréal, QC, Canada

The inelastic behavior of solid circular bars twisted to arbitrarily large strains is considered. Various phenomenological constitutive laws currently employed to model finite strain inelastic behavior are shown to lead to closed-form analytical solutions for torsion. These include rate-independent elastic-plastic isotropic hardening J_2 flow theory of plasticity, various kinematic hardening models of flow theory, and both hypoelastic and hyperelastic formulations of J_2 deformation theory. Certain rate-dependent inelastic laws, including creep and strain-rate sensitivity models, also permit the development of closed-form solutions. The derivation of these solutions is presented as well as numerous applications to a wide variety of time-independent and rate-dependent plastic constitutive laws.

1 Introduction

In recent years much attention has been focused on the development of constitutive laws for elastic-plastic solids, especially with regard to the modeling of finite strain behavior. Generally the aim has been to produce phenomenological theories which adequately model the essential features of material response, yet which remain simple enough for numerical applications. This has usually been achieved by appropriately extending the classical small strain theories of plasticity to the large strain regime. Examples of this approach are the finite strain versions of J_2 flow theory of plasticity, proposed by Budiansky (1970) and Hutchinson (1973) for isotropic hardening, and subsequently modified by Tvergaard (1978) for kinematic hardening, as well as the hypoelastic and hyperelastic versions of J_2 deformation theory of Stören and Rice (1975) and Hutchinson and Neale (1978a). Extensions of such models to include the effects of material strain-rate sensitivity have also been proposed (Hutchinson and Neale (1978b)).

The kinematic hardening law first suggested by Tvergaard (1978) was a plausible finite strain generalization of the classical Prager-Ziegler rule of small strain plasticity. However, for simple shear deformations this law was shown to predict strongly oscillatory shear stresses (Nagtegaal and de Jong, 1982). To eliminate such oscillations, various modified kinematic hardening rules have been advanced (e.g., Lee et al., 1983; Dafalias, 1983).

A fundamental problem related to finite strain constitutive modeling is the behavior of solid circular bars in torsion. Interest in this problem stems from the fact that the torsion test is perhaps the most widely used for obtaining experimental data for metals at very large strains. In addition, the nonhomogeneity of this deformation process and the inherent nonproportional stressing histories involved are prime sources of interest into the basic mechanics of this problem.

In previous investigations of large strain torsion (Neale and Shrivastava, 1985, 1989) numerical results have been generated assuming rate-independent, elastic-plastic, isotropic hardening J_2 flow theory of plasticity (Budiansky, 1970; Hutchinson, 1973), the various kinematic hardening rules of flow theory (Tvergaard, 1978; Lee et al., 1983; Dafalias, 1983), and both the hypoelastic (Stören and Rice, 1975) and hyperelastic (Hutchinson and Neale, 1978a) formulations of J_2 deformation theory. We have since recognized that closed-form analytical solutions can, in many instances, be obtained for the inelastic behavior of solid circular bars twisted to arbitrarily large strains. For example, most of the aforementioned constitutive laws permit the development of such closed-form solutions. Certain rate-dependent inelastic laws, including creep and strain-rate sensitivity models, also lead to closed-form solutions for torsion. The derivation of these solutions is given in this paper, as well as numerous applications to a wide variety of time-independent and rate-dependent constitutive laws. The conditions which render a particular constitutive model amenable to such closed-form solutions for large strain torsion are also discussed.

2 Analysis and Method of Solution

We consider a homogeneous, incompressible solid circular bar of radius R subjected to an angle of twist ψ per unit length. The bar is constrained axially, thus allowing the possible development of axial stresses and a resultant axial force F. The lateral surface of the bar is traction free, and all properties are assumed to be axisymmetric. Although some of the con-

Contributed by the Applied Mechanics Division of THE AMERICAN SOCIETY OF MECHANICAL ENGINEERS for publication in the JOURNAL OF APPLIED MECHANICS.

Discussion on this paper should be addressed to the Technical Editor, Leon M. Keer, The Technological Institute, Northwestern University, Evanston, IL 60208, and will be accepted until two months after final publication of the paper itself in the JOURNAL OF APPLIED MECHANICS. Manuscript received by the ASME Applied Mechanics Division, October 10, 1988; final revision, July 1, 1989.

Copyright © 1990 by ASME
Downloaded 03 May 2010 to 171.66.16.244. Redistribution subject to ASME license or copyright; see http://www.asme.org/terms/Terms_Use.cfm

stitutive models to be considered give rise to deformation-induced anisotropies, the behavior in all cases remains axisymmetric.

A spatial cylindrical polar coordinate system (θ, z, r) with orthonormal base vectors $\mathbf{e}_\theta$, $\mathbf{e}_z$, $\mathbf{e}_r$ is used as a reference. These base vectors are associated with material elements in their current, deformed state so that the various components of stress, rate-of-deformation, etc., in what follows represent the respective physical components.

The kinematics of the above-posed torsion problem is readily determined. The deformation field is such that material points with coordinates (Φ, z, r) in the initial, undeformed configuration currently have coordinates (θ, z, r) in the deformed state, with $\theta = \Phi + \psi z$. Accordingly, the (Eulerian) rate-of-deformation tensor $(\dot{\epsilon})$ and material spin tensor (ω) are such that

$$\dot{\epsilon}_{\theta z} = \dot{\epsilon}_{z\theta} = \omega_{\theta z} = -\omega_{z\theta} = \frac{\dot{\gamma}}{2}, \tag{1}$$

where $\dot{\gamma} = r\dot{\psi}$. Thus, each element of the bar is in a state of simple shear in the $\theta - z$ plane, where the shear deformation γ is directly proportional to the radial distance r. That is,

$$\gamma(r) = \frac{r}{R}\Gamma \tag{2}$$

where $\Gamma = R\psi$ represents the shear at the outer radius of the bar.

Because of axisymmetry and the prescribed boundary conditions, the only equation of equilibrium which is not identically satisfied is the relation

$$r\frac{d\sigma_{rr}}{dr} + \sigma_{rr} - \sigma_{\theta\theta} = 0, \tag{3}$$

where σ_{ij} is the Cauchy stress tensor. Furthermore, we have $\sigma_{r\theta} = \sigma_{rz} = 0$ throughout the bar.

For simple shear deformations, the various constitutive models to be employed allow us to obtain explicit expressions for the deviatoric stress components s_{ij} as a function of γ (and $\dot{\gamma}$ for rate-dependent behavior). To this state an arbitrary hydrostatic pressure p can be superimposed. Since

$$\sigma_{ij} = s_{ij} - \delta_{ij}p, \tag{4}$$

where δ_{ij} is the Kronecker delta, the equilibrium equation (3) becomes

$$\frac{dp}{dr} = \frac{ds_{rr}}{dr} + \frac{1}{r}(s_{rr} - s_{\theta\theta}). \tag{5}$$

Solving this, together with the boundary condition $\sigma_{rr}(R) = 0$, gives the hydrostatic pressure distribution $p(r)$. Combining the pressure $p(r)$ with the previously determined stress deviator distributions $s_{ij}(\gamma(r))$ and using (2) and (4) gives the total stress distributions $\sigma_{ij}(r)$. The resultant torque T and axial force F are given by

$$T = 2\pi\int_0^R r^2\sigma_{z\theta}dr \tag{6}$$

and

$$F = 2\pi\int_0^R r\sigma_{zz}dr, \tag{7}$$

respectively. Obviously, since $\sigma_{z\theta} = s_{z\theta}$ the hydrostatic pressure has no influence on T.

For each of the constitutive models to be used we have $s_{rr} = 0$, or $\sigma_{rr} = -p$. As a result, the boundary condition becomes $p(R) = 0$ and the solution to (5) is

$$p(r) = -\int_R^r \frac{1}{r}s_{\theta\theta}(\gamma)dr. \tag{8}$$

In equation (8), $s_{\theta\theta}(\gamma)$ is the stress deviator component from the simple shear analysis at $\gamma = r\Gamma/R$ (and $\dot{\gamma} = r\dot{\Gamma}/R$ for rate-dependent behavior).

Since $s_{rr} = 0$, we have $s_{zz} = -s_{\theta\theta}$ or $\sigma_{zz} = -(s_{\theta\theta} + p)$. Substituting this and (8) in (7) and integrating by parts gives

$$F(\Gamma) = -\frac{3\pi R^2}{\Gamma^2}\int_0^\Gamma \gamma s_{\theta\theta}(\gamma)d\gamma. \tag{9}$$

Equation (6) can also be written as

$$T(\Gamma) = \frac{2\pi R^3}{\Gamma^3}\int_0^\Gamma \gamma^2 s_{z\theta}(\gamma)d\gamma. \tag{10}$$

Thus, for a bar twisted to a shear deformation Γ at its outer radius, the simple shear solution $s_{ij}(\gamma)$ together with (9) and (10) immediately give the axial force and twisting couple, without recourse to solving explicitly for the pressure distribution $p(r)$. However, to obtain the corresponding stress distributions $\sigma_{ij}(r)$ across the bar, the pressure distribution must be evaluated using (8).

3 Constitutive Models of Time-Independent and Rate-Dependent Plasticity

A number of models of time-independent and rate-dependent large strain plasticity will be considered. These include rigid-plastic and elastic-plastic forms of J_2 flow theory, with isotropic hardening and kinematic hardening, as well as hypoelastic and hyperelastic versions of J_2 deformation theory. Classical creep laws and certain models of material strain-rate sensitivity will also be employed. The various constitutive laws are summarized in this section. Throughout, incompressibility is assumed. Cartesian axes, with x_1, x_2, x_3 associated with the $\mathbf{e}_\theta$, $\mathbf{e}_z$, $\mathbf{e}_r$ directions in torsion, are used as a reference.

3.1 Isotropic Hardening J_2 Flow Theory. For this model the plastic strain-rate components are related to the stress deviator tensor as follows

$$\dot{\epsilon}_{ij}^p = \frac{\dot{\gamma}_e^p}{2\tau_e}s_{ij}. \tag{11}$$

Here, $\tau_e = (s_{ij}s_{ij}/2)^{1/2}$ and $\dot{\gamma}_e^p = (2\dot{\epsilon}_{ij}^p\dot{\epsilon}_{ij}^p)^{1/2}$ are the equivalent shear stress and plastic shear strain rate, respectively. These are related to the usual uniaxial equivalent stress (σ_e) and axial plastic strain rate $(\dot{\epsilon}_e{}^P)$ through $\tau_e = \sigma_e/\sqrt{3}$ and $\dot{\gamma}_e{}^P = \sqrt{3}\dot{\epsilon}_e{}^P$, where σ_e and ϵ_e reduce to the uniaxial true stress and logarithmic strain for simple tension.

Elastic effects are incorporated by adding the components

$$\dot{\epsilon}_{ij}^e = \frac{1}{2G}\overset{*}{s}_{ij}, \tag{12}$$

where G is the elastic shear modulus. The asterisk denotes the Jaumann rate which, for any second-order tensor, $\mathbf{T}$, and antisymmetric spin tensor, $\mathbf{\Omega}$, is related to the material rate, $\dot{\mathbf{T}}$, through

$$\overset{*}{\mathbf{T}} = \dot{\mathbf{T}} + \mathbf{T}\mathbf{\Omega} - \mathbf{\Omega}\mathbf{T}. \tag{13}$$

For rigid-plastic behavior the total stress deviator components are, from (11),

$$s_{ij} = \frac{2\tau_e}{\dot{\gamma}_e}\dot{\epsilon}_{ij}. \tag{14}$$

For elastic-plastic response, inverting the sum of (11) and (12) gives the incremental relation

$$\overset{*}{s}_{ij} = 2G\dot{\epsilon}_{ij} - \frac{1}{\tau_e{}^2}(G - G_t)s_{ij}s_{kl}\dot{\epsilon}_{kl}. \tag{15}$$

Here, G_t is the tangent shear modulus, that is the slope of the equivalent shear stress—shear strain curve at the current level $\tau = \tau_e$. Similarly, in (14) τ_e is regarded as a function of γ_e and can be computed at the current value of γ_e using the

Downloaded 03 May 2010 to 171.66.16.244. Redistribution subject to ASME license or copyright; see http://www.asme.org/terms/Terms_Use.cfm

equivalent shear stress—shear strain curve. Equivalently, the uniaxial true stress (σ_e) – logarithmic strain (ϵ_e) curve in simple tension could be used where $\sigma_e = \sqrt{3}\tau_e$, $\epsilon_e = \gamma_e/\sqrt{3}$ and the tangent modulus is $E_t = 3G_t$.

3.2 Kinematic Hardening J_2 Flow Theory. With this model the initial yield surface retains its shape and size but translates in stress space during plastic deformation. The current yield surface is given by

$$\frac{1}{2}\bar{s}_{ij}\bar{s}_{ij} = \tau_Y^2 = \text{const.}, \tag{16}$$

where

$$\bar{s}_{ij} = s_{ij} - \beta_{ij}. \tag{17}$$

Here, β_{ij} specifies the current position of the yield surface origin in deviatoric stress space and τ_Y is the initial yield stress in shear, equal to $\sigma_Y/\sqrt{3}$ where σ_Y is the tensile yield stress.

For elastic-plastic behavior the relation analogous to (15) becomes (Tvergaard, 1978)

$$\overset{*}{s}_{ij} = 2G\dot{\epsilon}_{ij} - \frac{1}{\tau_Y^2}(G - G_t)\bar{s}_{ij}\bar{s}_{kl}\dot{\epsilon}_{kl}. \tag{18}$$

Tvergaard (1978) proposed that G_t be computed at the stress level

$$\tau_e = \tau_Y + (\beta_e)_{\max} \tag{19}$$

where $\beta_e = (\beta_{ij}\beta_{ij}/2)^{1/2}$.

Alternatively, (but not equivalently!) G_t has been taken as a function of the von Mises equivalent plastic strain γ_e^p (as defined in rate form in the previous subsection) and computed from the equivalent shear stress—shear strain curve at the value γ_e^p (Nagtegaal and de Jong, 1982; Lee et al., 1983; Dafalias, 1983). The first alternative will be employed here.

The yield surface translation during an increment of plastic deformation is given by the Prager-Ziegler shift rule

$$\overset{*}{\beta}_{ij} = \bar{s}_{ij}\dot{\mu}\,, \quad \dot{\mu} > 0 \tag{20}$$

which, together with (18) and the consistency condition $\dot{\tau}_Y = 0$, gives

$$\dot{\mu} = \frac{1}{2\tau_Y^2}\bar{s}_{ij}\overset{*}{s}_{ij} = \frac{G_t}{\tau_Y^2}\bar{s}_{ij}\dot{\epsilon}_{ij}. \tag{21}$$

For the rigid-plastic case we have (c.f. equation (14))

$$\bar{s}_{ij} = \frac{2\tau_Y}{\dot{\gamma}_c}\dot{\epsilon}_{ij} \tag{22}$$

with $\dot{\gamma}_c = (2\dot{\epsilon}_{ij}\dot{\epsilon}_{ij})^{1/2}$. The expressions (20) and (21) simplify and can be conveniently written as

$$\overset{*}{\beta}_{ij} = 2G_t\dot{\epsilon}_{ij}. \tag{23}$$

The various kinematic hardening models (e.g., Tvergaard, 1978; Lee et al., 1983; Dafalias, 1983) differ only in the choice of spin tensor Ω used in the definition (13) of the Jaumann rate. These are detailed in Section 4.2.

3.3 Hypoelastic J_2 Deformation Theory. According to the hypoelastic version of finite strain J_2 deformation theory (Stören and Rice, 1975) we have, in incremental form,

$$\overset{*}{s}_{ij} = 2G_s\dot{\epsilon}_{ij} - \frac{1}{\tau_e^2}(G_s - G_t)\, s_{ij}s_{kl}\dot{\epsilon}_{kl}. \tag{24}$$

Here, τ_e is the equivalent shear stress, as defined in Section 3.1, and $G_s = \tau_e/\gamma_e$ is the secant shear modulus, computed from the equivalent shear stress—shear strain curve at the level τ_e. Note that (24) reduces to the isotropic hardening flow theory relation (15) when we put $G_s = G$. In the initial elastic range, we have $G_s = G_t = G$ and (24) reduces to the relation (12).

3.4 Hyperelastic J_2 Deformation Theory. The deformation theory of Hutchinson and Neale (1978a) represents a nonlinear elastic law which is truly path independent for arbitrarily large strains. It makes extensive use of Hill's (1970) theory for finitely deformed isotropic elastic solids. For such solids the principal directions of Cauchy stress must be aligned with the principal directions of Eulerian strain. Thus, to fully specify the constitutive behavior for an incompressible material we need only know the relations between the principal Cauchy stress deviators s_i and corresponding principal stretches λ_i. These are given by

$$s_i = \frac{2\tau_e}{\gamma_e}\epsilon_i \tag{25}$$

where $\epsilon_i = ln\lambda_i$ are the principal components of logarithmic strain, and $\tau_e = (s_i s_i/2)^{1/2}$ as previously. However, γ_e is now defined in terms of the total principal logarithmic strains as $\gamma_e = (2\epsilon_i\epsilon_i)^{1/2}$. The relationship between τ_e and γ_e is again that described by the equivalent shear stress—shear strain curve.

3.5 Rate Dependent Plasticity Laws. The relations that are often used to describe creep deformations or material strain-rate sensitivity are viscoplastic generalizations of the previous rate-independent models. For example, (14), i.e.,

$$\dot{\epsilon}_{ij} = \frac{\dot{\gamma}_e}{2\tau_e}s_{ij} \tag{26}$$

with $\tau_e = (s_{ij}s_{ij}/2)^{1/2}$, $\dot{\gamma}_e = (2\dot{\epsilon}_{ij}\dot{\epsilon}_{ij})^{1/2}$ and $\dot{\gamma}_e = k\tau_e^n$ (27)

is the classical nonlinear viscous creep law (Odqvist, 1966). Hutchinson and Neale (1978b) incorporate strain-rate sensitivity in (14) and (26) by taking τ_e to be a function of γ_e and $\dot{\gamma}_e$ as follows:

$$\tau_e = K\gamma_e^N\dot{\gamma}_e^m. \tag{28}$$

Here, N and m are the strain hardening exponent and strain-rate sensitivity index, respectively. This expression reduces to (27) when $N = 0$ and $m = 1/n$. Other equivalent shear stress—strain—strain-rate expressions of the form

$$\tau_e = \mathfrak{F}(\gamma_e, \dot{\gamma}_e) \quad \text{or} \quad \dot{\gamma}_e = \mathfrak{G}(\tau_e, \gamma_e) \tag{29}$$

may be adopted.

4 Solutions for Large Strain Torsion

As outlined in Section 2, knowing the stress deviator components s_{ij} as functions of γ in simple shear (and $\dot{\gamma}$ for rate-dependent behavior) is the key to the development of an analytical solution for the solid bar in torsion, as each element in the bar is in a state of simple shear (in the θ-z plane) with a superimposed hydrostatic pressure. The pressure distribution across the bar is given by (8), the stress components by (4), and the resultant axial force and twisting couple by (9) and (10), respectively.

4.1 Isotropic Hardening J_2 Flow Theory. For simple shear deformations (1), the elastic-plastic isotropic hardening flow theory law (15) leads to the following relations:

$$s_{\theta\theta} = -s_{zz}\,, \quad s_{rr} = s_{r\theta} = s_{rz} = 0 \tag{30}$$

$$\tau_e = (s_{\theta\theta}^2 + s_{z\theta}^2)^{1/2} \tag{31}$$

$$\dot{s}_{\theta\theta} = \left(1 - \frac{G - G_t}{\tau_e^2}s_{\theta\theta}\right)s_{z\theta}\dot{\gamma} \tag{32}$$

$$\dot{s}_{z\theta} = \left(G - s_{\theta\theta} - \frac{G - G_t}{\tau_e^2}s_{z\theta}^2\right)\dot{\gamma} \tag{33}$$

The initial "elastic" (in fact, hypoelastic) response corre-

Downloaded 03 May 2010 to 171.66.16.244. Redistribution subject to ASME license or copyright; see http://www.asme.org/terms/Terms_Use.cfm

sponding to (12) is obtained by putting $G_t = G$ in the above relations. The solution of the resulting equations is

$$s_{\theta\theta} = -s_{zz} = 2G\sin^2\frac{\gamma}{2}, \quad s_{z\theta} = G\sin\gamma. \tag{34}$$

Plastic yielding occurs when $\tau_e = 2G\sin(\gamma/2) = \tau_Y$, i.e., when

$$\gamma = \gamma_Y = 2\sin^{-1}\left(\frac{\tau_Y}{2G}\right). \tag{35}$$

To obtain a solution in the elastic-plastic range ($\gamma \geq \gamma_Y$), we introduce a parametric angle α as follows such that (31) becomes automatically satisfied:

$$s_{\theta\theta} = \tau_e\sin\alpha, \quad s_{z\theta} = \sigma_{z\theta} = \tau_e\cos\alpha. \tag{36}$$

Substituting (36) into (32) and (33) and solving for $\dot{\tau}_e$ and $\dot{\alpha}$ gives

$$\dot{\tau}_e = [G_t\cos\alpha]\dot{\gamma}, \quad \dot{\alpha} = \left[1 - \frac{G}{\tau_e}\sin\alpha\right]\dot{\gamma}. \tag{37}$$

Eliminating $\dot{\gamma}$ leads to the following differential equation

$$(\tau_e - G\sin\alpha)d\tau_e - (\tau_e G_t\cos\alpha)d\alpha = 0. \tag{38}$$

Using the standard techniques for solving linear first-order ordinary differential equations (Birkhoff and Rota, 1960), and taking into account the condition (35) at incipient plastic flow, we obtain the following solution:

$$\alpha(\tau_e) = \sin^{-1}\left\{\frac{1}{I(\tau_e)}\left[\int_{\tau_Y}^{\tau_e}\frac{I(\tau_e)}{G_t}\,d\tau_e + \frac{\tau_Y}{2G}\right]\right\}, \tag{39}$$

where

$$I(\tau_e) = \exp\left[\int_{\tau_Y}^{\tau_e}\frac{G}{G_t\tau_e}\,d\tau_e\right]. \tag{40}$$

At initial yield we have $\alpha = \alpha_Y = \sin^{-1}(\tau_Y/2G)$.

Given the equivalent shear stress—shear strain relation for the material, we substitute $G_t(\tau_e)$ in (40) and (39) to obtain $\alpha(\tau_e)$. Using (37), we then relate τ_e to the shear deformation γ as follows:

$$\gamma(\tau_e) = \gamma_Y + \int_{\tau_Y}^{\tau_e}\frac{1}{G_t\cos\alpha}\,d\tau_e. \tag{41}$$

The stress deviator components at this shear deformation γ are obtained from (36).

For a linear hardening material with $G_t = h = \text{const.}$, (39) can be integrated explicitly. This gives

$$\alpha(\tau_e) = \sin^{-1}\left\{\frac{\tau_e}{G+h}\left[1 - \frac{1}{2}\left(1 - \frac{h}{G}\right)\left(\frac{\tau_e}{\tau_Y}\right)^{-(1+G/h)}\right]\right\}. \tag{42}$$

For the solid bar subjected to a shear deformation $\gamma(R) \equiv \Gamma$ at its outer radius, we get from (9), (10), and (36) the resultant axial force and torque

$$F(\Gamma) = -\frac{3\pi R^2}{\Gamma^2}\int_0^\Gamma \gamma\tau_e(\gamma)\sin\alpha\,d\gamma$$

$$T(\Gamma) = \frac{2\pi R^3}{\Gamma^3}\int_0^\Gamma \gamma^2\tau_e(\gamma)\cos\alpha\,d\gamma. \tag{43}$$

From (8) and (36) the hydrostatic pressure distribution is

$$p(r) = \int_r^R \frac{1}{r}\,\tau_e(\gamma)\sin\alpha\,dr. \tag{44}$$

The normal stresses in the bar are obtained from (4).

For rigid plastic behavior, (14) leads to the classical solution (Nadai, 1950) according to which $\gamma_e = \gamma$ and the only nonzero stress component is $\sigma_{z\theta} = \tau_e$. This corresponds to $\alpha = 0$ in the foregoing elastic-plastic solution, and now $p = F = 0$. For an equivalent shear stress—shear strain curve of the form

$$\tau_e = f(\gamma_e), \tag{45}$$

the resulting twisting couple is

$$T(\Gamma) = \frac{2\pi R^3}{\Gamma^3}\int_0^\Gamma \gamma^2 f(\gamma)d\gamma. \tag{46}$$

4.2 Kinematic Hardening J_2 Flow Theory. In this case analytical solutions are readily obtained for the rigid-plastic model (22), (23). The solution in simple shear is such that all components of s_{ij} and β_{ij} are zero, except for those in the $\theta - z$ plane. Since $\dot{\gamma}_c = \dot{\gamma}$, (1) and (22) give

$$s_{\theta\theta} = \beta_{\theta\theta} = -s_{zz} = -\beta_{zz},$$

$$s_{z\theta} = \sigma_{z\theta} = \tau_Y + \beta_{z\theta}. \tag{47}$$

Form the shift rule (23), we get

$$\dot{\beta}_{\theta\theta} = -\dot{\beta}_{zz} = 2\beta_{z\theta}\overset{*}{\omega}$$

$$\dot{\beta}_{z\theta} = G_t\dot{\gamma} - 2\beta_{\theta\theta}\overset{*}{\omega}, \tag{48}$$

where $\overset{*}{\omega} = \Omega_{\theta z} = -\Omega_{z\theta}$ represents the components of the antisymmetric spin tensor Ω appearing in the definition (13) of the Jaumann rate. (All other $\Omega_{ij} = 0$ here.)

According to Tvergaard's (1978) model, the material spin ω (1) is employed in (13). As a result, $\overset{*}{\omega} = \dot{\gamma}/2$ and (48) can be written as

$$\dot{\beta}_{\theta\theta} = \beta_{z\theta}\dot{\gamma}, \quad \dot{\beta}_{z\theta} = (G_t - \beta_{\theta\theta})\dot{\gamma}. \tag{49}$$

In a manner analogous to (36), we introduce a parametric angle α as follows:

$$\beta_{\theta\theta} = \beta_e\sin\alpha, \quad \beta_{z\theta} = \beta_e\cos\alpha. \tag{50}$$

(Recall $\tau_e = \tau_Y + \beta_e$.) Substituting (50) into (49) gives (c.f. equations (37) and (38))

$$\dot{\beta}_e = [G_t\cos\alpha]\dot{\gamma}, \quad \dot{\alpha} = \left[1 - \frac{G_t}{\beta_e}\sin\alpha\right]\dot{\gamma} \tag{51}$$

$$(\beta_e - G_t\sin\alpha)d\beta_e - (\beta_e G_t\cos\alpha)d\alpha = 0. \tag{52}$$

Using a procedure similar to that used to solve (37) and (38) we obtain the following solution to (52)

$$\alpha(\beta_e) = \sin^{-1}\left[\frac{1}{\beta_e}\int_0^{\beta_e}\frac{\beta_e}{G_t}\,d\beta_e\right]. \tag{53}$$

Also, from (51),

$$\gamma(\alpha) = \int_0^\alpha\left[1 - \frac{G_t}{\beta_e}\sin\alpha\right]^{-1}d\alpha. \tag{54}$$

For a rigid-plastic power-law hardening material with an effective shear stress—shear strain curve of the form

$$\tau_e = \tau_Y + h\gamma_e{}^N \tag{55}$$

where h and N are constants, the above expressions give

$$\alpha = \frac{\gamma}{N+1}, \quad \beta_e = h\left[(N+1)\sin\left(\frac{\gamma}{N+1}\right)\right]^N. \tag{56}$$

From (47), (50), and (56) we immediately get the expressions for $\beta_{ij}(\gamma)$ and $s_{ij}(\gamma)$.

For the corresponding solid bar, the resultant torque and axial force for $\gamma(R) = \Gamma$ become

$$T(\Gamma) = \frac{2\pi R^3}{\Gamma^3}\int_0^\Gamma \gamma^2\left[\tau_Y + \beta_e\cos\left(\frac{\gamma}{N+1}\right)\right]d\gamma \tag{57}$$

and

$$F(\Gamma) = -\frac{3\pi R^2}{\Gamma^2}\int_0^\Gamma \gamma\beta_e\sin\left(\frac{\gamma}{N+1}\right)d\gamma, \tag{58}$$

respectively, with $\beta_e(\gamma)$ given by (56). From (8), (50), and (56) we obtain the following expression for hydrostatic pressure

Downloaded 03 May 2010 to 171.66.16.244. Redistribution subject to ASME license or copyright; see http://www.asme.org/terms/Terms_Use.cfm

$$p(r) = -\int_R^r \frac{1}{r}\beta_e \sin\left(\frac{\gamma}{N+1}\right) dr \tag{59}$$

where $\gamma = r\Gamma/R$. This result, combined with (4), gives the normal stresses across the bar for a given value of Γ.

For a linear hardening material ($N=1$), we recover the simple shear solution given by Dafalias (1983); i.e., the above relations reduce to

$$\beta_{\theta\theta} = h(1-\cos\gamma), \quad \beta_{z\theta} = h\sin\gamma \tag{60}$$

$$s_{\theta\theta} = -s_{zz} = h(1-\cos\gamma)$$

$$s_{z\theta} = \sigma_{z\theta} = \tau_Y + h\sin\gamma.$$

For the solid bar we have

$$T(\Gamma) = \frac{2\pi R^3}{3}\left[\tau_Y + \frac{3h}{\Gamma^3}(2\Gamma\sin\Gamma + 2\cos\Gamma - \Gamma^2\cos\Gamma - 2)\right] \tag{61}$$

$$F(\Gamma) = -\frac{3\pi R^2 h}{\Gamma^2}\left[1 + \frac{\Gamma^2}{2} - \Gamma\sin\Gamma - \cos\Gamma\right]. \tag{62}$$

The kinematic hardening model proposed by Dafalias (1983) employs the spin $\dot{\mathbf{R}}\mathbf{R}^T$($\mathbf{R}$ is the orthogonal part of the polar decomposition of the velocity gradient), instead of the material spin ω, in the Jaumann rate expression (13). For simple shear deformations, this gives

$$\overset{*}{\omega} = \frac{2\dot{\gamma}}{\gamma^2+4} \tag{63}$$

in (48). Assuming linear hardening, the resulting equations can be solved explicitly for s_{ij} as functions of γ. The expressions for $s_{ij}(\gamma)$ can be found in (Dafalias, 1983) and shall not be repeated here. The transition from the simple shear solution to that for the solid circular bar is as described previously. We simply substitute the simple shear results $s_{ij}(\gamma)$ in (8)–(10) and (4) to determine the total stresses σ_{ij} across the bar, as well as the corresponding resultants F and T.

Among the numerous other kinematic-hardening models that have been proposed, many can be shown to lead to closed-form solutions for the large strain torsion of solid circular bars. If analytical solutions can be obtained for simple shear deformations, then the procedure outlined previously will provide the solution for the solid bar. The kinematic-hardening theories of Fressengeas and Molinari (1983), Dienes (1979) and Key (1984) give rise to such closed-form solutions.

4.3 Hypoelastic J_2 Deformation Theory. Because of the similarity between the elastic-plastic isotropic-hardening J_2 flow theory law (15) and the hypoelastic J_2 deformation theory relation (24), putting $G = G_s$ in the solution derived in Section 4.1 immediately furnishes the torsion solution for a material obeying the hypoelastic version (Stören and Rice, 1975) of J_2 deformation theory. Thus, equations (39)–(41) apply, but with G replaced by the secant shear modulus $G_s(\tau_e)$ as determined by the equivalent shear stress—shear strain relation for the material.

In the elastic range ($\gamma \le \gamma_Y$), the response is again given by (34). The elastic-plastic solution is simplified considerably by substituting $G_t = d\tau_e/d\gamma_e$, $G_s = \tau_e/\gamma_e$ and expressing the result in terms of γ_e. This leads to the result

$$\alpha = \sin^{-1}\left(\frac{\gamma_e}{2}\right), \quad \gamma = 2\alpha = 2\sin^{-1}\left(\frac{\gamma_e}{2}\right). \tag{64}$$

Substituting this in (36) gives

$$s_{\theta\theta} = -s_{zz} = 2G_s(\gamma_e)\sin^2\left(\frac{\gamma}{2}\right), \quad s_{z\theta} = G_s(\gamma_e)\sin\gamma. \tag{65}$$

Note that, from (35) and (64), the effective strain at yield satisfies $\gamma_{eY} = \tau_Y/G$.

For the solid bar (8)–(10) together with the above give

$$p(r) = -\int_R^r \frac{2}{r} G_s(\gamma_e)\sin^2\left(\frac{\gamma}{2}\right) dr \tag{66}$$

with $\gamma = r\Gamma/R$,

$$F(\Gamma) = -\frac{3\pi R^2}{\Gamma^2}\int_0^\Gamma 2\gamma G_s(\gamma_e)\sin^2\left(\frac{\gamma}{2}\right) d\gamma \tag{67}$$

and

$$T(\Gamma) = \frac{2\pi R^3}{\Gamma^3}\int_0^\Gamma \gamma^2 G_s(\gamma_e)\sin\gamma\, d\gamma. \tag{68}$$

In all of the foregoing expressions, G_s is evaluated at $\gamma_e = 2\sin(\gamma/2)$.

4.4 Hyperelastic J_2 Deformation Theory. The solution associated with the hyperelastic version of J_2 deformation theory (Hutchinson and Neale, 1987a) entails a calculation of the principal stretches λ_i and principal directions of Eulerian strain. For simple shear deformations, the principal stretches in the plane of shear are easily shown to be

$$\lambda_I = \frac{1}{\lambda_{II}} = \frac{\gamma}{2} + \left[1 + \frac{\gamma^2}{4}\right]^{1/2}. \tag{69}$$

The direction normal to this plane, ϵ_r, is also a principal direction and $\lambda_{III} \equiv \lambda_r = 1$. The direction of major principal Eulerian strain is inclined at an angle $\phi = \tan^{-1}(\lambda_{II})$ relative to the $\mathbf{e}_\theta$-axis, and the principal stress deviators, from (25), become

$$s_I = -s_{II} = 2G_s \ln\lambda_I, \quad s_{III} = s_{rr} = 0. \tag{70}$$

We also have

$$\tau_e = s_I, \ \gamma_e = 2\epsilon_I = 2\ln\lambda_I. \tag{71}$$

Transforming (70) from the principal Eulerian directions to the $\Theta - z$ reference axes gives the following components:

$$s_{\theta\theta} = -s_{zz} = \frac{2\gamma}{\sqrt{(4+\gamma^2)}} G_s \ln\lambda_I$$

$$s_{z\theta} = \frac{4}{\sqrt{(4+\gamma^2)}} G_s \ln\lambda_I \tag{72}$$

For the solid bar subjected to a twist $R\psi = \Gamma = \gamma(R)$, the resulting twisting couple becomes

$$T(\Gamma) = \frac{2\pi R^3}{\Gamma^3}\int_0^\Gamma \frac{4\gamma^2}{\sqrt{(4+\gamma^2)}} G_s \ln\lambda_I d\gamma, \tag{73}$$

and the axial force is

$$F(\Gamma) = -\frac{3\pi R^2}{\Gamma^2}\int_0^\Gamma \frac{2\gamma^2}{\sqrt{(4+\gamma^2)}} G_s \ln\lambda_I d\gamma. \tag{74}$$

Note that the torque and axial force satisfy the relation

$$\frac{F}{T} = -\frac{3\Gamma}{4R}. \tag{75}$$

The hydrostatic pressure distribution across the bar is

$$p(r) = \int_r^R \frac{2G_s\gamma}{r\sqrt{(4+\gamma^2)}} \ln\lambda_I dr \tag{76}$$

with $\gamma = r\Gamma/R$. Again, combining this result with (4) gives the normal stresses in the bar as a function of Γ.

4.5 Rate-Dependent Plasticity Laws. The rate-dependent constitutive model (28) leads to the following simple solution for shear:

$$\sigma_{z\theta} = \tau_e, \quad \dot{\gamma}_e = \dot{\gamma}, \tag{77}$$

with all other components of $s_{ij} = 0$. Thus, for the solid bar the hydrostatic pressure p, normal stress components σ_{ij}, and axial force F, are all zero.

Downloaded 03 May 2010 to 171.66.16.244. Redistribution subject to ASME license or copyright; see http://www.asme.org/terms/Terms_Use.cfm

For a bar twisted at a rate such that $\dot{\gamma}(R)=\dot{\Gamma}$, the relation (28) implies that, at a radial distance r,

$$\sigma_{z\theta}=K\gamma^N\dot{\gamma}^m, \tag{78}$$

with $\gamma(r)=r\Gamma/R$. Substituting this in (6) gives

$$T(\Gamma,\dot{\Gamma})=\frac{2\pi R^3}{(3+N+m)}K\Gamma^N\dot{\Gamma}^m. \tag{79}$$

For rate-independent behavior ($m=0$) and a power-law hardening curve of the form $\tau_e=K\gamma_e{}^N$, (79) becomes a special case of the classical rigid-plastic result (46).

5 Numerical Results and Discussion

In order to illustrate the differences in the responses predicted by the various rate-independent plasticity laws, the analytical solutions of the previous section are applied to materials whose uniaxial response is represented by a power-law relation of the type:

$$\frac{\tau_e}{\tau_Y}=\left(\frac{G}{\tau_Y}\right)\gamma_e \quad ; \quad \gamma_e\le\gamma_{eY}=\frac{\tau_Y}{G}$$

$$\frac{\tau_e}{\tau_Y}=1+K(\gamma_e-\gamma_{eY})^N \quad ; \quad \gamma_e\ge\gamma_{eY}. \tag{80}$$

This representation includes the linear hardening case when $N=1$. The rigid plastic versions are obtained by taking $\gamma_{eY}=0$. Figure 1 shows the $\tau_e-\gamma_e$ curve employed here: (a) a linear hardening law with $G/\tau_Y=500$, $K=0.5$, $N=1$, and (b) a power-law relation with $G/\tau_Y=500$, $K=2.845$, $N=0.2$. To deal with possible negative values of γ_e, we assume that the $\tau_e-\gamma_e$ curves are symmetric with respect to the origin.

The simple shear and torsion responses according to the linear hardening law are shown in Figs. 2(*a*)–2(*d*), while those pertaining to power-law hardening are described by Figs. 3(*a*)–3(*d*). The simple shear results consist of the graphs of the normalized shear and axial stresses ($s_{z\theta}/\tau_y$ and s_{zz}/τ_y assuming zero hydrostatic pressure) as functions of γ. The torsion results are described by the variation of the mean shear stress and axial stress (τ/τ_Y and σ/τ_Y) with respect to Γ. These variables are related to the torque and axial force through equations (9) and (10) as follows:

$$\tau=\frac{3T}{2\pi R^3}=\frac{3}{\Gamma^3}\int_0^\Gamma\gamma^2 s_{z\theta}(\gamma)d\gamma \tag{81}$$

$$\sigma=\frac{F}{\pi R^2}=-\frac{3}{\Gamma^2}\int_0^\Gamma\gamma s_{\theta\theta}(\gamma)d\gamma. \tag{82}$$

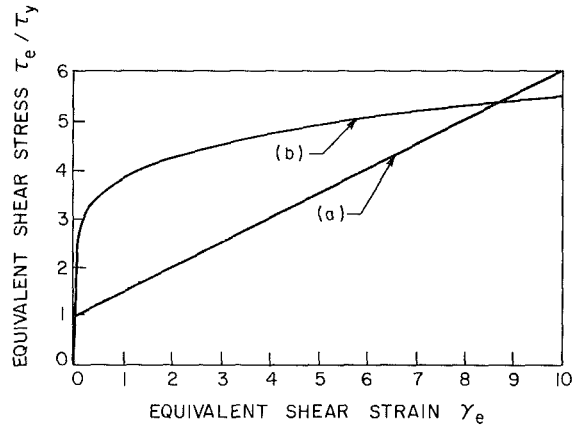


Fig. 1 Material models: (*a*) linear hardening, (*b*) power-law hardening

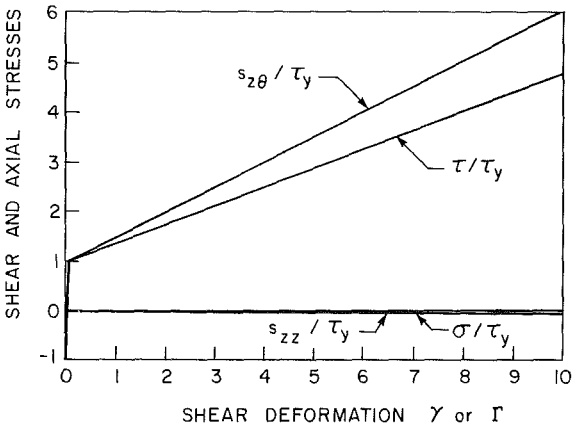


Fig. 2(*a*) Predicted responses in simple shear and torsion for J_2 isotropic-hardening theory (linear hardening)

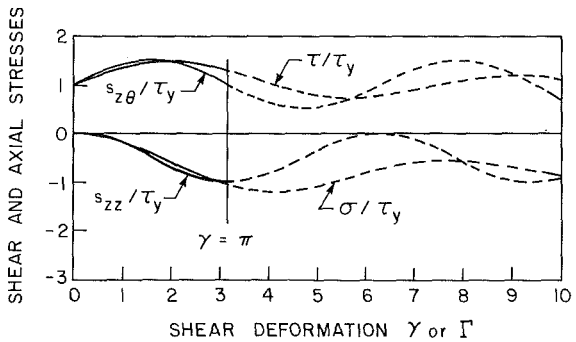


Fig. 2(*b*) Predicted responses in simple shear and torsion for J_2 kinematic-hardening theory (linear hardening)

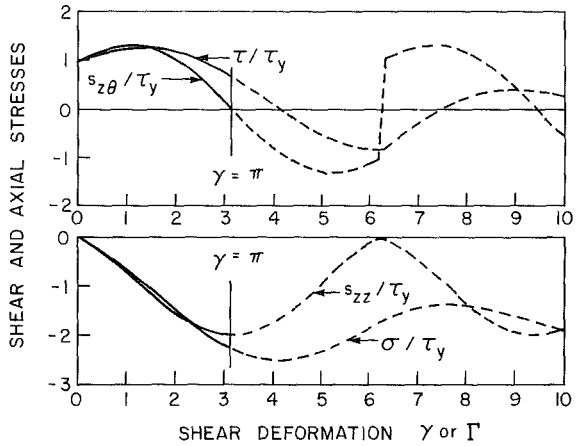


Fig. 2(*c*) Predicted responses in simple shear and torsion for J_2 hypoelastic theory (linear hardening)

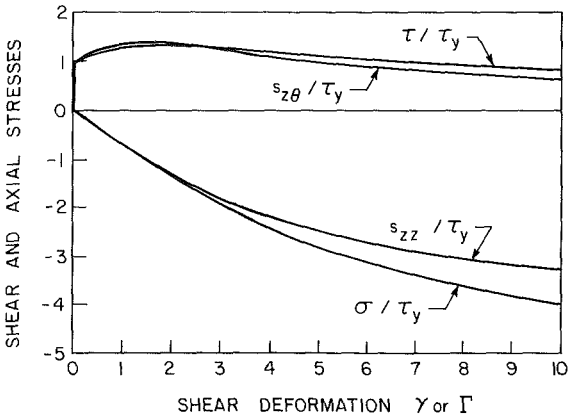


Fig. 2(*d*) Predicted responses in simple shear and torsion for J_2 hyperelastic theory (linear hardening)

Downloaded 03 May 2010 to 171.66.16.244. Redistribution subject to ASME license or copyright; see http://www.asme.org/terms/Terms_Use.cfm

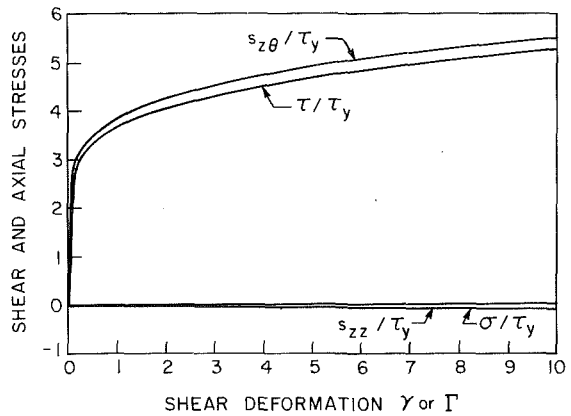


Fig. 3(a) Predicted responses in simple shear and torsion for J_2 isotropic-hardening theory (power-law hardening)

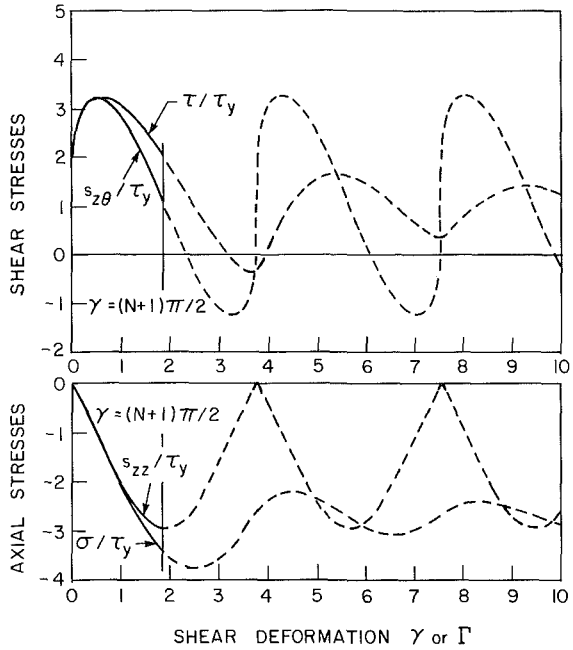


Fig. 3(b) Predicted responses in simple shear and torsion for J_2 kinematic-hardening theory (power-law hardening)

For simplicity, we do not show the radial distributions of σ_{rr}, σ_{zz}, $\sigma_{\theta\theta}$ in the twisted bar although, in the present case of fixed-end torsion, the radial variation of $\sigma_{z\theta}$ at any Γ can be inferred from the simple shear $s_{z\theta}-\gamma$ graph.

The results shown are for elastic-plastic material response, except those for the kinematic-hardening theory (Figs. 2(*b*) and 3(*b*)) which are obtained by treating the material as rigid plastic. In any case, since the elastic modulus is high ($G/\tau_y = 500$), the elastic-plastic results are very close to the rigid-plastic ones. Table 1 lists the rigid plastic solutions and their properties for simple shear and torsion assuming a rigid-plastic power-law material. Explicit closed-form expressions for τ and σ, although not listed here, can be obtained easily for the linear hardening material (for example, equations (61) and (62) for the kinematic hardening theory). Qualitatively, some of the results shown are similar to those reported in earlier work (Neale and Shrivastava 1985, 1989) except that previously they were obtained numerically. The dotted portions of the graphs indicate the regions for which the validity of the solutions is questionable on physical grounds as will be discussed later.

Table 1 may be used in conjunction with Figs. (2) and (3) for comparing the solutions from different theories, observing

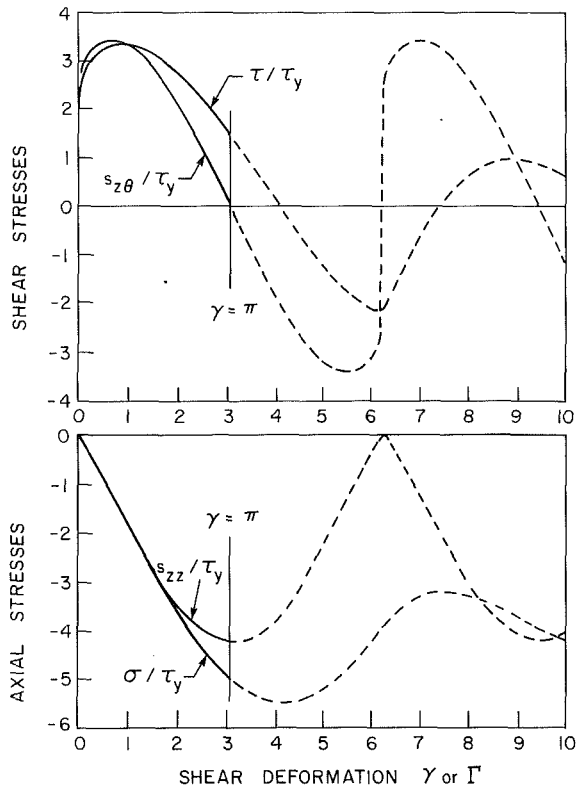


Fig. 3(c) Predicted responses in simple shear and torsion for J_2 hypoelastic theory (power-law hardening)

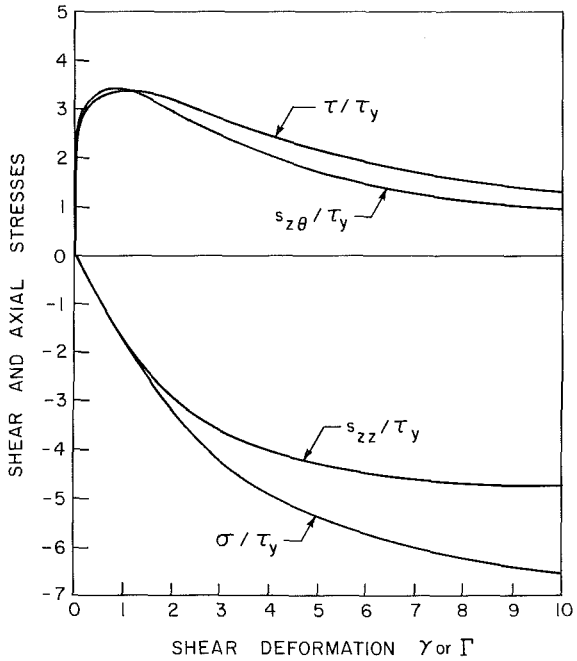


Fig. 3(d) Predicted responses in simple shear and torsion for J_2 hyperelastic theory (power-law hardening)

that essentially there are no qualitative differences in the responses with respect to the material models—linear or power law—and that we may consider the two sets of results together in the following discussion. We note first of all that both J_2 kinematic-hardening (Figs. 2(*b*) and 3(*b*)) and J_2 hypoelastic (Figs. 2(*c*) and 3(*c*)) theories predict periodic responses in simple shear, and hence oscillatory responses in torsion. The period is 2π for the hypoelastic theory and $(N+1)\pi$ for the kinematic-hardening theory. In contrast, the results obtained

Downloaded 03 May 2010 to 171.66.16.244. Redistribution subject to ASME license or copyright; see http://www.asme.org/terms/Terms_Use.cfm

Table 1 Predicted responses for a rigid plastic power-law material, $\tau_e/\tau_Y = f(\gamma_e) = [1 + K\gamma_e^N]$, in simple shear and fixed-end torsion

Variable	J_2 isotropic	J_2 kinematic	J_2 hypoelastic	J_2 hyperelastic
		SIMPLE SHEAR		
γ_e	γ	$(N+1)\sin\frac{\gamma}{(N+1)}$	$2\sin\frac{\gamma}{2}$	$2\,\text{sn}\left(\frac{\gamma}{2}+\left[1+\frac{\gamma^2}{4}\right]^{\frac{1}{2}}\right)$
s_{zz}/τ_Y	0	$-[f(\gamma_e)-1]\sin\frac{\gamma}{(N+1)}$	$-f(\gamma_e)\sin\frac{\gamma}{2}$	$-f(\gamma_e)\tanh\frac{\gamma_e}{2}$
$s_{z\theta}/\tau_Y$	$f(\gamma)$	$1+[f(\gamma_e)-1]\cos\frac{\gamma}{(N+1)}$	$f(\gamma_e)\cos\frac{\gamma}{2}$	$f(\gamma_e)\,\text{sech}\frac{\gamma_e}{2}$
		$\left(s_{z\theta}-\tau_Y=-\frac{ds_{zz}}{d\gamma}\right)$	$\left(s_{z\theta}=-\frac{2s_{zz}}{\gamma}\right.$ $\left.-2f(\gamma_e)\frac{ds_{zz}}{d\gamma}\right)$	$\left(s_{z\theta}=-\frac{2s_{zz}}{\gamma}\right)$
			$\overline{(N+1)f(\gamma_e)-N}$	
		TORSION		
σ/τ_Y	0	Eq.(82)	Eq.(82)	Eq.(82)
τ/τ_Y	$\frac{3f(\Gamma)+N}{N+3}$	Eq.(81)	Eq.(81)	Eq.(81)
		$\left(\tau-\tau_Y=-\frac{d\sigma}{d\Gamma}\right)$		$\left(\tau=-\frac{2\sigma}{\Gamma}\right)$

Table 2 Maximum $s_{z\theta}$ in simple shear and maximum τ in torsion and the corresponding s_{zz}, γ, and σ, Γ values for linear and power-law materials. (There is no maximum for isotropic hardening theory; the values given for this theory correspond to the maxima of the hyperelastic theory.)

Material Law	Simple Shear			Torsion		
Linear	max.$s_{z\theta}/\tau_Y$	γ	s_{zz}/τ_Y	max.τ/τ_Y	Γ	σ/τ_Y
Kine. Hardening	1.50	1.57	-0.50	1.46	2.0	-0.6
Hypoelastic	1.30	1.0	-0.71	1.28	1.3	-0.9
Hyperelastic	1.35	1.5	-1.02	1.34	1.9	-1.27
(Iso. Hardening	1.75	1.5	-0.006	1.71	1.9	-0.008)
Power-law	max.$s_{z\theta}/\tau_Y$	γ	s_{zz}/τ_Y	max.τ/τ_Y	Γ	σ/τ_Y
Kine. Hardening	3.25	0.5	-0.99	3.22	0.6	-1.17
Hypoelastic	3.42	0.7	-1.25	3.38	0.9	-1.59
Hyperelastic	3.44	0.8	-1.38	3.41	1.0	-1.71
(Iso. Hardening	3.72	0.8	-0.024	3.67	1.0	-0.033)

from the J_2 isotropic hardening (Figs. 2(*a*) and 3(*a*)) and J_2 hyperelastic (Figs. 2(*d*) and 3(*d*)) theories show mostly a monotonic variation, except that the shear stress or the torque for the hyperelastic material first rises to a maximum and then decreases monotonically.

We find that in all cases the axial stress (s_{zz} or σ) remains compressive. For a given γ or Γ it turns out to be the largest for the hyperelastic case. On the other hand, it remains negligibly small in the isotropic hardening case, thereby rendering the calculated response as approximately a pure shear one. For the kinematic-hardening and hypoelastic cases the s_{zz} stress component in simple shear varies periodically attaining a minimum value equal to zero. But in torsion, the stress σ corresponding to the axial force shows an attenuated variation with Γ.

Regarding the shear stress $s_{z\theta}$ in simple shear we note that, according to the hypoelastic theory, it undergoes a sign change at intervals of $\gamma = \pi$ regardless of the particular hardening law. The sign changes in $s_{z\theta}$ may or may not occur for the kinematic-hardening theory depending on the values of K and N in the power-law expression. The resulting torque from both of these theories, represented by the variation of τ, can also undergo sign changes depending on the material characteristics. It is evident that in the cases of hyperelastic and isotropic hardening theories, $s_{z\theta}$ and τ do not change sign and thus remain positive, though they do possess maximum values for the hyperelastic case.

It is interesting to observe that the initial responses in terms of shear stress are quite similar for the different theories (except for the isotropic hardening theory) and that the initial maximums of $s_{z\theta}$ or τ are not too different from each other. Table 2 provides a comparison of these maximums for the different theories and material models, together with the corresponding γ or Γ and s_{zz} or σ values. From this table we also notice that the maximum value of $s_{z\theta}$ in simple shear is quite close in value to the maximum value of τ of torsion. These observations then suggest that, at least in the initial stage, the shear stress response is rather insensitive to the constitutive law, and measurements of torque or shear stress in experiments may not be relied upon to discriminate between the intrinsic material characteristics in this range. However, the differences in s_{zz} or σ are quite significant even in the initial state, and it seems that their measurements would provide a better indication of the material characteristics.

With regard to the question of the physical validity of the solutions, we note that the solutions must be in accordance with the condition of continued plastic loading. For incremental theories of plasticity (Neale, 1981), neglecting elastic strains, these consist in requiring that $\dot{W} = s_{ij}\dot{\epsilon}_{ij} \geq 0$ and $\dot{\tau}_e \geq 0$ for the isotropic hardening theory, and $\dot{W} = \bar{s}_{ij}\dot{\epsilon}_{ij} \geq 0$ and $\dot{\beta}_e \geq 0$ for the kinematic hardening theory. On the other hand, for deformation theories (Neale, 1981), we have the single criterion requiring that $\dot{\tau}_e \geq 0$. On the basis of these criteria, we find that the solutions for the J_2 isotropic hardening incremental theory and J_2 hyperelastic deformation theory are valid for the entire $(0 \leq \gamma \leq 10)$ range of deformation. However, this is not the case with the other two theories. In the case of J_2 hypoelastic deformation theory, the range of validity is $0 \leq \gamma \leq \pi$ regardless of any particular material model. In the case of J_2 kinematic-hardening incremental theory, this range depends on the exponent of the power-law relation and is given by $0 \leq \gamma \leq (N+1)\pi/2$. It is obvious that exactly the same restrictions in terms of Γ apply to the torsional responses computed from these theories. For γ or Γ values higher than the upper limits we find that $\dot{\tau}_e < 0$ for the hypoelastic theory, and $\dot{\beta}_e < 0$ for the kinematic-hardening theory. The analysis of responses beyond the upper limits requires a closer examination of the assumptions involved in constitutive modeling of these two theories.

So far we have given explicit formulae for the torque T and axial force F, in terms of the shear deformation Γ, for the various constitutive theories. We shall now develop relations so that the simple shear results $s_{ij}(\gamma)$ can be extracted directly from experimentally measured axial force and torque-twist curves.

From (9) and (10), it follows that

$$\frac{\partial T}{\partial \Gamma} = \frac{1}{\Gamma}[-3T + 2\pi R^3 s_{z\theta}(\Gamma)] \tag{83}$$

$$\frac{\partial F}{\partial \Gamma} = \frac{1}{\Gamma}[2F - 3\pi R^2 s_{\theta\theta}(\Gamma)]. \tag{84}$$

As a result, to extract the simple shear relations we use

$$s_{z\theta}(\Gamma) = \frac{1}{2\pi R^3}\left[3T + \Gamma\frac{\partial T}{\partial \Gamma}\right] \tag{85}$$

$$s_{\theta\theta}(\Gamma) = -s_{zz}(\Gamma) = \frac{1}{3\pi R^2}\left[2F - \Gamma\frac{\partial F}{\partial \Gamma}\right]. \tag{86}$$

Recall that all other $s_{ij} = 0$.

The relation (85) is identical to that derived by Nadai (1950) and Hill (1950) on the basis of J_2 flow theory. This expression and (86), however, hold for all of the constitutive models considered here. They can be used together with the theoretical results (e.g., those summarized in Table 1) to interpret ex-

Downloaded 03 May 2010 to 171.66.16.244. Redistribution subject to ASME license or copyright; see http://www.asme.org/terms/Terms_Use.cfm

perimental data and determine material constants in the large strain range. For improved accuracy at small Γ, it is preferable to write (85) as

$$s_{z\theta}(\Gamma)=\frac{1}{2\pi R^3}\left[\Gamma^2\frac{\partial(T/\Gamma)}{\partial\Gamma}+4T\right] \tag{87}$$

as suggested by Hill (1950) and Störakers (1979), and

$$s_{\theta\theta}(\Gamma)=-s_{zz}(\Gamma)=-\frac{\Gamma^3}{3\pi R^2}\frac{\partial(F/\Gamma^2)}{\partial\Gamma}. \tag{88}$$

Also, substituting the above expressions in (31) and using the results of Table 1 allows us to construct the effective shear stress (τ_e)-effective shear strain (γ_e) curves from the experimentally measured axial force and torque-twist curves.

We conclude this study with a brief discussion concerning experiments involving large strain torsion. Although the torsion test is widely used for simulating large strain behavior of metals, for example, in rolling, the body of test data documenting the development of axial forces or length changes with the progression of twist is rather sparse. Swift (1947) was the first to conduct large-strain torsion tests on solid circular bars and tubes of several metals at room temperature. These were free-end tests allowing length changes, and the maximum shear attained before failure was of the order of $\Gamma=6$. He observed that, with the exception of lead specimens which shortened, all other specimens exhibited monotonic length increases. This observation, in terms of fixed-end torsion, implies that at room temperature one can expect the development of an axial compressive force which increases with twist. At elevated temperatures, the situation appears to be quite different. For example, Hardwick and Tegart (1961) in their tests observed that although initially ($\Gamma<6$), the specimens showed a length increase, in agreement with Swift's observations, further twisting to ultra large strains ($\Gamma\approx 20$) produced a net shortening of all the specimens (with the exception of aluminum which, after initial lengthening, showed no further lengthening or shortening). Their fixed-end tests were also consistent with the above finding in that the compressive force developed initially changed to a tensile force at large shear strains (again with the exception of aluminum).

The more recent fixed-end tests reported by Montheillet, Cohen, and Jonas (1984) on aluminum, copper, and iron bar specimens have confirmed the findings of Hardwick and Tegart. The typical experimental torque and axial force versus twist curves (Figs. 1 and 3 of Montheillet et al.) show first that a common characteristic of the torque-twist curves is that the torque attains a single maximum at a relatively small shear strain, and thereafter it begins to drop to an almost steady-state value. On the other hand, they observe that the axial force is initially compressive and attains a maximum at about the same strain at which maximum torque is reached. Another trend is that as the test temperature increases, the value of the maximum compressive force diminishes. With further twist, past the maximum point, the axial force either decreases to a steady-state tension value or displays a limited oscillatory behavior in the sense of reaching a minimum and then again attaining a maximum. The attainment of a steady-state tension value seems possible only at high enough temperatures.

A qualitative comparison of these experimental observations with the corresponding predictions of the theories considered in this investigation makes it quite clear that none of the constitutive laws examined is capable of accurately simulating the experimental behavior for arbitrarily large strains. On the other hand, the moderately large strain behavior (up to the point of maximum torque) is well-described by any of the theories (except by the J_2 isotropic hardening theory which does not display a maximum).

Acknowledgments

This work was supported by the Natural Sciences and Engineering Research Council of Canada (NSERC) and the government of the Province of Québec (Programme FCAR).

References

Birkhoff, G., and Rota, G. C., 1969, *Ordinary Differential Equations*, Blaisdell Publishing Company, Waltham, Mass.

Budiansky, B., 1970, unpublished work, (see Hutchinson, 1973).

Dafalias, Y. F. 1983, "Corotational Rates for Kinematic Hardening at Large Plastic Deformations," ASME JOURNAL OF APPLIED MECHANICS, Vol. 105, pp. 561–565.

Dienes, J. K., 1979, "On the Analysis of Rotation and Stress Rate in Deforming Bodies," *Acta Mechanica*, Vol. 32, pp. 217–232.

Fressengeas, C., and Molinari, A., 1983, "Modèles d'écrouissage cinématique en grande déformation," *Comptes Rendus, Academie des Sciences,* Paris, Vol. 297, Séries II, pp. 93–96.

Hardwick, D., and Tegart, W. J., 1961, "La déformation des métaux et alliages par torsion à haute température," *Memoires scientifiques, Revue de metallurgie*, Vol. 8, pp. 869–880.

Hill, R., 1950, *The Mathematical Theory of Plasticity*, Oxford University Press, London.

Hill, R., 1970, "Constitutive Inequalities for Isotropic Elastic Solids Under Finite Strain," *Proceedings of the Royal Society, London*, Vol. A314, pp. 457–472.

Hutchinson, J. W., 1973, "Finite Strain Analysis of Elastic-Plastic Solids and Structures," *Numerical Solution of Nonlinear Structural Problems*, R. F. Hartung, ed., AMD Vol. 6, ASME, New York, pp. 17–29.

Hutchinson, J. W., and Neale, K. W., 1978a, "Sheet Necking—II. Time-Independent Behavior," *Mechanics of Sheet Metal Forming*, D. P. Koistinen and N.-M. Wang, eds., Plenum Press, New York, pp. 127–153.

Hutchinson, J. W., and Neale, K. W., 1978b, "Sheet Necking—III. Strain-Rate Effects," *Mechanics of Sheet Metal Forming,* D. P. Koistinen, and N.-M Wang, eds., Plenum Press, New York, pp. 269–285.

Key, S. W., 1984, "Theoretical Foundations for Large Scale Computations for Nonlinear Material Behavior," *Mechanics of Elastic and Inelastic Solids*, S. Nemat-Nasser, R. J. Asaro, and G. A. Hegemier, eds., Martinus Nijhoff Publishers, Amsterdam.

Lee, E. H., Mallett, R. L., and Wertheimer, T. B., 1983, "Stress Analysis for Anisotropic Hardening in Finite-Deformation Plasticity," ASME JOURNAL OF APPLIED MECHANICS, Vol. 50, 1983, pp. 554–560.

Montheillet, F., Cohen, M., and Jonas, J. J., 1984, "Axial Stresses and Texture Development During the Torsion Testing of Al, Cu and α-Fe," *Acta Metallurgica*, Vol. 32, pp. 2077–2089.

Nadai, A, 1950, *The Theory of Flow and Fracture of Solids*, McGraw-Hill, New York.

Nagtegaal, J. C., and De Jong, J. E., 1982, "Some Aspects of Non-Isotropic Workhardening in Finite Strain Plasticity," Proceedings of the Workshop on *Plasticity of Metals at Finite Strain: Theory Experiment and Computation*, E. H. Lee and R. L. Mallett, eds., Division of Applied Mechanics, Stanford University, Stanford, Calif., and Department of Mechanical Engineering, Aeronautical Engineering and Mechanics, Rensselaer Polytechnic Institute, Troy, N.Y., pp. 65–102.

Neale, K. W., 1981, "Phenomenological Constitutive Laws in Finite Plasticity," *Solid Mechanics Archives*, Vol. 6, pp. 79–128.

Neale, K. W., and Shrivastava, S. C., 1985, "Finite Elastic-Plastic Torsion of a Circular Bar," *Engineering Fracture Mechanics*, Vol. 21, pp. 747–754.

Neale, K. W., and Shrivastava, S. C., 1989, "Kinematic Work-Hardening Models and Their Implications on Large Strain Plastic Behaviour in Torsion," *Yielding, Damage and Failure of Anisotropic Solids,* J. P. Boehler, ed., Mechanical Engineering Publications, London, pp. 131–143.

Odqvist, F. K. G., 1966, *Mathematical Theory of Creep and Creep Rupture*, Clarendon Press, Oxford, U.K.

Störakers, B., 1979, "An Explicit Method to Determine Response Coefficients in Finite Elasticity," *Journal of Elasticity*, Vol. 9, pp. 207–214.

Stören, S., and Rice, J. R., 1975, "Localized Necking in Thin Sheets," *Journal of the Mechanics and Physics of Solids*, Vol. 23, pp. 421–441.

Swift, H. W., 1947, "Length Changes in Metals Under Torsional Overstrain," *Engineering*, Vol. 163, pp. 253–257.

Tvergaard, V., 1978, "Effect of Kinematic Hardening on Localized Necking in Biaxially Stretched Sheets," *International Journal of Mechanical Sciences*, Vol. 20, pp. 651–658.

Downloaded 03 May 2010 to 171.66.16.244. Redistribution subject to ASME license or copyright; see http://www.asme.org/terms/Terms_Use.cfm

A Rudimentary Analysis of Improving Fatigue Life of Metals by Shot-Peening

Y. F. Al-Obaid
Dean, Faculty of Technological Studies,
Paaet, Kuwait

In this paper, a rudimentary analysis of improving fatigue life of metals is presented. The process is viewed as one of repeated impact of a stream of hard shots on to a target. The model considers first a single shot impinging upon a target and, on bouncing, it leaves a residual stress below the surface of the target. The problem is then generalized to consider the effect of a stream of shots by assuming their effect to be uniformly distributed over the entire surface. The analysis is highly simplified and it mainly aims at understanding the mechanics of this complicated process. Although rudimentary, the theoretical analysis is seen to be in reasonable agreement with experimental results performed with shots on targets of various materials.

Introduction

In shot-peening, a stream of metal or glass spherical particles are caused to impinge on the surface of the component. The object is to include compressive residual stresses in the surface layers of the target. The impact of the spherical particles, which usually takes place at a high velocity ≈ 100 m/sec, also causes plastic deformation which results in changes in the mechanical properties in the surface material. In other words, shot-peening can produce a substantial increase in surface hardness of a component, as well as produce favorable residual stresses to increase fatigue life considerably. The general form of residual stress in a typical shot-peening operation is shown in Fig. 1. Some typical increases gained in fatigue limit by shot-peening are given in Table 1.

The variety of items that are shot-peened is impressive: gears of all types and sizes, shafts with circlip grooves, bearing surfaces with section changes, steam and gas turbine parts, aircraft undercarriage parts, helicopter propeller drives and blades, compressor and high performance engine parts-pistons, crank shafts, connecting rods, valves and blocks. Probably the most exotic application of shot-peening is peen-forming. If you shot-peen one side of a shot of metal, the stretching of the peened surface causes the sheet to develop a spherical curvature, convex on the peened side. By exercising rigid controls in this process, panels that cover the wings of most of the larger aircraft are now peened to exact aerodynamic profiles.

There are many parameters involved in shot-peening which must be accurately controlled and regulated in order to produce a compressively stressed surface layer in which the amount of stress, the uniformity of the stress, and the depth of the layer can be held constant from piece to piece. These parameters are the type and size of shot, angle of impact, time of exposure, and the extent of surface coverage.

The parameters of the process are intricately related, and indeed they are beyond single analytical formulation. However, in order to understand the main features of the process, a simplified analysis is attempted and, as will be seen, it surprisingly agrees reasonably well with experiments.

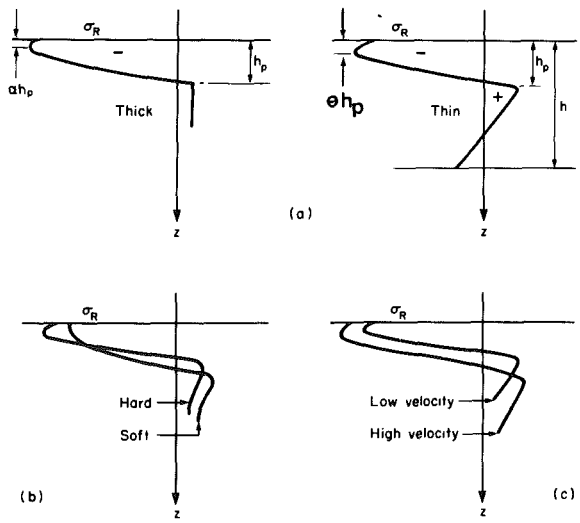


Fig. 1 Typical residual stress distributions

Contributed by the Applied Mechanics Division of THE AMERICAN SOCIETY OF MECHANICAL ENGINEERS for presentation at the Winter Annual Meeting, Dallas, Texas, November 25–30, 1990.

Discussion on this paper should be addressed to the Technical Editor, Leon M. Keer, The Technological Institute, Northwestern University, Evanston, IL 60208, and will be accepted until two months after final publication of the paper itself in the JOURNAL OF APPLIED MECHANICS. Manuscript received by the ASME Applied Mechanics Division, July 11, 1988; final revision, April 14, 1989.

Paper No. 90-WA/APM-8.

Copyright © 1990 by ASME
Downloaded 03 May 2010 to 171.66.16.244. Redistribution subject to ASME license or copyright; see http://www.asme.org/terms/Terms_Use.cfm

Mechanics of Shot-Peening

The sequence of events in the process can be summarized as follows: When a shot strikes the surface being peened, an identation at each point of impact is produced due to local plastic yielding (see Fig. 2). As the deformed regions tend to expand, they are restrained by adjacent, deeper metal that was not plastically deformed by the shot impact. As more and more shots impinge upon adjacent areas, the plastic zones are joined up to form a uniform layer when the whole of the surface is covered by impinging shots. Since the plastically deformed surface layer seeks to occupy more space, it is progressively compressed. This compressively stressed layer is extremely effective in preventing premature failure under conditions of cyclic loading, since the fatigue failure generally propagates from the free surface of a target and starts in a zone that is subjected to tensile stresses.

Table 1 Increase in fatigue limit, SAE Manual (1952)

Material	Fatigue Limit Unpeened MN/m^2	Fatigue Limit Peened MN/m^2	Percentage Increase
Carbon spring steel	517	793	54
Alloy spring steel	483	793	60
Stainless steel (302)	310	621	100
Phosphor bronze	103	207	100

When each shot rebounds, the balanced system of residual stresses are trapped in the specimen, the plastically deformed zone recovers only some part of the elastic portion of its total strain. The resulting trapped compressive stresses assume their position in a thin subsurface layer with tensile residual stresses distributed throughout the lower region. If the peening of a

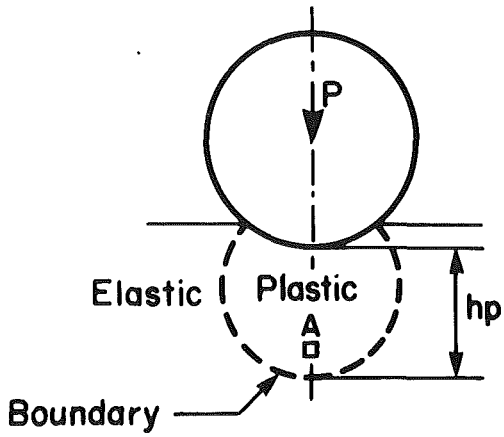
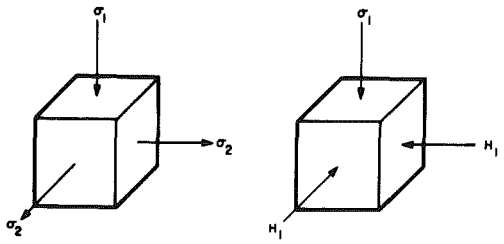
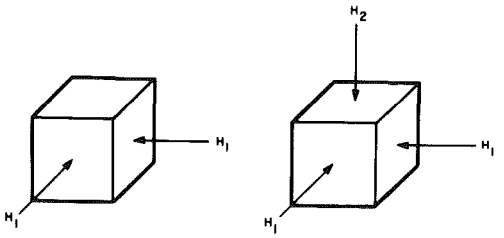


Fig. 2 Elastic-plastic boundary below contact zone



(a) Elastic before plastic flow (b) After plastic flow



(c) On removal of σ_1 (d) Secondary plastic flow

Fig. 3 Sequence of stress action in an element within a plastic zone

Nomenclature

E = Young's modulus
$\bar{F}$ = axial force in thin plate
L = length of plate
$\bar{M}$ = bending moment in thin plate
R = shot radius
Y = yield stress
b = width of plate
h_p = plate thickness
h = depth of plastic zone
m = strain rate index
P_o = maximum pressure
$\bar{p}$ = average pressure
t = time
v = impact velocity
z = depth
$\bar{z}$ = indentation
α = fraction of h_p where maximum residual stress occurs in a thick target
θ = fraction of h_p where maximum residual stress occurs in a thin target
δ = arc height
τ = h_p/h
ϵ = strain (suffix m—maximum)
$\dot{\epsilon}$ = strain rate (suffix o—reference)
ν = Poisson's ratio
σ = stress (suffix s—source, R—residual, b—bending, ax—axial)
ρ = density of shot

Downloaded 03 May 2010 to 171.66.16.244. Redistribution subject to ASME license or copyright; see http://www.asme.org/terms/Terms_Use.cfm

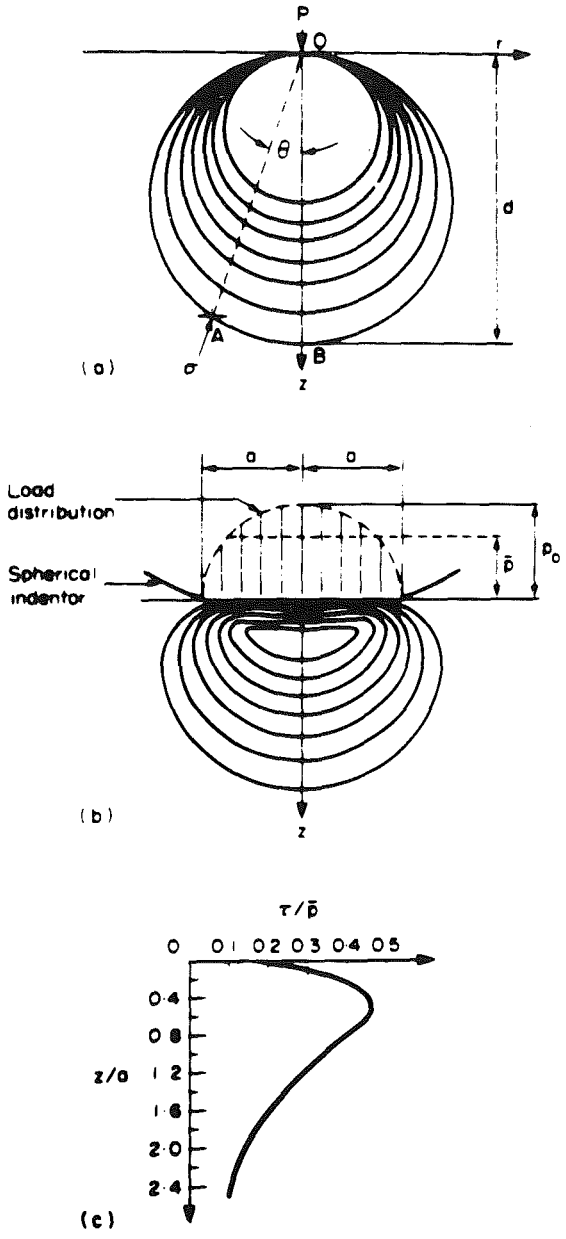


Fig. 4(*a*) Boussinesq solution for concentrated load *p*, (*b*) lines of constant $\tau/\bar{p}$, and (*c*) $\tau/\bar{p}$ versus *z/a* for vertical center line

specimen is continued excessively, the stress intensity developed may exceed a certain optimum value. This develops a tensile region of an increasing magnitude which ultimately causes fatigue failure of the subsurface layer.

In this paper, however, only a simplified analysis is considered. We first examine the stress field generated by a single spherical indenter and then a generalized approximation is made. Much of the discussion and philosophy focuses on what happens when a hard sphere impinges on an elastic-plastic target. The most important parameter, which at present we aim at predicting, is the depth of the plastic zone. This will be used to predict the residual stress distribution.

It is conceived in the analysis that when the shot presses on the surface, an element within the plastic/elastic field will go through a history as indicated in Fig. 3. First an elastic state of stress given by σ_1 and σ_2 and then by σ_1 and H_1 when plasticity develops. When the shot bounces off, the stress σ_1 is reversed as we have H_1 only. Of course, if H_1 is such that plasticity develops, then a condition of reversed plasticity develops. More discussion of this can be found in references Al-Hassani (1981) and Pope et al., (1975).

Statistical Aspects. Figure 4(*b*) shows lines of maximum elastic shear stress beneath a smooth spherical indenter as obtained from a Hertz analysis. The load distribution is hemispherical and the ratio of the mean $\bar{P}$ to maximum pressure P_o is 2/3. The maximum shear stress lines represent nondimensional values of $\tau/\bar{p}$ versus the nondimensional distance below the surface z/a from the vertical line. The base of the punch is drawn flat for convenience, even though it is a spherical surface of a larger radius. Plastic flow will occur first at a point beneath the surface ($z=0.47a$) corresponding to $\tau=0.468\ \bar{P}$, where a is the contact radius. By the maximum shear stress theory, this will occur when the stress at this point is equal to $Y/2$ and thus $\bar{P}=1.07$, where Y is the uniaxial yield stress.

The depth of the plastic zone is an elastic-plastic axisymmetric quasi-static solid caused by a rigid spherical punch is discussed by Shaw and de Salvo (1970a, 1970b). By matching the Hertz solution with that of the Boussinesque problem, they obtained an equivalent concentrated loading situation from which the required maximum shear stress contour, which defines the elastic-plastic boundary, is obtained. Consequently, the depth of the plastic boundary h_p was found to be $h_p=1.816a$. This relation corresponds to a $\tau/\bar{p}$ value of 0.177 in. Figure 4(*a*), in terms of the radius of the spherical indenter R and the depth of indentation $\bar{z}$, becomes (assuming $a^2=2\ \bar{z}\ R$):

$$h_p/R=2.57\ (\bar{z}/R)^{1/2}. \tag{1}$$

The 0.177 contours correspond to $\bar{p}=2.82$ (for $\tau=0.5Y$), which requires a maximum constant pressure at the center of the contact surface of $3/2\times 2.82Y=4.23Y$. After allowance for contour distortions near the edges of the indenter, a factor of 0.94 is predicted for correcting the value of $\bar{p}$ to become $2.82Y/0.94=3.0Y$, which is close to experimental values.

Dynamical Considerations

The problem of the response of an elastic-plastic semi-finite solid-to-rigid-sphere impact is one in which a number of difficulties exist. Apart from aspects of dynamic contact, there are still the processes of elastic and plastic stress waves due to a changing boundary condition unsolved. A single shot impinges obliquely and, thus, cratering of the target when being peened takes place under normal as well as tangential forces. It is beyond the scope of the present paper to address such aspects. However, one can gain a reasonable insight into the problem by considering the shot to be rigid, impinging upon a rigid-perfectly plastic target. This oversimplification assists us in predicting the depth of the dent produced in the target surface, and hence to later enable the estimation of the plastic zone h_p. With the latter predicted, it will be shown how one can predict the residual stress distribution in a shot-peened strip of metal.

Let us now assume that when a rigid spherical projectile indents a medium exhibiting a rigid plastic behavior, the resistance to its motion may be represented by an average pressure $\bar{p}=3Y$ (assumed constant), thus the equation of motion of the projectile is

$$M\ dv/dt=-\pi\ a^2\ \bar{p} \tag{2}$$

where M is the projectile mass $=4/3\ \rho\ \pi\ R^3$. We have, of course, neglected friction inertia of the moving metal ahead of the projectile and strain hardening. Equation (2) may be integrated in terms of the penetration (assumed to be small $z\simeq a^2/2R$) to give

$$\bar{z}/R=(2/3)^{1/2}(\rho\ v^2/\bar{p})^{1/2} \tag{3}$$

Downloaded 03 May 2010 to 171.66.16.244. Redistribution subject to ASME license or copyright; see http://www.asme.org/terms/Terms_Use.cfm

where $\bar{z}$ is the final indentation and v is the initial impact velocity.

The nondimensional number $(\rho v^2/\bar{p})$ comes in most impact problems. It gives a measure of the severity of impact and is sometimes called the "damage number." It may be used to identify dynamic similitudes in shot-peening situations. It was suggested earlier by Al-Hassani (1981) that different peened targets may be considered to have the same arc height if they have the same damage number.

Now, by assuming that quasi-static conditions still hold in the range of impact velocities and thus dynamic indentations which have the same value as those obtained from static tests produce similar plastic zones, if we combine equation (1) and equation (3), then we get the depth of the plastic zone as

$$h_p/R = (2.57)\ (2/3)^{1/4}(\rho\ v^2/\bar{p})^{1/4} \tag{4}$$

which is a most useful relationship for relating shot-peening parameters.

Residual Stress Distribution in a Shot-Peened Target

As previously explained, under each impact spot there will be a plastic zone constrained by an elastic field. After rebound of each shot the plastic zone interacts with the elastic field resulting in a residual stress distributed through the depth of the component. This residual stress is the sum of all the fields caused by repeated impacts at each spot as well as progressive impacts to cover the whole surface of the target. It is beyond any theoretical analysis to predict the instantaneous build-up of the residual stress distribution. But, by making use of the measured patterns of residual stress in shot-peened specimens, one is encouraged to make a brave assumption that the rest of the target reacts to the total sum of the residual stress distribution by exhibiting an equivalent direct and bending stresses acting in a manner to balance the internal stresses. Consequently, these cause bending and axial strains which are manifested by curvature of the target towards the impinging shots. This action continues until such time when the arc height levels off and a state of saturation is reached.

Thinking backward from the first state of stress we may find it justifiable to assume that the bending moment and axial force are reacting to a casual stress of "source stress." The latter term has been used by the French authors Flavanot and Nikulari (1977). This stress has a distribution similar to that found in a target which does not react by overall curvature, i.e., a semi-finite solid of an infinite overall bending and axial stiffnesses.

So, the residual stress distribution, $\sigma_R(z)$, in a thin plate may now be considered to be the result of further addition of the bending, σ_b, and axial stresses, σ_{ax}, on the source stress, σ_s. Hence,

$$\sigma_R(z) = \sigma_b + \sigma_{ax} + \sigma_s. \tag{5}$$

Figure 1(a) shows typical residual stress distribution in thin and thick plates due to peening. As is seen, σ_b and σ_{ax} are needed to produce σ_R.

From the experimental evidence, the shape of the residual stress distribution in a thick target can be represented by the first half of a cosine function. The strain produced by the source stress σ_s, which is acting in a plane parallel to the surface of the target, may be given by:

$$\epsilon(z) = \frac{(1-\nu)}{\mathrm{E}}\,\sigma_s \tag{6}$$

where ν is the Poission's ratio, E the Young's modulus and the negative sign indicates compressive.

The assumed cosine function has a peak at a depth αhp below the surface (see Fig. 1(a)) and may be described as follows:

$$\epsilon(z) = \epsilon_m \cos\pi\left[\frac{z-\alpha\ hp}{2(1-\alpha)hp}\right] \text{for } o \le z \le hp \tag{7}$$

and for $z > hp$, the function does not have a value.

In some shot-peened targets, the highest residual stress occurred at the top surface in which case $\alpha = o$.

The bending stress σ_b at depth z in a beam of width b and thickness h subjected to a bending moment $\bar{M}$ is given by

$\frac{12\bar{M}}{bh^3}\left(\frac{h}{2} - z\right)$ where

$$\bar{M} = \int_o^{hp} \sigma(z).\left(\frac{h}{2} - z\right).b.dz. \tag{8}$$

Similarly, the axial stress σ_{ax} is given by $\bar{F}/bh$

where $$\bar{F} = \int_o^{hp} \sigma(z).b.dz. \tag{9}$$

Integrating equations (8) and (9) over the range in which $\sigma(z)$ acts, i.e., $o \le z \le hp$ gives:

$$\sigma_b = \frac{E\ \epsilon_m\ 12(1-\alpha)\left(\frac{h}{2} - z\right)\lambda}{(1-\nu)\ \pi h}\ C_1 \tag{10}$$

and

$$\sigma_{ax'} = \frac{\mathrm{E}\ \epsilon_m}{(1-\nu)}\ \frac{2(1-\alpha)\lambda}{\pi}\ C_2 \tag{11}$$

where $\lambda = hp/h$,

$$C_1 = C_2 - 2\lambda + \frac{4\lambda}{\pi}(1-\alpha)\cos\frac{\pi\ \alpha}{2(1-\alpha)},$$

and $$C_2 = 1 + \sin\frac{\pi\ \alpha}{2(1-\alpha)}.$$

Substituting these in equation (5), we obtain the residual stress distribution as

$$\sigma_R(z) = \frac{\mathrm{E}\ \epsilon_m}{1-\nu}\left\{\frac{12\lambda}{\pi\ h}(1-\alpha)\left(\frac{h}{2} - z\right)C_1 + \frac{2\lambda}{\pi}(1-\alpha)C_2 - \frac{\epsilon\ (z)}{\epsilon_m}\right\}.$$

The maximum residual stress occurs at $z = \theta hp$ when

$\frac{d\sigma_R}{dz} = 0$. This condition is satisfied when

$$\frac{24\lambda^2(1-\alpha)^2 C_1}{\pi^2} = \sin\{\pi(\theta-\alpha)/2(1-\alpha)\}$$

$$\theta = \alpha + \frac{2(1-\alpha)}{\pi}\sin^{-1}\left[\frac{24\ \lambda^2(1-\alpha^2)C_1}{\pi^2}\right]. \tag{13}$$

For an infinitely thick target, i.e., $\lambda \to 0$, and we get $\theta = \alpha$ which is the condition prevalent at source stress.

From the foregoing analysis one can see that maximum residual stress occurs at θhp and is bound by the condition $\theta hp \le \alpha hp$. The amount by which the peak residual stress moves deeper into the body of the target depends on the right-hand term of equation (13) which is mainly decided by λ.

The value of ϵ_m in equation (12) is obtained by consideration of plane sections remaining plane in a beam of length L bent into an arc height, δ, and expressing the curvature by M/I E. The expression obtained is:

$$\epsilon_m = \frac{2}{3}\ \frac{\pi\ h\ \delta}{\lambda\ L^2(1-\alpha)C_1}. \tag{14}$$

Downloaded 03 May 2010 to 171.66.16.244. Redistribution subject to ASME license or copyright; see http://www.asme.org/terms/Terms_Use.cfm

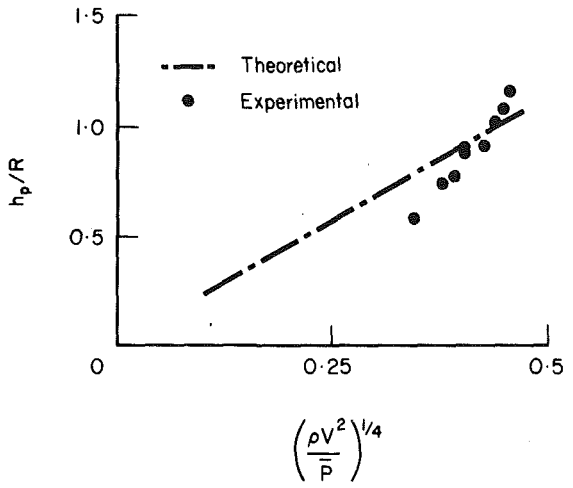


Fig. 5 Variation of depth of plastic zone with (damage number)

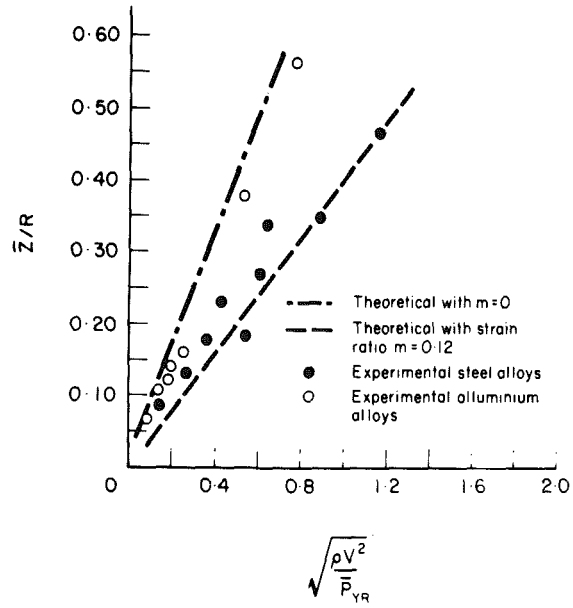


Fig. 6 Variation of indentation with the square root of the damage number

The importance of equation (14) now becomes clear. By substituting for hp from equation (4), we get

$$\lambda = 2.57\left(\frac{2}{3}\right)^{1/4}\left(\frac{R}{h}\right)\left(\frac{\rho V^2}{\bar{p}}\right)^{1/4} \tag{15}$$

which makes equation (12) most valuable in predicting the residual stress distribution from knowledge only of the arc height, for situations with $\alpha > o$, and shot density ρ, velocity, V, and the mean pressure, $\bar{p}$, as well as the thickness, h.

Results

Theoretical results on residual stress and plastic depth under various conditions can be found. A computer program incorporating equation (1) through equation (15) was written using Fortran IV language. A prime 750 computer was used to compile and execute the program and the input consisted of shot-peening parameters such as size and density of the shot, hardness, and thickness of the target. The program output consisted primarily of the calculated residual stresses in the target at each incremental thickness step. A second computer program was written to contour the calculated value of indentation depth (z), plastic depth (h_p) and the residual stress distribution (σ_R).

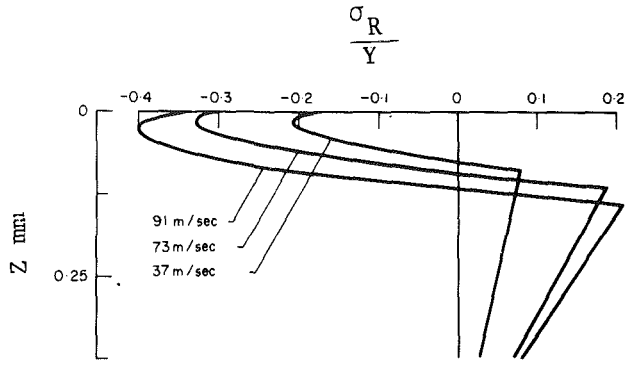


Fig. 7 Theoretically predicted residual stress distribution for different shot velocity

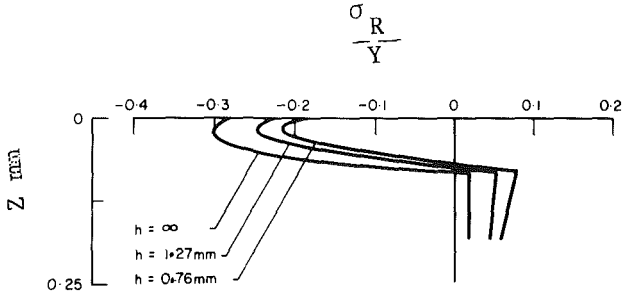


Fig. 8 Theoretically predicted stress distribution for different target thickness

First we find the value of the damage number from shot velocity, size and density, and target strength. The values of hp and z corresponding to this damage number are determined. The mean strain imposed by each shot is given by $(\bar{z}/4R)(1-V)$. If we assume that the average surface strain over the whole surface area is a fixed proportion of this, then the value of ϵ_m is selected. Thus, the distributions of bending, axial, and source stress are found individually and when combined, we get the distribution of the residual stress. It is convenient to plot results in nondimensional form.

The variation of indentation $\bar{z}$ with the damage number is shown in Fig. 5. The chain dotted line represents equation (3). The dotted line represents a theoretical line of a modified version of equation (3) allowing for strain rate with strain rate index $m = 0.12$ in a stress-strain relation of the form

$$\sigma = \sigma_o(\dot{\epsilon}/\dot{\epsilon}_o)^m \tag{16}$$

where σ_o is the flow stress at a reference strain rate ϵ_o.

It may be seen that the results for steel are closer to the strain-rate sensitive theory, but thet aluminum results, being not so sensitive to strain rate, are closer to equation (3) as would be expected.

Figure 6 shows a comparison between values of h_p obtained from etching nitrogen steel after single impacts. The theoretical results of equation (4) are also shown to agree reasonably well with the experiment.

A set of predicted residual stress distribution results from equation (12) are shown in Figs. 7 and 8. The conditions of peening for these results are for a shot of size $R = 0.36$ mm, density $\rho = 7740$ kg/m^3 and target material with $Y = 505$ MN/m^2, E = 200 GM/m^2, $\nu = 0.3$ assumed to be a plate of $L = 76$ mm. The value of α is chosen to be $= 0.2$. The surface strain factor used in the calculations was 0.6. In Fig. 7 the thickness of target was assumed to be 0.76 mm and the curves

Downloaded 03 May 2010 to 171.66.16.244. Redistribution subject to ASME license or copyright; see http://www.asme.org/terms/Terms_Use.cfm

are for shot impact velocities of 37, 73, and 91 m/s, respectively.

In Fig. 8 the influence of target thickness is demonstrated for an impact at 37 m/s for $h = 1.27$ mm and for a very thick target.

It is seen that the predicted figures agree with the common trends found in measured residual stress distributions. Other results may be obtained for glass beads and for targets of different materials.

Conclusion

A rudimentary analysis of the shot-peening process is presented. Simple expressions are obtained for the depth of the plastic zone, how it is influenced by the density of the shot and the thickness, and hardness of the target. Useful expressions are also found for the residual stress distribution and the predictions are found to be in reasonable agreement with experimental results.

A more rigorous theoretical analysis is necessary for predicting practical shot-peening situations. However, the present work goes a long way into simplifying the mechanics so as to highlight the main variables and how they are interrelated.

References

Al-Hassani, S. T. S., 1981, "Mechanical Aspects of Residual Stress Development in Shot-Peening," *First International Conference on Shot-Peening*, Paris, September 14–17, Pergamon Press.

Flavenot, J. F., and Nikulari, 1977, "La Measure des contraintes residuelles, Methode de la (Fleche) methode de la (Sourse de Contraintes), *Les Memories Technique due CETIM*, No. 31.

Pope, J. A., and Mohamed, A. K., 1975, "Residual Plastic Strain Produced by Single and Repeated Spherical Impact," *J. Iron and Steel Inst.*, July, pp. 285–297.

SAE Manual on Shot-Peening, 1952, SAE J808a.

Shaw, M. C., and de Salvo, G., 1950, "A New Approach to Plasticity and Its Application to Blunt Two-Dimensional Indenters," ASME *Journal of Engineering for Industry*, Vol. 92, pp. 469–479.

Shaw, M. C., and de Salvo G., 1970, "On the Plastic Flow Beneath a Blunt Axisymmetric Indenter," ASME *Journal of Engineering for Industry*, Vol. 92, pp. 480–493.

Downloaded 03 May 2010 to 171.66.16.244. Redistribution subject to ASME license or copyright; see http://www.asme.org/terms/Terms_Use.cfm

Effects of State Recovery on Creep Buckling Under Variable Loading[1]

D. N. Robinson[2]
Professor,
University of Akron,
Akron, OH 44325

S. M. Arnold[3]
Lewis Research Center,
Cleveland, OH 44135

Structural alloys embody internal mechanisms that allow recovery of state *with varying stress and elevated temperature; that is, they can return to a* softer state *following periods of* hardening. *Such material behavior is known to strongly influence structural response under some important thermomechanical loadings; for example, those involving thermal ratcheting. Here, we investigate the influence of* dynamic *and* thermal *recovery on the creep buckling of a column under variable loading. The column is taken as the idealized (Shanley) sandwich column. The constitutive model, unlike the commonly employed Norton creep model, incorporates a representation of both dynamic and thermal (state) recovery. The material parameters of the constitutive model are chosen to characterize NARloy-Z, a representative copper alloy used in thrust nozzle liners of reusable rocket engines. Variable loading histories include rapid cyclic unloading/reloading sequences and intermittent reductions of load for extended periods of time; these are superimposed on a constant load. The calculated results show that state recovery significantly affects creep buckling under variable loading. Failure to account for state recovery in the constitutive relations can lead to nonconservative predictions of the critical creep-buckling time.*

Introduction

The influence of dynamic and thermal recovery on the high temperature behavior of structural alloys is well recognized (for example, see Pugh and Robinson (1976); Robinson et al. (1976)). (See Figs. 1 and 2.) For example, recovery is believed to play a major role in one of the central structural problems relating to liquid metal breeder reactor design, the problem of thermal ratcheting. Failure to account for recovery effects in structural analyses involving repeated thermal transients has been shown to give qualitatively incorrect and nonconservative predictions of ratcheting in some instances (Sartory, 1980). Special provisions for taking recovery into account (e.g., the so-called α-reset procedure, see Robinson, 1979) are now finding their way into documents guiding structural analysis in the U.S. nuclear industry. The effects of thermal ratcheting have also been observed in thrust nozzle liners of reusable rocket engines.

A second area in which recovery effects are thought to play a primary role, and one that impacts essentially all high temperature system design, is that of creep crack growth under creep-fatigue (variable stress) conditions. Creep (state) recovery is believed to be one of the main causes of acceleration of crack growth in the creep regime and under variable loads. A study by Kubo (1983), using the same constitutive relations (see Robinson et al., 1976 and Robinson and Swindeman, 1982) employed in the present work, shows that the experimentally observed acceleration of creep cracks under variable stress can be predicted through the inclusion of appropriate mechanisms of recovery in the constitutive relations.

In this paper we discuss a third area of mechanics in which recovery is expected to have significant influence, that is, the problem of creep buckling under variable loading. The presence of mechanisms of recovery can allow creep strain rates to increase following periods of hardening and thus cause acceleration of creep buckling. Load reversals may be accompanied by dynamic recovery as in Fig. 1, and load reductions by thermal recovery as in Fig. 2; in either case, creep rates are increased upon reloading, which tends to reduce the critical time to buckling.

In the vast majority of creep-buckling studies the constitutive model used has been of the Norton type, see Hoff (1958), Hayman (1973) and Hoff (1978), wherein the (steady-state) creep rate is taken as a function of stress and temperature alone. Some investigations have made use of hardening theories that include a primary creep phase, for example Libove (1952), Jahsman (1970) and Hoff and Levi (1972). However, these theories do not generally allow for inelastic *state recovery* and, consequently, for rejuvenation of primary creep. These constitutive theories are adequate in the case of constant loading but may significantly overpredict the time to buckling under certain types of variable loading.

Here, we examine the elevated temperature creep-buckling

[1]This work was funded under NASA Grant NAG3-379.
[2]NASA Resident Research Associate.
[3]Formerly, graduate student at the University of Akron.
Contributed by the Applied Mechanics Division of THE AMERICAN SOCIETY OF MECHANICAL ENGINEERS for publication in the JOURNAL OF APPLIED MECHANICS.
Discussion on this paper should be addressed to the Technical Editor, Leon M. Keer, The Technological Institute, Northwestern University, Evanston, IL 60208, and will be accepted until two months after final publication of the paper itself in the JOURNAL OF APPLIED MECHANICS. Manuscript received by the ASME Applied Mechanics Division, May 26, 1988; final revision, May 17, 1989.

Copyright © 1990 by ASME
Downloaded 03 May 2010 to 171.66.16.244. Redistribution subject to ASME license or copyright; see http://www.asme.org/terms/Terms_Use.cfm

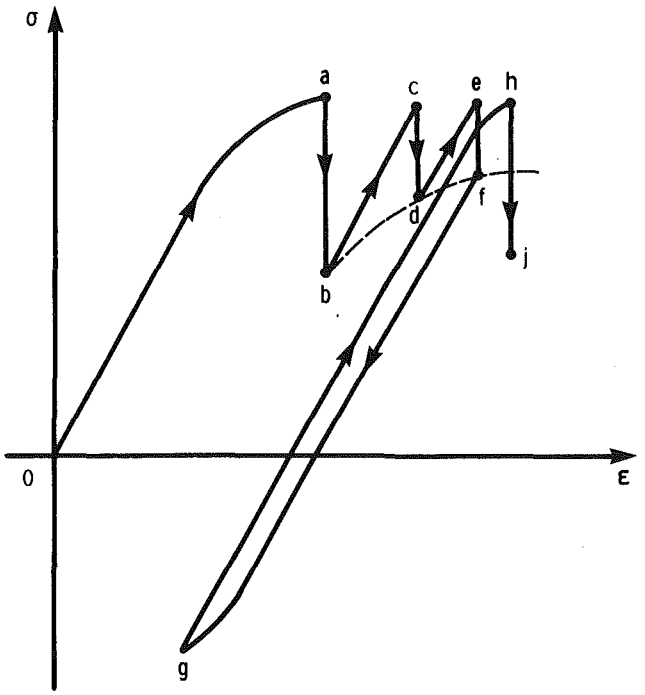


Fig. 1 Schematic representation of dynamic recovery. In the absence of stress reversals, the stress relaxations over a fixed time ab, cd, and ef show successive hardening. After the stress reversal fgh, stress relaxation hj shows evidence of (creep) softening, that is, evidence of *recovery of state* (see Pugh and Robinson, 1976).

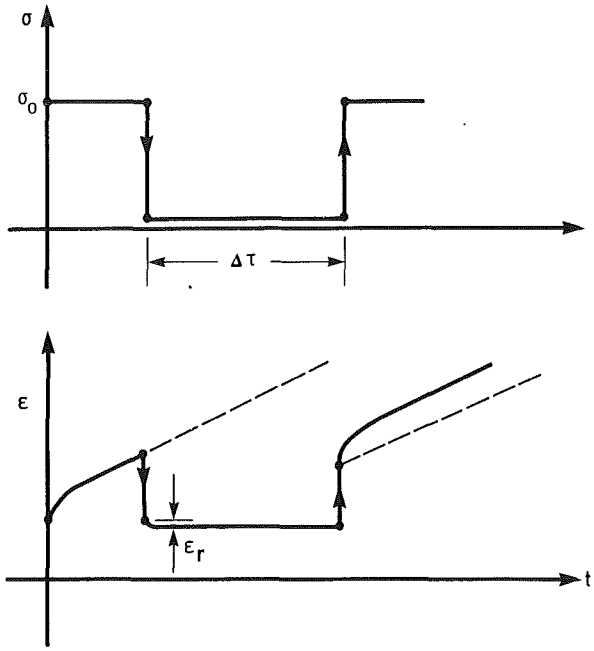


Fig. 2 Schematic representation of thermal recovery. Response in an interrupted creep test typically exhibits relatively small strain recovery ϵ_r but measurable softening (depending on the interval $\Delta\tau$) following a stress reduction, that is, *recovery of state* (see Robinson, 1976).

problem under variable loading using the simple Shanley model (see Shanley, 1960) of a column but with a constitutive model (Robinson and Swindeman, 1982) that embodies a representation of both dynamic and thermal recovery. The constitutive model is that developed principally by Robinson at Oak Ridge National Laboratory and NASA Lewis Research Center; and that used by Kubo (1983) in studies concerning creep crack growth.

The present study was motivated partly by the occurrence of what appears to be local ratcheting-buckling in the throat liner of the main thrust nozzles of reusable rocket engines, notably the NASA Space Shuttle main engine. For that reason the material parameters used in the constitutive equations are chosen to approximate a copper alloy, NARloy-Z, which is typical of materials used in rocket engine thrust nozzle liners.

We shall first state the constitutive model and, secondly, specify the geometry of the Shanley column model. We then investigate creep-buckling behavior under constant loading; cyclic loading which includes relatively rapid load reductions and reversals (dynamic recovery); and cyclic loading which includes intermittent reductions of load for extended periods of time (thermal recovery). Some of the calculations, using a roughly equivalent Norton type creep model, are repeated for comparison. Some physical aspects associated with the constitutive model are discussed along with the results. Finally, we state the conclusions drawn from the study.

The Constitutive Theory

We make use of the constitutive law reported in Robinson and Swindeman (1982) and Arnold (1987), which gives a complete multiaxial statement of the model. Here, we state the model in uniaxial terms together with the corresponding parameter values approximating the copper alloy NARloy-Z at 538°C (1000°F).

Flow law:

$$\dot{\epsilon}^p = \begin{cases} AF^n \operatorname{sgn}(\sigma-\alpha) & ;F>0 \text{ and } \sigma(\sigma-\alpha)>0 \\ 0 & ;F\le 0 \text{ or } F>0 \text{ and } \sigma(\sigma-\alpha)\le 0 \end{cases} \tag{1}$$

Evolutionary law:

$$\dot{\alpha} = \begin{cases} \dfrac{H}{|\alpha|^\beta}\dot{\epsilon}^p - R\,|\alpha|^{m-\beta}\operatorname{sgn}\alpha; & |\alpha|>\alpha_0 \text{ and } \sigma\alpha>0 \\ \dfrac{H}{\alpha_0{}^\beta}\dot{\epsilon}^p - R\alpha_0^{m-\beta}\operatorname{sgn}\alpha; & |\alpha|\le\alpha_0 \text{ or } \sigma\alpha\le 0 \end{cases} \tag{2}$$

in which

$$F=\frac{(\sigma-\alpha)^2}{\kappa^2}-1 \tag{3}$$

and

$$\begin{aligned} A &= 1.60\times10^{-8} \\ n &= 4 \\ m &= 8.73 \\ \beta &= 2.30 \\ \kappa &= 6.89 \\ H &= 1.46\times10^{7} \\ R &= 1.06\times10^{-7} \\ \alpha_0 &= 0.2. \end{aligned} \tag{4}$$

$\dot{\epsilon}^p$ denotes the inelastic strain rate in hr^{-1} and σ, the applied uniaxial stress in MPa. In the general form of the theory, κ (MPa) is a (Bingham-Prager) threshold stress playing the role of a scaler state variable; here it is taken to have the constant value given above. The quantity α (MPa) denotes the *single inelastic state variable*. It represents the uniaxial component of a tensorial state variable (internal stress) in the multiaxial formulation of the theory. The material parameter α_0 plays a

Downloaded 03 May 2010 to 171.66.16.244. Redistribution subject to ASME license or copyright; see http://www.asme.org/terms/Terms_Use.cfm

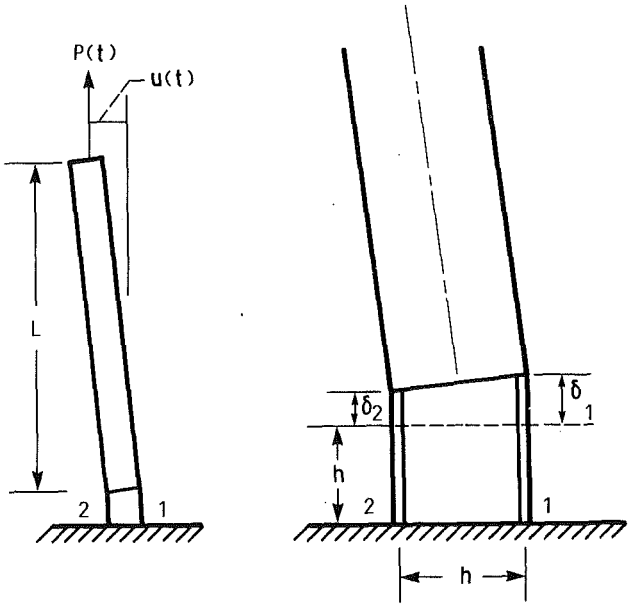


Fig. 3 Geometry of the Shanley sandwich column

primary role in the representation of dynamic recovery. (See Discussion.) The remaining parameters, in general functions of temperature, correspond to the isothermal behavior of NARloy-Z at 538°C (1000°F) and are consistent with the units MPa and hr. The Young's modulus at 538°C (1000°F) is

$$\mathrm{E} = 89{,}824 \text{ MPa}. \tag{5}$$

Equations (1) to (4) incorporate both dynamic and thermal recovery and are capable of predicting the behavior illustrated in Figs. 1 and 2.

The parameter values for NARloy-Z were determined from uniaxial tensile and stress relaxation test data. As the complete data base required for characterization was not available, these tensile and relaxation data had to be considered sufficient.

Tensile data at a strain rate of 0.002/sec, were found in Esposito and Zabora (1975) over a wide temperature range (−243 to 538°C). Stress relaxation data at 538°C (1000°F) were reported in Conway et al. (1975); these were used in the absence of creep data. The most serious data deficiency is the lack of tests giving a *direct* measurement of recovery effects; for example, strain or stress transient dip tests or open loop cyclic tests involving partial stress reversals. Nevertheless, it is believed that the material characterization is adequate for a reasonably quantitative study of creep-buckling behavior under variable stress.

The Shanley Column

The column model adopted here is the *sandwich* idealization introduced by Shanley (1960) and used by Kachanov (1967) and others. The column geometry is indicated in Fig. 3. All of the deformation is presumed to occur in the slender bar elements 1 and 2 of length h and cross-sectional area $A/2$. The remainder of the column of length $L(L>>h)$ remains rigid. The width of the column, that is, the distance separating bars 1 and 2, is also taken as h.

The column is loaded by a time-dependent load $P(t)$ (shown positive); the lateral displacement of the load point at any time is denoted by $u(t)$. The stress and total strain in bars 1 and 2 are denoted by σ_1, σ_2, and $e_1 = \delta_1/h$ and $e_2 = \delta_2/h$, respectively.

Equilibrium requires that

$$\sigma_2 + \sigma_1 = 2\sigma_0 \tag{6}$$

and

$$\sigma_2 - \sigma_1 = \frac{4\sigma_0 u}{h} \tag{7}$$

where $\sigma_0 = P/A$.

Differentiation with respect to time provides the rate form of the equilibrium equations,

$$\dot{\sigma}_2 + \dot{\sigma}_1 = 2\dot{\sigma}_0 \tag{8}$$

and

$$\dot{\sigma}_2 - \dot{\sigma}_1 = \frac{4u}{h}\,\dot{\sigma}_0 + 4\sigma_0\,\frac{\dot{u}}{h}\,. \tag{9}$$

From the geometric considerations (Fig. 3), the compatibility condition is obtained as

$$\frac{\delta_1 - \delta_2}{h} = \frac{u - u_0}{L} \tag{10}$$

or

$$e_1 - e_2 = \frac{u - u_0}{L} \tag{11}$$

in which u_0 is the initial displacement (imperfection). The rate form of the compatibility relation is

$$\dot{e}_1 - \dot{e}_2 = \frac{\dot{u}}{L}\,. \tag{12}$$

Decomposing the total strain rates in each bar into elastic and inelastic contributions gives

$$\dot{e}_1 = \frac{\dot{\sigma}_1}{\mathrm{E}} + \dot{\epsilon}_1^p \tag{13}$$

$$\dot{e}_2 = \frac{\dot{\sigma}_2}{\mathrm{E}} + \dot{\epsilon}_2^p \tag{14}$$

where E is the Young's modulus as specified in equation (5). The inelastic strain rates $\dot{\epsilon}_1^p$ and $\dot{\epsilon}_2^p$ are obtained by applying the inelastic constitutive equations (1) to (4) to each bar.

Combining the equilibrium equations (8) and (9), the compatibility equation (12), and the constitutive relationships (13) and (14) leads to

$$\dot{\sigma}_1\left(1 + \frac{4L}{\mathrm{E}h}\,\sigma_0\right) = \dot{\sigma}_0\left(1 + \frac{4L}{\mathrm{E}h}\sigma_0 - \frac{2u}{h}\right) - \frac{2L}{h}\,\sigma_0\left(\dot{\epsilon}_1^p - \dot{\epsilon}_2^p\right). \tag{15}$$

Under constant compressive stress (i.e., $\sigma_0 < 0$ and $\dot{\sigma}_0 = 0$), and in the absence of inelasticity ($\dot{\epsilon}_1^p = \dot{\epsilon}_2^p = 0$), equation (15) gives the Euler critical stress for the idealized column as

$$\sigma_c = \frac{\mathrm{E}h}{4L}\,. \tag{16}$$

Further, calling

$$\rho = \frac{\sigma_0}{\sigma_c} \tag{17}$$

and

$$\eta = \frac{2u}{h} \tag{18}$$

where η is termed the nondimensional displacement, we have from equation (15)

$$\dot{\sigma}_1 = \frac{\dot{\sigma}_0}{1+\rho}\,(1 + \rho - \eta) - \frac{\rho}{1+\rho}\,\frac{\mathrm{E}}{2}\,(\dot{\epsilon}_1^p - \dot{\epsilon}_2^p). \tag{19}$$

Now, from equation (6)

Downloaded 03 May 2010 to 171.66.16.244. Redistribution subject to ASME license or copyright; see http://www.asme.org/terms/Terms_Use.cfm

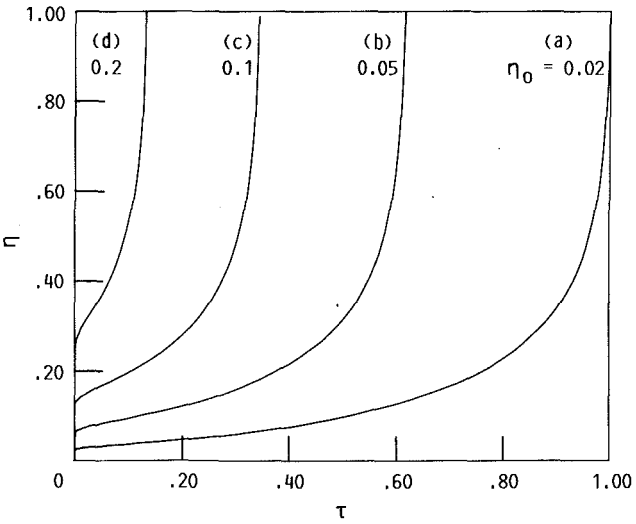


Fig. 4 Nondimensional displacement versus time for initial imperfections of $\eta_0 = 0.02$ (a), 0.05 (b), 0.1, (c), and 0.2 (d)

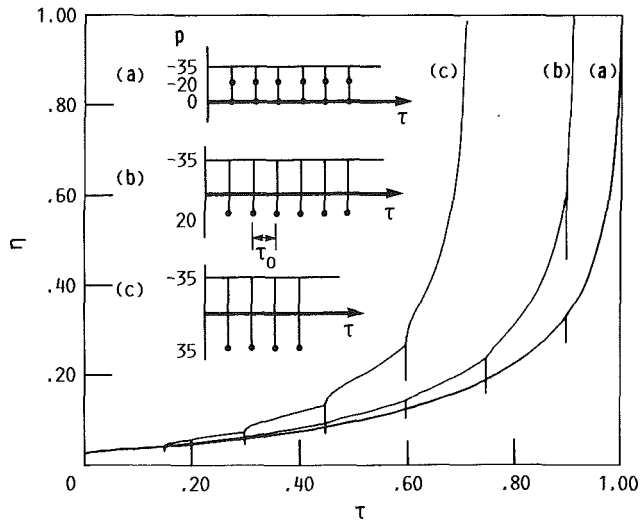


Fig. 5 Nondimensional displacement versus time for loading histories depicted in inserts (a), (b), and (c)

$$\dot{\sigma}_2 = 2\dot{\sigma}_0 - \dot{\sigma}_1, \tag{20}$$

and from equations (12) to (14) and (18),

$$\dot{\eta} = \frac{E}{2\sigma_c}\left(\frac{\dot{\sigma}_1}{E} + \dot{\epsilon}_1^p - \frac{\dot{\sigma}_2}{E} - \dot{\epsilon}_2^p\right). \tag{21}$$

The coupled system of equations (1) to (3) and (19) to (21) together with the appropriate initial conditions, including the initial imperfection $\eta_0 = \eta(0)$, allow the (nondimensional) displacement $\eta(t)$ to be calculated for a specified Euler critical stress σ_c and history of loading $\sigma_0(t)$. The results of several such calculations for various loading histories are presented in the following section.

Results

All of the calculated results represent the isothermal response of NARloy-Z at 538°C (1000°F). The Euler critical stress σ_c is 200 MPa and the loading/unloading ramp rate $|\dot{\sigma}_0|$ is 96 MPa/sec. This ramp rate was selected so that the strain rates nominally correspond to that in the characterization data. A discussion of the effect of variations in ramp rate as well as nonisothermal conditions is given in Arnold (1987).

The governing system of equations was integrated using a self-adapting fourth-order Adams-Bashforth predictor-corrector method with a fourth-order Runge-Kutta method as a starter. The calculations were performed in double precision on a Prime 850 computer with an upper error bound of 10^{-4}.

In all cases, the criterion defining the critical time to buckling t_c is taken as

$$\eta = \frac{2u}{h} = 1. \tag{22}$$

This is equivalent, under constant load, to the criterion

$$\sigma_1 = 0, \tag{23}$$

that is, the stress in bar element 1 becoming zero.

Behavior Under Constant Load. In all calculations the compressive load is first applied from zero, where the deforming elements are considered in a virgin state (i.e., $\alpha_1 = \alpha_2 \approx \alpha_0$), to a nominal value of the applied stress ($\sigma_0 = P/A$) of -35 MPa. Thus, with the Euler stress $\sigma_c = 200$ MPa the nominal value of the ratio ρ (equation (17)) is

$$\rho = \frac{\sigma_0}{\sigma_c} = \frac{-35}{200} = -0.175. \tag{24}$$

In this section we present the calculated results for a constant load ρ held at the value indicated in equation (24). Figure 4 shows the response $\eta(\tau)$ under these conditions for four different values of the initial (nondimensional) displacement $\eta_0 = 0.02$, 0.05, 0.10, and 0.2. The time $\tau = t/t_0$ in Fig. 4 is nondimensional, normalized with respect to the critical time for $\eta_0 = 0.02$; that is, $t_0 \approx 6$ hr.

Figure 4 shows that the critical time to buckling is reduced by a factor of almost 8 with an order of magnitude increase in the initial displacement.

For the sake of comparison, all subsequent calculations are taken to have the initial imperfection $\eta_0 = 0.02$ and are presented in terms of the nondimensional time $\tau = t/t_0$.

Behavior Under Variable Load. We first consider the effect of rapid load reductions and reversals superimposed on the constant load $\sigma_0 = -35$ MPa ($\rho = -0.175$). As shown in the inserts of Fig. 5, load interruptions occur at time intervals of $\tau_0 = 0.15$ with varying amplitude. These include reductions (in the tensile direction) of σ_0 to -20 MPa and to 0 MPa (insert (a)), to $+20$ MPa (insert (b)), and a complete reversal to $+35$ MPa (insert (c)). The calculated effects of these histories on the creep-buckling response $\eta(\tau)$ are shown as the respective curves (a), (b), and (c) of Fig. 5.

Curve (a) corresponds to the loading histories indicated in insert (a); reductions to -20 and 0 MPa. The response curve for each is identical to that of Fig. 4 for the same initial displacement 0.02, thereby indicating that no change in the buckling response has occurred. Response curve (b) corresponds to insert (b) in which there is a load reversal to $\sigma_0 = +20$ MPa. Here, we begin to see a measurable change in the calculated creep-buckling response, the critical time having diminished from the constant load case by about ten percent. Finally, in curve (c) we observe a reduction of more than 30 percent in the time to buckling. This corresponds to the history of insert (c) where a complete load reversal from $\sigma_0 = -35$ MPa to $\sigma_0 = +35$ MPa occurs at each load interruption. Immediately following each reversal, we see evidence of the reappearance of primary creep. This is attributed to the presence of dynamic recovery (Fig. 1) where creep (or relaxation) is observed to be accelerated by stress reversals—even in the absence of significant reversed inelastic strain. Although, to the knowledge of the authors, these effects have not been observed directly in creep-buckling phenomena, it is expected that such effects can occur, on the basis of the experimental observations illustrated schematically in Fig. 1.

Downloaded 03 May 2010 to 171.66.16.244. Redistribution subject to ASME license or copyright; see http://www.asme.org/terms/Terms_Use.cfm

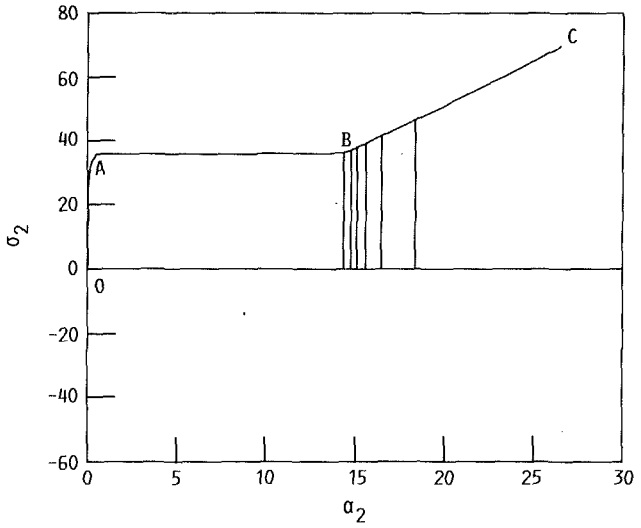


Fig. 6 State space for bar 2 showing state path corresponding to loading histories of insert (a), Fig. 5. Units MPa.

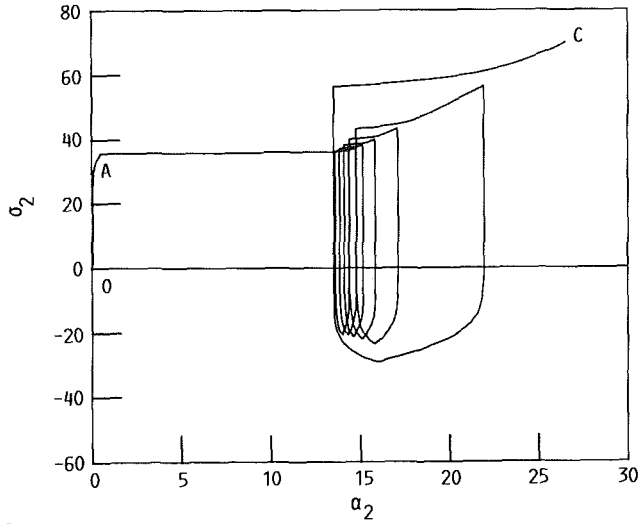


Fig. 7 State space for bar 2 showing state path corresponding to loading history of insert (c), Fig. 5. Units MPa.

The influence of dynamic recovery is best understood by considering the *state space* (σ, α) of Fig. 6. Note that in Fig. 6 and all subsequent representations of the state space, compressive σ and α are shown as positive and are plotted upward and to the right, respectively. Hereafter, the relevant quadrants of the state space will be referred to as the first ($\sigma\alpha > 0$) and the fourth ($\sigma\alpha < 0$). In Fig. 6 the trajectory of the state point, path OABC, (σ_2, α_2) for bar element 2 is shown corresponding to the constant load response curve (a) in Fig. 4. The segment OA traces the path of the state point during initial load-up to $\sigma_0 = -35$ MPa. Some inelasticity is indicated over path OA by the increase in the inelastic state variable, α_2. As σ_0 is held constant, bar 2 creeps under nearly constant stress, and the state point moves toward B. As the geometric nonlinearity becomes prevalent, the stress in bar 2 increases (as that in bar 1 decreases), and the state point moves toward C. Point C corresponds to the buckled condition $\eta = 1$ in Fig. 4 (curve (a)).

Figure 6 also shows the trajectory of the state point for the loading histories illustrated in insert (a) of Fig. 5; load reductions to $\sigma_0 = -20$ MPa and to $\sigma_0 = 0$. Here we see the effect of the abrupt load changes as vertical (elastic) trajectories in the state space, resulting in no overall change in the state path OABC from that just considered for a constant load. This, of course, results in the same creep-buckling response observed earlier for the constant load.

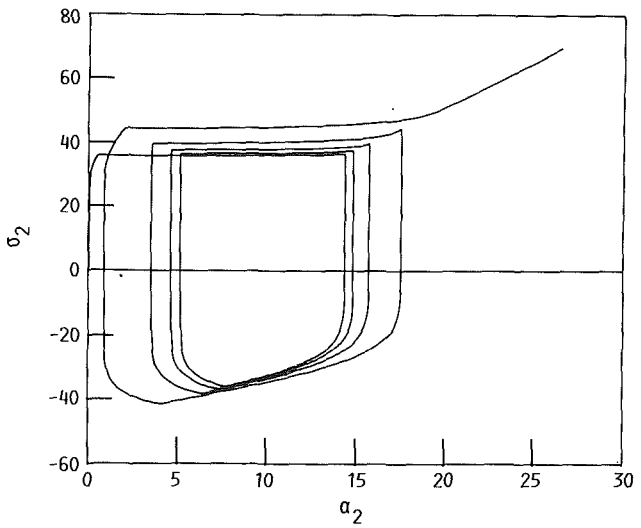


Fig. 8 State space for bar 2 showing path corresponding to loading history of insert (c), Fig. 5. Units MPa.

The state path of Fig. 7 relates to the loading history of insert (b) in Fig. 5. Here we begin to see evidence of *state recovery*. The load variations now produce stress reversals in bar 2 and the state point trajectories are not simply vertical (elastic) lines as before, but now follow curved paths as the state point penetrates into the fourth quadrant ($\sigma\alpha < 0$) corresponding to a reversal of stress. The state *recovers* with the stress reversal, resulting in a relatively *softer state* (smaller α_2) upon reloading. Correspondingly, the creep rate is increased in response to each load cycle. Evidence of increased creep rate following reloading is apparent in curve (b) (Fig. 5).

Load histories involving larger stress reversals produce increased state recovery. Figure 8 shows the state path in bar 2 for the fully reversed load depicted in insert (c) (Fig. 5). In Fig. 8, the effect of dynamic recovery at each unloading/reloading cycle returns the state point well back into the primary creep regime. As observed earlier, clear evidence of the rejuvenation of primary creep after each loading cycle is seen in curve (c) of Fig. 5, with the total effect of diminishing the critical buckling time by about 30 percent.

Since the period of application of the rapid loading cycles ($\tau_0 = 0.15$) was chosen quite arbitrarily, we now investigate the effect of the frequency of load cycles. Figure 9 shows the buckling response curves $\eta(\tau)$ for load histories involving a full reversal; that is, $\sigma_0 = -35$ to $+35$ MPa (as in insert (c) Fig. 5), with periods τ_0, $\tau_0/2$, $\tau_0/4$, and $\tau_0/8$. (The constant load response curve is also shown for reference.) We see the pronounced effect of more frequent (shorter period) stress reversals. Reversals with period $\tau_0/8$ reduce the time to buckling by more than a factor of 3.

Next, we examine the influence of load reductions of extended duration on the creep-buckling time. The loading histories considered are shown in the inserts of Fig. 10. Case (a) (i.e., insert (a) and response curve (a)) is equivalent to one of those considered previously (insert (a) of Fig. 5), where the time duration at the reduced load $\sigma_0 = 0$ is effectively zero. This history produces no change in the buckling response over the constant load case.

Insert (b) depicts the history where the load, having been applied for period τ_0, is abruptly removed (at a rate $|\dot{\sigma}_0| = 96$ MPa/sec) and held at zero for a period τ_1; a time comparable to the actual critical time ($\tau_0 = 6$ hr) of the column under constant load. The sequence is then repeated. This history reduces the critical time as shown in curve (b) by about

Downloaded 03 May 2010 to 171.66.16.244. Redistribution subject to ASME license or copyright; see http://www.asme.org/terms/Terms_Use.cfm

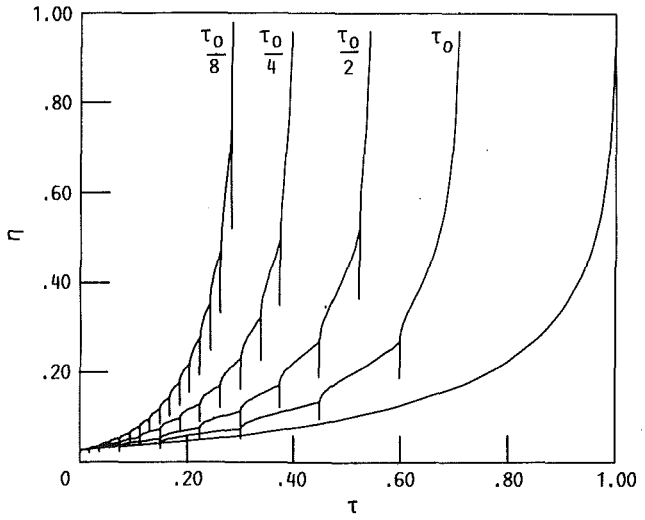


Fig. 9 Nondimensional displacement versus time showing the effect of the frequency of load reversals. Response curves for constant load (−35 MPa) and periods of τ_0, $\tau_0/2$, $\tau_0/4$, and $\tau_0/8$.

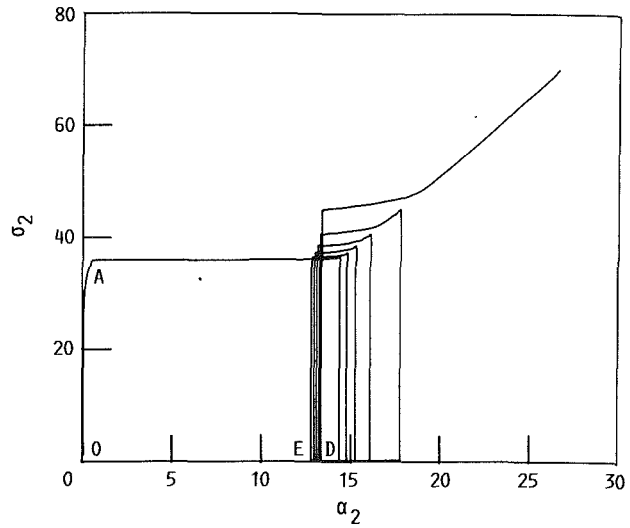


Fig. 11 State space for bar 2 showing state path corresponding to insert (b), Fig. 10. Units MPa.

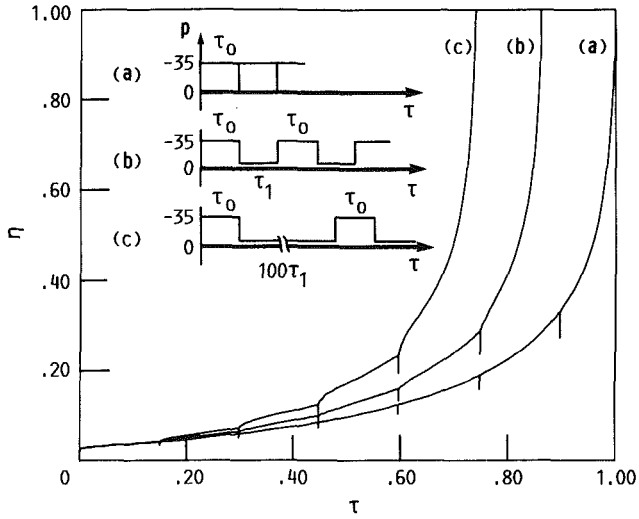


Fig. 10 Nondimensional displacement versus time for loading histories depicted in inserts (a), (b), and (c)

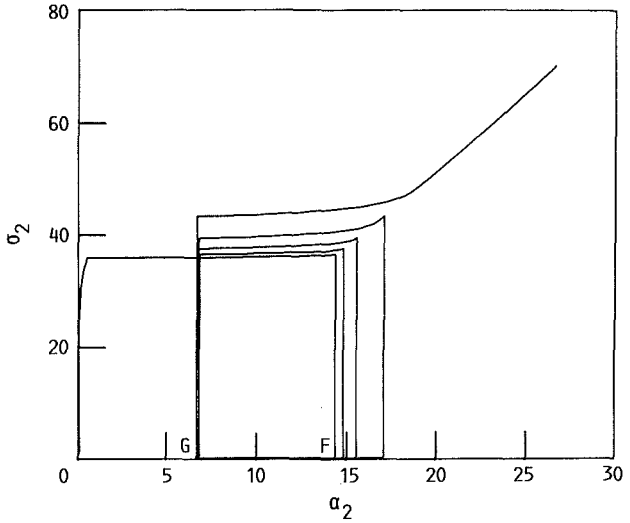


Fig. 12 State space for bar 2 showing state path corresponding to insert (c), Fig. 10. Units MPa.

15 percent. Here, the time τ includes only that time in which the load $\sigma_0 = -35$ MPa is applied.

This behavior is best visualized in the state space (σ_2, α_2), Fig. 11. State recovery is observed as, in time, the state point moves at zero stress toward smaller α_2; for example, on the first load reduction from point D to E. Reloading returns the state point to a softer state than before the load reduction and correspondingly, to a higher creep rate. Repetition of the sequence thus causes acceleration of the creep-buckling process.

Insert (c) of Fig. 10 shows a loading history in which the time at zero stress is now increased one-hundredfold to $100\tau_1$. The corresponding response curve (c) shows a further decrease in the critical time, about 30 percent. The related state point trajectory shown in Fig. 12 is qualitatively similar to that of Fig. 11 but now shows significantly increased recovery with the hundredfold increase in hold time at the reduced stress.

Comparison With Predictions by Norton Law. In this section we compare the results presented with those for identical loading histories based on a classical creep law of the Norton-Bailey type; that is,

$$\dot{\epsilon}^p = B\sigma^N \mathrm{sgn}(\sigma). \tag{25}$$

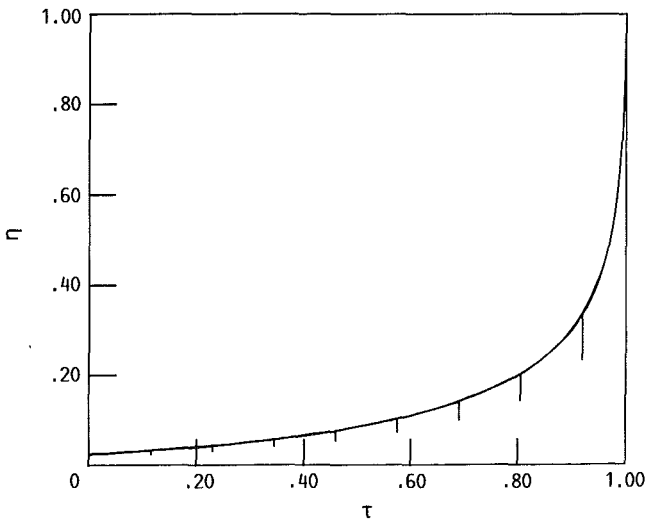


Fig. 13 Nondimensional displacement versus time for all loading histories using classical Norton-type creep law

Downloaded 03 May 2010 to 171.66.16.244. Redistribution subject to ASME license or copyright; see http://www.asme.org/terms/Terms_Use.cfm

A roughly equivalent representation was obtained by calculating the steady-state creep rates for various stress levels using equations (1) to (4) and fitting equation (25) to these "data" by choosing optimal values of B and N in a least squares sense. This process yielded the following:

$$B = 2.03 \times 10^{-19}$$
$$N = 9.375$$

which are consistent with units of σ in MPa and $\dot{\epsilon}^p$ in hr^{-1}. By using equation (25), the critical time to buckling (corresponding to the constant load case of curve (a) Fig. 4) turned out to be $t_0' = 7.8$ hr; slightly greater than the earlier reference $t_0' = 6$ hr. Thus, in the calculated results presented here (Fig. 13), the nondimensional time τ is obtained by normalization with respect to t_0'. The time plotted is that for which the load $\sigma_0 = -35$ MPa is applied. On this basis, calculations of creep-buckling response, $\eta(\tau)$, for all of the loading histories presented earlier have been included in Fig. 13. As expected, the time to buckling is completely unaffected by any of the variable loading histories. This is because the classical Norton-Bailey representation (equation (25)) fails to account for state recovery in any form.

Discussion

Dynamic recovery, as illustrated in Fig. 1 and by the state point trajectories of Figs. 7 and 8, is characterized in the present constitutive model through the dual analytical forms of the evolutionary law (equations (2)). This description is consistent with the viewpoint of Onat (1981) in representing inelastic behavior through the specification of analytically different mathematical forms corresponding to various *regions of the state space*. Here, different analytical forms are specified depending on whether the state point lies in the first (third) quadrant $\sigma\alpha > 0$ or the fourth (second) quadrant $\sigma\alpha < 0$ of the state space. In effect, this permits the state point to recover rapidly upon reversing the stress, even in the absence of significant reversed inelastic strain (Fig. 1). This formulation is intended as an idealization of a physical process wherein the dislocation structure (or the associated structure of internal stress) is abruptly altered with a reversal of the applied stress, because previously immobilized dislocations are remobilized on their slip planes, see Orowan (1959). Since the inelastic state variable α is taken as an averaged, phenomenological measure of the dislocation microstructure (or its associated internal stress state), it too should reflect a rapid change as the stress is reversed.

The specific functional form of the first of equations (2) is formulated in accordance with the experimental results of Mitra and McLean (1966). The second of equations (2) can be considered an analytical continuation of the first equation, evaluated at α_0 (small α) in the first quadrant of the state space, into the second quadrant; or with symmetrical response in tension and compression, at $-\alpha_0$ in the third quadrant into the fourth quadrant. This amounts to an idealized representation of the underlying physical process, but captures, nevertheless, the essential feature—that abrupt microstructural rearrangements occur with stress reversals.

The path of the state point in the fourth quadrant $\sigma\alpha < 0$ in Figs. 8 and 9, and, thus the *extent of recovery*, depend on the total strain rate and, critically, on the parameter α_0. Ideally α_0, or, more comprehensively, a function of σ and α replacing it, should be determined from experiments in which the recovery of creep rate or flow stress under stress reversals is measured directly; and not inferred indirectly from available monotonic tensile, creep and/or relaxation data as was done here. The present representation, however, is believed to be adequate, and consistent with the objective of demonstrating the strong influence of state recovery in creep buckling. A more comprehensive description of dynamic recovery, in the same spirit as that described, and the relevant experimentation are topics of continuing research.

Thermal recovery, as depicted in Fig. 2 and in the state paths shown in Figs. 11 and 12, is manifested in the second (negative) term of the Bailey-Orowan evolutionary equations (2). In the applications considered, the state point recovers, in time, under constant (zero) reduced stress, giving rise to an increased creep rate on reapplication of stress (Fig. 2). Physically, this macroscopic behavior is associated with thermally activated, diffusion controlled, microscopic processes such as climb of edge dislocations; which allow dislocations, in time, to bypass immobilizing obstacles, thus producing a *softer state* (smaller α). The important material parameters in equations (2) are R, m, and β. Ideally, these parameters are determined from both creep data and information obtained from stress or strain *transient dip tests* (see Robinson and Swindeman, 1982) that provide a *direct* measurement of thermal recovery. Again, as these data were not readily available for the alloy NARloy-Z, the pertinent parameters were inferred *indirectly* from available data. This approach, although not optimal, is considered consistent with the present objectives.

Conclusions

We have examined the creep-buckling response of an idealized (Shanley) column under some special variable loadings. The two types of loading considered amount to superpositions of the following load sequences on a constant applied load: (1) rapid cyclic unloading/reloading sequences involving stress reversals and (2) cyclic loading that includes intermittent reductions of load for extended periods of time (at elevated temperature).

Although the sandwich column model used is highly idealized, the constitutive model is quite comprehensive in that it incorporates a representation of dynamic and thermal (state) recovery. There is substantial experimental evidence that many structural alloys embody internal mechanisms at elevated temperature that allow inelastic strain rates to increase (recover) following periods of hardening. In particular, this is believed to be true for the representative copper alloy NARloy-Z characterized here.

The loading sequences examined are not intended to represent prototypical loading histories for any particular structural component; instead, they were chosen to best illustrate the generic influence of both *dynamic* and *thermal* recovery on structural behavior in the presence of a creep-induced instability. We expect that qualitatively similar behavior will accompany more realistic variable loading conditions (and more realistic structures), and that neglect of state recovery effects in such cases lead, similarly, to nonconservative predictions of the critical time to creep buckling.

The following conclusions can be drawn from this study:

1 State recovery (dynamic and thermal) can have a significant effect on creep-buckling behavior, that is, on the critical time.

2 Failure to account for state recovery in the constitutive equations can lead to nonconservative predictions of the critical buckling time under variable loading.

3 A classical Norton-Bailey type creep law, commonly used in creep-buckling analyses, does not account for state recovery and, therefore, may significantly overpredict the time to creep buckling under variable loading.

4 It is important that constitutive models (which are to be used in creep-buckling analyses involving variable loading) allow for recovery effects, and furthermore, that the characterization tests used for determining the pertinent material parameters include direct measurements of state recovery.

Downloaded 03 May 2010 to 171.66.16.244. Redistribution subject to ASME license or copyright; see http://www.asme.org/terms/Terms_Use.cfm

References

Arnold, S. M., 1987, "Effects of State Recovery on Creep Buckling Induced by Thermomechanical Loading," Ph.D. dissertation, University of Akron, Akron, Ohio.

Conway, J. B., Stentz, R. H., and Berling, J. T., 1975, "High-Temperature, Low-Cycle Fatigue of Copper-Base Alloys for Rocket Nozzles: Part I—Data Summary for Materials Tested in Prior Programs," (MTI-003-3-1-PT-1, Mar-Test Inc.; NASA Contract NAS3-19720) NASA CR-134908.

Esposito, J. J., and Zabora, R. F., 1975, "Thrust Chamber Life Predictions," *Vol. I—Mechanical and Physical Properties of High Performance Rocket Nozzle Materials*, (D180-18673-1-VOL-1, Boeing Aerospace; NASA Contract NAS3-17838) NASA CR-134806.

Hayman, B., 1973, "Some Observations on Creep Buckling Analysis," (preprints), *2nd International Conference on Structural Mechanics in Reactor Technology*, Vol. 5, Part. L, T. A Jaeger, ed., Berlin, pp. 1–12.

Hoff, N. J.,1958, "A Survey of the Theories of Creep Buckling," *Proceedings of the Third U.S. National Congress of Applied Mechanics*, R. M. Haythornthwaite, ed., ASME, New York, pp. 29–49.

Hoff, N. J., 1978, "Rules and Methods of Stress and Stability Calculations in the Presence of Creep," ASME JOURNAL OF APPLIED MECHANICS, Vol. 45, pp. 669–675.

Hoff, N. J., and Levi, I. M., 1972, "Short cuts in Creep Buckling Analysis," *Int. J. Solids Struct.*, Vol. 8, pp. 1103–1114.

Jahsman, W. E., 1970, "Creep Stability of a Column with Coupled Geometric Imperfection and Material Behavior Effects," *Creep in Structures*, J. Hult, ed., Springer-Verlag, pp. 360–369.

Kachanov, L. M., (transl., E. Bishop), 1967, *Theory of Creep* (Teoriya Polzuchesti), Boston Spa, U.K.

Kubo, S., 1983, "Effects of Creep Recovery and Hardening on the Stress and Strain-Rate Fields Near a Crack Tip in Creeping Materials," *Elastic-Plastic Fracture: Second Symposium, Vol. 1—Inelastic Crack Analysis*, ASTM STP – 803, ASTM, pp. I-594 to I-614.

Libove, C., 1952, "Creep Buckling of Columns," *J. Aeronaut. Sci.*, Vol. 19, pp. 459–467.

Mitra, S. K., and McLean, D., 1966, "Work Hardening and Recovery in Creep," *Proc. Roy. Soc., London*, Vol. A295, pp. 288–299.

Onat, E. T., 1981, "Representation of Inelastic Behavior," *Creep and Fracture of Engineering Materials and Structures*, B. Wilshire and D. R. J. Owen, eds., Pineridge Press, Swansea, U.K., pp. 587–602.

Orowan, E., 1959, "Causes and Effects of Internal Stresses," *Internal Stresses and Fatigue in Metals*, G. M. Rasweiler and W. L. Grube, eds., Elsevier, pp. 59–80.

Pugh, C. E., and Robinson, D. N., 1976, "Modified Auxilliary Procedures for Cyclic Creep and Relaxation," Oak Ridge National Laboratory, ORNL-5281, pp. 17–40.

Robinson, D. N., 1979, "Additions and Modifications to Constitutive Equations in RDT Standard F9-5T," Oak Ridge National Laboratory, ORNL-5622, pp. 2–11.

Robinson, D. N., Pugh, C. E., and Corum, J. M., 1976, "Constitutive Equations for Describing High-Temperature Inelastic behavior of Structural Alloys," *Proceedings of Specialist Meeting on High-Temperature Structural Design Technology of LMFBRs*," IAEA Report IWGFR/11, (CONF-760451-2), pp. 44–57.

Robinson, D. N., and Swindeman, R. W., 1982, "Unified Creep/Plasticity Constitutive Equations for 2 1/4 Cr-1 Mo Steel at Elevated Temperature," Oak Ridge National Laboratory, ORNL TM-8444.

Sartory, W. K., 1980, "Analysis of the ORNL Two-Bar Thermal Ratcheting Test SBRI," Oak Ridge National Laboratory, ORNL-5683, pp. 9–13.

Shanley, F. R., 1960, *Weight-Strength Analysis of Aircraft Structures*, Dover.

Downloaded 03 May 2010 to 171.66.16.244. Redistribution subject to ASME license or copyright; see http://www.asme.org/terms/Terms_Use.cfm

Kinematics for Bodies Undergoing Residual Stress and its Applications to the Left Ventricle

Keiichi Takamizawa

Takehisa Matsuda

Department of Biomedical Engineering,
National Cardiovascular Center
Research Institute,
5-7-1 Fujishirodai, Suita, Osaka 565 Japan

Biological soft tissues are understood to be materials that are residually stressed and nonlinear, and finitely deformed. A generalized continuum kinematics is needed to analyze such materials. Here, we apply Riemann geometry to the analysis of the residual stress and the stress distributions under loading conditions in the left ventricular wall assuming the uniform strain hypothesis. The hypothesis we employ states that the strain is uniformly distributed through the wall thickness at the end diastole. In conventional analyses, in contrast, it has been implicitly assumed that an unloading state gives a stress-free configuration. The steep stress distributions obtained from the conventional assumption are considerably reduced in the present study due to our hypothesis. The results are physiologically more plausible.

Introduction

It is widely noted that there are residual stresses in tissues of the living organs (Fung, 1984a,b; Vaishnav and Vossoughi, 1987; Omens and Fung, 1987) because these organs grow and develop under physiological loading conditions. Chuong and Fung (1986), and Takamizawa and Hayashi (1986, 1987) analyzed stress distributions in the arterial wall using a thick-walled cylindrical model. They showed that steep stress distributions at physiological loadings obtained assuming no residual stress are greatly reduced if there are residual stresses. Mirsky (1973) analyzed the stress distribution in the left ventricular wall using a thick-walled spherical model and showed, on the basis of the finite deformation theory, that the stress in the left ventricular wall is much higher in the endocardial layers than in the epicardial layers. From today's perspective it is obvious that a consideration of residual stress in the left ventricular wall is also needed. Omens and Fung (1987) investigated the residual strain in the left ventricle. These authors analyzed the stress distribution in the wall on the basis of the infinitesimal deformation theory accounting for the residual stress and obtained an almost constant stress distribution at the end of diastole.

The principle of superposition applies to infinitesimally-deformed linear solids. In this situation, the stress caused by external forces can be calculated independently of the residual stresses. However, for a finitely-deformed material, a different approach is needed. Here we apply the ideas developed to analyze dislocations and yielding of materials (Kondo, 1949, 1950) to soft tissues with residual stress. We analyze the stress distribution in the heart wall using a thick-walled spherical model, which is often used to analyze the left ventricle in biomechanics. In this analysis we adopted the uniform strain hypothesis instead of the conventional zero initial stress assumption. The uniform strain hypothesis for the left ventricle states that the tangential strain uniformly distributes through the wall thickness at the end of diastole. The results are compared with those obtained from the conventional theory.

Kinematics Referred to Local Stress-Free Configurations

A body $\mathfrak{B}$ is a three-dimensional differentiable manifold of material points p. A diffeomorphism from $\mathfrak{B}$ onto a region in Euclidean space is called a configuration of $\mathfrak{B}$. A curvilinear coordinate system $[x^k; g_{kl}]$ is introduced into Euclidean space. Here x^k represents the kth component of coordinates and g_{kl} the (k, l) component of the metric tensor. The coordinate system and configurations used in this section are illustrated in Fig. 1. In the following, a boldface letter denotes a triple of real numbers, for example, $\mathbf{x} = (x^1, x^2, x^3)$, and a configuration χ should be regarded as a triple of functions from $\mathfrak{B}$ into the set of real numbers $\chi = (\chi^1, \chi^2, \chi^3)$, and so on. A constitutive law relates deformation to stress where the deformation is usually defined with respect to a stress-free state. There does not, however, necessarily exist a stress-free state as a whole for a bulk material, because the bulk material may undergo residual stress. Even in such a case, we can define a locally stress-free state by considering an infinitesimal part taken from the body. This means, mathematically, that for each material point $p \in \mathfrak{B}$, there exists a neighborhood U_p of p in $\mathfrak{B}$ and a local configuration κ_p from U_p onto a region of Euclidean space in which the stress is zero, at least, at $\kappa_p(p)$. We will call this mapping a local stress-free configuration.

Contributed by the Applied Mechanics Division of THE AMERICAN SOCIETY OF MECHANICAL ENGINEERS for publication in the JOURNAL OF APPLIED MECHANICS.

Discussion on this paper should be addressed to the Technical Editor, Leon M. Keer, The Technological Institute, Northwestern University, Evanston, IL 60208, and will be accepted until two months after final publication of the paper itself in the JOURNAL OF APPLIED MECHANICS. Manuscript received by the ASME Applied Mechanics Division, March 28, 1988; final revision, April 15, 1989.

Copyright © 1990 by ASME
Downloaded 03 May 2010 to 171.66.16.244. Redistribution subject to ASME license or copyright; see http://www.asme.org/terms/Terms_Use.cfm

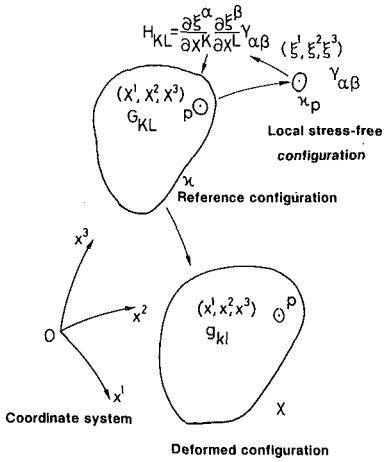


Fig. 1 Coordinate system and configurations. Coordinates of a material point p in each configuration and metric tensors at each position. (1) In a local stress-free configuration κ_p, the coordinates of the material point p are ξ^α and the metric tensor $\gamma_{\alpha\beta}$ at that position. (2) In the global reference configuration κ, the coordinates are X^K and the metric tensor G_{KL}. Another metric tensor H_{KL} is introduced. The infinitesimal quadratic form $H_{KL}dX^K dX^L$ gives the same infinitesimal length as that in the corresponding local stress-free configuration. The configuration κ carrying H_{KL} is called Riemannian stress-free configuration. (3) In an arbitrary deformed configuration χ, the coordinates are x^k and the metric tensor g_{kl}.

Truesdell and Noll (1965) defined a local configuration as a linear transformation from a tangential space of $\mathfrak{B}$ onto Euclidean space. The present definition is essentially the same as theirs, because in our analysis, only the tangential space at a point p is noted. We take a family of local stress-free configurations $\mathcal{C}=\{(U_p, \kappa_p)\}_{p\in\mathfrak{B}}$ for the whole body $\mathfrak{B}$. If there exists a global stress-free configuration κ_o, we can take $U_p=\mathfrak{B}$, $\kappa_p=\kappa_o$ for every point p, i.e., $\mathcal{C}=\{(\mathfrak{B}, \kappa_o)\}$. Although this family is regarded as a collection of local stress-free configurations in general, we can introduce the Riemannian manifold which is isometric to the family of local configurations in a sense and formally use it in the same manner as a global stress-free configuration embedded in Euclidean space.

Let κ_p^{-1} denote the inverse mapping of κ_p. The deformation gradient for the configuration χ is defined for the locally stress-free configuration

$$x_\alpha^k(p)=\left.\frac{\partial\chi^k(\kappa_p^{-1}(\xi))}{\partial\xi^\alpha}\right|_{\xi=\kappa_p(p)}, \tag{1}$$

where the differentiation is locally defined in $\kappa_p(U_p)$ and p is fixed, $x^k=\chi^k(p)$ represents the kth component of coordinates of the particle p in the deformed state χ and ξ^α the αth component of coordinates of a particle $q\in U_p$ in the locally stress-free configuration χ_p, i.e., $\xi^\alpha=\kappa_p^\alpha(q)$. We introduce the reciprocal gradients in the same manner,

$$\xi_k^\alpha(p)=\left.\frac{\partial\kappa_p^\alpha(\chi^{-1}(\mathbf{x}))}{\partial x^k}\right|_{\mathbf{x}=\chi(p)}. \tag{2}$$

The notation $\partial\xi^\alpha/\partial x^k$ is used to represent $\xi_k^\alpha(p)$ in this paper although this notation is rather confusing when we treat ξ_k^α as a field on $\chi(\mathfrak{B})$. That is because the gradient ξ_k^α defined at p and the gradient at $q\neq p$ may be concerned with different local configurations, in general, even if $q\in U_p$.

Let a fixed configuration κ be a global reference. The Kth component of $\kappa(p)$ is represented by $X^K=\kappa^K(p)$ and the metric tensor at $\mathbf{X}$ is represented by G_{KL}, i.e., $G_{KL}=g_{KL}(\kappa(p))$. We can introduce a Riemannian manifold

Nomenclature

Kinematics Referred to Local Stress-Free Configurations

$\mathfrak{B}$ = material body which is a set of material points and defined as a differentiable manifold
p, q = material points of $\mathfrak{B}$
$[x^k; g_{kl}]$ = coordinate system with metric tensor g_{kl}
κ_p = local stress-free configuration for a material point p
U_p = material neighborhood of a material point p
ξ^α = coordinates of a material point, p, in a local configuration, κ_p
$\gamma_{\alpha\beta}$ = metric tensor at $\kappa_p(p)$
$\mathcal{C}$ = family of local stress-free configurations
Ω = rotation for a local stress-free configuration, κ_p
κ = global reference configuration
X^K = coordinates of a material point, p, in a global reference configuration
G_{KL} = metric tensor at $\kappa(p)$
H_{KL} = metric tensor which gives with dX^K the same length as that in a local stress-free configuration at the corresponding point. This metric tensor and coordinates $(X^1, X^2, X^3)\in\kappa(\mathfrak{B})$ result in Riemannian stress-free configuration.
χ = deformed configuration
x^k = coordinates of a material point, p, in a deformed configuration
g_{kl} = metric tensor at $\chi(p)$
x_α^k, X_α^K = deformation gradients of a deformed configuration and a reference configuration in reference to a local stress-free configuration
$E_{\alpha\beta}$ = Green's strain tensor of a deformed configuration in reference to a local stress-free configuration
$\overset{*}{E}_{KL}$ = Green's strain tensor of a deformed configuration in reference to Riemannian stress-free configuration
$[KN, \mathcal{L}]^*$ = Christoffel symbols of the first kind for a Riemannian stress-free configuration
$\overset{*}{R}_{KLMN}$ = Riemann-Christoffel tensor for a Riemannian stress-free configuration
ρ_o, ρ = mass densities of stress-free and deformed configurations, respectively
$J, \tilde{J}$ = Jacobians, $\det(x_\alpha^k)$, $\det\left(\frac{\partial x^k}{\partial X^K}\right)$, respectively
γ, g, G, H = determinants, $\det(\gamma_{\alpha\beta})$, $\det(g_{kl})$, and so on

Stress Tensor Referred to Riemannian Stress-Free Configuration

t^{kl} = Cauchy's stress tensor in configuration χ
$T^{\alpha k}$ = first Piola-Kirchhoff stress tensor when a local stress-free configuration is taken as a reference
$\tilde{T}^{Kk}$ = first Piola-Kirchhoff stress tensor when global reference κ with G_{KL} is taken as a reference

Downloaded 03 May 2010 to 171.66.16.244. Redistribution subject to ASME license or copyright; see http://www.asme.org/terms/Terms_Use.cfm

that plays the role of a global stress-free configuration for a simple solid, even if there is not a global stress-free configuration in a physical sense. It is $\kappa(\mathfrak{B})$ with the metric tensor H_{KL} which satisfies the following condition at each material point $p \in \mathfrak{B}$,

$$H_{KL} dX^K dX^L = \gamma_{\alpha\beta} d\xi^\alpha d\xi^\beta. \tag{3}$$

This is equivalent to

$$H_{KL} X^K_\alpha X^L_\beta = \gamma_{\alpha\beta}, \tag{4}$$

where X^K_α is the deformation gradient defined by equation (1) for the configuration κ, and $\gamma_{\alpha\beta} = g_{\alpha\beta}(\kappa_p(p))$. From the definition the linear transformation defined by X^K_α, from the tangential space of $\kappa_p(U_p)$ at $\kappa_p(p)$ to the tangential space of $\kappa(\mathfrak{B})$ with H_{KL} at $\kappa(p)$, is an isometric transformation.

A locally stress-free configuration is not unique, since one can obtain stress-free configuration by a rigid body movement. However, the metric tensor H_{KL} is determined independently of any translation and/or rotation of a local configuration. We introduce an equivalence relation among families of local configurations by the condition that $\mathcal{C} = \{(U_p, \kappa_p)\}_{p\in\mathfrak{B}}$ is equivalent to $\bar{\mathcal{C}} = \{(\bar{U}_p, \bar{\kappa}_p)\}_{p\in\mathfrak{B}}$ if for every $p \in \mathfrak{B}$ there exists a locally isometric mapping Ω in Euclidean space such that for any $q \in U_p \cap \bar{U}_p$

$$\bar{\kappa}_p(q) = \Omega \circ \kappa_p(q), \tag{5}$$

where $\Omega \circ \kappa_p$ denotes the composition of Ω and κ_p. A locally-isometric mapping Ω for a local configuration κ_p should be a mapping which satisfies at $\kappa_p(p)$,

$$\Omega^\alpha_\mu \Omega^\beta_\nu \bar{\gamma}_{\alpha\beta} = \gamma_{\mu\nu}$$
$$\left(\Omega^\alpha_\mu = \frac{\partial \bar{\xi}^\alpha}{\partial \xi^\mu} = \frac{\partial \Omega^\alpha(\xi)}{\partial \xi^\mu}\bigg|_{\xi=\kappa_p(p)}\right), \tag{6}$$

where $\bar{\xi}^\alpha = \bar{\kappa}^\alpha_p(q)$ and $\bar{\gamma}_{\alpha\beta} = g_{\alpha\beta}(\bar{\kappa}_p(p))$. It should be noted that a rotation Ω may be defined for each local configuration independently of the others, nevertheless we did not explicitly represent the dependence of Ω on p in equation (5). If $\mathcal{C}$ is a family of stress-free configurations, an equivalent family $\bar{\mathcal{C}}$ results in another family of stress-free configurations. In the same manner as equation (4), we can define a metric tensor $\bar{H}_{KL}$ corresponding with $\bar{\mathcal{C}}$. This metric tensor $\bar{H}_{KL}$ coincides with the metric tensor H_{KL}:

$$\begin{aligned}\bar{H}_{KL} &= \frac{\partial \bar{\xi}^\alpha}{\partial X^K}\frac{\partial \bar{\xi}^\beta}{\partial X^L}\bar{\gamma}_{\alpha\beta} \\ &= \frac{\partial \xi^\mu}{\partial X^K}\frac{\partial \xi^\nu}{\partial X^L}\Omega^\alpha_\mu \Omega^\beta_\nu \bar{\gamma}_{\alpha\beta} \\ &= \frac{\partial \xi^\mu}{\partial X^K}\frac{\partial \xi^\nu}{\partial X^L}\gamma_{\mu\nu} \\ &= H_{KL}.\end{aligned} \tag{7}$$

A nontrivial example of equivalent families of local stress-free configurations for a body undergoing residual stress was given in a paper by Takamizawa and Hayashi (1988). We assume that the metric tensor H_{KL} is piecewise smooth on $\kappa(\mathfrak{B})$, and take the Riemannian connection. Nevertheless, other connections may be introduced (Truesdell and Noll, 1965).

The manifold $\kappa(\mathfrak{B})$ with the metric tensor H_{KL} may be non-Euclidean although $\kappa(\mathfrak{B})$ with G_{KL} is a region of Euclidean space. We shall call the manifold $\kappa(\mathfrak{B})$ with H_{KL} Riemannian

Nomenclature (cont.)

$\overset{*}{T}{}^{Kk}$ = first Piola-Kirchhoff stress tensor when a Riemannian stress-free configuration is taken as a reference

$\left\{ {k \atop lm} \right\}, \left\{ {K \atop LM} \right\}_\kappa$ = Christoffel symbols of the second kind for configurations χ and κ, respectively

$\left\{ {K \atop LM} \right\}^*$ = Christoffel symbols of the second kind for Riemannian stress-free configuration

Hyperelastic Material

W = strain energy stored per unit volume in a stress-free configuration

Π = hydrostatic pressure for material incompressibility

Application to a Spherical Model of the Left Ventricle

r, θ, ϕ; R, Θ, Φ = spherical coordinates for a deformed configuration of the spherical model of the left ventricle. Capital letters corresponding to these symbols denote coordinates for a global reference (end diastole).

λ_k, Λ_K = stretching ratios of a deformed configuration referred to stress-free configuration. Capital letters corresponding to these symbols denote stretching ratios of the global reference referred to the stress-free configuration.

σ_{kl} = physical components of Cauchy's stress

r_i, r_o; R_i, R_o = inner and outer radii of a deformed configuration and those of the end diastole, respectively

P_i, P_o = pressures at the inner and outer surfaces of the left ventricle

Results and Discussion

$\partial\kappa(\mathfrak{B})$ = boundary of $\kappa(\mathfrak{B})$

$\mathcal{E}$ = total strain energy stored in a given configuration κ

$\mathfrak{D}$ = total mass of the material body

t^{KL} = Cauchy stress in the configuration κ

τ^{KL} = external Cauchy stress acting on the surface of the body

dS = surface element of $\partial\kappa(\mathfrak{B})$

A_K = components of exterior unit normal vector of the surface element dS

δF = variation of a function F or a functional F

Ξ = Lagrangian multiplier for the constraint of mass conservation

Ψ_K = Lagrangian multipliers for the constraint of equilibrium condition

$\Psi_{K;L}$ = covariant derivatives of Ψ_K with X^L taking the metric G_{KL}

Appendix

$\hat{W}$ = strain energy density containing the energy increase by infinitesimal displacement, Ψ_K

e_{KL} = linear strain tensor defined from Ψ_K which is regarded as infinitesimal displacement

Downloaded 03 May 2010 to 171.66.16.244. Redistribution subject to ASME license or copyright; see http://www.asme.org/terms/Terms_Use.cfm

stress-free configuration to distinguish it from that with G_{KL}. The Riemannian stress-free configuration is uniquely defined in the sense of Riemann geometry even if we take any configuration as κ. If it is Euclidean, i.e., there exists a global stress-free configuration, the Riemann-Christoffel tensor vanishes. However, it may be a non-Euclidean manifold. The covariant components of Riemann-Christoffel tensor are given as follows (Sokolnikoff, 1964):

$$\overset{*}{R}_{KLMN} = \frac{1}{2}\left(\frac{\partial^2 H_{KN}}{\partial X^L \partial X^M} + \frac{\partial^2 H_{LM}}{\partial X^K \partial X^N} - \frac{\partial^2 H_{KM}}{\partial X^L \partial X^N} - \frac{\partial^2 H_{LN}}{\partial X^K \partial X^M}\right) + H^{\mathfrak{M}\mathfrak{N}}([KN,\mathfrak{M}]^*[LM,\mathfrak{N}]^* - [KM,\mathfrak{M}]^*[LN,\mathfrak{N}]^*), \tag{8}$$

where $H^{\mathfrak{M}\mathfrak{N}}$ represent the contravariant components of the metric tensor H_{KL} and $[KN,\mathfrak{M}]^*$ are the Christoffel symbols of the first kind with H_{KL}. The zero Riemann-Christoffel tensor means that the body $\mathfrak{B}$ can be completely relieved from the residual stress and strain by unloading and some cutting. We shall show this in the following paragraph.

Let V_p be a set of such points, $q \in U_p$, that the stress in the configuration κ_p is zero at $\kappa_p(q)$. It should be noted that V_p is not necessarily a neighborhood of p, nevertheless $p \in V_p \subset U_p$. For all points $q \in V_p$, we can adopt $U_q = U_p$, $\kappa_q = \kappa_p$ as a local stress-free configuration. If V_p is an open neighborhood of p, the Riemann-Christoffel tensor $\overset{*}{R}_{KLMN}$ is zero over $\kappa(V_p)$ since $\kappa(V_p)$ with H_{KL} is isometric to $\kappa_p(V_p)$ which carries the Euclidean metric $\gamma_{\alpha\beta}$. Therefore, if V_p is a neighborhood of p for every $p \in \mathfrak{B}$, $\overset{*}{R}_{KLMN}$ is zero over $\kappa(\mathfrak{B})$. This occurs in the case that the material body can be divided into some bulky parts which are completely free of stress—H_{KL} may be discontinuous on the boundaries of those parts. The converse is also true. We shall meet later with an example of the configuration which has nonzero Riemann-Christoffel tensor. In this case, the body is divided into infinitely small parts in order to completely relieve the residual strain.

When we adopt the locally stress-free configuration κ_p as a reference, Green's strain tensor is defined as follows:

$$E_{\alpha\beta} = \frac{1}{2}(g_{kl}\, x^k_\alpha\, x^l_\beta - \gamma_{\alpha\beta}). \tag{9}$$

In general, this strain must be defined for each point p with each reference configuration κ_p. However, we can introduce an equivalent but globally defined one. It is the strain defined with Riemannian stress-free configuration as a global reference,

$$\overset{*}{E}_{KL} = \frac{1}{2}\left(g_{kl}\frac{\partial x^k}{\partial X^K}\frac{\partial x^l}{\partial X^L} - H_{KL}\right) = \frac{\partial \xi^\alpha}{\partial X^K}\frac{\partial \xi^\beta}{\partial X^L} E_{\alpha\beta}. \tag{10}$$

This strain must be distinguished from the strain related to the configuration, $\kappa(\mathfrak{B})$, with the metric tensor, G_{KL}, as a reference because $\kappa(\mathfrak{B})$ with H_{KL} is a different geometrical object from that with G_{KL}. The strain tensor $\overset{*}{E}_{KL}$ may not satisfy the condition of compatibility since it is derived from the fact that the reference and deformed configurations convey Euclidean metrics, i.e., the Riemann-Christoffel tensors vanish in both of the configurations (Kondo, 1949).

The conservation law of mass is expressed by

$$\rho_o\sqrt{\gamma} = \rho\sqrt{g}\, J, \tag{11}$$

where ρ_o denotes the density in the locally stress-free configuration κ_p, $\gamma = \det(\gamma_{\alpha\beta})$, and ρ the density in the configuration χ, $g = \det(g_{kl})$, $J = \det(x^k_\alpha)$. Considering equation (4) and the relation

$$x^k_\alpha = \frac{\partial x^k}{\partial X^K} X^K_\alpha, \tag{12}$$

we reform equation (11) as follows

$$\rho_o\sqrt{H} = \rho\sqrt{g}\, \tilde{J}, \tag{13}$$

where $H = \det(H_{KL})$ and $\tilde{J} = \det(\partial x^k/\partial X^K)$. If the material is incompressible, the following equation is satisfied

$$\sqrt{H} = \sqrt{g}\, \tilde{J}. \tag{14}$$

Stress Tensor Referred to Riemannian Stress-Free Configuration

Because Piola-Kirchhoff stress tensors must be defined with a reference configuration, we will briefly consider stress, too. We note the stress at $\chi(p)$ in the deformed configuration χ. Let contravariant components of Cauchy stress tensor be represented by t^{kl}. If we adopt the configuration κ as a reference configuration in an ordinary sense, the first Piola-Kirchhoff stress tensor is defined by

$$\tilde{T}^{Kk} = \tilde{J}\sqrt{\frac{g}{G}}\frac{\partial X^K}{\partial x^l}\, t^{lk}. \tag{15}$$

If Riemannian stress-free configuration κ is taken, the stress should be defined as follows

$$\overset{*}{\tilde{T}}^{Kk} = \tilde{J}\sqrt{\frac{g}{H}}\frac{\partial X^K}{\partial x^l}\, t^{lk}. \tag{16}$$

The Piola-Kirchhoff tensor $T^{\alpha k}$ in reference to the locally stress-free configuration κ_p is related to the above tensor as follows

$$T^{\alpha k} = J\sqrt{\frac{g}{\gamma}}\frac{\partial \xi^\alpha}{\partial x^l}\, t^{lk} = \frac{\partial \xi^\alpha}{\partial X^K}\overset{*}{\tilde{T}}^{Kk}. \tag{17}$$

We can take the similar procedure for the second Piola-Kirchhoff stress.

The equation of equilibrium for the Cauchy stress is given by (Eringen, 1975)

$$t^{kl}_{;k} = \frac{\partial t^{kl}}{\partial x^k} + t^{km}\left\{{l \atop km}\right\} + t^{kl}\left\{{m \atop mk}\right\} = 0, \tag{18}$$

where $;k$ denotes the covariant differentiation with x^k, and $\left\{{l \atop km}\right\}$ the Christoffel symbols of the second kind with the metric tensor g_{kl}. For the Piola-Kirchhoff stress tensor $\tilde{T}^{Kk}$,

$$\frac{\partial \tilde{T}^{Kk}}{\partial X^K} + \tilde{T}^{Kl}\left\{{k \atop lm}\right\}\frac{\partial x^m}{\partial X^K} + \tilde{T}^{Kk}\left\{{L \atop LK}\right\}_\kappa = 0, \tag{19}$$

where $\left\{{L \atop KM}\right\}_\kappa$ represent the Christoffel symbols of the second kind with the metric tensor G_{KL}. Considering the relation between $\tilde{T}^{Kk}$ and $\overset{*}{\tilde{T}}^{Kk}$, we obtain

$$\frac{\partial \overset{*}{\tilde{T}}^{Kk}}{\partial X^K} + \overset{*}{\tilde{T}}^{Kl}\left\{{k \atop lm}\right\}\frac{\partial x^m}{\partial X^K} + \overset{*}{\tilde{T}}^{Kk}\left\{{L \atop LK}\right\}^* = 0, \tag{20}$$

where $\left\{{L \atop KM}\right\}^*$ represent the Christoffel symbols with the metric tensor H_{KL}.

We have just shown that a Riemannian stress-free configuration takes the formal role of a Euclidean global stress-free configuration.

Hyperelastic Material

We will consider a hyperelastic material, i.e., the stress-strain relation is derived from a strain energy density function. Using the deformation gradients referred to a locally stress-free state, Cauchy's stress is given as follows

$$t^{kl} = \frac{1}{J}\sqrt{\frac{\gamma}{g}}\, x^k_\alpha\, g^{lm}\frac{\partial W}{\partial x^m_\alpha}, \tag{21}$$

where W represents the strain energy per unit volume of the

Downloaded 03 May 2010 to 171.66.16.244. Redistribution subject to ASME license or copyright; see http://www.asme.org/terms/Terms_Use.cfm

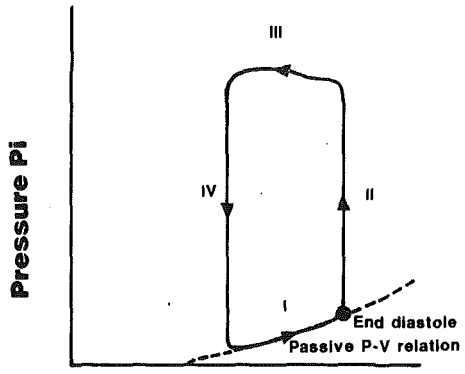


Fig. 2 Schematic diagram of the pressure-volume loop of the left ventricle. I: diastolic filling, II: isovolumic contraction, III: ejection, and IV: isovolumic relaxation.

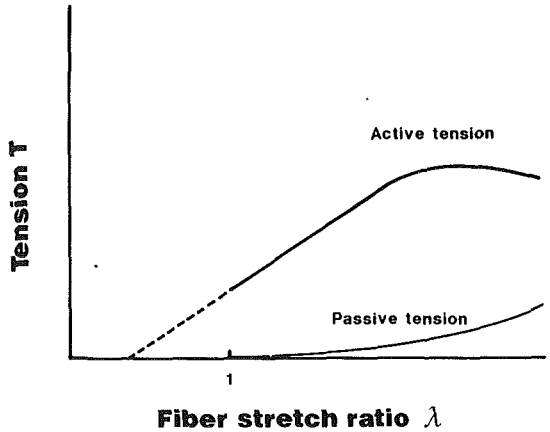


Fig. 3 Schematic diagram of the passive and isometric active tension-stretch relations in the cardiac muscle

stress-free configuration, and g^{kl} the reciprocal metric tensor corresponding to g_{kl}. Considering equations (4) and (12), we express the stress in the terms related to Riemannian stress-free configuration κ,

$$t^{kl} = \frac{1}{\bar{J}}\sqrt{\frac{H}{g}}\,\frac{\partial x^k}{\partial X^K}\,g^{lm}\,\frac{\partial W}{\partial\left(\dfrac{\partial x^m}{\partial X^K}\right)}. \tag{22}$$

For an incompressible material, a term of hydrostatic pressure Π is added to the above equations as a Lagrangian multiplier for the constraint (equation (14))

$$t^{kl} = -\Pi\, g^{kl} + \frac{\partial x^k}{\partial X^K}\,g^{lm}\,\frac{\partial W}{\partial\left(\dfrac{\partial x^m}{\partial X^K}\right)}. \tag{23}$$

Application to a Spherical Model of the Left Ventricle

The heart is a pump to push out blood to all parts of the body. Although it consists of four chambers and four valves, the main pumping function is performed by the left ventricle. The pressure-volume loop of the left ventricle is schematically shown in Fig. 2 (Parmley and Talbot, 1979). During the isovolumic contraction phase the active tension of the cardiac muscle increases from the end diastole until the opening of the aortic valve. The highest tension of the muscle fiber in a cardiac cycle is thought to be generated at the end of this phase. This estimate derives from a spherical model in which the total wall force is proportional to the pressure times the square of the inner radius of the chamber.

The fundamental unit of the muscle is called sarcomere and its length indicates the stretch of the muscle fiber. Fung (1984a,b) summarized several histological studies which suggested the nearly uniform distribution of the sarcomere length through the wall thickness at the end diastole. He also argued that the stretch of the muscle fibers should have a uniform distribution at the end diastole as an optimal condition of the contraction.

The active tension of the cardiac muscle depends on the length of the muscle fiber as shown schematically in Fig. 3 (Brady, 1979). The tension-length relation of the muscle is represented as a function of the fiber stretch ratio λ. The active tension is almost linearly related to λ below the maximum tension ratio. The slope of this curve is variable depending on the degree of activation. At the end of the isovolumic contraction the muscle fibers should be equally stretched to equally sustain the stress because they receive the severest load in a cardiac cycle. Since the fiber length is regarded to be almost unchanged during the isovolumic contraction, all fibers should undergo equal stretches at the end diastole.

We shall consider a thick-walled spherical model of the left ventricle in the diastole, i.e., the heart in a passive state. The wall material is assumed to be homogeneous, isotropic, incompressible, and hyperelastic. These assumptions are often used for the heart in biomechanics. Although the zero initial stress has been implicitly assumed in conventional analyses, we adopt the uniform strain hypothesis instead of it, i.e., assuming that the tangential strain is constant through the wall thickness at the end diastole. In this context, of course, the strain should be defined in reference to the stress-free configuration.

In this section, the symbols of the coordinates themselves are taken as the indices representing components of tensors.

(1) Deformation. It is assumed that there are only normal components of strain and stress in the spherical coordinate system $[r, \theta, \phi;\ g_{rr}=1,\ g_{\theta\theta}=r^2,\ g_{\phi\phi}=r^2\sin^2\theta,\ g_{kl}=0\ (k\neq l)]$, and deformation is given as follows

$$r = r(R), \quad \theta = \Theta, \quad \phi = \Phi, \tag{24}$$

where R, Θ, Φ denote the coordinates of a point in the end diastole, which is adopted as a global reference configuration κ. The radial, latitudinal, and longitudinal stretching ratios referred to the stress-free configuration are given as follows

$$\lambda_r = \sqrt{\frac{g_{rr}}{H_{RR}}}\,\frac{\partial r}{\partial R},$$

$$\lambda_\theta = \sqrt{\frac{g_{\theta\theta}}{H_{\Theta\Theta}}}\,\frac{\partial \theta}{\partial \Theta} = \sqrt{\frac{g_{\theta\theta}}{H_{\Theta\Theta}}}, \tag{25}$$

$$\lambda_\phi = \sqrt{\frac{g_{\phi\phi}}{H_{\Phi\Phi}}}\,\frac{\partial \phi}{\partial \Phi} = \sqrt{\frac{g_{\phi\phi}}{H_{\Phi\Phi}}},$$

where the coordinates $(R, \Theta, \Phi)\in\kappa(\mathfrak{B})$ with H_{KL} give the Riemannian stress-free configuration of the left ventricle.

If we set $r\equiv R$ in equation (25), it gives the stretching ratio of the global reference configuration (κ with G_{KL}) referred to the stress-free one, which is metrically equivalent to κ with H_{KL}. This results in the following equations

$$\Lambda_R = \sqrt{\frac{G_{RR}}{H_{RR}}},\quad \Lambda_\Theta = \sqrt{\frac{G_{\Theta\Theta}}{H_{\Theta\Theta}}},\quad \Lambda_\Phi = \sqrt{\frac{G_{\Phi\Phi}}{H_{\Phi\Phi}}}. \tag{26}$$

Downloaded 03 May 2010 to 171.66.16.244. Redistribution subject to ASME license or copyright; see http://www.asme.org/terms/Terms_Use.cfm

From the assumption of no shear and equation (26), we obtain the metric tensor

$$H_{RR}=\frac{1}{\Lambda_R^2},\quad H_{\Theta\Theta}=\frac{R^2}{\Lambda_\Theta^2},\quad H_{\Phi\Phi}=\frac{R^2\sin^2\Theta}{\Lambda_\Phi^2},$$
$$H_{KL}=0\ (K\neq L). \tag{27}$$

The uniform strain (stretch) hypothesis and the spherical symmetry imply that $\Lambda_\Theta=\Lambda_\Phi=$ constant through the wall thickness.

The condition of incompressibility (equation (14)) is written as follows

$$\sqrt{\begin{vmatrix}\frac{1}{\Lambda_R^2} & 0 & 0\\ 0 & \frac{R^2}{\Lambda_\Theta^2} & 0\\ 0 & 0 & \frac{R^2\sin^2\Theta}{\Lambda_\Phi^2}\end{vmatrix}}=\sqrt{\begin{vmatrix}1 & 0 & 0\\ 0 & r^2 & 0\\ 0 & 0 & r^2\sin^2\theta\end{vmatrix}}\begin{vmatrix}\frac{\partial r}{\partial R} & \frac{\partial r}{\partial\Theta} & \frac{\partial r}{\partial\Phi}\\ \frac{\partial\theta}{\partial R} & \frac{\partial\theta}{\partial\Theta} & \frac{\partial\theta}{\partial\Phi}\\ \frac{\partial\phi}{\partial R} & \frac{\partial\phi}{\partial\Theta} & \frac{\partial\phi}{\partial\Phi}\end{vmatrix},$$

that is,

$$\frac{R^2\sin\Theta}{\Lambda_R\Lambda_\Theta\Lambda_\Phi}=r^2\sin\theta\frac{\partial r}{\partial R}. \tag{28}$$

This equation is valid for the reference configuration κ, i.e., $r\equiv R$. Hence, $\Lambda_R\Lambda_\Theta\Lambda_\Phi=1$ (from the uniform stretch assumption, the radial stretching ratio Λ_R is also constant through the wall thickness). Therefore, we obtain the following from equation (28)

$$\frac{\partial r}{\partial R}\frac{r^2}{R^2}=1. \tag{29}$$

This implies that

$$r^3-R^3=\text{constant}. \tag{30}$$

The latitudinal, longitudinal, and radial stretching ratios are thus represented by

$$\lambda_\theta=\sqrt{\frac{g_{\theta\theta}}{H_{\Theta\Theta}}}=\Lambda_\Theta\frac{r}{R}=\frac{\Lambda_\Theta r}{(r^3+R_i^3-r_i^3)^{1/3}},$$
$$\lambda_\theta=\lambda_\theta,\quad \lambda_r=\frac{1}{\lambda_\theta\lambda_\phi}, \tag{31}$$

where R_i and r_i are internal radii of the ventricle at the end diastole and a certain loading state, respectively.

The configuration of the end diastole with the metric tensor H_{KL} is a non-Euclidean manifold, because covariant components of the Riemann-Christoffel tensor (equation (8)) don't vanish. For example, the component $\overset{*}{R}_{\Theta\Phi\Theta\Phi}$ is given by

$$\overset{*}{R}_{\Theta\Phi\Theta\Phi}=\frac{1}{\Lambda_\Phi^2}\left(1-\frac{\Lambda_R^2}{\Lambda_\Theta^2}\right)R^2\sin^2\Theta. \tag{32}$$

In contrast with this, every component of Riemann-Christoffel tensor vanishes for the similar model of the arterial wall. It corresponds to the result that we can obtain a global stress-free state for the cylindrical model by a longitudinal cutting (Takamizawa and Hayashi, 1988). The Riemannian stress-free configuration, however, is not globally Euclidean. Indeed, it is the product space of one-dimensional Euclidean space and a zone of a cone.

(2) Strain Energy Density Function. We adopted the following isotropic strain energy density function for the left ventricular wall in the diastole considering the functions proposed by Mirsky (1973) and Demiray (1984)

$$W=\frac{a}{2b}[\exp\{b(\mathrm{I}-3)\}-b(\mathrm{I}-3)], \tag{33}$$

where a,b represent constants, and I the first invariant of strain

$$\mathrm{I}=g_{kl}\,\gamma^{\alpha\beta}\,x^k_\alpha\,x^l_\beta=g_{kl}\,H^{KL}\frac{\partial x^k}{\partial X^K}\frac{\partial x^l}{\partial X^L}. \tag{34}$$

Cauchy's stress is derived from the above strain energy density function assuming the wall incompressibility

$$t^{kl}=-\Pi\,g^{kl}+H^{KL}\frac{\partial x^k}{\partial X^K}\frac{\partial x^l}{\partial X^L}Q(\mathrm{I}),$$
$$Q(\mathrm{I})=a[\dot{\exp}\{b(\mathrm{I}-3)\}-1]. \tag{35}$$

(3) Equilibrium Condition. The physical components of the Cauchy stress tensor are defined with no ambiguity in the orthogonal curvilinear coordinate system

$$\sigma_{kl}=\sqrt{g_{kk}g_{ll}}\,t^{kl}\quad(\text{no sum on } k,l). \tag{36}$$

We may omit one suffix of σ_{kl} because only the normal components are considered. Then the stress is represented by

$$\sigma_r=t^{rr},\quad \sigma_\theta=r^2\,t^{\theta\theta},\quad \sigma_\phi=r^2\sin^2\theta\,t^{\phi\phi}. \tag{37}$$

The constitutive law expressed in terms of physical components is given by

$$\sigma_k=-\Pi+\lambda_k^2\,Q(\mathrm{I}). \tag{38}$$

The invariant I can be also represented by the stretching ratios

$$\mathrm{I}=\lambda_r^2+\lambda_\theta^2+\lambda_\phi^2. \tag{39}$$

The equilibrium condition (18) for the physical components is reduced to

$$\frac{\partial\sigma_r}{\partial r}+\frac{2\sigma_r-\sigma_\theta-\sigma_\phi}{r}=0, \tag{40}$$

and the boundary conditions are

$$\sigma_r(r_i)=-P_i,\qquad \sigma_r(r_o)=-P_o=0, \tag{41}$$

where r_i and P_i represent the inner radius and pressure, r_o and P_o, the outer radius and pressure, respectively. Thus, each component of the stress is given as follows

$$\sigma_r(r')=-P_i+2\int_{r_i}^{r'}(\lambda_\theta^2-\lambda_r^2)Q(\mathrm{I})\frac{dr}{r},$$
$$\sigma_\theta-\sigma_r=(\lambda_\theta^2-\lambda_r^2)Q(\mathrm{I}),\qquad \sigma_\phi=\sigma_\theta. \tag{42}$$

The chamber pressure P_i is given by

$$P_i=2\int_{r_i}^{r_o}(\lambda_\theta^2-\lambda_r^2)Q(\mathrm{I})\frac{dr}{r}. \tag{43}$$

Results and Discussion

The isotropic mechanical properties of the wall of the left ventricle were assumed because we had limited data for the cardiac muscle and treated the ventricle as a spherical shell. The assumption of the wall incompressibility is common in the cardiovascular tissues. This makes the analysis simple in the cylindrical model and the spherical model, but in general the incompressibility assumption introduces difficulties, particularly, in the finite element method.

Using the experimental data of a canine heart obtained by Spotnitz et al. (1966), the constants a and b in equation (33) were determined by a least squares method. Nevertheless, the original data were given as the pressure-volume curve, we

Downloaded 03 May 2010 to 171.66.16.244. Redistribution subject to ASME license or copyright; see http://www.asme.org/terms/Terms_Use.cfm

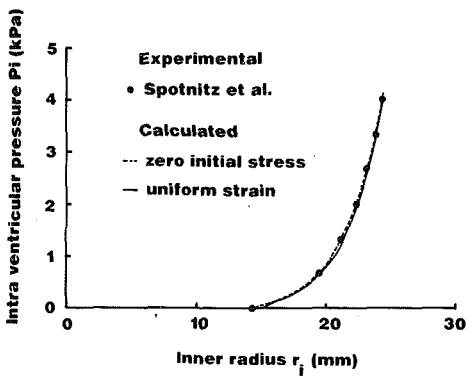
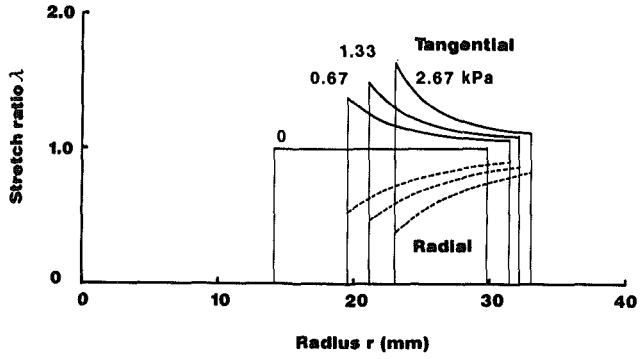


Fig. 4 Pressure-radius relation of the left ventricle in the diastole.



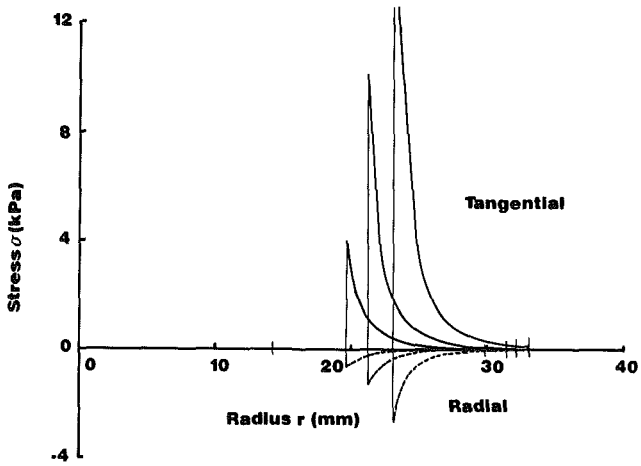
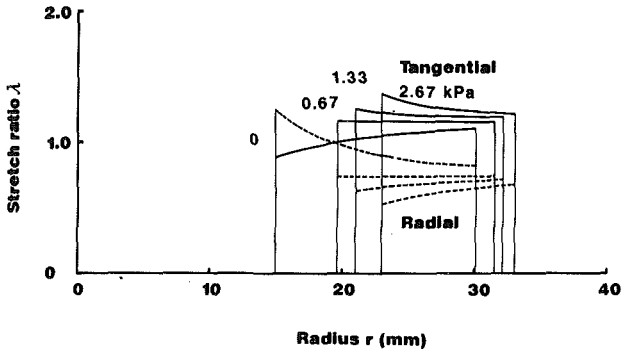


Fig. 5 Distributions of stretching ratios and stresses in the left ventricular wall at pressures $P_i = 0$, 0.67 kPa (5 mmHg), 1.33 kPa (10 mmHg), and 2.67 kPa (20 mmHg) (calculated on the basis of the zero initial stress assumption)



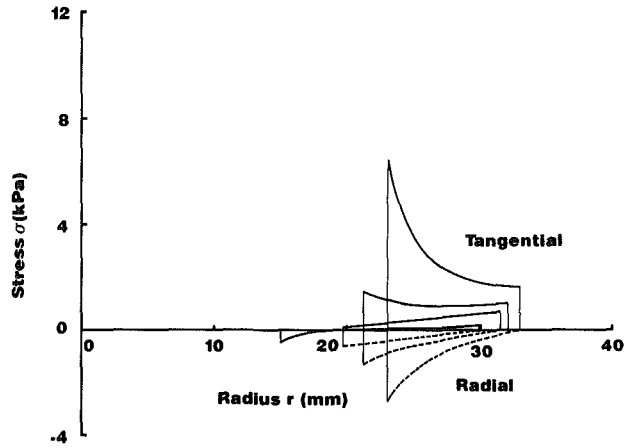


Fig. 6 Distributions of stretching ratios and stresses in the left ventricular wall at pressures $P_i = 0$, 0.67 kPa (5 mmHg), 1.33 kPa (10 mmHg), and 2.67 kPa (20 mmHg) (calculated on the basis of the uniform strain hypothesis)

redrew it into the pressure-radius relation assuming the spherical chamber. The experimental pressure-radius curve in the diastolic heart, and the calculated curves based on the conventional zero initial stress hypothesis and the uniform strain hypothesis are shown in Fig. 4. We assumed that the uniform strain (stretch) distribution occurs at 5 mmHg pressure loading. The determined constants were $a = 2.272$ kPa, $b = 0.749$ on the basis of the zero initial stress hypothesis, $a = 2.749$ kPa, $b = 1.094$ on the basis of the uniform strain hypothesis ($\Lambda = \Lambda_\Theta = \Lambda_\Phi = 1.16$ at 5 mmHg). Although the agreement seems to be better on the zero initial stress assumption than on the uniform strain hypothesis, it is very good except for the vicinity of zero pressure even on the uniform strain hypothesis.

The distributions of stress and stretching ratio calculated on the basis of the zero initial stress and uniform strain assumptions are shown in Figs. 5 and 6. The steep distributions in the stress are quite apparent even at 5 mmHg when we adopt the zero initial stress hypothesis. When we assume the uniform tangential stretching, the residual stress is introduced, i.e., compressive in the inner side and tensile in the outer side. The radial component of the residual stress is -0.06 kPa at the maximum in the middle region of the wall although it is zero at the inner and outer surfaces from the boundary condition. Janz and Waldron (1976) showed that the proper inhomogeneity of cardiac muscles results in the uniform stress distribution. The present results have shown that even if the material is homogeneous, the residual stress reduces the steep stress distribution of the left ventricular wall very much. It can be another maneuver for living organs to attain an optimized stress distribution under physiological conditions.

We analyzed the stress distributions in the left ventricular wall on the basis of the uniform strain hypothesis. The artery can be treated in the similar manner as the left ventricle. The difference between them is only that between the spherical and cylindrical coordinate systems. The stress distributions in the artery obtained from the present theory are the same as the results given in the study by Takamizawa and Hayashi (1987).

The uniform strain hypothesis is simple and plausible for geometrically simple models. Even if the uniform strain hypothesis is inadequate to a complex geometry, it is possible to start from a given residual strain and investigate the effect of the residual strain and/or stress. The residual strain is given by the metric tensor H_{KL} for the unloading configuration which is taken as a global reference κ. In this case, the residual

Downloaded 03 May 2010 to 171.66.16.244. Redistribution subject to ASME license or copyright; see http://www.asme.org/terms/Terms_Use.cfm

strain is calculated from equation (10) for the unloading configuration κ

$$\overset{*}{E}_{KL} = \frac{1}{2}(G_{KL} - H_{KL}). \tag{44}$$

Since the equilibrium condition must be satisfied in the unloading state, the residual strain cannot be arbitrarily chosen.

Another intriguing approach is an optimization theory. We may determine an optimal residual strain in the sense of the minimum of stored strain energy at given load and configuration. The given configuration is taken as κ, and the metric tensor H_{KL} is determined to provide the minimum strain energy at the given loading. This results in a variational problem with constraints, to which Lagrange's method of undetermined multipliers is applicable. Let the material be hyperelastic and the material constants be given. The total energy stored in the body is given by the following equation

$$\mathcal{E} = \iiint_{\kappa(\mathfrak{B})} W\sqrt{H}\, dX^1 dX^2 dX^3. \tag{45}$$

In the configuration κ, the equilibrium condition must be satisfied

$$t^{KL}_{;K} = 0, \tag{46}$$

where t^{KL} represents the Cauchy stress tensor and $;K$ means the covariant differentiation with X^K in the configuration κ with the metric tensor G_{KL} (cf., equation (18)). On the boundary of the configuration $\kappa(\mathfrak{B})$,

$$(t^{KL} - \tau^{KL})A_K = 0, \tag{47}$$

where τ^{KL} is the external stress acting on the surface and A_K is the covariant components of the exterior unit normal vector of the surface. The total mass of the material body $\mathfrak{B}$ should be conserved while we vary the metric tensor H_{KL}:

$$\mathfrak{D} = \iiint_{\kappa(\mathfrak{B})} \rho_o\sqrt{H}\, dX^1 dX^2 dX^3 = \text{constant}. \tag{48}$$

For the constraint conditions of equations (46) and (48), Lagrangian multipliers Ψ_L, which are the covariant components of an undetermined vector field, and Ξ, which is an undetermined constant, are introduced. The variation of $\mathcal{E}$ with the constraints is given as follows

$$\begin{aligned}
\delta\Sigma = \delta\mathcal{E} - \Xi\delta\mathfrak{D} - \iiint_{\kappa(\mathfrak{B})} \Psi_L\, \delta t^{KL}_{;K}\sqrt{G}\, dX^1 dX^2 dX^3 \\
= \iiint_{\kappa(\mathfrak{B})} \Big\{\delta(W\sqrt{H}) - \Xi\delta(\rho_o\sqrt{H}) \\
- \Psi_L \delta t^{KL}_{;K}\sqrt{G}\Big\} dX^1 dX^2 dX^3 \\
= \iiint_{\kappa(\mathfrak{B})} \Big[\Big(\frac{1}{2} WH^{MN} + \frac{\partial W}{\partial H_{MN}} \\
- \frac{1}{2}\Xi\rho_o H^{MN}\Big)\sqrt{H}\,\delta H_{MN} \\
- \{(\Psi_L \delta t^{KL})_{;K} - \Psi_{L;K}\delta t^{KL}\}\sqrt{G}\Big] dX^1 dX^2 dX^3 \\
= \iiint_{\kappa(\mathfrak{B})} \Big[\Big\{\frac{1}{2}(W - \Xi\rho_o)H^{MN} + \frac{\partial W}{\partial H_{MN}}\Big\}\sqrt{H} \\
+ \Psi_{L;K}\frac{\partial t^{KL}}{\partial H_{MN}}\sqrt{G}\Big]\delta H_{MN}\, dX^1 dX^2 dX^3 \\
- \iint_{\partial\kappa(\mathfrak{B})} \Psi_L\, \delta t^{KL}\, A_K\, dS,
\end{aligned} \tag{49}$$

where $\partial\kappa(\mathfrak{B})$ denotes the boundary of $\kappa(\mathfrak{B})$, and dS is the surface element, and this last integral vanishes since the boundary condition (47) is satisfied. Therefore, we obtain from $\delta\Sigma = 0$ the following equation

$$\frac{1}{2}(W - \Xi\rho_o)H^{MN} + \frac{\partial W}{\partial H_{MN}} + \sqrt{\frac{G}{H}}\,\Psi_{L;K}\frac{\partial t^{KL}}{\partial H_{MN}} = 0. \tag{50}$$

Since the stress t^{KL} is derived from the strain energy density function, we can determine six independent components of the metric tensor H_{KL} as a function of the material constants, an undetermined constant Ξ, and covariant derivatives of three undetermined functions Ψ_L. Thus, we obtain three differential equations imposed on Ψ_L from the equilibrium equation (46) including a parameter of Ξ. A given value of Ξ determines Ψ_L, and then the metric tensor H_{KL} and the total mass $\mathfrak{D}$ in equation (48). If the Riemann-Christoffel tensor derived from the metric tensor does not vanish, there exists the residual stress and strain.

In the case that the incompressible material equation (48) is automatically satisfied, then the term $\Xi\rho_o$ in equation (50) should be replaced with an undetermined function of a position because the incompressibility condition is the constraint to be satisfied at each point. Since the extra undetermined hydrostatic pressure Π appears in the relation between the stress and the derivatives of strain energy density function (equation (23)), we can obtain two independent equations from the three equilibrium equations if Π is eliminated. Thus, we must impose a condition on the Lagrange's multipliers, Ψ_K,

$$G^{KL}\Psi_{K;L} = \Psi^K_{;K} = 0. \tag{51}$$

The Lagrangian multipliers Ψ_K can be interpreted as components of infinitesimal displacement superposed on the configuration κ in a formal sense, although their values are not necessarily small.

The functional which is given in the Appendix is useful for the numerical analysis because all equations are derived from its stationary condition.

Acknowledgments

We wish to thank Prof. K. Hayashi, Department of Biomedical Control, Research Institute of Applied Electricity, Hokkaido University, for giving helpful information, Dr. H. Suga, Department of Cardiovascular Dynamics of our Institute, for inspiring comments from a physiological standpoint, and Drs. J. Seki and T. Kato, Biomedical Engineering, for valuable discussion. We also thank the reviewers for their valuable comments and criticism.

This study was supported financially in part by Research Grant for Cardiovascular Diseases from the Ministry of Health and Welfare.

References

Brady, A. J., 1979, "Mechanical Properties of Cardiac Fibers," *Handbook of Physiology*, Sec. 2, Vol. 1 R. M. Berne, N. Sperelakis, and S. R. Geiger, eds., American Physiological Society, Bethesda, Md., pp. 461-474.

Chuong, C. J., and Fung, Y. C., 1986, "On Residual Stress in Arteries," *ASME Journal of Biomechanical Engineering*, Vol. 108, pp. 189-192.

Demiray, H., 1984, "Incremental Elastic Modulus for Ventricles in Diastole," *Journal of Biomechanics*, Vol. 17, pp. 621-626.

Eringen, A. C., 1975, *Continuum Physics*, Vol. II, A. C. Eringen, ed., Academic Press, New York, pp. 42-44, 78-82.

Fung, Y. C., 1984a, "What Principle Governs the Stress Distribution in Living Organs?" *Biomechanics in China, Japan and U.S.A.* Edited by Y. C. Fung, E. Fukada, and Junjian, Wang eds., Science Press, Beijin, pp. 1-13.

Fung, Y. C., 1984b, *Biodynamics: Circulation*, Springer-Verlag, New York, pp. 53-68.

Janz, R. F., and Waldron, R. J., 1976, "Some Implications of a Constant Fiber Stress Hypothesis in the Diastolic Left Ventricle," *Bulletin of Mathematical Biology*, Vol. 38, pp. 401-413.

Kondo, K., 1949, "A Proposal of a New Theory concerning the Yielding of

Downloaded 03 May 2010 to 171.66.16.244. Redistribution subject to ASME license or copyright; see http://www.asme.org/terms/Terms_Use.cfm

Materials based on Riemannian Geometry, I" *Oyo Rikigaku, (Journal of Japan Society of Applied Mechanics)*, Vol. 2, pp. 123–128.

Kondo, K., 1950, "On the Dislocation, the Group of Holonomy and the Theory of Yielding," *Oyo Rikigaku (Journal of Japan Society of Applied Mechanics)*, Vol. 3, pp. 107–110.

Mirsky, I., 1973, "Ventricular and Arterial Wall Stresses Based on Large Deformation Theories," *Biophysical Journal*, Vol. 13, pp. 1141–1159.

Omens, J. H., and Fung, Y. C., 1987, "Residual Stress in the Left Ventricle," *Advances in Bioengineering*, A. G. Erdman, ed., ASME, New York, pp. 37–38.

Parmley, W. W., and Talbot, L., 1979, *Heart as a Pump, Handbook of Physiology*, Sec. 2, Vol. 1, R. M. Berne, N. Sperelakis, and S. R. Geiger, eds., American Physiological Society, Bethesda, Md., pp. 429–460.

Sokolnikoff, I. S., 1964, *Tensor Analysis*, John Wiley and Sons, New York, pp. 89–91, 326–327.

Spotnitz, H. M., Sonnenblick, E. H., and Spiro, D., 1966, "Relation of Ultrastructure to Function in the Intact Heart: Sarcomere Structure Relative to Pressure Volume Curves of Intact Left Ventricle of Dog and Cat," *Circulation Research*, Vol. 18, pp. 49–66.

Takamizawa, K., and Hayashi, K., 1986, "Constitutive Law of the Arterial Wall and Stress Distribution," *Proceedings of International Conference on Computational Mechanics '86*, Vol. 1, G. Yagawa and S. N. Atluri, eds., Springer-Verlag, Tokyo, pp. iv–149–154.

Takamizawa, K., and Hayashi, K., 1987, "Strain Energy Density Function and Uniform Strain Hypothesis for Arterial Mechanics," *Journal of Biomechanics*, Vol. 20, pp. 7–17.

Takamizawa, K., and Hayashi, K., 1988, "Uniformm Strain Hypothesis and Thin-walled Theory in Arterial Mechanics," *Biorheology*, Vol. 25, pp. 555–565.

Truesdell, C., and Noll, W., 1965, "The Nonlinear Field Theories of Mechanics," *Encyclopedia of Physics*, Vol. III/3, S. Flügge, ed., pp. 51–52, 81–92. Springer-Verlag, Berlin, pp. 51–52, 81–92.

Vaishnav, R. N., and Vossoughi, J., 1987, "Residual Stress and Strain in Aortic Segments," *Journal of Biomechanics*, Vol. 20, pp. 235–239.

APPENDIX

The equilibrium condition was treated as the constraint imposed on the variational problem in the Results and Discussion Section. However, the equilibrium and boundary conditions can be also derived considering that the metric tensor H_{KL} and the infinitesimal displacement Ψ_K are independently variable functions in the variational problem $\delta\Sigma=0$, if we define Σ as follows

$$\Sigma = -\Xi\mathfrak{D} + \iiint_{\kappa(\mathfrak{B})} \hat{W}\sqrt{H}\, dX^1 dX X^2 dX^3 - \iint_{\partial\kappa(\mathfrak{B})} \tau^{KL}\, \Psi_L\, A_K\, dS, \tag{A1}$$

where Ξ is the Lagrangian multiplier for the constraint of equation (48), but Ψ_K are not Lagrangian multipliers in this formulation. $\hat{W}$ can be regarded as the sum of the strain energy density W and the energy increase by the infinitesimal displacement Ψ_K

$$\hat{W} = W + e_{KL}\frac{\partial W}{\partial \overset{*}{E}_{KL}}, \tag{A2}$$

where e_{KL} represents components of the linear strain tensor defined by

$$e_{KL} = \frac{1}{2}(\Psi_{K;L} + \Psi_{L;K}). \tag{A3}$$

The displacement Ψ_K and the strain e_{KL} might be nominal quantities not corresponding to any physical reality.

In the case of incompressible material, $\Xi\mathfrak{D}$ is replaced with

$$\iiint_{\kappa(\mathfrak{B})} (\Xi\sqrt{H} + \Pi\, G^{KL} e_{KL}\sqrt{G}) dX^1 dX^2 dX^3, \tag{A4}$$

where Ξ and Π denote undetermined functions of a position as Lagrange's multipliers for the constraints

$$\sqrt{H} = \sqrt{G},\ G^{KL} e_{KL} = e^K_K = 0. \tag{A5}$$

Downloaded 03 May 2010 to 171.66.16.244. Redistribution subject to ASME license or copyright; see http://www.asme.org/terms/Terms_Use.cfm

The Effect of Contact Generation on the Elastic Properties of a Granular Medium

Anthony L. Endres
Department of Geophysics and Astronomy,
University of British Columbia,
Vancouver, BC, Canada V6T 1W5

Previous models for the elastic properties of a granular medium have assumed that all grain contacts are established in its undeformed configuration. Experimental data for the change in elastic properties as a function of confining pressure cannot be explained by these models. Contact creation is cited as one possible cause for this discrepancy. In this paper a model for a granular material is derived that allows for the creation of grain contacts during hydrostatic compression. This formulation allows for the use of general contact microphysics and a general statistical distribution of gap widths at the near-contact points. Numerical results show that for very small values of the average near-contact gaps (approximately 1/1000 of a sphere radius), there can be significant effects occurring in the range of confining pressures between 10^6 to 10^7 Pa. The results of this contact generating model are consistent with published experimental measurements.

Introduction

The modeling of granular materials by means of sphere packings has been the subject of numerous papers. Many authors (Gassmann (1951), Duffy and Mindlin (1957), Deresiewicz (1958), White (1965), and Walton (1975)) employed regular packings (e.g., hexagonal close packing, cubic packing). Brandt (1955) presented the first formulation for the elastic behavior of random packings; however, only the overall volumetric changes and the effective bulk modulus of the medium were considered. More recently, Digby (1981) Walton (1987) have presented more comprehensive treatments for the mechanical behavior of random sphere packings. In all of these studies, it was assumed that grain contacts were established in the initial, undeformed state and that no new grain contacts were generated during the compression of the medium. Further, some specific form of contact microphysics was always assumed.

Experimental evidence has shown that these mathematical models do not adequately describe the observed elastic behavior of sphere packings. In all of the above models, the hydrostatic strain and the effective elastic moduli are shown to be dependent on the 2/3 and 1/3 power, respectively, of the hydrostatic confining pressure. This infers that the elastic wave velocities are related to confining pressure by essentially a 1/6 power law. Duffy and Mindlin (1957) presented experimental data for the elastic wave velocities of a face-centered cubic packing of spheres. These data showed that the predicted elastic wave velocity was significantly higher than the measured velocity, and did not have a 1/6 power dependence of confining pressure. Further, as the allowable variation in sphere radii increased, the deviation between predicted and experimental velocity also increased. Domenico (1977) measured the elastic wave velocities of the random packing of air-saturated glass beads under hydrostatic confining pressures between 2.7 and 34.4 MPa. A least-squares fit to the data inferred that both compressional and shear wave velocities have approximately a 1/4 power relationship with the confining pressure. Murphy (1982) measured the compressional and shear wave velocities of a random packing of glass beads under vacuum and hydrostatic confining pressures between 0.1 and 35 MPa. A 1/4 power relationship was observed at low confining pressures, and a 1/6 power relationship was exhibited at high confining pressures.

Murphy (1982) stated that the 1/4 power relationship can be explained by the generation of contacts due to the closing of near-contact gaps and used a simple two-layer model to illustrate this point. However, a general formulation for a random packing was not derived. In this paper expressions are derived for the overall stress-strain relationship and the effective moduli of a granular medium under hydrostatic compression, which permit the generation of grain contacts due to the closure of near-contact gaps. The mathematical formulation of Walton (1987) provides a basis which can be expanded to include the effect of contact generation caused by the closing of near-contact gaps as the hydrostatic pressure increases. Further, Walton (1987) considers two cases of contact microphysics (i.e., perfectly smooth and infinitely rough spheres). The formulation presented here generalizes these results by allowing the use of general contact microphysics.

Contributed by the Applied Mechanics Division of THE AMERICAN SOCIETY OF MECHANICAL ENGINEERS for publication in the JOURNAL OF APPLIED MECHANICS.

Discussion on this paper should be addressed to the Technical Editor, Leon M. Keer, The Technological Institute, Northwestern University, Evanston, IL 60208 and will be accepted until two months after final publication itself in the JOURNAL OF APPLIED MECHANICS. Manuscript received by the ASME Applied Mechanics Division, January 13, 1989; final revision, June 19, 1989.

Copyright © 1990 by ASME
Downloaded 03 May 2010 to 171.66.16.244. Redistribution subject to ASME license or copyright; see http://www.asme.org/terms/Terms_Use.cfm

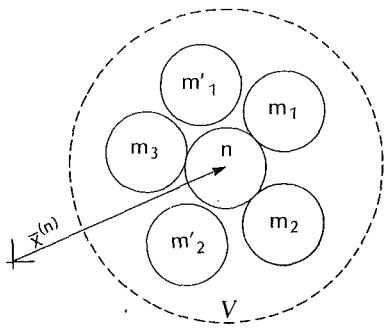


Fig. 1 Representative sphere in V (nth sphere), surrounded by neighboring spheres in contact (mth spheres) and near-contact (m'th spheres)

Undeformed Configuration

Consider a random packing of identical solid spheres of radius R. Each sphere is elastically isotropic and homogeneous with Lamé constants μ and λ. Let V be a volume within the packing containing N spheres and having dimensions which are very large compared to R. Within V, the random is assumed to be homogeneous.

Let $\mathbf{x}^{(n)}$ be the position of the center of the nth sphere relative to some given Cartesian coordinate system. The nth sphere is surrounded by neighboring spheres, some of which are in point contact with the nth sphere, while others are in near-contact, as in Fig. (1). In Fig. 2(a), the system of two spheres initially in point contact (in this case, the mth and nth spheres) is shown. Let the midpoint between sphere centers be denoted by O, with a position vector $\mathbf{x}^{(o)}$ given by

$$\mathbf{x}^{(o)} = \frac{1}{2}(\mathbf{x}^{(n)} + \mathbf{x}^{(m)}). \tag{1}$$

For this system, the inward unit vector along the line of the sphere centers, $\mathbf{i}^{(nm)}$, is defined by

$$\mathbf{i}^{(nm)} = (2R)^{-1}(\mathbf{x}^{(n)} - \mathbf{x}^{(m)}). \tag{2}$$

The system of two spheres in near-contact is illustrated in Fig. 2(b). In this case, let O' be the midpoint between the sphere centers, with a position vector $\mathbf{x}^{(o')}$ given by

$$\mathbf{x}^{(o')} = \frac{1}{2}(\mathbf{x}^{(n)} + \mathbf{x}^{(m')}). \tag{3}$$

Similarly, the inward unit vector along the line of the sphere centers, $\mathbf{i}^{(nm')}$, for this system is defined by

$$\mathbf{i}^{(nm')} = [2(R + g^{(nm')})]^{-1}(\mathbf{x}^{(n)} - \mathbf{x}^{(m')}), \tag{4}$$

where $2g^{(nm')}$ is the distance (or gap) between the surface of nth and m'th spheres along the line of the sphere centers.

Overall Stress-Strain Relationship

In order to derive the overall stress-strain relationship, consider an initial deformed state, obtained by subjecting the boundary of volume V to a displacement $\mathbf{u}$ consistent with a uniform, compressive hydrostatic strain $\epsilon\mathbf{I}$ (where $\mathbf{I}$ is the identity tensor). Hence, for a position vector $\mathbf{x}$ in V, the displacement at this point if V were a continuum is given by

$$\mathbf{u}(\mathbf{x}) = \epsilon\mathbf{I}\cdot\mathbf{x} = \epsilon\mathbf{x}. \tag{5}$$

It will be assumed that the sphere centers undergo a deformation which is consistent with this uniform strain and that all deformations are reversible. Then,

$$\mathbf{u}^{(n)} = \epsilon\mathbf{x}^{(n)} \tag{6}$$

defines the displacement of the nth sphere center. Similar expressions give the displacements for the centers of the mth and m'th sphere.

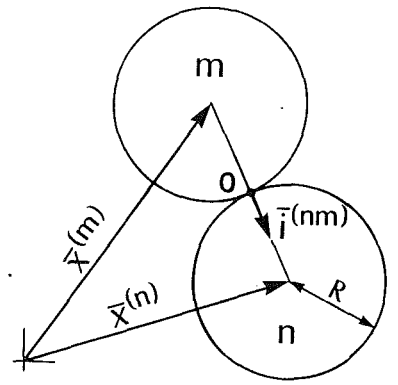


Fig. 2(a) The original point contact configuration

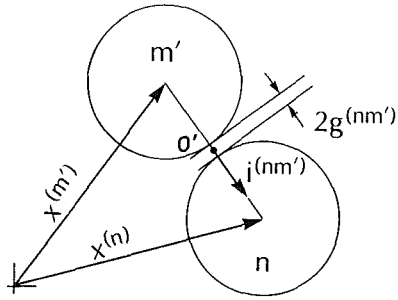


Fig. 2(b) The near-contact configuration

Consider the situation where two spheres are in point contact in the undeformed state. If $\Delta^{(no)}$ is the displacement of midpoint O with respect to the nth sphere center, then

$$\Delta^{(no)} = \frac{1}{2}(\mathbf{u}^{(m)} - \mathbf{u}^{(n)}) = -R\epsilon\mathbf{i}^{(nm)}. \tag{7}$$

As the hydrostatic strain increases, the contact area between spheres n and m becomes finite; and, a force, $\mathbf{F}^{(nm)}$, is exerted on the nth sphere due to its contact with the mth. Since the spheres are elastically isotropic and homogeneous, it can be assumed that $\mathbf{F}^{(nm)}$ is parallel to $\mathbf{i}^{(nm)}$. Hence,

$$\mathbf{F}^{(nm)} = F_N(\Phi^{(nm)})\mathbf{i}^{(nm)}, \tag{8}$$

where F_N is the magnitude of the normal component of $\mathbf{F}^{(nm)}$ and $\Phi^{(nm)}$ defines the state of the contact between the nth and mth spheres. Since all original contacts undergo identical deformations for a given hydrostatic strain ϵ, $\Phi^{(nm)} = \Phi$ for all these contacts.

For the spheres in near-contact, it is first necessary to establish a point contact before a force is exerted on the nth sphere. Since the relative displacement of one sphere center with respect to another is along the line of their centers, it can be shown that the point contact is obtained when

$$\|\Delta^{(no')}\| = g^{(nm')}, \tag{9}$$

where

$$\Delta^{(no')} = -(R + g^{(nm')})\epsilon\mathbf{i}^{(nm')}, \tag{10}$$

$\Delta^{(no')}$ being the displacement of the midpoint O' with respect to the nth sphere center. Once this occurs, a finite contact area will be established as the hydrostatic strain continues to increase; and, a force, $\mathbf{F}^{(nm')}$, is exerted on the nth sphere due to its contact with the m'th sphere. Given the previous assumptions, the force $\mathbf{F}^{(nm')}$ is given by

$$\begin{aligned}\mathbf{F}^{(nm')} &= F_N(\Phi^{(nm')})H(\|\Delta^{(no')}\| - g^{(nm')})\mathbf{i}^{(nm')} \\ &= F_N(\Phi^{(nm')})H(-(R + g^{(nm')})\epsilon - g^{(nm')})\mathbf{i}^{(nm')},\end{aligned} \tag{11}$$

where $\Phi^{(nm')}$ defines the state of the contact between spheres n and m', and H is the Heaviside step function.

Downloaded 03 May 2010 to 171.66.16.244. Redistribution subject to ASME license or copyright; see http://www.asme.org/terms/Terms_Use.cfm

Now that the forces on the nth sphere due to its contacts with its neighboring spheres are known, it is possible to relate the average stress within V to the average strain. The average stress, $\langle \sigma_{ij} \rangle$, within V is given by

$$\langle \sigma_{ij} \rangle = \frac{1}{V} \int_{\text{spheres}} \sigma_{ij} dV = \frac{1}{V} \sum_n \int_{V_n} \sigma_{ij}^{(n)} dV, \qquad (12)$$

where V_n is the volume of the nth sphere, $\sigma_{ij}^{(n)}$ are the components of the Cauchy stress within the nth sphere, and the summation is over all spheres in V. For the nth sphere, the stress within V_n can be related to the tractions on S_n, the surface of the nth sphere, in the following manner:

$$\int_{V_n} \sigma_{ij}^{(n)} dV = \frac{1}{2} \int_{S_n} (x_i' t_j^{(n)} + x_j' t_i^{(n)}) ds, \qquad (13)$$

where $\mathbf{t}^{(n)}$ is the traction on S_n and $\mathbf{x}' = \mathbf{x} - \mathbf{x}^{(n)}$ is the position of a point on S_n with respect to the center of the nth sphere. In general, it can be assumed that the contact areas will be small. This allows two simplifying assumptions. First, $\mathbf{x}'$ may be approximated by

$$\mathbf{x}' \approx \frac{1}{2} (\mathbf{x}^{(m)} - \mathbf{x}^{(n)}) = -R\mathbf{i}^{(nm)} \qquad (14)$$

for the original contacts and by

$$\mathbf{x}' \approx \frac{1}{2} \frac{R}{R + g^{(nm')}} (\mathbf{x}^{(m')} - \mathbf{x}^{(n)}) = -R\mathbf{i}^{(nm')} \qquad (15)$$

for the generated contacts. Secondly, the integration of the ith component of the traction over the contact surface is $F_i^{(nm)}$ for an original contact and $F_i^{(nm')}$ for the generated contacts.

Using these approximations, equation (13) becomes

$$\int_{V_n} \sigma_{ij}^{(n)} dV = \frac{-R}{2} \Big\{ \sum_m (i_i^{(nm)} F_j^{(nm)} + i_j^{(nm)} F_i^{(nm)}) + \sum_{m'} (i_i^{(nm')} F_j^{(nm')} + i_j^{(nm')} F_i^{(nm')}) \Big\}. \qquad (16)$$

In this expression, the first term of the right-hand side is the contribution of the original contacts and the second term represents the effect of created contacts. By using equation (16) in equation (12), and changing the summation from over the indices to over individual contacts, the following is obtained

$$\langle \sigma_{ij} \rangle = \frac{-R}{V} \Big\{ \sum_{\text{orig. cont.}} (i_i^{(nm)} F_j^{(nm)} + i_j^{(nm)} F_i^{(nm)}) + \sum_{\text{creat. cont.}} (i_i^{(nm')} F_j^{(nm')} + i_j^{(nm')} F_i^{(nm')}) \Big\}. \qquad (17)$$

The fact that the medium is undergoing hydrostatic compression is now introduced. This means

$$\langle \sigma_{ij} \rangle = -p\delta_{ij}, \qquad (18)$$

where p is the pressure applied to the surface of V and δ_{ij} is the Kronecker delta. By employing equations (8), (11), and (18), equation (17) becomes

$$p\delta_{ij} = \frac{2R}{V} \Big\{ \sum_{\text{orig. cont.}} F_N(\Phi) (i_i^{(nm)} i_j^{(nm)}) + \sum_{\text{creat. cont.}} F_N(\Phi^{(nm')}) H(-(R + g^{(nm')})\epsilon - g^{(nm')}) (i_i^{(nm')} i_j^{(nm')}) \Big\}. \qquad (19)$$

Since V contains a large number, N, of spheres, equation (19) can be expressed in terms of average values for the type of contact involved as follows:

$$p\delta_{ij} = \frac{RN}{V} \Big\{ \eta_o F_N(\Phi) \langle i_i^{(nm)} i_j^{(nm)} \rangle + \eta_c \langle F_N(\Phi^{(nm')}) H(-(R + g^{(nm')})\epsilon - g^{(nm')}) \rangle \langle i_i^{(nm')} i_j^{(nm')} \rangle \Big\}, \qquad (20)$$

where η_o and η_c are the average number of original contacts per sphere and the average number of near-contacts per sphere, respectively, and $<\ldots>$ represent average values taken over the contacts. Since it has been assumed that packing is statistically homogeneous and isotropic on the scale of the dimensions of V, then original and created contact points have a uniform probability distribution over a sphere surface. In this situation, Batchelor and O'Brien (1977) show that

$$\langle i_i^{(nm)} i_j^{(nm)} \rangle = \langle i_i^{(nm')} i_j^{(nm')} \rangle = \frac{1}{3} \delta_{ij}. \qquad (21)$$

Further, using

$$V = \frac{4\pi R^3 N}{3(1 - \phi)}, \qquad (22)$$

where ϕ is the porosity of the undeformed aggregate, equation (20) becomes

$$p = \frac{(1 - \phi)}{4\pi R^2} \{ \eta_o F_N(\Phi) + \eta_c \langle F_N(\Phi^{(nm')}) \times H(-(R + g^{(nm')})\epsilon - g^{(nm')}) \rangle \}. \qquad (23)$$

The average value of the normal force at the created contacts can be determined if the probability density function of $g^{(nm')}$, $f(g^{(nm')})$, is known. Since $g^{(nm')} \geq 0$ and the Heaviside step function is zero if

$$g^{(nm')} \geq -R\epsilon(1 + \epsilon)^{-1}, \qquad (24)$$

then equation (23) can be written as

$$p = \frac{(1 - \phi)}{4\pi R^2} \Big\{ \eta_o F_N(\Phi) + \eta_c \int_o^{-R\epsilon(1+\epsilon)^{-1}} F_N(\Phi^{(nm')}) f(g^{(nm')}) dg^{(nm')} \Big\}. \qquad (25)$$

In order to obtain the overall stress-strain relationship, the form of the contact microphysics must be defined. A specific example is considered in the following section on numerical results.

Effective Moduli

In order to determine the effective moduli of the granular medium, it is necessary to consider the effect of the application of an additional incremental deformation to the sphere packing after the initial hydrostatic deformation. Therefore, assume that the boundary of V is subjected to a further deformation $\delta\mathbf{u}$ which is consistent with a uniform strain tensor $\delta\mathbf{E}$. Then, the displacement of a point $\mathbf{x}$ in V, if it were in continuum, would be given by

$$\delta\mathbf{u}(x) = \delta\mathbf{E} \cdot \mathbf{x}, \text{ or } \delta u_i(\mathbf{x}) = \delta\epsilon_{ij} x_j. \qquad (26)$$

It will be assumed that this incremental deformation is small enough that effects of contact generation and destruction can be neglected, that the sphere centers undergo an incremental deformation which is consistent with a uniform incremental strain, and that all incremental deformations are reversible. Hence,

$$\delta\mathbf{u}^{(n)} = \delta\mathbf{E} \cdot \mathbf{x}^{(n)}, \text{ or } \delta u_i^{(n)} = \delta\epsilon_{ij} x_j^{(n)}. \qquad (27)$$

Downloaded 03 May 2010 to 171.66.16.244. Redistribution subject to ASME license or copyright; see http://www.asme.org/terms/Terms_Use.cfm

Given this as a starting point, then the incremental relative displacements of the midpoints O and O' with respect to the nth sphere center are given by

$$\delta\Delta^{(no)} = -R\delta\mathbf{E}\cdot\mathbf{i}^{(nm)} \tag{28}$$

and

$$\delta\Delta^{(no')} = -(R+g^{(nm')})\delta\mathbf{E}\cdot\mathbf{i}^{(nm')}. \tag{29}$$

Since the spheres are composed of homogeneous, isotropic material, it can be assumed that the incremental force at an original contact is given by

$$\delta\mathbf{F}^{(nm)} = \delta F_N(\Phi)\mathbf{i}^{(mn)} + \delta F_T(\Phi)\mathbf{j}^{(nm)}, \tag{30}$$

where

$$\mathbf{j}^{(nm)} = \frac{-R[\delta\mathbf{E}\cdot\mathbf{i}^{(nm)} - (\delta\epsilon_{kl}i_k{}^{(nm)}i_l{}^{(nm)})\mathbf{i}^{(nm)}]}{\|-R[\delta\mathbf{E}\cdot\mathbf{i}^{(nm)} - (\delta\epsilon_{kl}i_k{}^{(nm)}i_l{}^{(nm)})\mathbf{i}^{(nm)}]\|}. \tag{31}$$

Similarly, the incremental force at a created contact is

$$\delta\mathbf{F}^{(nm')} = \{\delta F_N(\Phi^{(nm')})\mathbf{i}^{(nm')} + \delta F_T(\Phi^{(nm')})\mathbf{j}^{(nm')}\} \times H(-(R+g^{(nm')})\epsilon - g^{(nm')}), \tag{32}$$

where

$$\mathbf{j}^{(nm')} = \frac{-(R+g^{(nm')})[\delta\mathbf{E}\cdot\mathbf{i}^{(nm')} - (\delta\epsilon_{kl}i_k{}^{(nm')}i_l{}^{(nm')})\mathbf{i}^{(nm')}]}{\|-(R+g^{(nm')})[\delta\mathbf{E}\cdot\mathbf{i}^{(nm')} - (\delta\epsilon_{kl}i_k{}^{(nm')}i_l{}^{(nm')})\mathbf{i}^{(nm')}]\|}, \tag{33}$$

and δF_N δF_T are the magnitude of the normal and tangential component of the incremental contact force $\delta\mathbf{F}$, respectively.

The concept of the contact stiffness is now introduced. Let D_N and D_T be the normal and tangential contact stiffness, respectively. Then,

$$D_N = \frac{dF_N}{dw}, \tag{34}$$

and

$$D_T = \frac{dF_T}{dr}, \tag{35}$$

where w is the magnitude of the normal component of the relative displacement of O or O' (i.e., parallel to $\mathbf{i}^{(nm)}$ or $\mathbf{i}^{(nm')}$) and r is the magnitude of the tangential component of the relative displacement of O or O' (i.e., perpendicular to $\mathbf{i}^{(nm)}$ or $\mathbf{i}^{(nm')}$). Since the incremental displacement is small, then

$$\delta F_N = D_N\delta w, \tag{36}$$

and

$$\delta F_T = D_T\,\delta r. \tag{37}$$

Hence, the contact forces can be rewritten as

$$\delta\mathbf{F}^{(nm)} = -R\{(D_N(\Phi) - D_T(\Phi))(\delta\epsilon_{kl}i_k{}^{(nm)}i_l{}^{(nm)})\mathbf{i}^{(nm)} + D_T(\Phi)\delta\mathbf{E}\cdot\mathbf{i}^{(nm)}\} \tag{38}$$

for the original contacts, and

$$\delta\mathbf{F}^{(nm')} = -(R+g^{(nm')})\{(D_N(\Phi^{(nm')}) - D_T(\Phi^{(nm')}))(\delta\epsilon_{kl}i_k{}^{(nm')}i_l{}^{(nm')})\mathbf{i}^{(nm')} + D_T(\Phi^{(nm')})\delta\mathbf{E}\cdot\mathbf{i}^{(nm')}\}H(-(R+g^{(nm')}\epsilon - g^{(nm')})) \tag{39}$$

for the created contacts.

Using the same procedure as was used to determine the relationship between pressure and hydrostatic strain, the following relationship is found between the average incremental stress, $\langle\delta\sigma_{ij}\rangle$, and the incremental average strain $\langle\delta\epsilon_{kl}\rangle$:

$$\langle\delta\sigma_{ij}\rangle \equiv \frac{3(1-\phi)}{8\pi R^2}\{\eta_o R[2(D_N(\Phi) - D_T(\Phi))\langle\delta\epsilon_{kl}\rangle\langle i_i{}^{(nm)}i_j{}^{(nm)}i_k{}^{(nm)}i_l{}^{(nm)}\rangle + D_T(\Phi)(\langle\delta\epsilon_{jk}\rangle\langle i_i{}^{(nm)}i_k{}^{(nm)}\rangle + \langle\delta\epsilon_{ik}\rangle\langle i_j{}^{(nm)}i_k{}^{(nm)}\rangle)] + \eta_c[2\langle(D_N(\Phi^{(nm')}) - D_T(\Phi^{(nm')}))(R+g^{(nm')}) \times H(-(R+g^{(nm')})\epsilon - g^{(nm')})\rangle\langle\delta\epsilon_{kl}\rangle\langle i_i{}^{(nm')}i_j{}^{(nm')}i_k{}^{(nm')}i_l{}^{(nm')}\rangle + \langle D_T(\Phi^{(nm')})(R+g^{(nm')})H(-(R+g^{(nm')})\epsilon - g^{(nm')})\rangle \times(\langle\delta\epsilon_{jk}\rangle\langle i_i{}^{(nm')}i_k{}^{(nm')}\rangle + \langle\delta\epsilon_{ik}\rangle\langle i_j{}^{(nm')}i_k{}^{(nm')}\rangle)]\}. \tag{40}$$

Since the initial deformation was hydrostatic, the homogeneous and isotropic nature of the random packing is retained during the incremental deformation. Hence, equation (21) and another result from Batchelor and O'Brien (1977),

$$\langle i_i{}^{(nm)}i_j{}^{(nm)}i_k{}^{(nm)}i_l{}^{(nm)}\rangle = \langle i_i{}^{(nm')}i_j{}^{(nm')}i_k{}^{(nm')}i_l{}^{(nm')}\rangle \equiv \frac{1}{15}(\delta_{ij}\delta_{kl} + \delta_{ik}\delta_{jl} + \delta_{il}\delta_{jk}) \tag{41}$$

may be used.

By inserting equations (21) and (41) into (40), the resulting expression can be compared with

$$\langle\delta\sigma_{ij}\rangle = C^*_{ijkl}\langle\delta\epsilon_{kl}\rangle, \tag{42}$$

where the effective moduli, C^*_{ijkl}, can be expressed in terms of the effective Lamé constants, μ^* and λ^*, as follows

$$C^*_{ijkl} = \lambda^*\delta_{ij}\delta_{kl} + \mu^*(\delta_{ik}\delta_{jk} + \delta_{il}\delta_{jk}). \tag{43}$$

Hence, it can be found that

$$\lambda^* = \frac{(1-\phi)}{20\pi}\left\{\frac{\eta_o}{R}(D_N(\Phi) - D_T(\Phi)) + \frac{\eta_c}{R^2}\langle(D_N(\Phi^{(nm')}) - D_T(\Phi^{(nm')}))H(-(R+g^{(nm')})\epsilon - g^{(nm')})\rangle\right\}, \tag{44}$$

and

$$\mu^* = \frac{(1-\phi)}{20\pi}\left\{\frac{\eta_o}{R}\left(D_N(\Phi) + \frac{3}{2}D_T(\Phi)\right) + \frac{\eta_c}{R^2} \times\langle(D_N(\Phi^{(nm')}) - D_T(\Phi^{(nm')})) \times H(-(R+g^{(nm')})\epsilon - g^{(nm')})\rangle\right\}. \tag{45}$$

Letting $f(g^{(nm')})$ again be the probability density function of $g^{(nm')}$, then, as was done previously, λ^* and μ^* can be written as

$$\lambda^* = \frac{(1-\phi)}{20\pi}\left\{\frac{\eta_o}{R}(D_N(\Phi) - D_T(\Phi)) + \frac{\eta_c}{R^2}\int_o^{-R\epsilon(1+\epsilon)^{-1}}\left(D_N(\Phi^{(nm')}) + \frac{3}{2}D_T(\Phi^{(nm')})\right) \times(R+g^{(nm')})f(g^{(nm')})dg^{(nm')}\right\}, \tag{46}$$

and

$$\mu^* = \frac{(1-\phi)}{20\pi}\left\{\frac{\eta_o}{R}\left(D_N(\Phi) + \frac{3}{2}D_T(\Phi)\right) + \frac{\eta_c}{R^2}\int_o^{-R\epsilon(1+\epsilon)^{-1}}\left(D_N(\Phi^{(nm')}) + \frac{3}{2}D_T(\Phi^{(nm')})\right) \times(R+g^{(nm')})f(g^{(nm')})dg^{(nm')}\right\}. \tag{47}$$

Downloaded 03 May 2010 to 171.66.16.244. Redistribution subject to ASME license or copyright; see http://www.asme.org/terms/Terms_Use.cfm

Numerical Results

From the foregoing analysis, it can be seen that the general elastic behavior of a contact generating granular medium is described by equations (25), (46), and (47). In order to obtain numerical results, it is necessary to define the nature of the contact microphysics and $f(g^{(nm')})$, the probability density function of $g^{(nm')}$, for the sphere packing.

The contact microphysics gives the form of the interaction between spheres in contact. Let us assume that spheres are infinitely rough (i.e., no slippage along the contact surfaces). Then, using the results of Walton (1978), the following expressions can be derived for the contact forces and contact stiffness:

$$F_N(\Phi) = \frac{4R^2(-\epsilon)^{3/2}}{3\pi B}, \tag{48}$$

$$F_N(\Phi^{(nm')}) = \frac{4R^{1/2}}{3\pi B}\,(-R\epsilon - g^{(nm')}(1+\epsilon))^{3/2}, \tag{49}$$

$$D_N(\Phi) = \frac{2R(-\epsilon)^{1/2}}{\pi B}, \tag{50}$$

$$D_T(\Phi) = \frac{4R(-\epsilon)^{1/2}}{\pi(2B+C)}, \tag{51}$$

$$D_N(\Phi^{(nm')}) = \frac{2[R(-g^{(nm')}(1+\epsilon) - R\epsilon)]^{1/2}}{\pi B}, \tag{52}$$

$$D_T(\Phi^{(nm')}) = \frac{4[R(-g^{(nm')}(1+\epsilon) - R\epsilon)]^{1/2}}{\pi(2B+C)}, \tag{53}$$

where

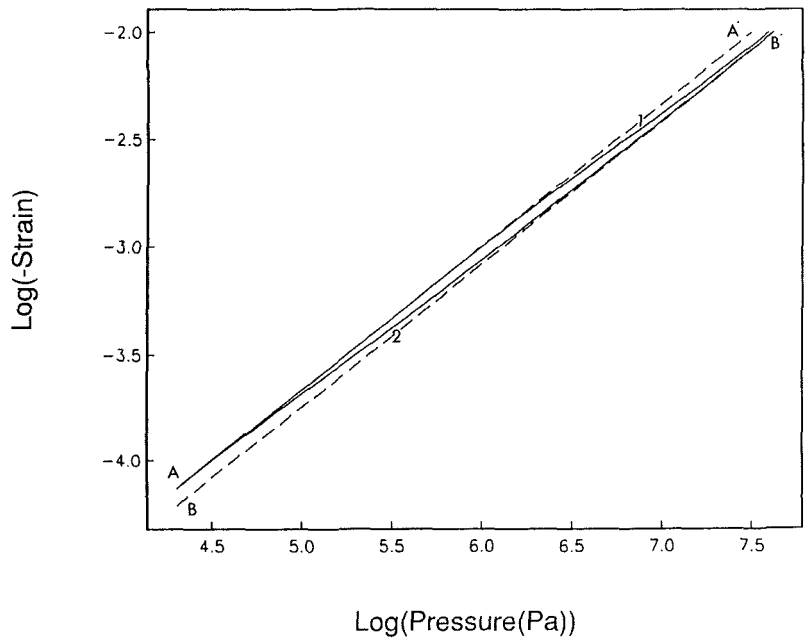


Fig. 3(a)

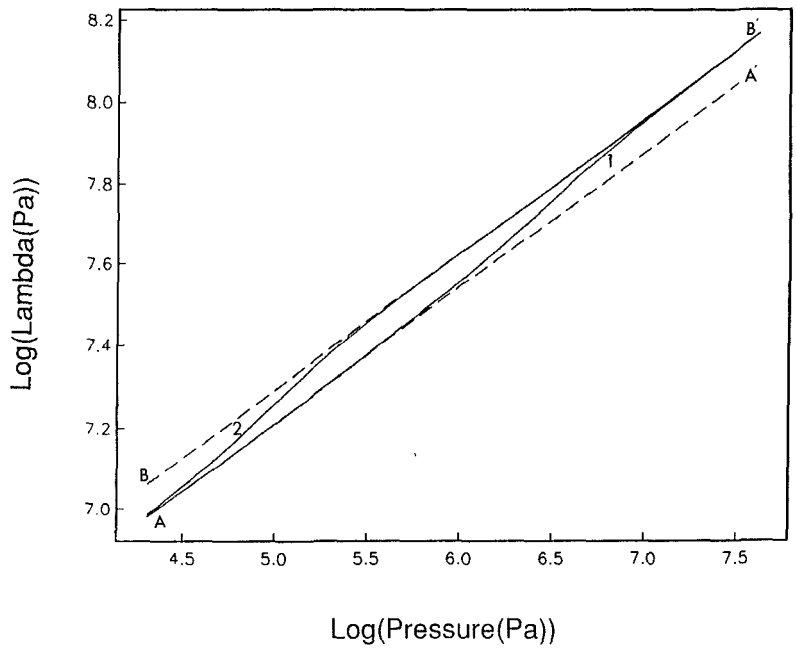


Fig. 3(b)

Downloaded 03 May 2010 to 171.66.16.244. Redistribution subject to ASME license or copyright; see http://www.asme.org/terms/Terms_Use.cfm

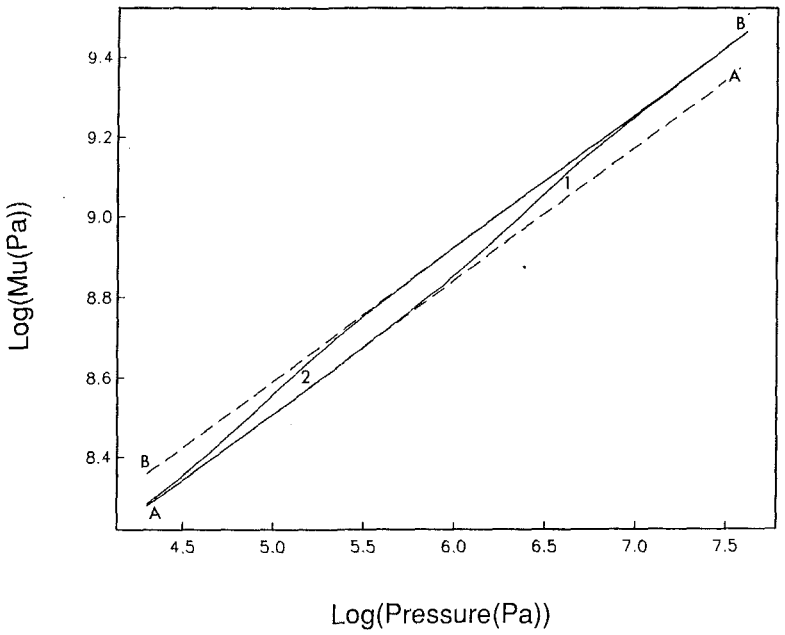


Fig. 3(c)

Fig. 3 Numerical results for contact generating model for cases: (1)$\alpha = 0.001$ R and (2) $\alpha = 0.0001$ R, dashed lines are Walton (1987) model for $\eta = \eta_o$ (line A – A′) and $\eta = \eta_o + \eta_c$ (line B – B′); (a) log $(-\epsilon)$ as a function of log (p), (b) log (λ^*) as a function of log (p), (c) log (μ^*) as a function of log (p).

$$B = \frac{1}{4\pi}\left\{\frac{1}{\mu} + \frac{1}{\mu+\lambda}\right\}, \tag{54}$$

$$C = \frac{1}{4\pi}\left\{\frac{1}{\mu} - \frac{1}{\lambda+\mu}\right\}. \tag{55}$$

The nature of the probability density function, $f(g^{(nm')})$, has not been established. However, given the nature of the problem, it is plausible that $g^{(nm')}$ has a Maxwell distribution. Hence, $f(g^{(nm')})$ is given by (Papoulis (1965)):

$$f(g^{(nm')}) = \frac{2^{1/2}}{\alpha^3\pi^{1/2}}\,(g^{(nm')})^2 \times \exp[-(g^{(nm')})^2(2\alpha^2)^{-1}]H(g^{(nm')}). \tag{56}$$

The maximum of $f(g^{(nm')})$ occurs at $\alpha\cdot 2^{1/2}$ and has a value of $2^{3/2}\,(\alpha e\pi^{1/2})^{-1}$. By using equations (48) through (53), and (56), the following expressions can be derived for the confining pressure p and the effective moduli λ^* and μ^*:

$$p = \frac{(1-\phi)(-\epsilon)^{3/2}}{3\pi^2 B}\left\{\eta_o + \eta_c \frac{2^{1/2}}{\alpha^3\pi^{1/2}}\left(\frac{-R\epsilon}{1+\epsilon}\right)^3 \int_o^1 (1-x)^{3/2}x^2\exp(-\beta x^2)dx\right\}, \tag{57}$$

$$\lambda^* = \frac{(1-\phi)C(-\epsilon)^{1/2}}{10\pi^2 B(2B+C)}\left\{\eta_o + \eta_c \frac{2^{1/2}}{\alpha^3\pi^{1/2}}\left(\frac{-R\epsilon}{1+\epsilon}\right)^3 \times \left[\int_o^1 (1-x)^{1/2}x^2\exp(-\beta x^2)dx + \left(\frac{-\epsilon}{1+\epsilon}\right)\int_o^1 (1-x)^{1/2}x^3\exp(-\beta x^2)dx\right]\right\}, \tag{58}$$

$$\mu^* = \frac{(1-\phi)(5B+C)(-\epsilon)^{1/2}}{10\pi^2 B(2B+C)}\left\{\eta_o + \eta_c \frac{2^{1/2}}{\alpha^3\pi^{1/2}}\left(\frac{-R\epsilon}{1+\epsilon}\right)^3 \times \left[\int_o^1 (1-x)^{1/2}x^2\exp(-\beta x^2)dx + \left(\frac{-\epsilon}{1+\epsilon}\right)\int_o^1 (1-x)^{1/2}x^3\exp(-\beta x^2)dx\right]\right\}, \tag{59}$$

where

$$\beta = (2\alpha^2)^{-1}\left(\frac{-R\epsilon}{1+\epsilon}\right)^2. \tag{60}$$

Table 1 Parameters used in numerical results

λ	2.1474×10^{10} Pa
μ	2.9655×10^{10} Pa
R	4.064×10^{-5} m
ϕ	0.383
η_o	6.4
η_c	2.1

The integrals in equations (57)–(59) can be shown to reduce to generalized hypergeometric functions (Gradshteyn and Ryzhik (1965)). However, to evaluate these expressions, it is much more practical to perform a numerical integration.

Table 1 gives the values of parameters used in evaluating equations (57)–(59). These values are typical of those used for dense packings of glass beads in Domenico (1977) and Murphy (1982). Values for η_o and η_c were obtained from Bernal and Mason (1960). Figures 3(*a*), 3(*b*), and 3(*c*) illustrate log $(-\epsilon)$, log (λ^*), and log (μ^*) as functions of log (p), respectively. In each case, $\alpha = 0.001$R and 0.0001R were used. In addition, the results for the model of Walton (1987) are also shown for two cases: the number of contacts $\eta = \eta_o + \eta_c$ and $\eta = \eta_o$.

In each case, the model of Walton (1987) gives linear relationships in terms of log (p), corresponding to the 2/3 power law for $(-\epsilon)$ and the 1/3 power law for the effective moduli

Downloaded 03 May 2010 to 171.66.16.244. Redistribution subject to ASME license or copyright; see http://www.asme.org/terms/Terms_Use.cfm

λ^* and μ^*. From Figs. 3(*a*)-3(*c*), it can be seen that three distinct regions exist in the response of the contact generating model. At low pressures, the contact generating model asymptotically approaches Walton's model for $\eta = \eta_o$ as p decreases. At high pressures, the contact generating model asymptotically approaches the completely contacted model, $\eta = \eta_o + \eta_c$, as p increases. Between the two, a transition zone exists. The onset of the transition zone as pressure increases is related to the mean value $g^{(nm')}$ (i.e., once a significant portion of the possible contacts are established, the transition begins). This behavior of the transition is independent of the choice of the probability density function, as it is a general response of the sphere packing due to contact generation.

If an attempt were made to describe the response of the model in the transition zone by means of a power-law relationship, Figs. 3(*b*) and 3(*c*) show that the effective exponent would be greater than 1/3 for the relationship between the effective moduli and the confining pressure. Hence, the effective power law between confining pressure and elastic wave velocities would have an exponent greater than 1/6. This is consistent with the experimental results of Domenico (1977) and Murphy (1982).

Conclusions

In this paper, a model for the elastic behavior of a granular medium which allows the generation of grain contacts during hydrostatic compression is presented. The form of this model permits the use of a variety of contact microphysics and statistical distributions for the gap width of the near-contact. Numerical results for this model display significant differences in comparison with models that assume no contact generation, particularly in the transition region. Further, it can be observed that this transition zone will occur over the range of confining pressures of interest in geological and geophysical problems ($10^6 - 10^7$ Pa) for values of α small in comparison to the sphere radius. This means that extremely small near-contact gaps can have a significant effect on the elastic behavior of a granular medium. The behavior of the contact generating model is consistent with experimental results for random packings of glass beads.

References

Batchelor, G. K., and O'Brien, R. W., 1977, "Thermal or Electrical Conduction through a Granular Material," *Proc. R. Soc. Lond.*, Vol. A355, pp. 313-333.

Bernal, J. D., and Mason, J., 1960, "Co-ordination of Randomly Packed Spheres," *Nature*, Vol. 188, pp. 910-911.

Brandt, H., 1955, "A Study of the Speed of Sound in a Porous Granular Media," ASME JOURNAL OF APPLIED MECHANICS, Vol. 22, pp. 479-486.

Deresiewicz, H., 1958, "Stress-Strain Relations for a Simple Model of a Granular Medium," ASME JOURNAL OF APPLIED MECHANICS, Vol. 25, pp. 402-405.

Digby, P. J., 1981, "The Effective Elastic Moduli of Porous Granular Rocks," ASME JOURNAL OF APPLIED MECHANICS, Vol. 48, pp. 803-808.

Domenico, S. N., 1977, "Elastic Properties of Unconsolidated Porous Sand Reservoirs," *Geophysics*, Vol. 42, pp. 1339-1368.

Duffy, J., and Mindlin, R. D., 1957, "Stress-Strain Relations of a Granular Medium," ASME JOURNAL OF APPLIED MECHANICS, Vol. 24, pp. 585-593.

Gassmann, F., 1951, "Elastic Waves through a Packing of Spheres," *Geophysics*, Vol. 16, pp. 673-685.

Gradshteyn, I. S., and Ryzhik, I. M., 1965, *Table of Integrals, Series, and Products*, Academic Press Inc., New York.

Murphy, W. F., 1982, "Effects of Microstructure and Pore Fluids on Granular Sedimentary Materials," Ph.D. dissertation, Stanford University, Palo Alto, Calif.

Papoulis, A., 1965, *Probability, Random Variables, and Stochastic Process*, McGraw-Hill, New York.

Walton, K., 1975, "The Effective Elastic Moduli of Model Sediments," *Geophys. J. R. Astro. Soc.*, Vol. 43, pp. 293-306.

Walton, K., 1978, "The Oblique Compression of Two Elastic Spheres," *J. Mech. Phys. Solids*, Vol. 26, pp. 139-150.

Walton, K., 1987, "The Effective Elastic Moduli of a Ramdom Packing of Spheres," *J. Mech. Phys. Solids*, Vol. 35, pp. 213-226.

White, J. E., 1965, *Seismic Waves: Radiation, Transmission and Attenuation*, McGraw-Hill, New York.

Downloaded 03 May 2010 to 171.66.16.244. Redistribution subject to ASME license or copyright; see http://www.asme.org/terms/Terms_Use.cfm

A Method for Identifying Parameters of Mechanical Joints

J. Wang
Research Assistant.

P. Sas
Professor and NFWO Research Associate.

Department of Mechanical Engineering,
Katholieke Universiteit Leuven
B-3030 Heverlee, Belgium

A method for identifying the physical parameters of joints in mechanical systems is presented. In the method, a multi-d.o.f. (degree-of-freedom) system is transformed into several single d.o.f. systems using selected eigenvectors. With the result from modal testing, each single d.o.f. system is used to solve for a pair of unknown physical parameters. For complicated cases where the exact eigenvector cannot be obtained, it will be proven that a particular physical parameter has a stationary value in the neighborhood of an eigenvector. Therefore, a good approximation for a joint physical parameter can be obtained by using an approximate eigenvector and the exact value for the joint parameters can be reached by carrying out this process in an iterative way.

1 Introduction

When conducting structural dynamic analysis such as the FEM (finite element method), one is required to know the physical characteristics (inertial, stiffness, and damping properties) of the analyzed systems. For some special mechanical parts (e.g., joints or connections), it is hardly possible to derive the associated physical parameters from the material data, in such cases the experimental identification of these parameters is necessary.

Conventional methods to determine these parameters, proposed by Levina (1965), Dolbey (1971), and Thornley (1984), consist of isolating the joints from the system and testing it with static load or sinusoidal excitation. However, often these joints cannot be separated from the system in which they are incorporated. Furthermore, if some joints could be separated, it is difficult to install them into a test structure without any additional joint. On the other hand, the physical characteristics of a joint are nonlinear and dependent upon different conditions such as preload, surface mating position, external load condition, temperature, and other conditions, so that the characteristics determined in a test environment normally cannot be applied in another environment. Yoshimura (1977) developed an iteration method to identify the stiffness and damping parameters of joints by comparing the theoretical simulation and experiment results of resonance frequencies and damping ratios. Zhou et al. (1986) identified the joint parameters through a least-square fit of measured and calculated frequency response functions. But, the identified joint parameters are limited to a few d.o.f.'s and the processes require much computational effort.

This paper addresses a method for experimentally determining the physical characteristics of joints in systems. In this approach, a multi-d.o.f. system will be converted to several single d.o.f. systems by imposing selected eigenvectors on it. Such a single d.o.f. system is recognized as an alternative form of the Rayleigh's quotient and is represented by both physical parameters of the original system and modal parameters of the selected mode. With measured modal parameters (resonance frequency and damping ratio), and assuming that the physical characteristics of the structure are known except those related the joint, one single d.o.f. system can be used to solve for one or one pair of physical parameters of the joint. Consequently, the total physical characteristics of the joint can be solved.

To explain the principle of the method, a simple free-free system consisting of two mass blocks joined by an unknown elastic element is treated. This system has a practical significance and can be used to characterize joints which can be isolated from the incorporated system as will be illustrated by an example. Finally, the method will be extended and applied to more complicated systems where the characterized joint cannot be separated from it, or must be kept in that condition. In this case, the solutions will no longer be "exact." However, using the stationary property of a Rayleigh's quotient, it will be proven that, with an approximate eigenvector, the solution is a good approximation, and when solved in an iterative way, it will converge quickly toward the "exact" values.

Two examples are given at the end of this paper. The first one illustrates the characterization of a rubber vibration isolator connection with the two mass-blocks system. The second one shows the application of the method in an iterative way for the characterization of bolted joints which connect two rectangular cross-section beams in particular conditions.

2 Two-Mass-Block System

For actual mechanical systems, the two-mass-block system, as shown in Fig. 1, is the simplest free-free vibration system. But, to completely describe its three-dimensional motion, 12 d.o.f.'s are required. They are

Contributed by the Applied Mechanics Division of THE AMERICAN SOCIETY OF MECHANICAL ENGINEERS for publication in the JOURNAL OF APPLIED MECHANICS.

Discussion on this paper should be addressed to the Technical Editor, Leon M. Keer, The Technological Institute, Northwestern University, Evanston, IL 60208, and will be accepted until two months after final publication of the paper itself in the JOURNAL OF APPLIED MECHANICS. Manuscript received by the ASME Applied Mechanics Division, November 3, 1988; final revision, June 28, 1989.

Copyright © 1990 by ASME
Downloaded 03 May 2010 to 171.66.16.244. Redistribution subject to ASME license or copyright; see http://www.asme.org/terms/Terms_Use.cfm

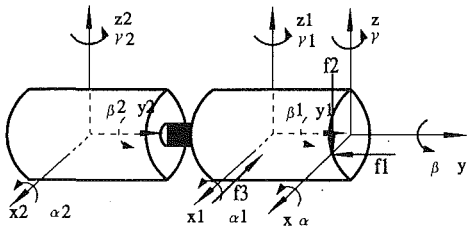


Fig. 1 Two-mass-block and elastic element system

$$(x_1,y_1,z_1,\alpha_1,\beta_1,\gamma_1,x_2,y_2,z_2,\alpha_2,\beta_2,\beta_2)^t$$

and are shown in Fig. 1. However, depending on the direction of the excitation force, the d.o.f.'s for describing the motion of the system can be reduced to a subset of the total 12 d.o.f.'s. For example, when an excitation force acts in the xy-plane, the number of the d.o.f.'s is reduced to six, $(x_1,y_1,\gamma_1,x_2,y_2,\gamma_2)^t$, because the d.o.f.'s out of the xy-plane really have no relation with the excitation force. Furthermore, if the excitation force is parallel to the y-axis in the xy-plane, the number of system d.o.f.'s reduces to 4, $(y_1,\gamma_1,y_2,\gamma_2)^t$.

Consider the free vibration of the situation with 4 active d.o.f.'s. In this case, the cross-terms between the translational d.o.f., y, and rotational d.o.f., γ, in the system matrices (mass, stiffness, and damping matrix) may be omitted by assuming that the length of the joint element is relatively short. The equations of motion for the free vibration of the system are written as

$$\begin{bmatrix} \mathbf{m} & \mathbf{0} \\ \mathbf{0} & \mathbf{J}_\gamma \end{bmatrix} \begin{Bmatrix} \ddot{\mathbf{y}} \\ \ddot{\boldsymbol{\gamma}} \end{Bmatrix} + \begin{bmatrix} \mathbf{c}_y & \mathbf{0} \\ \mathbf{0} & \mathbf{c}_\gamma \end{bmatrix} \begin{Bmatrix} \dot{\mathbf{y}} \\ \dot{\boldsymbol{\gamma}} \end{Bmatrix} + \begin{bmatrix} \mathbf{k}_y & \mathbf{0} \\ \mathbf{0} & \mathbf{k}_\gamma \end{bmatrix} \begin{Bmatrix} \mathbf{y} \\ \boldsymbol{\gamma} \end{Bmatrix} = \mathbf{0} \tag{1}$$

where

$$\mathbf{m} = \begin{bmatrix} m_1 & 0 \\ 0 & m_2 \end{bmatrix}; \quad \mathbf{J}_\gamma = \begin{bmatrix} J_{\gamma 1} & 0 \\ 0 & J_{\gamma 2} \end{bmatrix};$$

$$\mathbf{c}_y = \begin{bmatrix} c_y & -c_y \\ -c_y & c_y \end{bmatrix}; \quad \mathbf{c}_\gamma = \begin{bmatrix} c_\gamma & -c_\gamma \\ -c_\gamma & c_\gamma \end{bmatrix};$$

$$\mathbf{k}j_y = \begin{bmatrix} k_y & -k_y \\ -k_y & k_y \end{bmatrix}; \quad \mathbf{k}_\gamma = \begin{bmatrix} k_\gamma & -k_\gamma \\ -k_\gamma & k_\gamma \end{bmatrix};$$

$$\mathbf{y} = \begin{Bmatrix} y_1 \\ y_2 \end{Bmatrix}; \quad \boldsymbol{\gamma} = \begin{Bmatrix} \gamma_1 \\ \gamma_2 \end{Bmatrix}.$$

Equation (1) can be split into two

$$\mathbf{m}\ddot{\mathbf{y}} + \mathbf{c}_y\dot{\mathbf{y}} + \mathbf{k}_y\mathbf{y} = 0 \tag{2}$$

$$J_\gamma\ddot{\boldsymbol{\gamma}} + \mathbf{c}_\gamma\dot{\boldsymbol{\gamma}} + \mathbf{k}_\gamma\boldsymbol{\gamma} = 0. \tag{3}$$

Now, let us consider the undamped case of equation (2) and solve the eigenvalue problem

$$\omega_y^2\mathbf{m}\boldsymbol{\psi} + \mathbf{k}_y\boldsymbol{\psi} = 0. \tag{4}$$

We obtain two modes: a rigid body mode with a zero eigenfrequency and an eigenvector $(1, 1)^t$, and a normal mode (call it mode y) with an eigenfrequency ω_{ny} and eigenvector $\boldsymbol{\psi}_y = (1, m_1/m_2)^t$. For characterizing the connection (the elastic element), the rigid body mode can be ignored since the sensitivities for the mode, with respect to the parameters of the connection are always zero. With the proportional damping assumption ($\mathbf{C} = \alpha\mathbf{M} + \beta\mathbf{K}$) and $y = \boldsymbol{\psi}_y q$, and premultiplying equation (2) by $\boldsymbol{\psi}_y^t$, the equation becomes a single d.o.f. one and the corresponding eigenproblem can be written as

$$(\omega_y^2 m_{yy} + j\omega_y c_{yy} + k_{yy})q = 0 \tag{5}$$

where $m_{yy} = \boldsymbol{\psi}_y^t\mathbf{m}\boldsymbol{\psi}_y$; $c_{yy} = \boldsymbol{\psi}_y^t\mathbf{c}_y\boldsymbol{\psi}_y$; $k_{yy} = \boldsymbol{\psi}_y^t\mathbf{k}_y\boldsymbol{\psi}_y$ are, respectively, the modal mass, damping, and stiffness of mode y. This leads to the eigenfrequency

$$\omega_{ny} = \sqrt{(k_{yy}/m_{yy})} \tag{6}$$

and damping ratio

$$\zeta_y = \frac{c_{yy}}{2m_{yy}\omega_{ny}}. \tag{7}$$

In fact, equation (5) is an alternative form of the Rayleigh's quotient which contains both physical and modal parameters of the system. Hence, a pair of unknown physical parameters can be solved for with the real and imaginary part of the quotient.

In the case of characterizing the elastic element joining the two masses, the inertial properties of the two masses ($m1$ and $m2$) can be measured, and the eigenfrequency ω_{ny} and damping ratio ζ_y can be obtained from modal testing with different excitation configurations. With those, the term k_{yy} and c_{yy} are calculated, and hence the stiffness k_y and viscous damping c_y of the joint elastic element can be calculated by the following equations:

$$k_y = \frac{k_{yy}}{(\psi_{y1} - \psi_{y1})^2} = \omega_{ny}^2\frac{m_1 m_2}{m_1 + m_2} \tag{8}$$

$$c_y = \frac{c_{yy}}{(\psi_{y1} - \psi_{y1})^2} = 2\zeta_y\omega_{ny}\frac{m_1 m_2}{m_1 + m_2}. \tag{9}$$

Equation (5) is an alternative form of the Rayleigh's quotient. A Rayleigh's quotient is said to be stationary if the applied constant λ and vector ψ are the exact eigenvalue and eigenvector of a mode of the system. In this case, the Rayleigh's quotient for equation (5) is stationary because ω_{ny}, ζ_y, and $\boldsymbol{\psi}_y$ belong to the exact eigenvalue and eigenvector of the original system. Hence, the resulting k_y and c_y are exact for the system.

In the experimental identification, the accuracy of the identified k_y and c_y is dependent on that of experimental results ω_{ny} and ζ_y (k_y only depends on ω_{ny} while c_y depends on both of ω_{ny} and ζ_y). With respect to experimental modal analysis, the measured resonance frequencies are much more accurate than the measured damping ratios. Hence, k_y will be much more accurate than c_y.

Applying the same procedure to equation (3), expressions for calculating the stiffness k_γ and the damping c_γ of the elastic element in the direction around the natural axis parallel to the z axis can be derived. The formulas are similar to equation (8) and (9), provided that m_1 and m_2 are replaced by $J_{\gamma 1}$ and $J_{\gamma 2}$. Applying the procedure in the other planes, the stiffness and damping of the elastic element in the associated directions can be obtained.

3 Systems With Large Number of d.o.f.'s

The approach presented previously can be directly extended to more complicated cases where the system matrices in the final form have many d.o.f.'s instead of only two. Similar to equation (8) and (9), the stiffness and damping parameter between d.o.f. i and j, k_{ij}, and c_{ij}, can be calculated using the following equations if the corresponding Rayleigh's quotient is stationary, i.e., the exact $\boldsymbol{\psi}_r$, ω_{nr}, and ζ_r are known and the modal stiffness and damping, k_{rr} and c_{rr}, can be calculated.

Downloaded 03 May 2010 to 171.66.16.244. Redistribution subject to ASME license or copyright; see http://www.asme.org/terms/Terms_Use.cfm

$$k_{ij} = \frac{k_{rr} - \psi_r^t \mathbf{K}_o \psi_r}{(\psi_{ri} - \psi_{rj})^2} \tag{10}$$

$$c_{ij} = \frac{c_{rr} - \psi_r^t \mathbf{C}_o \psi_r}{(\psi_{ri} - \psi_{rj})^2} \tag{11}$$

where $\mathbf{K}_o$ and $\mathbf{C}_o$ are, respectively, the stiffness and damping matrix of the system with empty entries at the coordinates *ii*, *jj*, *ij*, and *ji*.

When stiffness parameters between several pairs of d.o.f. (several k_{ij}'s) have to be identified, the same procedure can be followed, i.e., one mode solves for one parameter, if it is possible to find the modes with eigenvectors where the relative modal displacement is active for one pair of d.o.f. and zero or negligible for the rest. In the cases where such modes cannot be found (i.e., the relative modal displacements are active in those pairs of d.o.f. for every mode), a set of simultaneous equations has to be set up and solved for the unknown joint stiffness parameters. This will be beyond the scope of this paper and will not be discussed here.

But, in practice, it is impossible for such complicated cases to obtain an eigenvector in function of the known physical parameters as in the case of the eigenvalue problem of equation (4). Neither, a full exact eigenvector can be obtained from both experiment and analysis. This is due to the fact that an experimental eigenvector is subjected to measurement errors and incompleteness, while an exact analytical eigenvector is not available because of the uncertainty of the identified parameters. However, a good approximate solution can be obtained by using an alternative eigenvector. An alternative eigenvector actually is a vector which has the same dimension as, and closely resembles, the exact eigenvector. It can be obtained from the eigensolution of an alternative system which differs from the original system only in the identified parameters or from a measured normal modal vector with interpolation at unmeasured d.o.f.'s. Furthermore, the "exact" solution can be reached when the approach is carried out in an iterative way, i.e., by rendering the corresponding Rayleigh's quotient stationary.

The idea behind this approach is enlightened by the theory of the stationary value for a Rayleigh's quotient (Meirovitch, 1980) which states that the Rayleigh's quotient has a stationary value in the neighborhood of an eigenvector such that for a vector with the same dimension and closely resembling the eigenvector, the stationary value is the eigenvalue associated with that eigenvector. In an alternative way, it can be proven that a particular parameter in the system matrices (for example, the stiffness k between d.o.f. i and j) has a stationary value in the neighborhood of an particular eigenvector. It is essential for using the approach to obtain a good approximate solution of the particular parameter when using an alternative eigenvector, or the "exact" solution if it is carried out in an iterative way.

Suppose that an n-d.o.f. system has a mass matrix $\mathbf{M}$ and a stiffness matrix $\mathbf{K}$

$$\mathbf{M}\ddot{\mathbf{q}} + \mathbf{K}\mathbf{q} = 0. \tag{12}$$

Its rth eigenvalue λ_r and the associated eigenvector ψ_r satisfy equation (13), a stationary Rayleigh's quotient.

$$\lambda_r m_{rr} + k_{rr} = 0 \tag{13}$$

where $m_{rr} = \psi_r^t \mathbf{M} \psi_r$ and $k_{rr} = \psi_r^t \mathbf{K} \psi_r$.

Suppose that a stiffness parameter in $\mathbf{K}$ has to be identified and an alternative eigenvector ψ_a, which closely resembles ψ_r, is used for the identification. To carry out the identification, ψ_r is replaced by ψ_a in the equation (13). In this case, the Rayleigh's quotient with ψ_a similar to equation (13) is no longer stationary. The equation for the Rayleigh's quotient must be compensated with an error term, denoted as $\Delta\mathbf{K}$, as in the following equation:

$$\lambda_r \psi_a^t \mathbf{M} \psi_a + \psi_a^t \mathbf{K} \psi_a + \psi_a^t \Delta\mathbf{K} \psi_a = 0. \tag{14}$$

$\Delta\mathbf{K} = \mathbf{K}_a - \mathbf{K}$ where $\mathbf{K}_a$ is the approximate solution of $\mathbf{K}$. The eigenvectors resulting from equation (12) form an n-dimension linear vector space and the vector ψ_a can be written as the linear combination of the eigenvectors.

$$\psi_a = \sum_{l=1}^{n} a_1 \psi_1 \tag{15}$$

Substitute equation (15) into equation (14):

$$\lambda_r \sum_{l=1}^{n} a_l^2 m_{ll} + \sum_{l=1}^{n} a_l^2 k_{ll} + \sum_{l=1}^{n} a_l \psi_l^t (\Delta\mathbf{K}) \sum_{l=1}^{n} a_l \psi_l = 0 \tag{16}$$

where $m_{ll} = \psi_l^t \mathbf{M} \psi_l$ and $k_{ll} = \psi_l^t \mathbf{K} \psi_l$.

Divide equation (16) by a_r^2. Meanwhile, remember that the vector ψ_a resembles the vector ψ_r closely. This implies that $|a_r| >> |a_l|$ $(l = 1, \ldots, n;\ l \neq r)$. Introduce the notation $\epsilon_l = a_l / a_r$ $(l = 1, \ldots, n;\ l \neq r)$, equation (16) becomes

$$\sum_{\substack{l=1 \\ l \neq r}}^{n} \epsilon_l^2 m_{ll} (\lambda_r - \lambda_l) + \sum_{l=1}^{n} \epsilon_l \psi_l^t (\Delta\mathbf{K}) \sum_{l=1}^{n} \epsilon_l \psi_l = 0. \tag{17}$$

When the identified stiffness parameter is related to the stiffness between d.o.f. i and j, the matrix $\Delta\mathbf{K}$ only has nonzero elements Δk at the position *ii* and *jj* and $-\Delta k$ at *ij* and *ji*. Equation (17) becomes

$$\sum_{\substack{l=1 \\ l \neq r}}^{n} \epsilon_l^2 m_{ll} (\lambda_r - \lambda_l) + \Delta k [(\psi_{ri} - \psi_{rj}) + \sum_{\substack{l=1 \\ l \neq r}}^{n} \epsilon_l (\psi_{ri} - \psi_{rj})]^2 = 0. \tag{18}$$

Equation (18) can be written in the form

$$\Delta k = \frac{0(\epsilon^2)}{[(\psi_{ri} - \psi_{rj}) + 0(\epsilon)]^2} = \frac{0'(\epsilon^2)}{(\psi_{ai} - \psi_{aj})^2} \tag{19}$$

where $0(\epsilon^2)$ and $0(\epsilon)$ are, respectively, the summation of the terms with a small second order and first order form. From equation (19), it can be seen that when ψ_a tends to ψ_r with a small first order deviation in ϵ_1, $(\psi_a - \psi_r) \to \mathbf{0}(\epsilon)$, and if $(\psi_{ai} - \psi_{aj}) \neq 0$, Δk tends to zero with a small second order deviation in ϵ_1, $\Delta k \to 0(\epsilon_2)$. Similarly, it can be proven that Δm at location i tends to zero with a small second order deviation in ϵ_1 if $\psi_{ai} \neq 0$.

Now the conclusion can be made that a particular parameter (k between d.o.f. i and j or m at location i) in the system matrices has a stationary value in the neighborhood of an eigenvector where the elements of alternative eigenvectors satisfy $\psi_{ai} - \psi_{aj} \neq 0$ or $\psi_{ai} \neq 0$. This is equivalent to the following statements: When using an alternative eigenvector which closely resembles the exact eigenvector directly in the procedure, the results will be a good approximation to the "exact" values, and when the procedure is carried out in an iterative way, as will be shown in the later section, the solution converges to the "exact" value of the identified parameters.

In practice, the applied mode should be chosen to be the one which has a maximum sensitivity with respect to the identified parameter. For example, when the stiffness k_{ij} between d.o.f. i and j is to be identified, the applied mode must be the one having the maximum sensitivity with respect to k_{ij}. This implies that the modal displacement between d.o.f. i and j of the mode has a maximum relative motion, i.e. $(\psi_{ri} - \psi_{rj})$ is maximum. On the other hand, when the mass m at location i has to

Downloaded 03 May 2010 to 171.66.16.244. Redistribution subject to ASME license or copyright; see http://www.asme.org/terms/Terms_Use.cfm

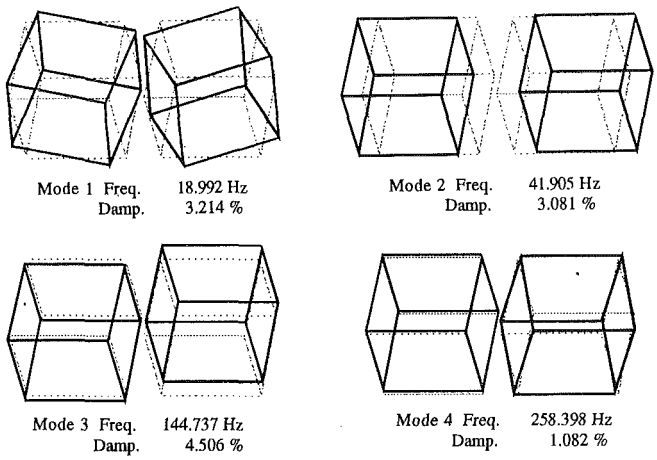


Fig. 2 The four modes for characterizing the rubber pad

Table 1 The equivalent inertial properties of the two mass blocks

Mass block 1		Mass block 2	
m_1	4.145 kg	m_2	4.377 kg
$J_{\beta 1}$	.4876E-2 kgm^2	$J_{\beta 2}$	.5711E-2 kgm^2
$J_{\alpha 1}, J_{\gamma 1}$	.4215E-2 kgm^2	$J\alpha 2, J\gamma 2$	.4813E-2 kgm^2

Table 2 The identified *k* and *c* of the rubber pad and applied modes

Dir.	k (N/m)	c (Ns/m)	Corresponding mode No. freq.(Hz) ζ
x	1.7643E+6	1.7466E+2	3 144.737 4.5062
y	1.4773E+5	3.4556E+1	2 41.905 3.0809
z	1.7643E+6	1.7466E+2	3 144.737 4.5062
	(Nm/rad)	(Nms/rad)	
α	3.2034E+1	1.7247E-2	1 18.992 3.2139
β	6.9347E+3	9.2426E-2	4 258.398 1.0819
γ	3.2034E+1	1.7247E-2	1 18.992 3.2139

be identified, the mode to be selected is the one with an eigenvector where the location i is far from the vibration nodes, i.e., $\psi_{ri} >> 0$. In this way, a better approximation or a fast convergence for the approach is guaranteed.

4 Applications

4.1 Characterization of a Rubber Vibration Isolator. The test structure, as shown in Fig. 1, consists of two steel cylindrical mass blocks joined by a rubber pad, which is commonly used in automobile industries for vibration isolation between body and engine. In this example, the physical characteristics of this vibration isolator have to be identified. It is assumed, that the analytical model of the isolator connection is a massless elastic element (the joint model with six Voight models). The inertial effects of the rubber pad will be taken into account by adding the equivalent amount to both mass blocks. The equivalent inertial properties are measured or calculated and given in Table 1.

The test is performed by suspending the structure from the gravity centers of both mass blocks, which are coinciding with the natural rotation axes in order to reduce the additional damping and stiffness and eliminate static distortion of the rubber. When the excitation force is applied in the xy-plane and parallel to the y-axis (f_1 in Fig. 1), two distinct modes are measured. The first mode (mode 1 in Fig. 2) is a rotational mode around the z-axis (γ-direction). In this mode, each mass block rotates around its own natural rotation axis parallel to the z-axis. The second mode (mode 2 in Fig. 2) is, obviously, a translational mode in the y-direction. When the excitation force is applied in the xy-plane but parallel to the x-axis (f_3 in Fig. 1), besides the mode 1 another mode is measured. The mode (mode 3 in Fig. 2) is a translational mode in the x-direction. Because the mass blocks and rubber pad are all cylindrical, the test structure is symmetric and three modes similar to modes 1, 2, and 3 are measured in the yz-plane as expected. Finally, applying the excitation force parallel to, but out of the yz-plane in the z-direction (f_2 in Fig. 1), a mode characterized by a rotation around the y-axis is measured (mode 4 in Fig. 2).

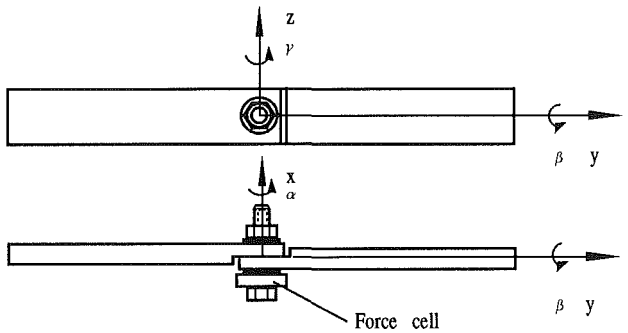


Fig. 3 Beam with the bolted joint

With the inertial properties of the mass blocks given in Table 1, the physical parameters (stiffness k and equivalent viscous damping c) of the rubber pad in six directions (x, y, z, α, β, and γ) are calculated by equation (8) and (9) in correspondence with the measured resonance frequencies and damping ratios of mode 3, 2, 3, 1, 4, and 1. These values and corresponding modes are given in Table 2.

4.2 Characterization of Bolted Joints in a Beam. Bolted joints are one of the most commonly used connections in mechanical constructions. However, such a joint normally can hardly be separated from the adjacent parts which form or support it. If the joint could be separated, it will be difficult to install it into a test structure such as the two-mass-block structure without any additional joint or connection.

This example illustrates the application of the iteration procedure for the identification of the stiffness and damping of a bolted joint in a beam structure. The structure consists of two beams with length of 500 mm and rectangular cross-section of 12 by 40 mm^2 connected by a bolt, as shown in Fig. 3. The

Downloaded 03 May 2010 to 171.66.16.244. Redistribution subject to ASME license or copyright; see http://www.asme.org/terms/Terms_Use.cfm

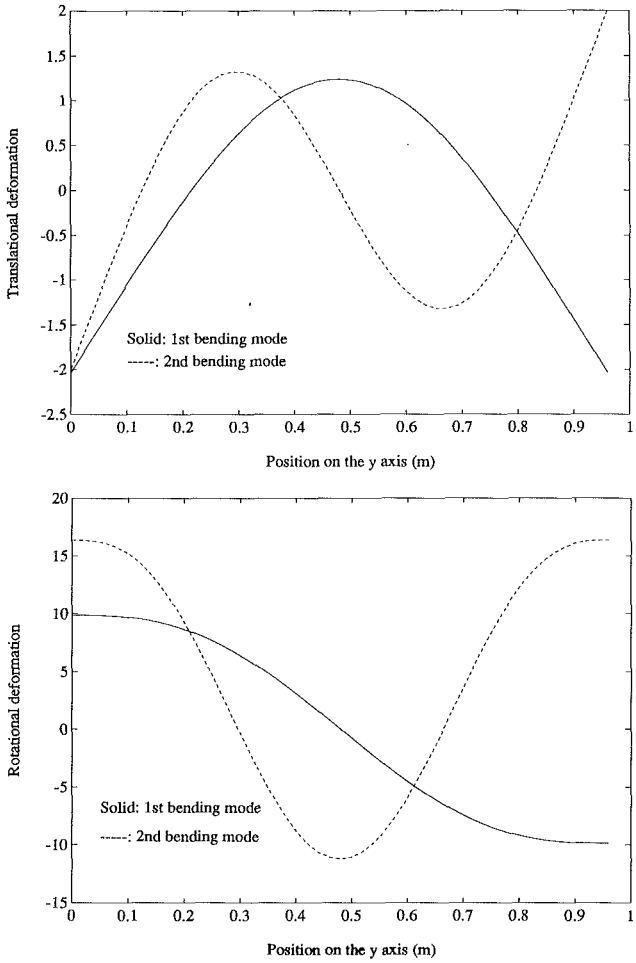


Fig. 4 Deformation of the first and second bending of a beam

physical parameters of the FE model for the beams are obtained from measurements and optimization techniques. The contacting area is about 40 by 40 mm^2. A load cell is installed, as seen in Fig. 3, to measure the preload of the contact pressure. Its mass-loading effect is taken into account by adding a lumped mass in the mass matrix.

In order to carry out the procedure of one mode solving for one parameter as in the previous example, several points of the physical configuration of the structure must be clarified. First, for such a structure, the d.o.f.'s in a plane have no inner relations with the d.o.f.'s out of the plane during free vibration as stated in Section 2. Thus, this spatial problem can be split into two planar problems if the rotation around the y-axis is omitted.

Second, for a lap joint as in this case, the length of the joint region cannot be neglected, consequently, the cross-term stiffness parameters, for example in the xy-plane, between d.o.f. x and γ, cannot be omitted. However, these cross-stiffness parameters can be considered to be proportional to a parameter, e.g., the elastic modulus E_j for the joint. Therefore, the joint elastic modulus E_x and translational stiffness k_x will be identified in the xy-plane for the joint.

Third, in order to select the applied modes, the physical configuration of the available modes should be inspected. When the deformation of the beam takes the shape of the first bending mode as shown in Fig. 4, the middle part of the beam is subjected to a maximum bending moment and minimum shear force (the shear force is zero in the exact middle of the beam). Hence, the rotational deformation is dominant there. As for the joint, since its both ends are located symmetrically with respect to the middle of the beam, the relative displacement of the rotational d.o.f. between the two ends of the joint becomes maximum (they are opposite in direction) while that of the translational d.o.f. are equal to zero, just as if the two beams are connected flexibly in the rotation direction and rigidly in the translation direction. Therefore, the mode is independent upon the stiffness of the joint in the translational direction and is equivalent to mode 1 in Section 2. The stiffness of the joint in the rotational d.o.f. can be solved with this mode. However, for the second bending mode, as shown in Fig. 4, the corresponding statement will be opposite to the above. The mode shape is equivalent to mode 3 in Section 2 and the problem in the translational d.o.f. can be solved.

Finally, the present example is defined in the frequency range of 0 to 640 Hz where the available modes of the structure are all bending modes which relate to the physical parameters associated d.o.f.'s in four directions, x, z, α, and γ. Therefore, only four parameters need to be identified for solving this problem in that frequency range. They are E_x, E_z, k_x, and k_z. Consequently, only four modes are required and

Table 3 The resonance frequencies and damping ratios of the bolt jointed beam measured in two particular conditions

Mode	Case 1		Case 2	
	Freq.(Hz)	Damp.ζ(%)	Freq.(Hz)	Damp.ζ(%)
1	62.406	0.2065	59.898	0.4658
2	188.827	0.0116	188.295	0.0234
3	213.715	0.0121	207.087	0.7083
4	622.504	0.0130	620.349	0.0247
Surfaces	ground,ground		milled,milled	
Preload	10000 N		3000 N	
Temprature	24.9°C		24.6°C	

Table 4(a) The resulting E_j, k, and Δf for each iterative step (Case 1)

Case	step	E_x(N/m^2)	k_x(N/m)	Δf_1	Δf_2
2	initial	7.0000E10	5.8728E7	1.112	0.888
xy	1	6.0489E10	5.0532E7	-0.126	-0.021
plane	2	6.1349E10	5.1258E7	0.000	0.000

Case	step	E_z(N/m^2)	k_z(N/m)	Δf_3	Δf_6
2	initial	9.0000E10	2.6637E8	1.864	1.205
yz	1	8.2693E10	2.4392E8	-0.128	-0.034
plane	2	8.3130E10	2.4523E8	0.000	0.000

Table 4(b) The resulting E_j, k, and Δf for each iterative step (Case 2)

Case	step	E_x(N/m^2)	k_x(N/m)	Δf_1	Δf_2
1	initial	9.0000E10	7.5508E7	0.487	0.421
xy	1	8.3666E10	7.0089E7	-0.029	-0.004
plane	2	8.3997E10	7.0367E7	0.000	0.000

Case	step	E_z(N/m^2)	k_z(N/m)	Δf_3	Δf_6
1	initial	1.0000E11	2.9596E8	-2.442	-0.720
yz	1	1.1157E11	3.3060E8	-0.207	-0.032
plane	2	1.1275E11	3.3409E8	-0.002	0.000
	3	1.1276E11	3.3412E8	0.000	0.000

Downloaded 03 May 2010 to 171.66.16.244. Redistribution subject to ASME license or copyright; see http://www.asme.org/terms/Terms_Use.cfm

Table 5 Damping factors of the joint for the two particular cases

Damping	Case 1	Case 2
c_x(Ns/m)	2.0627	6.6511
c_y(Ns/m)	12.2570	26.4330
c_γ(Nms/rad.)	0.2736	0.5715
c_α(Nms/rad.)	0.0900	6.1663

measured in two particular conditions (case 1 and case 2), which are modes 1, 2, 3, and 4 corresponding to the first and second bending mode in the *xy*-plane and first and second bending mode in the *yz*-plane. The measured results and test conditions of the two cases are listed in Table 3.

The iterative procedure for solving the problem, for example, in the *xy*-plane, is illustrated in the flow chart of Fig. 5, where the subscript *e* indicates the experimental. In the procedure, the initial values for alternative eigenvectors ψ_{a1} and ψ_{a2} corresponding to eigenvector ψ_1 and ψ_2 are obtained by inputting the initial value of E_x as listed in Table 4 into the FE package for the joint, and solving this eigenproblem of the overall model.

Once the alternative eigenvalues ψ_{a1} and ψ_{a2} are obtained, the approximate values of E_x and k_x, E_{ax}, and k_{ax} are calculated and used to solve for alternative eigenvectors ψ_{a1} and ψ_{a2} in the next iterative cycle until the desired accuracy is reached. Tables 4(*a*) and (*b*) show the calculated joint model parameters and the differences of the resulting natural frequencies with respect to the measured for case 1 and 2, respectively.

From Table 4, it can be seen that the results converge very fast. The results carried out with one step calculation were already a good approximation to the "exact" ones.

To finalize this procedure, the equivalent viscous damping factors of the joint in the two cases will be calculated. Assume that the damping contributed by the beams themselves is proportional, i.e., $\mathbf{C}=\alpha\mathbf{M}+\beta\mathbf{K}$. The matrix $\mathbf{C}$ with empty entries in the region of the joint can be derived. Then, with the matrix $\mathbf{C}$ and the measured damping ratios in Table 3, the equivalent viscous damping factors of the joint in the cases of Table 3 are solved according to the procedure described in Sections 2 and 3 and given in Table 5.

5 Conclusion

This paper presents a method for solving problems where a few physical parameters have to be determined. The method is well suited for the identification and the dynamic modeling of the special mechanical parts such as joints or connections. Normally, the characteristics of these parts are nonlinear and their physical or design parameters in a certain condition cannot be predicted. The method has proven to be efficient. For example, in the test phase, if the mode shapes are known in advance (for example, it is sure that the first normal mode of a rectangular beam is the first bending mode in the weak direction, etc.), one transfer function or one time domain response will be sufficient to determine the resonance frequencies and damping ratios required for the solution of the method. The calculations involved are straightforward. The iteration procedure, converges very fast if the applied mode is selected properly.

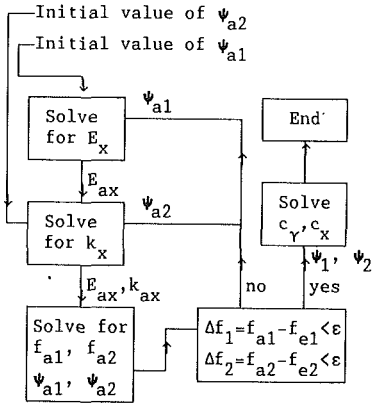


Fig. 5 Flow chart for solving E_x and k_x

References

Dolbey, M. P., and Bell, R., 1971, "The Contact Stiffness of Joints at Low Apparent Interface Pressure," *Ann. of C.I.R.P.*, Vol. 19, pp. 67–79.

Levina, E. M., 1965, "Calculation of Contact Deformation in Slideways," *Machines and Tooling*, Vol. 36, pp. 8–17.

Meirovitch, L., 1980, *Computational Methods in Structural Dynamics*, Sijthoff and Noordhoff, pp. 74–82.

Soukry, S. M., and Thornley, R. H., 1984, "The Stiffness and Damping of Lubricated Joints Subject to Normal Loads," *Proc. of the 25th M.T.D.R. Conference*, pp. 369–377.

Yoshimura, M., and Okushima, K., 1977, "Measurement of Dynamic Rigidity and Damping Property for Simplified Joint Models and Simulation by Computer," *Ann. of C.I.R.P.*, Vol. 25, pp. 193–198.

Zhou, C. S., Touratier, M., and Coffinal, G., 1986, "Identification of Dynamic Characteristics of Joints," *Proceedings of the 4th IMAC Conference*, Los Angeles, pp. 316–328.

Downloaded 03 May 2010 to 171.66.16.244. Redistribution subject to ASME license or copyright; see http://www.asme.org/terms/Terms_Use.cfm

The Dynamic Energy Release Rate for a Steadily Propagating Mode I Crack in an Infinite, Linearly Viscoelastic Body[1]

J. R. Walton
Department of Mathematics,
Texas A&M University,
College Station, TX 77843
Mem. ASME

An analysis is presented for the dynamic, steady-state propagation of a semi-infinite, mode I crack in an infinite, linearly viscoelastic body. For mathematical convenience, the material is assumed to have a constant Poisson's ratio, but the shear modulus is only assumed to be decreasing and convex. An expression for the Stress Intensity Factor (SIF) is derived for very general tractions on the crack faces and the Energy Release Rate (ERR) is constructed assuming that a fully developed Barenblatt type failure zone with nonsingular stresses exists at the crack tip and the loadings have a simple exponential form. For comparative purposes, expressions for the ERR are derived for the special cases of dynamic steady-state crack propagation in elastic material and quasi-static crack propagation in viscoelastic material, both with and without a failure zone. Sample calculations are included for power-law material and a standard linear solid in order to illustrate the combined influence of inertial effects, material viscoelasticity, and a failure zone upon the ERR.

1 Introduction

A number of analytical studies of dynamically propagating, semi-infinite cracks in linearly viscoelastic material have been reported in the literature in the twenty years since Willis (1967) presented a dynamic, steady-state analysis of a semi-infinite, mode III crack propagating in an infinite viscoelastic body. Employing transform methods and the Wiener-Hopf technique, Willis constructed the dynamic SIF for a special class of crack face loadings and for a standard material model.

Subsequently, Atkinson and his co-workers generalized Willis' mode III analysis by considering transient effects, more general constitutive assumptions, and a strip geometry (Atkinson and List (1972), Atkinson (1979), and Atkinson and Popelar (1979)). The principal objective of these works was the calculation of the dynamic SIF and, following Willis, the principal tools were integral transforms and the Wiener-Hopf technique along with various approximate and asymptotic methods. Additionally, an expression for the ERR was derived from the singular stress solution and a local work argument at the crack tip. This program was then applied to the physically more interesting but mathematically more difficult mode I counterparts (Atkinson and Coleman (1977), Atkinson (1979) and Popelar and Atkinson (1980)).

More recently, Walton and co-workers reconsidered dynamic mode III crack propagation in a series of papers (Walton (1982, 1983, 1985, 1987), Herrmann and Walton (1988), and Schovanec and Walton (1987b)). This work differed from previous studies in that it: allowed for more general crack face loadings and was valid for a broader class of shear moduli; obtained in many cases closed-form expressions for important physical quantities by using the Riemann-Hilbert rather than Wiener-Hopf methodology; and most importantly, computed the ERR based upon a Barenblatt failure zone model. Indeed, it was shown in Walton (1987) for dynamic, steady-state, mode III crack propagation and in Herrmann and Walton (1988) for the corresponding transient problem that whether or not a failure zone is incorporated into the model can significantly affect, both qualitatively and quantitatively, the behavior of the ERR as a function of crack speed. Furthermore, example calculations performed in Walton (1987) illustrate that the dynamic steady-state ERR based upon a failure zone model shows a dramatic initial decrease with increasing crack speed. This suggests that a fracture criterion based upon a critical ERR would predict relatively slow, stable, steady-state crack speeds in viscoelastic material, which is in agreement with experiments on real material. It should be remarked that the importance of incorporating a failure zone into viscoelastic fracture models has been noted previously by Knauss (1973) and Schapery (1975, 1984) in the context of quasi-static mode I crack propagation.

In the present paper, the Riemann-Hilbert/Barenblatt failure zone program carried out in Walton (1982, 1987) for a

[1]This research was supported by the Office of Naval Research under Contract No. N00014-K-0298 and the Science and Engineering Research Council of the United Kingdom under Grant No. GR/E/40538.

Contributed by the Applied Mechanics Division of THE AMERICAN SOCIETY OF MECHANICAL ENGINEERS for publication in the JOURNAL OF APPLIED MECHANICS.

Discussion on this paper should be addressed to the Technical Editor, Leon M. Keer, The Technological Institute, Northwestern University, Evanston, IL 60208, and will be accepted until two months after final publication of the paper itself in the JOURNAL OF APPLIED MECHANICS. Manuscript received by the ASME Applied Mechanics Division, February 1, 1988; final revision, June 20, 1989.

Copyright © 1990 by ASME
Downloaded 03 May 2010 to 171.66.16.244. Redistribution subject to ASME license or copyright; see http://www.asme.org/terms/Terms_Use.cfm

semi-infinite, mode III crack is applied to the corresponding mode I problem. For mathematical convenience the material is assumed to have a constant Poisson's ratio and a shear modulus that is continuous and decreasing as a function of time.

The plan of the paper is first to construct for very general, crack face loadings the singular stress solution, and in particular, the SIF. Next, a Barenblatt failure zone is incorporated into the model and an expression for the ERR is derived for crack face loads of a simple decreasing exponential type. The extension to a much wider class of crack face loads offers no serious difficulty (Walton, 1987) and is omitted for the sake of brevity.

2 Problem Formulation and Stress Analysis

The specific problem to be solved is the steady propagation to the right of a semi-infinite mode I crack in an infinite, isotropic, homogeneous, linearly viscoelastic body. The stress field is assumed to vanish at infinity and the crack is driven by a traveling system of crack face tractions. The equations of motion are

$$\sigma_{ij,j} = \rho \ddot{u}_i, \quad i = 1,2$$

and the boundary conditions are

$$\sigma_{12}(x_1,0,t) = 0, \quad -\infty < x_1 < \infty$$

$$\sigma_{22}(x_1,0,t) = f(x_1 - vt), \quad x_1 < vt$$

$$u_2(x_1,0,t) = 0, \quad x_1 > vt$$

$$\sigma_{ij} \to 0, \text{ as } x_1^2 + x_2^2 \to \infty,$$

where u_i and σ_{ij} are the displacement and stress tensor components, ρ is the mass density, and f is the crack face normal traction. The constitutive relations are given by

$$\sigma_{ij} = 2\mu * d\epsilon_{ij} + \delta_{ij}\lambda * d\epsilon_{kk}$$

in which μ and λ are positive, decreasing functions of $t > 0$ and $\mu * d\epsilon$ denotes the Stieltjes convolution.

Let us adopt the moving coordinate system $x = x_1 - vt$, $y = x_2$, define the functions u and v by $u(x,y) = u_1(x_1,x_2,t)$ and $v(x,y) = u_2(x_1,x_2,t)$, and introduce the Helmholtz decomposition

$$u(x,y) = \theta_{,x} + \phi_{,y}, \quad v(x,y) = \theta_{,y} - \phi_{,x} \tag{1}$$

where θ and ϕ are potential functions satisfying

$$v^2\theta_{,xx} = \frac{(\lambda + 2\mu)}{\rho} * d(\Delta\theta)$$

$$v^2\phi_{,xx} = \frac{\mu}{\rho} * d(\Delta\phi). \tag{2}$$

In equations (2), Δ denotes the Laplacian $\partial^2/\partial x^2 + \partial^2/\partial y^2$, $\theta_{,xx}$ denotes $\partial^2\theta/\partial x^2$, and $*d(\ )$ denotes convolution with respect to x.

Application of the Fourier transform

$$F(p) = \hat{f}(p) = \int_{-\infty}^{\infty} e^{ipx} f(x)\,dx$$

to equations (2) produces ordinary differential equations in y with solutions

$$\hat{\theta}(p,y) = A(p)\exp(-|p|y\gamma_1(ipv))$$

$$\hat{\phi}(p,y) = B(p)\exp(-|p|y\gamma_2(ipv)) \tag{3}$$

where

$$\gamma_j^2(z) = 1 - (v/\bar{c}_j(z))^2,$$

$$\bar{c}_1^2(z) = (\bar{\lambda}(z) + 2\bar{\mu}(z))/\rho,$$

$$\bar{c}_2^2(z) = \bar{\mu}(z)/\rho,$$

and $\bar{r}(z)$ denotes the Carson transform

$$\bar{r}(z) = r(0) + \int_0^{\infty} e^{-tz}\,dr(t).$$

For stresses to vanish as $y \to \infty$, the square roots $\gamma_j, j = 1,2$, are chosen to have positive real parts.

The boundary condition $\sigma_{xy}(x,0) = 0$ requires that

$$B(p) = -2A(p)i\,\mathrm{sgn}(p)\gamma_1(ivp)/(1 + \gamma_2^2(ivp)) \tag{4}$$

where $\mathrm{sgn}(p)$ denotes the signum function. From equations (1), (4), and the transformed constitutive relations, it follows that

$$\hat{\sigma}_{yy}(p,0) = T(p)\hat{v}_{,x}(p,0) \tag{5}$$

with $T(p)$ given by

$$T(p) = i\,\mathrm{sgn}(p)(\bar{c}_2(ivp)/v)^2(\bar{\mu}(ivp)/\gamma_1(ivp))$$

$$(4\gamma_1(ivp)\gamma_2(ivp) - (1 + \gamma_2^2(ivp))^2). \tag{6}$$

Equation (5) can be recast as a Riemann-Hilbert (hereafter abbreviated R-H) problem by making use of natural analytic extensions $F^+(z) = \hat{\sigma}_{yy}^+(z,0)$ and $F^-(z) = \hat{v}_{,x}(z,0)$ for $\mathrm{Im}(z) \gtrless 0$, respectively, that vanish as $\mathrm{Im}(z) \to \pm\infty$. The problem is then to find $F^+(z)$, $F^-(z)$ analytic for $\mathrm{Im}(z) \gtrless 0$, respectively, and such that

$$F^+(p) = T(p)F^-(p) + g(p), \quad -\infty < p < \infty \tag{7}$$

$$\lim_{\mathrm{Im}(z) \to \pm\infty} F^{\pm}(z) = 0,$$

where

$$g(p) = -\hat{\sigma}_{yy}^-(p,0) = -\hat{f}(p), \quad F^{\pm}(p) = \lim_{\mathrm{Im}(z) \to 0\pm} F^{\pm}(z)$$

and $\sigma_{yy}^+(x,0)$, $\sigma_{yy}^-(x,0)$ denote the restriction of $\sigma_{yy}(x,0)$ to $x > 0$, $x < 0$, respectively.

Solving the R-H problem (7) by the methods of Walton (1982) it can be shown that for all $x > 0$

$$\sigma_{yy}^+(x,0) = \frac{1}{2\pi}\int_{-\infty}^{\infty} e^{-ixp}X^+(p)\,dp \frac{1}{2\pi i}\int_{-\infty}^{\infty} \frac{g(t)}{X^+(t)}\frac{dt}{t-p} \tag{8}$$

and asymptotically as $x \to 0+$, $\sigma_{yy}^+(x,0) \sim K/\sqrt{\pi x}$ where the SIF, K, is given by

$$K = \frac{X_\infty^+}{2\pi}\int_{-\infty}^{\infty} g(p)/X^+(p)\,dp \tag{9}$$

with $X_\infty^+ \equiv \lim_{p \to \infty}(X^+(p)/\omega^+(p))$.

The function $X^+(p)$ in (8) and (9) is half of the solution pair $X^{\pm}(p)$ of the homogeneous R-H problem

$$X^+(p) = T(p)X^-(p), \tag{10}$$

which is conveniently solved by writing $T(p) = \mathrm{sgn}(p)T_0(p)$ and constructing $X^{\pm}(z)$ as the product

$$X^{\pm}(z) = \omega^{\pm}(z)X_0^{\pm}(z)$$

where

$$X_0^+(p) = T_0(p)X_0^-(p)$$

and $\omega^{\pm}(z)$ denote the brances of $\sqrt{z}$ with branch cuts along the negative and positive imaginary axes, respectively. Also in (9), $X_\infty^+ \equiv \lim_{p \to \infty} X_0^+(p)$.

As shown further in Walton (1982), application of the Plancherel theorem to (9) yields

$$K = -\frac{1}{\sqrt{\pi}}\int_{-\infty}^{0} \sigma_{yy}^-(x,0)h(x)\,dx$$

Downloaded 03 May 2010 to 171.66.16.244. Redistribution subject to ASME license or copyright; see http://www.asme.org/terms/Terms_Use.cfm

with

$$\int_{-\infty}^{\infty} h(x)e^{-ixp}dx = \frac{X_{\infty}^{+}}{X^{+}(p)}.$$

Moreover, for $x>0$, the methods of Walton (1982) produce a relatively simple expression for $\sigma_{yy}^{+}(x,0)$ involving $h(x)$ and $\sigma_{yy}^{-}(x,0)$. Clearly, the chief difficulty in constructing $\sigma_{yy}^{+}(x,0)$ lies in determining $X_0^{+}(p)$ or $h(x)$. The corresponding mode III problem admits simple closed-form expressions for these functions assuming only that the shear modulus $\mu(t)$ is positive, convex, continuously differentiable and decreasing, with any rate of decay permissible. (Even these mild assumptions are stronger than necessary.) As will be shown next, in mode I such is not the case.

To solve the homogeneous R-H problem, it proves convenient to further factor $T(p)$ as the product

$$T(p) = \mathrm{sgn}(p)T_1(p)T_2(p)T_3(p)$$

with

$$T_1(p) = i(\bar{c}_2(ivp)/v)^2\bar{\mu}(ivp),$$

$$T_2(p) = \frac{1}{\gamma_1(ivp)},$$

$$T_3(p) = 4\gamma_1(ivp)\gamma_2(ivp) - (1+\gamma_2^2(ivp))^2,$$

and write

$$X^{\pm}(z) = \omega^{\pm}(z)X_1^{\pm}(z)X_2^{\pm}(z)X_3^{\pm}(z)$$

in which

$$X_j^{+}(p) = T_j(p)X_j^{-}(p), \quad j=1,2,3.$$

Since $T_1(p)$ has a natural analytic extension $T_1(z)$ without zeroes for $\mathrm{Im}(z)<0$, one may take $X_1^{+}(z)\equiv 1$ and $X_1^{-}(z) = 1/T_1(z)$. For $X_2^{\pm}(z)$, the analysis in Walton (1982) may be used to show that separate consideration of the two cases $0<v<c_L^{*}$ and $c_L^{*}<v<c_L$ is required where c_L^{*} and c_L are the equilibrium (rubbery) and instantaneous (glassy) longitudinal wave speeds.

For $0<v<c_L^{*}$, $\gamma_1(ivp)$ has a natural analytic extension $\gamma_1(ivz)$ without zeroes for $\mathrm{Im}(z)<0$. Thus, one may take $X_2^{+}(z)\equiv 1$ and $X_2^{-}(z) = \gamma_1(ivz)$, whereas for $c_L^{*}<v<c_L$,

$$X_2^{+}(z) = (1+iq_1/z)^{-1/2} \text{ and } X_2^{-}(z) = (1+iq_1/z)^{-1/2}\gamma_1(ivz)$$

where $q_1 = q_1(v)$ is the unique positive real root of

$$v^2 = \bar{c}_1^2(qv) = (\bar{\lambda}(qv) + 2\bar{\mu}(qv))/\rho \tag{12}$$

and the branch cut for $\sqrt{1+iq_1/z}$ is the interval $\mathrm{Re}(z)=0$, $0>\mathrm{Im}(z)>-iq_1(v)$. It is easily shown that $q_1(v)$ is an increasing function of v with $q_1(c_L^{*})=0$ and $q_1(c_L)=\infty$.

The construction of $X_3^{\pm}(z)$ requires careful analysis of the mapping properties in the complex plane of the "Rayleigh" function $T_3(p) = 4\gamma_1\gamma_2 - (1+\gamma_2^2)^2$. It is useful to indicate explicitly by $T_3 = T_3(ivp,v)$ that T_3 depends inpendently upon v and p through

$$\gamma_j = \gamma_j(ivp,v) = \sqrt{1-(v/\bar{c}_j(ivp))^2}.$$

One now sees that $T_3(0,v)$ and $T_3(\infty,v)$ are the (real-valued) Rayleigh functions corresponding to equilibrium and instantaneous material properties, respectively, and the equilibrium and instantaneous Rayleigh wave speeds, c_R^{*} and c_R, are the unique positive numbers for which $T_3(0,c_R^{*}) = T_3(\infty,c_R) = 0$. As is well known (Achenbach (1973)), $c_R^{*}<c_T^{*}<c_L^{*}$, and $c_R<c_T<c_L$, and it is also clear that $c_j^{*}\le c_j$ for $j=R,T,L$. Moreover, it is expected for many real materials that $c_L^{*}<c_R$. From these observations and the obvious fact that the analysis breaks down for $v\ge c_R$, it follows that the followng four cases must be considered:

(i) $0<v<c_R^{*}$
(ii) $c_R^{*}<v<c_T^{*}$
(iii) $c_T^{*}<v<c_L^{*}$
(iv) $c_L^{*}<v<c_R$.

The following properties of $\gamma_j(iv(p-iq))$ and $T_3(p-iq)$, readily proved by methods in Walton (1982), are needed in the construction of $X_3^{+}(p)$.

P1. The real and imaginary parts of $\gamma_j(vq+ivp)$ are even and odd functions of p, respectively, and for $p>0$, $\mathrm{Im}[\gamma_j(vq+ivp)]>0$ and $\mathrm{Re}[\gamma_j(vq)]<\mathrm{Re}[\gamma_j(vq+ivp)]<\gamma_j(\infty)$.

P2. $\lim_{q\to\infty}\gamma_j(vq+ivp) = \lim_{|p|\to\infty}\gamma_j(vq+ivp) = \gamma_j(\infty) = \sqrt{1-(v/c_j)^2}$.

P3. There exists $q_j = q_j(v)$ ($j=1,2$ or equivalently L,T) such that

(a) $q_j(v)=0$ for $0<v<c_j^{*}$,

(b) $q_j(v)$ is an increasing function of v with $\lim_{v\to c_j} q_j(v)=\infty$, and

$$\text{(c)} \quad \lim_{p\to 0\pm}\gamma_j(vq+ivp) = \begin{cases} \pm i\sqrt{(v/\bar{c}_j(vq))^2-1}, & 0<q<q_j(v) \\ \sqrt{1-(v/\bar{c}_j(vq))^2}, & q_j(v)<q. \end{cases}$$

Thus, $\gamma_j(vq+ivp)$ is analytic for $q>0$ except for a branch cut along the interval $p=0$, $0\le q\le q_j(v)$. From P1–P3, $T_3(p-iq)$ inherits the following properties.

P4 The real and imaginary parts of $T_3(p-iq)$ are even and odd functions of p, respectively.

P5 $\lim_{q\to\infty}T_3(p-iq) = \lim_{|p|\to\infty}T_3(p-iq) = T_3(\infty,v)$, the first limit uniform in p. Also, $\lim_{v\to c_3}T_3(\infty,v)=0$.

From well-known properties of the Rayleigh function (Achenbach (1973)), one also deduces:

P6 For $0<v<c_T^{*}$, $\lim_{p\to 0\pm}T_3(p-iq) = T_3(-iq)$ is real for $q<0$, and there exists a unique $q_3 = q_3(v)$ such that $q_3=0$ for $0<v\le c_R^{*}$, $q_3(v)$ increases monotonically to ∞ as $v\to c_R$, $T_3(-iq)<0$ for $0\le q<q_3(v)$, $T_3(-iq_3(v))=0$ and $T_3(-iq)>0$ for $q>q_3(v)$.

The parameters $q_j(v)$, $j=1,2,3$ play a fundamental role in the analysis of the Rayleigh function $T_3(p-iq)$. Their principal properties are listed in

P7 $q_j(v)=0$ for $0\le v\le c_j^{*}$ and $q_j(v)>0$ for $v>c_j^{*}$; $q_j(v)$ increases monotonically to ∞ as $v\to c_j$ and $q_1(v)\le q_2(v)\le q_3(v)$ with $q_j(v) = q_{j+1}(v)$, $j=1,2$, occurring only when each is zero.

The construction of $X_3^{+}(z)$ is done case by case.

Case 1. $0<v<c_R^{*}$

Here, $q_j(v)=0$ for $j=1,2,3$ (P3 and P7) and from P1–P6 one concludes that $T_3(p-iq)$ is analytic for $q>0$. One may then choose $X_3^{+}(z)\equiv 1$ and $X_3^{-}(z) = 1/T_3(z)$ provided $T_3(z)$ has no zeroes for $\mathrm{Im}(z)<0$. For $\mathrm{Im}(z)<0$, $T_3(z)$ is given by

$$T_3(z) = 4[1-(v/\bar{c}_T(ivz))^2]^{1/2}[1-(v/\bar{c}_L(ivz))^2]^{1/2} - [2-(v/\bar{c}_T(ivz))^2]^2. \tag{13}$$

For material with a constant Poisson's ratio, ν,

$$(\bar{c}_T/\bar{c}_L)^2 = \frac{(1-2\nu)}{2(1-\nu)}.$$

Introducing $\bar{d} \equiv \bar{c}_T/c_T = \bar{c}_L/c_L$, one then has

$$T_3(z) = 4\left[1-\left(\frac{(v/\bar{d}(ivz))}{c_T}\right)^2\right]^{1/2} \times \left[1-\left(\frac{(v/\bar{d}(ivz))}{c_L}\right)^2\right]^{1/2} - \left[2-\left(\frac{(v/\bar{d}(ivz))}{c_T}\right)\right]^2.$$

The only zeros in the complex s-plane of the Rayleigh function,

$$4(1-(s/c_T)^2)^{1/2}(1-(s/c_L)^2)^{1/2} - (2-(s/c_T)^2)^2,$$

occur at $s=\pm c_R$. Thus, for any zeros of $T_3(z)$ with

Downloaded 03 May 2010 to 171.66.16.244. Redistribution subject to ASME license or copyright; see http://www.asme.org/terms/Terms_Use.cfm

$\mathrm{Im}(z)<0$, $\bar{d}(ivz)$ must be real. But by property P1, $\bar{d}(ivz)=\bar{d}(vq+ivp)$ for $z=p-iq$ is real only for $p=0,\infty$ or $q=\infty$, and by P6, $T_3(-iq)$ is never zero for $q>0$ and $0\le v<c_R^*$. Finally, since $T_3(\infty)$ is also not zero, Case 1 is completed.

Case 2. $c_R^*<v<c_T^*$

Here, $q_j(v)=0$ for $j=1,2$ (P3) and $T_3(p-iq)$ is analytic for $q>0$. A similar argument to Case 1 shows that $T_3(p-iq)$ has one zero (counting multiplicity) for $q>0$, occurring for $p=0$ and $q=q_3(v)>0$. Finally, $X^{\pm}(z)$ will have the correct asymptotic form as $|z|\to\infty$ and $z\to 0$ provided one takes for $X_3^{\pm}(z)$, $X_3^{+}(z)=(z+iq_3(v))/z$ and $X_3^{-}(z)=(z+iq_3(v))/(zT_3(z))$.

Case 3. $c_T^*<v<c_L^*$

Here, $q_1(v)=0$, $q_3(v)$ is as in Case 2, and $q_2(v)>0$ is the unique number q such that $\gamma_2(vq)=0$. By P3, $T_3(p-iq)$ is analytic for $q>0$ except on the cut $p=0$, $0\le q\le q_2(v)$ across which it has a jump discontinuity. Also, for $q>q_2(v)$, $T_3(p-iq)$ has a unique zero at $p=0$, $q=q_3(v)>q_2(v)$. From P3 and (13), one has for $0\le q\le q_2(v)$,

$$\lim_{p\to 0\pm} T_3(p-iq)=\pm i4[(v/\bar{c}_T(vq))^2-1]^{1/2}\times[1-(v/\bar{c}_L(vq))^2]^{1/2}-[2-(v/\bar{c}_T(vq))^2]^2. \tag{14}$$

Defining $\theta(q)\equiv\arg(T_3(-iq+(0+)))$, one has from (14) that for $0<q<q_2(v)$, $\pi/2<\theta(q)<\pi$ and $\theta(q_2(v))=\pi$. Consequently, simple expressions for $X_3^{\pm}(z)$ do not exist, even for a standard linear solid or Maxwell fluid. However, as in Walton (1982), numerically convenient forms can be constructed from the general representation $X_3^{\pm}(z)=\exp(\Gamma_3^{\pm}(z))$ with

$$\Gamma_3^{\pm}(z)\equiv\frac{1}{2\pi i}\int_{-\infty}^{\infty}\log(T_3(t))\frac{dt}{t-z}.$$

Moving the integration to the horizontal line $t-iq_2(v)$ leaves a contribution along the cut $p=0$, $0\le q\le q_2(v)$ which, for $\mathrm{Im}(z)>0$ gives

$$\Gamma_3^{+}(z)=\frac{1}{\pi}\int_0^{q_2(v)}\theta(q)\frac{dq}{q-iz}+\frac{1}{2\pi i}\int_{-\infty-iq_2(v)}^{\infty-iq_2(v)}\log(T_3(s))\frac{ds}{s-z}. \tag{15}$$

Since for $q>q_2(v)$, $T_3(p-iq)$ is analytic with a unique zero at $p=0$, $q=q_3(v)$, the second integral in (15) is easily evaluated yielding

$$X_3^{+}(z)=\left[\frac{q_3(v)-iz}{q_2(v)-iz}\right]\exp(J_3(z)) \tag{16}$$

$$X_3^{-}(z)=\left[\frac{q_3(v)-iz}{q_2(v)-iz}\right]\frac{\exp(J_3(z))}{T_3(z)} \tag{17}$$

where

$$J_3(z)=\frac{1}{\pi}\int_0^{q_2(v)}\theta(q)\frac{dq}{q-iz}. \tag{18}$$

Case 4. $c_L^*<v<c_R$

Here $0<q_1(v)<q_2(v)<q_3(v)$ and, as with Case 3, $T_3(p-iq)$ is analytic in the plane $q>0$ cut along $p=0$, $0\le q\le q_2(v)$. By P3 and (13) one has, for $0\le q\le q_1(v)$, $\lim_{p\to 0-}T_3(p-iq)=\lim_{p\to 0+}T_3(p-iq)$ whereas for $q_1(v)<q<q_2(v)$, $T_3(p-iq)$ has the jump discontinuity in (14). Also, by an argument similar to that in Case 1, one concludes that for $0\le q\le q_1(v)$ or $q_2(v)\le q\le q_3(v)$, $\lim_{p\to 0+}\arg(T_3(p-iq))-\lim_{p\to 0-}\arg(T_3(p-iq))=2\pi$. As in Case 3, it follows that

$$X_3^{+}(z)=\left[\frac{z+iq_1(v)}{z}\right]\left[\frac{z+iq_3(v)}{z+iq_2(v)}\right]\exp(J_4(z)) \tag{19}$$

$$X_3^{-}(z)=X_3^{+}(z)/T_3(z) \tag{20}$$

where

$$J_4(z)=\frac{1}{\pi}\int_{q_1(v)}^{q_2(v)}\theta(q)\frac{dq}{q-iz}. \tag{21}$$

It should be noted that the factor $\exp(I(z))$ in (17) and (20) removes the apparent pole at $z=-iq_2(v)$.

Combining the foregoing results one has, for $X^{\pm}(z)$, the following formulas.

Case 1. $0\le v\le c_R^*$

$$X^{+}(z)=\omega^{+}(z) \tag{22}$$

Case 2. $c_R^*<v<c_T^*$

$$X^{+}(z)=\omega^{+}(z)\left[\frac{z+iq_3(v)}{z}\right] \tag{23}$$

Case 3. $c_T^*<v<c_L^*$

$$X^{+}(z)=\omega^{+}(z)\left[\frac{z+iq_3(v)}{z+iq_2(v)}\right]\exp(J_3(z)) \tag{24}$$

Case 4. $c_L^*<v<c_R$

$$X^{+}(z)=\sqrt{z+iq_1(v)}\left[\frac{z+iq_3(v)}{z+iq_2(v)}\right]\exp(J_4(z)). \tag{25}$$

In all cases,

$$X^{-}(z)=\frac{X^{+}(z)\omega^{-}(z)}{T_0(z)\omega^{+}(z)}. \tag{26}$$

From (22), one sees that for Case 1, $X^{+}(z)$ is independent of crack speed and material parameters. Moreover, since $\sigma_{yy}^{+}(x,0)$ depends only upon the applied tractions and $X^{+}(p)$, one concludes that $\sigma_{yy}^{+}(x,0)$ for steady-state crack speeds less than c_R^* is the same as occurs in the corresponding elastic analysis.

Given $X^{+}(p)$ from (22)–(25), the SIF K can be computed from (9). Moreover, for Cases 1 and 2 the form (11) is easily constructed producing a simple expression for $h(x)$ depending upon crack speed and material properties only through $q_3(v)$. No such simple form exists for Cases 3 and 4 because of the term $\exp(J(z))$ in (24) and (25). Since $q_3(v)\to\infty$ as $v\to c_R$, K must vanish at the short-time Rayleigh wave speed. Furthermore, numerical calculations of K for a variety of examples show it to be a decreasing function of v.

3 Energy Release Rate Calculation

A Barenblatt-type failure zone is introduced as a small interval $(-a_f,0)$ behind the crack tip on which cohesive stresses, $\sigma_f(x)$, act to oppose the opening of the crack. It is further required that a_f be small relative to a length scale a_e associated with the crack and that the SIF, K_f, resulting from $\sigma_f(x)$ cancels the SIF, K_e, from the applied tractions thereby producing a nonsingular stress field ahead of the crack and a smoothly closing, cusp-like crack opening displacement in the failure zone (cf., Barenblatt (1962)). As discussed in Walton (1987), the essential features of such a model are reflected by taking for the crack face traction $\sigma_e(x)=\sigma_{yy}^{-}(x,0)$ and failure zone stress $\sigma_f(x)$ the forms

$$\sigma_e(x)=L_e\exp(x/a_e)$$
$$\sigma_f(x)=-L_f\exp(x/a_f) \tag{27}$$

for $x<0$, where L_e, L_f, a_e, and a_f are constants with $a_f<<a_e$. The analysis is readily extended to more general loads of the form

Downloaded 03 May 2010 to 171.66.16.244. Redistribution subject to ASME license or copyright; see http://www.asme.org/terms/Terms_Use.cfm

$$\sigma(x) = L\int_0^\infty e^{sx/a} dh(s)$$

where $dh(s)$ is any signed measure resulting in a meaningful integral (Walton, 1987).

A global energy balance argument equates the (steady-state) ERR, G, to the work done by the cohesive stresses

$$G = -\int_{-a_f}^{0} \sigma_f(x) v_{,x}(x,0)\, dx. \tag{28}$$

(See Walton (1987) and Schovanec and Walton (1987b) for a more thorough discussion of these energy considerations.)

The transformed stesses $\hat{\sigma}_f(p)$ and $\hat{\sigma}_e(p)$ are

$$\hat{\sigma}_f(p) = \frac{-a_f L_f}{1 + ia_f p}$$

$$\hat{\sigma}_e(p) = \frac{a_e L_e}{1 + ia_e p}.$$

Evaluating (9) by residues (noticing from (22)-(25) that $X_\infty^+ = 1$) gives

$$K_e = L_e / X^+(i/a_e) \text{ and } K_f = -L_f / X^+(i/a_f).$$

Thus, cancellation of the stress singularity requires

$$L_e / X^+(i/a_e) = L_f / X^+(i/a_f). \tag{29}$$

For the tractions (27), G in (28) can be expressed through application of Parseval's formula as

$$G = -\int_{-\infty}^{\infty} \check{\sigma}_f(p)\, \hat{v}_{,x}(p)\, dp \tag{30}$$

where $\check{\sigma}_f(p)$ denotes the inverse Fourier transform

$$\check{\sigma}_f(p) = \frac{1}{2\pi}\int_{-\infty}^{0} \sigma_f(x) e^{-ixp} dx = \frac{-a_f L_f}{2\pi(1 - ia_f p)}. \tag{31}$$

Utilizing (31), (30) can be evaluated by residues giving

$$G = L_f F^-(-i/a_f)$$

where $F^-(z)$ is the analytic extension of $\hat{v}_{,x}(p)$ to the lower half-plane. A general method for constructing $F^-(-i/a_f)$ was developed in Schovanec and Walton (1987a) with the result that

$$G = \left[\frac{a_e - a_f}{a_e + a_f}\right] \frac{a_f L_e^2}{2} \frac{X^+(i/a_f) X^-(-i/a_f)}{[X^+(i/a_e)]^2}. \tag{32}$$

For numerical evaluation, it is useful to introduce dimensionless parameters. Let $m(t/\tau) \equiv \mu(t)/\mu_\infty$ where $\mu_\infty \equiv \mu(\infty)$, and τ is a characteristic time scale. One then has

$$\tilde{\mu}(r) = \mu_\infty \tilde{m}(r\tau) = \mu_\infty \left[m(0) + \int_0^\infty e^{-tr\tau} dm(t)\right].$$

Also, dimensionless parameters α, γ, δ, ω, ϵ, and β_j, $j = 1,2,3$ are defined by

$$\alpha = c_T^* \tau / a_e, \quad \gamma = v/c_T^*, \quad \epsilon = a_f/a_e, \quad \delta = c_L/c_T,$$

$$\omega = c_R/c_T, \text{ and } \beta_j = a_e q_j(v). \tag{33}$$

The equilibrium shear wave speed was chosen for the velocity normalizer to facilitate comparison with the mode III results in Walton (1987). For constant Poisson's ratio, one has $\delta = c_L^*/c_T^* = \sqrt{2(1-\nu)/(1-2\nu)}$, $\omega = c_R^*/c_T^*$, and ω is the unique positive root of the "Rayleigh" equation

$$(2-\omega^2)^2 = 4\sqrt{1-\omega^2}\sqrt{1-(\omega/\delta)^2}$$

with $\omega < 1 < \delta$. Also, $\gamma_1(s)$ and $\gamma_2(s)$ become

$$\gamma_1(s) = \sqrt{1 - (\gamma/\delta)^2/\tilde{m}(\tau s)}$$

$$\gamma_2(s) = \sqrt{1 - \gamma^2/\tilde{m}(\tau s)},$$

and the four cases that must be considered are

$$0 \le \gamma < \omega, \quad \omega \le \gamma < 1, \quad 1 \le \gamma < \delta, \text{ and } \delta \le \gamma < \omega c_T/c_T^*.$$

Incorporating dimensionless parameters and utilizing (22)-(26) and (32), one has

$$G = \frac{a_e L_e^2}{2\mu_\infty}\left[\frac{1-\epsilon}{1+\epsilon}\right] g \tag{34}$$

where

$$g = g_1 g_2 g_3 \tag{35}$$

with

$$g_1 = 1/[\tilde{m}(\alpha\gamma/\epsilon)]^2 \tag{36}$$

and g_2, g_3 varying from case to case.

Case 1. $0 \le \gamma \le \omega$

Here, $\beta_1 = \beta_2 = \beta_3 = 0$,

$$g_2 = \sqrt{1 - (\gamma/\delta)^2/\tilde{m}(\alpha\gamma/\epsilon)},$$

and

$$g_3 = \gamma^2 / R(\alpha\gamma/\epsilon) \tag{37}$$

where

$$R(s) = 4\sqrt{1-\gamma^2/\tilde{m}(s)}\sqrt{1-(\gamma/\delta)^2/\tilde{m}(s)} - (2 - \gamma^2/\tilde{m}(s))^2. \tag{38}$$

Case 2. $\omega < \gamma < 1$

Again, $\beta_1 = \beta_2 = 0$ and g_2 is given by (37). However, $\beta_3 > 0$ is now the unique positive root of the equation

$$\tilde{m}(\alpha\gamma\beta_3) = (\gamma/\omega)^2 \tag{39}$$

and from (23), (26), and (32) one has

$$g_3 = \frac{[1-(\epsilon\beta_3)^2}{[1+\beta_3]^2} \frac{\gamma^2}{R(\alpha\gamma/\epsilon)}. \tag{40}$$

Case 3. $1 \le \gamma < \delta$

Again, g_2, β_1, and β_3 are as in Case 2, but $\beta_2 > 0$ is now defined as the unique root of

$$\tilde{m}(\alpha\gamma\beta_2) = \gamma^2. \tag{41}$$

More care is required here in calculating g_3 than in Case 2. Equations (18), (24), (26), and (32) are relevant, and at issue is the evaluation of $\lim_{z \to -i/a_f} J_3(z)$. If $1 < \epsilon\beta_2$, the Plemelj formula must be used and the resulting integral is a principal value, whereas for $1 > \epsilon\beta_2$, $J_3(z)$ is analytic at $z = -i/a_f$. In the former case, one concludes that

$$\lim_{p \to 0+} J_3(p - i/a_f) = i\theta(-i/a_f) + J_3(-i/a_f)$$

where the last integral is a principal value. It follows that

$$\lim_{p \to 0+} \exp(J_3(p - i/a_f)) = \exp(i\theta(-i/a_f))\exp(J_3(-i/a_f)).$$

But

$$\exp(i\theta(-i/a_f))$$

$$= \exp(i\arg(T_3((0+) - i/a_f))) = \frac{R(\alpha\gamma/\epsilon)}{|R(\alpha\gamma/\epsilon)|} \tag{42}$$

where $R(s)$ denotes the complex "Rayleigh" function (cf., (14))

$$R(s) = i4\sqrt{\gamma^2/\tilde{m}(s) - 1}\sqrt{1-(\gamma/\delta)^2/\tilde{m}(s)} - (2 - \gamma^2/\tilde{m}(s))^2. \tag{43}$$

Combining (18), (24), (26), (32), (38), (42), and (43) it follows that

$$g_3 = \frac{[1-(\epsilon\beta_3)^2]}{[1-(\epsilon\beta_2)^2]} \frac{[1+\beta_2]^2}{[1+\beta_3]^2} \exp(I_1^3 + I_2^3 - 2I_3^3) g_4 \tag{44}$$

where

$$g_4 = \begin{cases} \gamma^2/R(\alpha\gamma/\epsilon), & \text{if } \epsilon\beta_2 < 1 \\ \gamma^2/|R(\alpha\gamma/\epsilon)|, & \text{if } \epsilon\beta_2 > 1, \end{cases} \tag{45}$$

Downloaded 03 May 2010 to 171.66.16.244. Redistribution subject to ASME license or copyright; see http://www.asme.org/terms/Terms_Use.cfm

and

$$I_1^3=\frac{1}{\pi}\int_0^{\epsilon\beta_2}\theta\left(\frac{\alpha\gamma}{\epsilon}t\right)\frac{dt}{t+1},$$

$$I_2^3=\frac{1}{\pi}\int_0^{\epsilon\beta_2}\theta\left(\frac{\alpha\gamma}{\epsilon}t\right)\frac{dt}{t-1}, \tag{46}$$

$$I_3^3=\frac{1}{\pi}\int_0^{\beta_2}\theta(\alpha\gamma t)\frac{dt}{t+1}.$$

In (45), $R(\alpha\gamma/\epsilon)$ is real and given by (38) when $\epsilon\beta_2<1$, whereas it is complex and defined by (43) when $\epsilon\beta_2>1$.

Case 4. $\delta\le\gamma<c_R/c_T^*=\omega c_T/c_T^*$

Here, as for Case 3, β_3 and β_2 are given by (39) and (41) but $\beta_1>0$ is now the unique positive root of

$$\bar{m}(\alpha\gamma\beta_1)=(\gamma/\delta)^2. \tag{47}$$

For g_2 one finds

$$g_2=\left[\frac{1-(\gamma/\delta)^2/\bar{m}(\alpha\gamma/\epsilon)}{1-(\epsilon\beta_1)^2}\right]^{1/2} \tag{48}$$

and by arguments similar to those made in Case 3,

$$g_3=\frac{[1-(\epsilon\beta_1)^2]}{[1-(\epsilon\beta_2)^2]}\frac{[1-(\epsilon\beta_3)^2]}{[1+\beta_1]}\frac{[1+\beta_2]^2}{[1+\beta_3]^2}\times\exp(I_1^4+I_2^4-2I_3^4)g_4 \tag{49}$$

where

$$g_4=\begin{cases}\gamma^2/R(\alpha\gamma/\epsilon), & \text{if } \epsilon\beta_2<1 \text{ or } \epsilon\beta_1>1\\ \gamma^2/|R(\alpha\gamma/\epsilon)|, & \text{if } \epsilon\beta_1<1<\epsilon\beta_2\end{cases} \tag{50}$$

$$I_1^4=\frac{1}{\pi}\int_{\epsilon\beta_1}^{\epsilon\beta_2}\theta\left(\frac{\alpha\gamma}{\epsilon}t\right)\frac{dt}{t+1},$$

$$I_2^4=\frac{1}{\pi}\int_{\epsilon\beta_1}^{\epsilon\beta_2}\theta\left(\frac{\alpha\gamma}{\epsilon}t\right)\frac{dt}{t-1}, \tag{51}$$

$$I_3^4=\frac{1}{\pi}\int_{\beta_1}^{\beta_2}\theta(\alpha\gamma t)\frac{dt}{t+1}.$$

As with Case 3, $R(\alpha\gamma/\epsilon)$ in (50) is real and given by (38) when $\epsilon\beta_2<1$ or $\epsilon\beta_1>1$, whereas it is complex and given by (43) when $\epsilon\beta_1<1<\epsilon\beta_2$.

4 Special Cases and Numerical Examples

The general results of the previous section are illustrated here by considering a few special cases and numerical examples: elastic material, quasi-static viscoelastic crack growth, and dynamic viscoelastic crack growth without a failure zone.

Elastic. Setting $\bar{m}(s)\equiv m(0)$ in the general result corresponds to an elastic material with shear modulus equal to the short-time viscoelastic value. One then concludes from (34)–(38) that

$$G_{el}=\frac{a_eL_e^2}{2\mu}\left[\frac{1-\epsilon}{1+\epsilon}\right]\sqrt{1-(\gamma/\delta)^2}\frac{\gamma^2}{R(\gamma)} \tag{52}$$

where $R(\gamma)=2\sqrt{1-\gamma^2}\sqrt{1-(\gamma/\delta)^2}-(2-\gamma^2)^2$. The influence of the failure zone occurs only in the term $(1-\epsilon)/(1+\epsilon)$. Also one can show that G_{el} is an increasing function of γ that becomes infinite as $\gamma\to\omega$, i.e., when the crack speed reaches the Rayleigh wave speed.

Quasi-Static Viscoelastic Crack Growth. One recovers the quasi-static, steady-state solution from the general result by letting $c_T^*\to\infty$ with v fixed. Since $\alpha\gamma/\epsilon=\tau v/a_f$ is independent of c_T^*, it follows from (34)–(38) that the quasi-static ERR for constant Poisson's ratio is

$$G_{qs}=\frac{a_eL_e^2}{2\mu_\infty}\left[\frac{1-\epsilon}{1+\epsilon}\right]\frac{(1-\nu)}{\bar{m}(\alpha\gamma/\epsilon)}. \tag{53}$$

If Poisson's ratio is not constant, then ν in (53) is replaced by $\bar{\nu}(v/a_f)$ where $\bar{\nu}(s)$ is defined by

$$\frac{(1-2\bar{\nu}(s))}{2(1-\bar{\nu}(s))}=\left[\frac{\bar{c}_T(s)}{\bar{c}_L(S)}\right]^2=\frac{\bar{\mu}(s)}{\bar{\lambda}(s)+2\bar{\mu}(s)}.$$

From (53) one readily recovers the well-known facts that as $\gamma\to0$, G_{qs} depends only upon the equilibrium material properties, while as $\epsilon\to0$, (no failure zone) G_{qs} depends only upon the instantaneous material properties. For constant Poisson's ratio, G_{qs} is a decreasing function of crack speed, whereas such may not be the case when Poisson's ratio is not constant.

Dynamic Crack Growth Without a Failure Zone. The limiting case of vanishing failure zone is extracted from the general result by letting $\epsilon\to0$. It then follows that

$$G_{nf}=\frac{a_eL_e^2}{2\mu_0}\frac{[1+\beta_2]^2[v/c_T]^2}{[1+\beta_1][1+\beta_3]^2}\frac{\sqrt{1-(v/c_T)^2}}{R_0}\exp(-2I_3) \tag{54}$$

where

$$R_0=4\sqrt{1-(v/c_T)^2}\sqrt{1-(v/c_L)^2}-(2-(v/c_T)^2)^2$$

and I_3 is given in either (46_3) or (51_3). The four different cases give

Case 1. $\beta_1=\beta_2=\beta_3=I_3=0$;

Case 2. $\beta_1=\beta_2=I_3=0$, and $\beta_3>0$ is given by (39);

Case 3. $\beta_1=0$, β_2, β_3, and $I_3=I_3^3$ are given by (41), (39), and (46_3) with $0<\beta_2<\beta_3$;

Case 4. β_1, β_2, β_3, and $I_3=I_3^4$ are given by (48), (41), (39), and (51_3) with $0<\beta_1<\beta_2<\beta_3$.

Finally, it can be shown that G_{nf} as given in (54) is equivalent to the result of Popelar and Atkinson (1980) derived by a local work argument based upon the singular stress field. However, the form (54) is quite different from theirs and exhibits more clearly the dependence of the ERR upon material parameters.

Numerical Examples. Numerical examples were computed for both a standard linear solid with shear modulus

$$\mu(t)=\mu_\infty m_s(t/\tau)=\mu_\infty(1+\eta\exp(-t/\tau)) \tag{55}$$

and a power-law material with shear modulus

$$\mu(t)=\mu_\infty m_p(t/\tau)=\mu_\infty(1+\eta(1+t/\tau)^{-n}) \tag{56}$$

where $n>0$. For comparison purposes, the two models are given the same short-time and long-time wave speeds and one has $c_R/c_R^*=c_T/c_T^*=c_L/c_L^*=\sqrt{1+\eta}$ and $c_R/c_T^*=\omega\sqrt{1+\eta}$. Thus, γ must lie on the interval $0\le\gamma<\omega\sqrt{1+\eta}$. The number of cases to be considered is determined by computing $\delta=\sqrt{2(1-\nu)/(1-2\nu)}$ from the given Poisson's ratio, ν, and then solving the Rayleigh equation for $\omega=c_R^*/c_T$. There are always at least the two cases where $0\le\gamma\le\omega$ and $\omega<\gamma\le\delta$, and if $\omega\sqrt{1+\eta}\le1$, that is all there are. However, if $1<\omega\sqrt{1+\eta}\le\delta$, there are exactly three cases and if $\delta<\omega\sqrt{1+\eta}$, all four cases occur.

Considering first the standard linear solid, one sees from (55) that

$$\bar{m}(s)=\frac{1+s(1+\eta)}{1+s} \tag{57}$$

and (39), (41), and (47) are easily inverted for β_3, β_2, and β_1 giving

Downloaded 03 May 2010 to 171.66.16.244. Redistribution subject to ASME license or copyright; see http://www.asme.org/terms/Terms_Use.cfm

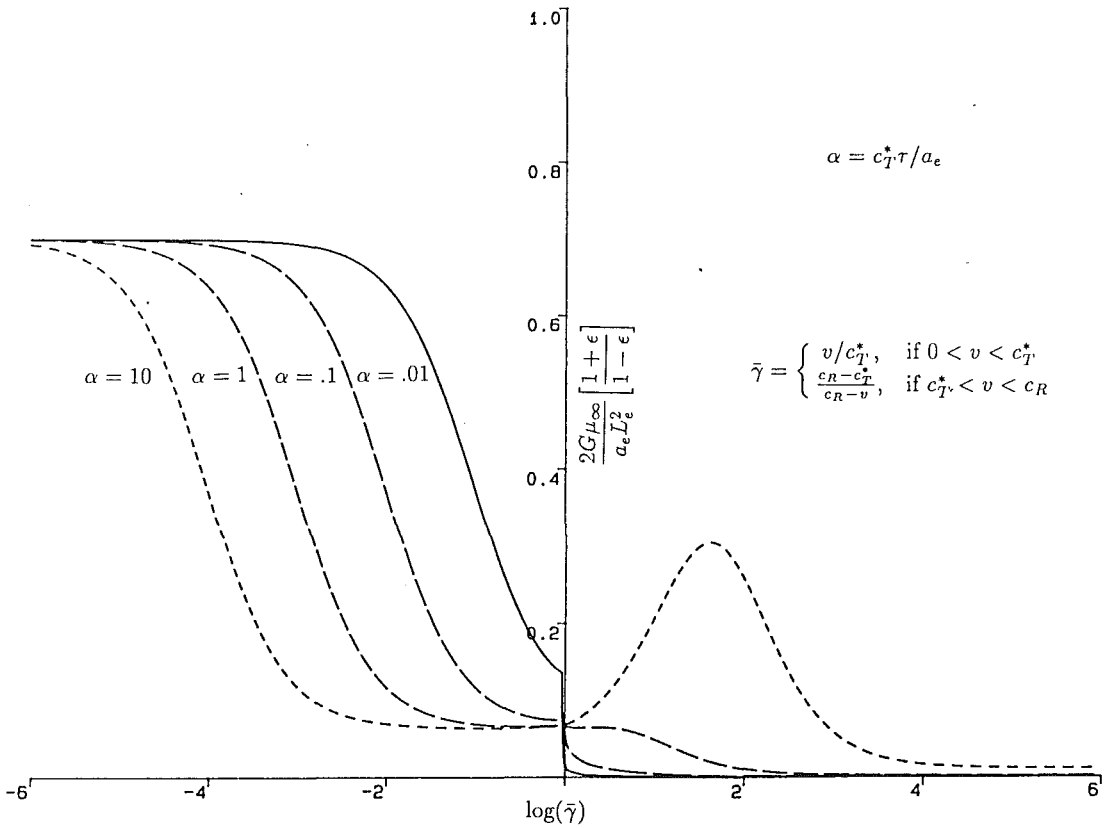


Fig. 1 Nondimensionalized ERR, g, versus (scaled) crack speed, $\bar{\gamma}$ (in 58), for a standard linear solid with $\epsilon = a_f/a_e = 0.1$, $\eta = (\mu(0) - \mu(\infty))/\mu(\infty) = 10$, ν = Poisson's ratio = .3, and $\alpha = c_T^* \tau / a_e = .01, .1, 1, 10$

$$\alpha\gamma\beta_1 = \left[\frac{(\gamma/\delta)^2 - 1}{1 + \eta - (\gamma/\delta)^2}\right],$$

$$\alpha\gamma\beta_2 = \left[\frac{\gamma^2 - 1}{1 + \eta - \gamma^2}\right],$$

$$\alpha\gamma\beta_3 = \left[\frac{(\gamma/\omega)^2 - 1}{1 + \eta - (\gamma/\omega)^2}\right].$$

One clearly has $\beta_1 < \beta_2 < \beta_3$.

The general result (34) is now readily applied. Since β_2 never gets very large in practice, the quadratures in (46) and (51) are not troublesome, allowing for I_2 to possibly be principal value integrals. Figure 1 shows plots of g versus a scaled crack speed, $\bar{\gamma}$, defined by

$$\bar{\gamma} = \begin{cases} \gamma, & \text{if } 0 < \gamma < 1, \\ \left[\dfrac{\omega\sqrt{1+\eta} - 1}{\omega\sqrt{1+\eta} - \gamma}\right], & \text{if } 1 < \gamma < \omega\sqrt{1+\eta} \end{cases} \tag{58}$$

$$= \begin{cases} v/c_T^*, & \text{if } 0 < v < c_T^*, \\ \dfrac{c_R - c_T^*}{c_R - v}, & \text{if } c_T^* < v < c_R. \end{cases}$$

Thus, $0 < \bar{\gamma} < \infty$ and $\bar{\gamma} = \infty$ corresponds to $v = c_R$. (c.f., Walton (1987))

For illustrative purposes and in the absence of any generally agreed upon constitutive model for the failure zone under dynamic conditions, it is more convenient to take $\epsilon \equiv a_f/a_e$ constant and allow $\lambda \equiv L_e/L_f$ to vary as required to cancel the stress singularity. Thus, in Fig. 1, ϵ was arbitrarily given the value $\epsilon = .01$. Taking λ constant (or some specified function of γ) and letting $\epsilon = \epsilon(\gamma)$ offers no difficultly, in principle; only a little extra computation is required (c.f., Walton (1987)).

It should be emphasized that the energy release rate function (in (34)) $g = g(\gamma)$ plotted in Fig. 1 is seen from (34) to be dimensionless. Moreover, if $g_{el}(\gamma)$ and $g_{qs}(\gamma)$ are the corresponding elastic and quasi-static viscoelastic ERR made dimensionless in the same manner, then from (52), (53), and (34)–(38) one has $g(0) = g_{el}(0) = g_{qs}(0) = 1 - \nu$.

The G versus γ curves in Figs. 1–7 have application to the question of stability of steady-state crack speeds since $G(\gamma)$ represents the energy from the applied tractions made available to the failure zone to propagate the crack tip. If, for example, one assumes that the energy required to propagate the crack tip is speed-independent, then speeds γ for which $dg/d\gamma < 0$ can be interpreted as stable crack speeds, whereas those for which $dg/d\gamma > 0$ would be unstable. For a more complicated required energy versus crack speed relationship, the above argument is easily modified in the obvious way.

It should also be observed that $\alpha = c_T^* \tau / a_f$ significantly affects the behavior of $g(\gamma)$. If $\alpha_1 < \alpha_2$, then $g(\gamma, \alpha_1) > g(\gamma, \alpha_2)$ for small γ, whereas $g(\gamma, \alpha_1) < g(\gamma, \alpha_2)$ for large γ. Moreover, for α small enough, $dG/d\gamma < 0$ for all $0 \le \gamma \le c_R/c_T^*$ and hence all crack speeds below the short-time Rayleigh wave speed would be stable. In contrast, for α large there exists an interval of crack speeds for which $dG/d\gamma > 0$ and which are thus unstable. (c.f., Walton (1987)).

Figure 2 displays calculations for power-law material corresponding to Fig. 1 for a standard linear solid. For the power-law model (56), $\tilde{m}(s)$ must be approximated by a quadrature and equations (39), (41), and (48) solved numerically for the β_j. Otherwise, g is computed as for the standard linear solid.

Downloaded 03 May 2010 to 171.66.16.244. Redistribution subject to ASME license or copyright; see http://www.asme.org/terms/Terms_Use.cfm

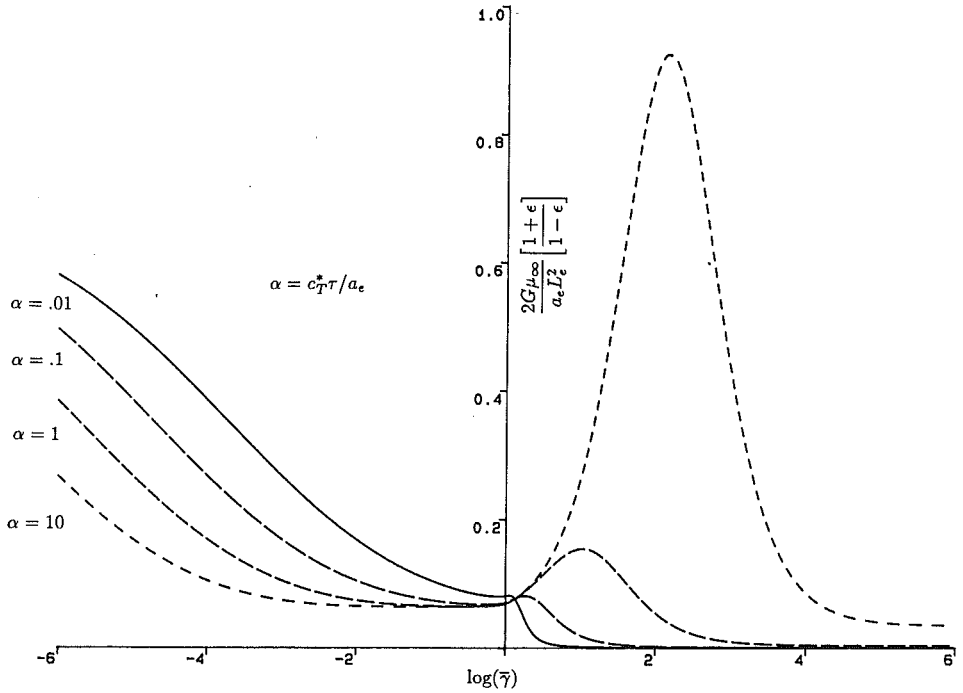


Fig. 2 Same as Fig. 1 except for a power-law material with exponent $n = .3$

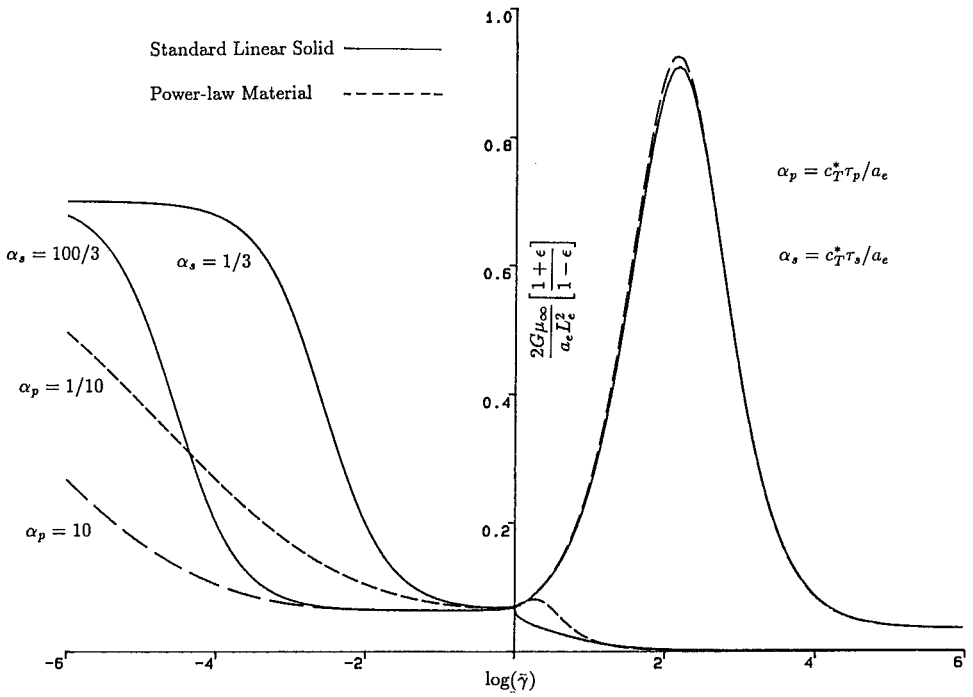


Fig. 3 Comparison of the power-law material in Fig. 2, with $\alpha_p = .1, 10$, to the standard linear solid in Fig. 1, with $\alpha_s/\alpha_p = 10/3$

For meaningful comparison of the power-law and standard linear solid models, it is useful to introduce separate relaxation times, τ_p and τ_s, respectively. The dimensionless α_p and α_s are defined accordingly. It is natural to chose τ_p and τ_s so that the shear modulus for each model has the same slope at $t = 0$. For $n = .3$, this requires that $\alpha_s/\alpha_p = 10/3$. These two models are compared in Fig. 3. Close agreement occurs for large α or large γ, whereas the opposite is the case for small α or small γ. This is due primarily to the significant influence $\bar{m}(\alpha\gamma/\epsilon)$ has upon $g(\gamma)$. The asymptotic behavior of $\bar{m}(s)$ for large s is determined by the asymptotic behavior of $m(t)$ for small t. Thus, when $\mu_s(t)$ and $\mu_p(t)$ have the same slope at $t = 0$, $\bar{m}_s(\alpha\gamma/\epsilon)$ and $\bar{m}_p(\alpha\gamma/\epsilon)$ are in close agreement when $\alpha\gamma/\epsilon$ is large and can differ greatly for $\alpha\gamma/\epsilon$ small. As Fig. 3 confirms, the standard linear solid model predicts significantly larger values for $g(\gamma)$ when γ is small than does the power-law model, with the reverse being true when α is small and $\gamma > \omega$. A similar effect is seen when two power-law models with different exponents are compared.

Figure 4 illustrates the influence of $\eta \equiv (\mu(0) - \mu(\infty))/$

Downloaded 03 May 2010 to 171.66.16.244. Redistribution subject to ASME license or copyright; see http://www.asme.org/terms/Terms_Use.cfm

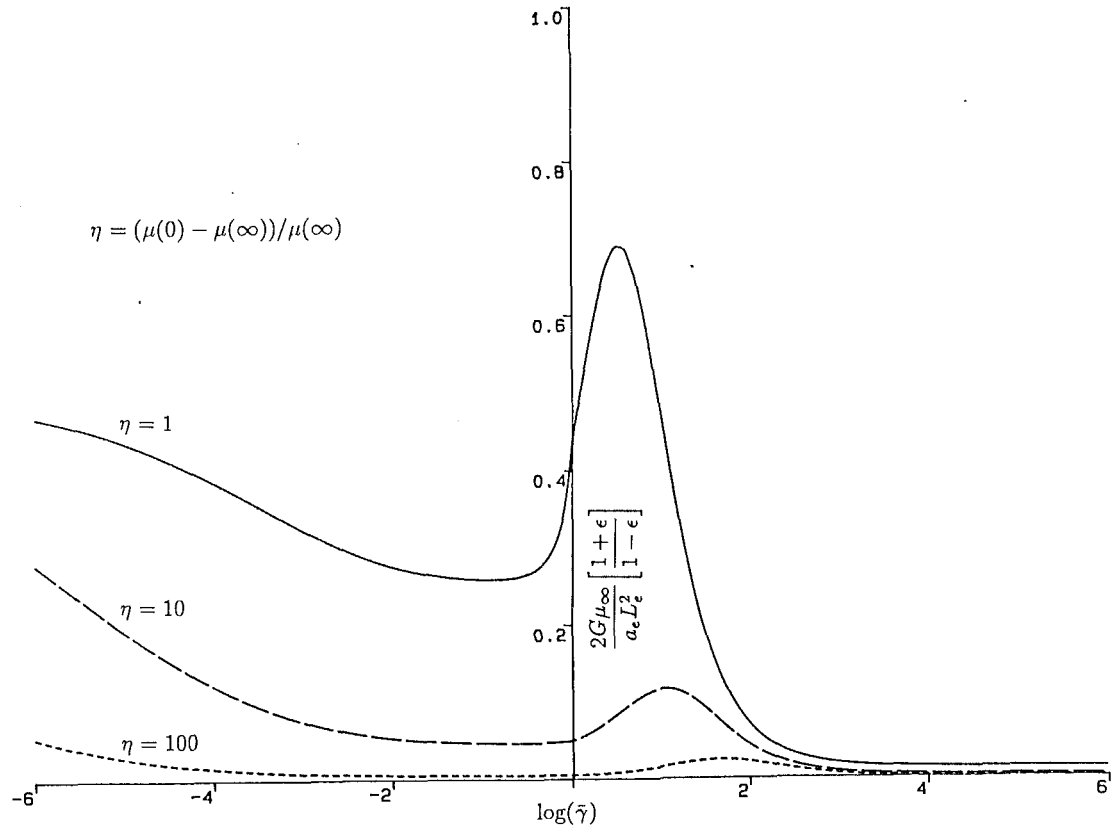


Fig. 4 Same as Fig. 2 except for a power-law material with $\alpha = 1$, $\nu = .49$, and $\eta = (\mu(0) - \mu(\infty))/\mu(\infty) = 1, 10, 100$

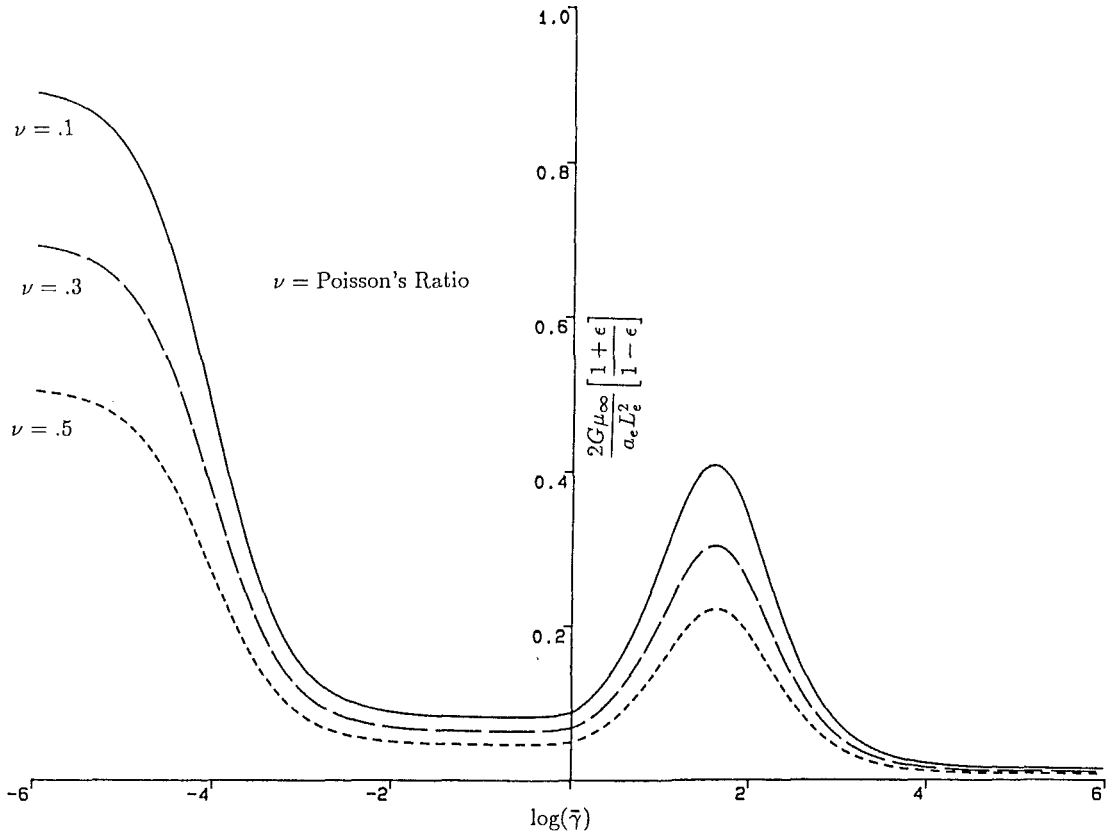


Fig. 5 Same as Fig. 1 except for a standard linear solid with $\alpha = 10$ and $\nu = .1, .3, .5$

Downloaded 03 May 2010 to 171.66.16.244. Redistribution subject to ASME license or copyright; see http://www.asme.org/terms/Terms_Use.cfm

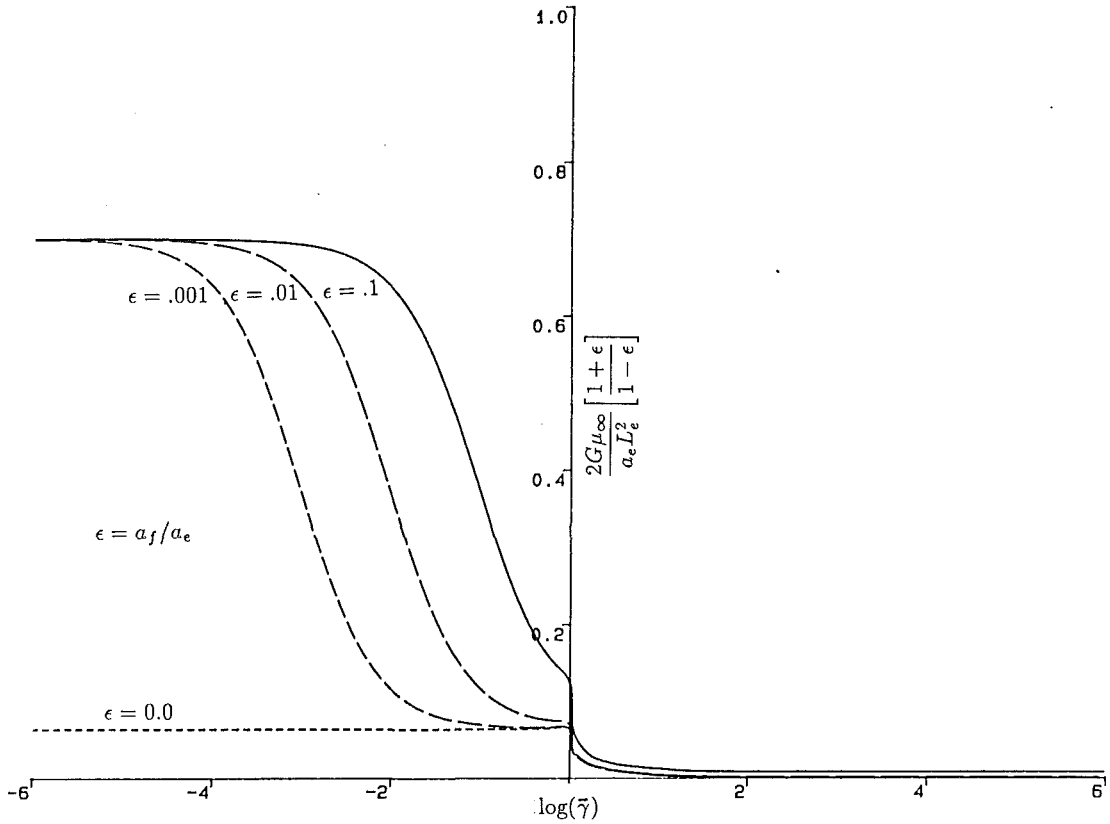


Fig. 6 Same as Fig. 1 except for a standard linear solid with $\alpha = .1$ and $\epsilon = .1, .01, .001, 0.0$

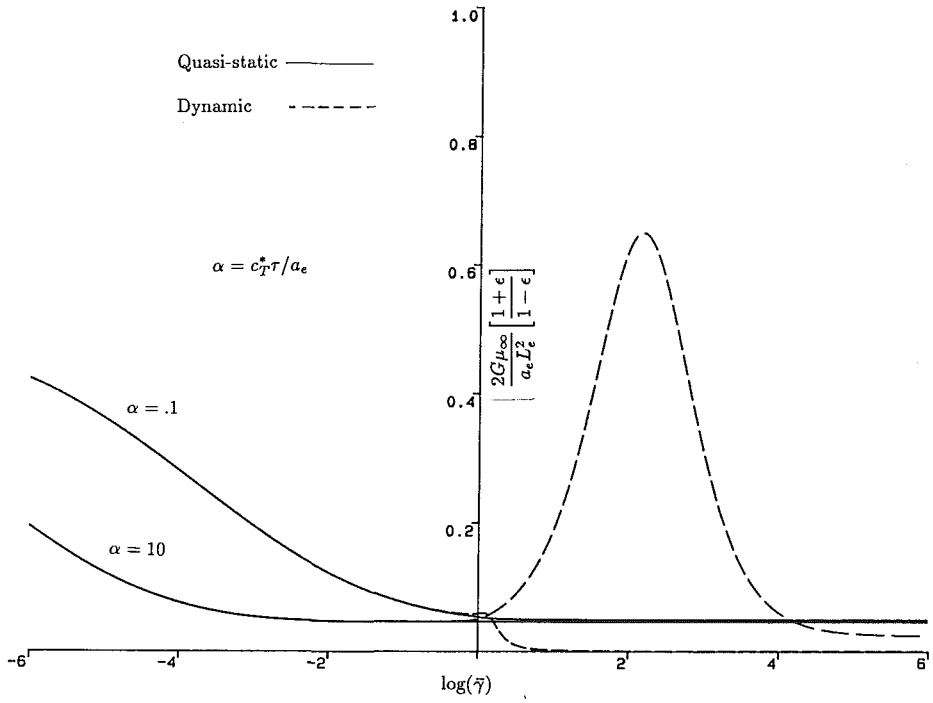


Fig. 7 Dynamic versus quasi-static comparison for a power-law material with $\epsilon = .01$, $\eta = 10$, $\nu = .49$, $n = .3$, and $\alpha = .1, 10$

$\mu(\infty)$ upon $g(\gamma)$. For small η, the response is more elastic like, whereas as η increases the effect of viscous energy dissipation becomes more pronounced. In Figs. 5 and 6, the standard linear solid model is used to illustrate the effect of Poisson's ratio and $\epsilon \equiv a_f/a_e$, respectively, upon $g(\gamma)$. The contrast between $\epsilon = 0$ and $\epsilon > 0$ in Fig. 6 merits comment. Again, the significant term is $\bar{m}(\alpha\gamma/\epsilon)$. For $\epsilon = 0$, it becomes $\bar{m}(\infty) = m(0) = 1 + \eta$ for all γ. Whereas, if $\epsilon > 0$,

Downloaded 03 May 2010 to 171.66.16.244. Redistribution subject to ASME license or copyright; see http://www.asme.org/terms/Terms_Use.cfm

$\lim_{\gamma \to 0} \tilde{m}(\alpha\gamma/\epsilon) = \tilde{m}(0) = 1$. Thus, predictions of $G(\gamma)$ not based upon a failure zone model will be significantly lower for small γ than those with a failure zone.

Figure 7 compares the quasi-static $g_{qs}(\gamma)$ and dynamic $g(\gamma)$ for power-law material. The quasi-static and dynamic predictions for $G(\gamma)$ are in close agreement for all crack speeds from zero to the equilibrium shear wave speed. The quasi-static analysis predicts that all crack speeds below c_R are stable, whereas the dynamic analysis for large α predicts an interval of unstable speeds. Moreover, there are values of α for which the quasi-static and dynamic predictions for $G(\gamma)$ are very close for nearly all crack speeds below c_R, though as $\gamma \to c_R/c_T^*$, the dynamic $G(\gamma)$ drops well below the quasi-static value. Finally, for small α, the quasi-static and dynamic $G(\gamma)$ agree up to nearly the equilibrium shear wave speed beyond which the dynamic values suddenly drop well below the quasi-static ones.

Acknowledgment

This author wishes to express his gratitude to Prof. J. R. Whiteman and the Brunel Institute of Computational Mathematics, Brunel University, for their hospitality, support, and assistance during the sabbatical year in which this paper was prepared.

References

Achenbach, J. D., 1973, *Wave Propagation in Elastic Solids*, North-Holland, Amsterdam.

Atkinson, C., 1979, "A Note on Some Dynamic Crack Problems in Linear Viscoelasticity," *Arch. Mech. Stos.*, Vol. 31, pp. 829–849.

Atkinson, C., and Coleman, C. J., 1977, "On Some Steady-State Moving Boundary Problems in the Linear Theory of Viscoelasticity," *J. Inst. Maths. Applics.*, Vol. 20, pp. 85–106.

Atkinson, C., and List, R. D., 1972, "A Moving Crack Problem in a Viscoelastic Solid," *Int. J. Engng. Sci.*, Vol. 10, pp. 309–322.

Atkinson, C., and Popelar, C. H., 1979, "Antiplane Dynamic Crack Propagation in a Viscoelastic Strip," *J. Mech. Phys. Solids*, Vol. 27, pp. 431–439.

Barenblatt, G. I., 1962, "The Mathematical Theory of Equilibrium Cracks in Brittle Fracture," *Advances in Applied Mechanics*, Vol. 7, Academic Press, pp. 55–129.

Herrmann, J. M., and Walton, J. R., 1989, "On the Energy Release Rate for Dynamic Transient Anti-Plane Shear Crack Propagation in a General Linear Viscoelastic Body," *J. Mech. Phys. Solids*, Vol. 37, No. 5, pp. 619–645.

Knauss, W. G., 1973, "On the Steady Propagation of a Crack in a Viscoelastic Sheet: Experiments and Analysis," *Deformation and Fracture of High Polymer*, H. H. Kausch, and R. Jaffee eds., Plenum Press, pp. 501–541.

Popelar, C. H., and Atkinson, C., 1980, "Dynamic Crack Propagation in a Viscoelastic Strip," *J. Mech. Phys. Solids*, Vol. 28, pp. 79–93.

Schapery, R. A., 1974, "A Theory of Crack Initiation and Growth in Viscoelastic Media I. Theoretical Development," *Int. J. Frac.*, Vol. 11, pp. 141–159.

Schapery, R. A., 1984, "Correspondence Principles and a Generalized J Integral for Large Deformation and Fracture Analysis of Viscoelastic Media," *Int. J. Frac.*, Vol. 25, pp. 195–223.

Schovanec, L., and Walton, J. R., 1987a, "The Energy Release Rate for a Quasi-Static Mode I Crack in a Nonhomogeneous Viscoelastic Body," *J. Eng. Frac. Mech.*, Vol. 54, pp. 635–541.

Schovanec, L., and Walton, J. R., 1987b, "The Dynamic Energy Release Rate for Two Parallel Steadily Propagating Mode III Cracks in a Viscoelastic Body," *Int. J. Frac.*, Vol. 41, pp. 133–155.

Walton, J. R., 1982, "On the Steady-State Propagation of an Anti-Plane Shear Crack in an Infinite General Linearly Viscoelastic Body," *Quart. Appl. Math.*, Vol. 40, pp. 37–52.

Walton, J. R., 1983, "Dynamic Steady-State Fracture Propagation in General Linear Viscoelastic Material," *Workshop on Dynamic Fracture*, W. G. Knauss, K. Ravi-Chandar, and A. J. Rosakis, eds., California Institute of Technology, pp. 197–204.

Walton, J. R., 1985, "The Dynamic Steady-State Propagation of an Anti-Plane Shear Crack in a General Linearly Viscoelastic Layer," ASME JOURNAL OF APPLIED MECHANICS, Vol. 52, pp. 853–856.

Walton, J. R., 1987, "The Dynamic Energy Release Rate for a Steadily Propagating Anti-Plane Shear Crack in a Linearly Viscoelastic Body," ASME JOURNAL OF APPLIED MECHANICS, Vol. 54, pp. 635–641.

Willis, J. R., 1967, "Crack Propagation in Viscoelastic Media," *J. Mech. Phys. Solids*, Vol. 15, pp. 229–240.

Downloaded 03 May 2010 to 171.66.16.244. Redistribution subject to ASME license or copyright; see http://www.asme.org/terms/Terms_Use.cfm

Effects of Crack Surface Heat Conductance on Stress Intensity Factors

An-Yu Kuo
Associate,
Structural Integrity Associates,
San Jose, CA 95118
Assoc. Mem. ASME

Effects of crack surface heat conductance on stress intensity factors of modes I, II, and III are investigated. The crack problem is first solved by assuming perfect (infinite) heat conductance at crack surfaces. Finite heat conductance at crack surfaces is then accounted for by imposing a set of distributed dipoles at the crack surfaces. Distribution function of the dipoles is the solution of a Fredholm integral equation. It is shown that, for cracks in a homogeneous, isotropic, linear elastic solid, the degree of thermal conductivity at crack surfaces will affect the magnitude of mode I and mode II stress intensity factors but not mode III stress intensity factor. It is also shown that, for a geometrically symmetric cracked solid, only the mode II stress intensity factor will be influenced by different crack surface heat conductance even if the thermal loading is not symmetric. More importantly, for a given material thermal conductivity (K) *and crack surface heat convection coefficient* (h), *effects of crack surface heat conductance on stress intensity factors is found to depend upon crack size. This "size effect" implies that, for a given set of* K *and* h, *an extremely small crack can be treated as if the crack surfaces are insulated and a very long crack can be treated as if the crack surfaces are perfectly heat conductive. As an example, the problem of a finite crack in an infinite plate subjected to a constant temperature gradient at infinity is studied.*

1 Introduction

Stress intensity factors caused by thermal stresses have been of prime interest in aerospace, nuclear, and electronic industries. Conventionally, crack surfaces have been assumed to be insulated (e.g., Sih, 1962) when solving for thermal stress intensity factors. Such an assumption often leads to a question of how much the stress intensity factors will change when a more realistic thermal conductivity is used for crack surfaces. Barber (1976, 1979) has obtained a steady-state thermal stress solution to the problem of a circular crack in an elastic solid with finite crack surface heat conductance. This paper outlines an analytical and numerical scheme for calculating thermal stress intensity factors (transient and steady-state) for cracks with surface heat conductance ranging from zero (insulated) to infinity (perfectly conductive) in the sense of the Biot number first employed by Barber (1976, 1979) to this class of problem.

2 Formulation

As illustrated in Fig. 1, we consider a homogeneous, isotropic, linear elastic body V with a boundary surface S and a crack surface S_c. It is assumed that the crack surface S_c lies in a plane. It is also assumed that the quasi-static thermoelasticity theory is valid. Therefore, governing equations and initial and boundary conditions for any point P in the elastic body are

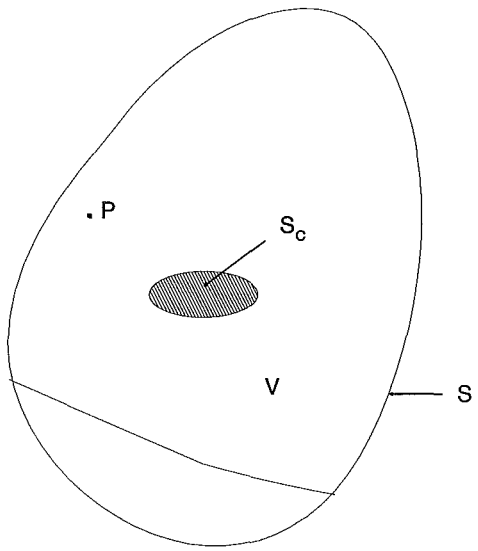


Fig. 1 A crack in an linear elastic solid

Contributed by the Applied Mechanics Division of THE AMERICAN SOCIETY OF MECHANICAL ENGINEERS for publication in the JOURNAL OF APPLIED MECHANICS.

Discussion on this paper should be addressed to the Technical Editor, Leon M. Keer, The Technological Institute, Northwestern University, Evanston, IL 60208, and will be accepted until two months after final publication of the paper itself in the JOURNAL OF APPLIED MECHANICS. Manuscript received by the ASME Applied Mechanics Division, July 11, 1989; final revision, June 26, 1989.

Copyright © 1990 by ASME
Downloaded 03 May 2010 to 171.66.16.244. Redistribution subject to ASME license or copyright; see http://www.asme.org/terms/Terms_Use.cfm

$$\xi \nabla^2 T = T_{,t} \qquad \xi = \frac{K}{\rho c} \tag{1}$$

$$\sigma_{ij,j} = 0 \tag{2}$$

$$\sigma_{ij} = 2G\left(\epsilon_{ij} + \frac{\nu}{1-2\nu}\epsilon_{mm}\delta_{ij} - \frac{\nu}{1-2\nu}\alpha T\delta_{ij}\right) \tag{3}$$

$$\epsilon_{ij} = (u_{i,j} + u_{j,i})/2 \tag{4}$$

$$T(P,0) = 0 \tag{5}$$

$$T(P,t) = T^o(P,t) \qquad P \text{ on } S_T \tag{6}$$

$$\frac{\partial T}{\partial n}(P,t) = q^o(P,t) \qquad P \text{ on } S_q \tag{7}$$

$$\frac{\partial T}{\partial n}(P,t) = \frac{\lambda}{L}[T(P^+,t) - T(P^-,t)] \qquad P \text{ on } S_c \tag{8}$$

$$\frac{\lambda}{L} = \frac{h}{K} \tag{9}$$

$$\sigma_{ij}n_j = F_i^o \qquad P \text{ on } S_\sigma \tag{10}$$

$$u_i = u_i^o \qquad P \text{ on } S_u \tag{11}$$

$$\sigma_{ij}n_j = 0 \qquad P \text{ on } S_c. \tag{12}$$

In the foregoing equations, K is thermal conductivity, ρ is mass density, c is specific heat, h is heat convection coefficient across the crack surface, P is a point within V, t is time, G is shear modulus, ν is Poisson's ratio, α is coefficient of thermal expansion, T^o is prescribed temperature on S_T, q^o is prescribed heat flux on S_q, $S = S_T + S_q$, P^+ and P^- stand for points at upper and lower crack surface, respectively, λ is the dimensionless Biot number (Barber, 1976, 1979), L is a characteristic length of the problem, F^o is prescribed traction on S_σ, u_i^o is the prescribed displacement on S_u, and $S = S_\sigma + S_u$. In equation (8), the crack surfaces are insulated when λ is zero and are perfectly heat conductive when λ is infinity. Since this is a linear problem, we can assume that

$$T(P,t) = T^{(1)}(P,t) + T^{(2)}(P,t) \tag{13}$$

$$\sigma_{ij}(P,t) = \sigma_{ij}^{(1)}(P,t) + \sigma_{ij}^{(2)}(P,t) \tag{14}$$

where functions with superscript (1) are solutions to the problem of $\lambda = \infty$ and functions with superscript (2) are complementary solutions which account for the proper crack surface thermal conductivity condition.

3 Solutions to Perfectly Conductive Crack Surfaces ($\lambda = \infty$)

$T^{(1)}$, $\sigma_{ij}^{(1)}$, and $u_i^{(1)}$ satisfy equations (1)–(12) except equation (8), which is replaced by

$$T^{(1)}(P^+,t) = T^{(1)}(P^-,t) \qquad P \text{ on } S_c. \tag{15}$$

In general, it is much easier to obtain temperature and stress intensity factor solutions to the problem of a perfectly heat conductive crack. Asymptotic stresses at the crack tip caused by thermal loading have been shown by Sih (1962) to have the same order of singularity ($-1/2$) and distribution functions. Kassir and Sih (1966) have shown that asymptotic stress solutions at the crack border are

$$\sigma_{nn}^{(1)} = [K_{\mathrm{I}}^{(1)} f_{nn}(\theta) + K_{\mathrm{II}}^{(1)} g_{nn}(\theta)]/\sqrt{2\pi r} \tag{16}$$

$$\sigma_{zz}^{(1)} = [K_{\mathrm{I}}^{(1)} f_{zz}(\theta) + K_{\mathrm{II}}^{(1)} g_{zz}(\theta)]/\sqrt{2\pi r} \tag{17}$$

$$\sigma_{ss}^{(1)} = [K_{\mathrm{I}}^{(1)} f_{ss}(\theta) + K_{\mathrm{II}}^{(1)} g_{ss}(\theta)]/\sqrt{2\pi r} \tag{18}$$

$$\sigma_{nz}^{(1)} = [K_{\mathrm{I}}^{(1)} f_{nz}(\theta) + K_{\mathrm{II}}^{(1)} g_{nz}(\theta)]/\sqrt{2\pi r} \tag{19}$$

$$\sigma_{sz}^{(1)} = [K_{\mathrm{III}}^{(1)} f_{sz}(\theta)]/\sqrt{2\pi r} \tag{20}$$

$$\sigma_{ns}^{(1)} = [K_{\mathrm{III}}^{(1)} f_{ns}(\theta)]/\sqrt{2\pi r} \tag{21}$$

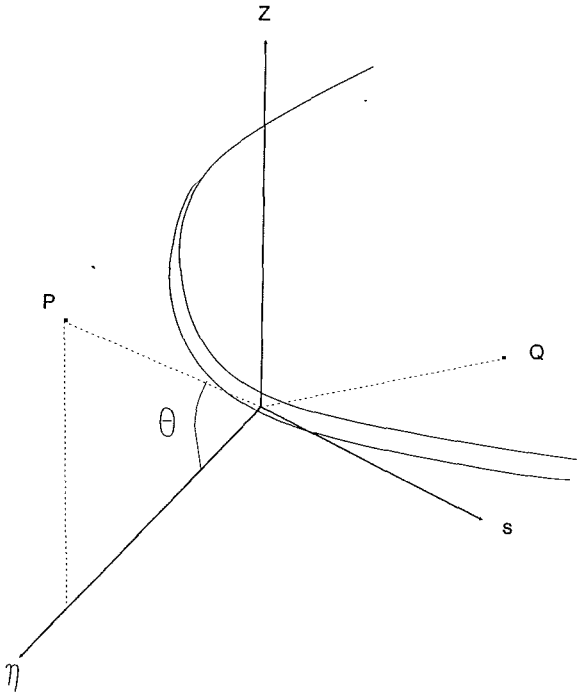


Fig. 2 Local coordinate at crack border

where, as depicted in Fig. 2, η(or n), s, and z are normal, tangential, and vertical coordinates of a local coordinate system at the crack border, and r and θ are distance to the crack border and angle with η-axis, respectively, in the $z-\eta$ plane. In equations (16)–(21), $f_{ij}(\theta)$ and $g_{ij}(\theta)$ are defined as

$$f_{nn}(\theta) = [3\cos(\theta/2) + \cos(5\theta/2)]/4 \tag{22}$$

$$f_{zz}(\theta) = [5\cos(\theta/2) - \cos(5\theta/2)]/4 \tag{23}$$

$$f_{ss}(\theta) = 2\nu\cos(\theta/2) \tag{24}$$

$$f_{nz}(\theta) = [-\sin(\theta/2) + \sin(5\theta/2)]/4 \tag{25}$$

$$f_{sz}(\theta) = \cos(\theta/2), \quad f_{ns}(\theta) = -\sin(\theta/2) \tag{26}$$

$$g_{mm}(\theta) = [-7\sin(\theta/2) + \sin(5\theta/2)]/4 \tag{27}$$

$$g_{zz}(\theta) = f_{nz}(\theta), \quad g_{ss}(\theta) = -2\nu\sin(\theta/2) \tag{28}$$

$$g_{nz}(\theta) = f_{nn}(\theta), \quad g_{sz}(\theta) = g_{ns}(\theta) = 0. \tag{29}$$

4 Partially Conductive Crack Surfaces (Finite λ)

In order to satisfy the actual crack surface thermal conductivity condition, equation (8), a complementary solution, $T^{(2)}$, $u_i^{(2)}$, and $\sigma_{ij}^{(2)}$ must be added to the solution of perfect crack surface thermal conductivity given in Section 3. The complementary solution has to satisfy equations (1)–(5) and the following boundary conditions:

$$\sigma_{ij}^{(2)}n_j = 0 \qquad P \text{ on } S_\sigma \text{ and } S_c \tag{30}$$

$$u_i^{(2)}(P,t) = 0 \qquad P \text{ on } S_u \tag{31}$$

$$T^{(2)}(P,t) = 0 \qquad P \text{ on } S_T \tag{32}$$

$$\frac{\partial T^{(2)}}{\partial n}(P,t) = 0 \qquad P \text{ on } S_q \tag{33}$$

$$\frac{\partial[T^{(1)} + T^{(2)}]}{\partial n}(P,t) = \frac{\lambda}{L}[T^{(2)}(P^+,t) - T^{(2)}(P^-,t)] \qquad P \text{ on } S_c. \tag{34}$$

From equaton (34) it is seen that, for a finite λ, temperature across the crack surfaces is not continuous, i.e., except at the crack tips, there is a temperature jump from one side of the

Downloaded 03 May 2010 to 171.66.16.244. Redistribution subject to ASME license or copyright; see http://www.asme.org/terms/Terms_Use.cfm

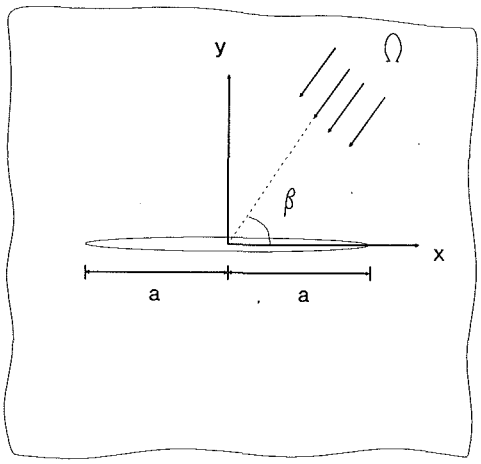


Fig. 3 A finite crack in an infinite plate

crack to the other. Such a temperature jump across the crack surface resembles the temperature jump caused by distributed dipoles situated at a surface in the solid (Carslaw and Jaeger, 1959). Therefore, equation (34) can be satisfied if we can find a set of dipoles properly distributed at the crack surfaces S_c.

It has been shown by Carslaw and Jaeger (1959) that, with a set of distributed dipoles of strength $M(Q,t)$ at crack surface S_c, temperature distribution in V is

$$T^{(2)}(P,t) = \int_{S_c} \int_0^t T^G(P,Q,t-\tau)\ M(Q,\tau)\ d\tau\ dS(Q) \quad (35)$$

where $T^G(P,Q,t)$ is the temperature solution at point P due to an instantaneous dipole of unit strength applied at point Q at $t=0$. In other words, T^G has to satisfy equations (1), (5), (32), and (33). With a method similar to that given by Carslaw and Jaeger (1959), it can be shown that $T^{(2)}$ given by equation (35) will create a temperature jump of $M(P,t)/(\rho c\xi)$ at point P of the crack surface where ξ is defined in equation (1). Therefore, equation (32) becomes

$$\int_{S_c} \int_0^t M(Q,\tau)\ \frac{\partial T^G(P,Q,t-\tau)}{\partial n(Q)}\ d\tau\ dS(Q)$$

$$+ q(P,t) = \frac{\lambda}{\rho c \xi L}\ M(P,t), \quad (36)$$

where

$$q(P,t) = \frac{\partial T^{(1)}(P,t)}{\partial n(P)} \quad (37)$$

is a known function from Section 3. Equation (36) is a Fredholm integral equation. It is worth noting that, except for problems with simple geometries such as an infinite space, it is often difficult to obtain T^G analytically. Thermal stresses due to $T^{(2)}$ can by written as

$$\sigma_{ij}^{(2)}(P,t) = \int_{S_c} \int_0^t \sigma_{ij}^G(P,Q,t-\tau) M(Q,\tau) d\tau\ dS(Q) \quad (38)$$

where $\sigma_{ij}^G(P,Q,t)$, which satisfies equations (2), (3), (4), (30), and (31), is the stress distribution at point P due to an instantaneous dipole of unit strength applied at point Q at $t=0$.

Since a dipole is a degenerated case of a heat source and a heat sink of the same strength situated at two adjacent points. It can be shown that

$$\sigma_{ij}^G(P,Q,t) = \frac{\partial}{\partial z(Q)}\ \sigma_{ij}^U(P,Q,t) \qquad Q \text{ on } S_c \quad (39)$$

where z is a local coordinate defined in Fig. 2 and $\sigma_{ij}^U(P,Q,t)$ is the stresses at point P due to an instantaneous heat source of unit strength applied at point Q at $t=0$. Asymptotically, ($r \to 0$), σ_{ij}^U must have the same format as equations (16)–(21), i.e.,

$$\sigma_{ij}^U(P,Q,t) = [C_{ij}\ f_{ij}(\theta) + D_{ij}\ g_{ij}(\theta)]/\sqrt{2\pi r(P)} \quad (40)$$

(no summation)

where $C_{ij} = C_{ij}\ (n(Q),\ s(Q),t)$ and $D_{ij} = D_{ij}(n(Q),s(Q),t)$ are scalar constants. Equations (39) and (40) lead to

$$\sigma_{ij}^G(P,Q,t) = \frac{1}{\sqrt{2\pi r(P)}}\ [E_{ij}\ f'_{ij}(\theta) + F_{ij}\ g'_{ij}(\theta)] \quad (41)$$

(no summation)

where $E_{ij} = C_{ij}\ [\eta(Q),\ s(Q),\ t]/r(Q)$, $F_{ij} = D_{ij}[\eta(Q),\ s(Q),\ t]/r(Q)$, and $r(Q) = [\eta(Q)^2 + s(Q)^2]^{0.5}$. By the definition of stress intensity factors and equations (38)–(40), we have

$$K_{\mathrm{I}}^{(2)} = \sqrt{2\pi r(P)}\ [\sigma_z^{(2)}]_{\theta=0}$$

$$= \int_{S_c} \int_0^t M(Q,\tau) F_{zz}(\eta(Q),s(Q),t-\tau) g'_{zz}(0) d\tau\ dS(Q)$$

$$= \frac{1}{2} \int_{S_c} \int_0^t M(Q,\tau) F_{zz}(\eta(Q),s(Q),t-\tau) d\tau\ dS(Q) \quad (42)$$

$$K_{\mathrm{II}}^{(2)} = \sqrt{2\pi r(P)}\ [\sigma_{nz}^{(2)}]_{\theta=0}$$

$$= \int_{S_c} \int_0^t M(Q,\tau) E_{nz}(\eta(Q),s(Q),t-\tau) f'_{nz}(0) d\tau\ dS(Q)$$

$$= \frac{1}{2} \int_{S_c} \int_0^t M(Q,\tau) E_{nz}(\eta(Q),s(Q),t-\tau) d\tau\ dS(Q) \quad (43)$$

$$K_{\mathrm{III}}^{(2)} = \sqrt{2\pi r(P)}\ [\sigma_{sz}^{(2)}]\theta = 0$$

$$= \int_{S_c} \int_0^t M(Q,\tau) E_{sz}(\eta(Q),s(Q),t-\tau) f'_{sz}(0) d\tau\ dS(Q)$$

$$= 0. \quad (44)$$

In equations (42)–(44), it is found that, in general, K_{I} and K_{II} will be affected by the degree of thermal conductivity at crack surfaces while K_{III} is independent of crack surface thermal conductivity. In other words, different λ values in equation (8) will generate different K_{I} and K_{II} solutions but will not change the K_{III} solution.

5 Cracked Solids With Geometrical Symmetry

For an elastic solid, of which the body V and all the boundary surfaces (S_σ, S_u, S_T, and S_q) are symmetric with respect to the plane containing the crack surface S_c, equations (42)–(44) can be further simplified. Under this geometrical symmetry condition, D_{ij} in equation (40) and thus F_{ij} in equation (41) must be equal to zero. Therefore, both $K_{\mathrm{I}}^{(2)}$ and $K_{\mathrm{II}}^{(2)}$ vanish in this case. Thus, for a geometrically symmetric cracked solid, its K_{I} and K_{III} solutions can be obtained by assuming that the crack surface is perfectly thermal-conductive or insulated. Such a behavior can greatly simplify the computational effort when only K_{I} and K_{III} is of major concern, e.g., pressurized thermal shock of a reactor pressure vessel in nuclear industry. Examples to geometrically symmetric cracked solids are: center-cracked plates, single-edge cracked plates, a semi-elliptical surface crack in an plate of finite thickness, an elliptical crack in an infinite space, a circumferentially cracked pipe, and an axially cracked pipe. It should be noted that, in the class of symmetric cracked structures, even though the geometry and boundary surfaces are assumed to be symmetric with respect to the crack plane, mechanical and thermal loadings can still be nonsymmetric, e.g., a finite crack in an infinite plate subjected to point heat sources at arbitrary locations (see Fig. 3).

Downloaded 03 May 2010 to 171.66.16.244. Redistribution subject to ASME license or copyright; see http://www.asme.org/terms/Terms_Use.cfm

6 Example Problem

Let us consider a finite crack of length $2a$ in an infinite plate subjected to a steady-state temperature gradient of Ω at infinity. As shown in Fig. 3, the thickness of the plate is assumed to be D and the temperature gradient Ω is assumed to have an angle of β with the x-axis. The plate is assumed to be stress-free at infinity.

For the case of $\lambda=\infty$, $T^{(1)}$ is a linear function of x and y. According to Boley and Weiner (1960), such a linear temperature field will not generate any stresses, i.e., $\sigma_{ij}^{(1)}=0$, $K_{\rm I}^{(1)}=K_{\rm II}^{(1)}=K_{\rm III}^{(1)}=0$. The next step is to solve the Fredholm equation defined by equation (36) for the dipole distribution function $M(x)$, $-a\le x\le a$. It is known (e.g., Carslaw and Jaeger, 1959) that for a dipole of unit strength applied at (0, 0) the steady-state temperature solution is

$$T^G=\frac{y}{2\pi K(x^2+y^2)}. \tag{45}$$

Thus, equation (36) becomes

$$\Omega D\sin\beta+\int_{-a}^{a}\frac{M(\bar{x})d\bar{x}}{2\pi K(x-\bar{x})^2}=\frac{\lambda M(x)}{2\rho c\xi a}. \tag{46}$$

Temperature jumps across crack surface (see Section 4) due to this distributed dipoles are

$$T^{(2)}(x,0^+)-T^{(2)}(x,0^-)=M(x)/(KD) \tag{47}$$

where $M(x)$ is in the units of energy per time, e.g. Btu/sec. It has been shown by Wilson and Yu (1977) that stress intensity factors due to thermal stresses can also be obtained by integrating, over the crack surface, the product of an influence function $m(x)$ and the stresses for the uncracked body under the same temperature field. For a finite crack of length $2a$ in an infinite plate, the influence function for all three crack modes at right crack-tip ($x=a$) is (e.g., Tada, Paris, and Irwin, 1985, or Sih, 1973)

$$m(x)=\left[\frac{(a+x)}{\pi a(a-x)}\right]^{1/2}. \tag{48}$$

Following the stress function method given by Boley and Weiner (1960) or Parkus (1968), it can shown that thermal stresses at $y=0$ due to a dipole of unit strength applied at (0,0) of an infinite plate (plane stress is implied) are

$$\sigma_{xy}^G(x,0)=\frac{G\alpha(1+\nu)}{2\pi KDx},\quad \sigma_{yy}^G(x,0)=\sigma_{yz}^G(x,0)=0. \tag{49}$$

By the definition of influence function and equation (38), stress intensity factors can be written as

$$K_{\rm I}^{(2)}=K_{\rm III}^{(2)}=0$$

$$K_{\rm II}^{(2)}=\frac{G\alpha(1+\nu)}{2\pi KD\sqrt{\pi a}}\int_{-a}^{a}\int_{-a}^{a}\frac{M(u)}{(x-u)}[(a+x)/(a-x)]^{1/2}du\,dx$$

$$=\frac{G\alpha(1+\nu)}{2KD\sqrt{\pi a}}\int_{-a}^{a}M(X)\,dx. \tag{50}$$

Since

$$M_0=2KD\Omega\sqrt{(a+x)(a-x)}\sin\beta \tag{51}$$

is the solution of

$$\Omega D\sin\beta+\int_{-a}^{a}\frac{M_0(\bar{x})d\bar{x}}{2\pi K(x-\bar{x})^2}=0, \tag{52}$$

it is reasonable to express $M(x)$ as:

$$M(x)=\sqrt{(a+x)(a-x)}\sum_{0}^{\infty}d_j\left(\frac{x}{a}\right)^j \tag{53}$$

where d_j are coefficients to be determined. Both equations (51) and (53) implicitly satisfy the crack-tip temperature condition, $T(\pm a,0^+)=T(\pm a,0^-)$ or $M(\pm a)=0$. It should be noted that, by integration with respect to x, equation (52) can be reduced to a Fredholm equation with a Cauchy kernel:

$$x\Omega D\sin\beta+A'=-\frac{1}{2\pi K}\int_{-a}^{a}\frac{M_o(\bar{x})}{x-\bar{x}}d\bar{x} \tag{54}$$

where A' is a constant to be determined. It is then relatively easy to show that equation (51) is the only solution of equation (54) (see Muskhelishivili, 1946). Substituting equation (53) into equation (46) and going through an algebraic and complex function manipulation, we find that the coefficients d_j in equation (53) can be determined by the following recurrence relations:

$$d_{2j-1}=e_{2j-1}=0,\qquad (j\ge 1)$$

$$d_0=\frac{2KD\Omega\sin\beta}{1+2\lambda}$$

$$d_{2j}=\frac{2\lambda}{2j+1+2\lambda}\sum_{m=1}^{j}(e_{2m}d_{2j-2m}),\qquad (j\ge 1) \tag{55}$$

$$e_0=1,\qquad e_2=1/2$$

$$e_{2m}=\frac{1}{2^m m!}\prod_{n=1}^{m}(2m-3),\qquad (m\ge 2).$$

Physically, equation (51) represents the dipole distribution for an insulated crack ($\lambda=0$) under a constant temperature gradient at infinity. Temperature jumps at the crack surface for the insulated crack can then be calculated by substituting equation (51) into equation (47) and is found to be

$$T(x,0^+)-T(x,0^-)=2\Omega\sqrt{(a+x)(a-x)}\sin\beta. \tag{56}$$

This temperature jump is identical to that given by Goodier and Florence (1959) ($m=1$ and $R=a/2$ in pages 26 and 27 of Goodier and Florence's report (1959)). Then, by equation (50), the stress intensity factor due to $M_0(x)$ is

$$K_{\rm II}^0=\frac{1}{2}G\alpha(1+\nu)a\sqrt{\pi a}\,\Omega\sin\beta. \tag{57}$$

$K_{\rm II}^0$ is equation (57) is the same as the solution to the same problem by Sih (1962) and Paris and Sih (1964).

For λ other than 0, $M(x)$, $T(x,0)$, as well as $K_{\rm II}$ can be solved numerically through equations (50), (54), and (55).

7 Numerical Results and Discussion

In the numerical calculation, it is found that, with the first 50 terms included in equation (53), the $K_{\rm II}$ solution converges to within 0.5 percent. Resulting mode II stress intensity factors for different λ values are plotted in Fig. 4 for λ up to 10. The stress intensity values shown in Fig. 4 have been normalized by the stress intensity factor solution for an insulated crack, $K_{\rm II}^0$ in equation (57). For λ value ranging from zero to infinity, the curve shown in Fig. 4 can be approximated, with error less than $0.02K_{\rm II}^0$, by

$$(K_{\rm II}/K_{\rm II}^0)=0.9827-2.247\phi+2.6513\phi^2-1.405\phi^3 \tag{58}$$

where $\phi=2/\pi\tan^{-1}\lambda$. For a given crack size a, as λ value increases the crack surface becomes more heat conductive and $K_{\rm II}$ value decreases toward zero monotonically. This phenomenon is similar to that observed by Barber (1979). Temperature jumps across the crack surface for $\lambda=0$, $\lambda=0.5$, and $\lambda=2$ are illustrated in Fig. 5. As expected, in Fig. 5,

Downloaded 03 May 2010 to 171.66.16.244. Redistribution subject to ASME license or copyright; see http://www.asme.org/terms/Terms_Use.cfm

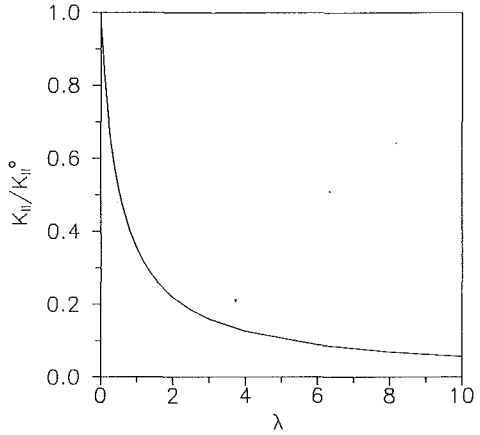


Fig. 4 Effects of crack surface thermal conductivity on K_{II}

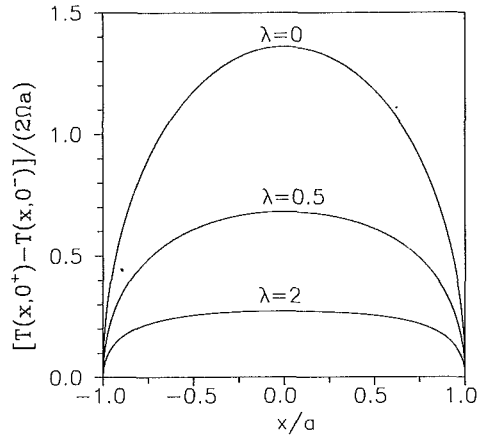


Fig. 5 Temperature jumps at the crack surface

temperature jumps decrease monotonically toward zero as the crack surface becomes more heat conductive. One important discovery out of Figs. 4 and 5 is that, in addition to the independent variables G, α, ν, $a^{3/2}$, Ω, and β given in equation (57), stress intensity factor K_{II} for a partially heat conductive crack has an additional independent variable of λ, which, for a constant crack length, represents the degree of crack surface thermal conductivity. For a given set of K and h ($\lambda/a = h/K = \text{constant}$), the degree of influence on K_{II} by crack surface thermal conductivity depends upon the length of the crack. Therefore, for a given set of K and h, small cracks act more like being insulated and long cracks tend to behave like being perfectly conductive. In other words, effects of crack surface thermal conductivity on stress intensity factors are crack-size dependent. This size effect could be a very important factor in designing a structural or electronic component for use in a transient temperature environment. For instance, if all the variables except crack size remain constant, the stress intensity factor is expected to reach a peak value and decay to zero as the crack length increases. Figure 6, K_{II} values have been normalized by the constant, $0.5G\alpha\sqrt{\pi}(1+\nu)\,(K/h)^{1.5}\Omega\,\sin\beta$.

To sum up this paper, a few conclusions can be drawn:

(1) For any crack geometries, K_{III} solution does not depend on crack surface thermal conductivity, only K_I and K_{II} do.

(2) For cracks in a geometrically symmetric solid, neither K_I nor K_{III} depends upon crack surface Biot number λ, i.e., K_I and K_{III} for elastic solids of this class can be calculated by assuming the crack surface is perfectly conductive ($\lambda=\infty$) or insulated ($\lambda=0$).

(3) Conclusions 1 and 2 are valid for both two and three-dimensional cracks.

(4) In general, conclusions 1-3 are not true for cracks in anisotropic materials because all the three fracture modes are coupled together in this case.

(5) For cracks (including interfacial cracks, e.g., Kuo, 1989) in a linear elastic, quasi-static solid (isotropic or anisotropic), the effects of crack surface thermal conductivity on stress intensity factors depend on the distribution of dipoles situated at the crack surfaces. Distribution function of the dipoles at the crack surfaces can be determined by a Fredholm integral equation.

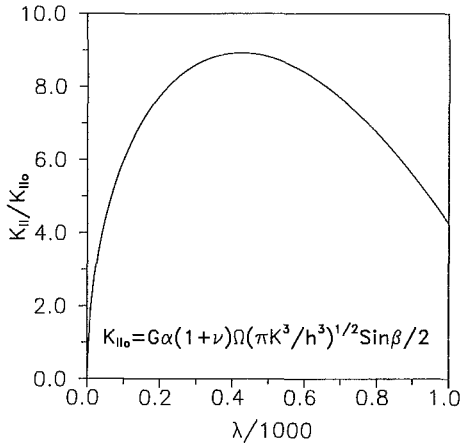


Fig. 6 Size effects

Acknowledgments

The support from Flight Dynamic Lab., Air Force Wright Aeronautica Lab., Aeronautical Systems Div. (AFSC), Wright-Patterson AFB of the U.S. Air Force under Grants F33615-86-C-3219 and F33615-87-C-3250 is gratefully acknowledged. The author wishes to thank Capt. C. Mazur and Dr. George P. Sendeckyj at the Air Force Wright Aeronautical Laboratories for their encouragement during the course of this research.

References

Barber, J. R., 1976, "The Disturbance of a Uniform Steady-State Heat Flux by a Partially Conducting Plane Crack," *Int. J. Heat Mass Transfer*, Vol. 19, pp. 956-958.

Barber, J. R., 1979, "Steady-State Stress Caused by an Imperfectly Conducting Penny-Shaped Crack in an Elastic Solid," *Journal of Thermal Stresses*, Vol. 3, pp. 77-83.

Boley, B. A., and Weiner, J. H., 1960, *Theory of Thermal Stresses*, John Wiley and Sons, New York.

Carslaw, H. S., and Jaeger, J. G., 1959, *Conduction of Heat in Solids*, Oxford University Press, London.

Goodier, J. N., and Florence, A. L., 1959, "Thermal Stress Due to Disturbance of Uniform Heat Flow by Cavities and Inclusions," Technical Report No. 120, Division of Engineering Mechanics, Stanford University, Stanford, Calif.

Kassir, M. K., and Sih, G. C., 1966, "Three-Dimensional Stress Distribution Around an Elliptical Crack Under Arbitrary Loadings," ASME JOURNAL OF APPLIED MECHANICS, Vol. 33, pp. 601-611.

Kuo, A. Y., 1990, "Interface Crack Between Two Dissimilar Half-Spaces Subjected to a Uniform Heat Flow at Infinity—Open Crack," ASME JOURNAL OF APPLIED MECHANICS, Vol. 57, pp. 359-364.

Muskhelishivili, N. I., 1946, *Singular Integral Equations*, translated by J. R. M. Radok, Groningen.

Parkus, H., 1968, *Thermoslasticity*, Blaisdell Publishing Co.

Paris, P. C., and Sih, G. C., 1964, "Stress Analysis of Cracks," *Fracture Toughness Testing and its Applications*, ASTM STP-381, p. 30-83.

Sih, G. C., 1962, "On the Singular Character of Thermal Stresses near a Crack Tip," ASME JOURNAL OF APPLIED MECHANICS, Vol. 29, pp. 587-589.

Sih, G. C., 1973, *Handbook of Stress Intensity Factors*, Lehigh University, Bethlehem, Penn.

Tada, H., Paris, P. C., and Irwin, G. R., 1985, *The Stress Analysis of Cracks Handbook*, 2nd ed., Paris Productions Inc., St. Louis, Mo.

Wilson, W. K., and Yu, I.-W., 1979, "The Use of the J-Integral in Thermal Stress Crack Problems," *International Journal of Fracture*, Vol. 15, pp. 377-387.

Downloaded 03 May 2010 to 171.66.16.244. Redistribution subject to ASME license or copyright; see http://www.asme.org/terms/Terms_Use.cfm

Interface Crack Between Two Dissimilar Half Spaces Subjected to a Uniform Heat Flow at Infinity—Open Crack

An-Yu Kuo
Associate,
Structural Integrity Associates,
San Jose, CA 95118
Assoc. Mem. ASME

The thermal stress problem of an "open" crack situated at the interface of two bonded, dissimilar, semi-infinite solids subjected to a uniform heat flow is studied. Heat transmission between adjacent crack surfaces is assumed to be proportional to the temperature difference between the crack surfaces with a proportional constant h, *which is defined as the contact coefficient or interface conductance. Temperature distribution of the problem is obtained by superimposing the temperature field for a perfectly bonded composite solid and the temperature fields for a series of distributed thermal dipoles at the crack location. The distribution function of the dipoles is obtained by solving a singular Fredholm integral equation. Stresses are then expressed in terms of a thermoelastic potential, corresponding to the temperature distribution, and two Muskhelishvili stress functions. Stress intensity factors are calculated by solving a Hilbert arc problem, which results from the crack surface boundary conditions and the continuity conditions at the bonded interface. Thermal stress intensity factors are found to depend upon an additional independent parameter, the Biot number* $\lambda = (ah/k)$, *on the crack surface, where* a *is half crack length and* k *is thermal conductivity. Dipole distribution and stress intensity factors for two example composite solids, Cu/Al and Ti/*Al_2O_3, *are calculated and plotted as functions of* λ. *Magnitude of the required mechanical loads to keep the interface crack open is also estimated.*

1 Introduction

Interface cracks between dissimilar materials under thermal loading is a major problem in the manufacturing of electronics devices and ceramic composites. For instance, cracking between the interface of the silicon substrate and either a bond pad or the aluminum metallization in an integrated circuit board has been known to cause significant reliability problems in the modern, high technology electronics industry. Also, there have been numerous incidents reported in the area of interface cracking between the ceramic fibers and matrix in a ceramic composite. This kind of interface cracking is mainly caused by the fact that there is an order-of-magnitude difference in thermal properties between two adjacent materials. By design, electronics boards and ceramic composites are most often used in environments with high temperature gradients. Therefore, a better understanding of interface cracks under thermal loading conditions is needed to guide the judicious selection of materials and fabrication methods which do not lead to interfacial failure.

As shown in Fig. 1, this paper considers the problem of an open interface crack of length $2a$ between two bonded, dissimilar, semi-infinite solids subjected to a uniform heat flow, q_o, at infinity. A homogeneous material case of this problem has been solved by Sih (1962), in which the crack surfaces were assumed to be completely insulated. Brown and Er-

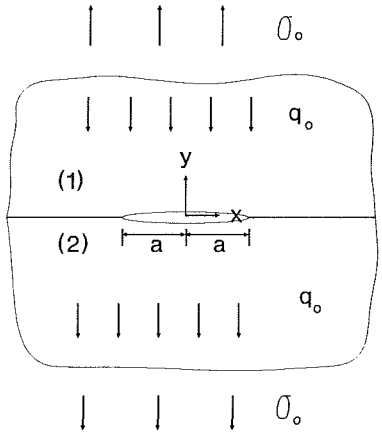


Fig. 1 An interface crack between two dissimilar materials

Contributed by the Applied Mechanics Division of THE AMERICAN SOCIETY OF MECHANICAL ENGINEERS for publication in the JOURNAL OF APPLIED MECHANICS.

Discussion on this paper should be addressed to the Technical Editor, Leon M. Keer, The Technological Institute, Northwestern University, Evanston, IL 60208, and will be accepted until two months after final publication of the paper itself in the JOURNAL OF APPLIED MECHANICS. Manuscript received by the ASME Applied Mechanics Division, March 8, 1989; final revision, June 5, 1989.

Copyright © 1990 by ASME
Downloaded 03 May 2010 to 171.66.16.244. Redistribution subject to ASME license or copyright; see http://www.asme.org/terms/Terms_Use.cfm

dogan (1968) have solved the interface crack problem by assuming zero (or finite) stresses at infinity. Brown and Erdogan also treated the partially-insulated crack surfaces by assuming that the heat flow passing through the crack surfaces was $(1-\delta)q_o$, where $0\le\delta\le 1$. However, due to the assumption of zero (or finite) stresses at infinity, Brown and Erdogan found the stress intensity factor solutions divergent. Physically, such a divergence in the stress solutions discovered by Brown and Erdogan (1968) is anticipated because, under a constant heat flow at infinity, both materials tend to bend up (or down) with different curvatures, reflecting the difference in thermal expansion coefficients. Under this thermal bending, the resulting displacement differential at infinity between the two materials represented a dislocation of infinite magnitude and thus made the stress solutions divergent. To ensure a convergent stress solution, Brown and Erdogan (1968) modified the problem by introducing two extra interfacial cracks, one from $x=b$ to $x=\infty$ and the other from $x=-b$ to $x=-\infty$ where $b>a$. However, solutions by Brown and Erdogan indicated that stress intensity factors of the modified problem were strongly dependent on the choice of b. Barber (1976, 1979) has presented a solution to the problem of a partially insulated crack in a homogeneous material with finite contact conductance. Barber and Comninou (1983) and Martin-Moran et al., (1983) have solved the problem of a partially closed penny-shaped crack with heat flow. In these two papers, the Barber's boundary conditions for thermoelastic contact (Comninou and Dundurs, 1979) were used for the contact region of a partially closed crack. Recently, Sturla and Barber (1988) have provided the solution to the problem of a plane crack in a homogeneous, anisotropic material subjected to heat flow.

In this paper, we reexamine the interface crack problem by introducing another kind of boundary conditions at infinity and by employing a contact coefficient h for the heat transmission between the adjacent crack surfaces. More specifically, it is assumed that

$$\sigma_{yy}^{\infty}=\sigma_{xy}^{\infty}=0,\ \epsilon_{xx}^{\infty}=0 \tag{1}$$

$$k_1\frac{\partial T(x,0^+)}{\partial y}=k_2\frac{\partial T(x,0^-)}{\partial y}=h[T(x,0^+)-T(x,0^-)] \tag{2}$$

where $|x|\le a$, and h is the contact coefficient (Holman, 1972) or interface conductance (Rohsenow and Hartnett, 1973) between the adjacent crack surfaces (see also Barber (1976, 1979)). In equation (1), it is implied that, at infinity, the composite solid is constrained in the x direction but is stress-free in the y direction. As will be shown in this paper, the constraint in the x direction at infinity makes the stress intensity factor solution convergent. In equation (2), $h=0$ and $h=\infty$ correspond to the cases of complete insulation and fully heat conductive, respectively, between the crack surfaces.

More importantly, it is also assumed that the interface crack is an "open" crack. An interface crack is open when the contact zone size (Comninou (1977, 1978, 1979) and Rice (1988)) at the crack tip is negligible compared with the nominal dimension of the problem. This assumption implies that, on top of the solution for the thermal stress problem, there might exist an implicit stress field caused by mechanical loads (e.g., a constant tensile stress σ_{yy} at infinity) such that the contact zone size for the total solution is infinitesimally small.

2 Temperature Solution

It is assumed that the uncoupled, quasi-static thermoelasticity theory is applicable to this problem. Thus, the first step of the solution procedure is to find a temperature distribution which satisfies the governing equations and boundary conditions. In addition to the boundary condition given by equation (2), governing equations and boundary conditions for the temperature problem are

$$\nabla^2 T_1(x,y)=\nabla^2 T_2(x,y)=0 \tag{3}$$

$$T_1(x,0^+)=T_2(x,0^-) \qquad |x|\ge a \tag{4}$$

$$k_1\frac{\partial}{\partial y}[T_1(x,0^+)]=k_2\frac{\partial}{\partial y}[T_2(x,0^-)] \qquad |x|\ge a \tag{5}$$

$$k_1\frac{\partial}{\partial y}[T_1(x,y)]=k_2\frac{\partial}{\partial y}[T_2(x,y)]=q_o \text{ at infinity} \tag{6}$$

where k_1 and k_2 are thermal conductivities of the upper and lower materials, respectively, and $T_1(x,y)$ and $T_2(x,y)$ are temperature distribution in the upper and lower halves of the composite plane, respectively. Solutions to equations (3)–(6) can be separated into two parts, one for a uniform heat flow in a perfectly bonded composite solid and the other for crack correction. For the perfect bonding case, it can be readily shown that

$$T_1(x,y)=(q_o y)/k_1 \text{ and } T_2(x,y)=(q_o y)/k_2 \tag{7}$$

are the temperature solutions for the upper and lower semi-infinite solids, respectively.

The corrective solution for the crack should still satisfy equations (2)–(6) except that q_o in equation (6) is replaced by zero. Physically, it can be envisioned that, for a completely or partially insulated crack, the temperatures on the adjacent surfaces of the crack are different, i.e., there is a temperature jump across the crack surfaces. Such a temperature jump across the crack region is analogous to the temperature jump created by a series of thermal dipoles distributed continuously at the crack region (Carslaw and Jaeger, 1959). Therefore, temperature solution to the crack correction problem can be expressed as the superposition of the temperature solutions of many distributed dipoles at the crack location. Hence, total temperature solutions to this problem become

$$T_j(x,y)=(q_o y)/k_j+\int_{-a}^{a}\frac{y\,M(t)}{2\pi k_j[(x-t)^2+y^2]}\,dt \tag{8}$$

where $j=1$ or 2 and $M(x)$ is the distribution function of the dipoles to be determined. The integrand in the second part of equation (8) corresponds to the temperature solution of a single thermal dipole of strength $M(t)$ situated at $(t,0)$. Substitution of equation (8) into equation (2) yields a singular Fredholm integral equation:

$$q_o+\int_{-a}^{a}\frac{y\,M(t)}{2\pi(x-t)^2}\,dt=\frac{h}{2}\left(\frac{1}{k_1}+\frac{1}{k_2}\right)M(x). \tag{9}$$

Since $M_o(x)=2q_o\sqrt{(a^2-x^2)}$ is an obvious solution to equation (9) when h is zero, it is reasonable to assume that the distribution function $M(x)$ of the dipoles is in the form of

$$M(x)=2q_o\sqrt{(a^2-x^2)}[d_0+d_1\xi+d_2\xi^2+\ \ldots\ +d_M\xi^M] \tag{10}$$

where $\xi=(x/a)$ and $|x|\le a$. From equations (9) and (10), a recurrence relation between d_js can be derived

$$\begin{aligned}
&d_0=\frac{1}{1+\lambda(1+\omega)}\\
&d_{2j}=\frac{\lambda(1+\omega)}{1+2j+\lambda(1+\omega)}\sum_{m=1}^{j}(e_{2m}\,d_{2j-2m}) && j\ge 1\\
&d_{2j-1}=0 && j\ge 1\\
&e_0=1,\ e_2=1/2\\
&e_{2m}=\frac{1}{2^m\,m!}\prod_{n=1}^{m}(2n-1) && m\ge 2
\end{aligned} \tag{11}$$

where $\omega=(k_1/k_2)$ is the ratio of the two thermal conductivities and $\lambda=(ha)/k_1$ is defined as the normalized contact coefficient or the Biot number on the crack surface. It can be shown that equation (11) degenerates to the recurrence relation presented by Kuo (1989) for the thermal cracking problem

Downloaded 03 May 2010 to 171.66.16.244. Redistribution subject to ASME license or copyright; see http://www.asme.org/terms/Terms_Use.cfm

in a homogeneous material (i.e., when the two materials are identical). Also, with equation (11), it can be shown that equation (10) is a convergent solution and that equation (10) reduces to $M_o(x)$ when the crack is completely insulated ($h=0$). It is worth mentioning that, for the case of an insulated crack in a homogeneous material, the distributed thermal dipoles $M_o(x)$ will lead to a temperature jump of $M_o(x)/k$ between two crack surfaces, which is identical to the solution given by Goodier and Florence (1959) for the same problem.

3 Stress Solution

The stress solution to this problem may be obtained by using the Muskhelishvili stress functions (Muskhelishvili, 1953) plus a thermoelastic displacement potential for the thermal expansions (see, e.g., Parkus, 1968). For problems with a straight boundary like the current one, stresses and displacements can be expressed in terms of a single stress function, ϕ, and a thermoelastic displacement potential, φ, as:

$$\sigma_{xx}+\sigma_{yy}=2[\phi(z)+\bar{\phi}(\bar{z})]-2\mu[\varphi_{,xx}+\varphi_{,yy}] \tag{12}$$

$$\sigma_{yy}-i\sigma_{xy}=2[(z-\bar{z})\bar{\phi}'(\bar{z})+\phi(z)-\phi(\bar{z})]-2\mu[\varphi_{,xx}+i\varphi_{,xy}] \tag{13}$$

$$2\mu(u'+iv')=\kappa\phi(z)+\phi(\bar{z})-(z-\bar{z})\bar{\phi}'(\bar{z})+2\mu[\varphi_{,xx}+i\varphi_{,xy}] \tag{14}$$

$$\nabla^2\varphi(x,y)=\eta\ T(x,y) \tag{15}$$

where $\phi(z)$ is an analytic function, μ is shear modulus of the material, u and v are displacements in the x and y directions, respectively, $u'=u_{,x'}$ $v'=v_{,x'}$ $\kappa=(3-\nu)/(1+\nu)$ and $\eta=\bar{\alpha}(1+\nu)$ for the plane-stress problem, $\kappa=(3-4\nu)$ and $\eta=\bar{\alpha}(1+\nu)/(1-\nu)$ for the plane-strain problem, ν is Poisson's ratio, and $\bar{\alpha}$ is coefficient of thermal expansion. It is worth noting that, for a plane-strain problem, $\bar{\alpha}(1+\nu)/k$ is defined as distortivity of the material (Dundurs and Panek, 1976). In addition to equation (1), boundary conditions and continuity conditions for the problem are

$$[\sigma_{yy}-i\sigma_{xy}]_1(x,0^+)=[\sigma_{yy}-i\sigma_{xy}]_2(x,0^-) \qquad |x|<\infty \tag{16}$$

$$[\sigma_{yy}-i\sigma_{xy}]_1(x,0^+)=[\sigma_{yy}-i\sigma_{xy}]_2(x,0^-)=0 \qquad |x|\le a \tag{17}$$

$$[u'+iv']_1(x,0^+)=[u'+iv']_2(x,0^-) \qquad |x|\ge a. \tag{18}$$

It can be shown, by integrating equation (15), that the displacement potentials φ_1 and φ_2 are

$$\varphi_j=\frac{q_o\eta_j y^3}{6k_j}+\frac{\eta_j}{8\pi k_j}\int_{-a}^{a} y\,M(t)\ln[(x-t)^2+y^2]dt \tag{19}$$

where $j=1$ or 2, and the distribution function $M(t)$ is defined in equations (10) and (11). Note that the boundary condition at infinity, equation (1), has been used implicitly during the derivation of equation (19). Hence, with equation (19), equations (16)–(18) can be rewritten as

$$\phi_1^+-\phi_1^--i\frac{\mu_1\eta_1}{4\pi k_1}f(x)=\phi_2^--\phi_2^+-i\frac{\mu_2\eta_2}{4\pi k_2}f(x), \qquad |x|<\infty \tag{20}$$

$$\phi_1^+-\phi_1^--i\frac{\mu_1\eta_1}{4\pi k_1}f(x)=0, \qquad |x|\le a \tag{21}$$

$$\frac{\kappa_1}{2\mu_1}\phi_1^++\frac{1}{2\mu_1}\phi_1^-+i\frac{\eta_1}{4\pi k_1}f(x)=\frac{\kappa_2}{2\mu_2}\phi_2^-+\frac{1}{2\mu_2}\phi_2^++i\frac{\eta_2}{4\pi k_2}f(x) \qquad |x|\ge a \tag{22}$$

where

$$f(x)=\int_{-a}^{a}\frac{M(t)}{x-t}dt=\begin{cases}2\pi q_o\cdot g_1(x) & |x|\le a\\ 2\pi q_o\cdot g_2(x) & |x|\ge a\end{cases} \tag{23a}$$

$$g_1(x)=|x|\sum_1^M C_{2j}\xi^{2j} \tag{23b}$$

$$g_2(x)=g_1(x)-\sqrt{(a^2-x^2)}\sum_1^M d_{2j}\xi^{2j} \tag{23c}$$

$$C_{2j}=\sum_{k=j}^{M}(d_{2k}b_{2k-2j}) \tag{23d}$$

$$b_0=1,\ b_2=-1/2,\ b_{2k}=-\frac{1\cdot3\cdot5\cdot\cdots(2k-3)}{2^k\,k!}, \tag{23e}$$

$\xi=(x/a)$, and d_{2k} are defined in equation (11). Equations (23a)–(23e) are derived by the standard analytical function integration in a complex domain and by the asymptotic expansion of $\sqrt{(a^2-x^2)}$ at infinity. From equation (20) and the Plemelj's formulae, it can be deduced that

$$\phi_1(z)+\phi_2(z)=\frac{1}{8\pi}\left(\frac{\mu_1\eta_1}{\pi k_1}-\frac{\mu_2\eta_2}{\pi k_2}\right)\int_{-\infty}^{\infty}\frac{f(t)}{t-z}dt. \tag{24}$$

Substituting equation (24) into equations (21) and (22) and eliminating ϕ_2, we have a pair of equations as follows

$$\phi_1^+-\phi_1^-=2\pi i q_o\,\Omega\,g_1(x) \qquad |x|\le a \tag{25}$$

$$\phi_1^++\tau\,\phi_1^-=2\pi i q_o\,\Gamma\,g_2(x) \qquad |x|\ge a \tag{26}$$

where

$$\tau=(1-\beta)/(1+\beta), \quad \Omega=\frac{\mu_1\eta_1}{4\pi k_1}$$

$$\Gamma=\left[\frac{\dfrac{(1+\alpha)(\kappa_1+1)}{(1+\alpha)(\kappa_2+1)}-2+\dfrac{\eta_2\,k_1}{\eta_1\,k_2}}{\dfrac{(1-\alpha)(\kappa_1+1)}{(1+\alpha)(\kappa_2+1)}+\kappa_1}\right]\Omega. \tag{27a}$$

In equation (27a), α and β are Dundurs constants (Dundurs, 1969) defined as follows:

$$\alpha=\frac{\mu_2(\kappa_1+1)-\mu_1(\kappa_2+1)}{\mu_2(\kappa_1+1)+\mu_1(\kappa_2+1)} \tag{27b}$$

$$\beta=\frac{\mu_2(\kappa_1-1)-\mu_1(\kappa_2-1)}{\mu_2(\kappa_1+1)+\mu_1(\kappa_2+1)}. \tag{27c}$$

The Plemelj's formulae and the relationship of $\oint f(t)/t-x\,dt=\pi i f(x)$ have been used to derive equation (26). Equations (25) and (26) are a typical set of equations for the Hilbert arc problem and their solution can be written as (Muskhelishvili, 1953)

$$\phi_1(z)=q_o\,R(z)\left[\int_{-a}^{a}\frac{\Omega\,g_1(t)}{(t-z)R^+(t)}dt-\left\{\int_{-\infty}^{-a}+\int_{a}^{\infty}\right\}\frac{\Gamma\,g_2(t)}{(t-z)R^+(t)}dt\right] \tag{28}$$

where

$$R(z)=(z-a)^{-1/2-i\epsilon}(z+a)^{-1/2+i\epsilon} \tag{29}$$

$$\epsilon=\frac{-1}{2\pi}\ln(\tau) \tag{30}$$

and τ is defined in equation (27). From equation (24), the solution for $\phi_2(z)$ can also be obtained subsequently.

Downloaded 03 May 2010 to 171.66.16.244. Redistribution subject to ASME license or copyright; see http://www.asme.org/terms/Terms_Use.cfm

Table 1 Material properties

	$\mu(10^{11}$ N/m$^2)$	ν	$\bar{\alpha}(10^{-6}/°C)$	k(W/m/°C)	$\delta(10^{-6}$m/W)
Cu	0.478	0.345	17.00	40.0	0.572
Al	0.305	0.330	7.22	130.0	0.074
Ti	0.434	0.322	9.00	16.0	0.744
Al_2O_3	1.792	0.207	9.00	2.9	3.746

Table 2 Bimaterial constants

	α	β	γ	ϵ
Cu/Al	0.226	0.0787	0.771	−0.0208
Ti/Al_2O_3	−0.581	−0.1849	−0.669	0.039

4 Stress Intensity Factor

The complex stress intensity factor K definition defined by Hutchinson et al. (1987) is used in this paper, i.e.,

$$K = \lim_{r\to 0} r^{-\epsilon}\sqrt{2\pi r}(\sigma_{22} + i\sigma_{12}) \tag{31a}$$

where r is the radial distance to the crack tip. According to Sih and Rice (1964), Rice and Sih (1965), and Rice (1988), it can be shown that

$$\bar{K} = 2\sqrt{2\pi}\, e^{\pi\epsilon}\cosh(\pi\epsilon) \lim_{z\to a}(z-a)^{1/2+i\epsilon}\phi_1(z) \tag{31b}$$

where $\bar{K}$ is the complex conjugate of K. Substitution of equation (28) into equation (31) yields

$$K = i\pi a\sqrt{\pi a}\,(2a)^{-i\epsilon} q_o\left[2\Omega\,\overline{D_1} - \Gamma\left(1 - \frac{1}{\tau}\right)D_2\right] \tag{32}$$

where

$$D_1 = \sum_{j=-1}^{2M} w_j \tag{33a}$$

$$D_2 = \sum_{m=0}^{M} (d_{2m} \cdot b_{2m+2}) \tag{33b}$$

$$w_{2m} = \sum_{k=m}^{M} (C_{2k} \cdot t_{2k-2m}) \qquad m = 0,1,2,\ldots,M \tag{33c}$$

$$w_{2m-1} = \sum_{k=m}^{M} (c_{2k} \cdot t_{2k-2m+1}) \qquad m = 0,1,2,\ldots,M \tag{33d}$$

$$t_0 = 1$$

$$t_m = \sum_{n=0}^{m} [(-1)^n S_{m-n} \cdot \overline{S_n}] \qquad (m \geq 1) \tag{33e}$$

$$S_1 = 1,\ S_k = \frac{1}{k!}\prod_{n=0}^{k-1}\left(\frac{1}{2} - i\epsilon - n\right) \qquad (k \geq 1), \tag{33f}$$

Γ and Ω are defined in equation (27), c_{2j}'s are defined in equation (23d), b_{2j}'s are defined in equation (23e), and d_{2j}'s are defined in equation (11). Derivation of equations (32), and (33a)-(33f) involve the use of the integration technique given by Muskhelishvili (1953, Section 110) and that fact that $[\varphi_1(z)/R(z)] \to 0$ at infinity (zero-resultant forces at infinity). Equation (32) is clearly a convergent solution because C_j's is a convergent series. The relationship between the complex stress intensity factor K defined in equation (31a), and another complex stress intensity factors $(K_1 + iK_2)$ defined by Sih and Rice (1964) and Rice and Sih (1965), is (Rice, 1988)

$$K = (K_1 + i\,K_2)\sqrt{\pi}\cosh(\pi\epsilon). \tag{33g}$$

5 Applications and Discussion

The current interface crack problem degenerates into a crack problem in a homogeneous material if material 1 and material 2 are identical. For a completely insulated crack in a homogeneous material, $h = 0$, $d_0 = 1$, $d_j = 0$ $(j \geq l)$, and

$$K = i\,K_{II} = i\mu\eta q_o a\sqrt{\pi a}/(2k) \tag{34}$$

$$M(x) = 2q_o\sqrt{(a^2 - x^2)} \qquad |x| \leq a. \tag{35}$$

The stress intensity solution in equation (34) is identical to the solution provided by Sih (1962) and the temperature jumps across the crack surfaces due to the distributed dipoles with distribution function $M(x)$ of equation (35) can be shown to be the same as the temperature jumps predicted by Goodier and Florence (1959). Also, it can be easily shown that for a partially insulated crack $(h > 0)$ in a homogeneous material, the stress intensity factor solution, equation (32), as well as the dipole distribution function, equation (10), degenerate to the solutions obtained by Kuo (1989) in which the influence function method, instead of the stress function method, was used in calculating the stress intensity factor. It should be noted that, in the homogeneous material case, the stress intensity factor solutions remain unchanged whether, at infinity, the solid is stress-free or is restrained in the x direction according to equation (1).

Next, we consider the problem of an interface crack in two different composite solids, Cu/Al and Ti/Al_2O_3. Material properties of the four materials are depicted in Table 1. Bimaterial constants α, β, ϵ, and γ for the two composite solids are listed in Table 2, where γ is defined as $(\delta_1 - \delta_2)/(\delta_1 + \delta_2)$ (Martin-Moran et al., 1983). As shown in Table 2, the bimaterial constant, ϵ, for the two example problems are found to be -0.0208 for the Cu/Al case and 0.0394 for the Ti/Al_2O_3 case. Also, as shown in Fig. 1 and Table 2, when q_o is positive, the heat flow is into a less distortive material for the Cu/Al case and is into a more distortive material for the Ti/Al_2O_3 case. The resulting normalized thermal dipole distribution functions and normalized complex stress intensity factor under different degrees of crack surface conductance for the Cu/Al case are illustrated in Figs. 2 and 4, respectively. Similar results for the Ti/Al_2O_3 case are shown in Figs. 3 and 4. In Fig. 4, the complex stress intensity factors have been normalized by K_o, where

$$K_o = \mu_1\eta_1 q_o a\sqrt{\pi a}(2a)^{i\epsilon}/(2k_1) \tag{36}$$

and in Figs. 2 and 3, the dipole distribution functions have been normalized by M_o, where

$$M_o = 2q_o aD \tag{37}$$

and D is an unit thickness. In Figs. 2, 3, and 4, it is seen that, for a given half-crack length, a, the stress intensity factors, the magnitudes of the dipole intensities, and thus the temperature jumps across the crack surfaces, decrease as the crack surfaces become more heat conductive (greater h and λ values). Physically, this phenomenon is anticipated. Also, as already discussed by Kuo (1989), for a given interface conductance h at the crack surfaces, the interface crack behaves more like an insulated crack when it is relatively small (smaller λ) and more like a fully heat-conductive crack when it is relatively long (greater λ). In other words, there is a new parameter

Downloaded 03 May 2010 to 171.66.16.244. Redistribution subject to ASME license or copyright; see http://www.asme.org/terms/Terms_Use.cfm

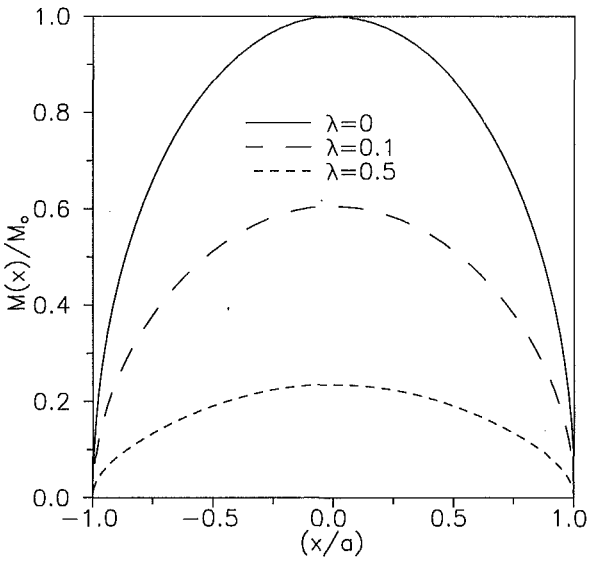


Fig. 2 Dipole distributions in Cu/Al composite

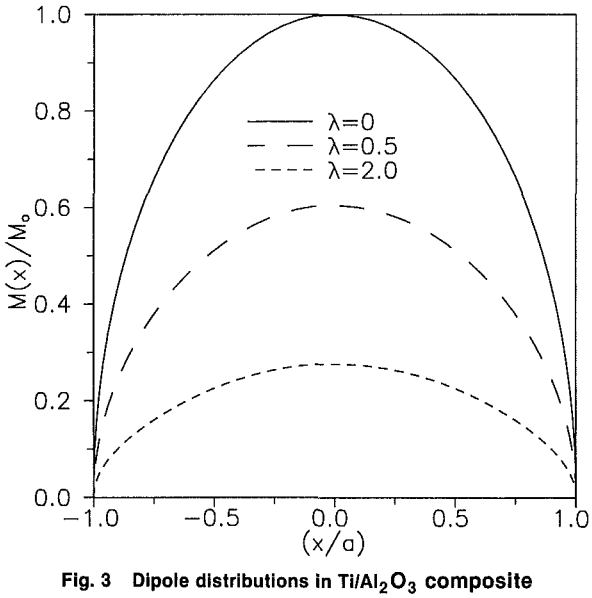


Fig. 3 Dipole distributions in Ti/Al_2O_3 composite

$\lambda = (ha/k_1)$ to the stress intensity factor solution of an interface crack subjected to thermal loading, reflecting the degree of heat conductance across the crack surfaces.

It is important to estimate the magnitude of the implicit mechanical load which, as discussed earlier in this paper, keeps the contact zone size negligible. An elementary estimate of the contact zone size r_c (Comninou, 1977, 1978, 1979) at the tip of an interface crack under isothermal condition has been given by Rice (1988) as

$$\mathrm{Re}[Kr_c^{-i\epsilon}/(1-2i\epsilon)] = 0. \tag{38}$$

Since equation (38) was derived from the asymptotic displacement field near the crack tip and the asymptotic solutions near the crack tip for the present problem share the same form as those for the isothermal problem, equation (38) should remain valid for the thermoelastic problem. As illustrated by the two example problems in this paper, the normalized contact zone size $(r_c/2a)$ is found to be negligible if $(q_o\epsilon) < 0$ but in the order of $o(1)$ if $(q_o\epsilon) > 0$. Thus, without other mechanical loading, the large contact zone for an interface crack under pure thermal loading may (if $q_o\epsilon > 0$) contradict the assumption of small contact zone and stress-free

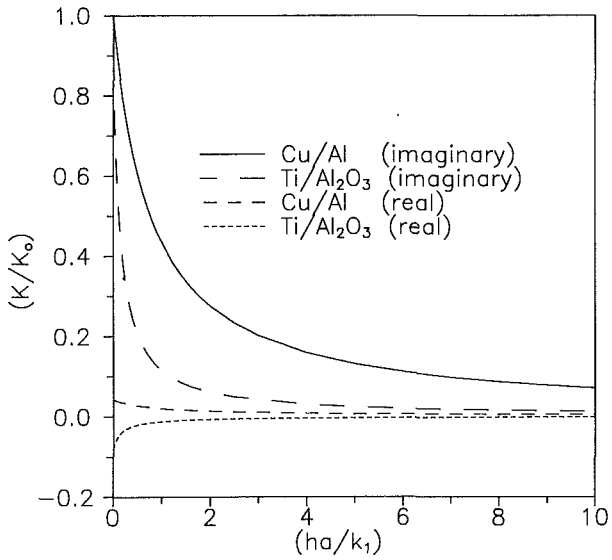


Fig. 4 Normalized complex stress intensity factors

boundary condition on the crack surfaces. Therefore, when $q_o\epsilon > 0$, an implicit mechanical loading is required to keep the interface crack open. For simplicity, it is assumed that the current thermal stress solution is to be superimposed with the stress solution of an interface crack subjected to a constant normal stress σ_{yy} $(=\sigma_o)$ at infinity. The total complex stress intensity factor for the interface crack under combined thermal and mechanical loading becomes

$$K = \{\sigma_o(1-2i\epsilon) + \mu_1\eta_1 \frac{q_o a}{2k_1}[E(\lambda) + iF(\lambda)]\}\sqrt{\pi a}(2a)^{i\epsilon} \tag{39}$$

where $E(\lambda)$ and $F(\lambda)$ are, respectively, the real and imaginary curves shown in Fig. 4. If we adopt $(r_c/2a) < 0.01$ as an acceptable limit for the contact zone size so that the small-scale contact zone concept may be applied, then, from equations (38) and (39), it is required that

$$\sigma_o \geq 0.31 \ \mathrm{sign}(\epsilon)\ [\mu_1\eta_1 q_o a F(\lambda)]/k_1 \tag{40}$$

approximately for both example problems. It is seen from equation (40) that, even without any tensile stress $(\sigma_o > 0)$ at infinity, the contact zone size is already negligible when the bimaterial constant ϵ is negative and the heat flux is into material 2 (lower material) or when the bimaterial constant ϵ is positive and the heat flux is into material 1 (upper material). However, if $(q_o\epsilon) > 0$, as far-field tensile stress greater than that given by equation (40) is needed to keep the interface crack "open." This restriction can generally be met in practical cases for which there exists some nonnegligible tensile component of the mechanical loading perpendicular to the crack. For instance, for a completely insulated interface crack of length 0.002 m under a constant heat flow of $q_o = 10000$ W/m^2, the minimum tensile stress σ_o at infinity to make the contact zone size negligible is only 0.129 MPa (18.6 psi) and 0.148 MPa (21.4 psi) for the cases of Cu/Al and Ti/Al_2O_3 composites, respectively. However, even though the aforementioned calculated tensile stresses needed to keep the crack open are very small, the applied heat flux are also small, and thus the tensile stresses required to keep the crack open should not be presumed to be small in actual application without checking. Under certain conditions, e.g., if there exists a big compressive stress perpendicular to the crack or if the crack is subjected to a heat flow of which $q_o\epsilon$ is greater than zero, the small-scale contact zone concept is no longer valid and the local contact model (Comninou, 1977, 1978, 1979 and Sturla and Barber, 1988) or the finite deformation theory (Knowles and Sternberg, 1983) must be used. For open inter-

Downloaded 03 May 2010 to 171.66.16.244. Redistribution subject to ASME license or copyright; see http://www.asme.org/terms/Terms_Use.cfm

face cracks, it seems more realistic, at least in the crack region near the crack tip, to assume that the crack surface contact conductance, h, be a function of the local crack opening displacement. Such a dependence of h on the crack opening displacement would not only make the thermoelastic problem nonlinear, but also make the heat conduction equations coupled with thermal stress equation. More studies, both experimentally and analytically, are thus needed on the effects of local crack opening displacement on temperature and thermal stress solutions. Finally, for a partially closed interface crack, it seems reasonable to assume that the interface conductance h on the crack surface is approximately a linear function of contact pressure as discovered by Thomas and Probert (1970). A solution for a partially closed interface crack under a constant heat flow will be reported in a separate paper.

Acknowledgment

The author is grateful to Prof. David Barnett of Stanford University for his helpful discussion on this topic. The author would also like to thank the reviewers of this paper for their valuable suggestions.

References

Barber, J. R., 1976, "The Disturbance of a Uniform Steady-State Heat Flux by a Partially Conducting Plane Crack," *Int. J. Heat Mass Transfer*, Vol. 19, pp. 956–958.

Barber, J. R., 1979, "Steady-State Stress Caused by an Imperfectly Conducting Penny-Shaped Crack in an Elastic Solid," *Journal of Thermal Stresses*, Vol. 3, pp. 77–83.

Barber, J. R., and Comninou, M., 1983, "The Penny-Shaped Interface Crack With Heat Flow: II—Imperfect Contact," ASME JOURNAL OF APPLIED MECHANICS, Vol. 50, pp. 770–776.

Brown, E. J., and Erdogan, F., 1968, "Thermal Stresses in Bonded Materials Containing Cuts on the Interface," *Int. J. Engng Sci.*, pp. 517–529.

Carslaw, H. S., and Jaeger, J. G., 1959, *Conduction of Heat in Solids*, Oxford University Press, London, U.K.

Comninou, M., 1977a, "The Interface Crack," ASME JOURNAL OF APPLIED MECHANICS, Vol. 44, pp. 631–636.

Comninou, M., 1977b, "Interface Crack With Friction in the Contact Zone," ASME JOURNAL OF APPLIED MECHANICS, Vol. 44, pp. 780–781.

Comninou, M., 1978, "The Interface Crack in a Shear Field," ASME JOURNAL OF APPLIED MECHANICS, Vol. 45, pp. 287–290.

Comninou, M., and Schmueser, D., 1979, "The Interface Crack in a Combined Tension-Compression and Shear Field," ASME JOURNAL OF APPLIED MECHANICS, Vol. 46, pp. 345–348.

Comninou, M., and Dundurs, J., 1979, "On the Barber Boundary Conditions for Thermoelastic Contact," ASME JOURNAL OF APPLIED MECHANICS, Vol. 46, pp. 849–853.

Dundurs, J., 1969, "Discussion on Edge-Bonded Dissimilar Orthogonal Elastic Wedges Under Normal and Shear Loading," ASME JOURNAL OF APPLIED MECHANICS, Vol. 36, pp. 650–652.

Dundurs, J., and Panek, C., 1976, "Heat Conduction Between Bodies with Wavy Surfaces," *International Journal of Heat and Mass Transfer*, Vol. 19, pp. 731–736.

Goodier, J. N., and Florence, A. L., 1959, "Thermal Stress Due to Disturbance of Uniform Heat Flow by Cavities and Inclusions," 1959, Technical Report No. 120, Division of Engineering Mechanics, Stanford University, Stanford, Calif.

Holman, J. P., 1972, *Heat Transfer*, 3rd ed., McGraw-Hill, New York.

Hutchinson, J. W., Mear, M. E., and Rice, J. R., 1987, "Crack Paralleling an Interface Between Dissimilar Materials," ASME JOURNAL OF APPLIED MECHANICS, Vol. 54, pp. 828–832.

Knowles, J. K., and Sternberg, E., 1983, "Large Deformation Near a Crack Tip of an Interface-Crack Between Two Neo-Hookian Sheets," *Journal of Elasticity*, Vol. 13, pp. 257–293.

Kuo, A. Y., et al., 1989, "Stress Intensity Factors for Cracking Metal Structures under Rapid Thermal Loading," Final Report WRDC-TR-89-3074 Flight Dynamics Lab., Wright-Patterson A.F.B., Ohio.

Martin-Moran, C. J., Barber, J. R., and Comninou, M., 1983, "The Penny-Shaped Interface Crack With Heat Flow: I—Perfect Contact," ASME JOURNAL OF APPLIED MECHANICS, Vol. 50, pp. 29–36.

Muskhelishvili, N. I., 1953, *Some Basic Problems of the Mathematical Theory of Elasticity*, P. Noordhoff Co., Groningen, Holland.

Parkus, H., 1968, *Thermoelasticity*, Blaisdell Publishing Co.

Rice, J. R., and Sih, G. C., 1965, "Plane Problems of Cracks in Dissimilar Media," ASME JOURNAL OF APPLIED MECHANICS, Vol. 32, pp. 418–423.

Rice, J. R., 1988, "Elastic Fracture Mechanics Concepts for Interfacial Cracks," ASME JOURNAL OF APPLIED MECHANICS, Vol. 55, pp. 98–103.

Rohsenow, W. M., and Hartnett, J. P., 1973, *Handbook of Heat Transfer*, McGraw-Hill New York.

Sih, G. C., 1962, "On the Singular Character of Thermal Stresses near a Crack Tip," ASME JOURNAL OF APPLIED MECHANICS, Vol. 29, pp. 587–589.

Sih, G. C., and Rice, J. R., 1964, "The Bending of Plates of Dissimilar Materials With Cracks," ASME JOURNAL OF APPLIED MECHANICS, Vol. 31, pp. 477–482.

Sturla, F. A., and Barber, J. R., 1988, "Thermal Stresses Due To a Plane Crack in General Anisotropic Material," ASME JOURNAL OF APPLIED MECHANICS, Vol. 55, pp. 372–376.

Thomas, T. R., and Probert, S. D., 1970, "Thermal Contact Resistance: The Directional Effect and Other Problems," *International Journal of Heat and Mass Transfer*, Vol. 13, pp. 789–807.

Downloaded 03 May 2010 to 171.66.16.244. Redistribution subject to ASME license or copyright; see http://www.asme.org/terms/Terms_Use.cfm

Effect of Material Properties on the Stability of Static Thermoelastic Contact

Ronggang Zhang

J. R. Barber

Department of Mechanical Engineering and Applied Mechanics, University of Michigan, Ann Arbor, MI 48109-2125

When heat is conducted across an interface between two different materials, the interaction between thermoelastic distortion and thermal contact resistance can cause the system to be unstable. This paper investigates the influence of material properties on the stability criterion for an interface between two half planes. It is found that most material combinations exhibit one or other of two kinds of stability behavior. In one of these, the stability criterion is closely related to that for uniqueness of the steady-state solution and instability is only possible for one direction of heat flow. In the other, instability can occur for either direction of heat flow and in one case is characterized by the oscillatory growth of a pressure perturbation.

1 Introduction

If two elastic bodies at different temperatures are pressed together, there will generally be some resistance to heat flow across the interface, which will be a function of the local contact pressure (Cooper et al. (1969), Shlykov and Ganin (1964)). However, the contact pressure is itself influenced by the thermal distortion, and hence by the temperature field in the bodies (Clausing (1966), Barber (1973)), so the heat conduction and elasticity solutions are coupled through the boundary conditions. An interesting consequence is that neither uniqueness nor existence theorems can be proved in general for steady-state solutions of such coupled problems (Barber (1978)), though Duvaut (1979) has proved existence for a particular contact resistance/pressure law.

Thermomechanical coupling also raises questions of stability, which have been investigated for various one-dimensional systems, using perturbation methods (Barber et al. (1980), Barber and Zhang (1988)). If one of the bodies is rigid, it is found that the criteria for stability and uniqueness are identical—in other words, steady-state solutions are only unstable when they are nonunique, in which case there exists another stable solution to which the system will gravitate. However, when both bodies are deformable, stability depends additionally on the ratio of thermal diffusivities of the materials and the behavior is more complex. For example, in the contact of two one-dimensional rods, several qualitatively different stability patterns are obtained, depending on diffusivity ratios and the rod lengths (Barber and Zhang (1988)). In particular, this system can exhibit instability even when the steady-state solution is unique, in which case numerical studies show that a steady nonlinear oscillatory behavior is obtained.

Two and three-dimensional problems are considerably more challenging, but it has been shown that a sinusoidal contact pressure perturbation on a nominally uniform (one-dimensional) pressure between two half spaces will be unstable for sufficiently large heat fluxes (Barber (1987)). The solution follows a method developed by Dow and Burton (1972) for the analogous problem of thermoelastic instabilities in contact pressure due to frictional heating.

2 Instability of a Sinusoidal Pressure Perturbation

Consider the one-dimensional problem of two half spaces of dissimilar materials in contact over their common interface, $y=0$, with a uniform contact pressure, p_0, and a uniform heat flux, $q_y=q_0$. We postulate the possibility of an exponentially growing small perturbation in the temperature field of the form

$$T(x,y,t)=f(y)e^{bt}\cos(mx) \tag{1}$$

where x is a spatial coordinate in the plane of the interface, t is time, and b, m are constants. The function $f(y)$ is determined from the requirement that the temperature must satisfy the transient heat conduction equation, after which the change in contact pressure due to thermal distortion can be calculated. The change in contact resistance, $R(p)$, due to this contact pressure perturbation can then be found. Finally, we deduce that a perturbation of the form (1) is possible if and only if the change in contact resistance is consistent with the corresponding thermal boundary conditions at the interface.

The analysis is given in (Barber (1987)) and will not be repeated here, but we note that the system is self-excited, and hence leads to a set of homogeneous equations which have a nontrivial solution only for certain eigenvalues of the exponential growth rate, b. The characteristic equation for the eigenvalues is found to be

Contributed by the Applied Mechanics Division of THE AMERICAN SOCIETY OF MECHANICAL ENGINEERS for publication in the JOURNAL OF APPLIED MECHANICS.

Discussion on this paper should should be addressed to the Technical Editor, Leon M. Keer, The Technological Institute, Northwestern University, Evanston, IL 60208, and will be accepted until two months after final publication of the paper itself in the JOURNAL OF APPLIED MECHANICS. Manuscript received and accepted by the ASME Applied Mechanics Division, March 27, 1989.

Copyright © 1990 by ASME

Downloaded 03 May 2010 to 171.66.16.244. Redistribution subject to ASME license or copyright; see http://www.asme.org/terms/Terms_Use.cfm

$$4MR'q_0 m\left[\frac{\delta_1}{a_1(a_1+m)}+\frac{\delta_2}{a_2(m-a_2)}\right]$$

$$+R_0+\frac{1}{K_1 a_1}-\frac{1}{K_2 a_2}=0 \tag{2}$$

where

$$a_1=\sqrt{m^2+b/k_1};\ a_2=-\sqrt{m^2+b/k_2} \tag{3}$$

$$\frac{1}{2M}=\frac{1-\nu_1}{\mu_1}+\frac{1-\nu_2}{\mu_2} \tag{4}$$

$$\delta_i=\frac{\alpha_i(1+\nu_i)}{K_i}. \tag{5}$$

R_0, R' denote the contact resistance, $R(p_0)$, and the derivative, $dR(p)/dp$, at the pressure, p_0, respectively, and K_i, k_i, α_i, ν_i, μ_i, $i=1, 2$, are the thermal conductivity, diffusivity, coefficient of thermal expansion, Poisson's ratio, and modulus of rigidity, respectively, for the two materials. The physical property δ is generally referred to as the distortivity, since it relates the thermoelastic distortion to the local heat flux in steady-state two-dimensional problems (Dundurs (1974)).

Equation (2) might have many solutions, some real and some complex, each of which would correspond to a possible perturbation (eigenfunction) of the form (1). The original one-dimensional system will be unstable if *any* of these solutions for b is positive or complex with positive real part. In the present paper, we shall investigate in some detail the conditions under which this can happen and, in particular, how the stability behavior is influenced by the properties of the contacting materials.

3 Dimensionless Presentation

It is convenient to restate equation (2) in dimensionless form, by defining the following dimensionless parameters

$$R^*=R_0K_1m \tag{6}$$

$$Q^*=-4MR'\alpha_1(1+\nu_1)q_0 \tag{7}$$

$$z=b/(m^2k_1) \tag{8}$$

$$r_1=k_2/k_1;\ r_2=\delta_2/\delta_1;\ r_3=K_2/K_1 \tag{9}$$

$$c_1=(1+z)^{1/2};\ c_2=(1+z/r_1)^{1/2}. \tag{10}$$

Notice that we have introduced a negative sign into the definition (7), since the contact resistance, $R(p)$, is generally a monotonically decreasing function of p, and hence R' is negative. The definition (7) will ensure that Q^* generally has the same sign as the heat flux q_0.

Substituting the expressions (6)–(10) into equation (2), we obtain

$$Q^*=\frac{R^*+\dfrac{1}{c_1}+\dfrac{1}{r_3c_2}}{\left[\dfrac{1}{c_1(1+c_1)}-\dfrac{r_2}{c_2(1+c_2)}\right]}. \tag{11}$$

This equation cannot be solved for z in closed form, but we can solve it inversely for Q^* if z is given. We first consider the simpler case in which z is assumed to be real.

4 Real Roots

The function $Q^*(z)$ defined by equation (11) can take any of the four forms illustrated in Fig. 1(*a–d*), depending upon the ratios of material properties, r_1, r_2, r_3 and the dimensionless resistance, R^*. It is convenient to label the materials in such a way that $r_1>1$. This involves no loss in generality.

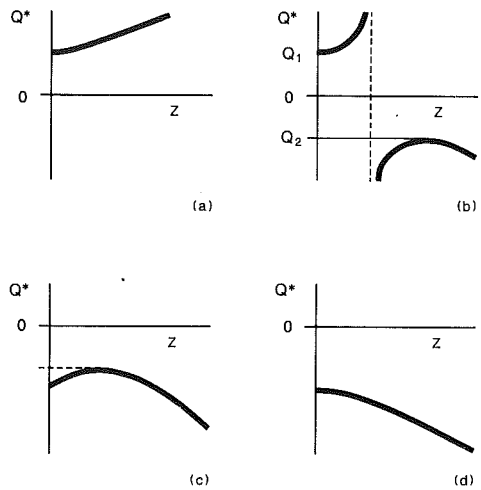


Fig. 1 Form of the function Q*(z) (equation (11)) for various ratios of material properties

If z is real and positive, it follows that c_1, c_2 are also real and positive and, hence, the numerator of the right-hand side of (11) is a positive decreasing function of z. The denominator of this expression can be written

$$D(z, r_1, r_2)=\frac{1}{c_1(1+c_1)}-\frac{r_2}{c_2(1+c_2)},$$

$$=f(z)-r_2\,f(z/r_1) \tag{12}$$

where

$$f(x)=\frac{1}{\sqrt{1+x}(1+\sqrt{1+x})}=\frac{1}{x}-\frac{1}{x\sqrt{1+x}} \tag{13}$$

is a monotonically decreasing function of z, with limiting behavior

$$f(0)=1/2;\ f(x)\to 1/x \text{ as } x\to\infty. \tag{14}$$

The corresponding limiting behavior of $D(z, r_1, r_2)$ is therefore

$$D(0, r_1, r_2)=(1-r_2)/2 \tag{15}$$

$$D(z, r_1, r_2)\to(1-r_2r_1)/z \text{ as } z\to\infty. \tag{16}$$

If a zero of equation (11) is to reach the real axis through the origin, the corresponding stability boundary will be determined by the condition $z=0$, i.e.,

$$Q^*=2(R^*+1+1/r_3)/(1-r_2) \tag{17}$$

which is possible only for the heat flow direction defined by $Q^*(1-r_2)>0$.

Recalling that $r_1>1$, we deduce immediately from equation (16) that at sufficiently large z, equation (11) will define values of Q^* of the opposite sign to (17), as in Fig. 1(*b*), provided that $1>r_2>1/r_1$. These zeros clearly cannot reach the real axis through the origin with increasing $|Q^*|$ and hence must pass into the right half plane across the imaginary axis. Material combinations whose property ratios fall into this range will exhibit instability for sufficiently large heat fluxes of *either* sign, the boundary for real roots being determined by equation (17) if $Q^*>0$ and by the *minimum* Q^* defined by (11) at larger z if $Q^*<0$. These values are labeled Q_1, Q_2, respectively, in Fig. 1(*b*).

Even for cases where a zero at the origin is possible, it can arise that the derivative of $|Q^*|$ with respect to z at the origin is negative as in Fig. 1(*c*), indicating that zeros occur on the positive real line at *lower* values of $|Q^*|$ than those needed to produce a zero at the origin. As before, these zeros must reach

Downloaded 03 May 2010 to 171.66.16.244. Redistribution subject to ASME license or copyright; see http://www.asme.org/terms/Terms_Use.cfm

Table 1 Type of behavior for different material combinations

Material No.	1	2	3	4	5	6	7	8	9	10	11	12	13	14	15	16	17	18	19
1																			
2	2																		
3	2	2																	
4	2	2	3																
5	2	2	2	1															
6	2	2	1	1	1														
7	1	3	2	2	3	2													
8	2	3	1	5	3	1	3												
9	1	2	2	2	2	2	1	2											
10	1	3	2	2	2	2	4	3	2										
11	1	2	2	2	2	2	1	2	1	2									
12	2	2	2	2	2	2	1	2	3	1	1								
13	2	2	2	2	2	2	1	2	4	1	1	1							
14	2	2	1	1	2	1	3	3	2	2	2	2	2						
15	1	2	2	2	2	2	1	2	1	1	1	1	1	2					
16	1	3	2	2	3	2	3	3	1	3	4	1	1	3	1				
17	1	1	4	5	1	3	1	5	1	1	1	1	1	5	1	1			
18	1	1	3	3	5	2	1	4	1	1	1	1	1	4	1	1	1		
19	1	3	2	2	2	2	2	3	1	2	3	1	1	2	1	1	1	1	
20	1	2	2	2	2	2	2	2	2	2	2	2	2	2	1	1	1	1	1
	1	2	3	4	5	6	7	8	9	10	11	12	13	14	15	16	17	18	19

Material No.

Table 2 Representative properties of some structural materials

No.	Material	ν	α $^{\circ}C^{-1} \times 10^{-6}$	K $W/m^{\circ}C$	k mm^2/s	δ $(m/W) \times 10^{-6}$
1	Zirconia	0.26	10.8	2.2	0.81	6.185
2	Nodular cast iron	0.31	13.7	48.9	16.05	0.367
3	Aluminium alloy	0.32	22.0	173.0	67.16	0.168
4	Beryllium/copper	0.29	17.0	147.0	42.17	0.149
5	Brass/bronze	0.33	19.0	78.0	21.35	0.324
6	Copper	0.33	17.0	381.0	101.93	0.059
7	Iron(gray cast)	0.26	12.0	50.0	12.86	0.302
8	Magnesium alloy	0.35	26.0	95.0	45.11	0.369
9	Nickel alloy	0.30	13.0	21.0	5.06	0.805
10	Carbon steel	0.30	12.0	47.0	13.27	0.332
11	Alloy steel	0.30	11.0	38.0	10.73	0.376
12	Stainless steel	0.30	14.0	21.0	5.93	0.867
13	Titanium alloy	0.33	9.0	12.0	5.45	0.998
14	Zinc alloy	0.33	27.0	111.0	36.56	0.324
15	Partially stabilized Zirconia	0.23	10.6	1.8	0.78	7.243
16	Alumina	0.20	7.7	34.0	8.52	0.272
17	SiC sintered	0.16	4.4	110.0	35.48	0.046
18	SiN Hot pressed	0.28	2.6	33.0	18.75	0.101
19	SiN Reaction bonded	0.24	2.9	10.0	8.00	0.360
20	Granite	0.28	6.5	2.5	1.09	3.328

the right half-plane by crossing the imaginary axis as $|Q^*|$ increases. Recalling that the numerator in (11) is a monotonically decreasing function of z, we note that $|Q^*|$ will decrease with z at small z for all values of R^*, r_3, provided that $|D(z, r_1, r_2)|$ *increases* with z in the same range. This in turn depends upon the sign of D and its first nonzero derivative at $z=0$. Differentiating (12) and setting z to zero, we obtain

$$D'(0, r_1, r_2) = 3(r_2/r_1 - 1)/8 \tag{18}$$

which will have the same sign as (15) if $r_1 > r_2 > 1$. We therefore conclude that the stability boundary will always be determined by a zero on the imaginary axis (corresponding to a growing oscillatory solution) if $r_1 > r_2 > 1$.

So far, we have only considered the influence of the denominator of equation (11) on the slope at $z=0$. By differentiating (11) and deleting multipliers known to be positive, we can show that $Q'(0)$ has the same sign as the expression

$$F(R^*) = 3R^*(1 - r_2/r_1) + 3(1 + 1/r_3)(1 - r_2/r_1) - 2(1 - r_2)(1 + 1/(r_1 r_3)) \tag{19}$$

which can also be regrouped in the form

$$F(R^*) = 3R^*(1 - r_2/r_1) + \{2(1 - 1/r_1) + (1 - r_2/r_1)\} + 3r_2(1 - 1/r_1) + (1 - r_2). \tag{20}$$

If $r_2 < 1$, every term in (20) is positive, as is (15), indicating that Q^* increases as we move away from the origin along the real line, as in Fig. 1(*a*, *b*). Figure 1(*b*) corresponds to the range $1 > r_2 > 1/r_1$, Fig. 1(*a*) to $r_2 < 1/r_1$.

We have already demonstrated from the properties of D alone that $Q^*(0)$ and $Q^{*\prime}(0)$ are of opposite sign for $r_1 > r_2 > 1$ and it therefore remains to consider the range $r_2 > r_1$. In this range, $Q^*(0)$ is negative (see (17)) and $F(R^*)$ will be negative for all R^* provided

$$3(1 + 1/r_3)(r_2/r_1 - 1) - 2(r_2 - 1)(1 + 1/(r_1 r_3)) > 0 \tag{21}$$

giving the form illustrated in Fig. 1(*d*). However, if $r_2 > r_1$ but (21) is not satisfied, there will be a range of values of R^* near $R^* = 0$, for which $F(R^*)$ is positive, and hence Fig. 1(*c*) behavior is obtained.

5 Summary of Stability Behavior

The preceding results enable us to characterize the stability behavior of an interface between dissimilar bodies on the basis of the dimensionless ratios of material properties. Three distinct kinds of behavior can be identified:

(*a*) Instability occurs for heat flow into the more distortive material, the stability boundary being determined by the passage of a zero through the origin in the complex plane, the corresponding criterion from (17) being

$$Q^*(1 - r_2) > 2(R^* + 1 + 1/r_3). \tag{22}$$

(*b*) Instability occurs for heat flow into the more distortive material, but at a smaller heat flux than that determined by (22). In this case, initial instability is characterized by a complex root, corresponding to a growing oscillatory solution.

(*c*) Instability occurs for heat flow into the *less* distortive material. Initial instability again corresponds to a complex root.

Labeling the bodies such that $r_1 > 1$, we find that

(1) For $0 < r_2 < 1/r_1$, type (a) behavior is always obtained.

(2) For $1/r_1 < r_2 < 1$, type (a) behavior is obtained for heat flow into the more distortive material and type (c) behavior for the opposite direction.

(3) For $1 < r_2 < r_1$, type (b) behavior is always obtained.

(4) If $r_1 < r_2$ *and* (21), type (a) behavior is always obtained.

(5) If $r_1 < r_2$ and (21) is *not* satisfied, there will be a critical value of R^* given by $F(R^*) = 0$, (see equation (19)), *below* which the behavior is of type (b) and *above* which it is of type (a).

Any given combination of materials at the interface must fall into one of these categories and we list the behavior obtained for interfaces between a representative selection of materials in Table 1. The material properties used in the development of this Table are given in Table 2.

We note from Table 1 that material combinations of type (1) and type (2) are about equally probable and together account for 89 percent of those considered. This is a consequence of the strong correlation between thermal conductivity, diffusivity, and distortivity.

6 Complex roots

For material combinations exhibiting behavior of type (b) or (c), the stability boundary corresponds to the heat flux at which a zero of equation (11) first crosses the imaginary axis. We must therefore examine the properties of this equation for complex values of z.

It is convenient to consider the more general case in which equation (11) has a solution of the form

$$z = we^{i\theta} \tag{23}$$

where w, θ are real.

Defining

$$H(z, r_1, r_3) = 1/c_1 + 1/(r_3 c_2), \tag{24}$$

we can rewrite equation (11) in the form

$$Q^* D(z, r_1, r_2) - H(z, r_1, r_3) - R^* = 0. \tag{25}$$

Separating real and imaginary parts and noting that Q^* and R^* must be real, we obtain

Downloaded 03 May 2010 to 171.66.16.244. Redistribution subject to ASME license or copyright; see http://www.asme.org/terms/Terms_Use.cfm

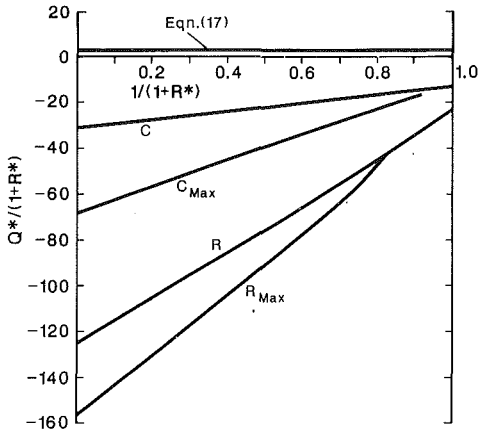


Fig. 2 Stability boundaries for an interface between aluminum alloy and stainless steel (type (2) behavior)

$$Q^*\mathrm{Re}(D) - \mathrm{Re}(H) - R^* = 0 \tag{26}$$

$$Q^*\mathrm{Im}(D) - \mathrm{Im}(H) = 0 \tag{27}$$

which can be solved inversely for a given value of z in the form

$$Q^* = \mathrm{Im}(H)/\mathrm{Im}(D) \tag{28}$$

$$R^* = Q^*\mathrm{Re}(D) - \mathrm{Re}(H). \tag{29}$$

The relation between Q^* and R^* at the complex stability boundary is then defined parametrically by setting $\theta = \pi/2$ and allowing w to take values in the range $w > 0$, noting that only those results in which $R^* > 0$ correspond to physically admissible solutions. This method also has the advantage that by setting θ to values in the range $0 < \theta < \pi/2$, we can find the conditions for unstable solutions elsewhere in the complex plane and hence track the motion of the zeros of equation (11) through the plane as Q^* increases. In particular, we can verify that they reach the positive real axis at the point corresponding to the minimum Q^* for a real root determined from Section 4 of this paper.

7 Results

Figure 2 shows the stability boundaries obtained for an interface between aluminum alloy and stainless steel, which exhibits type (2) behavior (see Table 1). Since R^* can take any positive value, it is convenient to condense the infinite range by plotting $Q^*/(1+R^*)$ against the function $1/(R^*+1)$, which is always between 0 and 1. Two curves are obtained for negative Q^*, one defining the minimum Q^* for a zero on the positive real line (curve R) and one for a zero on the imaginary axis (curve C). Curve C, of course, defines the true stability boundary for this direction of heat flow.

For positive Q^*, the stability boundary is defined by (17) and always corresponds to a real root.

Figure 3 shows the corresponding results for an interface between cast iron and brass, which exhibits type (3) behavior. Instability only occurs for $Q^* < 0$, and curves are shown for imaginary (C) and real (R) zeros as before.

8 Dominant Wavelengths

The stability behavior just described shows considerable similarity to that obtained in the related problem where heat is generated at the interface due to sliding (Dow and Burton (1972)). Azarkhin and Barber (1985) developed a numerical solution to investigate the behavior of such a system and noted that an initially smooth contact pressure distribution tends to develop wavy perturbations of a well-defined spatial wavelength, corresponding to the maximum exponential growth rate in Dow and Burton's perturbation analysis (Dow and Burton (1972)).

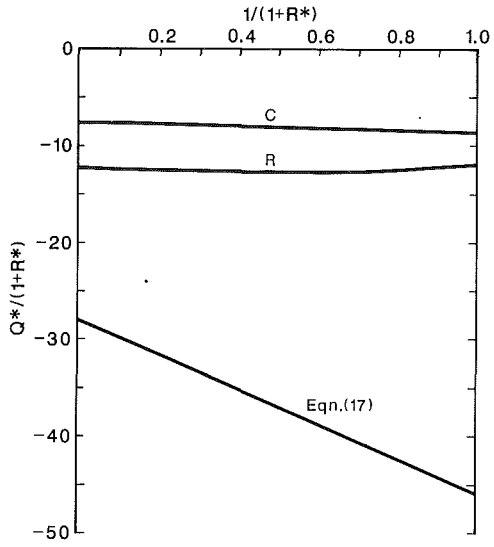


Fig. 3 Stability boundaries for an interface between cast iron and brass (type (3) behavior)

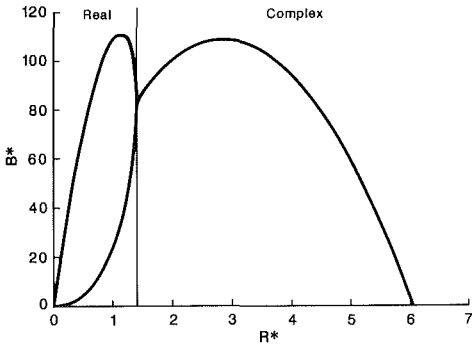


Fig. 4 Exponential growth rate of a perturbation as a function of wavelength for an aluminum alloy/stainless steel interface. Results are for a heat flux $Q^* = -200$.

We might anticipate a similar result for the present system. We note from equation (11) that instability occurs at a lower value of Q^* if R^* is small, corresponding to small values of m, and hence long wavelength perturbations. However, long wavelength perturbations involve changing the temperature of large masses of material and are likely to have low exponential growth rates.

We can investigate this question by using the inverse solution technique of Sections 4 and 6 iteratively to determine z for given values of Q^* and R^*. The results for an interface between aluminum alloy and stainless steel are presented in Fig. 4. We remove the wavelength dependence in the dimensionless parameter z by plotting the real part of the product

$$B^* = z(R^*)^2 = (R_0 K_1)^2 b/k_1 \tag{30}$$

as a function of R^* for various values of Q^*. For given values of R_0 and the material properties, B^* is proportional to b and R^* is proportional to m. Thus, Fig. 4 shows the effect of m on the real part of b, which defines the rate at which the magnitude of the perturbation grows. When the roots are real, two distinct curves are obtained, since the zeros of equation (11) bifurcate when they reach the real line, one moving towards the origin and one towards infinity. Of course, the root with the larger growth rate will dominate the transient behavior in this case.

The curve shows two maxima for B^*—one in the complex root range and one on the upper branch of the root curve. The

Downloaded 03 May 2010 to 171.66.16.244. Redistribution subject to ASME license or copyright; see http://www.asme.org/terms/Terms_Use.cfm

corresponding values of R^* are identified by the curves C_{max} and R_{max} in Fig. 2.

The two maximum values of B^* are relatively close, indicating that both wavelengths would play a significant part in the initial transient behavior of the system.

For the cast iron/brass interface, we find that the curves similar to Fig. 4 show a maximum at the complex/real transition, and hence the dominant wavelength corresponds to the curve R in Fig. 3.

9 Conclusions

An analysis of the stability criterion for the thermoelastic contact of two dissimilar materials shows that material combinations can be classified into one of five categories depending upon the ratios of the thermal conductivities, diffusivities, and distortivities.

The most common cases are:

(1) Stability behavior is similar to that for one material systems—i.e., the stability criterion is independent of the thermal diffusivities. In particular, instability only occurs when the heat flows into the material of higher distortivity, which is also the condition required for nonuniqueness of the steady-state solution.

(2) The same stability criterion is obtained for heat flow into the more distortive material, but instability is also possible for heat flow into the less distortive material. In the latter case, the steady-state solution is believed to be unique and the stability boundary is characterized by the growth of sinusoidal perturbations with complex growth rates, indicating oscillatory behavior.

When the system is unstable, the exponential growth rate depends upon the spatial wavelength of the perturbation and hence a range of preferred wavelengths is expected to dominate the transient behavior. This question is currently being investigated, using a direct numerical solution of the full nonlinear two-dimensional thermoelastic contact problem.

Acknowledgments

The authors are pleased to acknowledge the support of the National Science Foundation through grant number MSM-8719073.

References

Azarkhin, A., and Barber, J. R., 1985, "Transient thermoelastic contact problem of two sliding half-planes," *Wear*, Vol. 102, pp. 1–13.

Barber, J. R., 1973, "Indentation of the semi-infinite elastic solid by a hot sphere," *Int. J. Mech. Sci.*, Vol. 15, pp. 813–819.

Barber, J. R., 1978, "Contact problems involving a cooled punch," *J. Elasticity*, Vol. 8, pp. 409–423.

Barber, J. R., 1987, "Stability of thermoelastic contact," *Institution of Mechanical Engineers*, International Conference on Tribology, London, pp. 981–986.

Barber, J. R., and Zhang, R. G., 1988, "Transient behaviour and stability for the thermoelastic contact of two rods of dissimilar materials," *Int. J. Mech. Sci.*, Vol. 30, pp. 691–704.

Barber, J. R., Dundurs, J., and Comninou, M., 1980, "Stability considerations in thermoelastic contact," ASME Journal of Applied Mechanics, Vol. 47, pp. 871–874.

Clausing, A. M., 1966, "Heat transfer at the interface between dissimilar metals—the influence of thermal strain," *Int. J. Heat Mass Transfer*, Vol. 9, pp. 791–801.

Cooper, M. G., Mikic, B. B., and Yovanovich, M. M., 1969, "Thermal contact conductance," *Int. J. Heat Mass Transfer*, Vol. 12, pp. 279.

Dow, T. A., and Burton, R. A., 1972, "Thermoelastic instability of sliding contact in the absence of wear," *Wear*, Vol. 19, pp. 315–328.

Dundurs, J., 1974, "Distortion of a body caused by free thermal expansion," *Mech. Res. Comm.*, Vol. 1, pp. 121–124.

Duvaut, G., 1979, "Free boundary problem connected with thermoelasticity and unilateral contact," *Free boundary problems*, Vol. II, Pavia.

Shlykov, Yu. P., and Ganin, Ye. A., 1964, "Thermal resistance of metallic contacts," *Int. J. Heat Mass Transfer*, Vol. 7, pp. 921–929.

Downloaded 03 May 2010 to 171.66.16.244. Redistribution subject to ASME license or copyright; see http://www.asme.org/terms/Terms_Use.cfm

Cross-Approximation Method for Solving Dynamics Problems of Arbitrarily Shaped Plates

K. Poltorak
Institute of Machine Design Fundamentals,
Warsaw Technical University.
02-524 Warszawa, Poland

This paper deals with a new method for solving dynamics problems of arbitrarily shaped plates. The method consists in cross approximation of functions satisfying solely an equation of motion and functions satisfying solely boundary conditions on irregular plate edges. This approach is applied in the paper to the case of free and forced vibration of homogeneous and sandwich plates with edges of various shapes. Functions satisfying boundary conditions are determined by the Rvachev's R-*function method. The validity of the method is discussed.*

Introduction

Considering imperfections of all present methods for solving dynamics problems of arbitrarily shaped plates, developing of new competitive methods is still justified. Moreover, majority of the present methods is limited to the case of thin homogeneous plates, since they are based upon the classical plate theory. Therefore, it seems reasonable to develop such methods which comprise a broader class of plates like sandwich and laminated ones.

Recently a method for analyzing free and forced vibration of sandwich plates with irregular boundaries, based upon the Yan and Dowell (1972) theory of layered plates, has been given by Poltorak and Nagaya (1985, 1986). This method has turned out to be very effective (fast in computation and accurate) within certain limitations imposed on the shape of the plate areas.

This paper deals with another method which can be useful in the investigation of selected dynamics problems of both arbitrarily shaped homogeneous and sandwich plates.

Basic Principles

It is assumed in the current study that two families of functions are known for a given plate:

(1) a multiparametric family of functions which satisfy an equation of motion for a given forced vibration case but does not satisfy boundary conditions. Let it be put down in the form:

$$w = w(r,\theta,t,a_1,a_2,\ldots a_N) \tag{1}$$

where r and θ are polar coordinates, t = time, and $a_1,a_2,\ldots a_N$ are family parameters.

(2) a multiparametric family of functions which satisfy boundary conditions on irregular boundaries but does not satisfy the equation of motion. This can be written down as

$$u = u(r,\theta,t,b_1,b_2,\ldots b_M) \tag{2}$$

where $b_1,b_2,\ldots b_M$ are parameters of the family.

It is also assumed that a loading function varies periodically with time. Thus, one can write

$$w = \bar{w}(r,\theta,a_1,a_2,\ldots a_N)e^{i\omega t} \tag{3}$$

$$u = \bar{u}(r,\theta,b_1,b_2,\ldots b_M)e^{i\omega t}. \tag{4}$$

In general, when systems with internal damping are considered, parameters a_i and b_i are complex. In the current investigation, however, damping properties of materials are neglected, so these parameters become real.

Usually families of functions $\bar{w}$ and $\bar{u}$ are expressed in the form of infinite sums of convergent series. In such cases the number of parameters is $N=M=\infty$.

Let it be assumed for a while that such a set of parameters $a_1^*,a_2^*,\ldots$ is known, that function w satisfies exactly not only the equation of motion but the boundary conditions too, and such a set of parameters $b_1^*,b_2^*,\ldots$ is known that function u satisfies exactly not only boundary conditions but also the equation of motion. Then for a given time t^* the following expression is true

$$\iint_\Omega [\bar{w}(r,\theta,a_1^*,a_2^*,\ldots)e^{i\omega t^*} - \bar{u}(r,\theta,b_1^*,b_2^*,\ldots)e^{i\omega t^*}]^2 d\Omega = 0 \tag{5}$$

where Ω is a plate area. On dividing by $e^{i\omega t^*}$ one has

$$\iint_\Omega [\bar{w}(r,\theta,a_1^*,a_2^*,\ldots) - \bar{u}(r,\theta,b_1^*,b_2^*,\ldots)]^2 d\Omega = 0. \tag{6}$$

In practical problems, however, infinite sums of series are replaced by their partial sums. Then integral (6) takes a certain small value c which depends on the convergence of both series and on the number of terms included:

$$\iint_\Omega [\bar{w}(r,\theta,a_1^*,a_2^*,\ldots a_N^*) - \bar{u}(r,\theta,b_1^*,b_2^*,\ldots b_M^*)]^2 d\Omega = c \tag{7}$$

Contributed by the Applied Mechanics Division of THE AMERICAN SOCIETY OF MECHANICAL ENGINEERS for publication in the JOURNAL OF APPLIED MECHANICS.

Discussion on this paper should be addressed to the Technical Editor, Leon M. Keer, The Technological Institute, Northwestern University, Evanston, IL 60208, and will be accepted until two months after final publication of the paper itself in the JOURNAL OF APPLIED MECHANICS. Manuscript received by the ASME Applied Mechanics Division, April 1, 1988; final revision, April 3, 1989.

Copyright © 1990 by ASME
Downloaded 03 May 2010 to 171.66.16.244. Redistribution subject to ASME license or copyright; see http://www.asme.org/terms/Terms_Use.cfm

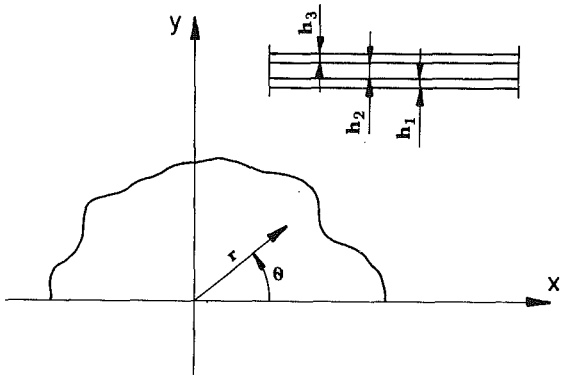


Fig. 1 Geometry of a sandwich plate with arbitrary shape

This suggests an idea that the unknown parameters $a_1^*, a_2^*, \ldots a_N^*, b_1^*, b_2^*, \ldots b_M^*$ can be found approximately as a result of seeking for minimum of the following functional

$$I(a_1, a_2, \ldots a_N, b_1, b_2, \ldots b_M) =$$

$$= \int\int_\Omega [\bar{w}(r,\theta,a_1,a_2,\ldots a_N) - \bar{u}(r,\theta,b_1,b_2,\ldots b_M)]^2 d\Omega. \quad (8)$$

Equation (8) has an analogy to the least square approximation with this difference, however, that the functions $\bar{w}$ and $\bar{u}$ are here both the approximating and approximated functions for each other.

The present method can be used for determination of a plate response to a dynamic excitation. It can also be used for determination of free vibration frequencies by detecting changes of vibration modes.

Functions Satisfying Equation of Motion

Let us take, for example, the solution of the Yan and Dowell (1972) equation of motion for three-layered plates (see Fig. 1) having at least one axis of symmetry and subject to uniformly distributed transverse loading given by Poltorak and Nagaya (1986). After dividing by $e^{i\omega t}$ this solution takes the following nondimensional form of a desired multiparametric family of functions:

$$\bar{w} = \sum_{n=0}^{\infty} \epsilon_n [A_n J_n(\mu' r') + B_n Y_n(\mu' r')$$

$$+ C_n I_n(\psi' r') + D_n K_n(\psi' r')] \cos n\theta - 1/4\beta(\mu'\psi')^2. \quad (9)$$

Here J_n, Y_n, I_n, and K_n are respective Bessel functions, $\epsilon_n = 1/2$ for $n = 0$ and $\epsilon_n = 1$ for $n \geq 1$, $r' = r/a$, where a is an arbitrarily selected in-plane dimension of the plate and A_n, B_n, C_n, D_n are family parameters. β is a dimensionless stiffness parameter and μ', ψ' are dimensionless quantities affected by plate proportions, material data, and by the nondimensional frequency of excitation:

$$\lambda = a(\rho_1 h_1 \omega^2 / D_1)^{1/4} \quad (10)$$

where ρ_1, h_1, and D_1 are density, thickness, and flexural rigidity of the first elastic layer, respectively.

If the origin of the plane coordinate system is located within the plate area, then $B_n = D_n = 0$ must be taken. Moreover, if the plate consists merely of a single elastic layer, then $\mu' = \psi' = \lambda$ and $\beta = 1$.

Functions Satisfying Boundary Conditions

Some specific functions satisfying simple boundary conditions on plate edges of simple shape can be found in the literature (e.g., in Leissa's book (1969)). But a general method for plates of arbitrary shape had not been known until Rvachev (1974, 1982) developed his R-function method. He defined so-called "structures of solution"—functions which satisfy given boundary conditions regardless of the plate shape. Information about the shape is transmitted into the structure by defining "contour functions" $v(r,\theta)$ which have to satisfy the following conditions:

$$v = 0 \text{ on all plate edges,} \quad (11a)$$

$$v > 0 \text{ inside the plate area,} \quad (11b)$$

and

$$dv/dn = 1 \text{ on all plate edges,} \quad (11c)$$

where n is a normal direction to an edge. If the plate boundary consists of segments related to different types of boundary conditions, the contour functions must be defined separately for each type of edges. Let us quote a few example structures.

(1) For homogeneous and sandwich plates with all-clamped edges:

$$u_s = v^2 \sum_{k+l=0}^{M} E_{kl}\phi_{kl}. \quad (12)$$

Here and in the following expressions E_{kl} are arbitrary constants and $\phi_{kl} = \varphi_k^1(r)\varphi_l^2(\theta)$ where φ_k^1 and φ_l^2 are terms of any convergent series.

(2) For homogeneous plates with simply-supported boundaries:

$$u_s = v \sum_{k+l=0}^{M} E_{kl}\left[\phi_{kl} - \frac{1}{2} v\phi_{kl}(D_2 v + \nu T_2 v) - v D_1 \phi_{kl}\right] \quad (13)$$

where D_n and T_n are differential operators of special type (see reference by Poltorak (1986)) of order n.

(3) For homogeneous plates with partly clamped and partly free edges:

$$u_s = v_1 \sum_{k+l=0}^{M} E_{kl}\{\phi_{kl} v_2^2 A_{kl} - [v_2^3/6(v_1^2 + v_2^2)]\,[D_3(v_1^2\phi_{kl})$$
$$+ 6[v_1^2(D_1 A_{kl} + A_{kl} D_2 v_2) + A_{kl} D_1(v_1^2)]$$
$$+ (2-\nu)[D_1 T_2(v_1^2\phi_{kl}) + 2v_1^2 A_{kl} T_2 v_2]]\}, \quad (14)$$

where

$$A_{kl} = [1/2(v_1^2 + v_2^2)]\,[D_2(v_1^2\phi_{kl}) + T_2(v_1^2\phi_{kl})].$$

v_1 is a contour function related to clamped edges and v_2 is a contour function related to free edges of the plate.

Other structures of solution for various combinations of boundary conditions are available from Rvachev's book (1974).

If the contour function is known for a given plate and series and φ^1 and φ^2 are defined, the structure u_s takes the form of a desired multiparametric family of functions $\bar{u}(r,\theta,E_{00},E_{01},\ldots)$. Of course, the unknown parameters can be determined by the use of Galerkin-Ritz procedure (see, for example, works by Rvachev (1974), Waberski (1979), Poltorak (1986)). But this would lead to a multiple differentiation of function $\bar{u}$ according to the order of the equation of motion. The current method enables one to avoid this troublesome operation.

According to the Rvachev's method functions $v(r,\theta)$ are determined by transformation of logical expressions describing the area of the plate into analytical ones by using properties of so-called R-functions. In this method the following logical operations are applied:

(1) product of two regions (see Fig. 2(*a*)): $\Omega_p = \Omega_1 \cap \Omega_2$;
(2) sum of two regions (see Fig. 2(*b*)): $\Omega_s = \Omega_1 \cup \Omega_2$;
(3) complement of a region (see Fig. 2(*c*)): $\Omega_c = \bar{\Omega}$.

If the shape of the region is simple, functions $v(r,\theta)$ satisfying conditions (11*a*) and (11*b*) can be found directly from

Downloaded 03 May 2010 to 171.66.16.244. Redistribution subject to ASME license or copyright; see http://www.asme.org/terms/Terms_Use.cfm

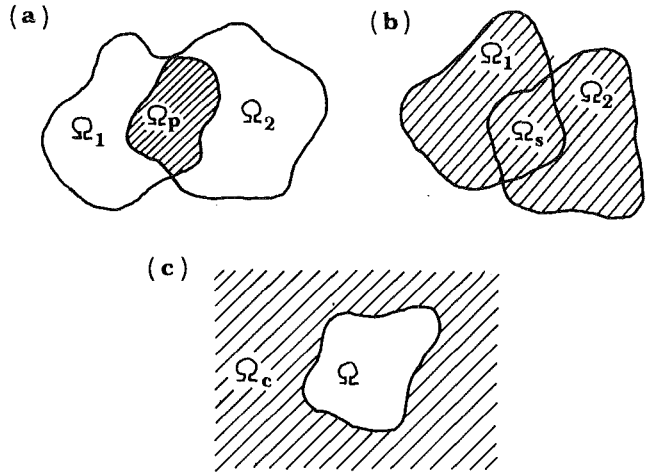


Fig. 2 Examples of logical operations: (a) product of two regions, (b) sum of two regions, and (c) complement of a region

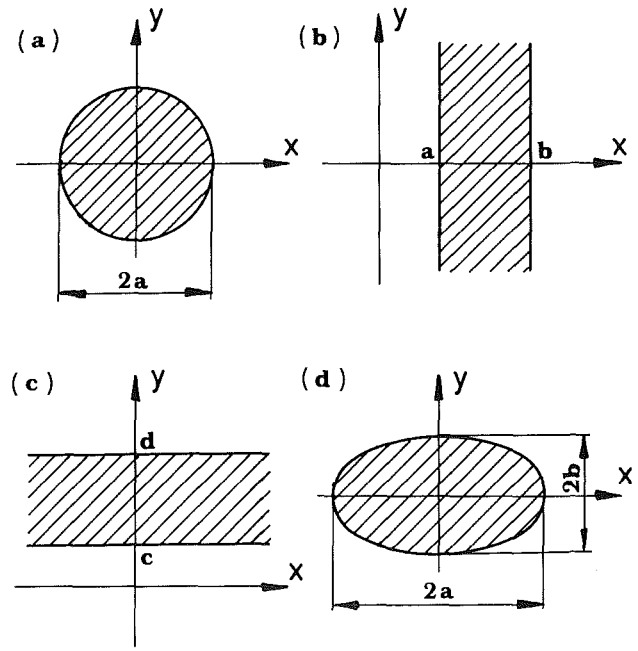


Fig. 3 Examples of elementary regions: (a) circle, (b) vertical belt, (c) horizontal belt, and (d) ellipse

analytical inequalities corresponding to these elementary regions. For example, one has:

(1) $v=a^2-r^2\geq 0$ for the circle of radius a (Fig. 3(a));

(2) $v=-ab+(a+b)x-x^2\geq 0$ where $x=r\cos\theta$ for a vertical belt (Fig. 3(b));

(3) $v=-cd+(c+d)y-y^2\geq 0$ where $y=r\sin\theta$ for a horizontal belt (Fig. 3(c));

(4) $v=1-x^2/a^2-y^2/b^2\geq 0$ where $x=r\cos\theta$ and $y=r\sin\theta$ for an ellipse (Fig. 3(d)).

A more complex area can be formed from elementary regions by applying a series of logical operations. Rvachev proposed to transform such logical expressions into analytical ones by replacing in them symbols of elementary regions by corresponding contour functions and by replacing logical operations by R-functions which transmit properties (11a) and (11b) of functions v on the resulting analytical expression. In the present study the following R-functions are used:

$$X\wedge Y=X+Y-(X^2+Y^2)^{1/2} \tag{15a}$$

$$X\vee Y=X+Y+(X^2+Y^2)^{1/2} \tag{15b}$$

$$\bar{X}=-X, \tag{15c}$$

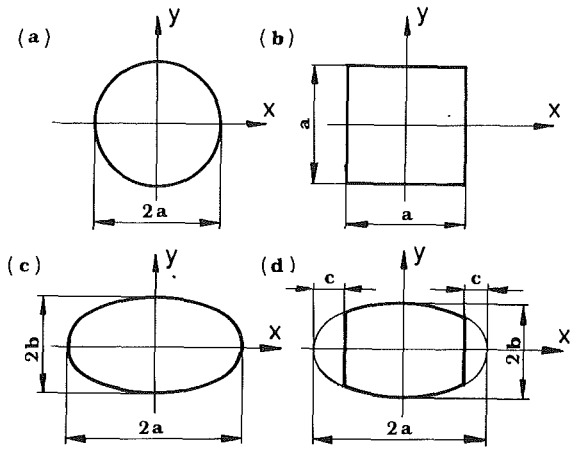


Fig. 4 Geometry of regions used in testing of the cross-approximation method: (a) circle, (b) square, (c) ellipse, and (d) ellipse truncated

referred to the logical product, sum, and complement, respectively.

It is also proven that condition (11c) will be satisfied by the resulting function when it is satisfied by all functions $v(r,\theta)$ of elementary regions. This can be achieved by introducing simple multipliers to functions $v(r,\theta)$ like, for example, $1/2a$ for the circular plate, $1/(b-a)$ for the vertical belt, or by applying the normalizing formula

$$v_n=v/[v^2+|\text{grad } v|^2]^{1/2}. \tag{16}$$

The procedure presented in this section is now applied to obtain the resulting functions $v(r,\theta)$ of several typical regions which are used next in testing of the cross-approximation method:

(1) circle (Fig. 4(a)). There is no need to apply R-functions.

$$v_c=(a^2-r^2)/2a \tag{17}$$

(2) square (Fig. 4(b)). The logical expression is $\Omega_s=\Omega_{hb}\cap\Omega_{vb}$, (product of a horizontal and vertical belt).

The corresponding analytical expression is

$$v_s=v_{hb}\wedge v_{vb}.$$

So, finally by utilizing R-function (15a), one has

$$v_s=v_{hb}+v_{vb}-(v_{hb}^2+v_{vb}^2)^{1/2} \tag{18}$$

where

$$v_{hb}=(a^2/4-r^2\cos^2\theta)/a,\ v_{vb}=(a^2/4-r^2\sin^2\theta)/a.$$

(3) ellipse (Fig. 4(c)). No need of R-functions. The analytical expression resulting directly from the equation of the ellipse is

$v_e=1-x^2-y^2/c^2$, where $x=r\cos\theta$, $y=r\sin\theta$, $c=b/a$, $a=1$.

However, it does not satisfy the condition (11c). So, by applying formula (16) one has

$$v_{el}=v_e/[v_e^2+4(x^2+y^2/c^4)]^{1/2}. \tag{19}$$

(4) ellipse truncated (Fig. 4(d)). The logical expression is $\Omega_{elt}=\Omega_{el}\cap\Omega_{vb}$ (product of an elliptical region and a vertical belt). The corresponding analytical expression is $v_{elt}=v_{el}\wedge v_{vb}$, where v_{el} is equivalent to expression (19) and $v_{vb}=(d^2/4-r^2\sin^2\theta)/d$, where $d=c/a$, $a=1$. Thus, finally by applying R-function (15a) one has

$$v_{elt}=v_{el}+v_{vb}-(v_{el}^2+v_{vb}^2)^{1/2}. \tag{20}$$

In order to complete forming of the functions satisfying boundary conditions, the selection of series φ^1 and φ^2 is required. In this paper Chebyshev's polynomials defined as

$$T(\xi x)=\cos[n\arccos\xi x] \text{ for each } n\geq 0,\ \xi x\in[-1,1], \tag{21}$$

where ξ is a normalizing factor are used as terms of those

Downloaded 03 May 2010 to 171.66.16.244. Redistribution subject to ASME license or copyright; see http://www.asme.org/terms/Terms_Use.cfm

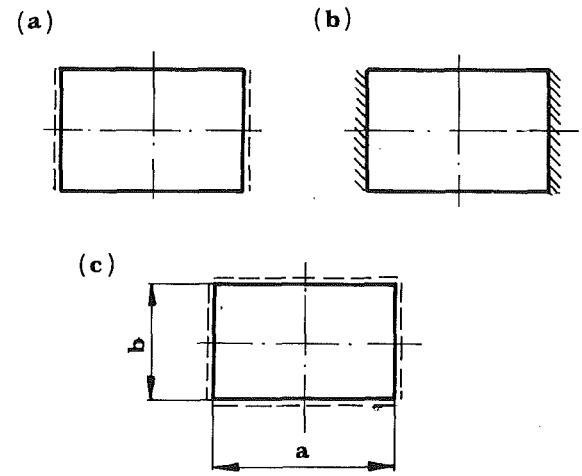


Fig. 5 Rectangular plates with (a) SS-F-SS-F, (b) C-F-C-F, and (c) SS-SS-SS-SS edges (SS-simply supported, C-clamped, F-free)

series. Of course, $x=r$ in the case of the series φ^1 and $x=\theta$ in the case of the series φ^2.

Examples

In order to illustrate the method and check its validity some numerical calculations are carried out for several examples of one and three-layered plates.

At first fundamental frequency parameters are calculated for one-layer rectangular plates with various combinations of boundary conditions (Fig. 5.) The required functional has the form:

$$I=\int\int_{\Omega}\left\{\sum_{n=0}^{N}\epsilon_n[A_nJ_n(\lambda r')+C_nI_n(\lambda r')]\cos n\theta-1/4\lambda^4-\bar{u}\right\}^2 d\Omega. \quad (22)$$

For the given problem the application of the R-function method is not yet necessary, and the following functions satisfying boundary conditions are sufficient:

$$\bar{u}=\sum_{k=1}^{M}E_k\sin^2 k\pi(r'\cos\theta+1/2) \text{ for the C-F-C-F plate;}$$

$$\bar{u}=\sum_{k=1}^{M}E_k\sin k\pi(r'\cos\theta+1/2) \text{ for the SS-F-SS-F plate;}$$

$$\bar{u}=\sum_{k+l=0}^{M}E_{kl}\sin k\pi(r'\cos\theta+1/2)\sin l\pi[(a/b)r'\sin\theta+1/2)]$$

for the SS-SS-SS-SS plate.

The minimization of functional (22), for a given value of nondimensional forcing frequency, λ, leads to the set of algebraic equations from which unknown parameters A_n, B_n, and E_{kl} can be determined. The fundamental frequency parameters are calculated by the bisectional method along the frequency axis, by checking the sign of the plate center displacement. The results for aspect ratio $b/a=0.8$ are collected in Table 1 and compared with results of other authors.

Secondly, the vibration of solid, homogeneous, and sandwich plates with all-clamped edges is considered. This time the functional is

$$I=\int\int_{\Omega}\left\{\sum_{n=0}^{N}\epsilon_n[A_nJ_n(\mu'r')+C_nI_n(\psi'r')]\cos n\theta-1/4\beta(\mu'\psi')^2-v^2(r,\theta)\sum_{k+l=0}^{M}E_{kl}T_k(\xi_1 r)T_l(\xi_2\theta)\right\}^2 d\Omega. \quad (23)$$

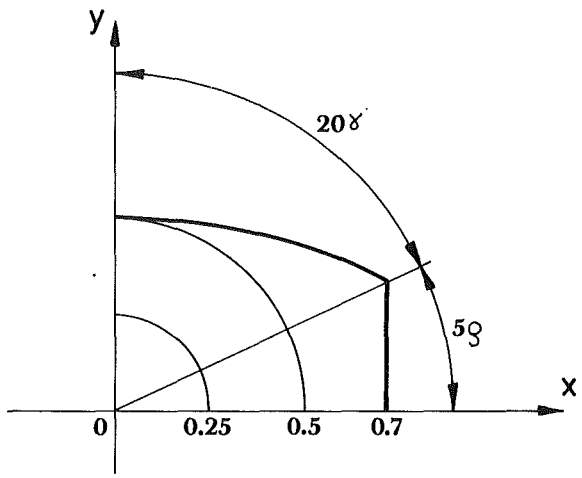


Fig. 6 Quarter of an elliptical truncated plate

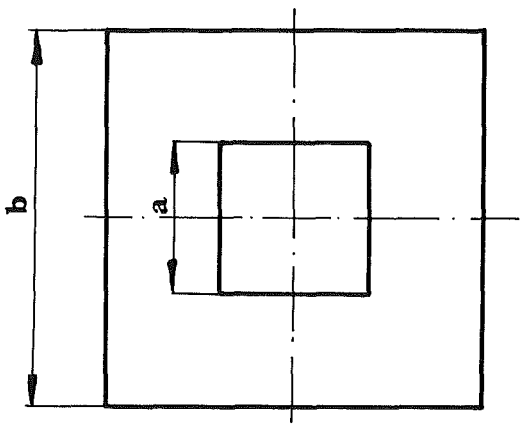


Fig. 7 Square plate with a square hole having clamped outer and free inner edges

Table 1 Comparison of fundamental frequency parameters λ_o for rectangular plates ($b/a=0.8$)

Plate	Present Results	Previous Results
SS-F-SS-F	9.87	9.87[a]
C-F-C-F	22.32	22.13[a]
SS-SS-SS-SS	25.26	25.29[a]

[a]Leissa (1969)

The calculations are carried out for circular, square, elliptical, and elliptical truncated plates. The contour functions, v, for those shapes have been derived in the previous section. In Table 2 nondimensional vibration amplitudes, $\bar{w}'$, at selected internal and boundary points of an elliptical truncated sandwich plate (see Figs. 4(*b*) and 6) obtained by the present method are compared with those of Poltorak and Nagaya (1986) calculated by the Fourier expansion collocation method for the same geometrical and material data. The assumed forcing frequency is $\lambda^2=0.5\lambda_o^2$ ($\lambda_o=5.391$ is the fundamental dimensionless resonance frequency). This comparison shows that the vibration amplitudes at the internal plate points calculated by both methods are in good agreement. Some discrepancy is observed when approaching the boundary line. The values $\bar{w}'$ at the boundary points indicate, however, that better results as regards satisfaction of the boundary condition $\bar{w}'=0$, are obtained by the present method. Table 3 shows dimensionless fundamental natural frequencies obtained by the present method for elastic homogeneous plates ($h_3/h_1=0$,

Downloaded 03 May 2010 to 171.66.16.244. Redistribution subject to ASME license or copyright; see http://www.asme.org/terms/Terms_Use.cfm

Table 2 Comparison of nondimensional vibration amplitudes $\bar{w}' \times 10^5$ at selected internal and boundary points of an elliptical, truncated sandwich plate with clamped edges, obtained by the present method with previous results of Poltorak and Nagaya (1986). Sign "−" indicates the opposite vibration phase. $\rho = 0.0595$, $\gamma = 0.0637$

No.	r / θ	0 previous/present	0.25 previous/present	0.5 previous/present	Points on the boundary line previous/present	
1	0	60.47/60.45	48.55/48.18	18.32/17.61	0.22/−0.09	straight-line segment
2	ρ	60.47/60.45	48.54/48.08	18.26/17.53	0.26/−0.04	
3	2ρ	60.47/60.45	48.17/47.81	18.06/17.29	0.32/0.06	
4	3ρ	60.47/60.45	47.72/47.38	17.68/16.84	0.25/0.12	
5	4ρ	60.47/60.45	47.14/46.82	17.06/16.16	−0.11/0.08	
6	5ρ	60.47/60.45	46.45/46.16	16.18/15.25	−0.84/0.02	corner
7	$5\delta+\gamma$	60.47/60.45	45.33/45.09	14.46/13.56	−1.24/0.13	
8	$5\rho+2\gamma$	60.47/60.45	44.91/44.69	13.76/12.90	−0.57/0.07	
9	$5\rho+3\gamma$	60.47/60.45	44.46/44.26	12.96/12.15	0.08/0.08	
10	$5\rho+4\gamma$	60.47/60.45	43.97/43.79	12.06/11.36	0.60/0.10	elliptical segment
11	$5\rho+5\gamma$	60.47/60.45	43.43/43.27	11.05/10.39	0.93/0.10	
12	$5\rho+10\gamma$	60.47/60.45	40.04/40.03	4.81/4.89	0.10/−0.02	
13	$5\rho+15\gamma$	60.47/60.45	36.16/36.26	0.32/0.65	−0.36/−0.02	
14	$5\rho+20\gamma=\pi/2$	60.47/60.45	34.24/34.37	0.35/−0.02	0.35/−0.02	

Table 3 Comparison of nondimensional fundamental natural frequencies for selected homogeneous plates with clamped edges

Plate	Form of the frequency	Present results	Previous results
circular	λ_o^2	10.217	10.216[a]
elliptical ($b/a=0.5$)	λ_o^2	27.403	27.378[a]
	$\lambda_o/2$	2.617	2.616[b]
			2.616[c]
square	λ_o^2	36.052	35.985[a]
	$\lambda o/2$	3.002	2.999[c]

[a]Leissa(1969), [b]Nagaya (1980), [c]Irie et al. (1978)

Table 4 Comparison of nondimensional fundamental natural frequencies λ_o for selected sandwich plates with symmetrically stacked layers and clamped edges

Plate	h_1/a	Results	h_2/h_1 0.5	1	2	5
circular	0.01	present	5.271	5.929	7.014	9.220
		previous	5.276	5.933	7.020	9.227
elliptical ($b/a=0.5$)	0.01	present	8.599	9.625	11.28	14.42
		previous	8.600	9.627	11.28	14.42
square	0.005	present	9.917	11.17	13.27	17.66
		previous	9.913	11.15	13.21	17.41

$h_2/h_1 = 0$) in comparison with other known results. In Table 4 dimensionless fundamental natural frequencies for selected configurations of sandwich plates (steel facings and fiber-reinforced plastic core) calculated by the cross-approximation method, with those given by Poltorak and Nagaya (1985), are compared.

Finally, a homogeneous square plate with a single central square hole is considered (Fig. 7). The outer edge of it is clamped and the inner one is free. In this case the function satisfying the equation of motion is taken in its full form (9) and the function $\bar{u}$ in form (14). The contour function v_1 for the outer edge is like this for a solid plate (18). The contour function v_2 for the inner edge has the same form but with a negative sign (consequence of logical complement). Table 5 shows the comparison of fundamental frequency paraemters for such a plate for various aspect ratios with those given by Nagaya (1981).

The values for N and M which decide on the series truncation has been taken as follows: M has been constant in all calculations and equal to 9, and N has varied in accordance with complexity of the plate shape from $N=6$ for the circular plate to $N=9$ for the truncated elliptical plate.

All of these comparisons show satisfactory agreement of both present and previous results.

Table 5 Comparison of fundamental frequency parameters λ_o for a square plate with a square hole having the outer edge clamped and the inner one free, $\nu = 0.3$.

a/b	Present results	Previous results
0.2	2.816	2.810[a]
0.3	3.073	3.067[a]
0.4	3.463	3.456[a]

[a]Nagaya (1981)

Conclusions

In the paper, the effective method for solving vibration problems of arbitrarily shaped homogeneous and sandwich plates with various boundary conditions has been proposed. No theoretical restrictions, except of symmetry, have been imposed upon the shape of the plate. Of course, even this restriction may be omitted by applying more general solutions of the equation of motion. The numerical results obtained for selected plate configurations have confirmed validity of the method.

References

Irie, T., Yamada, G., and Narita, Y., 1978, "Free Vibration of Clamped Polygonal Plates," *Bulletin of the Japan Society of Mechanical Engineers*, Vol. 21, pp. 1696–1702.

Leissa, A. W., 1969, "Vibration of Plates," NASA SP-160.

Nagaya, K., 1980, "Dynamic Response of a Plate With Arbitrary Shape," ASME JOURNAL OF APPLIED MECHANICS, Vol. 47, pp. 620–626.

Nagaya, K., 1981, "Simplified Method For Solving Problems of Vibrating Plates of Doubly Connected Arbitrary Shape, Part II: Applications and Experiments," *Journal of Sound and Vibration*, Vol. 74, pp. 553–564.

Downloaded 03 May 2010 to 171.66.16.244. Redistribution subject to ASME license or copyright; see http://www.asme.org/terms/Terms_Use.cfm

Poltorak, K., 1986, "Vibration of Plates With Straight-line, Clamped and Free Edges," *Journal of Sound and Vibration*, Vol. 104, pp. 437–447.

Poltorak, K., and Nagaya, K., 1985, "A Method for Solving Free Vibration Problems of Three-Layered Plates with Arbitrary Shape," *Journal of the Acoustical Society of America*, Vol. 78, pp. 2042–2048.

Poltorak, K., and Nagaya, K., 1986, "A Method for Solving Forced Vibration Problems of Arbitrarily Shaped Sandwich Plates," *Journal of the Acoustical Society of America*, Vol. 80, pp. 1408–1414.

Rvachev, V. L., 1974, *The Method of R-functions in Bending and Vibration Problems of Plates with Complex Boundaries*, (in Russian), Naukova Dumka, Kiev.

Rvachev, V. L., 1982, *Theory of R-functions and Some of its Applications*, (in Russian), Naukova Dumka, Kiev.

Waberski, A., 1978, "Vibration Statistics of Thin Plates With Complex Form," *AIAA Journal*, Vol. 16, pp. 788–794.

Yan, M. J., and Dowell, E. H., 1972, "Governing Equations for Vibrating Constrained-Layer Damping Sandwich Plates and Beams," ASME JOURNAL OF APPLIED MECHANICS, Vol. 39, pp. 1041–1046.

Downloaded 03 May 2010 to 171.66.16.244. Redistribution subject to ASME license or copyright; see http://www.asme.org/terms/Terms_Use.cfm

Analysis of Simply-Supported Orthotropic Cylindrical Shells Subject to Lateral Impact Loads

A. P. Christoforou

S. R. Swanson
Assoc. Mem. ASME

Department of Mechanical Engineering,
University of Utah,
Salt Lake City, UT 84112

An analytic solution is given for the problem of simply-supported orthotropic cylindrical shells subject to impact loading. The closed-form solution has not been obtained previously. The analysis is based on an expansion of the loads, displacements, and rotations in a double Fourier series which satisfies the end boundary conditions of simple support. Each expansion is assumed to be separable into a function of time and a function of position. By neglecting in-plane and rotary inertia the problem becomes a second-order ordinary differential equation in time for the Fourier coefficients of the radial deflection. For a given loading impulse the solution can be found by invoking the convolution integral. The results show that for impact by a heavy mass, the solution is equivalent to that obtained by an approximate procedure of neglecting the mass of the shell, which leads to a simple simple-degree-of-freedom analysis. For problems of impact by smaller masses, the higher response frequencies of the cylinder become important. The results show the importance of dynamic effects in the predicted impact duration, peak force, and peak deflection relative to the quasi-static response. The results show that the response amplitude varies linearly with the impact velocity, but the response characteristics depend on the mass of the impactor and the mass and stiffness of the cylinder.

1 Introduction

The response of laminated composite plates has been investigated more thoroughly than that of shells. The basic solution procedure, however, is quite similar to that applicable for shells. Thus, it is useful to examine analytic approaches used for problems in plates. The analysis of laminated composite plates subject to static and dynamic loads has been studied quite extensively in recent years. Lekhnitskii (1968), Whitney and Leissa (1970), and Jones (1975), have presented analyses with infinite transverse shear rigidity while Whitney and Pagano (1970) have presented a theory with transverse shear deformations. Sun and Chattopadhyay (1975) and Dobyns (1981) used the plate equations developed by Whitney and Pagano (1970) to analyze a simply-supported specially orthotropic plate subject to a center impact. The equations of motion are solved by assuming that the deflections at any point of the plate can be separated into a function of position and a function of time and expanded in terms of the mode shapes of the free vibrations. The transient response of the plate to impact is calculated by computing the impact force from the deceleration of the impactor mass. The derivation of the fundamental integral equation of motion was developed by Timoshenko (1928) for a rigid impact between a mass and a beam. The inclusion of the local deformation at the point of contact yields a nonlinear term in the integral equation and has to be solved numerically. In certain cases, however, the frequency of the structural response is very low when compared to the high frequencies associated with local deformation. In such situations the effects of local deformations can be neglected. Consequently, the resulting integral equation of motion during impact can be solved analytically.

The solution of the impact problem in cylindrical shells has not been obtained previously. Ramkumar and Thakar (1987) have presented an analysis on the dynamic response of curved laminated plates subjected to low velocity impact. They use Donnell's equations for thin shells, assume that the impact force varies linearly with time, and follow Dobyn's (1981) procedure to solve for the response. Kliger, Forristall, and Vinson (1973) and Vinson and Chou (1975) presented a double Fourier series solution of an orthotropic cylindrical shell subjected to a lateral concentrated static load.

In the present work an analysis is presented that predicts the response of a simply-supported orthotropic cylindrical shell to impact loads. The analysis uses a transient response due to the impact force to calculate the deflections and strains. The impact force is assumed to be distributed over a small rectangular area.

The present analysis is based on an expansion of the load, displacements, and rotations in a double Fourier series that satisfies the end boundary conditions of simple support. Each expansion is assumed to be separable into a function of time

Contributed by the Applied Mechanics Division of THE AMERICAN SOCIETY OF MECHANICAL ENGINEERS for publication in the JOURNAL OF APPLIED MECHANICS.

Discussion on this paper should be addressed to the Technical Editor, Leon M. Keer, The Technological Institute, Northwestern University, Evanston, IL 60208, and will be accepted until two months after final publication of the paper itself in the JOURNAL OF APPLIED MECHANICS. Manuscript received by the ASME Applied Mechanics Division, June 16, 1988; final revision, June 23, 1989.

Copyright © 1990 by ASME
Downloaded 03 May 2010 to 171.66.16.244. Redistribution subject to ASME license or copyright; see http://www.asme.org/terms/Terms_Use.cfm

and a function of position. Furthermore, by neglecting in-plane and rotary inertia, the problem becomes a second-order ordinary differential equation in time for the Fourier coefficients of the radial deflection. On the right-hand side of the differential equation are the Fourier coefficients of the loading function. For a given loading impulse, the solution can be found by invoking the convolution integral. In the case of impact, the impact force is computed from the deceleration of the impactor mass. This basically involves the equilibrium equation between the impactor and the shell during contact. By neglecting the local contact area deformation, the resulting integral equation can be solved algebraically for the impact force by using Laplace transforms. The expressions for the impact response and force in time are obtained by using the inversion theorem of the Laplace transforms in conjunction with the Cauchy residue theorem.

2 Governing Equations

Love's equations of motion for a circular cylindrical shell of length L, radius R, and thickness h subject to lateral loads generalized to include shear deformations, are (Bert and Birman, 1988):

$$N_{x,x}+\frac{1}{R}N_{x\theta,\theta}=\rho h\ddot{u}$$

$$N_{x\theta,x}+\frac{1}{R}N_{\theta,\theta}+\frac{1}{R}Q_{\theta}=\rho h\ddot{v}$$

$$Q_{x,x}+\frac{1}{R}Q_{\theta,\theta}-\frac{1}{R}N_{\theta}+q(x,\theta,t)=\rho h\ddot{w} \tag{1}$$

$$M_{x,x}+\frac{1}{R}M_{x\theta,\theta}-Q_x=\frac{\rho h^3}{12}\ddot{\beta}x$$

$$M_{x\theta,x}+\frac{1}{R}M_{\theta,\theta}-Q_{\theta}=\frac{\rho h^3}{12}\ddot{\beta}_{\theta}$$

where M_i and N_i are the stress couples and in-surface stress resultants, respectively; Q_i are the shear stress resultants; u, v, and w are the displacements along the axial x-axis, circumferential θ-axis and radial z-axis; β_x and β_θ are bending slopes in the x-z and θ-z planes, and t is time. A comma denotes differentiation with respect to the space variables, and a dot denotes differentiation with respect to time.

The constitutive equations for a specially orthotropic material ($B_{ij}=0$, $A_{16}=A_{26}=D_{16}=D_{26}=0$) are:

$$\begin{Bmatrix} N_x \\ N_\theta \\ N_{x\theta} \end{Bmatrix} = \begin{bmatrix} A_{11} & A_{12} & 0 \\ A_{12} & A_{22} & 0 \\ 0 & 0 & A_{66} \end{bmatrix} \begin{Bmatrix} \epsilon_x^o \\ \epsilon_\theta^o \\ \gamma_{x\theta}^o \end{Bmatrix}$$

$$\begin{Bmatrix} M_x \\ M_\theta \\ M_{x\theta} \end{Bmatrix} = \begin{bmatrix} D_{11} & D_{12} & 0 \\ D_{12} & D_{22} & 0 \\ 0 & 0 & D_{66} \end{bmatrix} \begin{Bmatrix} \kappa_x \\ \kappa_\theta \\ \kappa_{x\theta} \end{Bmatrix} \tag{2}$$

$$\begin{Bmatrix} Q_x \\ Q_\theta \end{Bmatrix} = \begin{bmatrix} kA_{55} & 0 \\ 0 & kA_{44} \end{bmatrix} \begin{Bmatrix} \gamma_{xz}^o \\ \gamma_{\theta z}^o \end{Bmatrix}$$

where A_{ij} and D_{ij} are the extensional and bending stiffnesses, and A_{ii} are the thickness shear stiffnesses

$$(A_{ij},D_{ij})=\int_{-h/2}^{h/2}(1,z^2)Q_{ij}dz \qquad (i,j=1,2,6)$$

$$A_{ii}=\int_{-h/2}^{h/2}Q_{ii}dz \qquad (i,i=4,5). \tag{3}$$

Q_{ij} are the plane stress reduced elastic stiffnesses, Q_{ii} are the thickness shear moduli and k is a shear correction factor introduced by Mindlin (1951) and is popularly taken to be $\pi^2/12$.

In equation (2), ϵ_i^o are the midsurface engineering strains, γ_{xz}^o and $\gamma_{\theta z}^o$ are the transverse shear strains and κ_i are the curvature and twist changes given by

$$\epsilon_x^o=u_{,x};\quad \epsilon_\theta^o=\frac{1}{R}v_{,\theta}+\frac{w}{R};\quad \gamma_{x\theta}^o=v_{,x}+\frac{1}{R}u_{,\theta}$$

$$\gamma_{xx}^o=\beta_x+w_{,x};\quad \gamma_{\theta z}^o=\beta_\theta+\frac{1}{R}w_{,\theta}-\frac{v}{R} \tag{4}$$

$$\kappa_x=\beta_{x,x};\quad \kappa_\theta=\frac{1}{R}\beta_{\theta,\theta};\quad \kappa_{x\theta}=\beta_{\theta,x}+\frac{1}{R}\beta_{x,\theta}.$$

The strain distributions throughout the shell are given as

$$\epsilon_x=\epsilon_x^o+z\kappa_x$$

$$\epsilon_\theta=\epsilon_\theta^o+z\kappa_\theta \tag{5}$$

$$\gamma_{x\theta}=\gamma_{x\theta}^o+z\kappa_{x\theta}$$

$$\gamma_{xz}=\gamma_{xz}^o;\quad \gamma_{\theta z}=\gamma_{\theta z}^o.$$

Substituting equations (4) and (2) into the equations of motion (1) results in a new set of equations in terms of deflections and rotations.

$$A_{11}u_{,xx}+\frac{A_{66}}{R^2}u_{,\theta\theta}+\left(\frac{A_{12}+A_{66}}{R}\right)v_{,x\theta}+\frac{A_{12}}{R}w_{,x}=\rho h\ddot{u}$$

$$\left(\frac{A_{66}+A_{12}}{R}\right)u_{,x\theta}+A_{66}v_{,xx}+\frac{A_{22}}{R^2}v_{,\theta\theta}-\frac{A_{44}}{R^2}v$$
$$+\left(\frac{A_{22}+A_{44}}{R^2}\right)w_{,\theta}+\frac{A_{44}}{R}\beta_\theta=\rho h\ddot{v}$$

$$-\frac{A_{12}}{R}u_{,x}-\left(\frac{A_{44}+A_{22}}{R^2}\right)v_{,\theta}+A_{55}w_{,xx}+\frac{A_{44}}{R^2}w_{,\theta\theta}$$
$$-\frac{A_{22}}{R^2}w+A_{55}\beta_{x,x}+\frac{A_{44}}{R}\beta_{\theta,\theta}+q(x,\theta,t)=\rho h\ddot{w} \tag{6}$$

$$-A_{55}w_{,x}+D_{11}\beta_{x,xx}+\frac{D_{66}}{R^2}\beta_{x,\theta\theta}-A_{55}\beta_x$$
$$+\left(\frac{D_{12}+D_{66}}{R}\right)\beta_{\theta,x\theta}=\frac{\rho h^3}{12}\ddot{\beta}_x$$

$$\frac{A_{44}}{R}v-\frac{A_{44}}{R}w_{,\theta}+\left(\frac{D_{66}+D_{12}}{R}\right)\beta_{x,x\theta}+D_{66}\beta_{\theta,xx}$$
$$+\frac{D_{22}}{R^2}\beta_{\theta,\theta\theta}-A_{44}\beta_\theta=\frac{\rho h^3}{12}\ddot{\beta}_\theta.$$

3 Solution Procedure

A closed-form solution of the governing equations will be developed in the following. The boundary conditions for a cylindrical shell that is freely supported (simply-supported without in-surface restraint) along its curved edges are given by

Downloaded 03 May 2010 to 171.66.16.244. Redistribution subject to ASME license or copyright; see http://www.asme.org/terms/Terms_Use.cfm

$$N_x(0,\theta,t)=N_x(L,\theta,t)=M_x(0,\theta,t)=M_x(L,\theta,t)=0$$

$$w(0,\theta,t)=w(L,\theta,t)=v(0,\theta,t)=v(L,\theta,t)=0 \tag{7}$$

$$\beta_\theta(0,\theta,t)=\beta_\theta(L,\theta,t)=0.$$

For a given load, the solution to equations (6) that satisfies the boundary conditions, equations (7), can be separated into a function of time and a function of position as follows:

$$u=U_{mn}(t)\cos n\theta\cos\frac{m\pi x}{L}$$

$$v=V_{mn}(t)\sin n\theta\sin\frac{m\pi x}{L}$$

$$w=W_{mn}(t)\cos n\theta\sin\frac{m\pi x}{L} \tag{8}$$

$$\beta_x=T_{mn}(t)\cos n\theta\cos\frac{m\pi x}{L}$$

$$\beta_\theta=B_{mn}(t)\sin n\theta\sin\frac{m\pi x}{L}$$

and the load as

$$q(x,\theta,t)=Q_{mn}(t)\cos n\theta\sin\frac{m\pi x}{L}. \tag{9}$$

Equations (8) and (9) are the double Fourier series expansions of the displacements, rotations and load, which are similar to the static case developed by Kliger, Forristall, and Vinson (1973) and Vinson and Chou (1975). This is known as the Navier solution.

In the present study the effects of in-surface rotary inertia will be assumed to be negligible. Bert and Birman (1988) mentioned these effects to be negligible in dynamic stability studies, while Dobyns (1981), by referring to Mindlin's (1951) finding made the same assumptions for the impact response of orthotropic plates. Thus, by substituting equations (8) and (9) into equations (6) and neglecting in-surface and rotary inertia yields the following set of equations:

$$\begin{bmatrix} C_{11} & C_{12} & C_{13} & C_{14} & C_{15} \\ & C_{22} & C_{23} & C_{24} & C_{25} \\ & & C_{33} & C_{34} & C_{35} \\ & & & C_{44} & C_{45} \\ \text{Sym} & & & & C_{55} \end{bmatrix} \begin{Bmatrix} U_{mn}(t) \\ V_{mn}(t) \\ W_{mn}(t) \\ B_{mn}(t) \\ T_{mn}(t) \end{Bmatrix}$$

$$= \begin{Bmatrix} 0 \\ 0 \\ \rho h\ddot{W}_{mn}(t)-Q_{mn}(t) \\ 0 \\ 0 \end{Bmatrix} \tag{10}$$

where C_{ij} are given as

$$C_{11}=-A_{11}\left(\frac{m\pi}{L}\right)^2-A_{66}\left(\frac{n}{R}\right)^2$$

$$C_{12}=C_{21}=(A_{12}+A_{66})\left(\frac{n}{R}\right)\left(\frac{m\pi}{L}\right)$$

$$C_{13}=C_{31}=\frac{A_{12}}{R}\left(\frac{m\pi}{L}\right)$$

$$C_{14}=C_{41}=C_{15}=C_{51}=0$$

$$C_{22}=-A_{66}\left(\frac{m\pi}{L}\right)^2-A_{22}\left(\frac{n}{R}\right)^2-\frac{A_{44}}{R^2}$$

$$C_{23}=C_{32}=-\left(\frac{A_{22}+A_{44}}{R}\right)\left(\frac{n}{R}\right)$$

$$C_{24}=C_{42}=\frac{A_{44}}{R}$$

$$C_{25}=C_{52}=0$$

$$C_{33}=-A_{55}\left(\frac{m\pi}{L}\right)^2-A_{44}\left(\frac{n}{R}\right)^2-\frac{A_{22}}{R^2}$$

$$C_{34}=C_{43}=A_{44}\left(\frac{n}{R}\right)$$

$$C_{35}=C_{53}=-A_{55}\left(\frac{m\pi}{L}\right)$$

$$C_{44}=-D_{66}\left(\frac{m\pi}{L}\right)^2-D_{22}\left(\frac{n}{R}\right)^2-A_{44}$$

$$C_{45}=C_{54}=-(D_{66}+D_{12})\left(\frac{n}{R}\right)\left(\frac{m\pi}{L}\right)$$

$$C_{55}=-D_{11}\left(\frac{m\pi}{L}\right)^2 D_{66}\left(\frac{n}{R}\right)^2-A_{55}. \tag{11}$$

Note that the fifth and fourth equations in (6) are fourth and fifth, respectively, in (10).

Bert and Birman (1988) obtained equations similar to (10) for a dynamic stability problem, and showed that they can be reduced to a single linear second-order differential equation by the following transformation:

$$\begin{aligned} &U_{mn}(t)=K_U W_{mn}(t); \quad V_{mn}(t)=K_V W_{mn}(t) \\ &B_{mn}(t)=K_B W_{mn}(t); \quad T_{mn}(t)=K_T W_{mn}(t) \end{aligned} \tag{12}$$

where the coefficients K_i are given by (Bert and Birman, 1988)

$$K_U=S_1+S_2K_B+S_3K_T; \quad K_V=S_4+S_5K_B+S_6K_T$$

$$K_B=\Delta_B/\Delta; \quad K_T=\Delta_T/\Delta$$

$$\Delta_B=(C_{35}+C_{15}S_1+C_{25}S_4)(C_{45}+C_{14}S_3+C_{24}S_6)$$
$$-(C_{34}+C_{14}S_1+C_{24}S_4)(C_{55}+C_{15}S_3+C_{25}S_6)$$

$$\Delta_T=(C_{45}+C_{15}S_2+C_{25}S_5)(C_{34}+C_{14}S_1+C_{24}S_4)$$
$$-(C_{44}+C_{14}S_2+C_{24}S_5)(C_{35}+C_{15}S_1+C_{25}S_4)$$

$$\Delta=(C_{44}+C_{14}S_2+C_{24}S_5)(S_{55}+C_{15}S_3+C_{25}S_6)$$
$$-(C_{45}+C_{14}S_3+C_{24}S_6)(C_{45}+C_{15}S_2+C_{25}S_5) \tag{13}$$

$$S_1=(C_{12}C_{23}-C_{22}C_{13})/S \qquad S_2=(C_{12}C_{24}-C_{22}C_{14})/S$$

$$S_3=(C_{12}C_{25}-C_{22}C_{15})/S \qquad S_4=(C_{12}C_{13}-C_{11}C_{23})/S$$

$$S_5=(C_{12}C_{14}-C_{11}C_{24})/S \qquad S_6=(C_{12}C_{15}-C_{11}C_{25})/S$$

$$S=C_{11}C_{22}-C_{12}^2.$$

Downloaded 03 May 2010 to 171.66.16.244. Redistribution subject to ASME license or copyright; see http://www.asme.org/terms/Terms_Use.cfm

Substituting equations (12) into the third equations in (10) yields

$$\ddot{W}_{mn}(t)+\frac{K_{mm}}{\rho h}W_{mn}(t)=\frac{1}{\rho h}Q_{mn}(t) \tag{14}$$

where the coefficients, K_{mn}, are given by

$$K_{mn}=-(C_{13}K_U+C_{23}K_V+C_{33}+C_{34}K_B+C_{35}K_T). \tag{15}$$

The terms of the Fourier series representation for the load, applied uniformly over a small rectangular area, $2R\phi_1(l_2-l_1)$, at the center of the cylindrical shell, $(L/2, 0)$, are

$$Q_{mn}(t)=P_{mn}\frac{F(t)}{2R\phi_1(l_2-l_1)} \tag{16}$$

where

$$P_{mn}=\frac{8}{mn\pi}\sin\frac{m\pi}{2}\sin\frac{m\pi}{2L}(l_2-l_1)\sin n\phi_1 \quad m\neq 0,\ n\neq 0 \tag{17}$$

and the P_{mo} term is obtained by replacing $(\sin n\phi_1)/n$ with ϕ_1.

Substituting equation (16) into (14) and by rearranging yields

$$\ddot{W}_{mn}(t)+\omega_{mn}^2W_{mn}(t)=\frac{P_{mn}\pi RL}{R\phi_1(l_2-l_1)}\frac{F(t)}{m_1} \tag{18}$$

where $\omega_{mn}^2=K_{mn}/\rho h$ are the fundamental frequencies of the shell and m_1 is the mass of the shell.

For zero initial displacement and velocity, the solution of equation (18) is

$$W_{mn}(t)=\frac{P_{mn}\pi RL}{R\phi_1(l_2-l_1)m_1\omega_{mn}}\int_0^t F(\tau)\sin\omega_{mn}(t-\tau)d\tau. \tag{19}$$

Using equations (19) and (12) with (8) results in expressions for the deformations in a shell under transverse loading; for example, the transverse deflection at any point of the shell is given by

$$w(x,\theta,t)=\frac{\pi RL}{R\phi_1(l_2-l_1)m_1}\sum_m\sum_n\frac{P_{mn}}{\omega_{mn}}\sin\frac{m\pi x}{L}\cos n\theta \times\int_0^t F(\tau)\sin\omega_{mn}(t-\tau)d\tau. \tag{20}$$

4 Impact Loading

The response of a cylindrical shell to impact loading may be computed from the transient response, equation (20), by computing the impact force from the deceleration of the impactor mass. The equilibrium equation between the impactor and the shell during contact is given by

$$F(t)=-m_2\ddot{W}\left(\frac{L}{2},0,t\right). \tag{21}$$

Integrating equation (21) twice yields

$$V_0t-\frac{1}{m_2}\int_0^t F(\tau)(t-\tau)d\tau=w\left(\frac{L}{2},0,t\right) \tag{22}$$

where V_0 is the initial velocity of the impactor with mass m_2, $w(L/2,0,t)$ is the deflection of the shell evaluated at the impact point as a function of time, and $F(t)$ is the impact force.

Combining equations (20) and (22) yields

$$V_0t-\frac{1}{m_2}\int_0^t F(\tau)(t-\tau)d\tau=\frac{\pi RL}{R\phi_1(l_2-l_1)m_1}\sum_m\sum_n\frac{P_{mn}}{\omega_{mn}}\sin\frac{m\pi}{2}\cos n\theta\int_0^t F(\tau)\sin\omega_{mn}(t-\tau)d\tau. \tag{23}$$

For a given impact situation equation (23) can be solved for the impact force and response of the shell.

The exact solution of equation (23) can be obtained by taking its Laplace transform, which after some algebra yields

$$F(s)=\frac{-m_2V_o}{1+\dfrac{\pi RL}{R\phi_1(l_2-l_1)}\dfrac{m_2}{m_1}\displaystyle\sum_q\sum_r P_{qr}\sin\frac{q\pi}{2}\frac{s^2}{s^2+\omega_{qr}^2}}. \tag{24}$$

The impact force history can now be determined by using the inversion theorem of the Laplace transforms in equation (24)

$$F(t)=\frac{1}{2\pi i}\int_{\gamma-i\infty}^{\gamma+i\infty}e^{ts}F(s)ds. \tag{25}$$

It follows from Cauchy's residue theorem (Arpaci, 1966) that

$$F(t)=\sum_j Res(a_j) \tag{26}$$

where $Res(a_j)$ is the residue of $e^{ts}F(s)$ evaluated at a_j, which are the simple poles of $e^{ts}F(s)$. These poles are the zeros of the denominator of $F(s)$ and are found numerically using a root-finding algorithm.

For a single pole the residue is found as

$$Res(a_j)=\lim_{s\to a_j}[(s-a_j)e^{ts}F(s)]. \tag{27}$$

Combining equations (24), (26), and (27) yields

$$F(t)=\sum_j\lim_{s\to a_j}\left[(s-a_j)\frac{-m_2V_0e^{ts}}{1+\dfrac{\pi RL}{R\phi_1(l_2-l_1)}\dfrac{m_2}{m_1}\displaystyle\sum_q\sum_r P_{qr}\sin\frac{q\pi}{2}\frac{s^2}{s^2+\omega_{qr}^2}}\right]. \tag{28}$$

Using L'Hospital's rule, equation (28) becomes

$$F(t)=\sum_j\frac{-m_2V_0e^{a_jt}}{\dfrac{\pi RL}{R\phi_1(l_2-l_1)}\dfrac{m_2}{m_1}\displaystyle\sum_q\sum_r P_{qr}\sin\frac{q\pi}{2}\frac{2a_j\omega_{qr}^2}{(a_j^2+\omega_{qr}^2)^2}}. \tag{29}$$

The simple poles a_j of $e^{ts}F(s)$ are the response frequencies and they are imaginary, $a_j=\pm i\omega_j$. Substituting in (29) and using the identity

$$\frac{e^{i\omega_jt}-e^{-i\omega_jt}}{i}=2\sin\omega_jt \tag{30}$$

yields

$$F(t)=\frac{-m_2V_0}{\dfrac{\pi RL}{R\phi_1(l_2-l_1)}\dfrac{m_2}{m_1}}\sum_j\frac{\sin\omega_jt}{\displaystyle\sum_q\sum_r P_{qr}\sin\frac{q\pi}{2}\frac{\omega_j\omega_{qr}^2}{(\omega_{qr}^2-\omega_j^2)^2}}. \tag{31}$$

Note in equation (31) that for each response frequency ω_j, the double summation in the denominator is just a constant, so in order to avoid any further calculation of this sum let

Downloaded 03 May 2010 to 171.66.16.244. Redistribution subject to ASME license or copyright; see http://www.asme.org/terms/Terms_Use.cfm

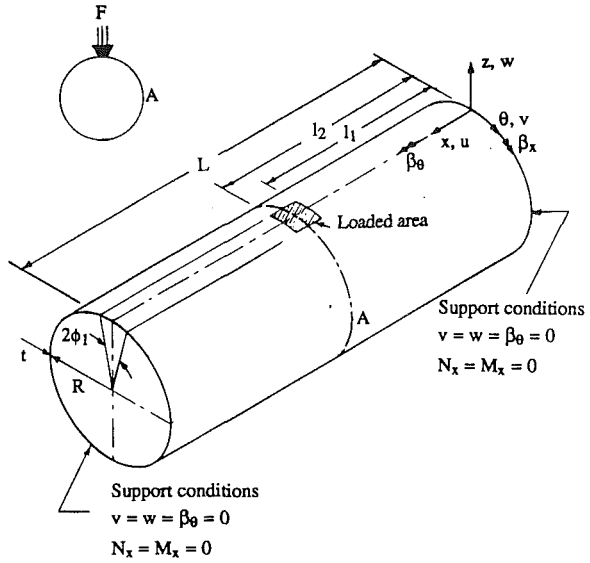


Fig. 1 Geometry of analyzed cylindrical shell

$$F_j = \frac{-m_2 V_0}{\dfrac{\pi RL}{R\phi_1(l_2-l_1)}\dfrac{m_2}{m_1}\displaystyle\sum_q\sum_r P_{qr}\sin\frac{q\pi}{2}\frac{\omega_j\omega_{qr}^2}{(\omega_{qr}^2-\omega_j^2)^2}}, \tag{32}$$

which makes equation (31)

$$F(t) = \sum_j F_j \sin \omega_j t. \tag{33}$$

Finally, the impact response can be determined by taking the Laplace transform of equation (19) as

$$W_{mn}(s) = \frac{P_{mn}\pi RL}{R\phi_1(l_2-l_1)m_1}\frac{F(s)}{s^2+\omega_{mn}^2}. \tag{34}$$

Substituting the Laplace transform of (33) into (34) yields

$$W_{mn}(s) = \frac{P_{mn}\pi RL}{R\phi_1(l_2-l_1)m_1}\sum_j \frac{F_i\omega_j}{(s^2+\omega_{mn}^2)(s^2+\omega_j^2)}. \tag{35}$$

Using the inverse theorem of the Laplace transform on equation (35) yields

$$W_{mn}(t) = \frac{P_{mn}\pi RL}{R\phi_1(l_2-l_1)m_1} \sum_j F_j\omega_j \frac{1}{2\pi i}\int_{\gamma-1\infty}^{\gamma+i\infty}\frac{e^{ts}}{(s^2+\omega_{mn}^2)(s^2+\omega_j^2)}ds. \tag{36}$$

Invoking Cauchy's residue theorem, the integral in (36) can be evaluated as

$$\frac{1}{2\pi i}\int_{\gamma-i\infty}^{\gamma+i\infty}\frac{e^{ts}}{(s^2+\omega_{mn}^2)(s^2+\omega_j^2)}ds = Res(\pm i\omega_{mn}) + Res(\pm i\omega_j). \tag{37}$$

Note that the expression inside the integral is of the form

$$f(s) = \frac{P(s)}{Q(s)R(s)} \tag{38}$$

where

$$P(s) = e^{ts}$$

$$Q(s) = s^2+\omega_{mn}^2 \tag{39}$$

$$R(s) = s^2+\omega_j^2.$$

From Arpaci (1966), the residues in equation (37) can be evaluated as follows:

$$Res(\pm i\omega_{mn}) + Res(\pm i\omega_j) = \frac{P(\pm i\omega_{mn})}{(dQ/ds)_{s=\pm i\omega_{mn}}R(\pm i\omega_{mn})} + \frac{P(\pm i\omega_j)}{Q(\pm i\omega_j)(dR/ds)_{s=\pm i\omega_j}}. \tag{40}$$

Combining equations (36), (37), (38), (39), and (40) yields

$$W_{mn}(t) = \frac{P_{mn}\pi RL}{R\phi_1(l_2-l_1)m_1}\sum_j F_j\omega_j\left[\frac{e^{i\omega_{mn}t}}{2i\omega_{mn}(\omega_j^2-\omega_{mn}^2)} + \frac{e^{-i\omega_{mn}t}}{-2i\omega_{mn}(\omega_j^2-\omega_{mn}^2)} + \frac{e^{i\omega_j t}}{(\omega_{mn}^2-\omega_j^2)(2i\omega_j)} + \frac{e^{-i\omega_j t}}{(\omega_{mn}^2-\omega_j^2)(-2i\omega_j)}\right]. \tag{41}$$

Using the identity equation of (30) in (41) yields, after some rearranging,

$$W_{mn}(t) = \frac{P_{mn}\pi RL}{R\phi_1(l_2-l_1)m_1}\sum_j \frac{F_j}{\omega_{mn}(\omega_j^2-\omega_{mn}^2)} \times(\omega_j \sin\omega_{mn}t - \omega_{mn}\sin\omega_j t). \tag{42}$$

Finally, by combining equations (42), (12), (8), (5), and (4), the deflection and strain histories at any point of the shell can be evaluated.

It can be noted that the static response can be obtained from (14) by dropping the acceleration term, and considering $F(t)$ in (16) to be a constant.

5 Results and Discussion

The major contribution of the analytic solution presented here is that it is very useful in parametric-type studies. By examining the resulting expressions one can gain a significant physical insight into the impact problem. For example, the response frequencies are the simple zeros to the denominator of equation (24). It can be seen that the response frequency, or impact duration, is independent of the impact velocity, and depends on the mass ratio and the material and geometrical parameters of the cylinder. From equations (24) and (42), it can also be seen that the impact velocity contributes only to the amplitude of the response and it is a linear contribution. Although this is a fundamental result, it has not been obvious previously.

Due to the relative calculational complexity the analytical solution presented previously has been coded into a computer program. The basic inputs to this computer program are the impact velocity, impactor mass, and the cylinder material and geometric parameters. Calculations were performed on 41.9-cm (16.5 in.) long and 96-mm (3.8 in.) I.D. cylindrical shells having a $[90/\pm 22]_{2T}$ layup of IM7/55A carbon/epoxy. Properties of this composite material system have been presented by Christoforou, Swanson, and Beckwith (1987). Fifty terms were used in each of the summations.

The problem of impact by a heavy mass much greater than that of the cylinder is a limiting case for the present analysis. In this situation the cylinder can be treated as equivalent to a massless spring, an approximation referred to as a "quasi-static" solution. Figure 2 shows a comparison between the impact force calculated by the analysis and the quasi-static force for a mass ratio of 15 and impact velocity of 3 m/sec (10 ft/sec). It can be seen that they are almost identical. Figure 3 shows the center deflection and strains versus time response. This also shows that the impact response is very similar to the static response, in that the peak deflection and strains occur at

Downloaded 03 May 2010 to 171.66.16.244. Redistribution subject to ASME license or copyright; see http://www.asme.org/terms/Terms_Use.cfm

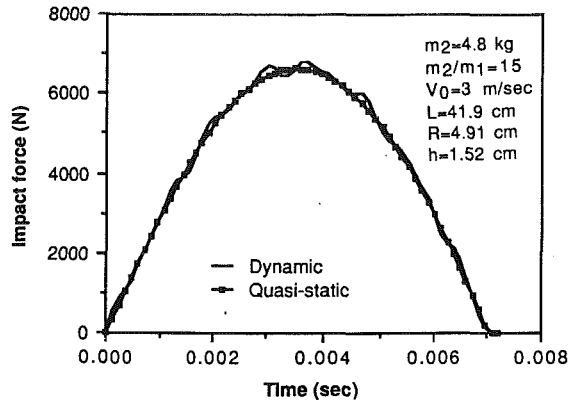


Fig. 2 Predicted force-time response of a carbon/epoxy cylindrical shell subject to impact by a heavy mass

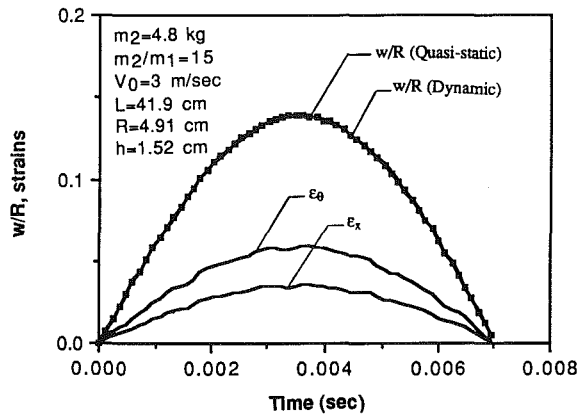


Fig. 3 Predicted center deflection and strain response of a carbon/epoxy cylindrical shell subject to impact by a heavy mass

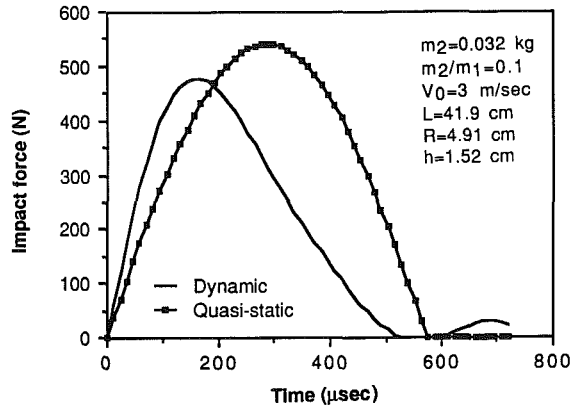


Fig. 4 Predicted force-time response of a carbon/epoxy cylindrical shell subject to impact by a small mass

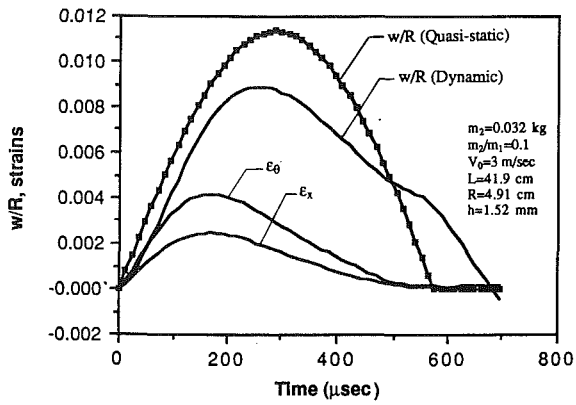


Fig. 5 Predicted center deflection and strain response of a carbon/epoxy cylindrical shell subject to impact by a small mass

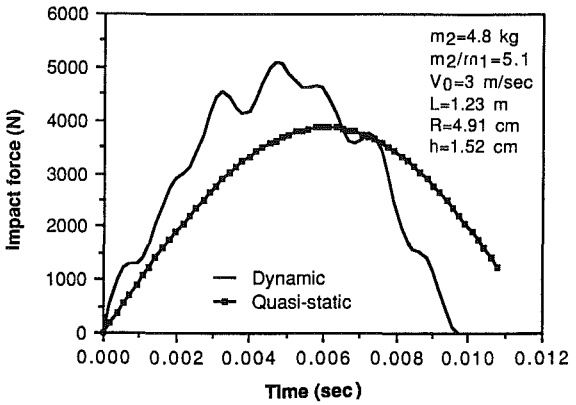


Fig. 6 Predicted force-time response of a long carbon/epoxy cylindrical shell subject to impact by a medium mass

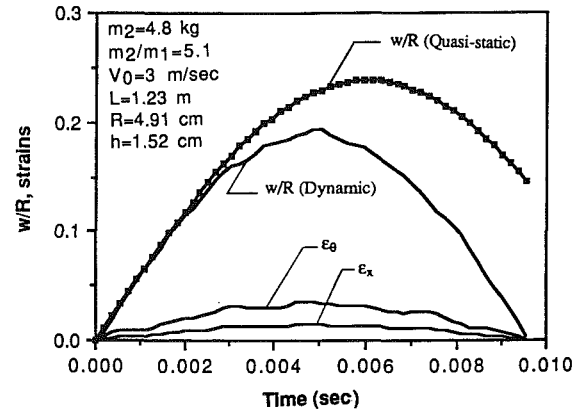


Fig. 7 Predicted center deflection and strain response of a long carbon/epoxy cylindrical shell subject to impact by a medium mass

the same time and the deflection shape is similar to the static deflection shape. Hence, in this case of impact by a heavy mass, the response can be simply obtained by neglecting the mass of the shell in a single-degree-of-freedom analysis. Although the results should not be surprising, in the past this type of behavior was attributed to "low velocity" impact, rather than directly to the mass of the impactor relative to the mass of the cylinder.

For a smaller impactor mass, higher response frequencies start to become important with dynamic effects becoming more evident. The results in Figs. 4 and 5 clearly show the importance of dynamic effects in the predicted impact duration, peak impact force, and peak impact deflection relative to the quasi-static response. Figure 4 shows the impact force versus time response for a mass ratio of 0.1. It is evident from the comparison shown there that the response is not quasi-static, and there is a 12 percent difference in the maximum force prediction between the dynamic analysis and the quasi-static analysis. This is also evident in Fig. 5, where there is 22 percent difference in the maximum deflection predictions.

So far, calculations have been made on a 41.9-cm (16.5 in.) long cylindrical shell subject to impact by different masses. It has been shown that as the impactor mass gets smaller, so does the impact duration with dynamic effects becoming more evident. As mentioned earlier, however, the impact response of the shell does not only depend on the mass ratio but also depends on the shell geometry and material properties. For example, if the length of the shell is increased, then the lateral

Downloaded 03 May 2010 to 171.66.16.244. Redistribution subject to ASME license or copyright; see http://www.asme.org/terms/Terms_Use.cfm

stiffness of the shell will be lower, which will change the impact response for a given impactor mass.

Figures 6 and 7 show the predicted impact force, deflection and strains of a 123-cm (48.5 in.) long circular cylindrical shell impacted by a 4.8 kg (10.8 lb) mass, which is the same impactor mass used in the example of Fig. 2. A comparison of Figs. 2 and 6 shows that a decrease in the lateral stiffness of the shell caused an increase in the contact duration. This result shows that the impact dynamic response is influenced by the stiffness of the cylinder (as affected by the length in this case) as well as the ratio of impactor mass to cylinder mass. The amplitude of the response is also affected by the stiffness change as expected. For the longer cylinder a lower impact force produces higher central deflection. Note that although the mass ratio became smaller by increasing the length, the impact duration became larger.

It is interesting to note the surprisingly good approximation to the actual dynamic impact problem available in the quasi-static solution, at least over the range of parameters considered here.

The method of solution presented here neglects local contact area deformations. Thus, the equilibrium equation between the shell and the impactor can be solved analytically, which has not been achieved previously. Shivakumar, Elber, and Illg (1985) showed the effects of local contact area deformation on the impact response of thin laminates to be negligible. The response was found to be flexural in nature and methods that included only contact area effects overestimated the impact force by several times. The contact duration for that particular case study was 600 μsec, with contact area effects appearing as high frequency noise with a half period of 50 μsec. In the case of thick laminates, or laminates having small thickness-to-length ratios, contact area effects are important and should be included in the analysis. It is an easy task to include in the analysis a linear spring, to provide an estimate of additional compliance due to local contact area deformation effects. Although the actual contact problem is nonlinear, bounds can be placed on the response with this linearized approach while still using an analytic solution.

In closing, it should be noted that in general there are high localized stresses associated with the contact area, even when relatively smooth indenters are used. These contact stresses can cause both fiber and matrix damage, and can lead to strength reductions. However, for relatively thin specimens such as those considered here, this contact area damage is small compared with the bending-induced damage. Christoforou, Swanson, Ventrello, and Beckwith (1987) showed experimentally that in the case of impact of cylinders supported internally by an aluminum mandrel, significant strength loss due to contact stresses could be observed even though bending stresses were eliminated. However, the load levels necessary to produce that damage were higher than those of the empty cylinder tests by an order of magnitude. Thus, while the contact stresses may well have to be considered in certain situations, they are not significant for the thin cylinders under study.

6 Conclusions

An analytical approach has been presented to solve for the force, deflection, and strains in a composite cylinder subjected to lateral impact loading. The resulting expressions have been coded into a Fortran computer program and a dynamic analysis can be easily accomplished. The model shows that in the case of impact be a heavy mass, the response of the cylinder is quasi-static. In the case of small impact masses, dynamic effects are evident. The impact duration is independent of the impact velocity and depends on the mass ratio and the material and geometric parameters of the cylinder. The impact velocity contributes only to the amplitude of the response. The major advantage of analytical methods is that they can be very useful in parametric-type studies. The present analytic solution is particularly useful in identifying the key variables of the impact problem.

References

Arpaci, V. S., 1966, *Conduction Heat Transfer*, Addison-Wesley, Reading, Mass., pp. 374–391.

Bert, C. W., and Birman, V., 1988, "Parametric Instability of Thick, Orthotropic, Circular Cylindrical Shells," *Acta Mechanica*, Vol. 71, pp. 67–76.

Christoforou, A. P., Swanson, S. R., Ventrello, S. C., and Beckwith, S. W., 1987, "Impact Damage of Carbon/Epoxy Composite Cylinders," *Proceedings of the 32nd International SAMPE Symposium and Exhibition*, Vol. 32, pp. 964–973.

Christoforou, A. P., Swanson, S. R., and Beckwith, S. W., 1987, "Lateral Impact of Composite Cylinders," Presented at the 2nd ASTM Symposium on Composite Materials: Fatigue and Fracture, Cincinnati, Ohio, April 27–28, 1987.

Dobyns, A. L., 1981, "Analysis of Simply-Supported Plates Subject to Static and Dynamic Loads," *AIAA Journal*, Vol. 19, pp. 642–650.

Jones, R. M., 1975, *Mechanics of Composite Materials*, Scripta, Washington, D.C.

Kliger, H. S., Forristall, G. Z., and Vinson, J. R., 1973, "Stresses in Circular Cylindrical Shells of Composite Materials Subjected to Localized Loads," AFOSR Tech. Report No. 73-0494.

Lekhnitskii, S. G., 1968, *Anisotropic Plates*, (translated by S. W. Tsai and T. Cheron), Gordon and Breach, New York.

Mindlin, R. D., 1951, "Influence of Rotary Inertia and Shear on Flexural Motions of Isotropic Elastic Plates," ASME JOURNAL OF APPLIED MECHANICS, Vol. 18, pp. 31–38.

Ramkumar, R. L., and Thakar, Y. R., 1987, "Dynamic Response of Curved Laminated Plates Subjected to Low Velocity Impact," ASME *Journal of Engineering Materials and Technology*, Vol. 109, pp. 67–71.

Shivakumar, K. N., Elber, W., and Illg, W., 1985, "Prediction of Impact Force and Duration Due to Low-Velocity Impact on Circular Composite Laminates," ASME JOURNAL OF APPLIED MECHANICS, Vol. 52, pp. 674–680.

Sun, C. T., and Chattopadhyay, S., 1975, "Dynamic Response of Anisotropic Plates Under Initial Stress Due to Impact of Mass," ASME JOURNAL OF APPLIED MECHANICS, Vol. 42, pp. 693–698.

Timoshenko, S., 1928, *Vibration Problems in Engineering*, D. Van Nostrand, New York.

Vinson, J. R., and Chou, T. W., 1975, *Composite Materials and Their Use in Structures*, Applied Science Pub., London.

Whitney, J. M., and Leissa, A. W., 1970, "Analysis of a Simply-Supported Laminated Anisotropic Rectangular Plate," *AIAA Journal*, Vol. 8, pp. 28–38.

Whitney, J. M., and Pagano, N. J., 1970, "Shear Deformation in Heterogeneous Anisotropic Plates," ASME JOURNAL OF APPLIED MECHANICS, Vol. 37, pp. 1031–1036.

Downloaded 03 May 2010 to 171.66.16.244. Redistribution subject to ASME license or copyright; see http://www.asme.org/terms/Terms_Use.cfm

C.-L. Tsai
Research Assistant.

I. M. Daniel
Professor,
Mem. ASME

Departments of Civil and Mechanical Engineering,
Northwestern University,
Evanston, IL 60208

G. Yaniv
Staff Scientist,
Simula, Inc.,
Tempe, AZ
Mem. ASME

Torsional Response of Rectangular Composite Laminates

The torsional response of a composite laminate of rectangular cross-section was analyzed by the Mindlin-Reissner theory. The analysis takes into account separately the shear properties of each layer. A general closed-form relationship was derived between torque and angle of twist in terms of the geometric parameters and shear properties of the laminae. In the case of unidirectional laminates, relations can be expressed involving the three principal shear moduli, G_{12}, G_{13}, and G_{23}. An experimental method was also developed for determining these moduli by measuring surface and edge strains with strain gages. Results for a typical graphite/epoxy composite show the validity of the usual assumption of transverse isotropy.

Introduction

Conventional shear test methods, such as the $[\pm 45]_{ns}$ coupon and the 10-deg off-axis test, are used to obtain the in-plane shear modulus of a unidirectional material. In some recent applications of thick composites it is necessary to determine out-of-plane or through-the-thickness properties as well. Out-of-plane shear moduli of laminates can be obtained by a single torsion test of a coupon of rectangular cross-section (Sumsion and Rajapakse, 1978). It has been shown that, contrary to some usual assumptions, out-of-plane shear moduli can be considerably lower than the in-plane modulus.

In the case of partial damage in a laminate, such as matrix cracking in one layer, it is of interest to determine the *in situ* properties of the damaged and undamaged layers. In this case the simple torsion test is proposed as a measure of property degradation.

Reissner (1945) and Mindlin (1951) solved the torsion problem of a homogeneous isotropic plate of rectangular cross-section. The theory takes into account the deformation due to transverse shear forces in addition to that due to in-plane forces, bending moments, and twisting moments. Seide derived the torsional rigidity of rectangular sandwich plates in series form (Seide, 1956). Lekhnitskii (1963) presented the solution to the torsion problem of a homogeneous anisotropic rod in series form. This solution, which relates applied torque to angle of twist, has been applied to the case of bars of rectangular cross-section (Sumsion and Rajapakse, 1978). However, it becomes unstable for very low aspect ratios of thickness to width. Furthermore, the reliance on a measured angle of twist introduces errors due to the effects of tabs and gripping conditions. Read and Dean described the determination of shear moduli from the torsional resonance frequency (Read and Dean, 1973). However, their equation is unstable for very low aspect ratios of thickness to width.

In this paper, a closed-form solution is derived for a general orthotropic laminate, based on the Mindlin-Reissner theory. An experimental procedure is proposed, insensitive to end effects, which gives two shear moduli with one specimen only. The effects of laminate thickness on shear moduli is investigated.

Laminate Constitutive Relations

In the classical lamination theory, the in-plane force resultants and moment resultants in a laminate are related to the midsurface strains and curvatures as follows (Fig. 1) (Jones, 1975).

$$\begin{bmatrix} N \\ M \end{bmatrix} = \begin{bmatrix} A & B \\ B & D \end{bmatrix} \begin{bmatrix} \epsilon^o \\ \kappa \end{bmatrix} \tag{1}$$

where

$[N] = [N_x, N_y, N_{xy}]$ in-plane forces per unit length,

$[M] = [M_x, M_y, M_{xy}]$ bending and twisting moments per unit length,

$[A] = [A_{ij}]$, $(i, j = 1, 2, 6)$ extensional stiffness matrix,

$[B] = [B_{ij}]$, $(i, j = 1, 2, 6)$ coupling stiffness matrix, and

$[D] = [D_{ij}]$, $(i, j = 1, 2, 6)$ flexural stiffness matrix.

The resultant transverse shear forces, not accounted for in classical lamination theory, can be related to the transverse shear strains of the middle surface as follows (Whitney, 1972):

$$\begin{bmatrix} V_x \\ V_y \end{bmatrix} = \begin{bmatrix} k^2{}_1 A_{44} & k_1 k_2 A_{45} \\ k_1 k_2 A_{45} & k^2{}_2 A_{55} \end{bmatrix} \begin{bmatrix} \bar{\gamma}_{xz} \\ \bar{\gamma}_{yz} \end{bmatrix} \tag{2}$$

Contributed by the Applied Mechanics Division of THE AMERICAN SOCIETY OF MECHANICAL ENGINEERS for presentation at the Winter Annual Meeting, Dallas, Tex., November 25-30, 1990.

Discussion on this paper should be addressed to the Technical Editor, Leon M. Keer, The Technological Institute, Northwestern University, Evanston, IL 60208, and will be accepted until two months after final publication of the paper itself in the JOURNAL OF APPLIED MECHANICS. Manuscript received by the ASME Applied Mechanics Division, October 10, 1988; final revision, April 1, 1989.

Paper No. 90-WA/APM-3.

Copyright © 1990 by ASME
Downloaded 03 May 2010 to 171.66.16.244. Redistribution subject to ASME license or copyright; see http://www.asme.org/terms/Terms_Use.cfm

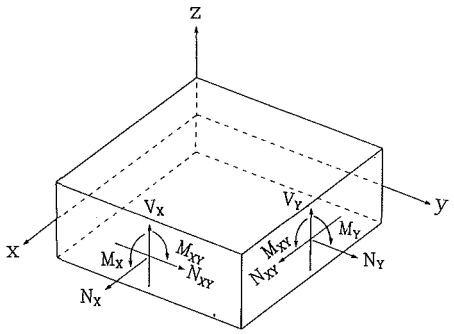


Fig. 1 Laminate element with force and moment resultants

where

V_x, V_y = resultant transverse shear forces,

$[A_{ij}]$ $(i, j = 4, 5)$ = shear stiffness matrix of laminate,

k_1, k_2 = shear correction factors, and

$\bar{\gamma}_{xz} = \bar{\gamma}_{yz}$ = average shear strains through thickness of laminate.

For a laminate of n layers of orientation ϕ and thickness t_k,

$$A_{ij} = \sum_{k=1}^{n} C^k{}_{ij}\, t_k \tag{3}$$

$C^k{}_{ij}$, $(i, j = 4, 5)$: shear stiffness of kth layer

$$\begin{bmatrix} C^k{}_{ij} \end{bmatrix} = \begin{bmatrix} m^2 G^k{}_{13} + n^2 G^k{}_{23} & mn(G^k{}_{23} - G^k{}_{13}) \\ mn(G^k{}_{23} - G^k{}_{13}) & n^2 G^k{}_{13} + m^2 G^k{}_{23} \end{bmatrix} \tag{4}$$

where

$m = \cos\phi$, $n = \sin\phi$,

ϕ = orientation of kth lamina

$G^k{}_{13}, G^k{}_{23}$ = out of plane shear moduli of kth layer, in the 1-3 and 2-3 planes, respectively.

Torsion of Rectangular Plate

A composite plate of length $2L$, width a, and thickness h is subjected to torque T about its longitudinal axis (x-axis in Fig. 2). If the plate is assumed to be midplane symmetric, the in-plane forces $[N]$ are zero. Assuming distortionless rotation, the out-of-plane deflection w is given by

$$w = \theta xy, \tag{5}$$

where θ is the angle of twist per unit length $\left(\frac{\alpha}{L}\right)$.

The distortionless condition also gives (Reissner, 1945)

$$\tau_{yz} = 0,$$

which also implies that

$$V_y = \int_{-h/2}^{h/2} \tau_{yz} dz = 0.$$

Inversion of equation (2) gives

$$\begin{bmatrix} \bar{\gamma}_{xz} \\ \bar{\gamma}_{yz} \end{bmatrix} = \begin{bmatrix} \frac{a_{44}}{k^2{}_1} & \frac{a_{45}}{k_1 k_2} \\ \frac{a_{45}}{k_1 k_2} & \frac{a_{55}}{k^2{}_2} \end{bmatrix} \begin{bmatrix} V_x \\ V_y \end{bmatrix} \tag{6}$$

where, $[a_{ij}]$, $(i, j = 4, 5)$ = shear compliance matrix.

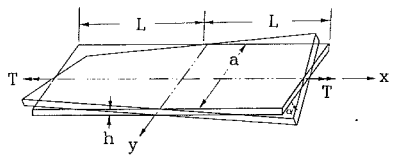


Fig. 2 Rectangular plate under torsion

From Read and Dean (1973) we can write

$$\begin{aligned} \bar{\gamma}_{xz} &= w_{,x} + \phi_x \\ \bar{\gamma}_{yz} &= w_{,y} + \phi_y \end{aligned} \tag{7}$$

where ϕ_x, ϕ_y are rotations of sections x = const. and y = const. The plate curvatures are related to these rotations as follows:

$$\begin{bmatrix} \kappa_x \\ \kappa_y \\ \kappa_{xy} \end{bmatrix} = \begin{bmatrix} \frac{\partial}{\partial x} & 0 \\ 0 & \frac{\partial}{\partial y} \\ \frac{\partial}{\partial y} & \frac{\partial}{\partial x} \end{bmatrix} \begin{bmatrix} \phi_x \\ \phi_y \end{bmatrix}. \tag{8}$$

Since there is not in-plane force, by setting $[N] = 0$ in equations (1) and eliminating $[\epsilon^o]$, we solve for the moments $[M]$:

$$\begin{bmatrix} M_x \\ M_y \\ M_{xy} \end{bmatrix} = \begin{bmatrix} R_{11} & R_{12} & R_{16} \\ R_{12} & R_{22} & R_{26} \\ R_{16} & R_{26} & R_{66} \end{bmatrix} \begin{bmatrix} \kappa_x \\ \kappa_y \\ \kappa_{xy} \end{bmatrix} \tag{9}$$

where, $[R] = [D] - [B][A]^{-1}[B]$.

From the plate equilibrium equations we obtain:

$$\begin{bmatrix} V_x \\ V_y \end{bmatrix} = \begin{bmatrix} \frac{\partial}{\partial x} & 0 & \frac{\partial}{\partial y} \\ 0 & \frac{\partial}{\partial y} & \frac{\partial}{\partial x} \end{bmatrix} \begin{bmatrix} M_x \\ M_y \\ M_{xy} \end{bmatrix}. \tag{10}$$

From equations (6) through (10), and noting that all stresses and strains are independent of x, we obtain

$$V_x = \left(R_{26} \frac{a_{45}}{k_1 k_2} + R_{66} \frac{a_{44}}{k^2{}_1}\right) \frac{\partial^2 V_x}{\partial y^2}, \tag{11}$$

the solution of which is

$$V_x = I_1 \sinh \frac{y}{\sqrt{W}} + I_2 \cosh \frac{y}{\sqrt{W}} \tag{12}$$

where I_1, I_2, are unknown coefficients and

$$W = R_{26} \frac{a_{45}}{k_1 k_2} + R_{66} \frac{a_{44}}{k^2{}_1}.$$

From equations (1), (6), (7), (8), and (9) we obtain

$$M_{xy} = W \frac{\partial V_x}{\partial y} - 2\,\theta\, R_{66}. \tag{13}$$

Substituting V_x from equation (12) we obtain

$$M_{xy} = \sqrt{W}\left(I_1 \cosh \frac{y}{\sqrt{W}} + I_2 \sinh \frac{y}{\sqrt{W}}\right) - 2\theta R_{66}. \tag{14}$$

Using the boundary conditions

$$M_{xy} = 0 \quad \text{at} \quad y = \pm a/2 \tag{15}$$

we obtain the solution

Downloaded 03 May 2010 to 171.66.16.244. Redistribution subject to ASME license or copyright; see http://www.asme.org/terms/Terms_Use.cfm

$$\left.\begin{aligned} I_2 &= 0 \\ I_1 &= \frac{2\theta R_{66}}{\sqrt{W}\cosh\dfrac{a}{2\sqrt{W}}} \end{aligned}\right\}, \tag{16}$$

and, therefore

$$\left.\begin{aligned} V_x &= I_1 \sinh\frac{y}{\sqrt{W}} \\ M_{xy} &= I_1\sqrt{W}\cosh\frac{y}{\sqrt{W}} - 2\theta R_{66} \end{aligned}\right\}. \tag{17}$$

The applied torque is related to the shear force and twisting moment above as

$$T = \int_{-a/2}^{a/2} (yV_x - M_{xy})\,dy,$$

from which we obtain

$$T = 4a\theta R_{66}\left(1 - \frac{2\sqrt{W}}{a}\tanh\frac{a}{2\sqrt{W}}\right). \tag{18}$$

For an isotropic material for which $k^2{}_1 = \dfrac{5}{6}$, we have

$$R_{66} = \frac{1}{12}Gh^3$$

$$\sqrt{W} = \frac{h}{\sqrt{10}}$$

with G the shear modulus. Then,

$$T = \frac{1}{3}a\theta Gh^3\left(1 - \frac{2h}{a\sqrt{10}}\tanh\frac{a\sqrt{10}}{2h}\right) \tag{19}$$

which is the same solution as that given by Reissner (1945).

For a unidirectional composite specimen twisted about an axis parallel to the fiber direction (0-deg specimen), the general relations (17) and (18) are simplified to:

$$\left.\begin{aligned} V_x &= \frac{1}{3a}\theta\, G_{12}\, h^3\, \beta\tanh\beta, \text{ at } y = a/2 \\ T &= \frac{1}{3}a\theta G_{12}h^3\left(1 - \frac{\tanh\beta}{\beta}\right) \end{aligned}\right\} \tag{20}$$

where,

$$\beta = \frac{a}{2h}\sqrt{10G_{13}/G_{12}}.$$

When the torque is applied about an axis normal to the fiber direction, G_{13} is replaced with G_{23} in the above relation. In this case it was shown that the shear correction factor $k^2{}_1 = 5/6$, as in the isotropic case (see Appendix). In equations (20) V_x and T are obtained from experimental measurements. The two equations are solved for G_{12} and G_{13} (or G_{12} and G_{23}) by the Newton-Raphson method.

A solution in series form, given by Lekhnitskii (1963) for a homogeneous anisotropic rod, agrees with the above closed-form solution. However, Lekhnitskii's solution becomes very sensitive to measured torque for very small h/a ratios typical of thin composite coupons.

Experimental Determination of Shear Moduli

The shear moduli of a unidirectional composite G_{12}, G_{13}, G_{23}, can be determined by conducting selected tests on unidirectional prismatic coupons and measuring the torque and angle of twist. A minimum of three tests would be needed, e.g., two tests with 0-deg specimens of different cross-sectional dimensions (h,a) and one test with a 90-deg specimen. However, direct measurement of the overall angle of twist does not yield accurate results because of end effects from the specimen tabs and grips.

A new experimental technique was developed, whereby the transverse shear, V_x, and angle of twist per unit length, θ, are determined from strain measurements on the surface and the edge of the specimen. These measurements are made near the center of the specimen and give the local values of V_x and θ. Therefore, they are not sensitive to end effects.

Assuming a parabolic distribution through the thickness of shear stress τ_{xz}, the shear force V_x at the edge of 0-deg specimen can be expressed as follows:

$$V_x = \frac{4}{3}G_{13}\epsilon^*{}_{45}, \text{ at } y = a/2, \tag{21}$$

where $\epsilon^*{}_{45}$ is the average strain measured with a strain gage on the edge of the specimen at 45 deg with the x-axis. This gage oriented at 45 deg with the specimen axis is mounted on the edge of the specimen near the center of the specimen.

The angle of twist per unit length, θ, is obtained by measuring, with a strain gage, the strain ϵ_{45} on the face of the specimen along the centerline at 45 deg with the x-axis. In equation (6) we note that $a_{45} = 0$ and $V_y = 0$. Then, from equations (6)–(8) we obtain

$$\kappa_{xy} = \phi_{x,y} + \phi_{y,x} = \frac{6}{5}a_{44}\, V_{x,y} - 2\, w_{,xy}. \tag{22}$$

Assuming the midplane shear strain $\gamma^o_{xy} = 0$ and $w = \theta xy$ for a distortionless twist, we obtain

$$\gamma_{xy} = Z\kappa_{xy} = Z\left(\frac{6}{5}a_{44}\, V_{x,y} - 2\theta\right). \tag{23}$$

On the surface of the specimen, $Z = h/2$,

$$\gamma_{xy} = \frac{3}{5}ha_{44}\, V_{x,y} - h\theta$$

and, using equations (17) for a 0-deg specimen,

$$\gamma_{xy} = h\theta\left[\frac{\cosh\left(\dfrac{y}{h}\sqrt{10\, G_{13}/G_{12}}\right)}{\cosh\left(\dfrac{a}{2h}\sqrt{10\, G_{13}/G_{12}}\right)} - 1\right]. \tag{24}$$

Along the centerline, $y = 0$,

$$\gamma_{xy} = h\theta\left(\frac{1}{\cosh\beta} - 1\right) \tag{25}$$

Since $\gamma_{xy} = 2\epsilon_{45}$,

$$\theta = \frac{2\cosh\beta}{1 - \cosh\beta}\cdot\frac{\epsilon_{45}}{h}. \tag{26}$$

Relations (21) and (26) are substituted into equations (20) to obtain a system, whereby G_{12} and G_{13} can be calculated in terms of the measured strains $\epsilon^*{}_{45}$ and ϵ_{45}, on the edge and the surface of the specimen. In the case of 90-deg specimen, G_{23} is substituted for G_{13} in all expressions above.

In the procedure outlined, it is assumed that the strain gages give the average strain on the edge and a point strain on the face of the coupon at the centerline. In reality, the gages give an average value over their gage area. More refined expressions have been developed taking into consideration the actual size of the gage.

This procedure was applied to the determination of shear moduli G_{12}, G_{13}, and G_{23} of unidirectional graphite/epoxy composite (AS4/3506-1, Hercules, Inc.). Sixteen-ply 0-deg and 90-deg coupons, 9 in. long and 1 in. wide, were in-

Downloaded 03 May 2010 to 171.66.16.244. Redistribution subject to ASME license or copyright; see http://www.asme.org/terms/Terms_Use.cfm

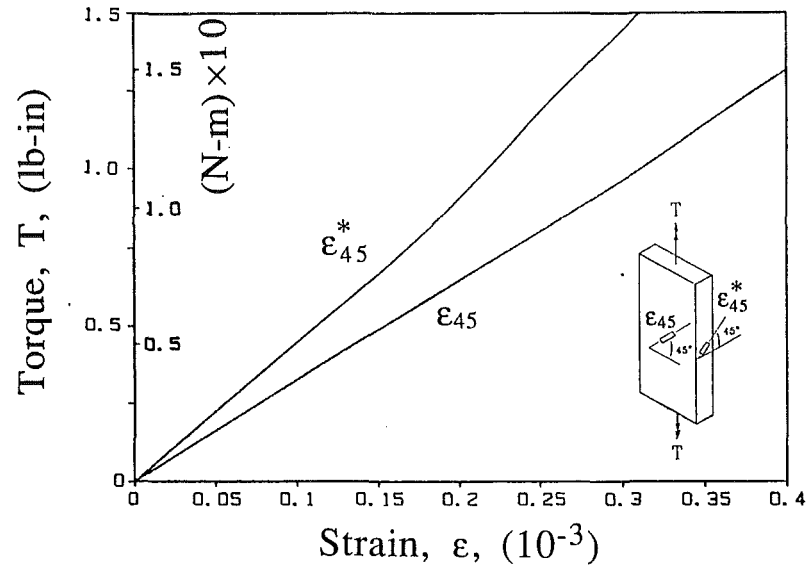


Fig. 3 Torque versus surface and edge strains at 45 deg with loading axis for $[0_{16}]$ graphite/epoxy specimen

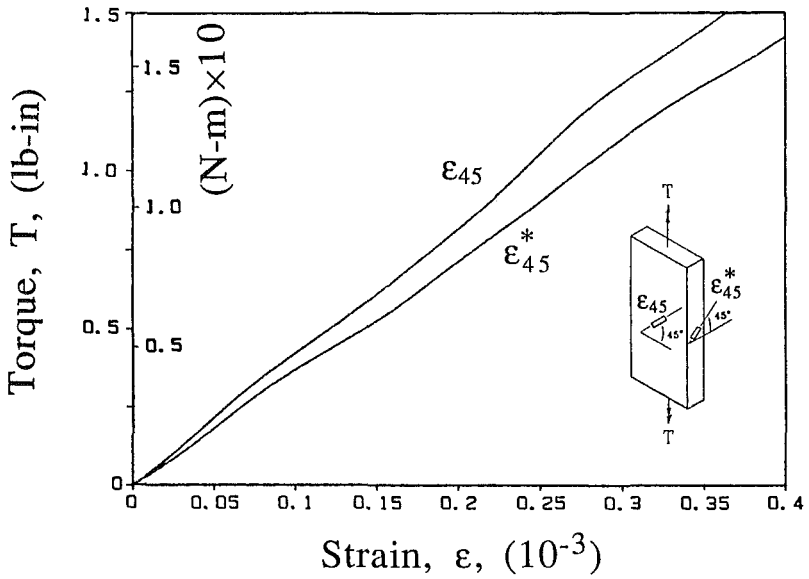


Fig. 4 Torque versus surface and edge strains at 45 deg with loading axis for $[90_{16}]$ graphite/epoxy specimen

strumented with strain gages on the wide surface and on the edge, oriented at 45 deg with the axial direction. They were loaded in a specially designed torsional fixture, equipped with a low-capacity torque cell.

Results were obtained in the form of curves of applied torque versus 45-deg surface and edge strains (Figs. 3 and 4). Three specimens of each type were tested. Results are tabulated in Table 1. It is seen from the results that the usual assumption of transverse isotropy is justified since $G_{12} \approx G_{13}$. The value of G_{23} is approximately half that of the in-plane shear modulus. It is conceivable, however, that the relative values of the in-plane and out-of-plane moduli may vary with laminate thickness, since that it related to the curing characteristics of the material.

Table 1 Shear moduli of unidirectional graphite/epoxy

Specimen	Modulus, GPa (10^6 psi)		
	G_{12}	G_{13}	G_{23}
$[0_{16}]$	7.31 (1.06)	7.25 (1.05)	
$[0_{16}]$	7.18 (1.04)	6.97 (1.01)	
$[0_{16}]$	6.76 (0.98)	6.62 (0.96)	
$[90_{16}]$	6.62 (0.96)		3.66 (0.53)
$[90_{16}]$	6.83 (0.99)		3.59 (0.52)
$[90_{16}]$	6.76 (0.98)		3.86 (0.56)
Average	6.90 (1.00)	6.97 (1.01)	3.73 (0.54)

Summary and Conclusions

A closed-form solution was obtained for a composite laminate under torsion, in terms of the lamination geometry and shear properties of the laminae.

In the case of unidirectional laminates, the solution was expressed in terms of the three principal shear moduli, G_{12}, G_{13}, and G_{23}. An experimental approach was also developed for determination of these moduli by measuring surface and edge strains in twisted prismatic coupons. The method is not sensitive to end effects since it is based on local measurements at

Downloaded 03 May 2010 to 171.66.16.244. Redistribution subject to ASME license or copyright; see http://www.asme.org/terms/Terms_Use.cfm

the center of the specimen. The specimen needs to be only long enough so that the middle is not effected by the ends.

Results for a typical graphite/epoxy material show that the usual assumption of transverse isotropy is justified, since $G_{12} \approx G_{13}$. The out-of-plane shear modulus G_{23} is approximately half the in-plane modulus.

Acknowledgment

The work described here was sponsored by the Office of Naval Research. We are grateful to Dr. Y. Rajapakse of ONR for his encouragement and cooperation and to Mrs. Yolande Mallian for typing the manuscript.

References

Jones, R. M., 1975, *Mechanics of Composite Materials*, Scripta Book Co., Wash.

Lekhnitski, S. G., 1963, *Theory of Elasticity of an Anisotropic Elastic Body*, Holden-Day, Oakland, Calif.

Mindlin, R. D., 1951, "Influence of Rotatory Inertia and Shear on Flexural Motions of Isotropic, Elastic Plates," ASME JOURNAL OF APPLIED MECHANICS, Vol. 18, pp. 336-343.

Read, B. E., and Dean, G. D., 1973, *Determination of Dynamic Properties of Polymers and Composites*, John Wiley and Sons, Inc., New York, pp. 139-141.

Reissner, E., 1945, "The Effect of Transverse Shear Deformation on the Bending of Elastic Plates," ASME JOURNAL OF APPLIED MECHANICS, Vol. 12, pp. 69-77.

Seide, P., 1956, "On the Torsion of Rectangular Sandwich Plates," ASME JOURNAL OF APPLIED MECHANICS, Vol. 23, pp. 191-194.

Sumsion, H. Theodore, and Rajapakse, Yapa D. S., 1978, "Simple Torsion Test for Shear Moduli Determination," *Proc. of the ICCM 2*, pp. 994-1002.

Whitney, J. M., 1972, "Stress Analysis of Thick Laminated Composite and Sandwich Plates," *J. Composite Materials*, Vol. 6, pp. 426-440.

APPENDIX

Shear Correction Factor

Since $[N] = 0$ in equation (1), we have

$[M] = [D][\kappa]$ or

$$[\kappa] = [d][M] \tag{A1}$$

where $[d]$ is the flexural compliance matrix. The stress-strain relations can be expressed as

$$[\sigma] = [\bar{Q}][\epsilon], \tag{A2}$$

where

$[\epsilon] = [\epsilon^o] + z[\kappa]$ and

$[\epsilon^o]$ = strains at middle plane, assumed to be zero.

z = distance from middle plane and

$[\bar{Q}]$ = stiffness matrix.

From equations (A1) and (A2) we obtain

$$[\sigma] = [\bar{Q}]z[d][M]. \tag{A3}$$

For an orthotropic laminate

$a_{45} = 0$

$R_{16} = R_{26} = 0$ (in equation (13))

$d_{16} = d_{26} = 0$

$\bar{Q}_{16} = \bar{Q}_{26} = 0.$

Then, we have

$M_x = M_y = 0$ and

$\sigma_x = 0$

$\sigma_y = 0$

$$\tau_{xy} = \bar{Q}_{66}\, d_{66}\, zM_{xy}. \tag{A4}$$

In the equilibrium equation,

$V_x = M_{x,x} + M_{xy,y}$,

we note that $M_{x,x} = 0$ since all stresses and strains are independent of x. Then

$V_x = M_{xy,y}$.

By integrating the equilibrium equation we obtain

$$\tau_{xz} = \int_z^{h/2} \left(\frac{\partial \sigma_x}{\partial x} + \frac{\partial \tau_{xy}}{\partial y} \right) d\zeta. \tag{A5}$$

Substituting $\sigma_x = 0$ and τ_{xy} from equation (A4), we obtain

$$\tau_{xy} = d_{66}\, V_x \int_z^{h/2} \bar{Q}_{66}\, \zeta\, d\, \zeta. \tag{A6}$$

From energy considerations we have:

$$\frac{1}{2}\, V_x \bar{\gamma}_{xz} = \frac{1}{2} \int_{-h/2}^{h/2} \tau_{xz}\gamma_{xz} dz \tag{A7}$$

where,

$\gamma_{xz} = \dfrac{\tau_{xz}}{C^k{}_{44}}$ shear strain of layer k,

$C^k{}_{44}$ as defined in equation (4),

$\bar{\gamma}_{xy} = V_x / A_{44} k_1{}^2$, average shear strain in laminate,

A_{44} as defined in equation (3), and

$k_1{}^2$ = shear correction factor in x-direction.

By substituting equation (A6) into (A7), we get:

$$k_1{}^2 = \left\{ A_{44} d_{66}{}^2 \int_{-h/2}^{h/2} \left[\int_z^{h/2} \bar{Q}_{66} \zeta\, d\, \zeta \right] \frac{1}{C_{44}{}^k}\, dz \right\}^{-1}. \tag{A8}$$

For isotropic specimen:

$$\bar{Q}_{66} = G,\ C_{44}{}^k = G,\ A_{44} = Gh,\ d_{66} = \frac{12}{Gh^3}$$

$$k_1{}^2 = \frac{5}{6}.$$

For 0-deg specimen:

$$\bar{Q}_{66} = G_{12},\ C^k{}_{44} = G_{13},\ A_{44} = G_{13}h,\ d_{66} = \frac{12}{G_{12}h^3}$$

$$k_1{}^2 = \frac{5}{6}.$$

For 90-deg specimen:

$$\bar{Q}_{66} = G_{12},\ C^k{}_{44} = G_{23},\ A_{44} = G_{23}h,\ d_{66} = \frac{12}{G_{12}h^3}$$

$$k_1{}^2 = \frac{5}{6}.$$

Downloaded 03 May 2010 to 171.66.16.244. Redistribution subject to ASME license or copyright; see http://www.asme.org/terms/Terms_Use.cfm

A High-Order Mixture Homogenization of Bi-laminated Composites

H. Murakami
Associate Professor of Applied Mechanics, Mem. ASME

A. Toledano
Research Assistant.

Department of Applied Mechanics and Engineering Sciences, University of California, San Diego, La Jolla, CA 92093

An asymptotic mixture theory of bi-laminated composites with periodic microstructure is presented for rate-independent inelastic responses, such as elastic-plastic deformation. Key elements are the modeling capability of simulating critical interaction between adjacent layers and the inclusion of the kinetic energy of microdisplacements. A variational procedure is adopted in order to construct a mixture model, which is deterministic, instead of phenomenological. The principle of virtual work is used for total quantities to construct mixture equations of motion, while Reissner's mixed variational principle (1984, 1986) applied to rate boundary value problems is used to yield mixture constitutive relations. In order to assess the model accuracy in the time domain, the predicted values were compared with experimental and numerically exact data. Good agreements between the predicted and experimental or numerically exact data for plastic as well as elastic waves were observed.

Introduction

Certain material and geometrical combinations lead to laminated composites having superior strength and ductility characteristics with respect to unit weight. As a result, laminated composites are frequently used in a dynamic load environment. This, in turn, requires a material model that can be used to simulate wave phenomena. The applications may also involve load amplitudes that induce global material nonlinearities. Consequently, a nonlinear material model is needed. For those cases where the composite consists of many laminae, it is computationally advantageous to describe the composite by a continuum model wherein the heterogeneities are "smoothed" or "homogenized."

In view of this, it is evident that a class of important problems concerning wave propagation in laminated composites requires a nonlinear continuum model. Further, due to the periodic microstructure of the composite, such a model needs to simulate the wave dispersion, which leads to "rounding" or "spreading" of the wave front. For laminated composites of elastic isotropic layers, the importance of wave dispersion was amply demonstrated analytically by Sun, Achenbach, and Herrmann (1968a) and Sve (1971). Deterministic high-order continuum models were also developed to include the dispersion for *arbitrary* wave motion, such as, the effective stiffness theories (Sun, Achenbach, and Herrmann, 1968b; Achenbach, Sun, and Herrmann, 1968; Drumheller and Bedford, 1974; Achenbach, 1975; Aboudi, 1981a,b) and the mixture theories (McNiven and Mengi, 1979a,b; Murakami, Maewal, and Hegemier, 1981; Murakami, 1985). These models, except the one by McNiven and Mengi (1979a,b), are fully deterministic in the sense that model constitutive relations are synthesized from the constituent and interface properties and geometries.

While several dispersive models are available for elastic responses, few models exist for nonlinear material responses. In extending the linear effective stiffness theory, Grot and Achenbach (1970) considered nonlinear elastic responses. For wave-guide propagation Hegemier (1974) modeled elastic-plastic-hydrodynamic material responses together with geometrical nonlinearities by using a mixture theory. Aboudi (1981b) adopted the first-order effective stiffness theory and considered viscoplastic material responses. To date, however, high-order mixture models have not been extended to include nonlinear material responses for arbitrary wave motion.

In this paper, an asymptotic mixture theory of bi-laminated composites with periodic microstructure is presented for rate-independent inelastic responses, such as elastic-plastic deformation. A procedure of constructing a mixture model is presented within the framework of homogenization theories. Key elements are the modeling capability of simulating critical interaction between adjacent layers and the inclusion of the kinetic energy of microdisplacements.

A variational procedure is adopted in order to construct a mixture model, which is deterministic, instead of phenomenological. The principle of virtual work is used for total quantities to construct mixture equations of motion, while Reissner's mixed variational principles (1950, 1984, 1986) applied to rate boundary value problems are used to yield mixture constitutive relations. The accuracy of the

Contributed by the Applied Mechanics Division of THE AMERICAN SOCIETY OF MECHANICAL ENGINEERS for publication in the JOURNAL OF APPLIED MECHANICS.

Discussion on this paper should be addressed to the Technical Editor, Leon M. Keer, The Technological Institute, Northwestern University, Evanston, IL 60208, and will be accepted until two months after final publication of the paper itself in the JOURNAL OF APPLIED MECHANICS. Manuscript received by the ASME Applied Mechanics Division, August 8, 1988; final revision, June 28, 1989.

Copyright © 1990 by ASME
Downloaded 03 May 2010 to 171.66.16.244. Redistribution subject to ASME license or copyright; see http://www.asme.org/terms/Terms_Use.cfm

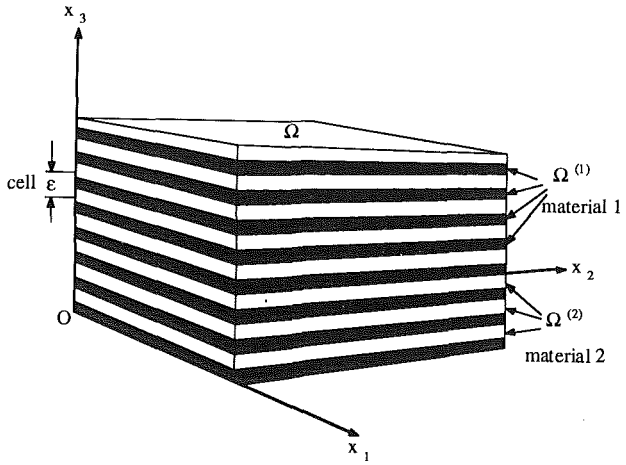


Fig. 1 A bi-laminated composite and the coordinate system

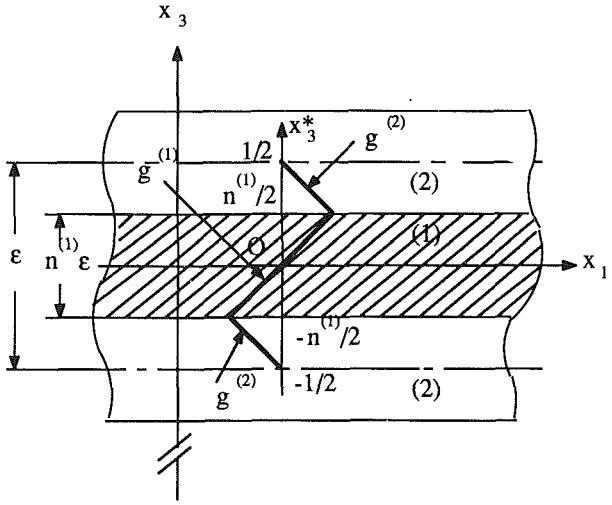


Fig. 2 A unit cell

resulting model depends on the accuracy of the trial displacement and transverse stress fields, which may be found accurately as solutions of a system of rate boundary value problems defined over a unit cell.

In order to assess the model accuracy in the time domain, numerical experiments were conducted for a half space subjected to step pressure loading on its surface. The prediction of the model was obtained by an explicit finite element code. DYNA2D, which was developed by Hallquist (1982), is used to furnish numerically exact data for the problem by discretizing the details of the composite microstructure. An excellent agreement between the predicted and exact data for plastic as well as elastic waves was observed. It is further noted that the mixture finite element code, which does not require the explicit discretization of the composite microstructure, is more than an order of magnitude faster than DYNA2D. While the treatment of viscoplastic composite response is straightforward, the application of the theory is deferred to later publications.

Formulation

Consider a bi-laminated composite of locally homogeneous laminae of material 1 and material 2, which occupies an open set V^ϵ of $\mathbf{R}^3$, as shown in Fig. 1. Let a rectangular Cartesian coordinate system x_1, x_2, and x_3 be selected with x_3 normal to the midplane of a lamina, which is defined by x_1 and x_2. A periodic microstructure in the macrocoordinate x_3 is defined by a cell or a unit period, shown in Figs. 1 and 2. Under the premise that the composite macro reference length or typical macrosignal wavelength is much larger than the cell dimension, it is convenient to introduce a microspace variable, x^*_3, rescaled by the cell length ϵ:

$$x^*_3 = x_3/\epsilon. \tag{1}$$

In equation (1) the microcoordinate is introduced to make the cell dimension O(1). Therefore, the parameter ϵ represents the ratio of micro-to-macro dimensions, and is considered to be small, $\epsilon \ll 1$. It is also assumed that material properties, such as density, elastic moduli, and inelastic material parameters, are periodic with a period of a unit cell. For example, elastic modulus tensor $\mathbf{C}$ is x^*_3-periodic:

$$\mathbf{C}(x_3 + \epsilon n) = \mathbf{C}(x_3) \tag{2}$$

where n is an integer.

Let $V^{(1)}$ denote the union of the domains occupied by laminae of material 1, while $V^{(2)}$ is the conjugate domain filled with laminae of material 2, as shown in Fig. 1. In the sequel, $(\,)^{(\alpha)}$ denotes $(\,)$ associated with material α. With respect to the microcoordinate, a cell domain consists of subdomains $A^{(1)}$ and $A^{(2)}$, occupied by material 1 and 2, respectively, as shown in Fig. 2:

$$A^{(1)} = \{x^*_3 \mid |x^*_3| < n^{(1)}/2\}, \quad A^{(2)} = \{x^*_3 \mid n^{(1)}/2 < |x^*_3| < 1/2\}, \tag{3}$$

where $n^{(\alpha)}$ is the volume fraction of material $\alpha(=1,2)$ and satisfies:

$$n^{(1)} + n^{(2)} = 1. \tag{4}$$

In the cell the interfaces, I^ϵ, are defined by $x^*_3 = \pm n^{(1)}/2$.

In the Cartesian indicial notation, Latin indices range from 1 to 3 and repeated indices imply the summation convention, unless otherwise stated. In addition, the notation $(\,)_{,i} = \partial(\,)/\partial x_i$ and $\dot{(\,)} = \partial(\,)/\partial t$, in which t represents time, will be employed.

The stress tensor, $\sigma^{[\alpha]}$, and displacement vector, $\mathbf{u}^{(\alpha)}$, satisfy:

(a) equations of motion

$$\sigma^{(\alpha)}_{ji,j} + f^{(\alpha)}_i = \rho^{(\alpha)} \ddot{u}^{(\alpha)}_i, \quad \sigma^{(\alpha)}_{ij} = \sigma^{(\alpha)}_{ji} \text{ in } V^{(\alpha)} \tag{5a,b}$$

where $f^{(\alpha)}_i$ is a constant body force, $\rho^{(\alpha)}$ denotes mass density;

(b) rate constitutive relations

$$\dot{\sigma}^{(\alpha)}_{ij} = C^{(\alpha)(ep)}_{ijkl}(x^*_3)\dot{e}_{kl}(\mathbf{u}^{(\alpha)}) \text{ in } V^{(\alpha)} \tag{6}$$

$$\dot{e}_{kl}(\mathbf{u}^{(\alpha)}) = \frac{1}{2}(\dot{u}^{(\alpha)}_{k,l} + \dot{u}^{(\alpha)}_{l,k}) \text{ in } V^{(\alpha)} \tag{7}$$

where $\mathbf{C}^{(\alpha)(ep)}$ is a tangent modulus tensor which becomes $\mathbf{C}^{(\alpha)}$ for elastic response; the change of the moduli is controlled by an appropriate loading-unloading criterion;

(c) interface continuity conditions

$$u^{(1)}_i = u^{(2)}_i, \quad \sigma^{(1)}_{3i} = \sigma^{(2)}_{3i} \text{ on } \Gamma^\epsilon; \tag{8a,b}$$

(d) appropriate boundary conditions on ∂V^ϵ;

(e) initial conditions on $\mathbf{u}^{(\alpha)}$ and $\dot{\mathbf{u}}^{(\alpha)}$ at $t=0$.

Conditions (a)-(e) define a well-posed initial boundary value problem on $V^\epsilon (= V^{(1)} \cup V^{(2)})$. However, due to the large number of lamina interfaces, the direct solution to this problem is extremely complicated and time consuming. In order to alleviate such difficulties by deriving a set of partial differential equations with constant coefficients, two levels of homogenization methods have been introduced. They are: (1) O(1) homogenization methods (Babuska, 1976; Bensoussan, Lions, and Papanicolaou, 1978; Sanchez-Palencia, 1980; Tartar, 1977), and (2) an asymptotic mixture model based upon an O(ϵ) homogenization method (Murakami, Maewal, and Hegemier, 1981; Murakami, 1985; Murakami

Downloaded 03 May 2010 to 171.66.16.244. Redistribution subject to ASME license or copyright; see http://www.asme.org/terms/Terms_Use.cfm

and Hegemier, 1986; Toledano and Murakami, 1987). Both methods are based upon an asymptotic scheme for $\epsilon \ll 1$. That is, for the case in which a typical cell length is much smaller than macro reference length or signal wavelength.

The basic results of the O(1) homogenization are the equations of motion for a single displacement field and the associated constitutive relations which include the effective tangent moduli. Therefore, the model is not capable of simulating the critical lamina interaction nor wave dispersion phenomena. On the contrary, the $O(\epsilon)$ homogenization method, an asymptotic mixture model, solves the shortcomings of the O(1) model *with minimal additional work* furnishing the capabilities of including the lamina interaction and wave dispersion effects.

The mixture model is characterized by the average displacement fields for material 1, material 2, and composite microdisplacement, $\mathbf{U}^{(\alpha)}$, $\alpha = 1,2$, and $\mathbf{S}$, respectively. The constituent's displacement fields interact through interaction body force, $\mathbf{P}$, as indicated by the mixture equations of motion, (31) and (32). The two homogenization methods utilize *multiscale representation* and *interior-domain asymptotic expansions* of dependent variables.

Multivariable Field Representation

In accordance with the introduction of macro and microcoordinates, $\mathbf{x}$ and x^*_3, respectively, it is assumed that stress and deformation fields vary significantly with respect to two basic length scales: (1) a "global" or "macro" length typical of the body size or loading condition, and (2) a "micro" length typical of "cell" length. Therefore, all field variables are considered to be functions of the microcoordinate x^*_3, as well as of $\mathbf{x}$ and time t:

$$h(\mathbf{x},t) = h^*(\mathbf{x},x^*_3,t) \tag{9}$$

where h is an arbitrary function of $\mathbf{x}$ and t.

Due to the multivariable field representation, spacial derivatives of a function h with respect to x_3 become:

$$h_{,3} = h^*_{,3} + \frac{1}{\epsilon} h^*_{,3*} \tag{10}$$

where $(\ )_{,3*} = \partial(\ )/\partial x_3{}^*$. In the sequel, h^* will be written as h for notational simplicity.

The multivariable field representation, (9), and the operation (10) yield the "synthesized" governing field relations, expressed for each constituent, as follows:

(a) equations of motion

$$\sigma^{(\alpha)}_{ji,j} + \frac{1}{\epsilon}\sigma^{(\alpha)}_{3i,3*} + f^{(\alpha)}_i = \rho^{(\alpha)}\ddot{u}^{(\alpha)}_i,\ \sigma^{(\alpha)}_{ij} = \sigma^{(\alpha)}_{ji} \text{ in } V^{(\alpha)}; \tag{11a,b}$$

(b) constitutive relations

$$\dot{\sigma}^{(\alpha)}_{ij} = C^{(\alpha)(ep)}_{ijkl}\{\dot{e}_{kl}(\mathbf{u}^{(\alpha)}) + \frac{1}{\epsilon}\dot{e}^*_{kl}(\mathbf{u}^{(\alpha)})\} \text{ in } V^{(\alpha)} \tag{12}$$

$$\dot{e}^*_{kl}(\mathbf{u}^{(\alpha)}) = \frac{1}{2}(\delta_{l3}\dot{u}^{(\alpha)}_{k,l*} + \delta_{k3}\dot{u}^{(\alpha)}_{l,k*}) \text{ in } V^{(\alpha)} \tag{13}$$

where δ_{ij} is the Kronecker delta, and the microstrain $\mathbf{e}^*$ in (13) yields nonzero components only for e^*_{33}, e^*_{23}, and e^*_{31};

(c) interface continuity conditions

$$u^{(1)}_i = u^{(2)}_i,\ \sigma^{(1)}_{3i} = \sigma^{(2)}_{3i} \text{ on } \Gamma. \tag{14a,b}$$

It is noted that synthesized displacement, stress, and strain tensors are all continuous with respect to the macrocoordinates, $\mathbf{x}$, while they retain discrete heterogeneous structure with respect to the microcoordinate, x^*_3, in each cell.

Further, being motivated by the Floquet and Bloch theorems (Brillouin, 1946) of harmonic waves in periodic structures, the variation of field variables which satisfy the periodicity with respect to x^*_3 is assumed.

$$h\left(\mathbf{x}, \frac{1}{2}, t\right) = h\left(\mathbf{x}, -\frac{1}{2}, t\right) \tag{15}$$

This x^*-*periodicity condition* allows one to analyze a single cell in an effort to determine the distribution of any field variable with respect to the microcoordinate. This assumption is adopted for elastic as well as inelastic deformations under the premise that a typical length of both elastic and inelastic domains is large compared with the cell dimension. This generalization is based upon the observation that, in an inelastic domain, tangent moduli of the two constituents may be well approximated by a locally periodic function of space variables. Since the tangent moduli depend also on the current stress state, exact periodicity conditions for tangent moduli might not hold, in general. However, under the premise that the variation of the tangent moduli with macrovariables is slow, inelastic tangent moduli may be approximated by a locally periodic function of space.

Variational Formulation

For the construction of a continuum model without x^*_3, it is convenient to cast the field equations in a variational form. Using the equations of motion, (11), Gauss' theorem, and the x^*-periodicity condition on the cell boundary, it can be demonstrated that the principle of virtual work, applied to the synthesized mixture fields by the multivariable representation, takes the form:

$$\iiint_V \Big[\sum_{\alpha=1}^{2}\int_{A^{(\alpha)}}\Big\{\Big(\delta e^{(\alpha)}_{ij} + \frac{1}{\epsilon}\delta e^{*(\alpha)}_{ij}\Big)\sigma^{(\alpha)}_{ij} - \delta u^{(\alpha)}_i(f^{(\alpha)}_i - \rho^{(\alpha)}\ddot{u}^{(\alpha)}_i)\Big\}dx^*_3 + \frac{1}{\epsilon}\Big[(\delta u^{(2)}_i - \delta u^{(1)}_i)T^*{}_i\Big|_{x^*_3 = -n^{(1)}/2}^{x^*_3 = n^{(1)}/2}\Big]dx_1dx_2dx_3$$

$$= \iint_{\partial V_T}\Big\{\sum_{\alpha=1}^{2}\int_{A^{(\alpha)}}\delta u^{(\alpha)\nu}_i T^{(\alpha)}_i dx^*_3\Big\}dS \tag{16}$$

where $A^{(\alpha)}$ denotes the x^*-domain of the cell occupied by material α, and is defined in (3), ${}^{\nu}T_i{}^{(\alpha)}$ denotes the traction vector acting on the surface ∂V_T whose outward normal is ν_i, dS is an infinitesimal surface element on ∂V_T. In addition, T^*_i is the traction vector on the interface, Γ. For arbitrary variation of $u_i{}^{(\alpha)}$, with (7) and (13) as definitions the Euler-Lagrange equations of (16) include (11), relation (d), and

$$\sigma^{(\alpha)}_{3i} = T^*{}_i \quad \text{on} \quad \Gamma \tag{17}$$

where Γ is the interface defined by $x^*_3 = \pm n^{(1)}/2$. The variational equation (16) for total quantities furnishes any order of homogenized models with corresponding equations of motion by substituting appropriate trial displacements. However, it will be pointed out for high-order homogenization models that the associated rate-constitutive relations are obtained either by the application of Reissner's mixed variational principle (Reissner, 1950, 1984, 1986) or a set of experiments.

Asymptotic Analysis

The premise that the composite microdimension is much smaller than the macrodimension, $\epsilon \ll 1$, and the form of governing equations, (11) and (12), suggest the expansion of the dependent variables in the asymptotic series (see for example, (Lene and Leguillon, 1982)):

$$\mathbf{u}^{(\alpha)}(\mathbf{x},x^*_3,t) = \mathbf{u}^{(\alpha)}_{(0)}(\mathbf{x},x^*_3,t) + \epsilon\mathbf{u}^{(\alpha)}_{(1)}(\mathbf{x},x^*_3,t) + \epsilon^2\mathbf{u}^{(\alpha)}_{(2)}(\mathbf{x},x^*_3,t) + \ldots \tag{18a}$$

Downloaded 03 May 2010 to 171.66.16.244. Redistribution subject to ASME license or copyright; see http://www.asme.org/terms/Terms_Use.cfm

$$\sigma^{(\alpha)}(\mathbf{x},x^*_3,t) = \frac{1}{\epsilon}\,\sigma^{(\alpha)}_{(-1)}(\mathbf{x},x^*_3,t) + \sigma^{(\alpha)}_{(0)}(\mathbf{x},x^*_3,t) + \epsilon\sigma^{(\alpha)}_{(1)}(\mathbf{x},x^*_3,t) + \ldots \tag{18b}$$

$$\mathbf{C}^{(\alpha)(ep)} = \mathbf{C}^{(\alpha)(ep)}_{(0)} + \epsilon\mathbf{C}^{(\alpha)(ep)}_{(1)} + \epsilon^2\mathbf{C}^{(\alpha)(ep)}_{(2)} + \ldots \tag{18c}$$

where $\sigma_{(n)}{}^{(\alpha)}$, $\mathbf{u}_{(n)}{}^{(\alpha)}$, and $\mathbf{C}_{(n)}{}^{(\alpha)}$ satisfy the x^*-periodicity condition, (15). In the sequel, a class of inelastic materials, including hardening elastoplastic materials, which have a rate potential and positive definite tangent modulus tensor is considered. Therefore, in the expansion, (18c), $\mathbf{C}_{(0)}{}^{(\alpha)(ep)}$ is also assumed to be symmetric and positive definite, which holds obviously for elastic response for which only $\mathbf{C}_{(0)}{}^{(\alpha)(ep)} = \mathbf{C}^{(\alpha)}$ is required in the expansion.

Substituting (18a,b,c) into (11) and grouping the terms of like power in ϵ, one finds a system of microboundary value problems (MBVPs) defined over a unit cell.

MBVP for O(ϵ^{-2}):

$$\sigma^{(\alpha)}_{3i(-1),3*} = 0 \quad \text{in} \quad A^{(\alpha)} \tag{19a}$$

$$\dot{\sigma}^{(\alpha)}_{ij(-1)} = C^{(\alpha)(ep)}_{ijkl(0)}\,\dot{e}^*{}_{kl}(\mathbf{u}^{(\alpha)}_{(0)}) \quad \text{in} \quad A^{(\alpha)} \tag{19b}$$

$$u^{(1)}_{i(0)} = u^{(2)}_{i(0)}, \quad \sigma^{(1)}_{3i(-1)} = \sigma^{(2)}_{3i(-1)} \quad \text{on} \quad \Gamma. \tag{19c,d}$$

From (19a) and (19b) the operator for $\mathbf{u}_0{}^{(\alpha)}$ may be expressed as:

$$L(\dot{\mathbf{u}}^{(\alpha)}_{(0)}) = \frac{\partial}{\partial x^*_j}\{C^{(\alpha)(ep)}_{ijkl(0)}\,\dot{e}^*{}_{kl}(\mathbf{u}^{(\alpha)}_{(0)})\} = 0 \quad \text{in} \quad A^{(\alpha)}. \tag{20}$$

Due to the positive definiteness of $\mathbf{C}_{(0)}{}^{(\alpha)(ep)}$, the operator $\mathbf{L}$ satisfies the ellipticity condition. The solution for (20) is:

$$\mathbf{u}^{(\alpha)}_{(0)} = \mathbf{u}_{(0)}(\mathbf{x},t) \tag{21a}$$

$$\sigma^{(\alpha)}_{(-1)} = \mathbf{0}, \quad \mathbf{e}^*(\mathbf{u}_{(0)}) = \mathbf{0}. \tag{21b,c}$$

Equation (21a) states that $\mathbf{u}_{(0)}$ is independent of x^*_3.

MBVP for O(ϵ^{-1}):

$$\sigma^{(\alpha)}_{3i(0),3*} = 0 \quad \text{in} \quad A^{(\alpha)} \tag{22a}$$

$$\dot{\sigma}^{(\alpha)}_{ij(0)} = C^{(\alpha)(ep)}_{ijkl(0)}\{\dot{e}^*{}_{kl}(\mathbf{u}^{(\alpha)}_{(1)}) + \dot{e}_{kl}(\mathbf{u}_{(0)})\} \quad \text{in} \quad A^{(\alpha)} \tag{22b}$$

$$u^{(1)}_{i(1)} = u^{(2)}_{i(1)}, \quad \sigma^{(1)}_{3i(0)} = \sigma^{(2)}_{3i(0)} \quad \text{on} \quad \Gamma. \tag{22c,d}$$

The form of forcing terms in (22b) suggests the following expression for $\mathbf{u}_{(1)}{}^{(\alpha)}$:

$$\dot{u}^{(\alpha)}_{i(1)}(x_k,x^*_3,t) = \dot{e}_{pq}(\mathbf{u}_{(0)}(x_k,t))\chi^{pq}_i(x^*_3) \tag{23}$$

where $\chi_i{}^{pq}$ is x^*-periodic. The substitution of (23) into (22) yields an MBVP for each $\chi_i{}^{pq}$, which is continuous over the cell. These problems are unique up to a constant vector with respect to x^*-variation. Therefore, it is customary, in O(1) theories, to choose $\chi_i{}^{pq}$ so that its average value over the cell vanishes:

$$\chi^{pq(a)}_i = \sum_{\alpha=1}^{2}\int_{A^{(\alpha)}}\chi^{pq}_i(x^*_3)dx^*_3 = 0. \tag{24}$$

Equations (22a) and (22d) imply that

$$\sigma^{(\alpha)}_{3i(0)} = \sigma_{3i(0)}(\mathbf{x},t). \tag{25}$$

Further, the positive definiteness of $\mathbf{C}_{(0)}{}^{(\alpha)(ep)}$ with (25) implies that $\dot{e}^*{}_{3i}(\mathbf{u}_{(1)}{}^{(\alpha)})$ is independent of x^*_3. Therefore, χ_i is linear in x^*_3 even for nonlinear responses. The integrability of $\mathbf{u}_{(1)}{}^{(\alpha)}$ can be checked by examining the operator for $\mathbf{u}_{(1)}{}^{(\alpha)}$ obtained by combining (22a) and (22b). It can be found that the same operator defined in (20) governs $\mathbf{u}_{(1)}{}^{(\alpha)}$, except with regard to the forcing vector due to the terms with $\mathbf{u}_{(0)}$. This RHS of the operator vanishes when integrated over the cell. Therefore, the integrability condition for $\mathbf{u}_{(1)}{}^{(\alpha)}$ is satisfied.

MBVP for O(1):

$$\sigma^{(\alpha)}_{ji(1),j*} = \rho^{(\alpha)}\ddot{u}_{i(0)} - f^{(\alpha)}_i - \sigma^{(\alpha)}_{ji(0),j} \quad \text{in} \quad A^{(\alpha)} \tag{26a}$$

$$\dot{\sigma}^{(\alpha)}_{ij(1)} = C^{(\alpha)(ep)}_{ijkl(0)}\{\dot{e}^*{}_{kl}(\mathbf{u}^{(\alpha)}_{(2)}) + \dot{e}_{kl}(\mathbf{u}^{(\alpha)}_{(1)})\} + C^{(\alpha)(ep)}_{ijkl(1)}\{\dot{e}_{kl}(\mathbf{u}_{(0)}) + \dot{e}^*{}_{kl}(\mathbf{u}^{(\alpha)}_{(1)})\} \tag{26b}$$

$$u^{(1)}_{i(2)} = u^{(2)}_{i(2)}, \quad \sigma^{(1)}_{3i(1)} = \sigma^{(2)}_{3i(1)} \quad \text{on} \quad \Gamma. \tag{26c,d}$$

It is necessary for O(1) homogenization methods to solve the MBVPs defined by (22) and (23) for χ^{pq}_i.

O(1) Homogenization Methods

The O(1) equations of motion are obtained by posing the integrability condition on (26a). According to the Fredholm alternative, the problem defined in (26) has a unique solution up to a constant vector with respect to x^*_3, if the operator for $\mathbf{u}_{(2)}$ in (26) satisfies the integrability condition, that is, the range of $L(\mathbf{u}_{(2)}{}^{(\alpha)})$ is orthogonal to its null space: $\mathbf{u}_{(0)}{}^{(\alpha)} = \mathbf{u}_{(0)}(\mathbf{x},t)$ (for example, see Sanchez-Palencia, 1980; Murakami and Toledano, 1988).

The O(1) equations of motion can also be obtained by substituting the displacement trial function:

$$u^{(\alpha)}_i(x_k,x^*_3,t) = u_{i(0)}(x_k,t) + \epsilon e_{pq}(\mathbf{u}_{(0)})\chi^{pq}_i(x^*_3) \tag{27}$$

into (16) and keeping only O(1) terms. The truncation of terms higher than the including O(ϵ) terms implies that the kinetic energy of the O(ϵ) displacement is not included. In order to improve the model capability in predicting dynamic response of composites over O(1) models, it is natural to include the kinetic energy due to $\mathbf{u}_{(1)}{}^{(\alpha)}$.

O(ϵ) Homogenization Methods: A Mixture Model

The development of an O(ϵ) homogenization commences with the definition of average displacements for each constituent, keeping terms up to and including O(ϵ^2) terms:

$$U^{(\alpha)}_i(x_k,t) = \frac{1}{n^{(\alpha)}}\int_{A^{(\alpha)}}\{u_{i(0)} + \epsilon e_{pq}(\mathbf{u}_{(0)})\chi^{pq}_i + \epsilon^2 u^{(\alpha)}_{i(2)}\}dx^*_3. \tag{28}$$

As displacement trial functions for each constituent, one adopts

$$u^{(\alpha)}_i(x_k,x^*_3.t) \approx U^{(\alpha)}_i(x_k,t) + \epsilon S_{pq}(x_k,t)\chi^{pq}_i(x^*_3) \tag{29a}$$

$$S_{pq} = S_{qp}. \tag{29b}$$

In (29), $U_i{}^{(\alpha)}$ is the O(1) displacement associated to each constituent, while S_{pq} represents the amplitude of the O(ϵ) displacement microstructure. It is noted that, for general periodic composites, equations (29) imply that the resulting model includes twelve macrodisplacements and corresponding equations of motion. The average displacement fields, $\mathbf{U}^{(\alpha)}$, $\alpha = 1,2$, take the form of mixture fields which interact with each other, while the six components of the displacement microstructure, S_{pq}, represent the microdeformation in the composite. Further, χ^{pq}_i, in general, depends on tangent moduli of the constituents.

Due to the positive definiteness of $\mathbf{C}_{(0)}{}^{(\alpha)(ep)}$, equations (25) and (22$b$) imply that $\dot{e}^*{}_{3i}(\mathbf{u}_{(1)}{}^{(\alpha)})$ is independent of x^*_3. Therefore, χ_i is linear in x^*_3 even for nonlinear responses. As a result, the O(ϵ) displacement microstructure is expressed by introducing only three amplitude functions, S_i, and expressing the microstructure with a simple function of x^*_3, which is independent of tangent moduli:

$$u^{(\alpha)}_i(\mathbf{x},x^*_3,t) \approx U^{(\alpha)}_i(\mathbf{x},t) + \epsilon S_i(\mathbf{x},t)g^{(\alpha)}(x^*_3) \tag{30a}$$

where

Downloaded 03 May 2010 to 171.66.16.244. Redistribution subject to ASME license or copyright; see http://www.asme.org/terms/Terms_Use.cfm

$$g^{(1)}(x^*_3)=\frac{x^*_3}{n^{(1)}},\quad g^{(2)}(x^*_3)=\frac{1}{n^{(2)}}\left(\frac{1}{2}\,\mathrm{sgn}\,x^*_3-x^*_3\right) \tag{30b}$$

in which sgn x^*_3 denotes the algebraic sign of x^*_3. In (30) the $O(\epsilon)$ displacement microstructure is represented by $g^{(\alpha)}$ which is a continuous zig-zag function over the cell, as shown in Fig. 2, and satisfies the x^*-periodicity condition and the normalization condition, (24).

The introduction of such an approximate displacement microstructure allows for the application of homogenization methods, even to nonlinear problems, without solving MBVPs for χ_i^{pq} which otherwise change at each load increment. A similar practice is commonly adopted in beam, plate, and shell theories, in which linear variation of in-plane displacement over the thickness is used even for nonlinear as well as linear problems.

Substituting (30*a*) into (16) and carrying out the integrations over a unit cell, one finds the following *nine* Euler-Lagrange equations:

$$n^{(\alpha)}\sigma_{ji,j}^{(\alpha a)}+(-1)^{\alpha+1}P_i+n^{(\alpha)}f_i^{(\alpha)}=n^{(\alpha)}\rho^{(\alpha)}\ddot{U}_i^{(\alpha)} \tag{31}$$

$$\epsilon^2 M_{ji,j}+\sigma_{3i}^{(2a)}-\sigma_{3i}^{(1a)}=\epsilon^2 I\ddot{S}_i \tag{32}$$

where

$$\sigma_{ij}^{(\alpha a)}=\frac{1}{n^{(\alpha)}}\int_{A^{(\alpha)}}\sigma_{ij}^{(\alpha)}dx^*_3 \tag{33a}$$

$$\epsilon M_{ij}=\sum_{\alpha=1}^{2}\int_{A^{(\alpha)}}\sigma_{ij}^{(\alpha)}g^{(\alpha)}(x^*_3)dx^*_3 \tag{33b}$$

$$P_i=\frac{1}{\epsilon}\left\{\sigma_{3i}^{(\alpha)}\left(\mathbf{x},\frac{n^{(1)}}{2},t\right)-\sigma_{3i}^{(\alpha)}\left(\mathbf{x},-\frac{n^{(1)}}{2},t\right)\right\} \tag{33c}$$

$$I=\sum_{\alpha=1}^{2}\int_{A^{(\alpha)}}\rho^{(\alpha)}(g^{(\alpha)})^2dx^*_3=\frac{1}{12}\sum_{\alpha=1}^{2}n^{(\alpha)}\rho^{(\alpha)}. \tag{33d}$$

Equation (31) indicates that two displacement fields $U_i^{(\alpha)}$, $\alpha=1,2$ interact through the interaction body force, P_i. Further, equation (32) governs the evolution of microdisplacements, S_i.

The associated boundary conditions are

$$\delta U_i^{(\alpha)}=0\quad\text{or}\quad n^{(\alpha)}\sigma_{ij}^{(\alpha a)}\nu_j=n^{(\alpha)}T_i^{(\alpha a)} \tag{34a}$$

$$\delta S_i=0\quad\text{or}\quad M_{ij}\nu_j={}^{\nu}T_i^{M} \tag{34b}$$

where

$$n^{(\alpha)}\,{}^{\nu}T_i^{(\alpha a)}=\int_{A^{(\alpha)}}{}^{\nu}T_i^{(\alpha)}dx^*_3,$$

$$\epsilon\,{}^{\nu}T_i^{M}=\sum_{\alpha=1}^{2}\int_{A^{(\alpha)}}{}^{\nu}T_i^{(\alpha)}g^{(\alpha)}(x^*_3)dx^*_3, \tag{35a,b}$$

and the initial conditions:

$$U_i^{(\alpha)},\ S_i,\ \dot{U}_i^{(\alpha)},\ \text{and}\ \dot{S}_i\ \text{given at}\ t=0\ \text{in}\ V. \tag{36}$$

Mixture Constitutive Relations

Variationally consistent model constitutive relations can be obtained by using Reissner's mixed variational principles (1950, 1984, 1986). The principles allow the use of the original constitutive relations together with the strain computed from the *trial displacements* and *trial transverse stresses* (Reissner, 1984; Murakami, 1986). The relevant mixed variational principle for laminated composites is based upon the variations of displacements $u_i^{(\alpha)}$ and transverse stresses, $\sigma_{3i}{}^{(\alpha)}$. Strains are computed, by definition, from displacements. Therefore, it is convenient to rewrite the rate-constitutive relation, (12), so that in-plane strains: e_{11}, e_{22}, and $2e_{12}$, and transverse stresses: σ_{31}, σ_{32}, and σ_{33} appear on the right-hand side. To this end, one first expresses (12) in the contracted form:

$$\dot{\boldsymbol{\sigma}}^{(\alpha)}=[C^{(\alpha)(ep)}]\dot{\mathbf{e}}^{(\alpha)} \tag{37a}$$

where

$$\boldsymbol{\sigma}=[\sigma_{11}\ \sigma_{22}\ \sigma_{12}\ \sigma_{31}\ \sigma_{23}\ \sigma_{33}]^T \tag{37b}$$

$$\mathbf{e}=[e_{11}\ e_{22}\ 2e_{12}\ 2e_{31}\ 2e_{23}\ e_{33}]^T \tag{37c}$$

in which $[\ ]^T$ denotes the transpose of $[\ ]$. A specific form of $[C^{(\alpha)(ep)}]$ for the von Mises yield criterion and the associative flow rule with isotropic strain hardening are shown in Appendix A.

By performing the required operation, one finds

$$\dot{\boldsymbol{\sigma}}_p^{(\alpha)}=[E_{11}^{(\alpha)}]\dot{\mathbf{e}}_p^{(\alpha)}+[E_{12}^{(\alpha)}]\dot{\boldsymbol{\sigma}}_t^{(\alpha)} \tag{38a}$$

$$\dot{\mathbf{e}}_t^{(\alpha)}=-[E_{12}^{(\alpha)}]^T\dot{\mathbf{e}}_p^{(\alpha)}+[E_{22}^{(\alpha)}]\dot{\boldsymbol{\sigma}}_t^{(\alpha)} \tag{38b}$$

where

$$\boldsymbol{\sigma}_p=[\sigma_{11}\ \sigma_{22}\ \sigma_{12}]^T,\quad \mathbf{e}_p=[e_{11}\ e_{22}\ 2e_{12}]^T \tag{38c,d}$$

$$\boldsymbol{\sigma}_t=[\sigma_{31}\ \sigma_{32}\ \sigma_{33}]^T \tag{38e}$$

$$\mathbf{e}_t=\left[2e_{31}+\frac{2}{\epsilon}e^*{}_{31}\ 2e_{23}+\frac{2}{\epsilon}e^*{}_{23}\ e_{33}+\frac{1}{\epsilon}e^*{}_{33}\right]^T \tag{38f}$$

and where the matrices $[E_{ij}]$, $i,j=1,2$ are functions of the elements of the tangent modulus matrix, $[C_{ij}]$, as shown in Appendix B.

Reissner's mixed variational principle applied to the rate boundary value problem defined by (11)–(14) yields

$$\begin{aligned}&\int\!\!\int\!\!\int_V\Bigg[\sum_{\alpha=1}^{2}\int_{A^{(\alpha)}}\{\delta\dot{\mathbf{e}}_p^{(\alpha)T}\dot{\boldsymbol{\sigma}}_p^{(\alpha)}+\delta\dot{\mathbf{e}}_t^{(\alpha)T}\dot{\boldsymbol{\sigma}}_t^{(\alpha)}-\delta\dot{\mathbf{u}}^{(\alpha)T}\rho^{(\alpha)}\dot{\mathbf{a}}^{(\alpha)}\\&+\delta\dot{\boldsymbol{\sigma}}_t^{(\alpha)T}(\dot{\mathbf{e}}_t^{(\alpha)}+[E_{12}^{(\alpha)}]^T\dot{\mathbf{e}}_p^{(\alpha)}-[E_{22}^{(\alpha)}]\dot{\boldsymbol{\sigma}}_t^{(\alpha)})\}dx^*_3\\&+\frac{1}{3}\Bigg[(\delta\dot{\mathbf{u}}^{(2)T}-\delta\dot{\mathbf{u}}^{(1)T})\dot{\mathbf{T}}^*+\delta\dot{\mathbf{T}}^{*T}(\dot{\mathbf{u}}^{(2)}\\&-\dot{\mathbf{u}}^{(1)})\Bigg|_{x^*_3=-n^{(1)}/2}^{x^*_3=n^{(1)}/2}\Bigg]dx_1dx_2dx_3\\&=\int\!\!\int_{\partial V_T}\left\{\sum_{\alpha=1}^{2}\int_{A^{(\alpha)}}\delta\dot{\mathbf{u}}^{(\alpha)T}{}^{\nu}\dot{\mathbf{T}}^{(\alpha)}dx^*_3\right\}dS\end{aligned} \tag{39a}$$

where

$$\mathbf{a}^{(\alpha)}=\ddot{\mathbf{u}}^{(\alpha)} \tag{39b}$$

and $\mathbf{u}$, $\mathbf{T}^*$, and ${}^{\nu}\mathbf{T}$ are the direct representations of u_i, $T^*{}_i$, and ${}^{\nu}T_i$, respectively. Further, the strains are all computed from the trial displacement field by (7) and (13). For arbitrary variation of $\dot{\mathbf{u}}^{(\alpha)}$ and $\dot{\boldsymbol{\sigma}}^{(\alpha)}$, the Euler-Lagrange equations of (39) yield the rate constitutive equations for $\dot{\mathbf{e}}_t{}^{(\alpha)}$ in (38*b*) as well as the rate equations of motion, (11), the rate boundary conditions, (*d*), and the rate form of (14) and (17). The remaining constitutive relations, (38*a*), are considered to be the definitions of $\dot{\boldsymbol{\sigma}}_p{}^{(\alpha)}$.

The mixed variational equation, (39), with appropriate trial functions $\dot{\mathbf{u}}^{(\alpha)}$ and $\dot{\boldsymbol{\sigma}}_t{}^{(\alpha)}$, yield the rate constitutive relations for a continuum model. Therefore, the variational equation for total quantities, (16), and the one for rates, (39), furnish a tool with which any deterministic high-order model can be constructed with appropriate trial displacements and transverse stresses. The basic requirements for the trial fields are the x^*-periodicity condition, (15). It is further noted that this procedure can also be extended to the cases without rate potentials by using the equivalent weighted residual form to Reissner's mixed variational principle.

The derivation of the rate constitutive relations for the mix-

Downloaded 03 May 2010 to 171.66.16.244. Redistribution subject to ASME license or copyright; see http://www.asme.org/terms/Terms_Use.cfm

ture model, (31) and (32), therefore, requires the approximation of transverse stresses:

$$\sigma_{3i}^{\{\alpha\}}(\mathbf{x},x_3^*,t) \approx \tau_{3i}^{(\alpha)}(\mathbf{x},t) + \epsilon\sigma_{3i(1)}^{\{\alpha\}}(\mathbf{x},x_3^*,t). \tag{40}$$

From (25) the O(1) transverse stresses are the same between the two constituents. However, with the same spirit as the construction of the trial displacement field, (30*a*), the difference of the average $O(\epsilon^2)$ transverse stresses is also included in $\tau_{3i}{}^{(\alpha)}$ of (40).

The $O(\epsilon)$ transverse stresses can also be constructed by solving the MBVP defined in (26) for $\mathbf{u}_{(2)}{}^{(\alpha)}$, and compute $\sigma_{3i(1)}{}^{(\alpha)}$ from (26*b*). However, this process becomes formidable for fiber-reinforced or particulate composites. Therefore, an attempt is made to construct a reasonable approximation of $\sigma_{3i(1)}{}^{(\alpha)}$ without solving for $\mathbf{u}_{(2)}{}^{(\alpha)}$. For laminated composites it is indeed possible to construct $\sigma_{3i(1)}{}^{(\alpha)}$ without knowing $u_{i(2)}{}^{(\alpha)}$. Since $\dot{\mathbf{e}}_{p(0)}{}^{(\alpha)}$ and $\dot{\sigma}_{l(0)}{}^{(\alpha)}$ are independent of $x^*{}_3$, equation (26*a*) indicates that

$$\dot{\sigma}_{3i(l),3*}^{\{\alpha\}} = D_i^{(\alpha)}(\mathbf{x},t) \tag{41}$$

where $D_i^{(\alpha)}$ is related to the rate of interaction body force, P_i, defined in (33*c*). Equation (33*c*) with (25) indicates that

$$P_i(\mathbf{x},t) = \sigma_{3i(l)}^{\{\alpha\}}\left(\mathbf{x}, \frac{n^{(1)}}{2}, t\right) - \sigma_{3i(l)}^{\{\alpha\}}\left(\mathbf{x}, -\frac{n^{(1)}}{2}, t\right). \tag{42}$$

As a result, the integration of (41) with the boundary conditions, (26*d*), (15), and (42) yields

$$\dot{\sigma}_{3i(l)}^{\{\alpha\}}(\mathbf{x},x_3^*,t) = \dot{P}_i(\mathbf{x},t)g^{(\alpha)}(x_3^*) \tag{43}$$

It is noted that the integrability condition for $\mathbf{u}_{(2)}{}^{(\alpha)}$, in (26), is satisfied automatically through the explicit introduction of the interaction body force, $\mathbf{P}$, in (43).

On substituting the rate form of (30*a*) and (40) with (43) into (39*a*), one obtains the rate form of (31), (32), and (34). In addition, the arbitrary variation of $\dot{\sigma}_l{}^{(\alpha)}$ yields the rate constitutive relations for the transverse stress variables, $\dot{\tau}^{(\alpha)}$ and $\dot{\mathbf{P}}$:

$$\begin{aligned}
&\int_{A^{(\alpha)}} [E_{22}^{\{\alpha\}}]dx_3^*\dot{\tau}^{(\alpha)} + \epsilon\int_{A^{(\alpha)}} [E_{22}^{\{\alpha\}}]g^{(\alpha)}dx_3^*\dot{\mathbf{P}} = n^{(\alpha)}\dot{\mathbf{e}}_{\{U\}l}^{\{\alpha\}} \\
&\quad + \int_{A^{(\alpha)}} [E_{12}^{\{\alpha\}}]^T dx_3^*\dot{\mathbf{e}}_{\{U\}p}^{\{\alpha\}} + (-1)^{\alpha+1}\dot{\mathbf{S}} \\
&\quad + \epsilon\int_{A^{(\alpha)}} [E_{12}^{\{\alpha\}}]^T g^{(\alpha)}dx_3^*\dot{\mathbf{e}}_{(S)p}
\end{aligned} \tag{44}$$

$$\begin{aligned}
&\epsilon\sum_{\alpha=1}^{2}\int_{A^{(\alpha)}} [E_{22}^{\{\alpha\}}]g^{(\alpha)}dx_3^*\dot{\tau}^{(\alpha)} \\
&+\epsilon^2\sum_{\alpha=1}^{2}\int_{A^{(\alpha)}} [E_{22}^{\{\alpha\}}](g^{(\alpha)})^2dx_3^*\dot{\mathbf{P}} = \dot{\mathbf{U}}^{(2)} - \dot{\mathbf{U}}^{(1)} \\
&+\epsilon\sum_{\alpha=1}^{2}\int_{A^{(\alpha)}} [E_{12}^{\{\alpha\}}]^T g^{(\alpha)}dx_3^*\dot{\mathbf{e}}_{\{U\}p}^{\{\alpha\}} \\
&+\epsilon^2\sum_{\alpha=1}^{2}\int_{A^{(\alpha)}} (g^{(\alpha)})^2dx_3^*\dot{\mathbf{e}}_{(S)l} \\
&+\epsilon^2\sum_{\alpha=1}^{2}\int_{A^{(\alpha)}} [E_{12}^{\{\alpha\}}]^T(g^{(\alpha)})^2dx_3^*\dot{\mathbf{e}}_{(S)p}
\end{aligned} \tag{45}$$

where

$$\tau^{(\alpha)} = [\tau_{31}^{\{\alpha\}}\ \tau_{23}^{\{\alpha\}}\ \tau_{33}^{\{\alpha\}}]^T,\quad \mathbf{P} = [P_1\ P_2\ P_3]^T \tag{46a,b}$$

$$\mathbf{e}_{\{U\}p}^{\{\alpha\}} = [U_{1,1}^{\{\alpha\}}\ U_{2,2}^{\{\alpha\}}\ U_{1,2}^{\{\alpha\}} + U_{2,1}^{\{\alpha\}}]^T \tag{46c}$$

$$\mathbf{e}_{\{U\}l}^{\{\alpha\}} = [U_{3,1}^{\{\alpha\}} + U_{1,3}^{\{\alpha\}}\ U_{2,3}^{\{\alpha\}} + U_{3,2}^{\{\alpha\}}\ U_{3,3}^{\{\alpha\}}]^T \tag{46d}$$

$$\mathbf{e}_{(S)p} = [S_{1,1}\ S_{2,2}\ S_{1,2} + S_{2,1}]^T \tag{46e}$$

$$\mathbf{e}_{(S)l} = [S_{3,1} + S_{1,3}\ S_{2,3} + S_{3,2}\ S_{3,3}]^T. \tag{46f}$$

It is noted that for hardening materials $[E_{22}{}^{(\alpha)}]$ on the LHS of (44) and (45) is positive definite and symmetric. The solution of (44) and (45) yields $\dot{\tau}^{(\alpha)}$ and $\dot{\mathbf{P}}$ in terms of $\dot{\mathbf{e}}_{(U)p}{}^{(\alpha)}$, $\dot{\mathbf{e}}_{(U)l}{}^{(\alpha)}$, $\dot{\mathbf{S}}$, $\dot{\mathbf{e}}_{(S)l}$, $\dot{\mathbf{e}}_{(S)p}$, and $\dot{\mathbf{U}}^{(2)} - \dot{\mathbf{U}}^{(1)}$. For elastic constituents it is possible to evaluate these relations explicitly (Murakami, 1985). However, for inelastic responses the integrals in (44) and (45) have to be evaluated numerically at each increment.

From (40) with (43) and (33*b*) one finds

$$\dot{\sigma}_{3i}^{\{\alpha a\}} = \dot{\tau}_{3i}^{\{\alpha\}},\quad \dot{M}_{3i} = \frac{1}{12}\dot{P}_i \quad i = 1-3, \tag{47a,b}$$

or, in the vector form:

$$\dot{\sigma}_l^{\{\alpha a\}} = \dot{\tau}^{(\alpha)},\quad \dot{\mathbf{M}}_l = \frac{1}{12}\dot{\mathbf{P}}. \tag{47a,b}$$

The constitutive relations for the in-plane stress variables are obtained from (38*a*), (30*a*), (7), and (33*a*,*b*). The results are

$$\begin{aligned}
n^{(\alpha)}\dot{\sigma}_p^{\{\alpha a\}} &= \int_{A^{(\alpha)}} [E_{11}^{\{\alpha\}}]dx_3^*\dot{\mathbf{e}}_{\{U\}p}^{\{\alpha\}} + \epsilon\int_{A^{(\alpha)}} [E_{11}^{\{\alpha\}}]g^{(\alpha)}dx_3^*\dot{\mathbf{e}}_{(S)p} \\
&\quad + \int_{A^{(\alpha)}} [E_{12}^{\{\alpha\}}]dx_3^*\dot{\tau}^{(\alpha)} + \epsilon\int_{A^{(\alpha)}} [E_{12}^{\{\alpha\}}]g^{(\alpha)}dx_3^*\dot{\mathbf{P}}
\end{aligned} \tag{48}$$

$$\begin{aligned}
\epsilon\dot{\mathbf{M}}_p &= \sum_{\alpha=1}^{2}\int_{A^{(\alpha)}} [E_{11}^{\{\alpha\}}]g^{(\alpha)}dx_3^*\dot{\mathbf{e}}_{\{U\}p}^{\{\alpha\}} \\
&+\epsilon\sum_{\alpha=1}^{2}\int_{A^{(\alpha)}} [E_{11}^{\{\alpha\}}](g^{(\alpha)})^2dx_3^*\dot{\mathbf{e}}_{(S)p} \\
&+\sum_{\alpha=1}^{2}\int_{A^{(\alpha)}} [E_{12}^{\{\alpha\}}]g^{(\alpha)}dx_3^*\dot{\tau}^{(\alpha)} \\
&+\epsilon\sum_{\alpha=1}^{2}\int_{A^{(\alpha)}} [E_{12}^{\{\alpha\}}](g^{(\alpha)})^2dx_3^*\dot{\mathbf{P}}
\end{aligned} \tag{49}$$

where

$$\mathbf{M}_p = [M_{11}\ M_{22}\ M_{12}]^T. \tag{50}$$

The accuracy of the resulting model in predicting elastic harmonic wave dispersion was amply demonstrated by Murakami, Maewal, and Hegemier (1981), and Murakami and Akiyama (1985). Therefore, the model accuracy will be assessed by comparing in time domain the predicted values with experimental and numerically exact data. It is noted that, compared with the effective stiffness theories developed by Sun, Achenbach, and Herrmann (1968b), Drumheller and Bedford (1974), and Aboudi (1981), the mixture model can furnish an accurate model by using the least number of displacement variables (Murakami, Maewal, and Hegemier, 1981). From the $O(\epsilon)$ model, the O(1) homogenized model can easily be obtained from the mixture model by introducing the kinematic constraints:

$$U_i^{(1)} = U_i^{(2)} = U_i \tag{51}$$

and taking the limit of $\epsilon \to 0$ as shown by Murakami and Toledano (1988).

Numerical Results

The accuracy of the present model is tested by comparing results with the experimental data reported by Lundergan and Drumheller (1971). Their experiment was performed on a

Downloaded 03 May 2010 to 171.66.16.244. Redistribution subject to ASME license or copyright; see http://www.asme.org/terms/Terms_Use.cfm

Table 1 Material properties (Lundergan and Drumheller, 1971)

Material α	Volume Fraction $n^{(\alpha)}$	Density $\rho^{(\alpha)}(kg/m^3)$	Young's Modulus $E^{(\alpha)}(GPa)$	Poisson's Ratio $\nu^{(\alpha)}$
1	0.7552	7896	124.3	0.293
2	0.2448	1200	6.464	0.285

Table 2 Material properties

Material α	Volume Fraction $n^{(\alpha)}$	Density $\rho^{(\alpha)}(kg/m^3)$	Young's Modulus $E^{(\alpha)}(GPa)$	Poisson's Ratio $\nu^{(\alpha)}$	Yield Stress $\sigma_Y(GPa)$	Hardening Parameter H'(GPa)
1	0.5	2200	69	0.17	—	—
2	0.5	1266	6.895	0.25	0.7	0.35

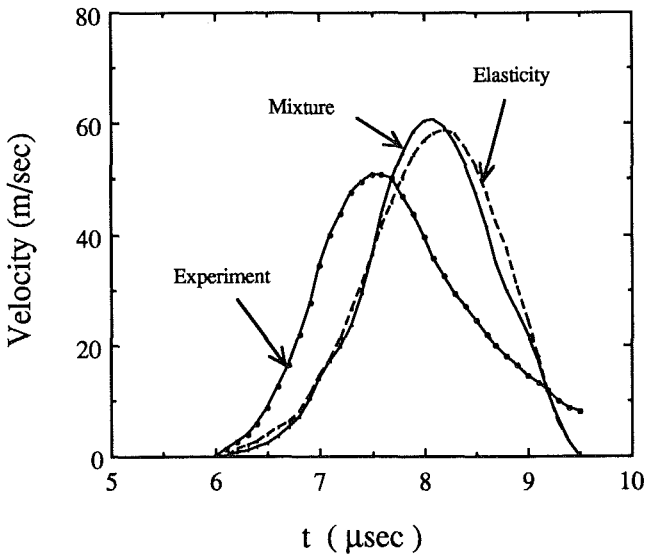


Fig. 3 Time variation of particle velocity

bilaminated plate made up of ten alternate layers of stainless steel and epon 828, and subjected to a pulse pressure loading of duration 1.7 μsec. The direction of wave propagation was perpendicular to the layering. Material properties are given in Table 1. Figure 3 shows the time variation of the particle velocity on the outer surface. An explicit finite element code was developed to solve the proposed mixture equations. The mixture results, which correspond to an elastic analysis are in close agreement with the elasticity solution obtained by the method of characteristics. The discrepancy between the elasticity solution and the experimental results is due to material nonlinearity and interface debonding (Lundergan and Drumheller, 1971).

In order to further assess the accuracy of the mixture model, a half space subjected to a step pressure loading of 1.4 GPa on its free surface was analyzed. Two cases have been considered: (1) wave propagation parallel to the interfaces of the composite (wave guide), and (2) propagation normal to the interfaces of the composite (wave reflect). DYNA2D (Hallquist, 1982) was used to furnish numerically exact data for the problem by discretizing the details of the composite microstructure.

The material properties of the composite are given in Table 2. For the wave-guide problem, due to the symmetry, only half a cell is discretized in DYNA2D where each material domain is subdivided into 285×9 quadrilateral plane-strain elements. The results of the mixture theory are obtained by using 225

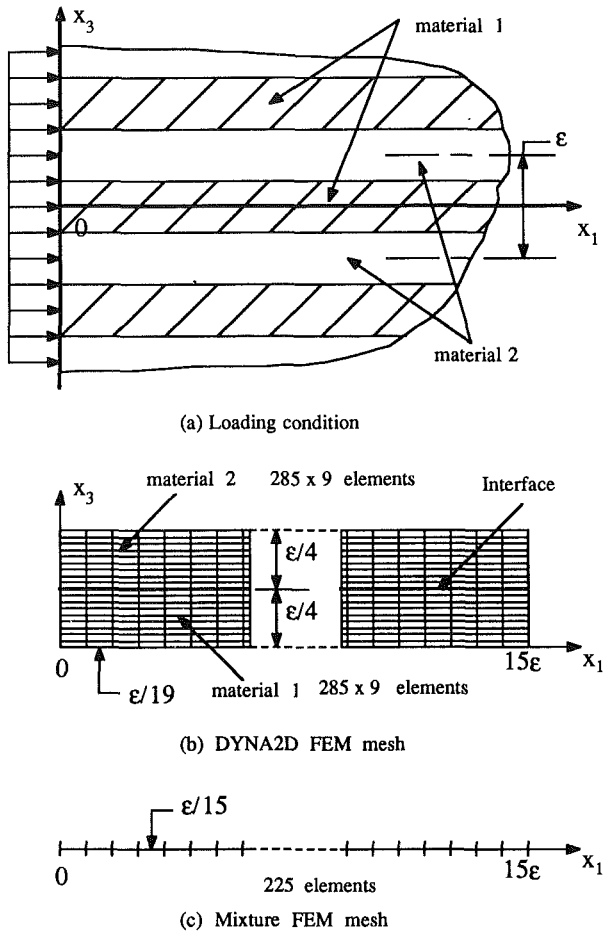


Fig. 4 Loading and finite element discretization for wave-guide analysis

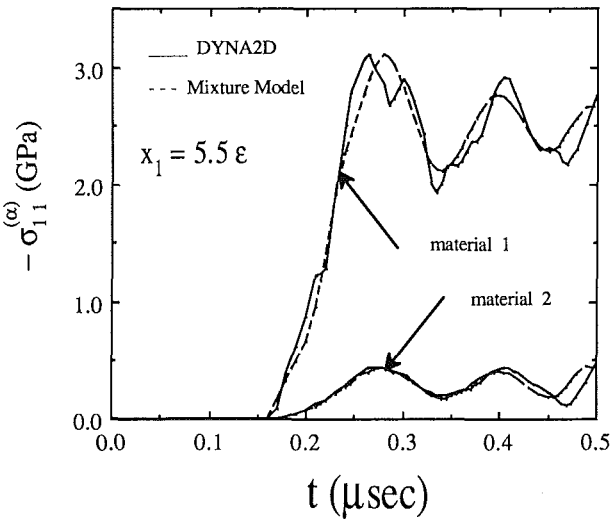


Fig. 5 Time variation of axial stress $\sigma_{11}^{(\alpha)}$ for elastic wave guide analysis

two-node, isoparametric elements. These meshes are shown in Fig. 4. The time variation of the axial stress $\sigma_{11}^{(\alpha)}$ is computed at a distance $x_1 = 5.5\epsilon$ from the loading surface, where the cell dimension $\epsilon = 180$ microns. For an elastic analysis, stress $\sigma_{11}^{(1)}$ in material 1 and $\sigma_{11}^{(2)}$ in material 2 are plotted in Fig. 5. It can be observed that the mixture model reasonably simulates the wave dispersion phenomenon and accurately predicts the shape of the wave front and maximum stresses. When material 2 is assumed elastoplastic obeying a von Mises yield criterion

Downloaded 03 May 2010 to 171.66.16.244. Redistribution subject to ASME license or copyright; see http://www.asme.org/terms/Terms_Use.cfm

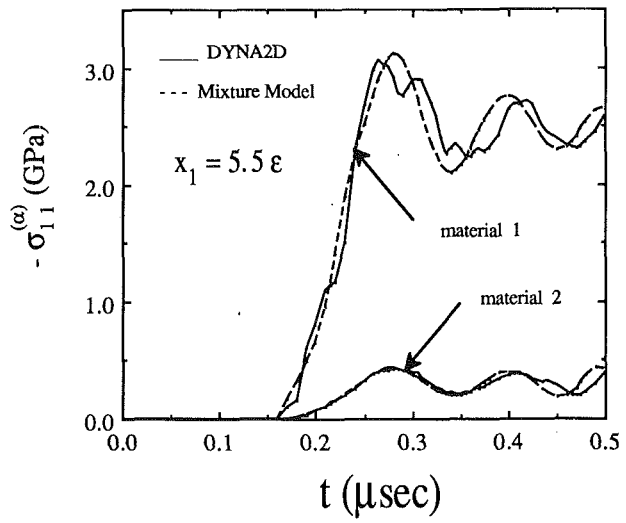


Fig. 6 Time variation of axial stress $\sigma_{11}{}^{(\alpha)}$ for elastoplastic wave guide analysis

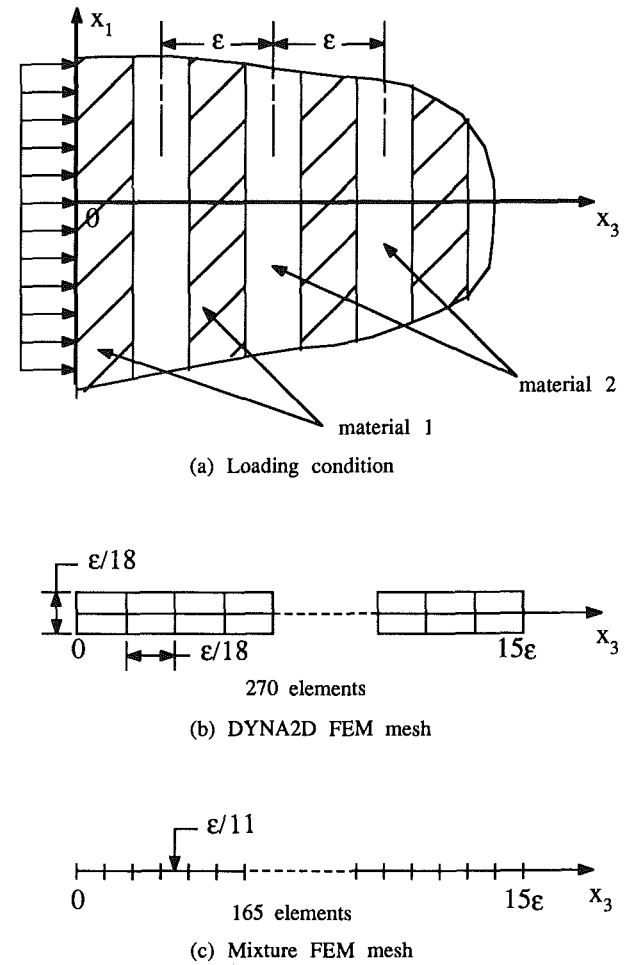


Fig. 7 Loading and finite element discretization for wave reflect analysis

with isotropic hardening, the time variations of the axial stress $\sigma_{11}{}^{(\alpha)}$ are plotted in Fig. 6. Again, good agreement is observed between the present model and DYNA2D computations. It is worth noting that in this case the plastic region is confined to an ϵ-distance from the loading surface, and hence does not propagate into the interior domain.

Next, the wave reflect problem, illustrated in Fig. 7, is considered wherein the same material properties are used except

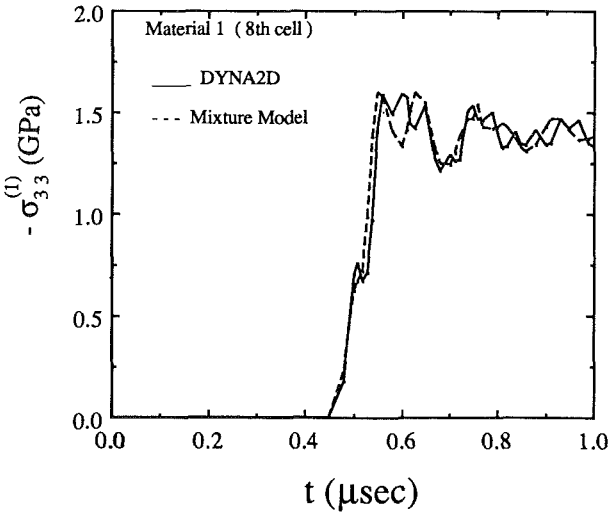


Fig. 8(a) Time variation of normal stress $\sigma_{33}{}^{(1)}$ for elastic wave reflect analysis

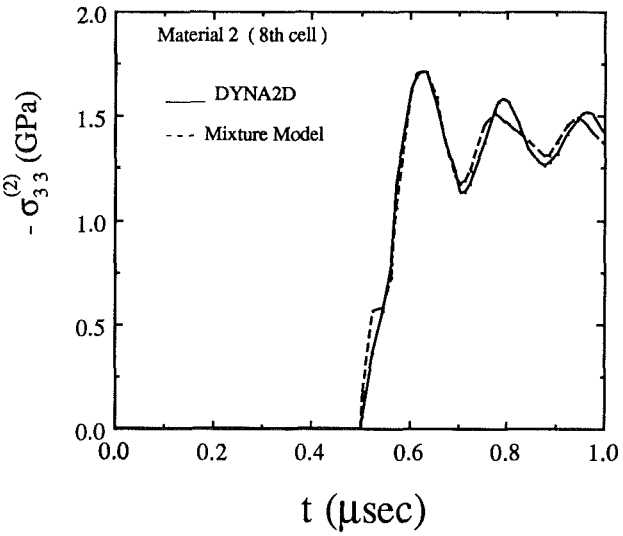


Fig. 8(b) Time variation of normal stress $\sigma_{33}{}^{(2)}$ for elastic wave reflect analysis

now $E^{(1)} = 15$GPa. In this case a 15-cell laminate is analyzed, with each cell subdivided into 18 quadrilateral plane-strain elements for the DYNA2D computations. The cell dimension is again $\epsilon = 180$ microns. For the present mixture model each cell is subdivided into 11 two-node linear isoparametric elements. The composite is assumed to undergo uniaxial strain deformation. The time variations of the normal stress $\sigma_{33}{}^{(\alpha)}$ are computed at the center of each material layer in the eighth cell from the loading surface. For an elastic analysis results are shown in Fig. 8(a) for material 1 and Fig. 8(b) for material 2, while for an elastoplastic analysis they are shown in Fig. 9(a) for material 1 and Fig. 9(b) for material 2. Good agreement is obtained between DYNA2D and the present mixture theory. A simple calculation based upon the effective tangent modulus theory demonstrates that the change in slope due to plastic deformation first occurs when $\sigma_{33}{}^{(2)} = 1.05$GPa, as Fig. 9($b$) also shows. It can be observed that, for the case of wave propagation normal to the interfaces of the composite, the ringing in the stiffer material (material 1) is more pronounced even for a lower ratio of $E^{(1)}/E^{(2)}$. It is noted that the mixture finite element code, which does not require the explicit discretization of the composite microstructure, is more than an order of magnitude faster than DYNA2D.

Downloaded 03 May 2010 to 171.66.16.244. Redistribution subject to ASME license or copyright; see http://www.asme.org/terms/Terms_Use.cfm

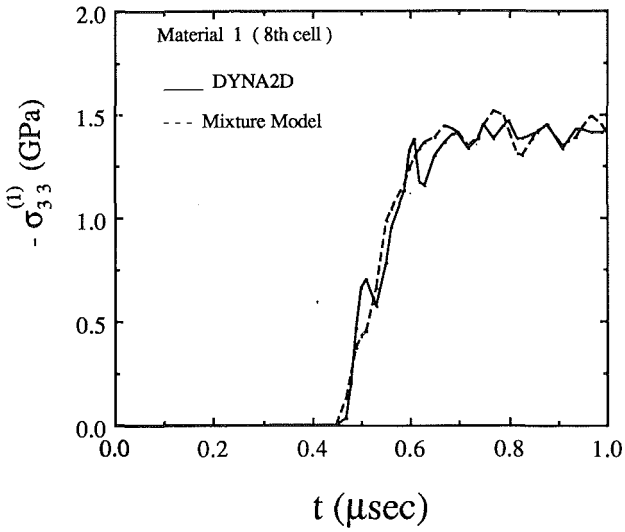


Fig. 9(*a*) Time variation of normal stress $\sigma_{33}^{(1)}$ for elastoplastic wave reflect analysis

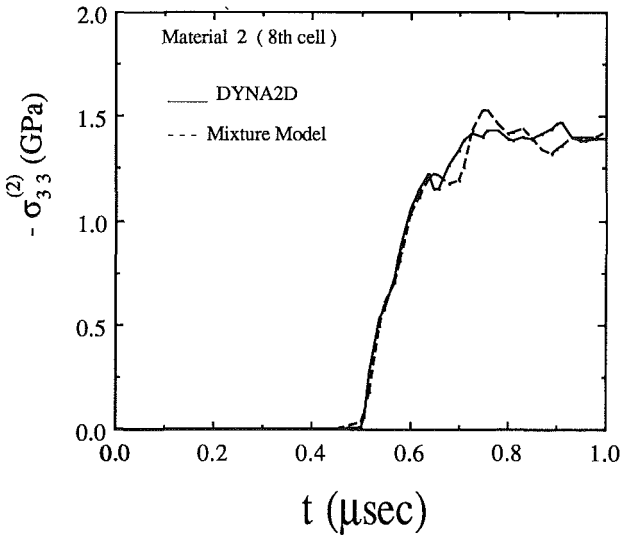


Fig. 9(*b*) Time variation of normal stress $\sigma_{33}^{(2)}$ for elastoplastic wave reflect analysis

Conclusions

A high-order homogenization model was introduced in order to furnish an improved model simulation capability for dynamic response of composites. A procedure of constructing a mixture model was presented systematically based upon the principle of virtual work for total quantities and Reissner's variational principle (Reissner, 1984) for bi-laminated composites. It was found that nine equations of motion are required for the mixture model. Good correlations with experimental and numerically exact data in the time domain, indicate that the mixture model may be used to simulate critical laminate interactions for static as well as dynamic problems.

Acknowledgment

The research was supported by the Office of Naval Research under Contract N00014-86-K-0468 to the University of California at San Diego. The authors are grateful to Dr. A. S. Kushner of ONR for his support.

References

Aboudi, J., 1981a, "Generalized Effective Stiffness Theory for Nonelastic Laminated Composites," *International Journal of Engineering Science*, Vol. 19, pp. 1269–1281.

Aboudi, J., 1981b, "Effective Stiffness Theory for a Laminated Elastic-Viscoplastic Work-Hardening Composite," *International Journal of Solids and Structures*, Vol. 17, pp. 421–431.

Achenbach, J. D., 1975, *A Theory of Elasticity with Microstructure for Directionally Reinforced Composites*, Springer-Verlag, New York.

Achenbach, J. D., Sun, C. T., and Herrmann, G., 1968, "On the Vibration of a Laminated Body," ASME Journal of Applied Mechanics, Vol. 35, pp. 689–696.

Babuska, I., 1976, "Solution of Interface Problems by Homogenization," *SIAM Journal of Applied Mathematics*, Vol. 7, Part I, pp. 603–634; Part II, pp. 635–645.

Bensoussan, A., Lions, J. L., and Papanicolaou, G., 1978, *Asymptotic Analysis for Periodic Structures*, North Holland, Amsterdam.

Brillouin, L., 1946, *Wave Propagation in Periodic Structure*. McGraw-Hill, New York (also published by Dover Publications, in 1953, New York).

Drumheller, D. S., and Bedford, D., 1974, "Wave Propagation in Elastic Laminates Using a Second Order Microstructure Theory," *International Journal of Solids and Structures*, Vol. 10, pp. 61–76.

Grot, R. A., and Achenbach, J. D., 1970, "Large Deformation of a Laminated Composite," *International Journal of Solids and Structures*, Vol. 6, pp. 641–659.

Hallquist, J. O., 1982, "User's Manual for DYNA2D—An Explicit Two-Dimensional Hydrodynamic Finite Element Code with Interactive Rezoning," University of California, Lawrence Livermore National Laboratory, Report UCID-18756.

Hegemier, G. A., 1974, "Finite Amplitude Elastic-Plastic Wave Propagation in Laminated Composites," *Journal of Applied Physics*, Vol. 45, pp. 4248–4253.

Lene, F., and Leguillon, D., 1982, "Homogenized Constitutive Law for a Partially Cohesive Composite Material," *International Journal of Solids and Structures*, Vol. 18, pp. 443–458.

Lundergan, C. D., and Drumheller, D. S., 1971, "Propagation of Stress Waves in a Laminated Plate Composite," *Journal of Applied Physics*, Vol. 42, No. 2, pp. 669–675.

McNiven, H. D., and Mengi, Y., 1979a, "A Mathematical Model for the Linear Dynamic Behavior of Two Phase Periodic Materials," *International Journal of Solids and Structures*, Vol. 15, pp. 271–280.

McNiven, H. D., and Mengi, Y., 1979b, "Propagation of Transient Waves in Elastic Laminated Composites," *International Journal of Solids and Structures*, Vol. 15, pp. 303–318.

Murakami, H., 1985, "A Mixture Theory for Wave Propagation in Angle-Ply Laminates, Part 1: Theory," ASME Journal of Applied Mechanics, Vol. 52, pp. 331–337.

Murakami, H., 1986, "Laminated Composite Plate Theory with Improved In-Plane Responses," ASME Journal of Applied Mechanics, Vol. 53, pp. 661–666.

Murakami, H., and Akiyama, A., 1985, "A Mixture Theory for Wave Propagation in Angle-Ply Laminates, Part 2: Application," ASME Journal of Applied Mechanics, Vol. 52, pp. 338–343.

Murakami, H., and Toledano, A., 1988, "A High-Order Mixture Homogenization of Bi-Laminated Composites," *Recent Advances in Macro- and Micro-Mechanics of Composite Materials*, D. Hui and J. R. Vinson, eds., ASME Winter Annual Meeting, Chicago, AD-Vol. 13, pp. 243–253.

Murakami, H., and Hegemier, G. A., 1986, "A Mixture Model for Unidirectionally Fiber-Reinforced Composites," ASME Journal of Applied Mechanics, Vol. 53, pp. 765–773.

Murakami, H., Maewal, A., and Hegemier, G. A., 1981, "A Mixture Theory with a Director for Linear Elastodynamics of Periodically Laminated Media," *International Journal of Solids and Structures*, Vol. 17, pp. 155–173.

Reissner, E., 1950, "On a Variational Theorem in Elasticity," *Journal of Mathematics and Physics*, Vol. 29, pp. 90–95.

Reissner, E., 1984, "On a Certain Mixed Variational Theorem and a Proposed Application," *International Journal for Numerical Methods in Engineering*, Vol. 20, pp. 1366–1368.

Reissner, E., 1986, "On a Mixed Variational Theorem and On Shear Deformable Plate Theory," *International Journal for Numerical Methods in Engineering*, Vol. 23, pp. 193–198.

Sanchez-Palencia, E., 1980, *Non-Homogeneous Media and Vibration Theory*, (Lecture Notes in Physics, 127), Springer-Verlag, Berlin, Heidelberg.

Sun, C. T., Achenbach, J. D., and Herrmann, G., 1968a, "Time-Harmonic Waves in a Stratified Medium Propagating in the Direction of the Layering," ASME Journal of Applied Mechanics, Vol. 35, pp. 408–411.

Sun, C. T., Achenbach, J. D., and Herrmann, G., 1968b, "Continuum Theory for a Laminated Medium," ASME Journal of Applied Mechanics, Vol. 35, pp. 467–475.

Sve, C., 1971, "Time Harmonic Waves Travelling Obliquely in a Periodically Laminated Medium," ASME Journal of Applied Mechanics, Vol. 38, pp. 477–482.

Tartar, L., 1977, *Cours Pecot*, College de France.

Toledano, A., and Murakmi, H., 1987, "A High-Order Mixture Model for Periodic Particulate Composites," *International Journal of Solids and Structures*, Vol. 23, pp. 989–1002.

Downloaded 03 May 2010 to 171.66.16.244. Redistribution subject to ASME license or copyright; see http://www.asme.org/terms/Terms_Use.cfm

APPENDIX A

The Tangent Modulus Matrix $[C^{(\alpha)(ep)}]$

The von Mises yield criterion is expressed in terms of the effective stress, $\bar{\sigma}$, and the uniaxial yield stress, σ_Y, as follows

$$\bar{\sigma} = \sqrt{\frac{3}{2} s_{ij} s_{ij}} = \sigma_Y, \tag{A1}$$

where s_{ij} is the deviatoric stress

$$s_{ij} = \dot{\sigma}_{ij} - \frac{1}{3} \delta_{ij} \sigma_{kk}. \tag{A2}$$

The elastoplastic tangent modulus matrix in the contracted form can be easily obtained as

$$[C^{(\alpha)(ep)}] = [C^{(\alpha)}] - \frac{9\mu^{(\alpha)2}}{\bar{\sigma}^{(\alpha)2}(H' + 3\mu)^{(\alpha)}} \mathbf{s}^{(\alpha)} \mathbf{s}^{(\alpha)T} \tag{A3}$$

where H' is the strain-hardening parameter and $\mu^{(\alpha)}$ is the shear modulus and

$$\mathbf{s} = [s_{11}\ s_{22}\ s_{12}\ s_{31}\ s_{23}\ s_{33}]^T. \tag{A4}$$

For the stress state on the yield surface (A1), the plastic loading occurs when

$$s_{ij} \dot{s}_{ij} > 0, \tag{A5}$$

otherwise elastic response is assumed.

APPENDIX B

The Definitions of $[E_{ij}]$ in Equation (38)

It is convenient to rewrite (12) in the contracted form by introducing submatrices, $[D_{ij}]$, $i,j = 1,2$, as follows:

$$\dot{\sigma}_p = [D_{11}]\dot{\mathbf{e}}_p + [D_{12}]\dot{\mathbf{e}}_t \tag{B1}$$

$$\dot{\sigma}_t = [D_{12}]^T \dot{\mathbf{e}}_p + [D_{22}]\,\dot{\mathbf{e}}_t. \tag{B2}$$

Equation (B2) can be used to solve for $\dot{\mathbf{e}}_t$. By substituting the result into (B1) one obtains the desired form, (41a,b), and finds:

$$[E_{11}] = [D_{11}] - [D_{12}][D_{22}]^{-1}[D_{12}]^T$$

$$[E_{12}] = [D_{12}][D_{22}]^{-1},\ [E_{22}] = [D_{22}]^{-1}. \tag{B3}$$

Downloaded 03 May 2010 to 171.66.16.244. Redistribution subject to ASME license or copyright; see http://www.asme.org/terms/Terms_Use.cfm

M. Bouden
Mem. ASME

S. K. Datta
Fellow ASME

Department of Mechanical Engineering
and CIRES,
University of Colorado,
Boulder, CO 80309-0427

Rayleigh and Love Waves in Cladded Anistropic Medium

Guided waves in coated anisotropic medium are of interest in electronics. Also, in recent years, cladded fiber-reinforced composites are being developed for use as aerospace structures. This paper deals with guided wave propagation in a cladded or coated anisotropic medium. The cladding (coating) is assumed to be a thin isotropic layer, which is bonded to a transversely isotropic substrate with the axis of symmetry parallel to the layer. It is shown that the anisotropy of the substrate affects the dispersion behavior in a manner that is substantially different than in the case of isotropic substrate.

1 Introduction

Early work on dispersion of Rayleigh and Love waves was by Love (1911, 1926), who gave the first comprehensive treatment of the case of an elastic solid half space covered by a single solid layer.

Stoneley (1926) investigated the effect of the ocean on the transmission of Rayleigh waves. Many other authors considered the dispersion of surface waves in isotropic layered medium. Ewing et al. (1957) gave a review of the works done by many authors, such as Haskell (1953), Jeffreys (1935), Kanai (1951), Tolstoy and Usdin (1953), and Newlands (1952). In all the aforementioned publications the media were considered isotropic. Farnell and Adler (1972) discussed guided wave propagation in thin layers. Their discussion included a detailed description of Rayleigh and Love waves in isotropic layered medium, and a general description of Rayleigh and Love waves in anisotropic layered medium. As numerical examples, they discussed in detail the case of cubic crystals when the Love-Rayleigh mode separation was valid, and only one coupled case, when the direction of propagation was rotated 5 deg from the crystal axis. Earlier Crampin (1970) and Crampin and Taylor (1971) considered surface waves in layered anisotropic media. Of particular relevance to the present work is that of Crampin and Taylor (1971), who discussed several cases of anisotropic half spaces. However, they did not consider the case of an isotropic layer overlying a transversely isotropic half space when the axis of symmetry is parallel to the interface.

Among the more recent studies may be mentioned the works of Nayfeh et al. (1981) and Chimenti et al. (1982) which deal with deflection of acoustic waves in a fluid coupled half space with a thin solid layer between the fluid and solid half spaces. Also, Kundu and Mal (1986) and Nayfeh and Taylor (1988) have presented solutions for waves in a layered half space. In all these works, the authors have considered isotropic solids. Furthermore, a Thomson-Haskell (see, Thomson (1950) and Haskell (1953)) matrix approach has been adapted in the last two works.

In this paper we investigate the effect of anisotropy of the transversely isotropic substrate on the dispersive wave propagation in the isotropic layer. This problem is of interest in electronics and in space structures (Farnell and Adler (1972) and Pelka (1986)). The two substrates considered here, beta-quartz and graphite fiber-reinforced epoxy, are transversely isotropic. It is assumed that in both cases the axis of symmetry is parallel to the layer. Numerical results are presented for two cases: a gold layer on beta-quartz and an aluminum cladding on graphite-epoxy.

There are well-known precision problems associated with the straightforward application of the Thomson-Haskell procedure. Various modifications of the procedure have been proposed to avoid the precision problem (for a discussion of this reference (see Xu and Mal (1987)). The difficulty associated with the Thomson-Haskell method can be avoided by using a global matrix that is obtained by simultaneous enforcement of boundary (or, continuity) conditions at the surfaces (interfaces). This has been successfully used by Mal (1988) to study guided waves in a layered isotropic solid. In this paper we have used the same approach and have found that the method is quite stable for a wide range of frequency.

2 Problem Formulation

We consider here a layered half space as shown in Fig. 1. This is composed of an isotropic layer of thickness H bonded to a half space of a transversely isotropic material, where the x-axis is the unique axis.

If $\mathbf{U} = (u, v, w)$ is the displacement vector referred to as the cartesian coordinate system $O(x, y, z)$, then the equations of motion are

$$\frac{\partial \sigma_{xx}}{\partial x} + \frac{\partial \sigma_{xy}}{\partial y} + \frac{\partial \sigma_{xz}}{\partial z} + \rho X = \rho \ddot{u} \tag{1}$$

Contributed by the Applied Mechanics Division of THE AMERICAN SOCIETY OF MECHANICAL ENGINEERS for presentation at the Winter Annual Meeting, Dallas, Texas, November 25–30, 1990.

Discussion on this paper should be addressed to the Technical Editor, Leon M. Keer, The Technological Institute, Northwestern University, Evanston, IL 60208, and will be accepted until two months after final publication of the paper itself in the JOURNAL OF APPLIED MECHANICS. Manuscript received by the ASME Applied Mechanics Division, July 11, 1988; final revision, May 31, 1989.

Paper No. 90-WA/APM-4.

Copyright © 1990 by ASME
Downloaded 03 May 2010 to 171.66.16.244. Redistribution subject to ASME license or copyright; see http://www.asme.org/terms/Terms_Use.cfm

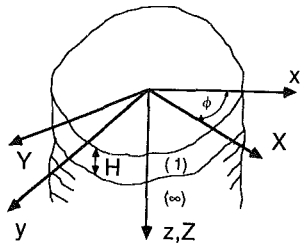


Fig. 1 Geometry of the problem; layered half space

$$\frac{\partial \sigma_{yx}}{\partial x}+\frac{\partial \sigma_{yy}}{\partial y}+\frac{\partial \sigma_{yz}}{\partial z}+\rho Y=\rho \ddot{v} \tag{2}$$

$$\frac{\partial \sigma_{zx}}{\partial x}+\frac{\partial \sigma_{yz}}{\partial y}+\frac{\partial \sigma_{zz}}{\partial z}+\rho Z=\rho \ddot{w}, \tag{3}$$

where σ_{ij} are the stress components, (X, Y, Z) are the components of the force per unit mass, and

$$(\cdot)\equiv\frac{\partial(\ )}{\partial t}.$$

In a transversely isotropic material, the stresses can be written in terms of the displacements as follows:

$$\sigma_{xx}=c_{11}\frac{\partial u}{\partial x}+c_{12}\frac{\partial v}{\partial y}+c_{12}\frac{\partial w}{\partial z} \tag{4}$$

$$\sigma_{yy}=c_{12}\frac{\partial u}{\partial x}+c_{22}\frac{\partial v}{\partial y}+c_{23}\frac{\partial w}{\partial z} \tag{5}$$

$$\sigma_{zz}=c_{12}\frac{\partial u}{\partial x}+c_{23}\frac{\partial v}{\partial y}+c_{22}\frac{\partial w}{\partial z} \tag{6}$$

$$\sigma_{yz}=c_{44}\left(\frac{\partial v}{\partial z}+\frac{\partial w}{\partial y}\right) \tag{7}$$

$$\sigma_{xz}=c_{55}\left(\frac{\partial u}{\partial z}+\frac{\partial w}{\partial x}\right) \tag{8}$$

$$\sigma_{xy}=c_{55}\left(\frac{\partial u}{\partial y}+\frac{\partial v}{\partial x}\right) \tag{9}$$

where c_{ij} are the stiffness tensor components in the contraction notation and

$$c_{44}=\frac{1}{2}(c_{22}-c_{23}).$$

By substitution of the foregoing stress expressions into the equations of motion, we get

$$c_{11}\frac{\partial^2 u}{\partial x^2}+c_{12}\frac{\partial^2 v}{\partial x\partial y}+c_{12}\frac{\partial^2 w}{\partial x\partial z}+c_{55}\left(\frac{\partial^2 u}{\partial y^2}+\frac{\partial^2 v}{\partial x\partial y}\right)+c_{55}\left(\frac{\partial^2 u}{\partial z^2}+\frac{\partial^2 w}{\partial x\partial z}\right)+\rho X=\rho \ddot{u} \tag{10}$$

$$c_{55}\left(\frac{\partial^2 u}{\partial x\partial y}+\frac{\partial^2 v}{\partial x^2}\right)+c_{12}\frac{\partial^2 u}{\partial x\partial y}+c_{22}\frac{\partial^2 v}{\partial y^2}+c_{23}\frac{\partial^2 w}{\partial y\partial z}+c_{44}\left(\frac{\partial^2 v}{\partial z^2}+\frac{\partial^2 w}{\partial y\partial z}\right)+\rho Y=\rho \ddot{v} \tag{11}$$

$$c_{55}\left(\frac{\partial^2 u}{\partial x\partial z}+\frac{\partial^2 w}{\partial x^2}\right)+c_{44}\left(\frac{\partial^2 v}{\partial y\partial z}+\frac{\partial^2 w}{\partial y^2}\right)+c_{12}\frac{\partial^2 u}{\partial x\partial z}+c_{23}\frac{\partial^2 v}{\partial y\partial z}+c_{22}\frac{\partial^2 w}{\partial z^2}+\rho Z=\rho \ddot{w}. \tag{12}$$

The displacements can be written in terms of three potential functions as in Buchwald (1961) in the form

$$u=\frac{\partial \Theta}{\partial x} \tag{13}$$

$$v=\frac{\partial \Phi}{\partial y}+\frac{\partial \Psi}{\partial z} \tag{14}$$

$$w=\frac{\partial \Phi}{\partial z}-\frac{\partial \Psi}{\partial y}. \tag{15}$$

Eliminating the displacements from equations (10)-(15) we get

$$\left[c_{55}\frac{\partial^2}{\partial x^2}+c_{44}\nabla^2-\rho\frac{\partial^2}{\partial t^2}\right]\nabla^2\Psi+\rho\left(\frac{\partial Y}{\partial z}-\frac{\partial Z}{\partial y}\right)=0 \tag{16}$$

$$(c_{12}+c_{55})\frac{\partial^2}{\partial x^2}\nabla^2\Phi+\left[c_{55}\nabla^2+c_{11}\frac{\partial^2}{\partial x^2}-\rho\frac{\partial^2}{\partial t^2}\right]\frac{\partial^2\Theta}{\partial x^2}+\rho\frac{\partial X}{\partial x}=0 \tag{17}$$

$$(c_{12}+c_{55})\frac{\partial^2}{\partial x^2}\nabla^2\Theta+\left[c_{22}\nabla^2+c_{55}\frac{\partial^2}{x^2}-\rho\frac{\partial^2}{\partial t^2}\right]\nabla^2\Phi+\rho\left(\frac{\partial Y}{\partial y}+\frac{\partial Z}{\partial z}\right)=0 \tag{18}$$

where

$$\nabla^2=\frac{\partial^2}{\partial z^2}+\frac{\partial^2}{\partial y^2}.$$

It can be noted from equation (16) that the equation governing Ψ is independent of the equations satisfied by Θ and Φ.

In this paper we seek homogeneous solutions for Φ, Θ, and Ψ in the absence of body forces, i.e.,

$$X=Y=Z=0.$$

In particular, we assume potentials of the following form, representing propagating waves in the plane of x, y.

$$\Theta=g_1(z)e^{i(kx+\xi y-\omega t)} \tag{19}$$

$$\Phi=g_2(z)e^{i(kx+\xi y-\omega t)} \tag{20}$$

$$\Psi=g_3(z)e^{i(kx+\xi y-\omega t)} \tag{21}$$

By substitution these assumed potentials into equations (16), (17), and (18), we get a second-order ordinary differential equation in $g_3(z)$ and a second-order system of differential equations in $g_1(z)$ and $g_2(z)$. It can be shown that the solutions have the following forms:

$$g_1(z)=F_1\Omega_1^+ + G_1\Omega_2^+ \tag{22}$$

$$g_2(z)=F_2\Omega_1^+ + G_2\Omega_2^+ \tag{23}$$

$$g_3(z)=F_3\Omega_3^-. \tag{24}$$

Here,

$$\Omega_1^+=A_{11}e^{is_1 z}+A_{12}e^{is_1(H-z)} \tag{25}$$

$$\Omega_2^+=A_{21}e^{is_2 z}+A_{22}e^{is_2(H-z)} \tag{26}$$

$$\Omega_3^-=A_{31}e^{irz}-A_{32}e^{ir(H-z)}. \tag{27}$$

Using equations (19)-(21) and the expressions for $g_1(z)$, $g_2(z)$, and $g_3(z)$ in equations (16)-(18), we get

$$r=\sqrt{\frac{k_2^2-k^2-\epsilon\xi^2}{\epsilon}} \tag{28}$$

Downloaded 03 May 2010 to 171.66.16.244. Redistribution subject to ASME license or copyright; see http://www.asme.org/terms/Terms_Use.cfm

$$s_{1,2}^2 = \frac{-[\gamma k^2 - k_2^2(1+\beta)]}{2\beta}$$

$$\pm \frac{\sqrt{[\gamma k^2 - k_2^2(1+\beta)]^2 - 4\beta(k^2 - k_2^2)\,(\alpha k^2 - k_2^2)}}{2\beta} - \xi^2, \quad (29)$$

where the nondimensional material constants have been defined as

$$\alpha = \frac{c_{11}}{c_{55}}, \quad \beta = \frac{c_{22}}{c_{55}}, \quad \delta = 1 + \frac{c_{12}}{c_{55}}$$

$$\epsilon = \frac{c_{44}}{c_{55}}, \quad \gamma = 1 + \alpha\beta - \delta^2.$$

Also, we have defined

$$k_2^2 = \frac{\rho\omega^2}{c_{55}}.$$

The constants appearing in equations (22)-(24) may be taken as

$$F_1 = G_1 = F_3 = 1 \quad (30)$$

$$F_2 = \frac{k_2^2 - \alpha k^2 - \xi^2 - s_1^2}{\delta(\xi^2 + s_1^2)} \quad (31)$$

$$G_2 = \frac{k_2^2 - \alpha k^2 - \xi^2 - s_2^2}{\delta(\xi^2 + s_2^2)}. \quad (32)$$

Using (19)-(24) in (13)-(15), and turn in (4)-(9), the displacement and traction components can be written in matrix form as follows:

$$\{\mathbf{u}\}_m = [E]_m [D]_m \{\mathbf{v}\}_m. \quad (33)$$

Here, m is the layer identifier (1 or ∞),

$$\{\mathbf{u}\}_m = [u, w, v, \sigma_{yz}, \sigma zz, \sigma_{xz}]_m^T \quad (34)$$

$$\{\mathbf{v}\}_m = [A_{11}, A_{21}, A_{31}, A_{12}, A_{22}, A_{32}]_m^T, \quad (35)$$

and $[D]_m$ is a (6×6) diagonal matrix

$$\text{diag}[D]_m = [e^{is_1 z}, e^{is_2 z}, e^{irz}, e^{is_1(H-z)}, e^{is_2(H-z)}, e^{ir(H-z)}]_m, \quad (36)$$

and

$$[E]_m = \begin{bmatrix} ikF_1 & ikG_1 & 0 \\ is_1F_2 & is_2G_2 & -i\xi F_3 \\ i\xi F_2 & i\xi G_2 & irF_3 \\ -2\xi s_1 \epsilon c_{55} F_2 & -2\xi s_2 \epsilon c_{55} G_2 & (\xi^2 - r^2)\epsilon c_{55} F_3 \\ c_{55}\Gamma_1 & c_{55}\Gamma_2 & 2\xi r \epsilon c_{55} F_3 \\ -ks_1 c_{55}(F_1 + F_2) & -ks_2 c_{55}(G_1 + G_2) & k\xi c_{55} F_3 \end{bmatrix}$$

$$\begin{bmatrix} ikF_1 & ikG_1 & 0 \\ -is_1F_2 & -is_2G_2 & i\xi F_3 \\ i\xi F_2 & i\xi G_2 & irF_3 \\ 2\xi s_1 \epsilon c_{55} F_2 & 2\xi s_2 \epsilon c_{55} G_2 & -(\xi^2 - r^2)\epsilon c_{55} F_3 \\ c_{55}\Gamma_1 & c_{55}\Gamma_2 & 2\xi r \epsilon c_{55} F_3 \\ ks_1 c_{55}(F_1 + F_2) & ks_2 c_{55}(G_1 + G_2) & -k\xi c_{55} F_3 \end{bmatrix}_m \quad (37)$$

Γ_1 and Γ_2 are given by

$$\Gamma_1 = (1-\delta)k^2 F_1 + [(2\epsilon - \beta)\xi^2 - \beta s_1^2] F_2 \quad (38)$$

$$\Gamma_2 = (1-\delta)k^2 G_1 + [(2\epsilon - \beta)\xi^2 - \beta s_2^2] G_2. \quad (39)$$

The vectors, $\{\mathbf{u}\}_m$, $\{\mathbf{v}\}_m$, and matrices, $[E]_m$, $[D]_m$, in equation (33) are partitioned to improve the efficiency and accuracy of the numerical computations. We write

$$\{\mathbf{u}\}_m = \begin{Bmatrix} \mathbf{u}_D \\ \cdots \\ \mathbf{u}_S \end{Bmatrix}_m \qquad \{\mathbf{v}\}_m = \begin{Bmatrix} \mathbf{v}^- \\ \cdots \\ \mathbf{v}^+ \end{Bmatrix}_m \quad (40)$$

$$[E]_m = \begin{bmatrix} Q_{11}^m & \vdots & Q_{12}^m \\ \cdots & \cdots & \cdots \\ Q_{21}^m & \vdots & Q_{22}^m \end{bmatrix},$$

$$[D]_m = \begin{bmatrix} (D_{11}^m)_z & \vdots & 0 \\ \cdots & \cdots & \cdots \\ 0 & \vdots & (D_{22}^m)_z \end{bmatrix} \quad (41)$$

where the subscript z stands for the level at which the $[D]$ matrices are evaluated, and the subscripts D and S denote displacements and tractions, respectively.

Using the solution given by equation (33) and applying the appropriate boundary conditions of continuity of tractions and displacements at the interface between the layer and the half space, the traction-free boundary condition at the upper surface, and the radiation condition as $z \to \infty$, one arrives at the following dispersion equation:

$$\det[B - AC^{-1}D] = 0 \quad (42)$$

where

$$[A] = Q_{11}^{\infty}(D_{11}^{\infty})_0 \quad (43)$$

$$[B] = Q_{11}^1(D_{11}^1)_H \{Q_{21}^1(D_{11}^1)_0\}^{-1} Q_{22}^1(D_{22}^1)_0 - Q_{12}^1(D_{22}^1)_H \quad (44)$$

$$[C] = Q_{21}^{\infty}(D_{11}^{\infty})_0 \quad (45)$$

$$[D] = Q_{21}^1(D_{11}^1)_H \{Q_{21}^1(D_{11}^1)_0\}^{-1} Q_{22}^1(D_{22}^1)_0 - Q_{22}^1(D_{22}^1)_H. \quad (46)$$

Given the properties of the materials, equation (42) can be solved to obtain the dispersion curves showing the dependence of the phase velocity on frequency. This is discussed in the following section.

3 Numerical Results and Discussion

In this paper, two cases are studied: a beta-quartz transversely isotropic substrate coated with a gold layer and an

Downloaded 03 May 2010 to 171.66.16.244. Redistribution subject to ASME license or copyright; see http://www.asme.org/terms/Terms_Use.cfm

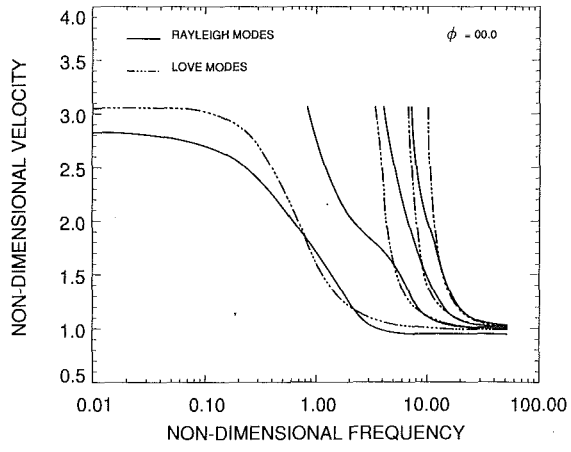


Fig. 2(a)

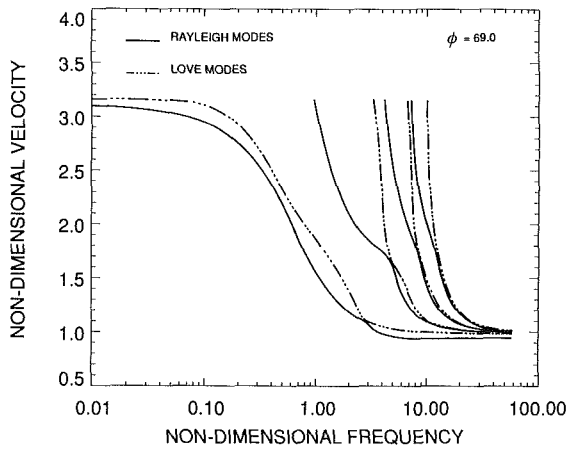


Fig. 2(b)

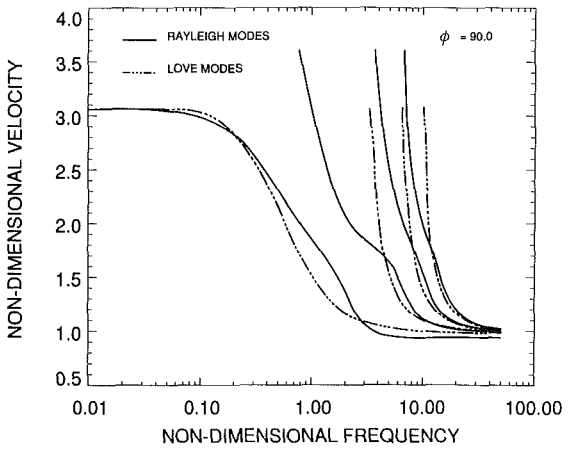


Fig. 2(c)

Fig. 2 Phase velocity dispersion of the eight first modes of gold on beta-quartz; (a) direction of propagation along the symmetry axis, (b) direction of propagation rotated 69 deg from the symmetry axis, and (c) direction of propagation normal to the symmetry axis

aluminum cladded graphite-epoxy where the material properties are listed in Table 1.

For a gold layer on the beta-quartz, three angles of propagation are considered. The corresponding Love and Rayleigh-mode dispersion curves are plotted in Figs. 2(*a*)–2(*c*). The nondimensional velocity is (c/β^1), and KH (c/β^1) is the nondimensional frequency where $K^2 = k^2 + \xi^2$ is the wave number along the X-direction in the plane of propagation. The superscript on the shear velocity is the layer identifier. For gold $\beta^1 = 1.2045$ km/s, Fig. 2(*a*) shows the dispersion curves

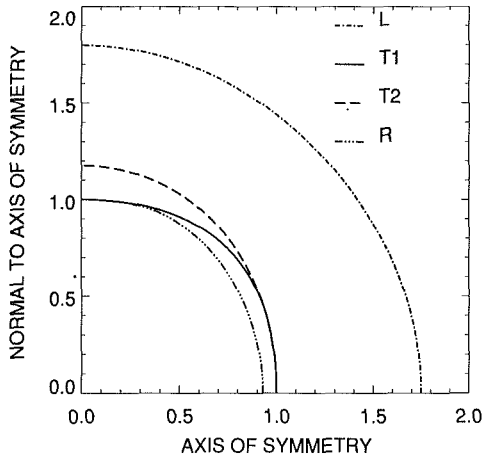


Fig. 3 Wave velocities in beta-quartz half space. The quasi-longitudinal quasi-transverse, true transverse, and Rayleigh waves are labeled, L, T_2, T_1, and R, respectively.

Table 1 Material properties (all the stiffnesses are in the units 10^9 N/m^2)

Material	ρ(g/cm^3)	c_{11}	c_{22}	c_{12}	c_{44}	c_{55}
Gold	19.3	203.0	203.0	147.0	28.0	28.0
Beta-quartz	2.65	110.4	116.6	32.8	49.95	36.1
Aluminum	2.7	109.0	109.0	56.0	26.5	26.5
Graphite-epoxy	1.7	160.7	13.92	6.44	3.5	7.07

for the first eight modes when the direction of propagation is along the symmetry axis ($\phi = 0$ deg). The Love modes start at the horizontally-polarized shear wave velocity of the substrate ($\beta_{55}^{\infty} = 3.6909$ km/s) and approach asymptotically the shear velocity of the layer β^1 as $KH \to \infty$. The two subscripts on the shear velocity are the subscripts of the stiffness constant that relates the direction of propagation to the direction of polarization.

The first Rayleigh mode starts at the velocity of the Rayleigh wave of the substrate in the direction of symmetry, $c_R^{\infty} = 3.4320$ km/s as $KH \to 0$ and approaches the free-surface Rayleigh wave velocity of the layer $c_R^1 = 1.1374$ km/s. The higher Rayleigh-modes start at the vertically-polarized shear wave velocity of the substrate, β_{55}^{∞}, and approach the shear velocity of the layer β^1 for high wave numbers. Figure 3 shows a polar plot of the nondimensional velocities for the beta-quartz. These velocities are nondimensionalized with respect to β_{55}^{∞}.

In Fig. 2(*c*) the dispersion curves for a direction of propagation normal to the symmetry axis ($\phi = 90$ deg) are shown. In this case and the previous one (Fig. 2(*a*)), the Love modes and the Rayleigh modes separate, which is a very useful check for our three-dimensional formulation. The Love modes start at the horizontally-polarized shear wave velocity, β_{55}^{∞}, of the substrate and approach the shear wave velocity, β^1, of the layer. The first Rayleigh mode starts at the velocity of the Rayleigh wave of the substrate in the direction perpendicular to the symmetry axis, which is determined to be equal to β_{55}^{∞} from Fig. 3. As $KH \to \infty$, it approaches c_R^1 of gold. The higher modes start at the vertically-polarized shear wave velocity ($\beta_{44}^{\infty} = 4.3415$ km/s) and as $KH \to \infty$, they approach β^1 asymptotically.

The dispersion curves for a 69 deg angle of propagation are shown in Fig. 2(*b*). This specific angle was chosen, because the free-surface Rayleigh wave velocity of the beta-quartz is maximum. The fundamental mode tends to the surface wave velocity in the half space, $c_R^{\infty} = 3.7440$ km/s, at low frequency and approaches c_R^1 at high frequency. The higher modes start at the lowest quasi-transverse velocity in the half space, $\beta^{T_1} = 3.7804$ km/s. It is noticeable that the modes do not cross

Downloaded 03 May 2010 to 171.66.16.244. Redistribution subject to ASME license or copyright; see http://www.asme.org/terms/Terms_Use.cfm

each other as in the previous cases, but they pinch as observed by Crampin and Taylor (1971).

For the aluminum cladded graphite-epoxy half space, results for five different directions of propagation are shown in Figs. 4(*a*)–4(*e*). For this combination of material properties, the layer is found to stiffen the substrate as mentioned by Farnell and Adler (1972), when they discussed the isotropic case. The common thing about these dispersion curves is that there is only one Rayleigh-like mode that propagates in a very limited range of KH. They all start at the free-surface Rayleigh velocity and end at the lowest shear velocity of the substrate, which happens to be the quasi-transverse wave velocity for the graphite-epoxy shown in Fig. 5. The slopes of the dispersion curves are negative for ($\phi = 0$ deg) as $KH \to 0$ and increase to become positive as the direction of propagation makes larger angles with the symmetry axis. It is also observed that the phase velocity becomes nearly independent of frequency for a small range of frequency as ϕ increases to 90 deg.

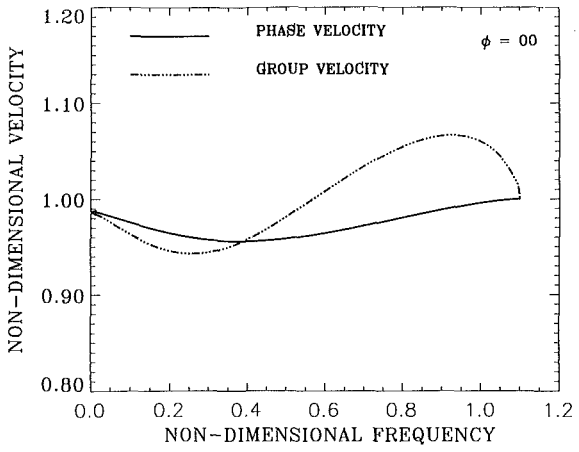


Fig. 4(*a*)

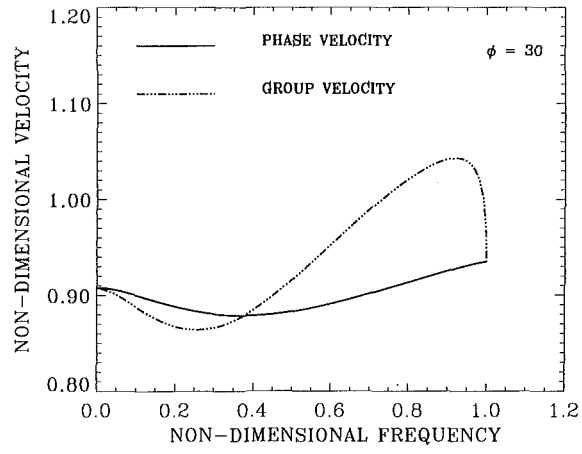


Fig. 4(*b*)

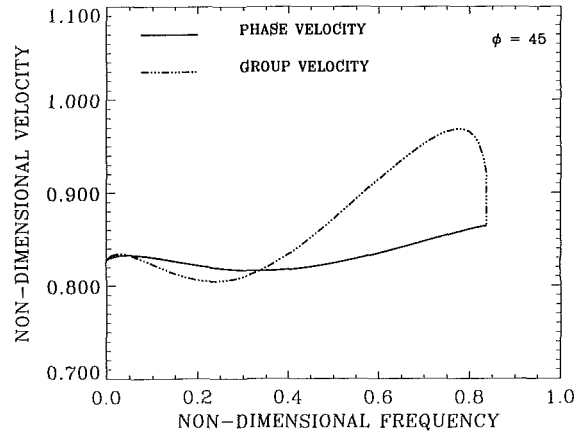


Fig. 4(*c*)

4 Conclusion

The effect of anisotropy of the substrate on the surface wave propagation in the isotropic layer has been studied in this paper. Two cases are considered: one relevant for electronic applications and the other for aerospace structures. It is shown that the relative material property differences in the two cases give rise to quite different behaviors of the surface waves. Implications of these differences to the scattering by defects (interface or surface cracks) will be reported in a subsequent paper. It may be noted also that the dispersion characteristics presented in this paper could be used to characterize thin films or coating by ultrasonic means. This will be explored in a future communication.

5 Acknowledgment

The work reported here was supported in part by grants from the Office of Naval Research (#N00014-86-K-0280), from the National Science Foundation (MSM-8609813, INT-8521422, and INT-8610487), and NASA (NAGW-1388).

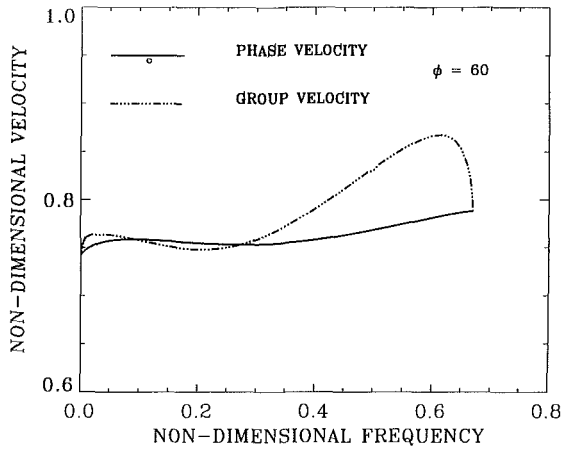


Fig. 4(*d*)

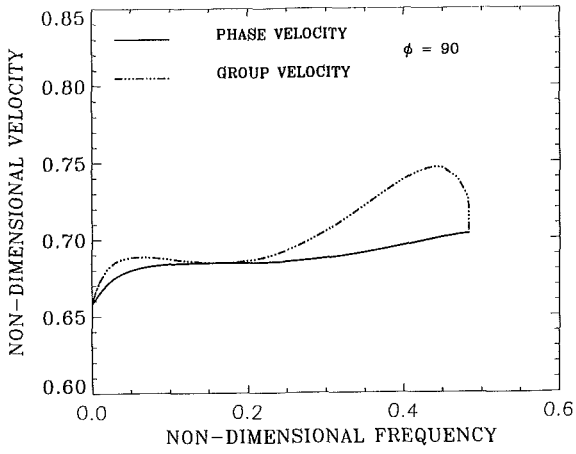


Fig. 4(*e*)

Fig. 4 Phase and group velocities for a layer of aluminum on graphite-epoxy; (*a*) direction of propagation along the fiber axis, direction of propagation rotated 30 deg from the fiber axis, (c) direction of propagation rotated 45 deg from the fiber axis, (*d*) direction of propagation rotated 60 deg from the fiber axis, and (*e*) direction of propagation normal to fiber axis

Downloaded 03 May 2010 to 171.66.16.244. Redistribution subject to ASME license or copyright; see http://www.asme.org/terms/Terms_Use.cfm

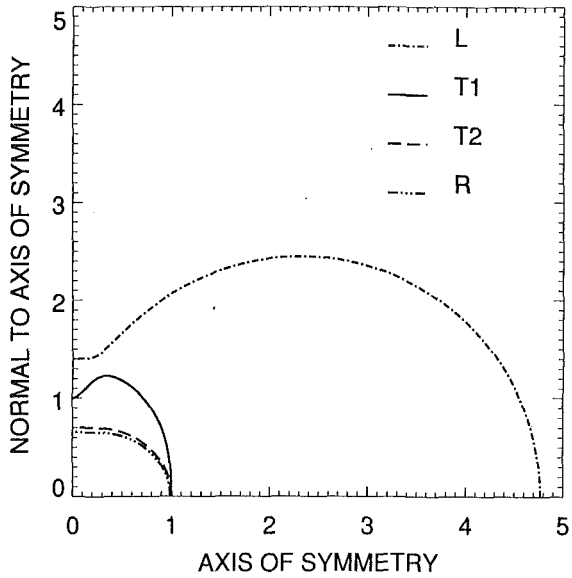


Fig. 5 Wave velocities in graphite epoxy space. The quasi-longitudinal quasi-transverse, true transverse, and Rayleigh waves are labeled, L, T_2, T_1, and R, respectively

The work was initiated when the second author visited the University College, Galway, Ireland where he had fruitful discussions with Dr. P. M. O'Leary. The first author is grateful to the Tunisian government for granting a scholarship for his graduate studies.

References

Buchwald, V. T., 1961, "Rayleigh Waves in Transversely Isotropic Media," *Quart. J. Mech, and Applied Math.*, Vol. 14, Pt. 3, pp. 35–127.

Chimenti, D. E., Nayfeh, A. H., and Butler, D. L., 1982, "Leaky Rayleigh Waves on a Layered Halfspace," *J. Appl. Phys.*, Vol. 53, pp. 170–176.

Crampin, S., 1970, "The Dispersion of Surface Waves in Multilayered Anisotropic Media," *Geophys. J. R. Astr. Soc.*, Vol. 21, pp. 387–402.

Crampin, S., and Taylor, B. D., 1971, "The Propagation of Surface Waves in Anisotropic Media," *Geophys. J. R. Astr. Soc.*, Vol. 25, pp. 71–87.

Ewing, W. M., Jardetszky, W. S., and Press, F., 1957, *Elastic Waves in Layered Media*, McGraw Hill, New York.

Farnell, G. W., and Adler, E. L., 1972, "Elastic Wave Propagation in Thin Layers," *Physical Acoustics*, Vol. 9, Academic Press, New York, pp. 35–127.

Haskell, N. A., 1953, "The Dispersion of Surface Waves in Multilayered Media," *Bull. Seism. Soc. Amer.*, Vol. 43, pp. 17–34.

Jeffreys, H.,.1935, "The Surface Waves of Earthquakes," *Monthly Notices Roy., Astron. Soc., Geophys. Suppl.*, Vol. 3, pp. 253–261.

Kanai, K., 1951, "On the Group Velocity of Dispersive Surface Waves," *Bull. Earthquake Research Inst.*, Tokyo, Vol. 29, pp. 49–60.

Kundu, T., and Mal, A. K., 1986, "Acoustic Material Signature of a Layered Plate," *Int. J. Eng. Sci.*, Vol. 24, pp. 1819–1829.

Love, A. E. H., *1911*, *1926*, *Some Problems of Geodynamics*, Cambridge University Press, London.

Mal, A. K., 1988, "Guided Waves in Layered Solids with Interfaces Zones," *Int. J. Eng. Sci.*, Vol. 26, pp. 257–266.

Nayfeh, A. H., Chimenti, D. E., Adler L., and Crane, R. L., 1981, "Ultrasonic Leaky Waves in the Presence of a Thin Layer," *J. Appl. Phys.*, Vol. 52, pp. 4985–4994.

Nayfeh, A. H., and Taylor, T. W., 1988, "Surface Wave Characteristics of Fluid-loaded Multilayered Media," *J. Acoust. Soc. Am.*, Vol. 84, pp. 2187–2191.

Newlands, M., 1952, "The Disturbance Due to a Line Source in a Semi-infinite Elastic Medium with a Single Surface Layer," *Phil. Trans. Roy. Soc.*, London, Vol. 245A, pp. 213–308.

Pelka, E. J., 1986, "Space Station Assembly: Techniques and Structures," *Lockheed Horizons*, pp. 33–49.

Stoneley, R., *1926*, "The Effect of the Ocean on Rayleigh Waves," *Monthly Notices Roy. Astron. Soc., Geophys. Suppl.*, Vol. 1, pp. 349–356.

Thomson, W. T., 1950, "Transmission of Elastic Waves through a Stratified Solid Medium," *J. Appl Phys.*, Vol. 21, pp. 89–93.

Tolstoy, I., and Usdin, E., 1953, "Dispersive Properties of Stratified Elastic and Liquid Media: A Ray Theory," *Geophysics*, Vol. 18, pp. 844–870.

Xu, P.-C., and Mal, A. K., 1987, "Calculation of the Inplane Green's Functions for a Layered Viscoelastic Solid," *Bull. Seism. Soc. Am.*, Vol. 77, pp. 1823–1837.

Downloaded 03 May 2010 to 171.66.16.244. Redistribution subject to ASME license or copyright; see http://www.asme.org/terms/Terms_Use.cfm

G. Krishnasamy
Graduate Student.

L. W. Schmerr
Professor.
Assoc. Mem. ASME

T. J. Rudolphi
Associate Professor.

F. J. Rizzo[1]
Professor and Chairman,
Mem. ASME

Department of Engineering Science and Mechanics,
Iowa State University,
Ames, IA 50011

Hypersingular Boundary Integral Equations: Some Applications in Acoustic and Elastic Wave Scattering

The properties of hypersingular integrals, which arise when the gradient of conventional boundary integrals is taken, are discussed. Interpretation in terms of Hadamard finite-part integrals, even for integrals in three dimensions, is given, and this concept is compared with the Cauchy Principal Value, which, by itself, is insufficient to render meaning to the hypersingular integrals. It is shown that the finite-part integrals may be avoided, if desired, by conversion to regular line and surface integrals through a novel use of Stokes' theorem. Motivation for this work is given in the context of scattering of time-harmonic waves by cracks. Static crack analysis of linear elastic fracture mechanics is included as an important special case in the zero-frequency limit. A numerical example is given for the problem of acoustic scattering by a rigid screen in three spatial dimensions.

1 Introduction

The Boundary Integral Equation (BIE) formulation for many problems in mechanics and the Boundary Element Method (BEM) of solution of the integral equations enjoy a measure of confidence and applicability today, counter to the predictions and expectations of many early observers, including several of the present authors. This early skepticism was not without foundation, considering the challenges to computing posed by at least the weak singularities, not to mention the stronger ones of the Cauchy Principal Value (CPV) type, which appear in many (vector) problems with the BIE/BEM. However, easy processes of regularization, singularity removal before computation, and/or analytical computation of singular integrals, together with careful use of good algorithms for numerical computation, have made the BIE/BEM an efficient and generally well-conditioned numerical solution procedure.

Despite this measure of success, researchers have had less confidence in computing with equations obtained by taking the gradient or normal derivative of the conventional (singular) BIE's. Such equations, which involve derivatives of an already singular kernel, lead to so-called hypersingular equations and arise, for example, in the study of cracks in an elastic solid and scattering of acoustic and electromagnetic waves by arbitrarily thin screens. Here regularization procedures are far from straightforward, and singularity removal is problematic, especially when one encounters integrals the very existence of which appears to (often) be in question.

In this paper we consider the occurrence of certain hypersingular integral equations in the context of acoustic wave scattering by thin screens and elastic wave scattering by cracks. Both problems are in the frequency domain. The static problems of linear elastic fracture mechanics are included in the elastic crack category in the zero-frequency limit. Our treatment of the hypersingular equations themselves is applicable, however, to such equations in whatever context they might arise. Indeed, although they are not needed in some applications where regular BIE's suffice, there is indication that hypersingular equations, if we could compute with them, might be more convenient and lead to systems of algebraic equations with better numerical properties. In any case, the following discussion should be applicable to any situation where the gradient or normal derivative of an ordinary (singular) BIE is indicated.

Specifically, all hypersingular integrals in what follows arise from taking the gradient of a representation integral for an acoustic or elastic field in the vicinity of a crack and moving the source point to the boundary (crack itself) through careful limiting processes. Two such limiting processes are discussed. In the first, called "Conversion," two terms in a Taylor series expansion of the density function in the integrals are subtracted and added back before any limit is taken. The added-back terms, the only ones more than weakly singular now, are

[1] Presently Professor and Head of the Department of Theoretical and Applied Mechanics, University of Illinois, Urbana, IL 61801.

Contributed by the Applied Mechanics Division of THE AMERICAN SOCIETY OF MECHANICAL ENGINEERS for presentation at the Winter Annual Meeting, Dallas, Texas, November 25-30, 1990.

Discussion on this paper should be addressed to the Technical Editor, Leon M. Keer, The Technological Institute, Northwestern University, Evanston, IL 60208, and will be accepted until two months after final publication of the paper itself in the JOURNAL OF APPLIED MECHANICS. Manuscript received by the ASME Applied Mechanics Division, March 1, 1989; final revision, May 31, 1989.

Paper No. 90-WA/APM-7.

Copyright © 1990 by ASME
Downloaded 03 May 2010 to 171.66.16.244. Redistribution subject to ASME license or copyright; see http://www.asme.org/terms/Terms_Use.cfm

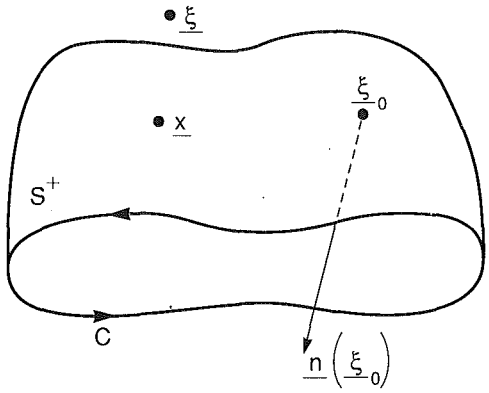


Fig. 1 An arbitrarily shaped scatterer

converted to regular line integrals around the crack edge and less severely singular integrals on the crack surface using Stokes' theorem. In the second process, called "Finite Parts," it is shown that the finite part of a divergent surface integral may be defined in the sense of Hadamard. This finite part is then shown to lead to exactly the same formula involving line and surface integrals as before. Throughout, the difference is noted between truly divergent integrals and those which have a hypersingular kernel but nevertheless are well-defined, albeit in a special sense, and are computable. The smoothness requirements on the density function as demanded by the two methods are discussed. The validity of the two methods is demonstrated by solving a three-dimensional acoustic wave scattering problem and comparing the results with theory.

2 Acoustic Wave Scattering: Context for a Hypersingular Integral

Let ϕ be the (complex) potential for the time-harmonic acoustic field existing in the unbounded region exterior to a scattering obstacle, S, of finite size. Here we regard S as a plate or screen with vanishingly small thickness and not necessarily planar in form. The subsequent designations "+" and "−" correspond to the two sides of S. Points $\mathbf{x}$ and ξ_o are on S^+ or S^-, points ξ are elsewhere, and $k=\omega/c$ is the wave number with ω the circular frequency and c the wave speed. We are interested in problems where an incident field ϕ^i impinges upon S and we seek the scattered field ϕ^s (where $\phi \equiv \phi^i + \phi^s$) exterior to and possibly on (the two sides of) S. The scatterer S is characterized by a suitable prescription of the normal gradient $\partial\phi/\partial n$ on each side of S, e.g., if S is rigid, $\partial\phi/\partial n = 0$ on each side of S (see Fig. 1).

The starting point for our treatment of such problems is the representation integral

$$\phi^s(\xi) = \int_{S^+} \left[G^D(\mathbf{x},\xi)\left(\frac{\partial\phi^+(\mathbf{x})}{\partial n^+} + \frac{\partial\phi^-(\mathbf{x})}{\partial n^-}\right) - (\phi^+(\mathbf{x}) - \phi^-(\mathbf{x}))\frac{\partial G^D(\mathbf{x},\xi)}{\partial n(\mathbf{x})}\right] dS(\mathbf{x}) \tag{1}$$

which arises from a careful application of Green's theorem to ϕ^s and G^D, wherein $G^D(\mathbf{x},\xi) = e^{ikR}/4\pi R$ is the free-space Green's function, $R \equiv |\mathbf{x}-\xi|$ (dependence of all variables on k is understood but suppressed (et. seq.)) and appropriate behavior of ϕ^s and its derivatives at infinity is assumed. Positive directions of the normal to S^+ point away from the acoustic material as shown in Fig. 1 with a specific positive normal shown at a point ξ_o on S^+. Having specified $(\partial\phi^+/\partial n^+ + \partial\phi^-/\partial n^-)$ on S, $\phi^s(\xi)$ is given by equation (1) once the surface potential discontinuity $u \equiv \phi^+ - \phi^-$ is known on S, since G^D and its normal derivative (with respect to n^+ at $\mathbf{x}$ et. seq.) are as given. Thus it remains to determine $u(\mathbf{x})$.

It is sufficient for our purposes here to limit the discussion to rigid scatterers such that the first integral in equation (1) containing known boundary data vanishes. Then the limiting procedure where $\xi \to \xi_o$ leads to the familiar BIE, the kernels of which are at most weakly singular (Appendix B). This action is, by itself, ineffective to determine $u(\mathbf{x})$, since the resulting BIE contains the two unknowns $u(\mathbf{x})$ and ϕ^+. However, if the gradient in the component direction $\xi_r (r=1,2,3)$ at ξ of $\phi^s(\xi)$ is taken, i.e.,

$$\frac{\partial\phi^s(\xi)}{\partial\xi_r} = -\frac{\partial}{\partial\xi_r}\int_{S^+} \frac{\partial G^D(\mathbf{x},\xi)}{\partial n(\mathbf{x})} u(\mathbf{x})\, dS(\mathbf{x}) \tag{2}$$

and the point ξ moved to a point ξ_o on S, then there is sufficient information in the inner product of equation (2) with the normal $n(\xi_o)$ (i.e., $(\partial/\partial\xi_r)n_r(\xi_o) \equiv \partial/\partial n_o$; (the summation convention on repeated subscripts, et. seq.) $\partial\phi^s/\partial n_o = -\partial\phi^i/\partial n_o$) to solve for the single unknown $u(\mathbf{x})$ provided, of course, that suitable meaning can be attached to the right side of equation (2). Note, if the ξ_r derivative is taken under the integral sign, the integral becomes hypersingular (Kutt, 1975); Filippi, 1977; Ioakimidis, 1982; Kaya and Erdogan, 1987; Nishimura and Kobayashi, 1988) in the limit as $\xi \to \xi_o$. Interpretations of such an integral as an ordinary improper one or as a CPV fail (Appendix B). The important issue now, and this is the central issue in this paper, is meaningful analytical treatment and effective numerical computation of the right side of equation (2) and its vector counterparts for elastic wave analysis. Static problems in the zero-frequency limit form an important special case.

3 Analytical Options

Consider the expression[1]

$$\frac{\partial\phi^s(\xi_o)}{\partial\xi_r} = -\lim_{\xi\to\xi_o}\int_S \frac{\partial^2 G^D(\mathbf{x},\xi)}{\partial\xi_r\partial n(\mathbf{x})} u(\mathbf{x})\, dS \overset{?}{=} -\int_S \frac{\partial^2 G^D(\mathbf{x},\xi_o)}{\partial\xi_r\partial n(\mathbf{x})} u(x)\, dS \tag{3}$$

and note that there is little conceptual difficulty with the first integral since ξ is not on S and thus there is no difficulty with the first equality, assuming that the (proper) integral may be evaluated, transformed, or regularized (somehow) to yield a function of ξ which would *then* be well behaved in the indicated limit. However, the second equality is invalid since, as already observed, the singularity in the kernel is $(1/R^3)$ and the second integral diverges if interpreted as an ordinary improper integral or as a CPV. Thus it appears that the "*limit of the integral*" $\neq$ "*integral of the limit*" in expression (3).

Strategies to deal with this state of affairs have amounted to the following. Perform an integration by parts on the first of the integrals of equation (3), wherein the ξ_r derivative of $\partial G^D/\partial n$ is, in effect, transferred to a tangential derivative of $u(x)$. This "regularization" process (Maue, 1949; Burton Miller, 1971; Bui, 1977; Weaver, 1977; Terai, 1980; Sladek et al., 1986) lowers the integrand singularity to at most $(1/R^2)$ so that the integral of the limit exists, but this is at the expense of the unknown being the tangential derivative of $u(\mathbf{x})$ over S rather than $u(\mathbf{x})$ itself. This quantity is unbounded at the scatterer edges (cracks) and the regularization process is complicated, and may not be possible, for all vector problems. Computations (Polch and Cruse, 1987; Cruse, 1988) based on such a strategy are reported to be delicate at best.

Another strategy centers around first making simplifying assumptions in the vicinity of the singularity regarding the geometry (e.g., a flat boundary element) and/or regarding the

[1] In the sequel, $dS \equiv dS(x)$ and $S \equiv S^+$ only are understood.

Downloaded 03 May 2010 to 171.66.16.244. Redistribution subject to ASME license or copyright; see http://www.asme.org/terms/Terms_Use.cfm

variation of $u(\mathbf{x})$ in that vicinity (element). Then the first of the integrations of equation (3) can be performed, in simple cases (Kitahara, 1986), to yield an approximate analytical algebraic function of ξ. This can be subsequently differentiated with respect to ξ_r and the limit as $\xi \to \xi_o$ taken to yield a meaningful result. A variant of this strategy (Takakuda et al. (1985), Lin and Keer (1987), Budreck and Achenbach (1988)), again based on *a priori* simplifying discretization assumptions, is to transform the first of the integrals of equation (3) to a line integral around the edge of a (flat) element, over which $u(x)$ is assumed constant, and then take the limit $\xi \to \xi_o$ without difficulty.

In this paper we offer two analytical options in interpreting expression (3). The first, which we call "Conversion," is in the spirit of "do the integrations and/or convert to line integrals before taking the limit $\xi \to \xi_o$" as described above. However, here we convert our integrals in general fashion with methods independent of any simplifying (discretization) assumptions. The second, which we term "Finite Parts," is in the spirit of a special interpretation of the second integral in equation (3), much as the CPV is a special interpretation of an otherwise divergent integral. Our interpretation involves the definition of the finite part of a divergent integral as originally introduced by Hadamard (1923) for integrals of a single variable. It is shown (Appendix C), we believe for the first time, that the limit of the first integral in equation (3) is equal to the Hadamard Finite Part (HFP) of the second integral in equation (3). This is done for integrals over arbitrarily shaped S. It is done also for a one-dimensional version of the present integrals in Martin and Rizzo (1989). Finite part integrals are also identified by Takakuda (1985) and Lin and Keer (1987) for integrals over crack surface in a three-dimensional medium but only under the special simplifying assumptions mentioned above.

We also show how the HFP is a generalization of the CPV and explicitly show, if there ever was any doubt, why the CPV is inadequate to render meaning to the second of the integrals of equation (3). Finally, we show in this section that an effective formula for computation of hypersingular integrals arising out of the BIE method is available and is the same whether the "Conversion" process or the "Finite Part" interpretation is explicitly used.

Before proceeding with either approach, we subtract and add back the fundamental solution $G(\mathbf{x},\xi) \equiv 1/4\pi \mathrm{R}$ for the zero-frequency (static) case to formula (2) such that

$$\frac{\partial \phi^s(\xi)}{\partial \xi_r} = -\int_S \left[\frac{\partial^2 G^D(\mathbf{x},\xi)}{\partial \xi_r \partial n(\mathbf{x})} - \frac{\partial^2 G(\mathbf{x},\xi)}{\partial \xi_r \partial n(\mathbf{x})}\right] u(\mathbf{x}) dS - \int_S \frac{\partial^2 G(\mathbf{x},\xi)}{\partial \xi_r \partial n(\mathbf{x})} u(\mathbf{x}) dS. \quad (4)$$

Now as $\xi \to \xi_o$, the first integral is weakly singular in the limit while the second is hypersingular. The advantage of dealing with equation (4) as compared with equations (2) or (3) is that we are dealing with a hypersingular integral whose kernel is real and less complicated. This advantage is more pronounced in vector problems.

The remainder of this section of the paper is concerned with treatment of the last (hypersingular) integral in equation (4).

3.1 Conversion. Consider the key term of equation (4) which we designate

$$I_r(\xi) \equiv -\int_S \frac{\partial^2 G(\mathbf{x},\xi)}{\partial \xi_r \partial n(\mathbf{x})} u(\mathbf{x}) dS(\mathbf{x}). \quad (5)$$

The practice of subtracting and adding the first term of a Taylor series expansion of a density function in a singular integral, such as occurs in a conventional BIE, is an old one (Muskhelishvili, 1953; Cruse and Van Buren, 1971) to more effectively isolate and study the properties of the CPV. An extension of that basic idea, using two terms of the series expansion, is effective for the integral of equation (5) and, except for Brandão (1986) and Kaya and Erdogan (1987) who used it on a one-dimensional hypersingular integral, it is an idea apparently not heretofore explored. Expanding u about ξ_o we have

$$I_r(\xi) = -\int_S \frac{\partial^2 G(\mathbf{x},\xi)}{\partial \xi_r \partial n(\mathbf{x})} [u(\mathbf{x}) - u(\xi_o) - u_{,p}(\xi_o)(x_p - \xi_{op})] dS - u(\xi_o) \int_S \frac{\partial^2 G(\mathbf{x},\xi)}{\partial \xi_r \partial n(\mathbf{x})} dS - u_{,p}(\xi_o) \int_S \frac{\partial^2 G(\mathbf{x},\xi)}{\partial \xi_r \partial n(\mathbf{x})} (x_p - \xi_{op}) dS \quad (6)$$

such that if ξ_o is not on the edge of S and $u(\mathbf{x}) \in C^{1,\alpha}$ at ξ_o, i.e., $|u(\mathbf{x}) - u(\xi_o) - u_{,k}(\xi_o)(x_k - \xi_{ok})| \le B|\mathbf{x} - \xi_o|^{\alpha+1}$, $0 < \alpha \le 1$, $|B| < \infty$, then in the limit as $\xi \to \xi_o$ the first surface integral in equation (6) is at most weakly singular. The second integral has, of course, the same hypersingular character as the original one in equation (5) but with unit density, whereas the third integral, also with unit density, is $0(1/R^2)$ and is a CPV in the limit.

Now if $F_{pq} \ldots ,_i$ signifies the first derivative with respect to x_i of a function $F_{pq} \ldots$ on S (invoking the comma notation for derivatives, et. seq.), Stokes' integral theorem in the form

$$\int_S (F_{pq} \ldots ,_i n_j - F_{pq} \ldots ,_j n_i) dS = \epsilon_{kji} \oint_c F_{pq} \ldots dx_k, \quad (7)$$

(ϵ_{kji} is the alternating symbol) may be used to convert the last two integrals in equation (6) to line integrals, another surface integral, and a solid angle. The details of this conversion are found in Appendix A, and the result is

$$I_r(\xi) = -\int_S \frac{\partial^2 G(\mathbf{x},\xi)}{\partial \xi_r \partial n(\mathbf{x})} [u(\mathbf{x}) - u(\xi_o) - u_{,p}(\xi_o)(x_p - \xi_{op})] dS - u_{,p}(\xi_o) \int_S \frac{\partial G(\mathbf{x},\xi)}{\partial \xi_r} n_p(\mathbf{x}) dS + u_{,r}(\xi_o) \left(\frac{\Omega(\xi)}{4\pi}\right) + u(\xi_o) \epsilon_{qkr} \oint_C \frac{\partial G(\mathbf{x},\xi)}{\partial x_k} dx_q + u_{,p}(\xi_o) \epsilon_{qrp} \oint_C G(\mathbf{x},\xi) dx_q + u_{,p}(\xi_o) \epsilon_{qkr} \oint_C \frac{\partial G(\mathbf{x},\xi)}{\partial x_k} (x_p - \xi_{op}) dx_q \quad (8)$$

where $\Omega(\xi)$ is the solid angle subtended by the surface S from ξ. The second surface integral and the line integrals around the edge C of S are in the limit, of course, regular. We note that derivatives of u occur only at ξ_o and may be taken outside of all integrals. Thus, a computational strategy built on equation (4), with I_r as given by equation (8) as the key ingredient, contains regular and at most weakly singular integrals. This strategy has none of the weaknesses of the integration-by-parts regularization mentioned before and is free of any discretization assumptions for S. It demands only sufficient smoothness on u at ξ_o for the Taylor series expansion and the conversion by Stokes' theorem. The smoothness issue is far from incidental, however, as will be discussed further in the Finite Part Section and in Appendix D.

3.2 Finite Parts. Consider the integral in equation (5) and partition S into a small part S_ϵ which includes ξ_o, assumed locally flat as shown in Fig. 2, and the remaining part $S - S_\epsilon$.

Downloaded 03 May 2010 to 171.66.16.244. Redistribution subject to ASME license or copyright; see http://www.asme.org/terms/Terms_Use.cfm

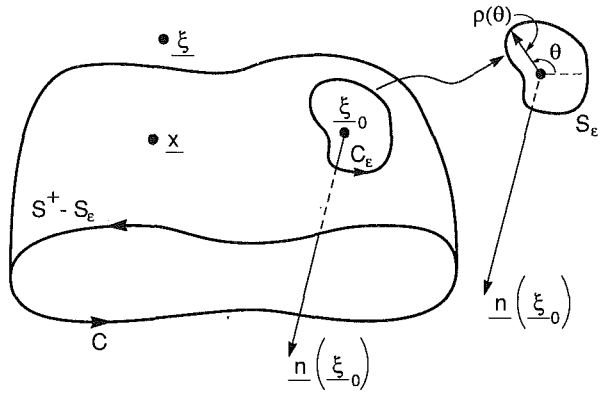


Fig. 2 The scatterer surface divided into two parts S^+ and $S^+ - S_\epsilon$

Then the limit as $\xi \to \xi_o$ of the integral of equation (5) can be expressed [2] as

$$I_r(\xi_o) = -\lim_{S_\epsilon \to 0}\left\{\lim_{\xi \to \xi_o}\int_{S-S_\epsilon} \frac{\partial^2 G(\mathbf{x},\xi)}{\partial \xi_r \partial n(\mathbf{x})} u(\mathbf{x})\, dS + \lim_{\xi \to \xi_o}\int_{S_\epsilon} \frac{\partial^2 G(\mathbf{x},\xi)}{\partial \xi_r \partial n(\mathbf{x})}[u(\xi_o) + u_{,p}(\xi_o)(x_p - \xi_{op}) + \ldots] dS\right\}. \tag{9}$$

Consider first the integral over S_ϵ. To perform the integration, note that $u(\mathbf{x})$ is expanded about ξ_o, and integrals involving the first two terms give rise to expressions which are unbounded in the size parameter $\rho(\theta)$ (see Fig. 2) for S_ϵ as $S_\epsilon \to 0$. The rest of the terms of the integral over S_ϵ are of order $\rho(\theta)$ or higher and vanish as $S_\epsilon \to 0$.

Explicitly, in the limit as $\xi \to \xi_o$, the result is (see Appendix C for details)

$$I_r(\xi_o) = \lim_{S_\epsilon \to 0}\left\{-\int_{S-S_\epsilon} \frac{\partial^2 G(\mathbf{x},\xi_o)}{\partial \xi_r \partial n(\mathbf{x})} u(\mathbf{x})\, dS + u(\xi_o)\frac{n_r(\xi_o)}{4\pi}\int_o^{2\pi} \frac{d\theta}{\rho(\theta)} - u_{,p}(\xi_o)\frac{n_r(\xi_o)}{4\pi}\int_o^{2\pi} \rho_{,p}(\theta)\ln|2\rho(\theta)|\, d\theta\right\}. \tag{10}$$

Note that both integrals from 0 to 2π on θ are unbounded as $S_\epsilon \to 0$. Upon examination of the integral in equation (10) over $S - S_\epsilon$ we find that it also is unbounded as $S_\epsilon \to 0$. To see this, and indeed to appreciate the essence of the present section, subtract and add the first two terms in the Taylor series expansion of $u(\mathbf{x})$ about ξ_o in the integral over $S - S_\epsilon$. The added-back terms, when integrated, have terms which are exactly the same as the last two in equation (10) except *with opposite sign* (Appendix C). Thus, the terms unbounded as $S_\epsilon \to 0$ *cancel* inside the brackets in equation (9) as well as equation (10) such that the limit as $S_\epsilon \to 0$ is rather benign, the troublesome terms already having canceled. The result is that $I_r(\xi_o)$ may be written as

$$I_r(\xi_o) = -\oint\!\!\!\!\!\!=_S \frac{\partial^2 G(\mathbf{x},\xi_o)}{\partial \xi_r \partial n(\mathbf{x})} u(\mathbf{x})\, dS(\mathbf{x}) \tag{11}$$

where the "double dash" on the integral signifies the finite part of the indicated integral according to Hadamard (1923), or the HFP. In effect, equation (10) serves to define the HFP of integral (5).

In the foregoing definition the density function is part of the integrand. There are other forms of expressing $I_r(\xi_o)$ and the one best suited for computation is under investigation. One form of expressing $I_r(\xi_o)$ in terms of FP and CPV, which does not include the density function as part of the integrand, follows clearly from equation (6), i.e.,

$$I_r(\xi_o) = -\int_S \frac{\partial^2 G(\mathbf{x},\xi_o)}{\partial \xi_r \partial n(\mathbf{x})}[u(\mathbf{x}) - u(\xi_o) - u_{,p}(\xi_o)(x_p - \xi_{op})]dS - u(\xi_o)\oint\!\!\!\!\!\!=_S \frac{\partial^2 G(\mathbf{x},\xi_o)}{\partial \xi_r \partial n(\mathbf{x})} dS - u_{,p}(\xi_o)\int_S \frac{\partial^2 G(\mathbf{x},\xi_o)}{\partial \xi_r \partial n(\mathbf{x})}(x_p - \xi_{op})dS \tag{12}$$

where the "single dash" is now used to signify the CPV.

It is important to note at this point that if $u(\mathbf{x})$ does not have continuous first derivatives at ξ_o, the limit as $\xi \to \xi_o$ that gives rise to equation (10) does not exist. That is (Appendix D), additional terms unbounded in the parameter $D \equiv |\xi - \xi_o|$ would appear in equation (10) and these are multiplied by a coefficient equal to zero only if $u(\mathbf{x})$ has continuous first derivatives at ξ_o. Thus, smoothness of u at ξ_o is not simply a matter of computational accuracy to be considered when selecting shape functions and elements. Moreover, the finite part in equation (11) and thus (12) depends, for its very definition, on $u(\mathbf{x})$ being $C^{1,\alpha}$ at ξ_o since the weak singularity of integrals such as the first of (12) and (B15) or (B19) require this even stronger condition. Similar remarks hold for the $C^{0,\alpha}$ smoothness requirement for the existence of the CPV (e.g., Muskhelishvili, 1953), although lack of attention to this, with common discretization procedures for CPV integrals, proves not to be troublesome. Such is not the case, however, with HFP integrals.

An obvious question at this point is: What is the relation between equation (8), with its line integrals, and equation (11) or (12), with its finite part integrals? Are they completely equivalent or separate roads to hypersingular integral computation?

3.3 Equivalence. To answer the above questions, note that the option of numerically computing a CPV or analytically converting (removing) one to a regular integral have long been part of the BIE literature (e.g., Lachat and Watson, 1976; Guiggiani, 1987). Similarly, special numerical techniques (Kutt, 1975) may be used directly on a HFP integral. Alternatively, in the spirit of singularity removal, note first that $I_n(\xi_o) = I_r(\xi_o) n_r(\xi_o)$. It can now be shown (Appendices B and C) that the last two integrals in (12) summed on $n_r(\xi_o)$ can be rewritten according to

$$u(\xi_o)\oint\!\!\!\!\!\!=_S \frac{\partial^2 G(\mathbf{x},\xi_o)}{\partial n(\xi_o)\partial n(\mathbf{x})} dS = -u(\xi_o) n_r(\xi_o)\oint_C \epsilon_{qkr}\frac{\partial G(\mathbf{x},\xi_o)}{\partial x_k} dx_q$$

$$u_{,p}(\xi_o)\oint\!\!\!\!\!\!=_S \frac{\partial^2 G(\mathbf{x},\xi_o)}{\partial n(\xi_o)\partial n(\mathbf{x})}(x_p - \xi_{op})dS = u_{,r}(\xi_o) n_r(\xi_o) \times \left(\frac{\Omega(\xi_o)}{4\pi} - \frac{1}{2}\right) + u_{,k}(\xi_o)\int_S \frac{\partial G(\mathbf{x},\xi_o)}{\partial n(\xi_o)} n_k(\mathbf{x})\, dS - u_{,p}(\xi_o) n_r(\xi_o)\oint_C \epsilon_{qkr}\frac{\partial G(\mathbf{x},\xi_o)}{\partial x_k} \times (x_p - \xi_{op})dx_q - u_{,p}(\xi_o) n_r(\xi_o)\oint_C \epsilon_{qrp} G(\mathbf{x},\xi_o) dx_q. \tag{13}$$

[2] It is worth noting that the smallness and flatness of S_ϵ and indeed, the limit as $S_\epsilon \to 0$ are not essential ideas in equation (9). Clearly, S may be arbitrarily partitioned and the important limit as $\xi \to \xi_o$ taken, for arbitrary S_ϵ, and $I_r(\xi_o)$ would still be well defined. Thus, there should be no confusion about the order of the two limits in equation (9). The flatness of S_ϵ and the limit as $S_\epsilon \to 0$ we have taken for convenience.

Downloaded 03 May 2010 to 171.66.16.244. Redistribution subject to ASME license or copyright; see http://www.asme.org/terms/Terms_Use.cfm

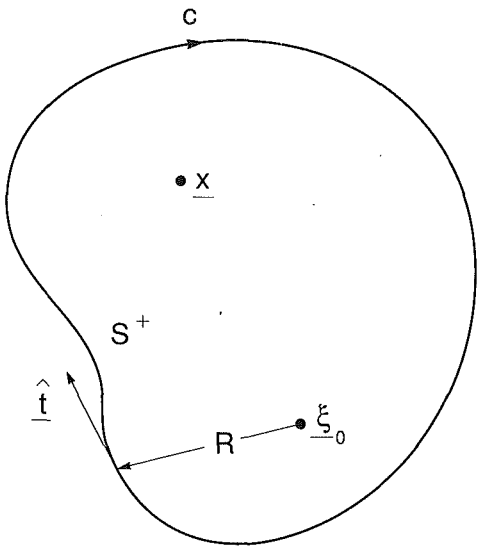


Fig. 3 A flat scatterer

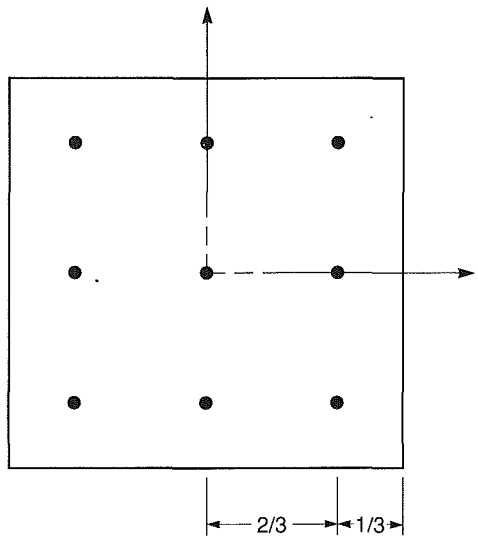


Fig. 4 An 8-node nonconforming element

To most easily see this, let $u(\xi)$ in (12) be identical with $-f(\xi)$ in (B19). Then note that in light of (B20) the HFP of $I_4(\xi_o)$, and hence of $I_n(\xi_o)$, is given by (B19) summed on $n_r(\xi_o)$ with the integrals involving θ missing. Therefore comparing terms in $u(\xi_o)$ and terms in $u_{,p}(\xi_o)$, respectively, expressions (13) follow at once. Thus the expression for $I_n(\xi_o)$ starting from either equation (8) or equation (12), i.e., by using the "Conversion" or the "Finite Parts" approach, is the same and both are given by

$$I_n(\xi_o) = -\int_S \frac{\partial^2 G(\mathbf{x},\xi_o)}{\partial n(\xi_o)\partial n(\mathbf{x})}[u(\mathbf{x}) - u(\xi_o) - u_{,p}(\xi_o)(x_p - \xi_{op})]dS - u_{,k}(\xi_o)n_r(\xi_o)\int_S \frac{\partial G(\mathbf{x},\xi_o)}{\partial \xi_r} n_k(\mathbf{x})dS + u(\xi_o)n_r(\xi_o)\epsilon_{qkr}\oint_C \frac{\partial G(\mathbf{x},\xi_o)}{\partial x_k}dx_q + u_{,p}(\xi_o)n_r(\xi_o)\epsilon_{qkr} + \oint_C \frac{\partial G(\mathbf{x},\xi_o)}{\partial x_k}(x_p - \xi_{op})dx_q + u_{,p}(\xi_o)n_r(\xi_o)\epsilon_{qrp}\oint_C G(\mathbf{x},\xi_o)dx_q. \quad (14)$$

Note that the second integral in equation (14) is not a CPV, since as $\mathbf{x}\to\xi_o$, the term $u_{,k}(\xi_o)n_k(\xi_o) \equiv \partial u/\partial n(\xi_o) = 0$ by hypothesis for a rigid scatterer.

Finally then, from our decomposition of equation (4), the expression for the normal gradient of the scattered field from a thin scatterer is given by

$$\frac{\partial \phi^s(\xi_o)}{\partial n(\xi_o)} = -\frac{\partial \phi^i(\xi_o)}{\partial n(\xi_o)} = -\int_S \left[\frac{\partial^2 G^D(\mathbf{x},\xi_o)}{\partial n(\xi_o)\partial n(\mathbf{x})} - \frac{\partial^2 G(\mathbf{x},\xi_o)}{\partial n(\xi_o)\partial n(\mathbf{x})}\right] u(\mathbf{x})dS + I_n(\xi_o) \quad (15)$$

with $I_n(\xi_o)$ given by (14).

4 Numerical Example

To validate the analysis done so far, a physical problem having a theoretical solution is solved using equation (15) and compared with theory. One such problem is the scattering of plane waves at normal incidence on a penny-shaped rigid scatterer. Equation (15), when specialized for a flat scatterer, results in

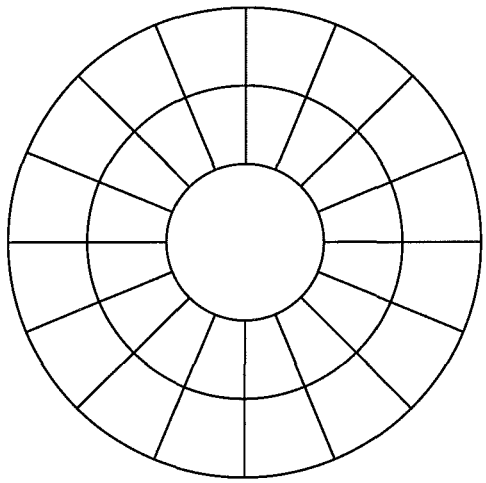


Fig. 5 Penny-shaped scatterer discretized by 33 nonconforming elements

$$4\pi\left(\frac{\partial \phi^i}{\partial n}\right) = \int_{S^+} \frac{1}{R^3}[e^{ikR} - 1 - ikRe^{ikR}]u(\mathbf{x})dS + \int_{S^+} \frac{1}{R^3}[u(\mathbf{x}) - u(\xi_o) - u_{,p}(\xi_o)(x_p - \xi_{op})]dS + \oint_C \frac{1}{R^3}\left[u(\xi_o) + \frac{\partial u(\xi_o)}{\partial \xi_p}(x_p - \xi_{op})\right]\{(x_1 - \xi_{o1})\hat{t}_2 - (x_2 - \xi_{o2})\hat{t}_1\}dl + \oint_C \frac{1}{R}\left\{\frac{\partial u(\xi_o)}{\partial x_1}\hat{t}_2 - \frac{\partial u(\xi_o)}{\partial x_2}\hat{t}_1\right\}dl \quad (16)$$

where R, C, and $\hat{t}$ are as shown in Fig. 3, $\partial\phi^i/\partial n = ik$ and k is the wave number of the incident wave.

Integral equation (16) can be treated like any other BIE and solved numerically through the familiar BEM, provided the smoothness requirements at the collocation points (see Appendix B) are satisfied. In the familiar BEM (Banerjee, 1981; Cruse, 1988) it is common practice to have the collocation points on the edges of the element where the density function is continuous but does not satisfy the smoothness require-

Downloaded 03 May 2010 to 171.66.16.244. Redistribution subject to ASME license or copyright; see http://www.asme.org/terms/Terms_Use.cfm

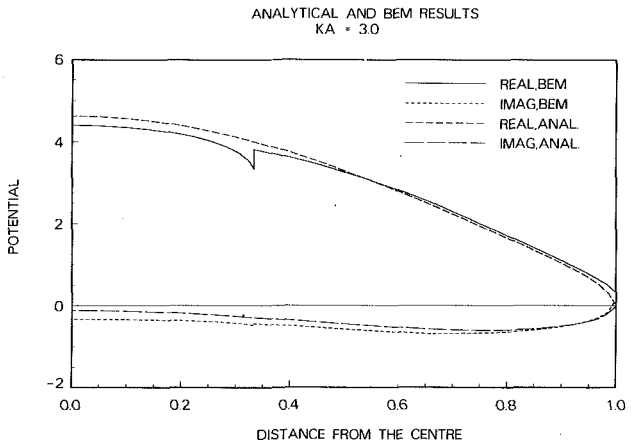


Fig. 6 Analytical and BEM results for KA = 3.0

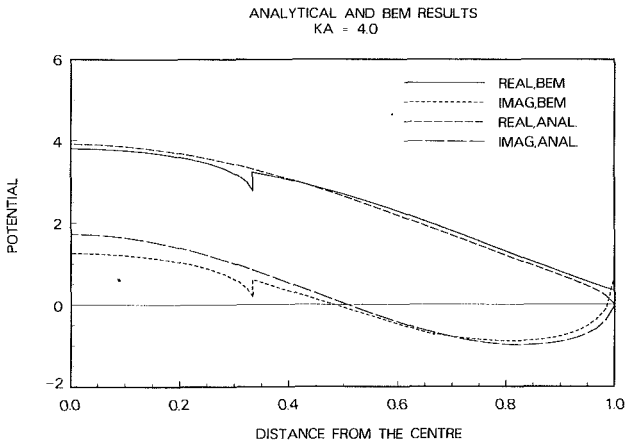


Fig. 7 Analytical and BEM results for KA = 4.0

ment. To circumvent this problem, one could either choose nonconforming elements, where the collocation points are away from the edges, or use splines. Though splines might give a more accurate and smooth result (Rudolphi et al., 1988), they are more difficult to implement in three-dimensional problems. On the other hand, nonconfirming elements are not only easy to generate, but also require little effort to incorporate into already existing BEM codes.

To solve the problem under discussion using the BEM, 8-node nonconforming elements (Fig. 4) were used to discretize the domain. The square root behavior of the solution near the crack edges is built into the shape functions of elements along the edges of the scatterer. A penny-shaped crack modeled by 33 elements (Fig. 5) is used to solve the scattering problem after using a model with five elements (not shown) resulted in errors as big as 11 percent at nodes close to the edges. For the 33-element model, the complex scattered field for different wave numbers was computed and compared with theory in Figs. 6 through 8. The discontinuities in the complex scattered field at 1/3 and 2/3 of the radius from the center are due to the nonconforming nature of the elements used. The discontinuity closest to the center can be reduced on further discretizing the center. The numerical solution of the complex potential at the crack tips as shown is nonzero. It should be zero there, and this can be easily corrected by incorporating the information about this zero into the shape functions of elements along the edges of the scatterer. As noted earlier, conforming elements with the proper smoothness would eliminate discontinuities completely if one wished to do the extra work required for implementation of such elements.

If one is interested in the equivalent static problem, for example, fluid flow obstructed by a flat disk, equation (16) can be used with $k=0$ and $\partial\phi^i/\partial n$ = constant.

If the collocation points were located at the edges of the element, i.e., when the smoothness requirements are not satisfied, spurious results would be obtained (Krishnasamy et al., 1987). Such results seem to change dramatically with changes in discretization pattern.

5 Elastic Wave Scattering: The Crack Problem

For acoustic wave scattering, it was shown in Section 3.3 that using either the "Conversion" process or the "Finite Parts" interpretation, equation (14) was the result for the key expression $I_n(\xi_o)$. An identical duality in approach exists for the (vector) problems of elastic wave scattering and linear elastic fracture mechanics, but we spare the reader the details of equivalence. Rather, we discuss only the "Conversion" process here and even that in limited detail.

The representation integral for scattered elastic waves from

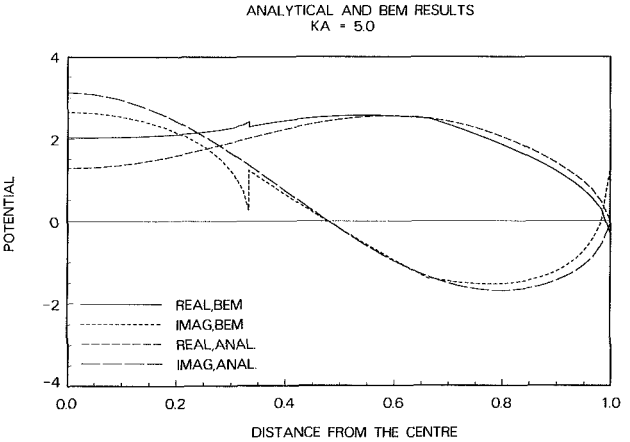


Fig. 8 Analytical and BEM results for KA = 5.0

an arbitrarily shaped, vanishingly thin crack S (cf., Fig. 1) is given by

$$u_m^s(\xi) = C_{ijkl}\int_S \left\{G_{im}^D\left(\frac{\partial u_k^+}{\partial x_l} - \frac{\partial u_k^-}{\partial x_l}\right)n_j^+(\mathbf{x}) - \frac{\partial G_{km}^D}{\partial x_l}(u_i^+ - u_i^-)n_j^+(\mathbf{x})\right\}ds \tag{17}$$

where u_m^s is the scattered displacement field, u_m^i the incident field, $u_m \equiv u_m^s + u_m^i$ the total field, G_{im}^D the components of the fundamental time-harmonic point-force solution for elastodynamics (cf., Pao and Varatharajulu, 1975; Rizzo, Rezayat, and Shippy, 1985), and C_{ijkl} the constants describing a linear elastic material. The designations "+" and "−" refer to the two sides of S as before. For a stress-free crack surface, (17) reduces to

$$u_m^s(\xi) = -C_{ijkl}\int_S \frac{\partial G_{km}^D}{\partial x_l}\Delta u_i(\mathbf{x})n_j(\mathbf{x})ds \tag{18}$$

where $\Delta u_i = u_i^+ - u_i^-$ is the crack-opening displacement, the primary dependent variable in a boundary value problem. In the limit as $\xi \to \xi_o$ equation (18) results in a familiar BIE, but this, for the same reason already discussed in the acoustics problem, is insufficient to determine Δu_i. As before, we take the gradient of the representation integral, i.e.,

$$\frac{\partial u_m^s(\xi)}{\partial \xi_r} = -C_{ijkl}\int_S \frac{\partial^2 G_{km}^D(\mathbf{x},\xi)}{\partial \xi_r \partial x_l}\Delta u_i(\mathbf{x})n_j(\mathbf{x})ds \tag{19}$$

Downloaded 03 May 2010 to 171.66.16.244. Redistribution subject to ASME license or copyright; see http://www.asme.org/terms/Terms_Use.cfm

which, in the limit as $\xi \to \xi_o$, has the same hypersingular character as equation (3) for acoustics. Virtually the entire discussion of the singularities following equation (3) above applies to (19) with only obvious modifications to account for the vector character of (19). Thus it sufficies here to first subtract and add back the Kelvin point-force solution for elastostatics (cf., Cruse, 1969) to obtain the counterpart of (4), i.e.,

$$\frac{\partial u_m^s(\xi)}{\partial \xi_r} = -C_{ijkl}\int_S \left[\frac{\partial^2 G_{km}^D(\mathbf{x},\xi)}{\partial \xi_r \partial x_l} - \frac{\partial^2 G_{km}(\mathbf{x},\xi)}{\partial \xi_r \partial x_l}\right] \times n_j(\mathbf{x})\Delta u_i(\mathbf{x})ds - C_{ijkl}\int_S \frac{\partial^2 G_{km}(\mathbf{x},\xi)}{\partial \xi_r \partial x_l} n_j(\mathbf{x})\Delta u_i(\mathbf{x})ds \quad (20)$$

wherein, as before, in the limit $\xi \to \xi_o$ the first integral in (20) is weakly singular, and the second integral whose kernel is real and frequency independent is hypersingular. Indeed, for problems of static loading of a cracked body, only the second integral pertains, so that the methods of this paper are relevant to much of static linear elastic fracture mechanics.

Next, following the methods of Section 3.1 only, if ξ_o is a point on S which does not fall on the crack edge and Δu_i is at least $C^{1,\alpha}$ at ξ_o, then Stokes' theorem in the form (7) (cf., Teodosiu, 1982) can be used to express (20), in the limit as $\xi \to \xi_o$, in the form

$$\frac{\partial u_m^s(\xi_o)}{\partial \xi_r} = -C_{ijkl}\int_S \left(\frac{\partial^2 G_{km}^D}{\partial \xi_r \partial x_l} - \frac{\partial^2 G_{km}}{\partial \xi_r \partial x_l}\right) n_j(\mathbf{x})\Delta u_i(\mathbf{x})ds$$

$$- C_{ijkl}\int_S \frac{\partial^2 G_{km}}{\partial \xi_r \partial x_l} n_j(\mathbf{x})[\Delta u_i(\mathbf{x}) - \Delta u_i(\xi_o)$$

$$- \Delta u_{i,p}(\xi_o)(x_p - \xi_{op})]ds + C_{ijkl}\int_S \frac{\partial G_{im}}{\partial x_r}\frac{\partial \Delta u_k(\xi_o)}{\partial \xi_l} n_j(\mathbf{x})ds$$

$$+ \Delta u_i(\xi_o)\epsilon_{jrq}C_{ijkl}\oint_C \frac{\partial G_{km}}{\partial x_l}dx_q + \frac{\partial \Delta u_i(\xi_o)}{\partial \xi_j}$$

$$\times \epsilon_{rlq}C_{ijkl}\oint_C G_{km}dx_q + \frac{\partial \Delta u_i(\xi_o)}{\partial \xi_p}\epsilon_{jrq}C_{ijkl}$$

$$\times \oint_C \frac{\partial G_{km}}{\partial x_l}(x_p - \xi_{op})dx_q - \frac{\partial \Delta u_i(\xi_o)}{\partial \xi_r}C_{ijkl}$$

$$\times \int_S \frac{\partial G_{km}}{\partial x_l} n_j(\mathbf{x})ds(\mathbf{x}) \equiv u_{m,r}^s(\xi_o) \quad (21)$$

where the last integral, which is a CPV, can be replaced for an isotropic material as

$$\frac{\partial \Delta u_i(\xi_o)}{\partial \xi_r}C_{ijkl}\int_S \frac{\partial G_{km}}{\partial x_l} n_j(\mathbf{x})ds(\mathbf{x}) = -\left(\frac{\Omega(\xi_o)}{4\pi}\right)\frac{\partial \Delta u_m(\xi_o)}{\partial \xi_r}$$

$$+ \frac{1}{8\pi}\frac{\partial \Delta u_j(\xi_o)}{\partial \xi_r}\oint_C \epsilon_{mji}R_{,pp}dx_i$$

$$+ \frac{1}{8\pi(1-\nu)}\frac{\partial \Delta u_j(\xi_o)}{\partial \xi_r}\oint_C \epsilon_{jpi}R_{,pm}dx_i \quad (22)$$

wherein $R \equiv |\mathbf{x} - \xi_o|$. For an anisotropic material, though an expression like equation (22) is more difficult to get, one can avoid direct computation of the CPV integral by replacing it by $-\partial \Delta u_i(\xi_o)/\partial \xi_r$ and the negative of an integral with the same integrand over S_c, where S_c is any surface such that $S\ U\ S_c$ is a closed surface with the normal to both surfaces pointing outwards. Equation (21) with (22) is the vector counterpart of equation (8). All integrals are regular, or at most weakly singular, as discussed in connection with equation (8). If desired, (21) could be converted to a form like (12) in which HFP and CPV integrals were explicit. These in turn could be transformed via the method of Section 3.2 (and Appendices B and C) such that again (21) would result.

Finally, since the scattered traction is given by

$$t_p^s(\xi_o) = C_{pqmr}u_{m,r}^s(\xi_o)n_q(\xi_o), \quad (23)$$

and since the total traction $t_p(\xi_o)$ across S is zero by hypothesis, it suffices to sum the terms in (21) with $C_{pqmr}n_q(\xi_o)$, set the sum equal to $-t_p^i(\xi_o)$ and regard formula (23) as our main BIE formula for numerical computation for the present class of problems, i.e., scattering of time-harmonic waves by cracks. For static loading of such cracks, by direct applied traction or by a remote field using superposition to fix the boundary data, a formula with obvious simplifications pertains.

Computational strategies based on (21) and (23) for representative vector problems are under way.

6 Discussion

We should emphasize the basic nature of the issues in this paper. The BIE/BEM solution procedures, most familiar in the literature, involve weakly singular or, at most, CPV integrals in contrast with the nonsingular integrals of most other methods such as the finite element method. One might view the singularities as the price one pays for the "reduction in dimension" or "reformulation of the problem on the boundary" so often mentioned as the big advantages with the BIE. Now, even higher-order singularities are being advocated for which even interpretations as CPVs are insufficient. Interpretation as Hadamard finite-part integrals is possible although, as shown in this paper, even this is not necessary. Nevertheless, such an interpretation and our suggested method of treatment of the integrals, using two terms in a Taylor series expansion, are a natural extension of the CPV idea; but there are important differences as have been shown. It appears that each step upwards in kernel singularity requires greater smoothness of the function multiplying the kernels for the integrals to exist in any sense. Practical implications of and clarification of this fact and the kinds of limits needed to define this hierarchy of singular integrals are, perhaps, the central issues of this paper.

It is possible now to treat wave scattering from an arbitrarily shaped (not flat) crack surface, the difficulties encountered in getting an analytical expression for finite parts due to the curvature of the surface having been overcome. Alternatively, we have also proposed a method which does not require any HFP or CPV interpretation and eliminates any numerical computation of HFP or CPV integrals. In this method, Stokes' theorem is used not to reduce the order of singularity by transferring a derivative on the fundamental solution to the density function, i.e., the usual regularization, but to convert surface integrals to line integrals. This method is valid regardless of how the surface is discretized and whether the surface is open or closed. The smoothness demanded of the density function by this method is required by the nature of the hypersingularity and hence needs to be satisfied no matter what method is used. Indeed, without this smoothness requirement, we believe that no meaningful value can be given to the hypersingular integrals involved in the gradient BIE (equation (2)) by any method. Moreover, we contend that the understanding in this paper regarding where and why smoothness is required permits stable and accurate computations with even nonconforming boundary elements. Our reported results, though preliminary, support this conclusion. This is in contrast to the delicate nontrivial numerical issues with the usual regularization methods, as mentioned earlier, wherein CPV's must be computed using very special interpolation procedures.

Finally, in addition to crack applications, hypersingular integral equations should prove useful for computing gradients

Downloaded 03 May 2010 to 171.66.16.244. Redistribution subject to ASME license or copyright; see http://www.asme.org/terms/Terms_Use.cfm

of potentials, and stresses in vector problems, right on the boundaries of bodies defined by closed surfaces, (cf., Cruse and Van Buren, 1971). Such equations are also useful in constructing a formulation for a unique solution at all frequencies for frequency-dependent, wave-scattering problems, (e.g., Burton and Miller, 1971; Terai (1980). They also appear in the acoustic and elastodynamic transmission problem in scattering theory (cf. Kleinman and Martin, 1988), and in computational models of thin shields in electroplating (e.g., Gray and Giles, 1988). We suspect that hypersingular integral equations will appear more frequently in many contexts as their properties become better understood, and when more confidence to treat them numerically is gained.

7 Acknowledgment

We are especially grateful to P. A. Martin of the University of Manchester for much communication on finite part integrals without which this work would have been impossible. Also, partial support was provided by the U.S. office of Naval Research under Contract N0014-86-K-0551. This research was also sponsored (for L.W.S., T.J.R) by the National Institute of Standards and Technology program for Integrated Design, NDE, and the Manufacturing Sciences at the Center for Nondestructive Evaluation, Iowa State University.

References

Brandão, M. P., 1986, "Improper Integrals in Theoretical Aerodynamics: The Problem Revisited," *AIAA J.*, Vol. 25, pp. 1258-1260.

Budreck, D. E., and Achenbach, J. D., 1988, "Scattering From Three-Dimensional Planar Cracks by the Boundary Integral Equation Method," ASME JOURNAL OF APPLIED MECHANICS, Vol. 55, pp. 405-411.

Bui, H. D., 1977, "An Integral Equations Method for Solving the Problem of a Plane Crack of Arbitrary Shape," *J. Mech. Phys. Solids*, Vol. 25, pp. 29-39.

Burton, A. J., and Miller, G. F., 1971, "The Application of the Integral Equation Methods to the Numerical Solution of Some Exterior Boundary-Value Problems," *Proc. Roy. Soc. Lond. A.*, Vol. 323, pp. 201-210.

Cruse, T. A., 1969, "Numerical Solution in Three-Dimensional Elastostatics," *Int. J. Solids and Structs.*, Vol. 5, pp. 1259-1274.

Cruse, T. A., and Van Buren, W., 1971, "Three-Dimensional Elastic Stress Analysis of Fracture Specimen with an Edge Crack," *Int. J. Fracture Mech.*, Vol. 7, pp. 1-15.

Cruse, T. A., 1988, *Boundary Element Analysis in Computational Fracture Mechanics*, Kluwer Academic Publishers, Boston, Mass.

Filippi, P. J. T., 1977, "Layer Potentials and Acoustic Diffraction," *J. Sound and Vib.*, Vol. 54, pp. 473-500.

Gray, L. R., and Giles, G. E., 1988, "Application of the Thin Cavity Method to Shield Calculations in Electroplating, Bergen Scientific Center," Allégaten 36,5007 Bergen, Norway.

Guiggiani, M., and Casalini, P., 1987, "Direct Computation of Cauchy Principle Value Integrals in Advanced Boundary Elements," *Int. Jou. Num. Meth. in Engng.*, Vol. 24, pp. 1711-1720.

Hadamard, J., 1923, *Lectures on Cauchy's Problem in Linear Partial Differential Equations*, Yale Univ. Press, New Haven, Conn.

Ioakimidis, N. I., 1982, "Application of Finite Part Integrals to the Singular Integral Equations of Crack Problems in Plane and 3-D Elasticity," *Acta Mechanica*, Vol. 45, pp. 31-47.

Kaya, A. C., and Erdogan, F., 1987, "On the Solution of Integral Equations with Strongly Singular Kernels," *Q. Appl. Math.*, Vol. 45, pp. 105-122.

Kitahara, M., 1986, private communication.

Kleinman, R. E., and Martin, P. A., 1988, "On Single Integral Equations for the Transmission Problem of Acoustics," *SIAM J. Appl. Math.*, Vol. 48, pp. 307-325.

Krishnasamy, G., Rudolphi, T. J., Schmerr, L. W., and Rizzo, F. J., 1988, "Hypersingular Integral Formulas and Wave Scattering with the Boundary Element Method," *Proc. 1st Japan-US Symposium on Boundary Elements*, Tokyo.

Kutt, H. R., 1975, "The Numerical Evaluation of Principal Value Integrals by Finite-Part Integration," *Numer. Math.*, Vol. 24, pp. 20-210.

Lachat, J. C., and Watson, J. O., 1976, "Effective Numerical Treatment of Boundary Integral Equations: A Formulation for Three Dimensional Elastostatics," *Int. J. Num. Meth. Engng.*, Vol. 10, pp. 991-1005.

Lin, W., and Keer, L. M., 1987, Scattering by a Planar Three-Dimensional Crack, *J. Acoust. Soc. Am.*, Vol. 82, pp. 1442-1448.

Martin, P. A., and Rizzo, F. J., 1989, "On Boundary Integral Equations for Crack Problems," *Proc. Roy. Soc. London*, Vol. A421, pp. 341-355.

Maue, A. W., 1949, "Zur Formulierung eines allgemeinen Beugungsproblems durch eine Integralgleichung," *Z. Physics*, Vol. 126, pp. 601-618.

Muskhelishvili, N. I., 1953, *Some Basic Problems of the Mathematical Theory of Elasticity*, 3rd ed., Nordhoff, The Netherlands.

Nishimura, N., and Kobayashi, S., 1988, "An Improved Boundary Integral Equation Method for Crack Problems," Proc. IUTAM Symposium, San Antonio, *Adv. Boundary Element Meth.*, T. A. Cruse, ed., (IUTAM Symposium, San Antonio, Texas, Apr. 13-16, 1987), Springer-Verlag, Berlin, W. Germany.

Pao, Y. H., and Varatharajulu, V., 1975, "Huygens' Principle, Radiation Conditions and Integral for the Scattering of Elastic Waves," Department of Theoretical and Applied Mechanics, Cornell University.

Polch, E. Z., Cruse, T. A., and Huang, C. J., 1987, "Traction BIE Solutions for Flat Cracks," *Comput. Mech.*, Vol. 2, pp. 253-267.

Rizzo, F. J., Shippy, D. J., and Rezayat, M., 1985, "A Boundary Integral Equation Method for Radiation and Scattering of Elastic Waves in Three Dimensions," *International Journal for Numerical Methods in Engineering*, Vol. 21, pp. 115-129.

Rudolphi, T. J., Krishnasamy, G., Schmerr, L. W., and Rizzo, F. J., 1988, "On the Use of Strongly Singular Integral Equations for Crack Problems," Proc. 10th Int. Conf. Boundary Elements, Southampton, U.K., Sept., 1988.

Sládek, V., Sládek, J., and Balas, J., 1986, "Boundary Integral Formulation of Crack Problem," *ZAMM.Z.angew. Math. Mech.*, Vol. 66, pp. 83-94.

Takakuda, K., Koizumi, T., and Shibuya, T., 1985, "On Integral Equation Methods for Crack Problems," *Bull. J.S.M.E.*, Vol. 28, Feb. 1985.

Teodosiu, C., 1982, *Elastic Models of Crystal Defects*, Springer-Verlag, New York.

Terai, T., 1980, "On Calculation of Sound Fields Around Three-Dimensional Objects by Integral Equation Methods," *J. Sound and Vib.*, Vol. 69, pp. 71-100.

Weaver, J., 1977, "Three-Dimensional Crack Analysis," *Int. J. Solids and Structures*, Vol. 13, pp. 321-330.

APPENDIX A

In the following, the integrals that occur in equation (6) are "converted" by Stokes' theorem. Let J be the second integral in equation (6). In indicial notation,

$$J = -\int_S G_{,kr}(\mathbf{x},\xi) n_k(\mathbf{x}) dS \tag{A1}$$

where $G_{,rk}(\mathbf{x},\xi) = \partial^2 G(\mathbf{x},\xi)/\partial x_r \partial x_k$. Subtracting and adding the term $G_{,kk}(\mathbf{x},\xi) n_r(\mathbf{x})$, we have

$$J = -\int_S [G_{,kr}(\mathbf{x},\xi) n_k(\mathbf{x}) - G_{,kk}(\mathbf{x},\xi) n_r(\mathbf{x})] dS - \int_S G_{,kk}(\mathbf{x},\xi) n_r(\mathbf{x}) dS \tag{A2}$$

where, since $G_{,kk}(\mathbf{x},\xi) = 0$ for ξ not on S, the second integral of (A2) is zero. Using Stokes' theorem of equation (7), equation (A2) reduces to the line integral

$$J = -\epsilon_{qkr} \oint_C G_{,k}(\mathbf{x},\xi) dx_q \tag{A3}$$

where C is the line bounding S.

Now let Z be the third integral in equation (6). In indicial notation it is

$$Z = -\int_S G_{,kr}(\mathbf{x},\xi)(\mathbf{x}-\xi_o)_p n_k(\mathbf{x}) dS, \tag{A4}$$

or equivalently,

$$Z = -\int_S [G_{,k}(\mathbf{x},\xi)(\mathbf{x}-\xi_o)_p]_{,r} n_k(\mathbf{x}) dS + \delta_{rp} \int_S G_{,k}(\mathbf{x},\xi) n_k(\mathbf{x}) dS. \tag{A5}$$

Subtracting and adding the term $[G_{,k}(\mathbf{x},\xi)(\mathbf{x}-\xi_o)_p]_{,k} n_r(\mathbf{x})$, we have

$$Z = -\int_S \{[G_{,k}(\mathbf{x},\xi)(\mathbf{x}-\xi_o)_p]_{,r} n_k(\mathbf{x}) - [G_{,k}(\mathbf{x},\xi) \times (\mathbf{x}-\xi_o)_p]_{,k} n_r(\mathbf{x})\} dS - \int_S G_{,kk}(\mathbf{x},\xi)(\mathbf{x}-\xi_o)_p n_r(\mathbf{x}) dS - \delta_{kp} \int_S G_{,k}(\mathbf{x},\xi) n_r(\mathbf{x}) dS - \delta_{rp} \frac{\Omega(\xi)}{4\pi} \tag{A6}$$

Downloaded 03 May 2010 to 171.66.16.244. Redistribution subject to ASME license or copyright; see http://www.asme.org/terms/Terms_Use.cfm

where $\Omega(\xi)$ is the solid angle made by the surface from the viewpoint ξ. Using Stokes' theorem on the first integral and recognizing that the second integral is zero, equation (A6) is

$$Z = -\epsilon_{qkr}\oint_C G_{,k}(\mathbf{x},\xi)(\mathbf{x}-\xi_o)_p dx_q - \delta_{kp}\int_S G_{,k}(\mathbf{x},\xi)n_r(\mathbf{x})dS - \delta_{rp}\frac{\Omega(\xi)}{4\pi}. \tag{A7}$$

Subtracting and adding the term $G_{,r}(\mathbf{x},\xi)n_k(\mathbf{x})$ from the second integral of equation (A7) and invoking Stokes' theorem again results in

$$Z = -\epsilon_{qkr}\oint_C G_{,k}(\mathbf{x},\xi)(\mathbf{x}-\xi_o)_p dx_q - \epsilon_{qrp}\oint_C G(\mathbf{x},\xi)dx_q - \int_S G_{,r}(\mathbf{x},\xi)n_p(\mathbf{x})dS - \delta_{rp}\frac{\Omega(\xi)}{4\pi}. \tag{A8}$$

APPENDIX B

The following are some types of improper integrals of interest in this paper and three-dimensional BIE/BEM analysis in general. Both $\mathbf{x}$ and ξ_o are on S. A limit as $\xi \to \xi_o$ is not an issue in this Appendix since such a limit is already understood as giving rise to the present integrals. Consider

$$I_1(\xi_o) \equiv \int_S \frac{f(\mathbf{x})}{r}dS \tag{B1}$$

where $f(\mathbf{x})$ is any density function which satisfies $f_{,p}(\mathbf{x})n_p(\mathbf{x}) = 0$, the rigid scatterer boundary condition, on the surface and $r \equiv |\mathbf{x}-\xi_o|$. $I_1(\xi_o)$ is weakly singular and the singularity can be removed by using polar coordinates to represent the differential area. Next, consider

$$I_2(\xi_o) \equiv \int_S f(\mathbf{x})\left(\frac{1}{r}\right)_{,k} n_k(\mathbf{x})dS \tag{B2}$$

which is no more than a weakly singular integral and can be reduced to a regular integral and a solid angle $\Omega(\xi_o)$ as follows:

$$I_2(\xi_o) \equiv \int_S [f(\mathbf{x}) - f(\xi_o)]\left(\frac{1}{r}\right)_{,k} n_k(\mathbf{x})dS + f(\xi_o)\int_S \left(\frac{1}{r}\right)_{,k} n_k(\mathbf{x})dS \tag{B3}$$

where the second integral is $-\Omega(\xi_o)$ as in equation (A5). Now consider

$$I_3(\xi_o) \equiv \int_S f(\mathbf{x})\frac{1}{r^2}(r_{,i}n_j - r_{,j}n_i)dS. \tag{B4}$$

As a result of the strong singularity in $I_3(\xi_o)$, we more formally write (see Fig. 2)

$$I_3(\xi_o) = \lim_{S_\epsilon \to 0}\left\{\int_{S-S_\epsilon} f(\mathbf{x})\frac{1}{r^2}(r_{,i}n_j - r_{,j}n_i)dS\right\} \tag{B5}$$

$$I_3(\xi_o) = \lim_{S_\epsilon \to 0}\left\{\int_{S-S_\epsilon} [f(\mathbf{x}) - f(\xi_o)]\frac{1}{r^2}(r_{,i}n_j - r_{,j}n_i)dS - f(\xi_o)\int_{S-S_\epsilon}\left[\left(\frac{1}{r}\right)_{,i}n_j - \left(\frac{1}{r}\right)_{,j}n_i\right]dS\right\} \tag{B6}$$

and trust that we may attach meaning to the indicated limit at least in the sense of the CPV (cf., Muskhelishvili, 1953 and (B9)). Invoking Stokes' theorem, equation (B6) reduces to

$$I_3(\xi_o) = \lim_{S_\epsilon \to 0}\left\{\int_{S-S_\epsilon} [f(\mathbf{x}) - f(\xi_o)]\frac{1}{r^2}(r_{,i}n_j - r_{,j}n_i)dS - f(\xi_o)\oint_C \epsilon_{jik}\left(\frac{1}{r}\right)dx_k - f(\xi_o)\oint_{C_\epsilon}\epsilon_{jik}\left(\frac{1}{r}\right)dx_k\right\}. \tag{B7}$$

Using the local polar coordinates over S_ϵ, as in Fig. 2, it can be shown that

$$\epsilon_{jik}\oint_{C_\epsilon}\left(\frac{1}{r}\right)dx_k = n_j(\xi_o)\int_o^{2\pi}\rho_{,i}(\theta)\ln|2\rho(\theta)|\,d\theta \tag{B8}$$

where $\rho(\theta)$ is as shown in the figure and $\rho_{,i}(\theta)$ is either $\sin\theta$ or $\cos\theta$.

Actually, there are two ways to interpret $I_3(\xi_o)$. If $\rho(\theta)$ is a constant, then the terms in (B8) vanish and for sufficiently smooth $f(\mathbf{x})$ at ξ_o, i.e., $C^{0,\alpha}$, the surface integral in (B7) is at most weakly singular in the limit. This is usually referred to as the CPV and is denoted by

$$I_3^*(\xi_o) = \oint_S f(\mathbf{x})\frac{1}{r^2}(r_{,i}n_j - r_{,j}n_i)dS. \tag{B9}$$

However, suppose $\rho(\theta)$ were assumed not to be a constant, then one can define the HFP of $I_3(\xi_o)$ as (cf., Hadamard, 1925)

$$I_3^{**}(\xi_o) = \lim_{S_\epsilon \to 0}\left\{\int_{S-S_\epsilon} f(\mathbf{x})\frac{1}{r^2}(r_{,i}n_j - r_{,j}n_i)dS + f(\xi_o)n_j(\xi_o)\int_o^{2\pi}\rho_{,i}(\theta)\ln|2\rho(\theta)|\,d\theta\right\} \tag{B10}$$

which again reduces equation (B7) to one which is finite in the limit $S_\epsilon \to 0$ and is denoted by

$$I_3^{**}(\xi_o) = \oint_S f(\mathbf{x})\frac{1}{r^2}(r_{,i}n_j - r_{,j}n_i)dS. \tag{B11}$$

Thus, interpreting $I_3(\xi_o)$ either as a CPV or a HFP results in

$$I_3^*(\xi_o) = I_3^{**}(\xi_o) = \int_S [f(\mathbf{x}) - f(\xi_o)]\frac{1}{r^2}(r_{,i}n_j - r_{,j}n_i)dS - f(\xi_o)\oint_C \epsilon_{jik}\left(\frac{1}{r}\right)dx_k. \tag{B12}$$

Note that $I_3(\xi_o)$ without either interpretation is unbounded. Finally, consider the even more strongly singular integral

$$I_4(\xi_o) \equiv \int_S f(\mathbf{x})\frac{\partial^2 G(\mathbf{x},\xi_o)}{\partial\xi_r \partial n(\mathbf{x})}dS \equiv -\int_S f(\mathbf{x})G_{,rk}(\mathbf{x},\xi_o)n_k(\mathbf{x})dS \tag{B13}$$

for which we hope to find meaning in the following limits.

$$I_4(\xi_o) = -\lim_{S_\epsilon \to 0}\int_{S-S_\epsilon} f(\mathbf{x})G_{,rk}(\mathbf{x},\xi_o)n_k(\mathbf{x})dS \tag{B14}$$

$$I_4(\xi_o) = -\lim_{S_\epsilon \to 0}\left\{\int_{S-S_\epsilon}[f(\mathbf{x}) - f(\xi_o) - f_{,p}(\xi_o)(\mathbf{x}-\xi_o)_p] \times G_{,rk}(\mathbf{x},\xi_o)n_k(\mathbf{x})dS - f(\xi_o)J - f_{,p}(\xi_o)Z\right\}, \tag{B15}$$

Downloaded 03 May 2010 to 171.66.16.244. Redistribution subject to ASME license or copyright; see http://www.asme.org/terms/Terms_Use.cfm

where J and Z are as defined by (A3) and (A8) with the surface and line integrals now over $S-S_\epsilon$ and $C+C_\epsilon$, respectively. The integrals over C_ϵ in J and Z are expressed in local coordinates, Fig. 2, over S_ϵ as follows:

$$\epsilon_{qkr}\oint_{C_\epsilon} G_{,k}(\mathbf{x},\xi_o)dx_q = -\frac{n_r(\xi_o)}{4\pi}\int_o^{2\pi}\frac{d\theta}{\rho(\theta)} \tag{B16}$$

$$\epsilon_{qkr}\oint_{C_\epsilon} G_{,k}(\mathbf{x},\xi_o)(\mathbf{x}-\xi_o)_p dx_q = 0 \tag{B17}$$

$$\epsilon_{qrp}\oint_{C_\epsilon} G(\mathbf{x},\xi_o)dx_q = \frac{n_r(\xi_o)}{4\pi}\int_o^{2\pi}\rho_{,p}(\theta)\ln|2\rho(\theta)|d\theta. \tag{B18}$$

On substituting (B16), (B17), and (B18) in equation (B15), we get

$$\begin{aligned} I_4(\xi_o) = \lim_{S_\epsilon\to 0}\Big[&-\int_{S-S_\epsilon}[f(\mathbf{x})-f(\xi_o)-f_{,p}(\xi_o)(\mathbf{x}-\xi_o)_p] \\ &\times G_{,rk}(\mathbf{x},\xi_o)n_k(\mathbf{x})dS + f(\xi_o)\Big\{-\epsilon_{qkr}\oint_C G_{,k}(\mathbf{x},\xi_o)dx_q \\ &+\frac{n_r(\xi_o)}{4\pi}\int_o^{2\pi}\frac{d\theta}{\rho(\theta)}\Big\} + f_{,p}(\xi_o)\Big\{\delta_{rp}\Big[-\frac{\Omega(\xi_o)}{4\pi}+\frac{1}{2}\Big] \\ &-\int_{S-S_\epsilon} G_{,r}(\mathbf{x},\xi_o)n_p(\mathbf{x})dS - \epsilon_{qkr}\oint_C G_{,k}(\mathbf{x},\xi_o)(\mathbf{x}-\xi_o)_p dx_q \\ &-\epsilon_{qrp}\oint_C G(\mathbf{x},\xi_o)dx_q - \frac{n_r(\xi_o)}{4\pi}\int_o^{2\pi}\rho_{,p}(\theta)\ln|2\rho(\theta)|d\theta\Big\}\Big] \end{aligned} \tag{B19}$$

in which the first surface integral is at most weakly singular, if $f(\mathbf{x})$ is at least $C^{1,\alpha}$ at ξ_o. In the limit as $S_\epsilon\to 0$, the terms explicitly involving θ in (B19) are unbounded. Assuming $\rho(\theta)\equiv\epsilon$, a constant, does not help as equation (B16), and so (B19), are of order $1/\epsilon$, though (B18) is zero identically. Hence, $I_4(\xi_o)$, as given by (B15), does not exist as a CPV. Instead for $\rho(\theta)$ not a constant, the finite part of $I_4(\xi_o)$ can be defined as

$$\begin{aligned} I_4^{**}(\xi_o) = \lim_{S_\epsilon\to 0}\Big\{ &-\int_{S-S_\epsilon} f(\mathbf{x})G_{,rk}(\mathbf{x},\xi_o)n_k(\mathbf{x})dS \\ &-f(\xi_o)\frac{n_r(\xi_o)}{4\pi}\int_o^{2\pi}\frac{d\theta}{\rho(\theta)} + f_{,p}(\xi_o)\frac{n_r(\xi_o)}{4\pi}\int_o^{2\pi}\rho_{,p}(\theta) \\ &\times\ln|2\rho(\theta)|d\theta\Big\} \end{aligned} \tag{B20}$$

so that $I_4^{**}(\xi_o)$ is at most weakly singular. This is denoted by

$$I_4^{**}(\xi_o) = \oint\!\!\!\!\!\!=_S f(\mathbf{x})\frac{\partial^2 G(\mathbf{x},\xi_o)}{\partial\xi_r\partial n(\mathbf{x})}dS. \tag{B21}$$

Additional motivation for this HFP definition, for the problems treated in this paper, is given in Appendix C.

APPENDIX C

In Appendix B, both $\mathbf{x}$ and ξ_o were already on S and we took special limits involving $S_\epsilon\to 0$ to define the CPV and HFP. In this Appendix we consider the limit as $D\to 0$, $D\equiv|\xi-\xi_o|$, where $\xi\notin S$ for certain integrals. Hopefully, our work in this Appendix motivates and renders more intutive the definition of the HFP in Appendix B, especially for BIE/BEM analysts who are first concerned with the limit as $D\to 0$ in physical problems.

Thus, consider the integral

$$J_3(\xi_o) = \lim_{D\to 0}\int_S f(\mathbf{x})\frac{1}{r^2}(r_{,i}n_j - r_{,j}n_i)dS \tag{C1}$$

where r, n, and S are as defined in Appendix B. Expanding $f(\mathbf{x})$ using Taylor's series over S_ϵ (Fig. 2), we have

$$\begin{aligned} J_3(\xi_o) = &\int_{S-S_\epsilon} f(\mathbf{x})\frac{1}{|\mathbf{x}-\xi_o|^2}(r_{,i}n_j - r_{,j}n_i)dS \\ &+\lim_{D\to 0}\Big\{f(\xi_o)\int_{S_\epsilon}\frac{1}{|\mathbf{x}-\xi|^2}(r_{,i}n_j - r_{,j}n_i)dS + 0(S_\epsilon)\Big\}. \end{aligned} \tag{C2}$$

If we let $S_\epsilon\to 0$ so as to eliminate all terms of order S_ϵ, we have

$$\begin{aligned} J_3(\xi_o) = &I_3(\xi_o) \\ &+\lim_{S_\epsilon\to 0}\Big\{f(\xi_o)\lim_{D\to 0}\int_{S_\epsilon}\frac{1}{|\mathbf{x}-\xi|^2}(r_{,i}n_j - r_{,j}n_i)dS\Big\} \end{aligned} \tag{C3}$$

where $I_3(\xi_o)$ is as defined in equation (B7). The second term in local coordinates, as in Fig. 2, is given by

$$\begin{aligned} &\lim_{D\to 0}\int_{S_\epsilon}\frac{1}{|\mathbf{x}-\xi|^2}(r_{,i}n_j - r_{,j}n_i)dS \\ &\qquad = n_j(\xi_o)\int_o^{2\pi}\rho_{,i}(\theta)\ln|2\rho(\theta)|d\theta. \end{aligned} \tag{C4}$$

In the limit as $S_\epsilon\to 0$, both $I_3(\xi_o)$ and the second term of equation (C3) are unbounded. But these unbounded terms are equal and opposite in sign (equations (B8) and (C4)) which results in cancellation and $J_3 = I_3^{**}$. This is the motivation for defining $I_3^{**}(\xi_o)$ as in equation (B10).

Next consider

$$\begin{aligned} J_4(\xi_o) &\equiv \lim_{D\to 0}\int_S f(\mathbf{x})\frac{\partial^2 G(\mathbf{x},\xi)}{\partial\xi_r\partial n(x)}dS \\ &\equiv -\lim_{D\to 0}\int_S f(\mathbf{x})G_{,rk}(\mathbf{x},\xi)n_k(x)dS. \end{aligned} \tag{C5}$$

Expanding $f(\mathbf{x})$ using Taylor's series as before,

$$\begin{aligned} J_4(\xi_o) = &-\int_{S-S_\epsilon} f(\mathbf{x})G_{,rk}(\mathbf{x},\xi_o)n_k(\mathbf{x})dS \\ &+\lim_{D\to 0}\Big\{-f(\xi_o)\int_{S_\epsilon} G_{,rk}(\mathbf{x},\xi)n_k(\mathbf{x})dS \\ &-f_{,p}(\xi_o)\int_{S_\epsilon} G_{,rk}(\mathbf{x},\xi)(\mathbf{x}-\xi_o)_p n_k(\mathbf{x})dS + 0(S_\epsilon)\Big\}. \end{aligned} \tag{C6}$$

For the same reason as before for $J_3(\xi_o)$, taking the limit $S_\epsilon\to 0$ and using the relations for ξ_o close to the boundary, Fig. 2, i.e.,

$$\begin{aligned} &f(\xi_o)\int_{S_\epsilon} G_{,rk}(\mathbf{x},\xi)n_k(\mathbf{x})dS \\ &= f(\xi_o)\frac{n_r(\xi_o)}{4\pi}\int_0^{2\pi}\Big\{\frac{1}{\sqrt{\rho^2(\theta)+D^2}} - \frac{D^2}{[\rho^2(\theta)+D^2]^{3/2}}\Big\} \\ &\qquad d\theta + 0(D) \end{aligned} \tag{C7}$$

$$\begin{aligned} &f_{,p}(\xi_o)\int_{S_\epsilon} G_{,rk}(\mathbf{x},\xi)(\mathbf{x}-\xi_o)_p n_k(\mathbf{x})dS \\ &= f_{,p}(\xi_o)\frac{n_r(\xi_o)}{4\pi}\int_o^{2\pi}\rho_{,p}(\theta)\Big\{\frac{2\rho(\theta)}{\sqrt{\rho^2(\theta)+D^2}} - \ln|\rho(\theta) \\ &+\sqrt{\rho^2(\theta)+D^2}| - \frac{\rho(\theta)D^2}{[\rho^2(\theta)+D^2]^{3/2}} + \ln D\Big\}d\theta + 0(D), \end{aligned} \tag{C8}$$

Downloaded 03 May 2010 to 171.66.16.244. Redistribution subject to ASME license or copyright; see http://www.asme.org/terms/Terms_Use.cfm

we get

$$J_4(\xi_o) = I_4(\xi_o) + \lim_{S_\epsilon \to 0}\left\{-f(\xi_o)\frac{n_r(\xi_o)}{4\pi}\int_o^{2\pi}\frac{d\theta}{\rho(\theta)}\right.$$

$$\left.+f_{,p}(\xi_o)\frac{n_r(\xi_o)}{4\pi}\int_o^{2\pi}\rho_{,p}(\theta)\ln|2\rho(\theta)|\,d\theta\right\}. \quad \text{(C9)}$$

In the limit as $S_\epsilon \to 0$, $I_4(\xi_o)$ and the last two terms of equation (C9) are unbounded. But these unbounded terms are equal and opposite in sign (equations (B16) and (B18)), and as a result $J_4(\xi_o) = I_4^{**}(\xi_o)$. This observation on the cancellation of the infinities is the motivation for defining $I_4^{**}(\xi_o)$ as in equation (B20).

To encapsulate all of this, we may write

$$\lim_{S_\epsilon \to 0}\left\{\int_{S-S_\epsilon} H(\mathbf{x},\xi_o)g(\mathbf{x})dS(\mathbf{x}) + A(\xi_o,S_\epsilon)\right\} \equiv L(\xi_o) \quad \text{(C10)}$$

where $L(\xi_o)$ is the finite value of a singular integral with singular kernel $H(\mathbf{x},\xi_o)$ and density $g(x)$. If H is only weakly singular, A may be zero and no restrictions on the shape of S_ϵ or how it goes to zero are needed. If H is more strongly singular, A may still be zero provided $S_\epsilon \to 0$ in a special (CPV) manner and $g(\mathbf{x})$ is $C^{0,\alpha}$. If H is hypersingular, a nonzero A is required to cancel the unbounded terms in the integral and the precise form of A can be (intuitively) provided if $L(\xi_o)$ arises in a BIE/BEM context. For this a price on $g(\mathbf{x})$ is extracted. Now $g(\mathbf{x})$ must be $C^{1,\alpha}$ (see Appendix B) and the result of this is the HFP. Clearly, special restrictions on S_ϵ to yield a finite L, with zero A, a process called the CPV, could be regarded as a special case of the HFP.

APPENDIX D

Consider the term $J_4(\xi_o)$ as in equation (C5). Let S_ϵ be a small neighborhood about the point ξ_o such that the density function $f(\xi_o)$ is continuous about ξ_o but $f_{,p}(\xi_o)$ is not continuous across the line abc as in Fig. 9. (Such would be the case if the line abc were the junction between two conforming isoparametric elements with nodes at a, b, and c.) Let $f_{,p}^1(\xi_o)$ and $f_{,p}^2(\xi_o)$ represent the gradient of the density function over S_ϵ^1 and S_ϵ^2, respectively, about ξ_o. For S_ϵ as defined above, and expanding the density function on each side of the line abc, one obtains

$$J_4(\xi_o) = -\int_{S-S_\epsilon} f(\mathbf{x})G_{,rk}(\mathbf{x},\xi_o)n_k(\mathbf{x})dS$$

$$+\lim_{D\to 0}\left\{-f(\xi_o)\int_{S_\epsilon} G_{,rk}(\mathbf{x},\xi)n_k(\mathbf{x})dS\right.$$

$$-f_{,p}^1(\xi_o)\int_{S_\epsilon^1} G_{,rk}(\mathbf{x},\xi)(\mathbf{x}-\xi_o)_p n_k(\mathbf{x})dS$$

$$\left.-f_{,p}^2(\xi_o)\int_{S_\epsilon^2} G_{,rk}(\mathbf{x},\xi)(\mathbf{x}-\xi_o)_p n_k(\mathbf{x})dS + 0(D)\right\} \quad \text{(D1)}$$

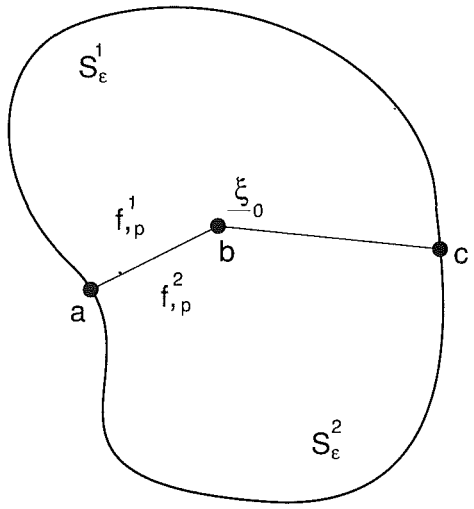


Fig. 9 Smoothness requirement not satisfied across line abc

where the first term is equal to $I_4(\xi_o)$, equation (B14), and the second term is as given in equation (C7). The third and the fourth terms when combined give

$$-f_{,p}^1(\xi_o)\frac{n_r(\xi_o)}{4\pi}\int_0^{\theta_1}\rho_{,p}(\theta)\left\{\frac{2\rho(\theta)}{\sqrt{\rho^2(\theta)+D^2}} - \ln|\rho(\theta)\right.$$

$$\left.+\sqrt{\rho^2(\theta)+D^2}| - \frac{\rho D^2}{[\rho^2(\theta)+D^2]^{3/2}}\right\}d\theta - f_{,p}^2(\xi_o)\frac{n_r(\xi_o)}{4\pi}$$

$$\times\int_{\theta_1}^{2\pi}\rho_{,p}(\theta)\left\{\frac{2\rho(\theta)}{\sqrt{\rho^2(\theta)+D^2}} - \ln|\rho(\theta)+\sqrt{\rho^2(\theta)+D^2}|\right.$$

$$\left.-\frac{\rho D^2}{[\rho^2(\theta)+D^2]^{3/2}}\right\}d\theta - \ln D\left\{f_{,p}^2(\xi_o)\int_o^{\theta_1}\rho_{,p}(\theta)d\theta\right.$$

$$\left.+f_{,p}^1(\xi_o)\int_{\theta_1}^{2\pi}\rho_{,p}(\theta)d\theta\right\}. \quad \text{(D2)}$$

The above expression does not exist in the limit as $D\to 0$ as the term multiplying $\ln D$ is never zero for $f_{,p}^2(\xi_o)$ not equal to $f_{,p}^1(\xi_o)$, i.e., when the gradient of the density function is not continuous. If $f_{,p}^2(\xi_o) = f_{,p}^1(\xi_o)$, then the term multiplying $\ln D$ in (D2) vanishes, and in the limit as $D\to 0$, the entire expression (D2) reduces to the last term of equation (C9).

It has been shown by P. A. Martin (private communication), for a one-dimensional case, that continuity of derivatives C^1, although sufficient to eliminate the (comparable) $\ln D$ term as shown, is still insufficient to give a finite limit as $D\to 0$. The stronger condition $C^{1,\alpha}$ is required for a finite limit.

Downloaded 03 May 2010 to 171.66.16.244. Redistribution subject to ASME license or copyright; see http://www.asme.org/terms/Terms_Use.cfm

Analysis of Surface Wave Generation by Laser Interference

K. J. Faran[1]
Mechanical Engineering Department.

R. J. Dwayne Miller
Chemistry Department and Laboratory for Laser Energetics.

S. M. Gracewski
Mechanical Engineering Department, Assoc. Mem. ASME

University of Rochester, Rochester, NY 14627

An analytical solution for thermal excitation of elastic waves in an homogeneous, isotropic, elastic half-space resulting from a pulsed laser interference pattern incident on the solid surface is presented. The spacially-periodic laser field absorbed by the surface causes rapid heating within the optical penetration depth. Thus, a temperature field is generated which can be modeled as being spacially harmonic along the free edge, decaying exponentially with depth, and having a Heaviside dependence on time. Transform techniques yield expressions for the resulting transverse and normal displacements within the laser interference region in terms of infinite integrals over frequency. The integrands contain poles indicating the expected Rayleigh waves propagating along the surface, as well as branch points corresponding to the bulk longitudinal and transverse wave speeds. The solution is obtained by integrating numerically in the complex frequency plane with an appropriate contour around the poles and branch cuts. Normal and transverse displacements are plotted as functions of time and depth for various materials and temperature fields.

Introduction

Surface acoustic wave (SAW) generation by laser-induced spacially-periodic heating has been proposed by Lee and White (1968). A mask, with alternating transparent and opaque strips, placed between the laser and sample was used to create a spacially-periodic illumination and demonstrate the technique. Laser interference was suggested as an alternate means of producing a periodic optical pattern. Ash et al. (1980) and Cashier (1970) have also reported on SAW generation by periodic surface illumination using a mask and laser interference, respectively. In both, a one-dimensional approximation was used to predict the normal surface displacement due to thermal expansion.

A two-dimensional plane-strain solution was presented by Lee and Jackson (1975) for elastic waves generated by a time-harmonic spacially-periodic optical radiation incident on the surface of a half-space. The induced temperature field was used as a boundary condition only. Royer and Dieulesaint (1984) and White (1986) both consider a finite optical penetration depth, but incident on a plate with thickness comparable to the spatial peak-to-peak spacing of the incidient light. In both cases, the solution is presented for time-harmonic excitation.

In the present paper, the transient plane-strain elastic wave solution will be presented for a spacially-harmonic optical pattern with finite penetration incident on the surface of an isotropic half-space. The optical pattern is created by the interference of two picosecond laser pulses separated by an angle θ incident on the solid surface (Fig. 1). A similar technique used to generate bulk ultrasonic waves has been described theoretically and verified experimentally by Nelson and Fayer (1980) and Nelson et al. (1982). The resulting SAW wavelength $\Lambda = \lambda_0/[2 \sin(\theta/2)]$ is equal to the interference pattern spacing, where λ_0 is the wavelength of the laser light. By adjusting the angle θ, continuously tunable, coherent ultrasonic waves can be obtained. The amplitude of the resulting SAW can be determined by diffraction of a third time-delayed laser pulse. From measurements of diffraction efficiency as a function of the time delay of the detection pulse, the SAW wave speed and attenuation can be determined. Therefore, this technique provides a method of measuring surface properties in a highly-localized region.

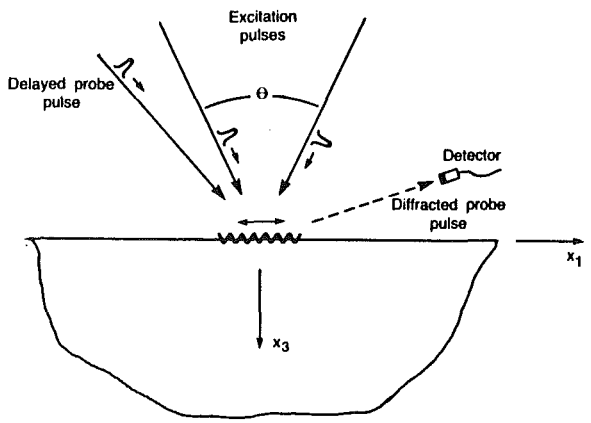


Fig. 1 Solid half-space showing the generation and detection laser pulse configuration

[1]Currently with the U. S. Army.

Contributed by the Applied Mechanics Division of THE AMERICAN SOCIETY OF MECHANICAL ENGINEERS for publication in the JOURNAL OF APPLIED MECHANICS.

Discussion on this paper should be addressed to the Technical Editor, Leon M. Keer, The Technological Institute, Northwestern University, Evanston, IL 60208, and will be accepted until two months after final publication of the paper itself in the JOURNAL OF APPLIED MECHANICS. Manuscript received by the ASME Applied Mechanics Division, May 26, 1988; final revision, March 3, 1989.

Copyright © 1990 by ASME
Downloaded 03 May 2010 to 171.66.16.244. Redistribution subject to ASME license or copyright; see http://www.asme.org/terms/Terms_Use.cfm

Problem Formulation

The plane-strain solution will be derived for an isotropic, linear elastic half-space with a traction-free surface subject to the temperature field $T(\mathbf{x}, t)$ induced by the optical interference pattern. This temperature field within the illuminated area can be represented by

$$(T-T_0)=\frac{\Delta T_{\max}}{2}\left[1+\sin\left(\frac{2\pi x_1}{\Lambda}\right)\right]e^{-ax_3}H(t), \qquad (1)$$

where $H(t)$ is the unit step function, T_0 is the initial temperature, a is the decay constant determined by the optical absorption, and $\Delta T_{\max}$ is the maximum temperature rise. This expression is similar to the temperature profile used to model bulk wave generation by laser interference (see Nelson and Fayer, 1980), but with the exponential decay with depth included to account for absorption. For this representation to closely approximate the actual temperature distribution, the following assumptions must hold: (1) the excitation pulse and molecular relaxation times are much shorter than the acoustic time constant such that the heat deposition can be considered instantaneous; (2) the time scale for thermal diffusion is longer than the experimental time-scale so that diffusion can be neglected; (3) the temperature variations due to material strain are negligible, and therefore the thermoelastic equations decouple; and (4) the laser interference region is much larger than the peak-null spacing such that peak-to-peak intensity variations can be neglected.

The governing equations are reduced to wave equations by introducing the displacement potentials ϕ and ψ and for plain strain take the form:

$$\nabla^2\phi-\frac{1}{c_l^2}\frac{\partial^2\phi}{\partial t^2}=\frac{a'(3\lambda+2\mu)}{\lambda+2\mu}(T-T_0), \qquad (2)$$

$$\nabla^2\psi-\frac{1}{c_t^2}\frac{\partial^2\psi}{\partial t^2}=0,$$

with

$$\mathbf{u}=\nabla\phi+\nabla\times(\psi\mathbf{e}_2),$$

$$\tau=\lambda\nabla\cdot\mathbf{u}\mathbf{I}+\mu[\nabla\mathbf{u}+(\nabla\mathbf{u})^T]-a'(3\lambda+2\mu)(T-T_0)\mathbf{I},$$

$$\nabla=\frac{\partial}{\partial x_1}\mathbf{e}_1+\frac{\partial}{\partial x_3}\mathbf{e}_3,$$

where $\mathbf{u}$ is the displacement vector, τ is the stress tensor, λ and μ are the Lamé constants, ρ is the density, a' is the coefficient of linear thermal expansion, and c_l and c_t are the longitudinal and transverse wave speeds, respectively. These governing equations with the temperature field given by equation (1) must be solved subject to zero initial conditions, traction-free boundary conditions along the surface $x_3=0$, and the appropriate radiation conditions as $x_3\to\infty$.

Spacially-Harmonic Solution

The potentials resulting from the spacially-harmonic term of the applied temperature field given in equation (1) will also be spacially harmonic and of the form, $\phi(x_1, x_3, t)=\Phi(x_3, t)\sin(\beta x_1)$, $\psi(x_1, x_3, t)=\Psi(x_3, t)\cos(\beta x_1)$, where $\beta=2\Pi/\Lambda$. This form reduces the governing equations to partial differential equations of x_3 and t.

The solution of the equations of motion, obtained by using Laplace Transforms in time and substituting the resulting displacements into the displacement-potential relations, is

$$u_1(x_1, x_3, t)=\frac{A\cos(\beta x_1)}{2\Pi i}\lim_{\gamma\to\infty}\int_{\zeta-i\gamma}^{\zeta+i\gamma}\left[\beta e^{-ax_3}+\beta C_1 e^{-b_l x_3}-b_t C_2 e^{-b_t x_3}\right]\frac{e^{\omega t}d\omega}{(a^2-b_t^2)\omega}, \qquad (3)$$

$$u_3(x_1, x_3, t)=\frac{A\sin(\beta x_1)}{2\Pi i}\lim_{\gamma\to\infty}\int_{\zeta-i\gamma}^{\zeta+i\gamma}\left[ae^{-ax_3}+b_l C_1 e^{-b_l x_3}+\beta C_2 e^{-b_t x_3}\right]\frac{e^{\omega t}d\omega}{(a^2-b_t^2)\omega},$$

where $c_l^2=(\lambda+2\mu)/\rho$, $c_t^2=\mu/\rho$, $b_l^2=\beta^2+\omega^2/c_l^2$, $b_t^2=\beta^2+\omega^2/c_t^2$ and $A=\Delta T_{\max}a'(3\lambda+2\mu)/2(\lambda+2\mu)$. The coefficients $C_1(\omega)$ and $C_2(\omega)$ are found by substituting the solution into the boundary conditions to obtain $C_1(\omega)=[4\beta^2 b_t a-(b_t^2+\beta^2)^2]/R$, $C_2(\omega)=2\beta(\beta^2+b_t^2)(b_l-a)/R$, where $R(\omega)=(\beta^2+b_t^2)^2-4\beta^2 b_l b_t$ is the Rayleigh wave equation. The branches of the square-root functions b_l and b_t must be chosen such that the radiation condition is satisfied and the solution is finite as $x_3\to\infty$.

One-Dimensional Solution

The remaining term of the applied temperature field (equation (1)) is independent of x_1, the coordinate parallel to the half-space boundary. The governing equations and boundary conditions for this temperature field reduce to a one-dimensional system of equations for the normal displacements $u_3'(x_3, t)$. The tangential displacement u_1' is identically zero.

Laplace transforms can be used to obtain the closed-form solution

$$u_3'(x_3, t)=-(A/a)\left[e^{-ax_3}-\frac{1}{2}e^{-a(c_l t+x_3)}-\frac{1}{2}e^{-a|c_l t-x_3|}\right]H(t). \qquad (4)$$

The total normal displacement field, $u_3{}^T$, can then be obtained by adding u_3' to the normal displacement field, u_3, for the spacially-harmonic solution given in equation (3).

Numerical Integration

The equations were nondimensionalized before numerical results were obtained. The nondimensional variables are

$$\hat{x}_1=\beta x_1,\ \hat{x}_3=ax_3,\ \hat{t}=t/\tau_R,$$

$$\hat{\omega}=\omega/\omega_R,\ \hat{u}_1=\beta u_1,\ \hat{u}_3=\beta u_3$$

$$\hat{c}_l=c_l/c_R,\ \hat{c}_t=c_t/c_R$$

where c_R is the Rayleigh wave speed, $\omega_R=\beta c_R$ is the frequency of the Rayleigh wave, and $\tau_R=2\pi/\omega_R$ is the period of the Rayleigh wave. In nondimensional form, there is one parameter a/β which defines the length-scale ratios of the temperature profile. The material is defined by Poisson's ratio ν and the coefficient A which arises only as a constant factor proportional to the incident energy.

A change of variables $\bar{\omega}=-i\hat{\omega}$ was used to write the solution in terms of integrals along the real axis. The contour of integration was deformed into the complex $\bar{\omega}$ plane to avoid the poles and branch cuts on the real axis. The contour used, which is deformed into the lower half plane to satisfy the radiation conditions, is shown in Fig. 2.

Results and Discussion

Numerical results are presented for normal and transverse displacements versus time and depth for various values of the parameters a/β and ν. The solid curve in Fig. 3(*a*) shows the variation with time of the normal surface displacement at $x_1=\pi/2$ for a spacially-harmonic applied temperature field with $\nu=0.062$, $a/\beta=6.0$, $a'=9.943\times10^{-6}/°C$, and the average heat input per unit surface area $Q=5\times10^4$ J/cm^2. These parameters were chosen to match the experimental conditions for surface wave generation in the (001) plane of an n-

Downloaded 03 May 2010 to 171.66.16.244. Redistribution subject to ASME license or copyright; see http://www.asme.org/terms/Terms_Use.cfm

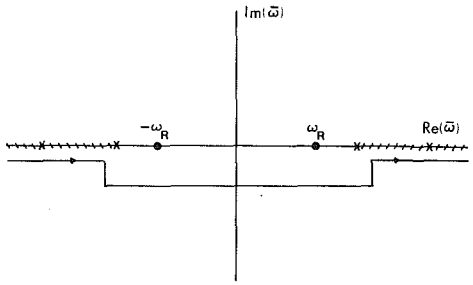


Fig. 2 · Contour of integration

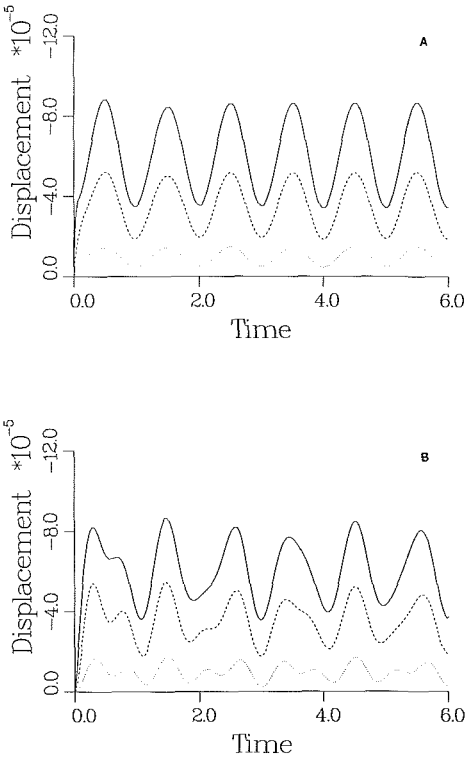


Fig. 3 Nondimensional surface displacements versus nondimensional time for $a/\beta = 6.0$ (solid line), $a/\beta = 1.0$ (dashed line), and $a/\beta = 1/2\pi$ (dotted line): (*a*) normal displacement and (*b*) transverse displacement. For all curves, $\nu = 0.062$ and $Q = 5 \times 10^4$ J/cm^2.

TiO_2 crystal by the interference of two 100 psec, 355 nm laser pulses (Kasinski et al.). This value of Poisson's ratio yields the correct wave speeds in the (001) plane and a' was set equal to the coefficient of linear expansion normal to this plane. Results for the spacially-harmonic temperature field are presented here, since the spacially-uniform term of the temperature field will not generate surface waves and the uniform field results cannot be detected by the probe laser pulse.

The solid curve in Fig. 3(*a*) shows an initial rapid rise in displacements followed by a nearly-harmonic oscillation at the Rayleigh wave frequency ($\omega_R = c_R\beta$ with nondimensional period $\tau/\tau_R = 1.0$). The other curves in Fig. 3(*a*) demonstrate that the surface wave amplitude and initial rise decrease as a/β decreases. For constant Λ, decreasing a/β corresponding to increasing optical penetration depth. As the penetration depth increases, more energy is transformed into bulk waves and therefore smaller SAW displacements are expected. For $a/\beta = 1/2\pi$, the optical penetration depth is equal to the interference pattern spacing.

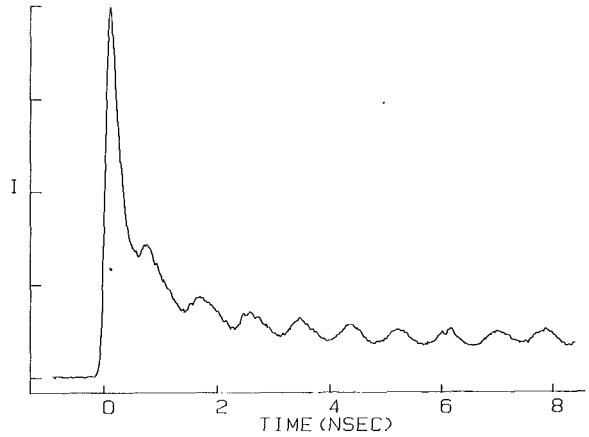


Fig. 4 Intensity of the diffracted detection laser pulse versus time delay for an n-TiO_2 surface (doping concentration 4×10^{18}/cc) in air. Excitation power = 2×10^{15} photons/cm^2, optical penetration depth = 700Å and laser interference pattern spacing = 2.7 μm ($a/\beta = 5.9$).

In Fig. 3(*b*), the transverse surface displacements at $x_1 = 0$ are plotted versus time for the same parameters as in Fig. 3(*a*). The presence of bulk wave contributions causes the initial non-periodic displacements. Superimposed on the harmonic oscillation with normalized period $\tau/\tau_R = 1.0$ is another oscillation with normalized period $\tau/\tau_R \sim 0.6$. This period corresponds to the longitudinal wave speed and therefore is evidence that a longitudinal wave component propagating parallel to the surface is initially generated. The ratio of the longitudinal-wave to Rayleigh-wave contributions increases as penetration depth increases, as expected. The longitudinal wave contribution decreases with time. Bulk waves eventually propagate away from the surface, and therefore at large times, the transverse displacements will also be harmonic with a period equal to τ_R.

Experimental results in Fig. 4 show a harmonic modulation superimposed on an initially large, but rapidly decaying signal resulting from the diffraction grating generated by free carriers. (See Kasinski et al. for a discussion of the free carrier diffraction grating.) The nonexponential behavior of the free carrier grating results from three-body Auger recombination of the photogenerated carriers. The harmonic modulation has a beat frequency which corresponds to a wave speed equal to $4.84 \pm 0.01 \times 10^5$ cm/sec which is in excellent agreement with the known SAW speed for $Ti0_2(001)$ surfaces (4.81×10^5 cm/sec). This indicates the existence of coherent surface acoustic waves. From the measured diffraction intensity, the surface displacement is determined to be 0.05 ± 0.02 nm. This measured value is in good agreement with the calculated value 0.022 nm determined from the peak to null distance of the solid curve in Fig. 3(*a*).

Figures 5(*a*) and 5(*b*) show the effect of Poisson's ratio on the normal and transverse surface displacements, respectively. As Poisson's ratio increases, the normal surface displacement also increases, but the amplitude of the surface wave (peak-null distance) decreases. Also, the transverse displacements show a larger second peak as Poisson's ratio increases, possibly indicating a larger bulk wave contribution.

Normal displacement versus depth is plotted for spacially uniform and spacially-harmonic heating in Figs. 6(*a*) and 6(*b*), respectively. It is obvious from Fig. 6(*a*) and the result in equation (4) that the spacially-uniform heating results in a wave traveling away from the surface with the longitudinal wave speed, superimposed upon a time-invariant displacement which decays exponentially with depth. The displacement field for the spacially-harmonic heating is more complex, however, the wave propagating away from the surface can still be identified.

Downloaded 03 May 2010 to 171.66.16.244. Redistribution subject to ASME license or copyright; see http://www.asme.org/terms/Terms_Use.cfm

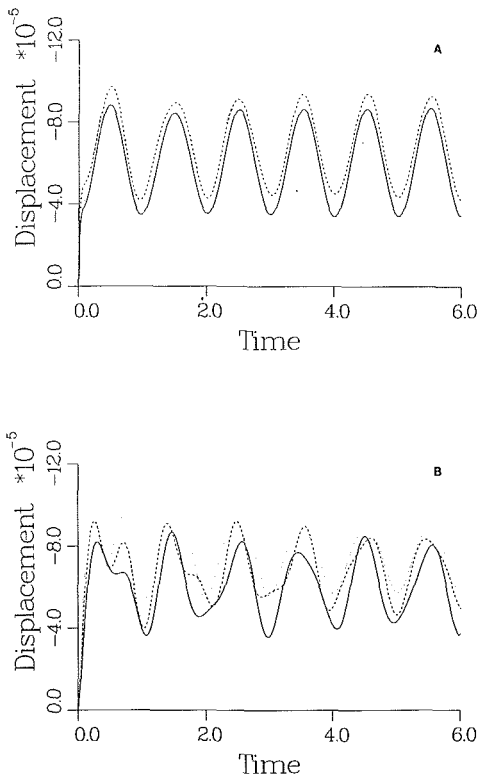


Fig. 5 Nondimensional surface displacements versus nondimensional time for $\nu = 0.062$ (solid line), $\nu = 0.2$ (dashed line), and $\nu = 0.3$ (dotted line): (*a*) normal displacement and (*b*) transverse displacement. For all curves, $a/\beta = 6.0$ and $Q = 5 \times 10^4$ J/cm^2.

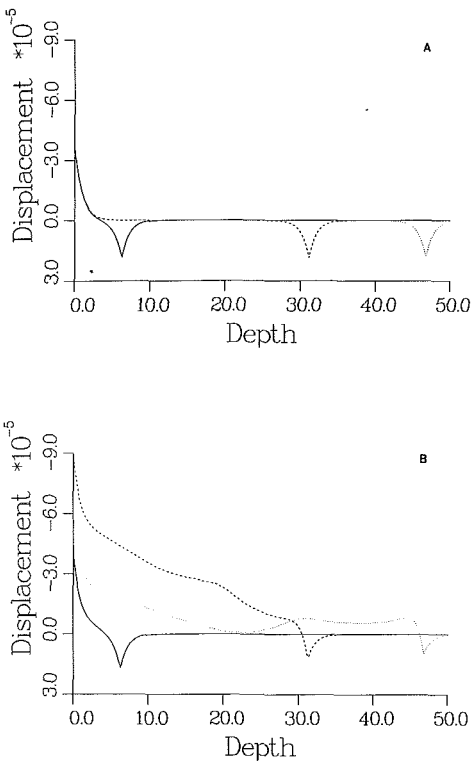


Fig. 6 Nondimensional normal displacements versus nondimensional depth for $t = 0.1$ (solid line), $t = 0.5$ (dashed line), and $t = 0.75$ (dotted line): Results for (*a*) spacially-uniform excitation and (*b*) spacially-harmonic excitation. For all curves $\nu = 0.062$, $a/\beta = 6.0$, $Q = 5 \times 10^4$ J/cm^2.

Summary

A transient solution is presented for the elastic wave fields in a half-space resulting from an applied temperature field generated by the interference of two laser pulses. The temperature profile is spacially harmonic parallel to the free surface and decays exponentially with depth. Numerical results are presented for normal and transverse displacements as functions of time and depth. The calculated surface wave amplitude compares well with experiments on an n-TiO_2 crystal, even without accounting for the crystal anisotropy. Contributions from both the Rayleigh surface wave and a wave traveling parallel to the surface at the longitudinal wave speed are evident in the surface displacement plots. In these plots, the effect of the longitudinal wave component decays with time as the energy propagates away from the surface. The effect of the two parameters ν and a/β was also studied. For constant heat input, the amplitude of the surface wave decreases as the ratio of penetration depth to interference pattern spacing increases (or a/β decreases). Also, the surface wave amplitude decreases as Poisson's ratio ν increases.

References

Ash, E. A., Dieulesaint, E., and Rakouth, H., 1980, "Generation of Surface Acoustic Waves by Means of a C. W. Laser," *Elect. Lett.*, Vol. 16, No. 12, pp. 470–472.

Cachier, G., 1970, "Optical Excitation of High-Amplitude Surface Waves," *Appl. Phys. Lett.*, Vol. 17, No. 10, pp. 419–421.

Kasinski, J. J., Gomez-Jahn, L. A., Faran, K. J., Gracewski, S. M., and Miller, R. J. D., 1989, "Picosecond dynamics of surface electron transfer processes: Surface restricted transient grating studies of the $n-T_iO_2/H_2O$ interface," J. Chem. Phys., Vol. 90, pp. 1253–1269.

Lee, R. E., and Jackson, D. W., 1975, "An Optical Detector Based on Surface-Acoustic-Wave Generation," IEEE *Ultrasonics Symp. Proc.*, Cat. #75 CHO 994-4SU, pp. 126–129.

Lee, R. E., and White, R. M., 1968, "Excitation of Surface Elastic Waves by Transient Surface Heating," *Appl. Phys. Lett.*, Vol. 12, No. 1, pp. 12–14.

Nelson, Keith A., and Fayer, M. D., 1980, "Laser-induced Phonons: A Probe of Intermolecular Interactions in Molecular Solids," *J. Chem. Phys.*, Vol. 72, No. 9, pp. 5202–5218.

Nelson, Keith A., Miller, R. J., Dwayne, Lutz, D. R., and Fayer, M. D., 1982, "Optical Generation of Tunable Ultrasonic Waves," *J. Appl. Phys.*, Vol. 53, No. 2, pp. 1144–1149.

Royer, D., and Dieulesaint, E., 1984. "Analysis of Thermal Generation of Rayleigh Waves," *J. Appl. Phys.*, Vol. 9, No. 1, pp. 2507–2511.

White, Richard M., 1986, "Thermoelastic Coupling to Lamb Waves," *IEEE Ultrasonics Symp.*, pp. 411–415.

Downloaded 03 May 2010 to 171.66.16.244. Redistribution subject to ASME license or copyright; see http://www.asme.org/terms/Terms_Use.cfm

On the Free Vibrations of Suspended Cables With Frictional End Restraint

H. M. Irvine

Professor and Head,
School of Civil Engineering,
The University of New South Wales,
Kensington, N.S.W. 2033, Australia

Results are obtained for the free vibrations of suspended cables for which longitudinal end restraint is supplied by friction. The problem is germane to submarine telecommunication cables. It is shown that all modes of vibration are independent of any characteristic dimensionless parameters, at least insofar as the linear theory applies to flat-sag cables, and the friction capability of the soil at the mudline is low. This sets the problem apart from the traditional, firmly founded suspended cable where, for some of the important in-plane modes, there is variability in the results. The theory is of importance in determining the vortex-induced vibratory response of suspended cable spans to currents of various sorts.

Introduction

In recent years there have been a lot of investigations of the vibrational behavior of suspended cables, typically of rather flat sag—for these are of the most structural importance—in which the nature of the in-plane modes of vibration has been thoroughly explored. The dual effects of Hookean stiffness and gravity stiffness make the problems unusual and, indeed, this interplay of gravity and elasticity may be expressed by a dimensionless coefficient, called λ^2 in the literature, the size of which determines the physical behavior of the cable. The engineering theory of flat-sag cables is now fairly well developed (Irvine, 1981), and a recent series of studies (see, for example, Triantafyllou, 1984, 1987) have now more or less completed our understanding of the dynamical behavior of cables.

In all of this, the cables are assumed to be firmly anchored or, if some anchorage compliance is evident, then this may be accounted for by an equivalent spring.

The purpose of this paper is to investigate the in-plane free vibrations of cables which, outside of the suspended span, do not stop abruptly but, rather, continue on and longitudinal restraint is supplied by skin friction in these anchor regions. The problem is relevant to conditions in some parts of the sea floor where spans occur intermittently in bottom-hugging submarine cables.

Static Equilibrium Profile

The cable is modeled as shown in Fig. 1.

From the classical theory for flat-sag uniform cables we have

$$y=\frac{mgl^2}{2H}\,\frac{x}{l}\left(1-\frac{x}{l}\right),$$

in which the sag (at midspan) d is

$$d=\frac{mgl^2}{8H}. \tag{1}$$

The length of the anchor regions, L, is given by the statement of longitudinal equilibrium $fL=H$.

The frictional capability of submarine sediments is not well understood but is believed to frequently be quite low, with the result that the influence of the suspended span extends a considerable distance into the regions to each end of the span. That is, typically, $L \gg l$.

The problem is closed, in the sense of finding another equation, apart from equation (1), in which the two unknowns, (namely, d, and horizontal component of cable tension, H) occur, by writing an equation of longitudinal displacement compatibility.

The extra length of cable in the suspended span, over and above the span itself, is given by

$$\int_o^l (ds-dx) = \int_o^l \left(\frac{ds}{dx}-1\right)dx$$

$$\approx \frac{1}{2}\int_o^l \left(\frac{dy}{dx}\right)^2 dx$$

$$\approx \frac{8}{3}\left(\frac{d}{l}\right)^2 l.$$

This extra length is supplied by the stretching of the cable in the (assumed lengthy) anchor regions, namely

$$2\times\frac{1}{2}\,\frac{HL}{EA}=\frac{H^2}{fEA}.$$

Therefore, the second equation reads

Contributed by the Applied Mechanics Division of THE AMERICAN SOCIETY OF MECHANICAL ENGINEERS for publication in the JOURNAL OF APPLIED MECHANICS.

Discussion on this paper should be addressed to the Technical Editor, Leon M. Keer, The Technological Institute, Northwestern University, Evanston, IL 60208, and will be accepted until two months after final publication of the paper itself in the JOURNAL OF APPLIED MECHANICS. Manuscript received by the ASME Applied Mechanics Division, November 15, 1988; final revision, June 6, 1989.

Copyright © 1990 by ASME
Downloaded 03 May 2010 to 171.66.16.244. Redistribution subject to ASME license or copyright; see http://www.asme.org/terms/Terms_Use.cfm

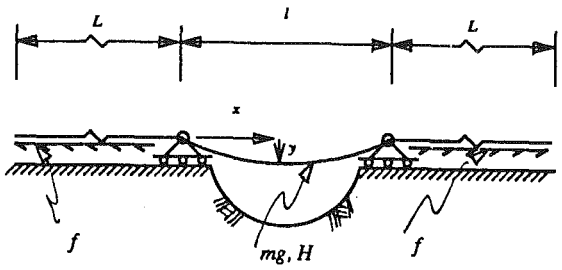


Fig. 1 Model of cable

$$\frac{H^2}{fEA}=\frac{8}{3}\left(\frac{d}{l}\right)^2 \cdot l.$$

which can be recast, with the help of equation (1), into an equation in which only H, for example, appears as an unknown. That is,

$$\frac{H^2}{fEA}=\frac{l}{24}\cdot\left(\frac{mgl}{H}\right)^2 \tag{3}$$

The static profile of the cable may now be evaluated explicitly.

Free Vibrations

Free vibrations about the static equilibrium profile may be separated into two components which, to first order, are uncoupled. These are the out-of-plane components and the in-plane components. The in-plane components may be further separated into symmetric and antisymmetric modes of vibration. This distinction is necessary because it is only the symmetric in-plane modes that generate additional cable tension. In point of fact, it is only these modes that give rise to a vibration problem that is, in any way, different from the standard free vibrational problem of the suspended, firmly anchored, cable (Irvine, 1981).

The out-of-plane modes of the present problem are the same as those for the classical taut string (viewed in plan, the suspended cable is a taut string and we assume sufficient lateral restraint at the span ends to force nodes there). We have, therefore, (see Irvine, 1981, for example, for the theory) for the nth out-of-plane mode

$$w_n(x)=A_n \sin\frac{n\pi x}{l} \quad , \quad n=1,2,3\ldots \tag{4a}$$

with the corresponding natural frequency given by

$$\omega_n=\frac{n\pi}{l}\left(\frac{H}{m}\right)^{1/2} \quad , \quad n=1,2,3\ldots . \tag{4b}$$

The in-plane modes have modal components that are largely vertical when the sag-to-span ratio is small: That is, longitudinal inertia may be ignored. This is a standard assumption for flat-sag cable systems and has been borne out by experiments and field observations.

The antisymmetric in-plane modes are those that do not induce additional cable tension. This may be shown to be satisfied by the requirement

$$\int_o^l v(x)dx=0$$

where $v(x)$ is the vertical component of displacement in an in-plane mode.

The foregoing closure condition is satisfied by mode shapes of the form

$$v_n(x)=A_n \sin\frac{n\pi x}{l} \quad , \quad n=2,4,6\ldots \tag{5a}$$

with the corresponding natural frequencies

$$\omega_n=\frac{n\pi}{l}\left(\frac{H}{m}\right)^{1/2} \quad , \quad n=2,4,6\ldots . \tag{5b}$$

Like the out-of-plane modes, these in-plane modes are identical to those of the standard, firmly founded, suspended cable.

In the case of the symmetric in-plane modes we start with the equation of motion in the suspended span, namely

$$H\frac{\partial^2 v}{\partial x^2}+h\frac{d^2y}{dx^2}-m\frac{\partial^2 v}{\partial t^2}=0.$$

The middle term represents the contribution made to vertical equilibrium by the product of additional tension and the original, or static, profile curvature. In a taut string this term is negligibly small because the static profile, $y(x)$, is very small.

Letting

$$v(x,t)=v(x)e^{i\omega t}$$

$$h(t)=he^{i\omega t}$$

and noting that

$$\frac{d^2y}{dx^2}=\frac{-mg}{H},$$

yields

$$H\frac{d^2v}{dx^2}+m\omega^2 v=mg\frac{h}{H},$$

which is to be solved as a boundary value problem subject to boundary conditions of $v(0)=v(l)=0$. The solution is (see Irvine, 1981)

$$v(x)=\frac{h}{H}\cdot\left(\frac{mgl^2}{H}\right)\cdot\frac{1}{(\alpha l)^2}\left\{-\tan\frac{\alpha l}{2}\sin\alpha x-\cos\alpha x\right\} \tag{6}$$

where

$$(\alpha l)^2=\frac{m\omega^2 l^2}{H}.$$

We need another equation because we cannot establish the mode shape until $\alpha l(ie, \omega)$ is known. This, again, is derived from the requirements of compatibility. To first order the cable in the suspended span is longer than its static profile by the amount

$$\int_o^l \frac{dy}{dx}\frac{dv}{dx}dx=\frac{mg}{H}\int_o^l vdx$$

when vibration in a symmetric in-plane mode occurs.

This additional cable length is provided by further (periodic) stretching in the cable that comprises the anchor regions. Originally we had a stretch of

$$2\times\frac{1}{2}\frac{HL}{EA}=\frac{H^2}{fEA}.$$

For small variations in H, the static tension, we have a variation in stretch by the amount

$$\frac{2H\Delta H}{fEA}$$

or, in terms of the present dynamic problem,

$$\frac{2Hh}{fEA}$$

or, since $H=fL$, where L is the length of the anchor region to one end of the span, we have

Downloaded 03 May 2010 to 171.66.16.244. Redistribution subject to ASME license or copyright; see http://www.asme.org/terms/Terms_Use.cfm

$$h\frac{2L}{EA}.$$

If we wished to include the stretch of the suspended span itself, we would write this expression as

$$\frac{h(l+2L)}{EA}$$

but, for the reasons given at the start, it is often true that in submarine cables $L \gg l$. (See Appendix for further discussion of this point.)

Hence, the compatibility equation becomes

$$h\frac{2L}{EA} \approx \frac{mg}{H}\int_o^l v\,dx \tag{7}$$

and this may be compared with the standard, firmly anchored, suspended cable in which the compatibility equation is

$$\frac{hl}{EA} \approx \frac{mg}{H}\int_o^l v\,dx.$$

After substitution of equation (6) into equation (7), integration and rearrangement, we have the well-known result

$$\tan\frac{\alpha l}{2} = \frac{\alpha l}{2} - \frac{4}{\lambda^2}\left(\frac{\alpha l}{2}\right)^3 \tag{8}$$

in which, for the standard, firmly anchored, suspended cable,

$$\lambda^2 = \left(\frac{mgl}{H}\right)^2\left(\frac{EA}{H}\right) \tag{9a}$$

and, for the present problem

$$\lambda^2 = \left(\frac{mgl}{H}\right)^2\left(\frac{lEA}{2LH}\right). \tag{9b}$$

For the standard suspended cable, λ^2 is the parameter which dictates the nature of the response. For example, when λ^2 is small, we have response akin to that for a taut string—a load applied at one point causes deflection of the same sign along the whole span—while, when λ^2 is large, we have response akin to that of a suspension bridge cable—a load applied at one point causes the cable to lift up in other regions of the span (see Irvine (1981) for a full discussion of the physics of cable response). However, with the suspended cable anchored by end friction we note that equation (3) may be rearranged to

$$\frac{HL}{EA} = \frac{l}{24}\left(\frac{mgl}{H}\right)^2$$

or

$$\left(\frac{mgl}{H}\right)^2\left(\frac{lEA}{2LH}\right) = 12$$

or

$$\lambda^2 = 12. \tag{10}$$

In other words, λ^2 is not variable, even though the span profile geometry can vary significantly. This is unusual.

Our transcendental frequency equation (8) becomes

$$\tan\frac{\alpha l}{2} = \left(\frac{\alpha l}{2}\right) - \frac{1}{3}\left(\frac{\alpha l}{2}\right)^3$$

and the first nonzero root is

$$(\alpha l)_1 = 1.403\pi$$

while the second and higher symmetric modes are given quite accurately by

$$(\alpha l)_n \approx (2n-1)\pi \quad n = 2,3,4\ldots .$$

This may be expressed, insofar as the natural frequencies are concerned, as

$$\omega_1 = \frac{1.403\pi}{l}\left(\frac{H}{m}\right)^{1/2}$$

$$\omega_n \approx \frac{(2n-1)\pi}{l}\left(\frac{H}{m}\right)^{1/2}, \quad n = 2,3,4\ldots .$$

Discussion and Conclusions

Suspended cables that are anchored by frictional restraint have modes of vibration that are identical to those of the traditional, firmly founded suspended cable, with one notable exception. In the case of the symmetric (i.e., additional tension generating) in-plane modes the frequencies and mode shapes are fixed and are not dependent on the characteristic dimensionless parameter, λ^2, because it has been shown that λ^2 is constant for cables with this type of end restraint.

This is an unusual result that has one important ramification: In the case of in-line and cross-flow vortex induced vibration of suspended cable spans on the ocean floor, the fundamental natural frequencies are different. For in-line motion (i.e., vibration in the first out-of-plane mode), the natural frequency is

$$\omega_1 = \frac{\pi}{l}\left(\frac{H}{m}\right)^{1/2}$$

while, for cross-flow motion (i.e., vibration in the first in-plane mode), the natural frequency is

$$\omega_1 = \frac{1.403\pi}{l}\left(\frac{H}{m}\right)^{1/2}.$$

Futhermore, the difference is fixed and not variable. This information may be utilized when vortex-induced vibration studies are undertaken on spans which lie close to the ocean floor. In this area the fluid mechanics of the process is far from straightforward, although this is ameliorated to some degree because it appears that, for spans that satisfy the assumptions made in this paper (particularly that relating to low skin friction in the anchor regions), a reasonably accurate cable dynamics model can be constructed for the suspended span. It is assumed, of course, that buoyancy effects and added mass effects will be included in the cable model.

References

Irvine, H. H., 1981, *Cable Structures*, M.I.T. Press, Cambridge, Mass., p. 256.

Triantafyllou, M. S., 1984, "Linear Dynamics of Cables and Chains," *The Shock and Vibration Digest*, Vol. 16.

Triantafyllou, M. S., 1987, Dynamics of Cables and Chains," *The Shock and Vibration Digest*, Vol. 19.

APPENDIX

Results When Skin Friction is Not Low

(a) Only One Anchor Span. If, for example, one end of the cable is firmly anchored by its passage over a rock outcrop, there is only one anchor span.

Equation (3) becomes

$$\frac{1}{2}\frac{H^2}{fEA} = \frac{l}{24}\left(\frac{mgl}{H}\right)^2.$$

Equation (7) becomes

Downloaded 03 May 2010 to 171.66.16.244. Redistribution subject to ASME license or copyright; see http://www.asme.org/terms/Terms_Use.cfm

$$\frac{hL}{EA} \approx \frac{mg}{H} \int_o^l v dx,$$

and equation (9*b*) becomes

$$\lambda^2 = \left(\frac{mgl}{H}\right)^2 \left(\frac{lEA}{LH}\right),$$

and this leads to $\lambda^2 = 12$ as before.

(b) High Skin Friction in the Anchor Spans. In the main body of the paper we assumed low skin friction in the anchor spans. However, *if* the skin friction was high, we should obtain, in this limit, the result for a firmly founded cable, namely equation (8). This is not possible from the result $\lambda^2 = 12$.

If we go back to the compatibility equation, we have, in allowing for stretching *in* the span as well as in the anchor regions,

$$\frac{h(l+2L)}{EA} = \frac{mg}{H} \int_o^l v dx.$$

Following through with the analysis we have, for the symmetric in-plane modes, the transcendental equation

$$\tan \frac{\alpha l}{2} = \frac{\alpha l}{2} - \frac{4}{\lambda_*^2} \left(\frac{\alpha l}{2}\right)^3$$

where λ_*^2 is given by

$$\lambda_*^2 = \frac{12\lambda^2}{12+\lambda^2}$$

in which $\lambda^2 = (mgl/H)^2(EA/H)$. This definition of λ^2 is the traditional one (Irvine, 1981).

When the cable is taut and flat in the suspended span (implying high skin friction in the anchor spans) we have $\lambda^2 \to 0$ and so $\lambda_*^2 \to 0$ and we recover the classical result for the first mode of a taut string, namely

$$\omega_1 \approx \frac{\pi}{l} \left(\frac{H}{m}\right)^{1/2}.$$

On the other hand, when a reasonable sag is evident in the suspended span, implying low friction in the anchor spans, we have $\lambda^2 \to \infty$ and so $\lambda_*^2 \to 12$ which is the result in the main body of this paper.

Downloaded 03 May 2010 to 171.66.16.244. Redistribution subject to ASME license or copyright; see http://www.asme.org/terms/Terms_Use.cfm

Nonclassically Damped Dynamic Systems: An Iterative Approach

Firdaus E. Udwadia
Professor of Civil Engineering,
Decision Systems,
and Mechanical Engineering.
University of Southern California,
Los Angeles, CA 90089-1114

Ramin S. Esfandiari
Assistant Professor of Mathematics.
Lecturer of Mechanical Engineering,
California State University,
Long Beach, CA 90840-5005

This paper presents a new, computationally efficient, iterative technique for determining the dynamic response of nonclassically damped, linear systems. Such systems often arise in structural and mechanical engineering applications. The technique proposed in this paper is heuristically motivated and iteratively obtains the solution of a coupled set of second-order differential equations in terms of the solution to an uncoupled set. Rigorous results regarding sufficient conditions for the convergence of the iterative technique have been provided. These conditions encompass a broad variety of situations which are commonly met in structural dynamics, thereby making the proposed iterative scheme widely applicable. The method also provides new physical insights concerning the decoupling procedure and shows why previous approximate approaches for uncoupling nonclassically damped systems have led to large inaccuracies. Numerical examples are presented to indicate that, even under perhaps the least ideal conditions, the technique converges rapidly to provide the exact time histories of response.

I Introduction

The analysis of structural and mechanical systems subjected to dynamic loads is an area of great interest to engineers so that safe and reliable designs can be generated. A large number of such systems are modeled by linear differential equations described by

$$M\ddot{x}(t)+C\dot{x}(t)+Kx(t)=a(t);$$
$$x(t_0)=x_0,\ \dot{x}(t_0)=\dot{x}_0,\ t\epsilon(t_0,\ T] \tag{1}$$

where, $x(t)$ is an N vector of displacements; $a(t)$ is an N vector of force each component of which is generally taken to be a continuous function of time, t; and, M, K, and C are the mass, the stiffness, and the damping matrices, respectively. The numerical solution of equation (1), when the matrices M, K, and C can be simultaneously diagonalized by a suitable transformation, is obtained by decoupling the system and solving for each "mode" of vibration separately. This modal superposition technique, besides being useful when the system response is dominated by a relatively few number of lower modes, provides a conceptual simplicity which lends itself to an enhanced intuitive understanding of the system's response. This conceptual decoupling is also pivotal in the use of the so-called spectrum methods which have gained considerable acceptance in various fields of application, like earthquake engineering and shock and vibration analysis.

In most physical systems, the matrix M is positive definite (being related to the inertial mass properties of the system) and symmetric. Also, the matrix K is real and symmetric, a consequence of the Betty-Maxwell reciprocity relations. Under such conditions we are guaranteed to find a transformation that simultaneously diagonalizes both M and K (Noble, 1969). However, to obtain a transformation that simultaneously diagonalizes M, K and the damping matrix C, requires that the matrix C have a special form (Caughey, 1960; Caughey and O'Kelly, 1963). For passive systems, the matrix C is positive definite.

Often our lack of knowledge about the damping mechanism in large, complex systems does not permit a detailed specification of the damping matrix C, and, based on experience, the analyst often prescribes percentages of critical damping related to the various modes, which he suspects control the system's response to a given sort of excitation. While this may be sufficient (and perhaps even the best one can do) in certain circumstances, there are other situations in which sufficient information may be available to describe the matrix C through more detailed experimental testing of materials and/or subcomponents and components. Thus, there arise situations (e.g., in the design of spacecraft components) in which a more sophisticated analysis may be warranted. It is these kinds of systems that this paper deals with.

In what follows we shall assume that the mass matrix, M, is positive definite and symmetric, and the stiffness matrix, K, is symmetric and real. When M, K, and C cannot be simultaneously diagonalized by a suitable matrix transformation, one is left with a coupled system of equations of the form

$$\ddot{z}(t)+F\dot{z}(t)+\Lambda z(t)=h(t);\ z(t_0)=z_0,\ \dot{z}(t_0)=\dot{z}_0,\ t\epsilon(t_0,\ T] \tag{2}$$

where the matrix F, in general, is now a full matrix, and

Contributed by the Applied Mechanics Division of THE AMERICAN SOCIETY OF MECHANICAL ENGINEERS for presentation at the Winter Annual Meeting, Dallas, Tex., November 25–30, 1990.

Discussion on this paper should be addressed to the Technical Editor, Leon M. Keer, The Technological Institute, Northwestern University, Evanston, IL 60208, and will be accepted until two months after final publication of the paper itself in the JOURNAL OF APPLIED MECHANICS. Manuscript received by the ASME Applied Mechanics Division, August 25, 1988; final revision, June 1, 1989.

Paper No. 90-WA/APM-5.

Copyright © 1990 by ASME
Downloaded 03 May 2010 to 171.66.16.244. Redistribution subject to ASME license or copyright; see http://www.asme.org/terms/Terms_Use.cfm

$\Lambda = \text{Diag}\ \{\lambda_1, \lambda_2, \ldots, \lambda_N\}$ is a diagonal matrix. For classically damped systems, the transformation $x = Tz$ will uncouple the system represented by equation (1) and cause F to be a diagonal matrix. Yet, in many practical applications, it turns out that such a complete decoupling of equation (1) cannot be accomplished. The loss of the decoupled form leads to two major problems. First, it causes an increased computational burden to obtain the solution of equation (1); secondly, and perhaps more importantly, it increases the conceptual complexity of the response of the system because it is no longer possible to think of the total response as a superposition in terms of the contributions from the real modes and real frequencies of vibration of the system (Clough and Mojtahedi, 1976; Foss, 1958). This has led to an intense activity among researchers in the fields of mechanical, civil, and aerospace engineering to develop approximate methods that can obtain the response of the coupled system through the integration of an "equivalent" uncoupled set of equations.

Two different approaches have so far been used to do this. The first approach conceives of equation (2) as a second-order matrix differential equation and attempts to use different methods to uncouple it. Most, if not all, of these techniques essentially revolve around replacing the general matrix F by an "equivalent" diagonal matrix, D (Thompson, Calkins, and Caravani, 1974). Several ways of arriving at the diagonal elements of D from the matrix F, have evolved. Among those more commonly employed are: (1) using the diagonal elements of F in the matrix D; (2) obtaining each of the diagonal elements of D by using suitable algebraic expressions involving the elements of the matrix F which belong to the row in which that diagonal element is found; and, (3) ascribing percentages of critical damping to various modes of vibration, thereby discarding, in large measure, the information provided by the damping matrix F. The most common of these methods is simply to ignore the off-diagonal elements of the matrix F which then naturally gives rise to errors in the calculation of the response quantities (Clough and Mojtahedi, 1976; Hasselman, 1976; Warburton and Soni, 1977). A good deal of literature has concentrated on the conditions under which these errors may be small (Foss, 1958; Warburton and Soni, 1977). Most such studies have centered around the development of criteria which principally involve the parameter values of the elements of Λ and F. They are generally concerned with the left-hand side of equation (2), either ignoring the forcing function on the right-hand side of equation (2) or assuming that the system is excited harmonically. Duncan and Taylor (1979) and Warburton and Soni (1977) appear to be some of the few people who have explicitly recognized that the error in such approximate response calculations is substantially affected by the nature of the forcing vector. Though they consider only harmonic excitations, they do treat the relative amplitudes of the components of the forcing vector in their formulations as a variable that may affect the error. Yet neither of them elaborates on this point in any detail. Hasselman (1976) provides a criterion for when modal coupling can be neglected. He shows that as two or more elements of the Λ matrix come closer to each other, substantial modal interaction may be anticipated and ignoring the off-diagonal terms of the matrix F would lead, in general, to substantial errors. Cronin (1976) develops an approach on the basis that the matrix F is almost diagonalizable by the transformation that diagonalizes M and K. Although this method may generate results of acceptable accuracy for some matrices C, its usefulness to general damping matrices is questionable.

The second category of approaches conceives of the system of equations (2) to be a system of $2N$ first-order differential equations. The dynamic response is then obtained by direct integration or through the determination of the complex eigenvalues and complex mode shapes. Although the generalized modal superposition method of Foss (1958) is thoroughly

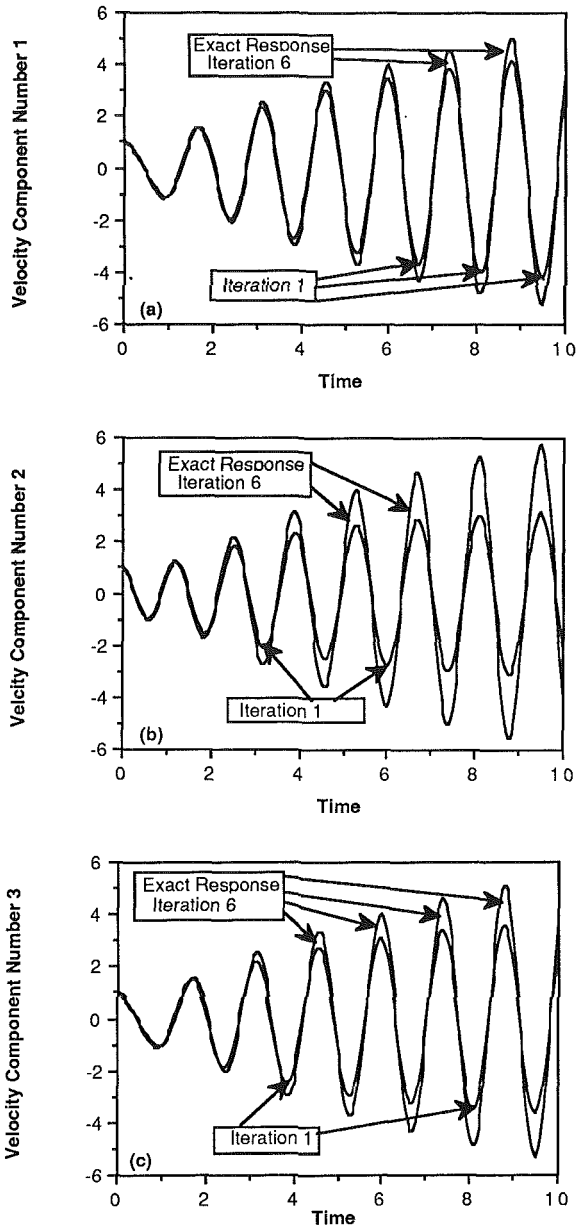


Fig. 1 Variations of the three velocity components corresponding to the exact response, first, and sixth iterations (example 1) relative to time

studied and well established, (*a*) it is computationally intensive, and (*b*) the physical significance of the various elements of the method is not as well understood as for the classical modal method. In a recent effort to clarify this significance, Veletsos and Ventura (1986) use the complex mode shape and complex frequency approach. They show that the corresponding transient displacement of a nonclassically damped multi-degree-of-freedom system can be expressed as a linear combination of displacements and the true relative velocities of a series of single degree-of-freedom systems subjected to similar excitations. Different approaches including modal superposition, complex mode shapes, direct integration, and weighted damping ratios have been compared in (Clough and Mojtahedi, 1976) where direct integration has been indicated as the preferred method. A recursive step-by-step approach in the time domain, again requiring information about the complex mode shapes and complex frequencies, has been introduced in (Singh and Ghafory-Ashtiany, 1976). P. D. Spanos, et al. (1988) deal with the decoupled analysis of classically

Downloaded 03 May 2010 to 171.66.16.244. Redistribution subject to ASME license or copyright; see http://www.asme.org/terms/Terms_Use.cfm

damped, large linear systems through an iterative predictor-corrector type scheme using substructuring.

All the approximate methods which use an uncoupled set of equations to represent the coupled set have at least two important shortfalls. Each of these techniques leads to inaccuracies, that, in general, increase as two or more of the elements of Λ approach each other. Thus, situations where multiple eigenvalues (or closely clustered eigenvalues) of Λ exist, lead to substantial errors (Hasselman, 1976). Further, it is difficult to assess, in general, the error that is caused in the computation of the response for arbitrary forcing functions $h(t)$ and matrices Λ thereby leaving the analyst ignorant of the extent of error caused by his approximation. In particular, as pointed out in (Duncan and Taylor, 1979), the extent of error generated by these currently available approximate techniques is extremely difficult to assess for large multi-degree-of-freedom systems.

In this paper we present a computationally efficient, iterative scheme for the numerical solution of coupled differential equations. Extensive numerical testing shows that the scheme works well. It is capable of handling arbitrary forcing vectors $h(t)$ and provides error bounds on the accuracy of the results obtained. More importantly, the method throws light on the uncoupling process and indicates that any coupled system of the form (2) can be replaced by an uncoupled system if and only if the forcing functions in the two systems are appropriately modified. *Thus the replacement of the matrix* F *by a diagonal matrix* D *requires concomitant changes in the forcing function* h(t) *if the responses obtained from the coupled and the uncoupled systems are to be identical.* The technique not only provides a simple computational method for handling coupled differential equations which cannot be represented by classical normal modes, but yields insight into the physics of the response of such systems. It indicates why previous efforts which involved uncoupling by concentrating on the properties of the system as represented in the left-hand side of equation (1) without explicit recognition of the forcing terms on the right-hand side, were bound to yield, in general, inaccurate results.

Section II of the paper presents the iterative approach on the basis of heuristic reasoning. For purposes of clarity in understanding and implementation, the algorithm is presented using pseudo-code. This is followed in Section III by a rigorous analysis of the sufficient conditions under which the iterative scheme is convergent. It is shown analytically that for a relatively large class of problems that are encountered in the analysis of structural and mechanical systems, the iterative scheme converges to the correct result. Section IV provides some numerical examples to show the efficacy of the proposed method. Among these examples are those with which previous investigators have found some measure of difficulty when using the usual uncoupling techniques described previously (Duncan and Taylor, 1979; Hasselman, 1976). We have chosen systems with multiple, undamped natural frequencies, and forcing functions whose frequencies coincide with these natural frequencies, thus providing rather stringent numerical tests of the technique proposed. Section V provides a discussion of the method and compares it with some of the methods proposed hereto.

II The Iterative Approach

As stated previously, under the assumption that M is positive definite and symmetric, and K is a real, symmetric matrix, equation (1) can always be cast into the form of equation (2). It will therefore suffice to begin with equation (2) in which F, Λ, $z(t_0)$, and $\dot{z}(t_0)$ are taken to be known. Let equation (2) be replaced by the system

$$\ddot{u}(t)+D\dot{u}(t)+\Lambda u(t)=f(t),\ u(t_0)=z_0,\ \dot{u}(t_0)=\dot{z}_0, \qquad (3)$$

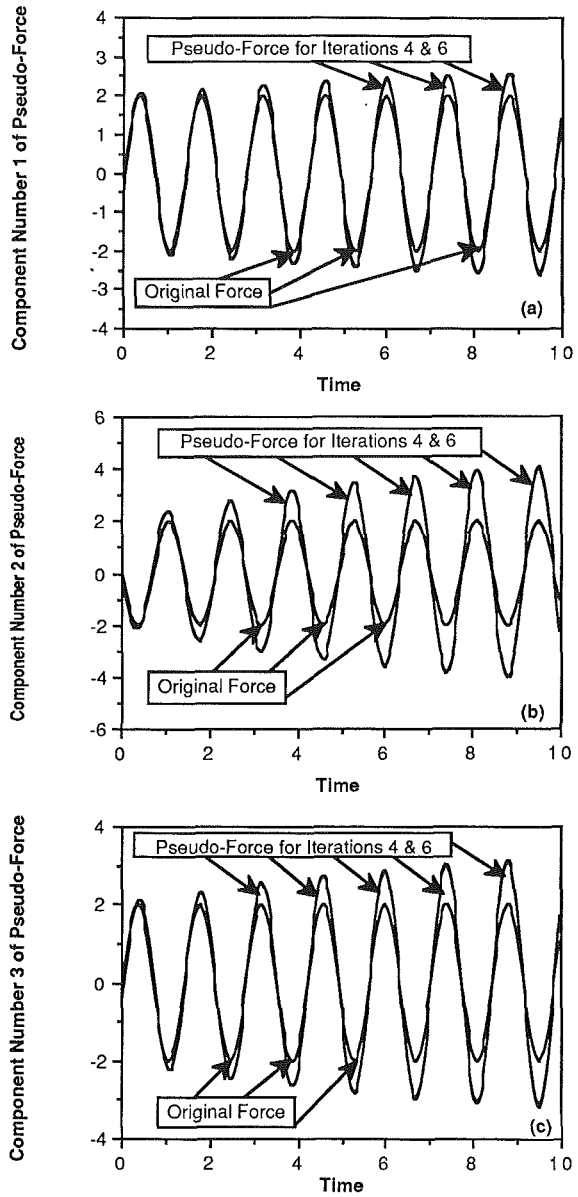


Fig. 2 Variations of the three velocity components of the pseudo-force corresponding to the first, fourth, and sixth iterations (example 1) as a *function of time*

where $D=\text{Diag}\ \{d_1, d_2, \ldots, d_N\}$ is the diagonal matrix obtained by taking the diagonal elements of F, and the function $f(t)$ is as yet unknown. Denoting the error in the response between equations (2) and (3) by the N-vector $\delta(t)=z(t)-u(t)$ and subtracting equation (3) from equation (2), we get

$$\ddot{\delta}(t)+D\dot{\delta}(t)+\Lambda\delta(t)$$
$$=h(t)-f(t)-(F-D)\dot{z},\ \delta(t)=\dot{\delta}(t)=0. \qquad (4)$$

Since (4) is a linear system of differential equations with zero initial conditions,

$$\delta(t)=0,\ t\in[t_0, T],\ \text{if and only if}\ f(t)=h(t)-(F-D)\dot{z}(t). \qquad (5)$$

This implies that the solutions of equations (2) and (3) will be identical, i.e., $z(t)\equiv u(t)$ if and only if the right-hand side of equation (3) is taken to be $f(t)$ as defined in equation (5). The only snag in performing such a replacement, is that the response $z(t)$ is not known, and in fact is obtained through a solution of equation (2), which is what we want to solve for in the first place. To circumvent this problem, we consider the following iterative scheme which uses successive approxima-

Downloaded 03 May 2010 to 171.66.16.244. Redistribution subject to ASME license or copyright; see http://www.asme.org/terms/Terms_Use.cfm

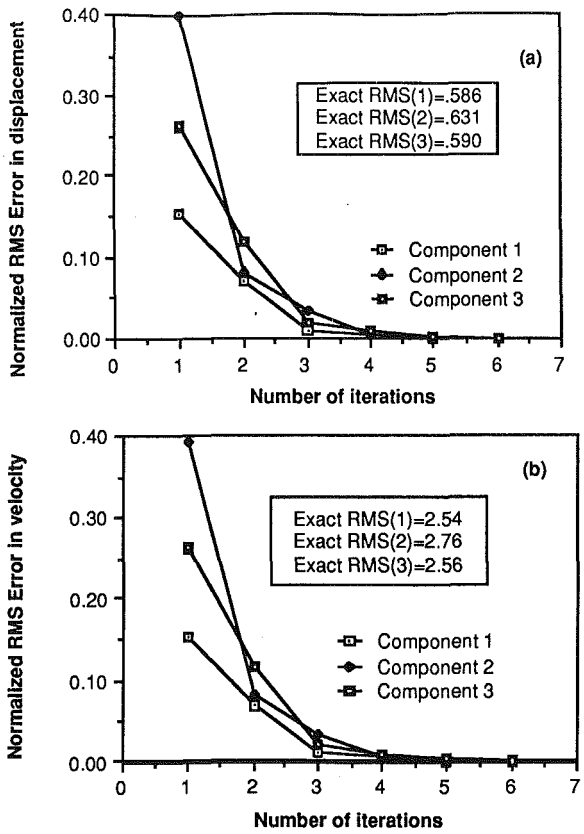


Fig. 3 RMS error of the three components of displacement (*a*) and velocity (*b*) (example 1) versus number of iterations

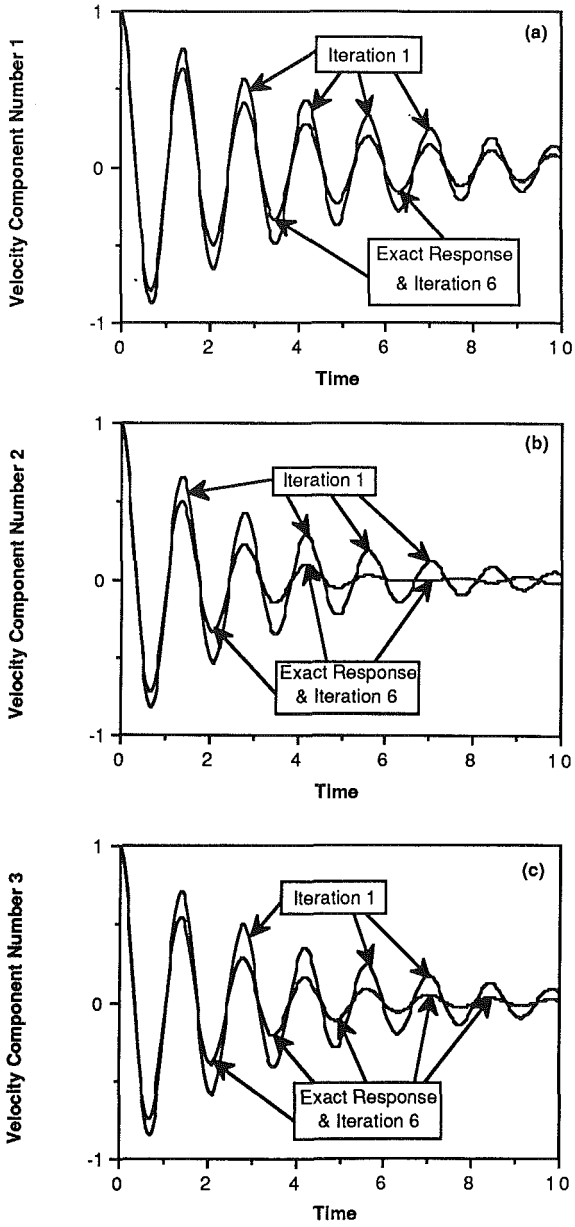


Fig. 4 Variations of the three velocity components corresponding to the exact response, first, and sixth iterations (example 2) versus time

tions for $z(t)$. The scheme can best be described in the following algorithmic form where the superscript n is used to denote quantities related to the nth iteration.

Step 1: Set $t_i = t_0,\ t_e = T$

$$u(t_i) = z_0,\ \dot{u}(t_i) = \dot{z}_0$$

Procedure I.

Step 2: Set $n = 1$;

$$\hat{f}^{(0)}(t) = h(t), t\epsilon(t_i,\ t_e]$$

Step 3: Solve the *uncoupled* system of equations:

$$\ddot{u}^{(n)}(t) + D\dot{u}^{(n)}(t) + \Lambda u^{(n)}(t) = \hat{f}^{(n-1)}(t), t\epsilon(t_i,\ t_e] \qquad (6)$$

$$u(t_i) = z_0,\ \dot{u}(t_i) = \dot{z}_0$$

Obtain:

$$\dot{u}^{(n)}(t),\ t\epsilon(t_i,\ t_e)$$

Set 4A: Set $\hat{z}^{(n)}(t) = \dot{u}^{(n)}(t),\ t\epsilon(t_i,\ t_e]$

Step 4B: Set $\hat{f}^{(n)}(t) = h(t) - (F - D)\hat{z}^{(n)}(t),\ t\epsilon(t_i,\ t_e]$

Set $n = n + 1$

Step 5: If:

$\hat{f}^{(n)}(t)$ converges {or $u^{(n)}(t)$ converges}

Then:

$$z(t) \cong \hat{z}^{(n)}(t),\ \dot{z}(t) \cong \hat{z}^{(n)}(t),$$
$$f(t) \cong \hat{f}^{(n)}(t);\ t\epsilon(t_i,\ t_e]$$

Stop.

Else:

Go to Step 3.

The following important elements of the iterative scheme should be noted.

1 At each iteration a set of uncoupled equations (as per Step 3) are solved.

2 In Steps 4A and 4B of Procedure I we have explicitly indicated the iterative approximations of:

(*a*) $\hat{z}(t)$, the solution of coupled system of equations (2), and,

(*b*) $\hat{f}^{(n)}(t)$, the right-hand side of equation (3), which we shall refer to henceforth as *the pseudo-force.*

Perhaps the most significant contribution of such an iterative scheme is the conceptual understanding that the coupled system represented by equation (2), could be thought of in terms of an uncoupled system with an altered (and obviously diagonal) damping matrix *provided* that appropriate adjustments can be made to the vector, $h(t)$, on the right-hand side. Past efforts to replace the coupled system by a set of uncoupled equations have concentrated mainly on obtaining "equivalent" diagonal forms D corresponding to the

Downloaded 03 May 2010 to 171.66.16.244. Redistribution subject to ASME license or copyright; see http://www.asme.org/terms/Terms_Use.cfm

general matrix F without making appropriate alterations to the forcing function, $h(t)$ on the right-hand side of equation (2). Without such an adjustment, it is little wonder that previous approximate methods which were used to uncouple equation (2) led to solutions (responses) which were, at times, significantly different from those of the coupled system. We then obtain the following conceptual picture:

[coupled system with full matrix F and force vector $h(t)$] may be made equivalent to [uncoupled system with diagonal matrix D and pseudo-force vector $f(t)$].

Thus, our heuristically-developed scheme shows that it may be possible to think of the response of the system represented by equation (2) as being separable into different "modes" *provided* that it is subjected to the pseudo-force vector $f(t)$ rather than the actual forcing vector $h(t)$. Having developed the plausibility of the algorithm on heuristic grounds, we next investigate the conditions under which such a conceptual picture is guaranteed to be valid. In the following section, sufficient conditions for convergence of this iterative method are investigated, namely, the conditions under which the error $\delta^{(n)}(t) = z(t) - u^{(n)}(t) \to 0$ as $n \to \infty$.

III Convergence of the Iterative Scheme

The algorithm that was explained in step-wise form to expose the underlying heuristics can now be represented as

$$\ddot{u}^{(n)}(t) + D\dot{u}^{(n)}(t) + \Lambda u^{(n)}(t) = h(t) + (D-F)\dot{u}^{(n-1)}(t), \quad (7a)$$

with

$$u^{(n)}(t_0) = z_0, \; n = 0, 1, 2, \ldots, \quad (7b)$$

$$\dot{u}^{(n)}(t_0) = \dot{z}_0, \; n = 1, 2, 3, \ldots, \text{ and,} \quad (7c)$$

$$\dot{u}^{(0)}(t) = 0, \; t \epsilon (t_0, T]. \quad (7d)$$

Also, equation (2) can be rewritten as

$$\ddot{z}(t) + D\dot{z}(t) + \Lambda z(t) = h(t) + (D-F)\dot{z}(t), \; t \epsilon (t_0, T] \quad (8a)$$

$$\text{with } \dot{z}(t_0) = \dot{z}_0, \text{ and } z(t_0) = z_0. \quad (8b)$$

Subtracting equation (7) from equation (8), and noting that $\delta^{(n)}(t) = z(t) - u^{(n)}(t)$, we obtain

$$\ddot{\delta}^{(n)}(t) + D\dot{\delta}^{(n)}(t) + \Lambda\delta^{(n)}(t) = -(F-D)\dot{\delta}^{(n-1)}(t),$$

$$n = 1, 2, \ldots \quad (9a)$$

$$\text{with } \dot{\delta}^{(0)}(t) = \dot{z}(t) - \dot{u}^{(0)}(t), \; t \epsilon (t_0, T]; \text{ and,} \quad (9b)$$

$$\dot{\delta}^{(n)}(t_0) = \delta^{(n)}(t_0) = 0, \; n = 1, 2, \ldots. \quad (9c)$$

Denoting Fourier Transforms with tildes so that

$$\tilde{\delta}(\omega) = \int_0^\infty \delta(t) e^{i\omega t} dt, \quad (10)$$

we obtain, by (9),

$$[-\omega D + i(\omega^2 I - \Lambda)]\tilde{\delta}^{(n)}(\omega) = \omega B \tilde{\delta}^{(n-1)}(\omega) \quad (11)$$

where $B = [b_{ij}] = F - D$. This then yields the recursion

$$\tilde{\delta}^{(n)}(\omega) = [S(\omega)]^n \, \tilde{\delta}^{(0)}(\omega), \quad (12)$$

where

$$S(\omega) = [\omega(\omega A)^{-1} B], \quad (13)$$

and

$$\omega A = -\omega D + i\omega G \quad (14)$$

is a diagonal matrix, with

$$D = \text{Diag}\{d_1, d_2, d_3, \ldots, d_N\} \quad (15)$$

and

$$\omega G = \text{Diag}\{\omega^2 - \lambda_1, \omega^2 - \lambda_2, \omega^2 - \lambda_3, \ldots, \omega^2 - \lambda_N\}. \quad (16)$$

Noting equation (9), the vector $\delta^{(0)}(t)$ corresponds to the error in the initial iterate. We are now ready to present the following convergence results.

Theorem 1: $u^{(n)}(t) \to z(t)$ almost everywhere (a.e.) if and only if $S(\omega)$ is quasi-nilpotent, i.e., $\{S(\omega)\}^n \to 0$, for all $\omega \epsilon \mathbf{R}$, as $n \to \infty$. (We denote the real line by $\mathbf{R}$).

This condition is equivalent to the spectral radius of $S(\omega)$, denoted $\rho_s(\omega)$, being less than unity for all $\omega \epsilon \mathbf{R}$ (Noble, 1969).

Proof: $u^{(n)}(t) \to z(t)$ almost everywhere implies that $\tilde{\delta}^{(n)}(\omega) \to 0$ for all ω, and for arbitrary $\tilde{\delta}^{(0)}(\omega)$. Noting equation (12) the result follows. Also if $S^n(\omega) \to 0$, then $\tilde{\delta}^{(n)}(\omega) \to 0$.

Since the determination of the spectral radius of $S(\omega)$ for all $\omega \epsilon \mathbf{R}$ is difficult, especially for large matrices, we present

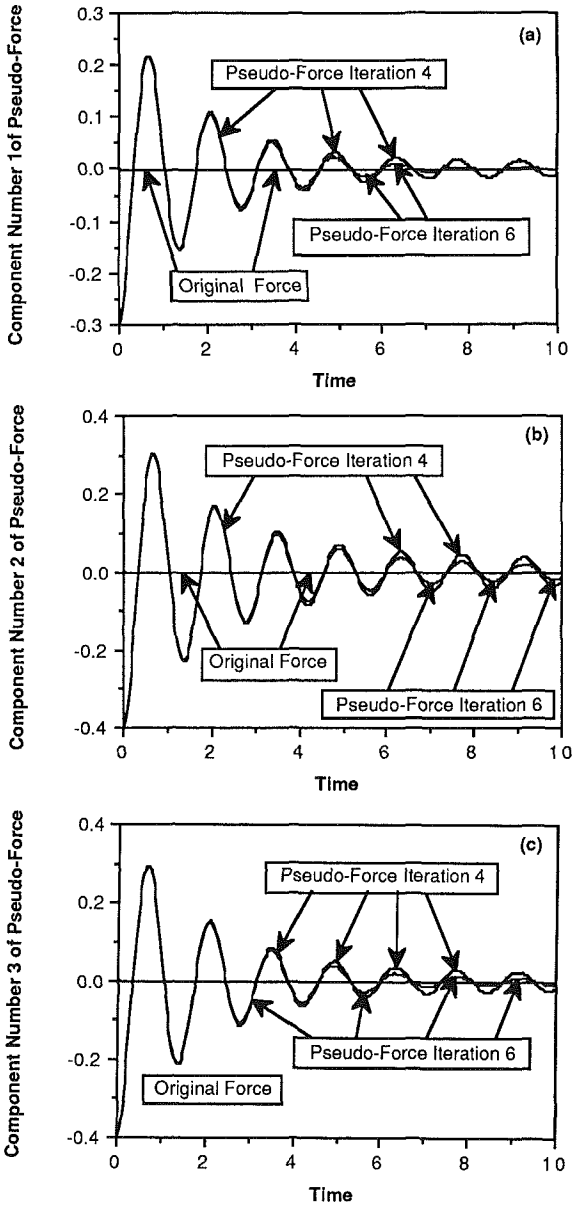


Fig. 5 Variations of the three components of the pseudo-force generated at the first, fourth, and sixth iterations (example 2) versus time

Downloaded 03 May 2010 to 171.66.16.244. Redistribution subject to ASME license or copyright; see http://www.asme.org/terms/Terms_Use.cfm

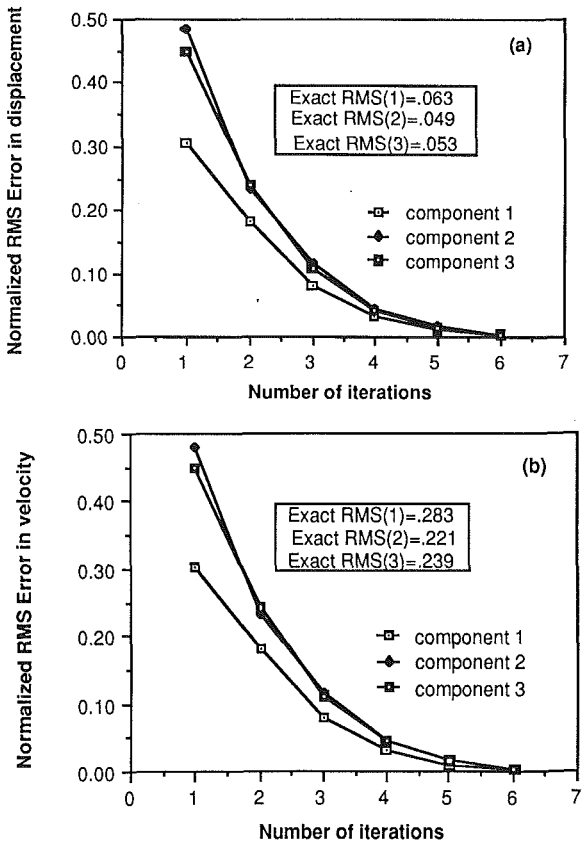


Fig. 6 RMS error of the components of displacement (*a*) and velocity (*b*) (example 2) versus number of iterations

here some sufficient conditions related to the matrix F which ensure convergence of the iterative scheme (9).

Lemma 1: The spectral radius of matrix $S(\omega)$ has the following property:

$$\rho_s(\omega) \le \max_{1\le i\le N}\left\{\frac{\omega}{|\alpha_i|}\sum_{j=1}^{N}|b_{ij}|\right\},\ \omega\epsilon\mathbf{R}, \tag{17}$$

where,

$$|\alpha_i| = \sqrt{\omega^2 d_i^2 + (\lambda_i - \omega^2)^2}. \tag{18}$$

Proof: We have (Noble, 1969)

$$\rho_s(\omega) \le \|\omega(A\omega)^{-1}B\|_\infty. \tag{19}$$

Noting that the matrix denoted by (ωA) is diagonal and that the matrix B has zeros along its diagonal, the result follows.

Lemma 2: If the matrix $\Lambda = \text{Diag}\ (\lambda_1, \lambda_2, \ldots, \lambda_N)$ is nonsingular, i.e., $\lambda_i \neq 0$, $i\epsilon\ (1,N)$, then

(*a*) $\rho_s(0) = 0$, and

(*b*) $\rho_s(\pm\infty) = 0$.

Proof: Using relation (17), and taking the appropriate limits, the result follows.

As a consequence, $\tilde{\delta}^{(n)}(0) \to 0$ as $n \to \infty$.

Theorem 2: If the matrix F is strictly diagonally dominant, then $u^{(n)}(t) \to z(t)$ almost everywhere.

Proof: We have, by Lemma 1,

$$\max_{\omega\epsilon\mathbf{R}}\{\rho_s(\omega)\} = \max_{\omega\epsilon\mathbf{R}}\left\{\max_{1\le i\le N}\frac{\omega}{|\alpha_i|}\sum_{j=1}^{j=N}|b_{ij}|\right\}. \tag{20}$$

However, the elements of the matrix B do not depend on ω. Also, using (18), we get

$$\left\{\frac{\omega}{|\alpha_i|}\right\} \le \frac{1}{|d_i|},\ i=1, 2, 3, \ldots, N;\ \omega\epsilon\mathbf{R}, \tag{21a}$$

with,

$$\max_{\omega\epsilon\mathbf{R}}\left\{\frac{\omega}{|\alpha_i|}\right\} = \frac{1}{|d_i|},\ i=1, 2, 3, \ldots, N. \tag{21b}$$

The maxima in (21*b*) occur at

$$\omega^2 = \lambda_i,\ i=1, 2, 3, \ldots, N. \tag{22}$$

Thus, we obtain

$$\max_{\omega\epsilon\mathbf{R}}\{\rho_s(\omega)\} \le \max_{1\le i\le N}\left\{\frac{1}{|d_i|}\sum_{j=1}^{j=N}|b_{ij}|\right\}. \tag{23}$$

We note that $[b_{ii}] = 0$, $[b_{ij}] = [f_{ij}]$ for $i \neq j$, and $d_i = [f_{ii}]$. Strict diagonal dominance of matrix F therefore requires that the right-hand side of (23) be less than unity. We thus obtain $\rho_s(\omega) < 1$, for all $\omega\epsilon\mathbf{R}$. By Theorem 1, the result then follows.

We next prove that if F is a symmetric positive definite matrix an additional set of sufficient conditions can be obtained to ensure convergence of the iterative scheme. In view of Lemma 2, we shall concentrate on the case $\omega \neq 0$.

Lemma 3: Let F be a positive definite matrix. Then

$$\rho_s(\omega) = \rho_{A^{-1}B}(\omega) \le \rho_{D^{-1}B}. \tag{24}$$

Proof: Let $|\lambda_0|$ be the spectral radius of $A^{-1}B$. Thus,

$$Bx = \lambda_0 Ax = \lambda_0(-D+iG)x \tag{25}$$

where x is the eigenvector corresponding to λ_0. Therefore, we have

$$|\lambda_0| = \frac{|x^H Bx|}{|x^H(-D+iG)x|} = \frac{|x^H Bx|}{\left|\sum_{k=1}^{k=N}(-d_k + ig_k)\,|x_k|^2\right|}$$

$$\le \frac{|x^H Bx|}{\left|\left\{\sum_{k=1}^{k=N} -d_k\,|x_k|^2\right\}\right|}. \tag{26}$$

Denoting the spectral radius of $D^{-1}B$ by $|\mu_0|$, we then get

$$|\lambda_0| \le \max_{\forall y}\left\{\frac{|y^H By|}{\left|\left\{\sum_{k=1}^{k=N} -d_k\,|y_k|^2\right\}\right|}\right\} = |\mu_0|, \tag{27}$$

and hence the result.

Lemma 4: If F is positive definite and symmetric, then the eigenvalues of $-D^{-1}B$ are all less than unity.

Proof: Let λ be an eigenvalue of $-D^{-1}B$. Then

$$-D^{-1}(F-D)x = \lambda x. \tag{28}$$

Let $D^{-1/2}y = x$. Then

$$-D^{1/2}(F-D)D^{-1/2}y = \lambda y, \text{ and}$$

$$-y^T[D^{-1/2}F\,D^{-1/2}]y + y^T y = \lambda y^T y.$$

Normalizing $y^T y = 1$ and noting that F is positive definite, we get

$$\lambda < 1. \tag{29}$$

Hence, the result.

Downloaded 03 May 2010 to 171.66.16.244. Redistribution subject to ASME license or copyright; see http://www.asme.org/terms/Terms_Use.cfm

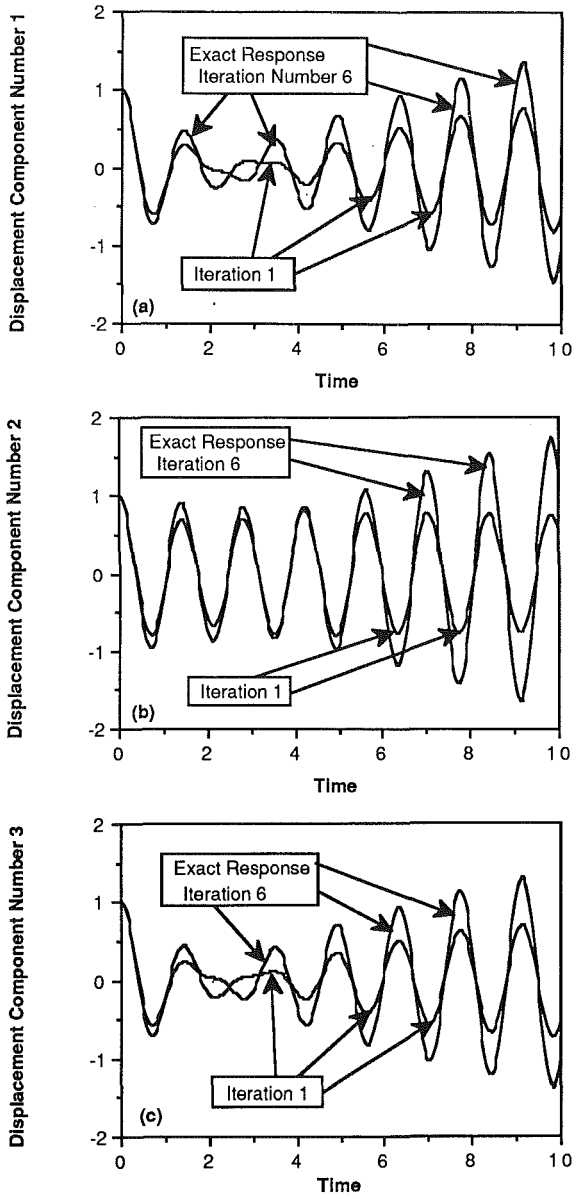


Fig. 7 Variations of the displacement components for the exact response, first, and sixth iterations (example 3) as a function of time

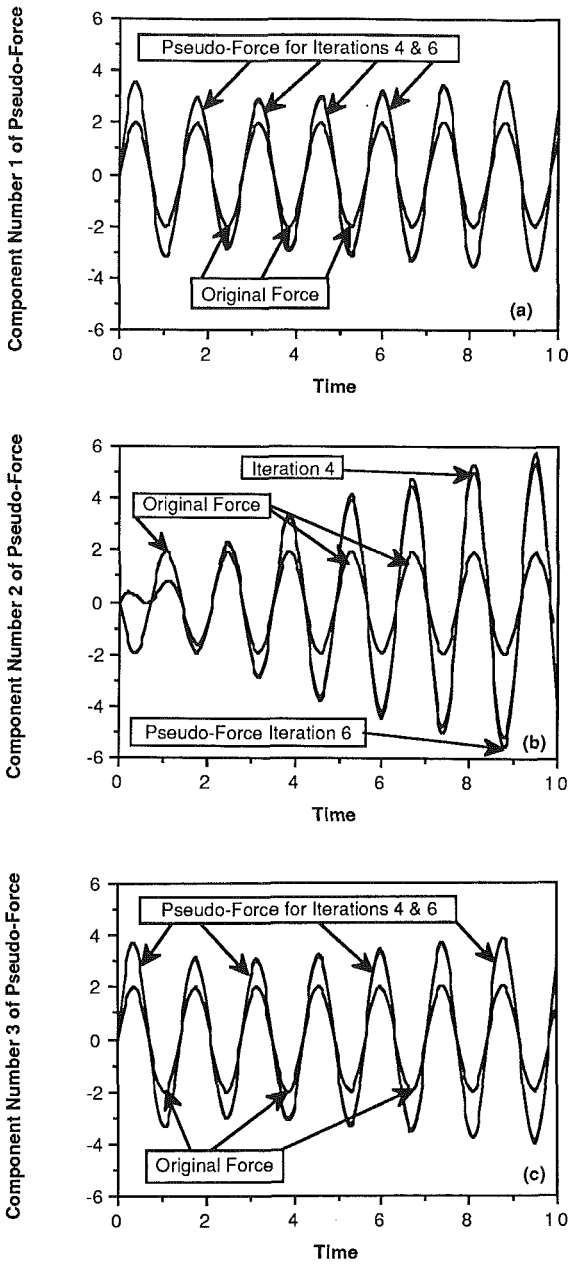


Fig. 8 Variations of the components of the pseudo-force generated at the first, fourth, and sixth iterations (example 3) versus time

Lemma 5: If $\lambda_k(D^{-1}F) < 2$, $k = 1, 2, \ldots, N$, then $\rho_{D^{-1}B} < 1$.

Proof: From the previous result, we get

$$\lambda = 1 - y^T D^{-1/2} F D^{-1/2} y. \tag{30}$$

Noting that $D^{-1}F$ and $D^{-1/2}F D^{-1/2}$ have the same eigenvalues, the result follows.

Theorem 3: If F is symmetric and positive definite and if all the eigenvalues of $D^{-1}F$ are less than 2, then the iterative scheme (9) converges.

Proof: The result follows from Lemmas 3 and 5.

IV Numerical Results

In this section we present some numerical results on three nonclassically damped systems. The three successive systems considered in this section correspond, roughly speaking, to increasing levels of generality of the nature of the damping matrix F. In each case, the matrix F is far from a diagonal matrix, the off-diagonal terms being appreciable compared to those on the diagonal. These examples have been specifically chosen so that the system responses are strongly coupled through the damping terms. Customary uncoupling methods in N-space fail miserably in these situations (Duncan and Taylor, 1979; Hasselman, 1976). We find that in all the examples studied, the iterated results, after only a few iterations, are almost the same as those obtained from using the fourth-order Runge-Kutta Integration Scheme (Press et al., 1986).

Direct use of the fourth-order Runge-Kutta procedure to obtain the response of the linear system given by equation (1) requires that it be first cast in $2N$-order form. The number of multiplications involved for each time-step in this direct approach is then approximately $(16N^2 + 18N)$. The iterative technique developed in this paper utilizes the Nigam-Jennings algorithm (Nigam and Jennings, 1968) for numerical computations. This requires, for each time-step, a total of

Downloaded 03 May 2010 to 171.66.16.244. Redistribution subject to ASME license or copyright; see http://www.asme.org/terms/Terms_Use.cfm

$(8N+N^2)I$ multiplications, where I is the number of iterations. Thus, for large N, when convergence occurs within 16 iterations, the iterative method becomes computationally superior. The numerical work reported here was performed on a MacIntosh microcomputer. Throughout this section it shall be assumed that the various parameter values are provided in consistent physical units.

Example 1: Consider a three degree-of-freedom system, which has the following parameter values:

$$F = \begin{bmatrix} 0.4 & 0.2 & 0.1 \\ 0.1 & 0.6 & 0.3 \\ 0.1 & 0.3 & 0.5 \end{bmatrix}, \text{ and, } \Lambda = \text{Diag}\{20.0,\ 20.0,\ 20.0\}. \tag{31}$$

The matrix F is thus *nonsymmetric* but diagonally dominant. (It should be noted that the off-diagonal terms cannot be thought of as "small" compared to the diagonal elements). It is also positive definite, and its eigenvalues are $\mu_1 = 0.914$, $\mu_2 = 0.334$, and $\mu_3 = 0.252$. Its spectral norm is therefore less than unity. Theorem 2 of Section III thus ensures that the iterative scheme developed herein will converge.

The parameters t_0 and T are taken to be zero and 10 units (seconds), respectively. The initial displacements and velocities are taken to be

$$z_i(0) = 0,\ i = 1,\ 2,\ 3;\ \text{and, } \dot{z}_i(0) = 1.0,\ i = 1,\ 2,\ 3. \tag{32}$$

The system is subjected to the force vector $h(t)$ given by

$$h_1(t) = 2\sin\sqrt{20}t,\ h_2(t) = -2\sin\sqrt{20}t,$$
$$\text{and } h_3(t) = 2\sin\sqrt{20}t,\ t\epsilon(0,\ 10]. \tag{33}$$

The diagonal elements of the matrix Λ are all equal, and had there been no damping in the system (i.e., if F were zero), the three undamped frequencies of the uncoupled system would all be equal and have a value of $\sqrt{20}$ units. The identical values of these diagonal elements (Hasselman, 1976) show that intense interaction is to be expected through the coupling created by the matrix F. This would be all the more prominent because the excitation is also taken to have a frequency of $\sqrt{20}$ units. Standard decoupling methods used to date have been known to provide totally erroneous results in this situation (Hasselman, 1976).

The technique that was described in Section II is utilized to obtain the response of the coupled system. At each step the uncoupled system is integrated using the algorithm first presented by Nigam and Jennings (1968) which requires only eight multiplications for each time-step. At each iteration the pseudo-forces are obtained and are then used to obtain the response of the system at the next iteration, as described by equation (7). The matrix D is comprised of the diagonal elements of the matrix F. For the first iteration, the pseudo-force vector is taken to be the same as the given forcing vector, namely $h(t)$. Results from the first iteration therefore provide a measure of the extent of error in determining the system's response had all the off-diagonal elements of the matrix F been ignored. Along with the results obtained by the iterative scheme, we also provide the results obtained by using the fourth-order Runge-Kutta method with an error tolerance of 10^{-3}. In this sequel we shall refer to the results obtained from this Runge-Kutta Integration as "Exact Response," for short.

Figures 1(a), 1(b), and 1(c) show a comparison of the three components of the velocity of the system as calculated by the Runge-Kutta method and the iterative scheme developed. The differences in the responses obtained at the first iteration and the sixth iteration using the uncoupled system are substantial and therefore noteworthy. The error at the first iteration would be identical to that obtained by ignoring all the off-diagonal elements of the matrix F. Convergence to the response calculated using the Runge-Kutta scheme results within about six iterations. Figure 2 shows the components of the original forcing vector and the pseudo-forces used to determine the response of the uncoupled system at the fourth and sixth iterations. *We thus note that the response of the coupled system can be correctly obtained through an integration of the uncoupled equations if proper modification of the right-hand sides of these uncoupled equations is made.* The lack of such an appropriate modification of the forcing vector on the right-hand side of equation (2) is the cause of the poor accuracies arrived at by methods used by several previous investigators. As expected, the pseudo-forces at the fourth and sixth iterations are almost identical.

Figures 3(a) and 3(b) show the rate of convergence of each component of the displacement and velocity response as a function of the iteration number. The normalized root mean square (RMS) error, e_i, in each displacement component is defined by the relation

$$\text{normalized RMS error at iteration } n \text{ in component } i = \frac{\text{RMS of } \{u_i^{(n)} - z_i^{RK}\}}{\text{RMS of } \{z_i^{RK}\}} \tag{34}$$

where $u_i^{(n)}$ is the nth iterate of component i, and z_i^{RK} is the ith component of the response of equation (2) calculated using the direct Runge-Kutta Method. A similar relation is used for the normalized RMS error in the velocity components. The RMS responses obtained using the Runge-Kutta method are also provided in the figures.

Example 2: Next, the same system described in equations (31) and (32) is used, except that the forcing vector $h(t)$ is set to zero. Thus the coupled system's response to an initial velocity is sought. Figures 4(a)-4(c) again show the responses obtained by the Runge-Kutta method and those obtained from the Iterative Method. Again, the first iteration result is seen to be substantially different from that of the sixth; convergence to the Runge-Kutta response is observed within six iterations. Since $h(t) = 0$, the components of the original forcing function are zero. Figures 5(a)-5(c) show the pseudo-forces that are generated at each iteration corresponding to the uncoupled system of equations (7), clearly indicating that they are not negligible and therefore cannot be ignored if the response of the coupled system is to be approximated by the response of the uncoupled system. Furthermore, these pseudo-forces depend on the forcing function $h(t)$ of the coupled system. Figure 6 again shows the nature of the convergence of the scheme with iteration number.

Example 3: Here we consider a symmetric matrix F with the elements given by

$$F = \begin{bmatrix} 0.40 & 0.30 & 0.10 \\ 0.30 & 0.60 & 0.34 \\ 0.10 & 0.34 & 0.50 \end{bmatrix} \text{ and } \Lambda = \text{Diag}\{20.0,\ 20.0,\ 20.0\}. \tag{35}$$

along with the initial conditions

$$z_i(0) = 1.0,\ i = 1,\ 2,\ 3;\ \text{and, } \dot{z}_i(0) = 0,\ i = 1,\ 2,\ 3. \tag{36}$$

The forcing vector $h(t)$ is the same as that in equation (33).

The matrix F though symmetric is no longer diagonally dominant. The eigenvalues of F are 0.12, 0.347, and 1.033. Yet the eigenvalues of $D^{-1}F$($\mu_1 = 1.9909$, $\mu_2 = 0.7764$, and $\mu_3 = 0.2327$) are all less than 2 and by Theorem 3 of Section III the iterative scheme of Section I is ensured of convergence. Again, the elements of the matrix Λ are identical and the forcing function has a frequency identical to the undamped uncoupled fundamental frequency (i.e., $\sqrt{20}$ units). These sets of conditions promise a large interaction in the modes through the matrix F (Hasselman, 1976; Warburton and Soni, 1977). Figures 7(a)-7(c) show the displacement responses of the

Downloaded 03 May 2010 to 171.66.16.244. Redistribution subject to ASME license or copyright; see http://www.asme.org/terms/Terms_Use.cfm

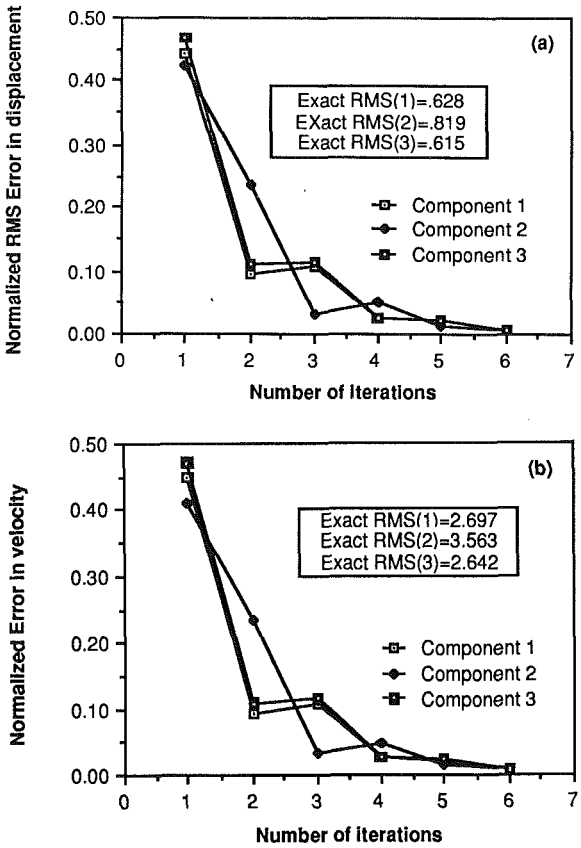


Fig. 9 Normalized RMS error of the displacement (*a*) and velocity (*b*) components (example 3) versus the number of iterations

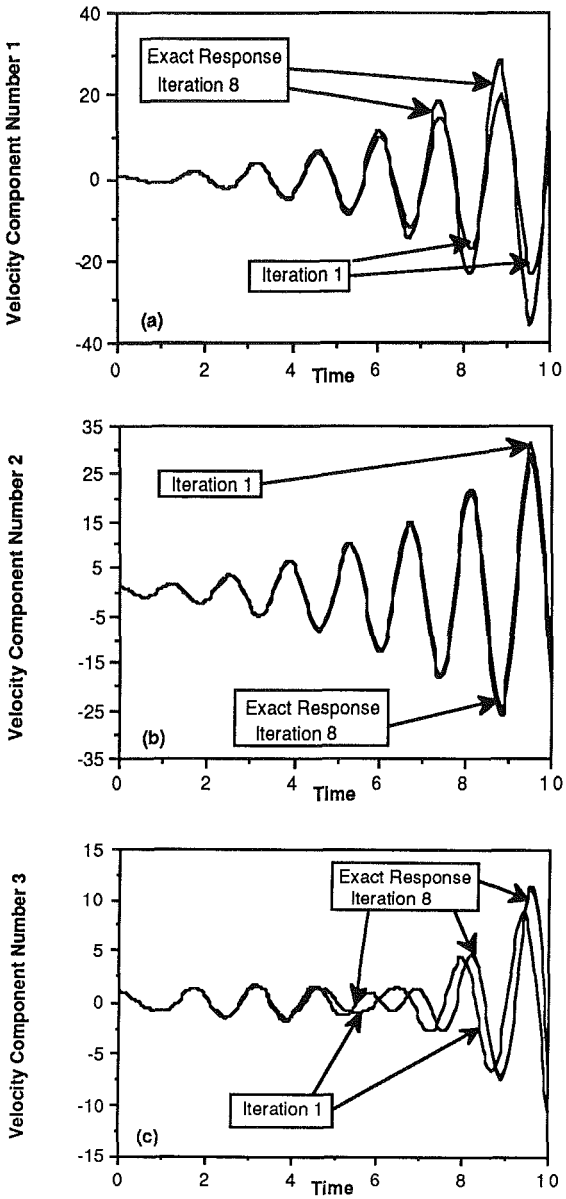


Fig. 10 Variations of the velocity components corresponding to the exact response, first, and eighth iterations (example 4) versus time

various components. Again, convergence of the response at the sixth iteration to the response computed by direct integration is shown. In Figs. 8(*a*)-8(*c*) the pseudo-force components at the fourth and sixth iterations are shown along with the components of the original forcing vector $h(t)$. The manner in which the convergence occurs is indicated in Figs. 9(*a*) and 9(*b*).

Example 4: To amplify the nature of the results obtained in Section III, we next consider a three degree-of-freedom system defined by the following matrices:

$$F = \begin{bmatrix} 0.2 & 0.7 & 0.6 \\ 0.5 & 0.1 & 0.3 \\ 0.4 & 0.4 & 0.3 \end{bmatrix}, \text{ and, } \Lambda = \text{Diag}\{20.0,\ 20.0,\ 20.0\} \tag{37}$$

along with the initial conditions

$$z_i(0) = 0,\ i = 1,\ 2,\ 3;\ \text{and,}\ \dot{z}_i(0) = 1.0,\ i = 1,\ 2,\ 3. \tag{32}$$

The forcing vector $h(t)$ is taken to be the same as that in relation (33).

Here the matrix F is nonsymmetric and nonpositive definite. In spite of this, Figs. 10(*a*)-10(*c*) show the convergence of the various components of the response of the system to results obtained from the Runge-Kutta computations. Figures 11(*a*)-11(*c*) show the pseudo-forces that need to be used to compensate for ignoring the off-diagonal terms of the matrix F. Figures 12(*a*) and 12(*b*) show the convergence of displacement and velocity components, respectively.

It should be noted that the results presented in Section III provide only the sufficient conditions for convergence of the iterative scheme. This means that convergence is possible and often does occur, in such schemes, even when these sufficient conditions are not satisfied. This is exemplified in this example where we find that neither Theorem 2 nor 3 of Section III is applicable. A brief summary of all four examples is provided in Table 1.

V Conclusions and Discussion

A simple, new, computationally efficient and heuristically-motivated iterative method is developed for the numerical solution of general, linear vibratory systems modeled by coupled differential equations. It is shown to be a better alternative to the approximate methods that have so far been used by previous investigators. Most, if not all, of the previous investigations have focused on the modification of the left-hand side of the system represented by equation (2) in such a way that the transformed damping matrix is diagonal. This generates unacceptable computational errors for certain cases. The iterative scheme presented here shows that by appropriately adjusting the right-hand side of the equation in each iteration, the exact solutions can be rapidly obtained. Furthermore, to simplify the use of the proposed scheme to

Downloaded 03 May 2010 to 171.66.16.244. Redistribution subject to ASME license or copyright; see http://www.asme.org/terms/Terms_Use.cfm

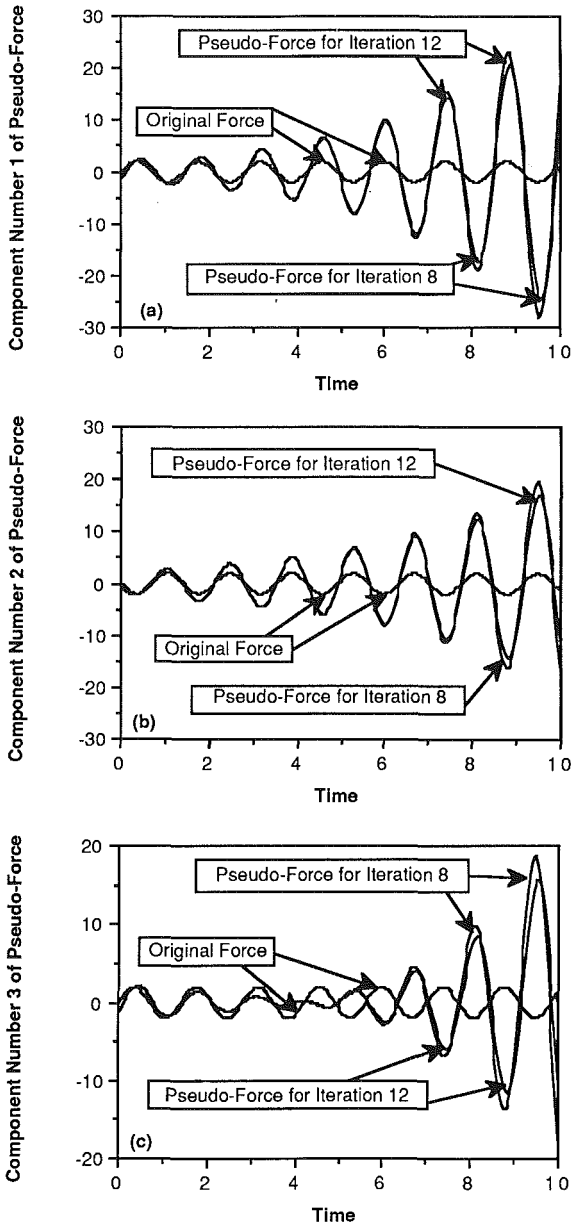


Fig. 11 Variations of the three components of the pseudo-force generated at the first, eighth, and twelveth iterations (example 4) with response to time

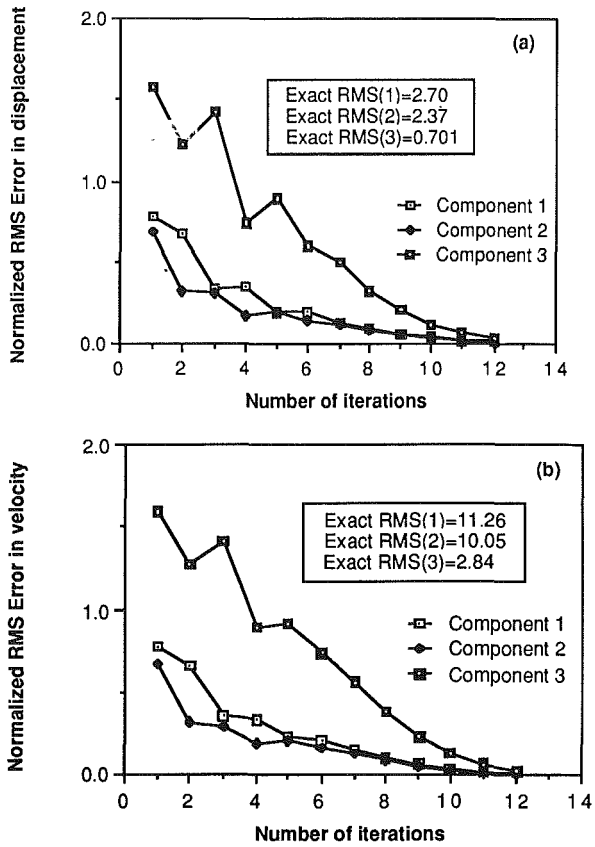


Fig. 12 Normalized RMS error for the displacement (*a*) and velocity (*b*) components (example 4) with respect to the number of iterations

Table 1 Summary of numerical results

Example Number	F Matrix and Its Characteristics	Diagonal Λ Matrix	Forcing Vector h(t)	Initial Conditions	*Normalized* RMS Error (Displacement)
1	$\begin{bmatrix} 0.4 & 0.2 & 0.1 \\ 0.1 & 0.6 & 0.3 \\ 0.1 & 0.3 & 0.5 \end{bmatrix}$ Nonsymmetric; Positive Definite; Diagonally Dominant; THEOREM 2 OF SECTION III APPLIES	$\lambda_1 = 20.0$ $\lambda_2 = 20.0$ $\lambda_3 = 20.0$	$h_1(t) = 2\sin\sqrt{20}\,t$ $h_2(t) = -2\sin\sqrt{20}\,t$ $h_3(t) = 2\sin\sqrt{20}\,t$	$z_1(0) = 0$ $z_2(0) = 0$ $z_3(0) = 0$ $\dot{z}_1(0) = 1$ $\dot{z}_2(0) = 1$ $\dot{z}_3(0) = 1$	$e_1 = 0.47E\text{-}03$ $e_2 = 0.51E\text{-}03$ $e_3 = 0.71E\text{-}03$ (Iteration 6)
2	Same as in Example Number 1	Same as in Example Number 1	$h_i(t) = 0,\ i = 1, 2, 3$	Same as in Example Number 1	$e_1 = 0.28E\text{-}02$ $e_2 = 0.41E\text{-}02$ $e_3 = 0.39E\text{-}02$ (Iteration 6)
3	$\begin{bmatrix} 0.4 & 0.3 & 0.1 \\ 0.3 & 0.6 & 0.34 \\ 0.1 & 0.34 & 0.5 \end{bmatrix}$ Symmetric; Positive Definite: Non–Diagonally Dominant; THEOREM 3 OF SECTION III APPLIES	Same as in Example Number 1	Same as in Example Number 1	$z_1(0) = 1$ $z_2(0) = 1$ $z_3(0) = 1$ $\dot{z}_1(0) = 0$ $\dot{z}_2(0) = 0$ $\dot{z}_3(0) = 0$	$e_1 = 0.58E\text{-}02$ $e_2 = 0.77E\text{-}02$ $e_3 = 0.60E\text{-}02$ (Iteration 6)
4	$\begin{bmatrix} 0.2 & 0.7 & 0.6 \\ 0.5 & 0.1 & 0.3 \\ 0.8 & 0.4 & 0.3 \end{bmatrix}$ Nonsymmetric; Nonpositive; Non Diagonally Dominant; RESULTS OF SECTION III DO NOT APPLY	Same as in Example Number 1	Same as in Example Number 1	Same as in Example Number 1	$e_1 = 0.96E\text{-}02$ $e_2 = 0.63E\text{-}02$ $e_3 = 0.28E\text{-}01$ (Iteration 12)

practical problems in structural and mechanical engineering, we have provided the algorithm in the form of a pseudo-code. We list the important features of the work presented here as follows:

(*i*) An important aspect of the presently introduced method is the conceptual understanding that many coupled systems of differential equations which are met with in structural dynamics can be interpreted in terms of uncoupled systems, *provided* that they are subjected to an appropriately calculated *pseudo-forcing vector*. This yields considerable physical insight into the dynamic behavior of large-scale, nonclassically damping structural and mechanical systems.

(*ii*) Unlike several approaches (Singh and Ghafory-Ashtiany, 1986; Veletsos and Ventura, 1986) requiring calculation of complex frequencies and complex mode shapes, thus making the physical interpretation of the elements of the solution difficult, the method presented here is straightforward, computationally efficient, and does not require computations involving complex variables.

(*iii*) Much of the previous effort to uncouple the equations of nonclassically damped systems has been based on replacing the damping matrix by a diagonal matrix. For certain systems and certain types of excitations, this leads to unacceptable computational errors (Hasselman, 1976). Or,

Downloaded 03 May 2010 to 171.66.16.244. Redistribution subject to ASME license or copyright; see http://www.asme.org/terms/Terms_Use.cfm

approximate solutions have been obtained by incorporating the contributions from only a finite number of modes. This may result in acceptable approximations for classically damped systems, but not necessarily for nonclassical systems (Duncan and Taylor 1979). The approach introduced here explains physically why such behavior is to be commonly expected from nonclassically damped systems.

(*iv*) Analytical results are provided giving sufficient conditions for the convergence of the iterative method. Such conditions are indeed necessary to provide, since convergence is of crucial importance in obtaining numerically accurate dynamic responses. It is shown that for diagonally-dominant general damping matrices, F, the method converges. Further results are given for passive systems in which the damping matrix is positive-definite and symmetric. These conditions cover a wide range of commonly occurring structural and mechanical systems.

(*v*) Several numerical examples are presented and it is shown that even under the least ideal conditions the iterative method works well and converges rapidly to the exact solution. The examples illustrate the important role played by the pseudo-force for such convergence. The figures show the extent of error created if the pseudo-force is not taken into account and point out why previous approaches have failed to obtain higher numerical accuracies. It is shown that the iterative approach presented here holds high promise for obtaining very accurate responses to nonclassically damped linear systems, within a few iterations.

References

Caughey, T. K., 1960, "Classical Normal Modes in Damped Linear Structures," ASME JOURNAL OF APPLIED MECHANICS, Vol. 27, pp. 269–271.

Caughey, T. K., and O'Kelly, M. J., 1963, "General Theory of Vibrations of Damped Linear Dynamic Systems," Report of the Dynamics Laboratory, California Institute of Technology, Pasadena, Calif.

Clough, R. W., and Mojtahedi, S., 1976, "Earthquake Response Analysis Considering Non-Proportional Damping," *Earthquake Engineering and Structural Dynamics*, Vol. 4, pp. 489–496.

Cronin, D. L., 1976, "Approximation for Determining Harmonically Excited Response of Non-Classically Damped Systems," *ASME Journal of Engineering for Industry*, pp. 43–47.

Duncan, P. E., and Taylor, R. Eatock, 1979, "A Note on the Dynamic Analysis of Non-Proportioanlly Damped Systems," *Earthquake Engineering and Structural Dynamics*, Vol. 7, pp. 99–105.

Foss, K. A., 1958, "Co-Ordinates that Uncouple the Equations of Motion of Damped Linear Dynamic Systems," ASME JOURNAL OF APPLIED MECHANICS, Vol. 25, pp. 361–364.

Hasselman, T. K., 1976, "Modal Coupling in Lightly Damped Structures," *AIAA Journal*, Vol. 14, pp.

Nigam, N., and Jennings, P. C., 1968, "Digital Calculation of Response Spectra From Strong Motion Earthquake Records," EERL Report No. 700-00, California Institute of Technology, Pasadena, Calif.

Noble, B., 1969, *Applied Linear Algebra*, Prentice-Hall, Englewood Cliffs, N. J.

Press, W. H., Flannery, B. P., Teukolsky, S. A., and Vetterling, W. T., 1986, *Numerical Recipes*, Cambridge University Press, Cambridge, U.K.

Singh, M. P., and Ghafory-Ashtiany, M., 1986, "Modal Time History of Non-Classically Damped Structures for Seismic Motions," *Earthquake Engineering and Structural Dynamics*, Vol. 13, pp. 133–146.

Spanos, P. D., Cao, T., Jacobson, C., Nelson, D., and Hamilton, D., 1988, "Decoupled Dynamic Analysis of Combined Systems by Iterative Determination of Interface Accelerations," *Earthquake Engineering and Structural Dynamics*, Vol. 16, pp. 491–500.

Thomson, W. T., Calkins, T., and Caravani, P., 1974, "A Numerical Study of Damping," *Earthquake Engineering and Structural Dynamics*, Vol. 3, pp. 97–103.

Veletsos, A. S., and Ventura, C. E., 1986, "Modal Analysis of Non-Classically Damped Linear Systems," *Earthquake Engineering and Structural Dynamics*, Vol. 14, pp. 217–243.

Warburton, G. B., and Soni, S. R., 1977, "Errors in Response Calculations for Non-Classically Damped Structures," *Earthquake Engineering and Strucutral Dynamics*, Vol. 5, pp. 365–376.

Downloaded 03 May 2010 to 171.66.16.244. Redistribution subject to ASME license or copyright; see http://www.asme.org/terms/Terms_Use.cfm

Modal Sensors/Actuators

C.-K. Lee
IBM Research Division,
Almaden Research Center,
San Jose, CA 95120-6099
Assoc. Mem. ASME

F. C. Moon
Department of Mechanical and
Aerospace Engineering,
Cornell University,
Ithaca, NY 14853-7501
Mem. ASME

A piezoelectric laminate theory that uses the piezoelectric phenomenon to effect distributed control and sensing of structural vibration of a flexible plate has been used to develop a class of distributed sensor/actuators, that of modal sensors/actuators. The one-dimensional modal sensors/actuator equations are first derived theoretically and then examined experimentally. These modal equations indicate that distributed piezoelectric sensors/actuators can be adopted to measure/excite specific modes of one-dimensional plates and beams. If constructed correctly, actuator/observer spillover will not be present in systems adopting these types of sensors/actuators. A mode 1 and a mode 2 sensor for a one-dimensional cantilever plate were constructed and tested to examine the applicability of the modal sensors/actuators. A modal coordinate analyzer which allows us to measure any specific modal coordinate on-line real-time is proposed. Finally, a way to create a special two-dimensional modal sensor is presented.

Introduction

Investigating the use of discrete point sensors/actuators to control the vibrations of flexible structures has been a major research subject in the last ten years (Balas, 1978a, 1978b, 1979; Oz and Meirovitch, 1980; Bar-Kana et al., 1983; Meirovitch et al., 1983; Schafer, 1985; Natori et al., 1988). These control strategies often suffer from actuator/observer spillover as shown by Balas (1978b), where actuator and observer spillover due to the residual (uncontrolled) models leads to instabilities in the closed-loop system. Techniques such as prefiltering (Balas, 1978b) and modal-filtering (Meirovitch and Baruh, 1982) have been developed over the years to overcome the spillover of the independent modal-space control method. It should be noted that the modal filtering is carried out in space and not in time (Meirovitch and Baruh, 1985). Use of PZT (lead, zirconate, titanate) ceramic and PVDF (polyvinylidene fluoride) thin film as a distributed active damper for beam vibration have been studied (Bailey and Hubbard, 1985; Burke and Hubbard, 1987; Plump et al., 1987; Hanagud et al., 1985, 1986; Crawley and de Luis, 1985, 1986; Fanson and Caughey, 1987; Fanson and Garba, 1988). In this paper, using a concept similar to modal-filtering, a novel class of distributed sensors/actuators, modal sensors/actuators for certain types of beams and plates will be presented. These modal sensors/actuators will sense or actuate the modal coordinate of a particular mode of the beam or plate directly without extensive on-line real-time computational requirements. These types of sensors/actuators can be easily implemented into structural systems using piezoelectric laminae, such as PZT, PVDF, etc.

Contributed by the Applied Mechanics Division of THE AMERICAN SOCIETY OF MECHANICAL ENGINEERS for publication in the JOURNAL OF APPLIED MECHANICS.

Discussion on this paper should be addressed to the Technical Editor, Leon M. Keer, The Technological Institute, Northwestern University, Evanston, IL 60208, and will be accepted until two months after final publication of the paper itself in the JOURNAL OF APPLIED MECHANICS. Manuscript received by the ASME Applied Mechanics Division, June 30, 1988; final revision, February 15, 1989.

Theory of One-Dimensional Distributed Sensors/Actuators

There are two essential ideas in this paper: first, to use the directional properties of a piezoelectric material to design a composite structure, and second, to shape the electrodes to achieve the desired input-output characteristics of the sensor. The basic configuration of the laminates that will be studied in this paper is shown in Fig. 1, where the shim metal layer (layer 2) is made from isotropic material such as aluminum, stainless steel, etc., and can be considered here as part of the existing structure. The piezoelectric laminae can be made from any piezoelectric materials and are considered as added layers for sensing, actuating, and even controlling the structure vibration. An interesting fact about PVDF worth mentioning is that the Young's modulus of PVDF manufactured under certain conditions is the same in all directions (Tamura et al., 1977; Kepler, 1978). These types of mechanically isotropic PVDF will be used as the piezoelectric laminae in this paper. Even if mechanically anisotropic PVDF is used as the piezoelectric laminae, the mechanical stiffness of PVDF is usually ten times smaller than the existing structure, thus the mechanical anisotropy of the PVDF can generally be neglected.

Since all the laminae are made from isotropic material, the laminates constructed will be transverse isotropic in the xy-plane as shown in Fig. 1. The skew angle θ in Fig. 1 is defined as an angle rotating from the x-axis to the x'-axis and obeying the sign convention of the right-hand rule with respect to the z-axis. One thing that should be noted is that the z'-axis can either point to the positive or the negative z-axis direction. These facts will be used later to develop the modal sensors/actuators.

Extending the Kirchoff hypothesis (Ashton, et al.), which results in a plane stress state for a thin plate, to piezoelectric laminae will yield the following constitutive equations for piezoelectric laminae (Lee, 1987, 1988) written in IEEE compact matrix notation (IEEE std., 1978):

Copyright © 1990 by ASME
Downloaded 03 May 2010 to 171.66.16.244. Redistribution subject to ASME license or copyright; see http://www.asme.org/terms/Terms_Use.cfm

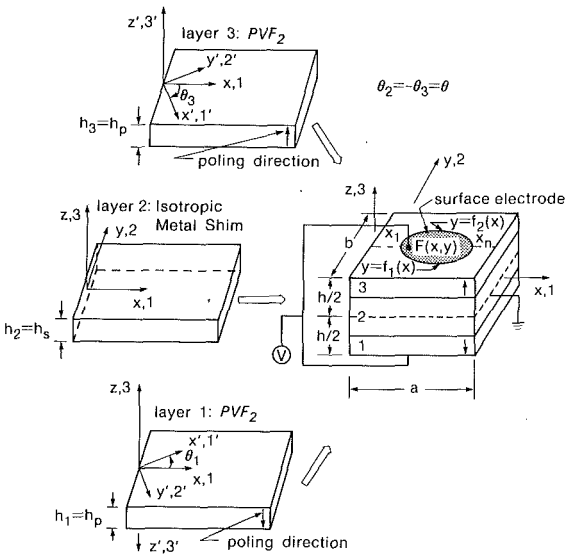


Fig. 1 Three-layer PVDF-shim metal composites (*x, y, z* represent laminate axes; *x', y', z'* represent laminae axes)

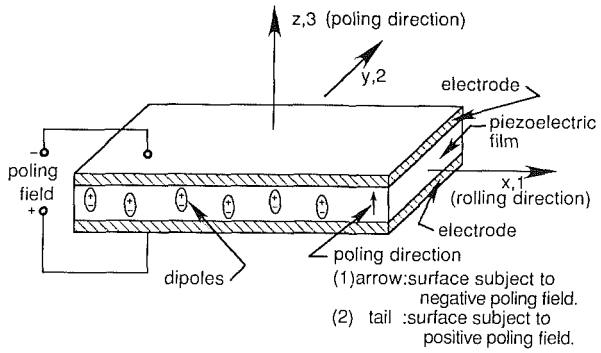


Fig. 2 Coordinate axes of PVDF film

$$\begin{bmatrix} \mathbf{T}_{1'} \\ \mathbf{T}_{2'} \\ \mathbf{T}_{6'} \end{bmatrix} = [c] \begin{bmatrix} \mathbf{S}_{1'} \\ \mathbf{S}_{2'} \\ \mathbf{S}_{6'} \end{bmatrix} - \mathbf{E}_{3'} \begin{bmatrix} e^0_{3'1'} P_o(x,y) \\ e^0_{3'2'} P_o(x,y) \\ e^0_{3'6'} P_o(x,y) \end{bmatrix}, \quad (1)$$

$$\mathbf{D}_{3'} = \epsilon_{3'3'} \mathbf{E}_{3'} + d^0_{3'1'} P_o \mathbf{T}_{1'} + d^0_{3'2'} P_o \mathbf{T}_{2'} + d^0_{3'6'} P_o \mathbf{T}_{6'}, \quad (2)$$

where the vectors **T, S, D, E** represent the stress, strain, electric displacement, and electric field, respectively, ϵ is the permitivity constant of a piezoelectric lamina, and the prime on the subscript is used to designate that the constant is written with respect to the laminae axes. In addition,

$$[c] = \begin{bmatrix} Y_p/(1-\nu_p^2) & \nu_p Y_p/(1-\nu_p^2) & 0 \\ \nu_p Y_p/(1-\nu_p^2) & Y_p/(1-\nu_p^2) & 0 \\ 0 & 0 & Y_p/2(1+\nu_p) \end{bmatrix}, \quad (3)$$

is the stiffness matrix of the piezoelectric lamina, $[e^0_{3'1'}\ e^0_{3'2'}\ e^0_{3'6'}]^t = [c][d^0_{3'1'}\ d^0_{3'2'}\ d^0_{3'6'}]^t$, where the superscript "t" represents the transposition of a matrix, the constants e and d are the piezoelectric stress/charge and strain/charge constants of the piezoelectric laminae, the superscript "0" indicates that the piezoelectric quantity specified is a constant, while the variation of the polarization profile of the laminae is modeled solely by $P_o(x,y)$. More specifically, $P_o(x,y)$ represents the polarization profile which is introduced to model the effect that PVDF is ferroelectric (Kepler and Anderson, 1978), which means that the piezoelectric strength can be changed or reversed by poling. One thing that should be noted

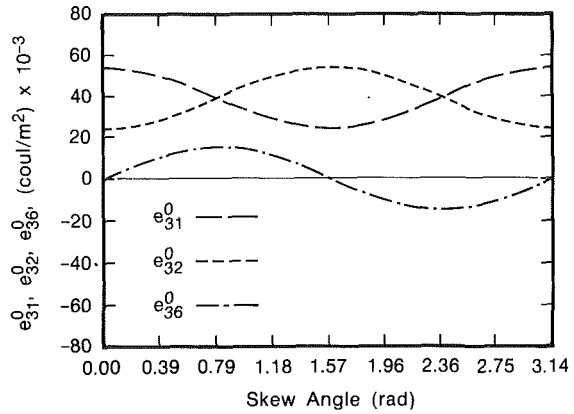


Fig. 3 Piezoelectric stress/charge constant of PVDF versus skew angle

for PVDF is that experimental data published by Fukada and Sakurai (1971) showed that the polarization profile can have the same variation for different piezoelectric constants. Thus, we can use the same function $P_o(x,y)$ to model the variations in this paper. The skew angle effect (Fig. 1) is modeled by performing coordinate transformation for the piezoelectric constants between the laminae and laminate axes:

$$\begin{bmatrix} e^0_{31} \\ e^0_{32} \\ e^0_{36} \end{bmatrix} = [\mathbf{T}_m(\theta)] \begin{bmatrix} e^0_{3'1'} \\ e^0_{3'2'} \\ e^0_{3'6'} \end{bmatrix}, \quad (4)$$

$$\begin{bmatrix} d^0_{31} \\ d^0_{32} \\ d^0_{36} \end{bmatrix} = [\mathbf{T}_m(\theta)] \begin{bmatrix} d^0_{3'1'} \\ d^0_{3'2'} \\ d^0_{3'6'} \end{bmatrix}, \quad (5)$$

where the transformation matrix $[\mathbf{T}_m(\theta)]$ has the following form:

$$[\mathbf{T}_m(\theta)] = \begin{bmatrix} m^2 & n^2 & -2mn \\ n^2 & m^2 & 2mn \\ mn & -mn & m^2-n^2 \end{bmatrix}, \quad (6)$$

$m = \cos\theta$, $n = \sin\theta$, and θ is the skew angle. For the commercially available PVDF thin film (Kynar Film Manual, 1983) used in this paper, when written with respect to the coordinate system shown in Fig. 2, $d^0_{3'1'} = 23 \times 10^{-12}$m/V (or coul/N) and $d^0_{3'2'} = 3 \times 10^{-12}\ m/V$, and $d^0_{3'6'} = 0$. Therefore, the change of the e constants versus the skew angle can be shown in Fig. 3. Equations (1) and (2) allow us to introduce the piezoelectric property into the classical laminated plate theory (Ashton et al.). In fact, equation (1) forms the base of the distributed actuator equation and equation (2) the base of the distributed sensor equation.

Upon introducing equation (1) into the classical laminated plate theory and using equations (4) and (5) to model the skew angle effect, the actuator equation for a laminated piezoelectric plate as shown in Fig. 1 can be obtained as follows (Lee, 1987, 1988):

$$\mathbf{D}_{11}\left\{\frac{\partial^4 w}{\partial x^4} + 2\frac{\partial^4 w}{\partial x^2 \partial y^2} + \frac{\partial^4 w}{\partial y^4}\right\} + \rho h \frac{\partial^2 w}{\partial t^2} =$$

$$-2h_p \bar{z}_p G(t)\left\{e^0_{31}\frac{\partial^2}{\partial x^2}(FP_o) + e^0_{32}\frac{\partial^2}{\partial y^2}(FP_o) + 2e^0_{36}\frac{\partial^2}{\partial x \partial y}(FP_o)\right\}, \quad (7)$$

where

Downloaded 03 May 2010 to 171.66.16.244. Redistribution subject to ASME license or copyright; see http://www.asme.org/terms/Terms_Use.cfm

$$\mathbf{D}_{11}=\left(\frac{h_s^3}{12}\right)\left[\frac{Y_s}{(1-\nu_s^2)}\right]+h_p\left(\frac{h_s^2}{2}+h_sh_p+\frac{2}{3}h_p^2\right)\left[\frac{Y_p}{(1-\nu_p^2)}\right] \quad (8)$$

is the flexural rigidity of the plate; $w=w(x, y, t)$ is the out-of-plane displacement of the plate; Y, ν, h represent the Young's modulus, Poisson's ratio, and the thickness of the laminae, respectively; subscripts p and s are used to designate that of the PVDF layer or the shim metal layer; $\bar{z}_p$ is the z-coordinate of the midplane of the third layer, i.e., $\bar{z}_p=(h_p+h_s)/2$ in Fig. 1; ρ represents the equivalent density of a laminate, e.g., for a three-layered PVDF-shim metal laminate as shown in Fig. 1

where $\rho=\left(\sum_{k=1}^{3}\rho_k h_k\right)/h=(2\rho_p h_p+\rho_s h_s)/h.$

When an electric field is connected to a piezoelectric lamina, only the portion of the lamina that is covered by electrode on both sides of the surfaces, termed effective surface electrode, will be affected by the externally applied electric field. Therefore, we can use the surface electrode to control the location of the force induced by the electromechanical interactions of the piezoelectric laminae. This effective surface electrode property is modeled by $F(x, y)$. More specifically, $F(x, y)$ equals one if (x, y) is covered by electrode on both sides of the lamina, otherwise it is zero. A similar effect can be found in the piezoelectric sensor. As the piezoelectric material is dielectric, the electric charge generated due to the external mechanical disturbance will be detected only if the charge is collected through the surface electrode to an external measurement device. In other words, this selective charge collecting phenomenon performed by a surface electrode is equivalent to doing signal processing through the integration of spatial domain. This is also one of the fundamental concepts that is used in this paper to create modal sensors/actuators.

If we assume that there is no y-dependence in the displacement w, i.e., $w=(x, t)$, equation (7) can be reduced to a one-dimensional version:

$$\mathbf{D}_{11}\frac{\partial^4 w}{\partial x^4}+\rho h\frac{\partial^2 w}{\partial t^2}=-2h_p\bar{z}_p G(t)e_{31}^0\frac{d^2\mathfrak{F}(x)}{dx^2}, \quad (9)$$

where

$$\mathfrak{F}(x)=\int_{-\frac{b}{2}}^{\frac{b}{2}}F(x,y)P_o(x,y)dy, \quad (10)$$

is introduced to represent the spatial dependent part of the interactions between PVDF and the electric field summed along the y-direction, b being the width of the beam. This one-dimensional plate equation, equation (9), when reduced to a single layer case, i.e., $h_p\to 0$ in $\mathbf{D}_{11}$, has the same form as that of the beam equation except that the flexural rigidity constant differs by a factor of $(1-\nu^2)$. That is, the cylindrical bending effect of a slender plate in the y-direction appears as an increase in stiffness since the flexural rigidity EI of a unit width beam is $(1-\nu^2)$ times the flexural rigidity, $\mathbf{D}_{11}$, of a one-dimensional slender plate. This $(1-\nu^2)$ factor can be further understood by using the concepts of plane-strain approximation and plane-stress approximation (Love, 1927). Taking a slender plate as an example, the plane-strain approximation is used along the width direction whenever the thin plate theory is used (Timoshenko and Woinowsky-Krieger, 1959). The plane-stress approximation, on the other hand, is used along the width direction of a beam. These two concepts indeed unearth the difference and similarity between a one-dimensional plate and a beam as a result of the $(1-\nu^2)$ factor between the formulation of the plane-stress and plane-strain approximation (Love, 1927; Chou and Pagano, 1967). Furthermore, these discussions also indicate that if the thickness of a slender plate as shown in Fig. 1 is much smaller than its width, a one-dimensional plate equation, (equation (9)), instead of the beam equation should be used to model the dynamic behavior (Pao, 1988).

Expanding this discussion and recognizing that the difference between a single-layer one-dimensional plate and a one-dimensional laminated plate is only in the definition of $\mathbf{D}_{11}$ used, we can use equation (9) to model a laminated piezoelectric beam of unit width simply by setting $\nu_p\equiv\nu_s\equiv 0$ in the definition of $\mathbf{D}_{11}$ presented in equation (8).

Substituting equation (2) into Gauss' law and recognizing the fact that the equivalent circuit of a piezoelectric lamina, while it is not resonant in its thickness mode, is a capacitor with a parallel leakage resistor, we can approximate the closed-circuit charge signal $q_k(t)$ measured through the electrode of the kth lamina (Fig. 1) as follows (Lee, 1987, 1988):

$$q_k(t)=-\bar{z}_k\int_s FP_o\left[e_{31}^0\frac{\partial^2 w}{\partial x^2}+e_{32}^0\frac{\partial^2 w}{\partial y^2}+2e_{36}^0\frac{\partial^2 w}{\partial x\partial y}\right]dxdy,\ k=1,3, \quad (11)$$

where $\bar{z}_k$ is the z-coordinate of the midplane of the kth layer, e.g., in Fig. 1, $\bar{z}_1=-\bar{z}_3=-\bar{z}_p=-(h_p+h_s)/2$, $\mathbf{S}$ is the area that is covered by the piezoelectric lamina (with and without electrode).

For a single-span slender plate with the same configuration as that shown in Fig. 1, $w=w(x, t)$ can again be substituted into equation (11) to obtain the one-dimensional sensor equation. Furthermore, since there is no moment or force resultants along the y-direction, the summation of $F(x, y)P_o(x,y)$ along the y-direction can again be adopted to represent the spatial dependent part of the interactions between the PVDF and the electrical field as that done in the actuator equation. In other words, one can use $\mathfrak{F}(x)$ in equation (10) to model the effect of the effective electrode $F(x, y)$ and the polarization profile $P_o(x, y)$ summed along the y-direction. Therefore, the sensor equation of a single span plate becomes

$$q_k(t)=-\bar{z}_k e_{31}^0\int_0^a\mathfrak{F}(x)\frac{\partial^2 w}{\partial x^2}dx, \quad (12)$$

where a is the length of the plate (Fig. 1).

Theory of Modal Sensors/Actuators

The transverse deformation of a one-dimensional plate w can be decomposed into the modal summation

$$w(x,t)=\sum_{m=1}^{\infty}A_m(t)\phi_m(x), \quad (13)$$

where $A_m(t)$ and $\phi_m(x)$ are the modal coordinate and mode shape of mode m, respectively. Substituting equation (13) into equation (9) yields that

$$q_k(t)=\sum_{m=1}^{\infty}A_m(t)B_m, \quad (14)$$

where

$$B_m=-\bar{z}_k e_{31}^0\int_0^a\mathfrak{F}(x)\left[\frac{d^2\phi_m(x)}{dx^2}\right]dx. \quad (15)$$

Since a one-dimensional plate as well as a beam is a self-adjoint system as discussed previously, the modes are orthogonal to each other. This property can be used to help us design a modal sensor/actuator. In addition, since the difference between a one-dimensional plate and beam (laminated or homogeneous) can be attributed to the value of the flexural rigidity used, the following discussions will remain valid for all cases (beam or plate, laminated or homogeneous) as long as the flexural rigidity is changed accordingly. For example, since the mode shapes of a beam and a one-dimensional plate (laminated or homogeneous) depend on the boundary conditions only, they will be identical for all these cases. However, since the

Downloaded 03 May 2010 to 171.66.16.244. Redistribution subject to ASME license or copyright; see http://www.asme.org/terms/Terms_Use.cfm

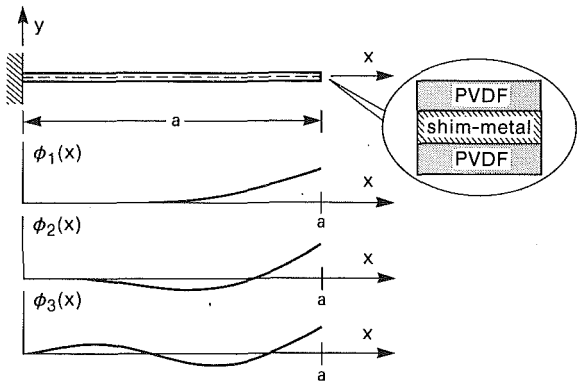


Fig. 4 Mode shape of a one-dimensional cantilever plate

natural frequencies are proportional to the square root of the flexural rigidity, they will have to be changed accordingly. Consider a one-dimensional cantilever slender plate with length a as shown in Fig. 4, i.e., $\mathbf{D}_{11}$ has the form of equation (8), the mode shapes $\phi_m(x)$ for both the one-dimensional cantilever plate and the cantilever beam are (Blevins, 1985)

$$\phi_m(x) = [\cosh(\lambda_m x/a) - \cos(\lambda_m x/a)] - \sigma_m[\sinh(\lambda_m x/a) - \sin(\lambda_m x/a)], \quad (16)$$

where $\lambda_1 = 1.87510407$, $\lambda_2 = 4.69409113$, etc. satisfy the transcendental equation $\cos\lambda\cosh\lambda + 1 = 0$, and $\sigma_1 = 0.734095514$, $\sigma_2 = 1.018467319$, etc. are obtained from the formula $\sigma_m = (\sinh\lambda_m - \sin\lambda_m)/(\cosh\lambda_m + \cos\lambda_m)$.

Combining equations (14) and (15) and the fact that

$$\int_0^a [d^2\phi_n(x)/dx^2][d^2\phi_m(x)/dx^2]dx = \delta_{nm}(\lambda_n^4/a^3), \quad (17)$$

where δ_{nm} is the Kronecker delta, we know that if we choose $\mathcal{F}(x)$ equal to a scaling constant μ_n times the second derivative of a particular mode shape, a modal sensor will be created. Physically, $\mathcal{F}(x)$ is proportional to the modal strain distribution along the length of the plate. In other words, if

$$\mathcal{F}(x) = \mu_n[d^2\phi_n(x)/dx^2], \quad (18)$$

equation (15) becomes

$$B_m = -(\tilde{z}_k e_{31}^0 \mu_n \lambda_n^4/a^3)\delta_{nm}. \quad (19)$$

Therefore, equation (14) reduces to the *modal sensor equation* as follows:

$$q_k(t) = -(\tilde{z}_k e_{31}^0 \mu_n \lambda_n^4/a^3)A_n(t). \quad (20)$$

This equation allows us to measure a particular modal coordinate directly. In other words, observer spillover will not be present in systems adopting this type of sensor.

Several concepts need to be cleared up before equation (20) can be turned into a real physical system. First, if we choose $P_o \equiv 1$, then $\mathcal{F}(x)$ can be achieved by varying the surface electrode pattern $F(x, y)$ according to equation (10). Second, simply varying the surface electrode pattern cannot generate a negative value for $\mathcal{F}(x)$ which is required for portions of $d^2\phi_n(x)/dx^2$. The answer is to vary the polarization profile $P_o(x, y)$. Several configurations that create a mode 2 sensor, which measures the mode 2 coordinate directly are shown in Fig. 5. As we can see, either re-poling the PVDF or wiring the output polarity of different portions of PVDF can be used to create negative values for $\mathcal{F}(x)$.

Instead of measuring a charge signal to create a modal sensor, we can apply voltage to the effective surface electrode (equation (18)) to create a modal actuator. Taking the one-dimensional modal sensor just discussed as an example, and substituting equation (18) into equation (9) yields that

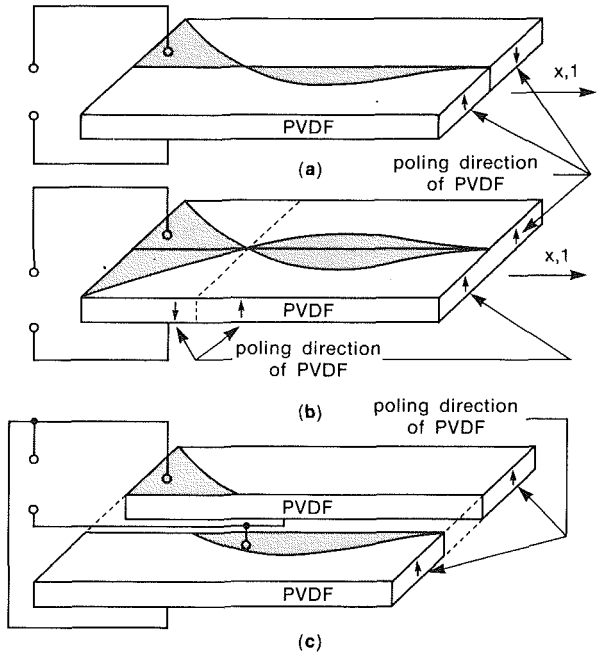


Fig. 5 Configurations for PVDF mode 2 sensors (the dotted area represents the effective surface electrode)

$$\mathbf{D}_{11}\frac{\partial^4 w}{\partial x^4} + \rho h\frac{\partial^2 w}{\partial t^2} = -2[h_p\tilde{z}_p G(t)e_{31}^0\mu_n]\frac{d^4\phi_n(x)}{dx^4}. \quad (21)$$

Substituting equation (13) into equation (21) and using the fact that

$$d^4\phi_m(x)/dx^4 = (\lambda_m/a)^4\phi_m(x), \quad (22)$$

we can obtain that

$$\mathbf{D}_{11}\sum_{r=1}^{\infty}A_r(t)(\lambda_r/a)^4\phi_r(x) + \rho h\sum_{r=1}^{\infty}\frac{d^2A_r(t)}{dt^2}\phi_r(x) = -2[h_p\tilde{z}_p e_{31}^0\mu_n(\lambda_n/a)^4]G(t)\phi_n(x). \quad (23)$$

Multiplying both sides of (23) by $\phi_m(x)$, integrating over the length of the one-dimensional plate and employing the fact that $\int_0^a \phi_m\phi_r dx = a\delta_{mr}$ yields the *modal actuator equation*:

$$\rho h\frac{d^2A_n(t)}{dt^2} + [\mathbf{D}_{11}(\lambda_n/a)^4]A_n(t) = -2[h_p\tilde{z}_p e_{31}^0\mu_m(\lambda_m/a)^4]G(t)\delta_{mn}. \quad (24)$$

This equation shows that if $\mathcal{F}(x)$ has the form of equation (18), only the modal coordinate $A_n(t)$ of mode n is under the influence of the PVDF mode n actuator. In other words, we can create a distributed actuator which excites each particular mode independently so that actuator spillover will not be an issue in one-dimensional flexible plates actuated by this type of actuator. The results shown can be easily extended to all other boundary conditions of one-dimensional plates and beams.

Experimental Setup and Procedures

An experimental setup as shown in Fig. 6 is used to check how well different modal sensors can distinguish different modes. Mode 1 and mode 2 sensors were fabricated by first pasting two pieces of 110-μm thick PVDF on both sides of a 203.2-μm (8 mil) thick stainless steel shim to form a 14.66 cm long, 1.0 cm wide cantilever slender plate. The surface electrode of PVDF is then etched according to equation (18) with $\mu_1 = (a/\lambda_1)^2/2$, $\mu_2 = (a/\lambda_2)^2/4$. From the discussion of the effective surface electrode concept, we know that only the electrode on one surface of the piezoelectric lamina needs to be etched to

Downloaded 03 May 2010 to 171.66.16.244. Redistribution subject to ASME license or copyright; see http://www.asme.org/terms/Terms_Use.cfm

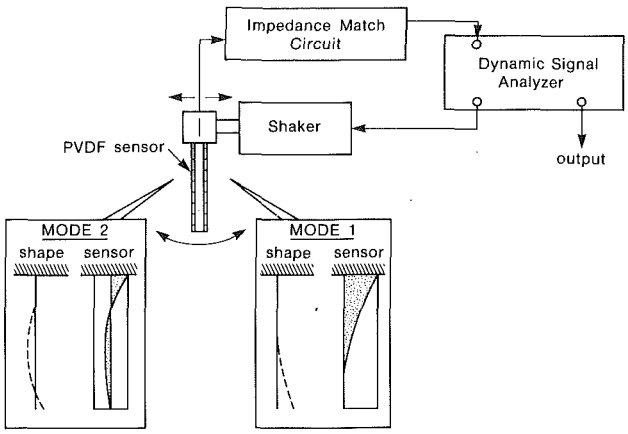


Fig. 6 Experimental setup for modal sensors (the dotted area represents the effective surface electrode)

achieve the selective charge collecting phenomenon predicted by the theory. Therefore, only the electrode on the two outer surfaces of the piezoelectric laminates was etched. The PVDF film used in this experiment was sputtered with a nickel-aluminum electrode (150 Å nickel base layer and 400 Å aluminum cover layer). The most common etchant for printed circuit board processing—ferric chloride ($FeCl_3$) was used to etch the nickel-aluminum electrode despite the fact that nickel is generally considered not to react to $FeCl_3$ solution. It is believed that the thin film nature of the electrode and the strong chemical activity of the aluminum are the main reason that $FeCl_3$ is usable here. This finding makes the physical implementation of the surface electrode effect readily available.

A HP 3562 dynamic signal analyzer is used to perform the sweep sine measurement. The sine wave from 5 Hz to 55 Hz with a sweep rate of 6.87 mHz/sec is used to drive the shaker which in turn drives the PVDF modal sensors. The PVDF sensor signal is measured by connecting the PVDF surface electrode such as shown in Figs. 5 and 6 into the impedance match circuit. This in-house impedance match circuit is made from a National Semiconductor LM163 precision instrument amplifier. The twin shield drivers of this 16-pin dual-in-line package eliminates the capacitive loading to PVDF and reduces sensor signal bandwidth loss due to cable capacitance. Also, the high input impedance of LM163, 20 GΩ for both the common and differential mode with a gain of 10, makes the corner frequency of the high pass filter circuit formed by PVDF sensor and the LM163 below 0.1 Hz. Thus, for a frequency higher than 1 Hz, the signal measured will not be subjected to distortion due to the electronics used. More specifically, the closed-circuit charge signal predicted by equation (20) is obtained by measuring the open-circuit voltage signal based on the fact that the sensor source capacitance equals the ratio of the closed-circuit charge signal and the open-circuit voltage signal. The frequency response curves of mode 1 and mode 2 sensors are measured and displayed separately.

Experimental Results

The transfer function, magnitude ratio of the PVDF sensor signal and the dynamic signal analyzer output driving signal, is shown in Fig. 7. As can be seen here, the natural frequencies of mode 1 and mode 2 of this piezoelectric laminate are 7.270 Hz and 47.577 Hz, respectively. Substituting $Y_s = 200 \times 10^9 \text{N/m}^2$, $Y_p = 2 \times 10^9 \text{N/m}^2$, $\rho_s = 7800\ \text{Kg/m}^3$, $\rho_p = 1780\ \text{Kg/m}^3$, $h_s = 203.2\ \mu\text{m}$, $h_p = 110\mu\text{m}$, and $\nu_s = \nu_p = 1/3$, into equation (8) yields that the flexural rigidity, $\mathbf{D}_{11}$, equals 0.17 N-m. Therefore, the natural frequency of the first two modes can be calculated by substituting the corresponding constants into $f(\text{Hz}) = \lambda_i^2 (\mathbf{D}_{11}/\rho h)^{1/2}/(2\pi a^2)$. Therefore, the predicted natural

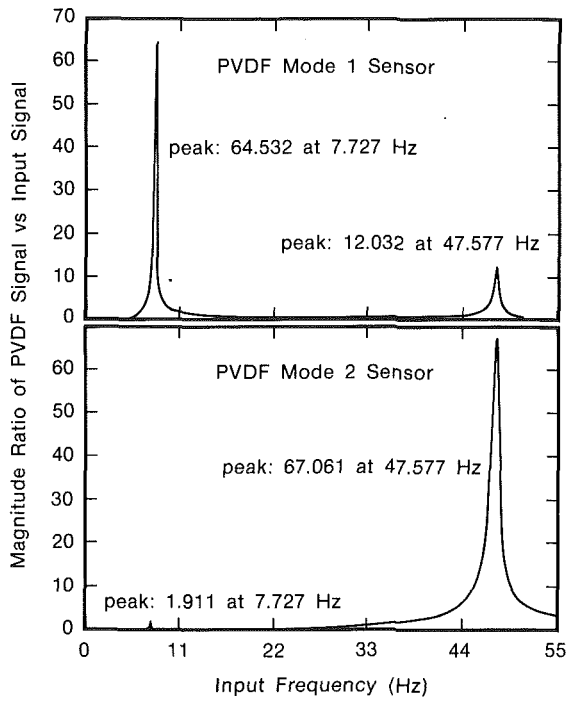


Fig. 7 Magnitude ratio of PVDF signal and shaker driving signal versus frequency

frequency are 7.635 Hz and 47.848 Hz which agrees with the experimental results. Furthermore, we can see that in Fig. 7 the mode 1 sensor responds to the mode 1 vibration much more than the mode 2 vibration. Also, the mode 2 sensor is much more sensitive to the mode 2 vibration than that of mode 1. Because there is no damping factor adopted in equations (20) and (24), the absolute magnitude shown in Fig. 7 is not comparable to the theoretical prediction. This disagreement can be overcome by introducing modal damping into equations (20) and (24) (Lee et al., 1989).

One thing that should be noted is that a detailed comparison is not the main purpose of Fig. 7. This experiment is designed to see if modal sensors will discern the contributions of different modes simply by shaping the surface electrode. These modal sensors can indeed distinguish the contributions of the different modes, and in effect shows the practicality of modal sensors. However, some leak-through phenomenon was found. That is, according to the theory that was developed previously, the mode 1 sensor should only respond to the mode 1 coordinate and the mode 2 sensor only to the mode 2 coordinate. However, experimental data shown in Fig. 7 indicates that the modal sensors constructed can have a small response to other modes. This discrepancy can be explained by observing the edges of the surface electrode pattern. The edges of the surface electrode pattern shown in Fig. 8 is not smooth enough to be considered a match with the theoretical predictions. However, even with such a rough etching process, the response of the mode 1 sensor is still more than five times larger than the mode 2 sensor response when the plate is vibrating at mode 1. This effect is even more significant when the system is vibrating at the second mode. The responses between the sensors have a more than 30 times difference at the vibration of that mode. The results from this experiment verify that different types of sensors can be created by changing the surface electrode pattern. In other words, these type of sensors/actuators can be used to reshape the transfer function so that a flexible plate control task can be easily implemented physically (Lee et al., 1989).

It is worth mentioning that a transfer function similar to Fig. 7 can also be achieved by strategically placing two accel-

Downloaded 03 May 2010 to 171.66.16.244. Redistribution subject to ASME license or copyright; see http://www.asme.org/terms/Terms_Use.cfm

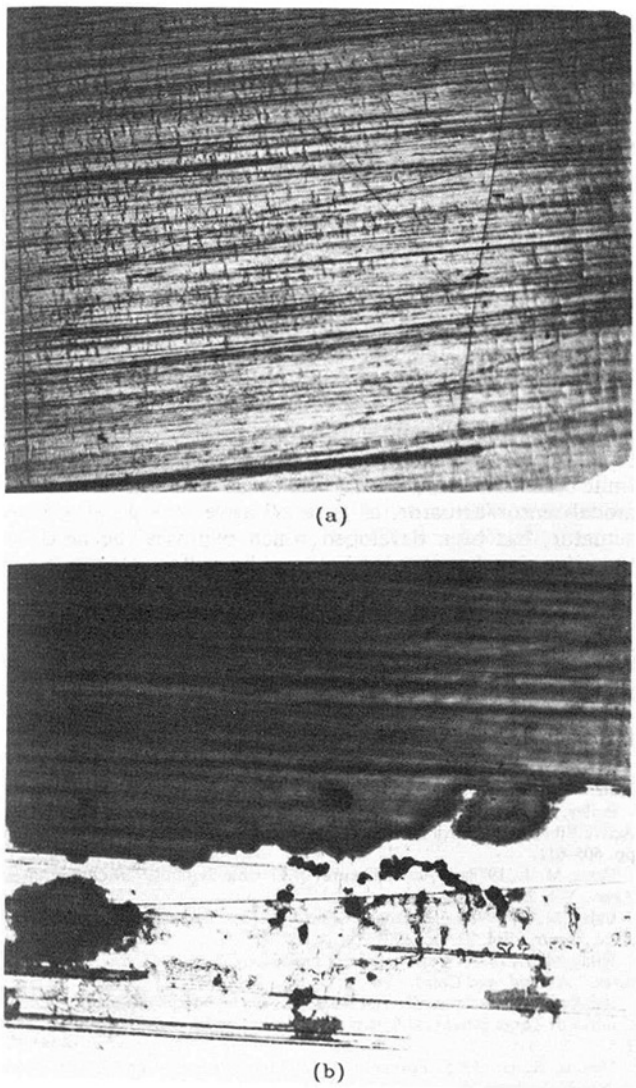


Fig. 8 One hundred times magnified PVDF surface electrode pattern (the dark area is the effective surface electrode): (*a*) before etching, (*b*) after etching

erometers at two locations. However, the output signal of a point sensor (e.g., an accelerometer) contains a spatial domain as well as a time-dependent portion. In order to obtain a modal coordinate, the spatially dependent part of the sensor signal needs to be integrated out. The integrated sensor can be considered a physical realization of the modal filtering method (Oz and Meirovitch, 1980; Meirovitch and Baruh, 1982, 1985). In other words, the charge collecting phenomenon performed by the shaped electrode (equation (18)) is in fact performing signal processing in the spatial domain. From this theory, we know that the modal coordinate can be measured directly by shaping the electrode according to equation (18). This effect cannot be achieved simply by placing accelerometers in strategic positions. The effect of shaped electrode is successfully verified by the experimental results shown in Fig. 7.

An On-Line Modal Coordinate Analyzer

From the previous discussions, we know that the combination of a particular electrode pattern and a corresponding polarization profile will create a modal sensor. Therefore, according to the results, we can either create a piezoelectric laminate with different modal sensors within different laminae or integrate several independent modal sensors at different portions of a lamina. However, we can also adopt the concept of

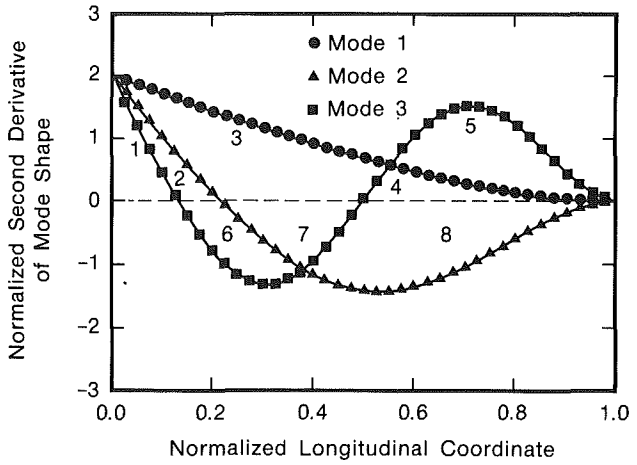


Fig. 9 Overlapped surface electrode pattern for modal sensors 1 to 3. The normalized longitudinal coordinate is the longitudinal coordinate divided by the length of the beam *a*, normalized second derivative of mode *n* is $(a/\lambda_n)^2 d^2\phi_n/dx^2$.

multiplexing signals in a spatial domain to combine several modal sensors, which share part of the surface electrode, into one lamina. More specifically, overlapping the surface electrode pattern needed for the first three modes of the slender cantilever plate (Fig. 9), we can see that the surface electrode can be separated into eight segments with the poling direction of segments $1 \sim 5$ and $6 \sim 8$ in the opposite directions. The combination of segments 1 to 4 will create a mode 1 sensor. The combination of segments 1, 2, 7, 8 and 1, 4, 5, 6, 7 will create a mode 2 and a mode 3 sensor, respectively. This suggests that we can use one group of electrode segments on the surface of PVDF to measure the modal coordinate of different modes on-line real-time simply by wiring the correspondent electrode segments together or by multiplexing the signal from each individual segment. The concept can be generalized as such: Digitize the surface electrode across space and use either a set of analog-digital-converters (ADC) to measure the signal transmitted from each individual pixel simultaneously or a single ADC to multiplex the signal from different pixels. The digitized time domain signal from each different pixel can then be stored to a random access memory (RAM) chip connected to a microprocessor. In this way, all the modal coordinates can be measured by using an internal pointer and an accumulator of the microprocessor to take the sum of all the values of each corresponding address in the RAM. This generalization provides us a method to retrieve modal coordinates of different modes on-line real-time without reshaping the surface electrodes.

Discussion of Modal Sensors/Actuators for Plates

In the foregoing derivations, we used the orthogonality principle of mode shapes of a one-dimensional laminated plates with cantilever boundary conditions to design modal sensors/actuators. Since the orthogonality principle can be easily proved for one-dimensional plates with other boundary conditions, modal sensors/actuators for one-dimensional plates with other boundary conditions can be easily developed following the same approach. A general orthogonality principle does not exist for the vibration mode shapes of thin plates (Blevins, 1985; Prakash, 1980) because of the complexity of the boundary conditions of the plates. However, the mode shapes of a thin uniform plate can be shown to be orthogonal, i.e.,

$$\int_s \phi_{rj}\phi_{mn}dxdy = 0 \text{ for } r \neq m,\ j \neq n, \tag{25}$$

where ϕ_{rj} is the mode shape of the rj mode, if (1) the natural frequencies of the modes are well separated and (2) either (*a*) the edges of the plate are clamped or (*b*) the portion of the

Downloaded 03 May 2010 to 171.66.16.244. Redistribution subject to ASME license or copyright; see http://www.asme.org/terms/Terms_Use.cfm

edges which are not clamped are straight segments, as those of a rectangular or polygonal plate, and these segments are simply supported (Blevins, 1985; Meirovitch, 1971; Prakash, 1980). The modes of plates which do not fall into these classes cannot generally be shown to be orthogonal because of the complexity of the rigorous boundary conditions. However, this lack of a general proof of orthogonality is not a serious practical limitation. Many of the modes of plates for which orthogonality cannot be proven in general can be shown to be orthogonal in specific cases. Generally, the mode shapes of plates with free boundaries cannot be expressed in a closed form. In order to facilitate the numerical solution, the boundary conditions associated with simply-supported and free edges are often simplified by neglecting some of the terms in the rigorous boundary conditions. Orthogonality can be proven for these approximate boundary conditions. Combining these arguments and the experience learned from the modal sensors of one-dimensional cantilever plates, we know that the modal sensor can be extended to plates with certain other boundary conditions using numerical methods or experimental methods to help us identify the mode shapes and orthogonality principle. Taking a four-sided simply-supported rectangular plate with length a and width b (Fig. 1) as an example, the mode shape function has the following form:

$$\phi_{rj}(x, y) = [\sin(r\pi x/a)][\sin(j\pi y/b)]. \tag{26}$$

Again, the transverse deformation of the plate w can be expressed as:

$$w(x,y,t) = \sum_{r=1}^{\infty} \sum_{j=1}^{\infty} A_{rj}(t)\phi_{rj}(x,y), \tag{27}$$

where $A_{rj}(t)$ is the modal coordinate of mode rj.

Substituting equation (27) into equation (11) yields that

$$q_k(t) = -\bar{z}_k \int_s FP_o \left\{ \sum_{r=1}^{\infty} \sum_{j=1}^{\infty} \left[e_{31}^0 \left(-\frac{\pi^2}{a^2} \sin\frac{r\pi x}{a} \sin\frac{j\pi y}{b} \right) + e_{32}^0 \left(-\frac{\pi^2}{b^2} \sin\frac{r\pi x}{a} \sin\frac{j\pi y}{b} \right) \right] + 2e_{36}^0 \left(\frac{\pi^2}{ab} \cos\frac{r\pi x}{a} \cos\frac{j\pi y}{b} \right) \right\} dxdy. \tag{28}$$

Due to the orthogonality of the sine and cosine function, equation (28) can be reduced to

$$q_k(t) = \delta_{lr}\delta_{mj} \left[\bar{z}_k \mu_{lm} \frac{\pi^2}{4} \right] \left[e_{31}^0 \frac{b}{a} + e_{32}^0 \frac{a}{b} \right], \tag{29}$$

if

$$FP_o(x,y) = \mu_{lm}[\sin l\pi x/a][\sin m\pi y/b], \tag{30}$$

where μ_{lm} is a scaling constant. This equation suggests a way to create a true two-dimensional modal sensor. Modal actuators for plates with this type of boundary condition can also be constructed using a similar approach. Furthermore, the reciprocal relationship of the distributed sensors and actuators (Lee, 1987, 1988; Lee and Moon, 1987, 1988) ensures that whenever a choice of $FP_o(x, y)$ is found to create a type of modal sensors, similar types of modal actuators can be created using exactly the same $FP_o(x, y)$. This reciprocal relationship between PVDF modal sensors and modal actuators suggests that those modal sensors/actuators can be combined to make a PVDF oscillator (Lee, 1987; Lee and Moon, 1987, 1988) which will vibrate at a specific mode. These reciprocal sensors/actuators can also be combined to make an active damper for flexible structure control (Lee et al., 1989). Even though a general solution for all boundary conditions is not available for a two-dimensional system, it is believed that the modal actuator for certain boundary conditions can be created.

Conclusion

A piezoelectric laminate plate theory was used to invent PVDF modal sensors/actuators. An on-line modal coordinate analyzer was proposed. The reciprocal relationship between PVDF modal sensors and modal actuators was also discussed. The methods presented in this paper are: (1) laminating the PVDF laminae to form a piezoelectric laminate, (2) changing the skew angle of each PVDF lamina, (3) reshaping the effective surface electrode, and (4) varying the polarization profile of PVDF. These methods are a realization of integrating system dynamics into the distributed sensors/actuators design process, which are used extensively in flexible structural control.

To summarize, one can say that a flexible structure is an infinite dimensional system as is a distributed sensor/actuator. Conventional point sensors/actuators, in contrast, are finite-dimensional systems and thus have intensive signal processing requirements, whereas distributed sensors/actuators being infinite dimensional systems to not. In conclusion, a distributed modal sensor/actuator, as an alternative to a point sensor/actuator, has been developed which bypasses the need for extensive signal processing because the surface electrode and the polarization profile of a distributed sensor/actuator can be used to integrate sensor/actuator signals in the spatial domain.

References

Ashton, J. E., Halpin, J. C., and Petit, P. H., 1969, *Primer on Composite Materials: Analysis*, (Progress in Materials Science Series), Technomic, Conn.

Bailey, T., and Hubbard, J. E., 1985, "Distributed Piezoelectric-Polymer Active Vibration Control of a Cantilever Beam," *J. Guid. and Contr.*, Vol. 8, pp. 605–611.

Balas, M. J., 1978a, "Active Control of Flexible Systems," *J. Optim. Theo. Appl.*, Vol. 25, pp. 415–436.

Balas, M. J., 1978b, "Feedback Control of Flexible Systems," *IEEE Trans. Auto. Contr.*, Vol. 23, pp. 673–679.

Balas, M. J., 1979, "Direct Velocity Feedback Control of Large Space Structures," *J. Guid. and Contr.*, Vol. 2, pp. 252–253.

Bar-Kana, I., Kaufman, H., and Balas, M., 1983, "Modal Reference Adaptive Control of Large Structural Systems," *J. Guid. and Contr.*, Vol. 6, pp. 112–118.

Blevins, R. D., 1985, *Formulas for Natural Frequency and Mode Shape*, Robert E. Krieger, Fla.

Burke, S. E., and Hubbard, J., 1987, "Active Vibration Control of a Simply Supported Beam Using a Spatially Distributed Actuator," *IEEE Contr. Syst. Mag.*, Aug., pp. 25–30.

Chou, P. C., and Pagano, N., 1967, *Elasticity: Tensor, Dyadic and Engineering Approaches*, (Univ. Series in Basic Eng)., W. W. Hagerty, ed., Van Nostrand, N. J.

Crawley, E. F., and de Luis, J., 1985, "Use of Piezo-Ceramics as Distributed Actuators in Large Space Structures," *Proc. of the 26th AIAA/ASME/ASCE/AHS Structures, Structural Dynamics and Materials Conf.*, pp. 126–133.

Crawley, E. F., and deLuis, J., 1986, "Experimental Verification of Distributed Piezoelectric Actuators for Use in Precision Space Structures," *Proc. of the 27th AIAA/ASME/ASCE/AHS Structures, Structural Dynamics and Materials Conf.*, pp. 116–124.

Fanson, J. L., and Caughy, T. K., 1987, "Positive Position Feedback Control for Large Space Structures," *Proc. of the 28th AIAA/ASME/ASCE/AHS Structures, Structural Dynamics and Materials Conf.*, pp. 588–598.

Fanson, J. L., and Garba, J. A., 1988, "Experimental Studies of Active Members in Control of Large Space Structures," *Proc. of the 29th AIAA/ASME/ASCE/AHS Structures, Structural Dynamics and Materials Conf.*, pp. 9–17.

Fukuda, E., and Sakurai, T., 1971, "Piezoelectricity in Polarized Poly(vinylidene Fluoride) Films," *Polymer J.*, Vol. 2, pp. 656–662.

Hanagud, S., Obal, M. W., and Meyyappa, M., 1985, "Electronic Damping Techniques and Active Vibration Control," *Proc. of the 26th AIAA/ASME/ASCE/AHS Structures, Structural Dynamics and Materials Conf.*, AIAA Paper No. 85-0752.

Hanagud, S., Obal, M. W., and Calise, A. J., 1986, "Optimal Vibration Control by the Use of Piezoceramic Sensors and Actuators," *Proc. of the 27th AIAA/ASME/ASCE/AHS Structures, Structural Dynamics and Materials Conf.*, pp. 177–185.

IEEE Standard on Piezoelectricity, 1978, Std. 176.

Kepler, R. G., 1978, "Pyroelectricity and Ferroelectricity in Organic Materials (Review)," *Ann. Rev. Phys. Chem.*, Vol. 29, pp. 497–518.

Kepler, R. G., and Anderson, R. A., 1978, "Ferroelectricity in Polyvinylidene Fluoride," *J. Appl. Phys.*, Vol. 49, pp. 1232–1235.

Kynar Piezo Film Technical Manual, 1983, Pennwalt Corp.

Downloaded 03 May 2010 to 171.66.16.244. Redistribution subject to ASME license or copyright; see http://www.asme.org/terms/Terms_Use.cfm

Lee, C.-K., 1987, "Piezoelectric Laminates for Torsional and Bending Modal Control: Theory and Experiment," Ph.D. dissertation, Cornell University, Ithaca, N.Y.

Lee, C.-K., and Moon, F. C., 1989, "Laminated Piezopolymer Plates for Torsional and Bending Modal Control," U.S. Patent No. 4,868,477.

Lee, C.-K., 1988, "Theory of Laminated Piezoelectric Plates for the Design of Distributed Sensors/Actuators: Part 1. Governing Equations and Reciprocal Relationships," IBM Research Division Report RJ 6332, to appear in *J. of Acoust. Soc. Am.*, Feb. 1990.

Lee, C.-K., and Moon, F. C., 1989, "Laminated Piezoelectric Plates for Torsion and Bending Sensors and Actuators," *J. of Acoust. Soc. Am.*, Vol. 85, pp. 2432–2439.

Lee, C.-K., Chiang, W.-W., and O'Sullivan, T. C., 1989, "Piezoelectric Modal Sensors and Actuators Achieving Critical Active Damping on a Cantilever Plate," (AIAA Paper No. 89-1390), *Proc. of the 30th AIAA/ASME/ASCE/AHS Structures, Structural Dynamics and Materials Conf.*, Apr., pp. 2018–2026.

Love, A. E. H., 1927, *A Treatise on the Mathematical Theory of Elasticity*, 4th ed., Cambridge Univ. Press, Cambridge, U.K.

Meirovitch, L., 1971, *Analytical Methods in Vibrations*, Macmillan, New York, p. 183.

Meirovitch, L., and Baruh, H., 1982, "Control of Self-Adjoint Distributed-Parameter Systems," *J. Guid. and Contr.*, Vol. 5, pp. 60–66.

Meirovitch, L., and Baruh, H., 1985, "The Implementation of Modal Filters for Control of Structures," *J. Guid. and Contr.*, Vol. 8, pp. 707–716.

Meirovitch, L., Barvin, H., Montgomery, R. C., and Williams, J. P., 1983, "Nonlinear Control of an Experimental Beam by IMSC," AIAA preprint, 83-0855.

Natori, M., Motohashi, S., Takahara, K., and Kuwao, F., 1988, "Vibration Control of Truss Beam Structures Using Axial Force Actuators," *Proc. of the 29th AIAA/ASME/ASCE/ASH Structures, Structural Dynamics and Materials Conf.*, pp. 491–499.

Oz, H., and Meirovitch, L., 1980, "Optimal Modal-Space Control of Flexible Gyroscopic Systems," *J. Guid. and Contr.*, Vol. 3, pp. 218–226.

Pao, Y.-H., 1988, Department of T&AM, Cornell University, private communication.

Plump, J. M., Hubbard, J. E., and Bailey, T., 1987, "Nonlinear Control of a Distributed System: Simulation and Experimental Results," ASME *J. Dyn. Sys. Mea. and Contr.*, Vol. 109, pp. 133–139.

Prakash, B. G., 1980, "Free Vibration of Rectangular Plates," *J. Sound and Vibration*, Vol. 70, pp. 303–305.

Schafer, B. E., and Holzach, H., 1985, "Experimental Research on Flexible Beam Modal Control," *J. Guid. and Contr.*, Vol. 8, pp. 597–604.

Tamura, M., Hagiwara, S., Matsumoto, S., and Ono, N., 1977, "Some Aspects of Piezoelectricity and Pyroelectricity in Uniaxially Stretched Poly(vinylidene Fluoride)," *J. Appl. Phys.*, Vol. 48, pp. 513–521.

Timoshenko, S., and Woinowsky-Krieger, S., 1959, *Theory of Plates and Shells*, 2nd ed., McGraw-Hill Book Co., New York.

von Flotow, A. H., and Schafer, B., 1986, "Wave Absorbing Controllers for a Flexible Beam," *J. Guid and Contr.*, Vol. 9, No. 6, pp. 673–680.

Downloaded 03 May 2010 to 171.66.16.244. Redistribution subject to ASME license or copyright; see http://www.asme.org/terms/Terms_Use.cfm

On Randomly Excited Hysteretic Structures

G. Q. Cai
Research Assistant.

Y. K. Lin
Charles E. Schmidt Professor and Director.

Center for Applied Stochastics Research,
Florida Atlanta University,
Boca Raton, FL 33431

Approximate probability distributions of certain response variables are obtained for hysteretic systems under Gaussian white-noise excitations. The approximate method used is a generalization of a dissipation-energy-balancing procedure, developed previously for nonlinear but basically nonhysteretic systems. Some new issues related particularly to hysteresis models are explained and resolved. The method is applicable to either bilinear or smooth-type hysteresis without the restriction that the response be a narrow-band process or the energy dissipation be small. Comparison of computed results with available simulation results indicates that the proposed method is accurate for wide ranges of excitation levels and system parameters.

Introduction

In structural dynamics, the term hysteresis is used to describe a nonconservative system behavior, in which the restoring force depends not only on the instantaneous deformation but also the past history of deformation. If motion is cyclic, then a plot of restoring force versus deformation forms a closed loop, the area within the loop being the energy loss per cycle. Excellent reviews of hysteresis characterisitics for various structural elements were given by Sozen (1974) and Iwan (1974).

The problem of hysteretic system under random excitation is difficult, and no mathematically exact solution is available at the present time. Published approximate solutions have been restricted to single-degree-of-freedom systems, governed typically by the following nondimensional equation of motion:

$$\ddot{x}+2\zeta\dot{x}+f(\tau)=\xi(\tau) \tag{1}$$

$$f(\tau)=\alpha x+(1-\alpha)z(\tau) \tag{2}$$

where τ is a nondimensional time, $\xi(\tau)$ is a stochastic process which will be taken as Gaussian white noise in what follows, and an overdot denotes one differentiation with respect to τ. Equation (2) describes a restoring force separable into a linear component and a hysteretic component. The hysteretic component $z(\tau)$ can often be modeled by a first-order differential equation,

$$\dot{z}=g(x,\dot{x},z). \tag{3}$$

One simple example is the widely used elastoplastic model,

$$\dot{z}=\begin{cases}0 & z\,\mathrm{sgn}\,\dot{x}=1\\ \dot{x} & |z|<1\end{cases} \tag{4}$$

shown in Fig. 1(*a*) where the elastic displacement limit has been chosen as the nondimensionalization length. The restoring force, $f(\tau)$, obtained from combining this hysteresis component, $z(\tau)$, and the linear component constitutes the well-known bilinear model shown in Fig. 1(*b*).

The first analysis of the response of a bilinear system to statistically stationary random excitation was due to Caughey (1960), who used the methods of equivalent linearization and slowly varying parameters. Accurate results were obtained for the mean-square response when the coefficient α in (2) is not too small; significant errors were found when this is not the case (Iwan and Lutes 1968).

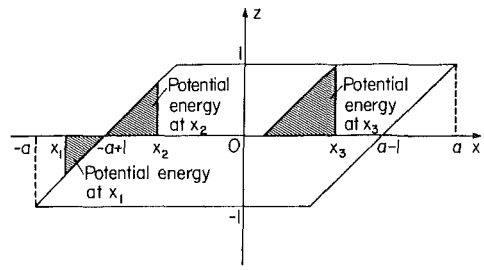


Fig. 1(*a*)

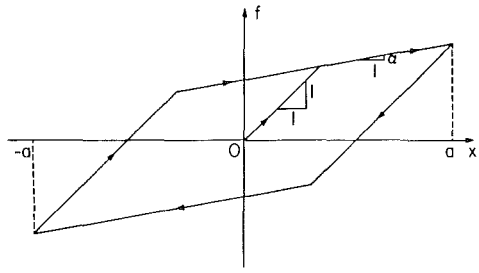


Fig. 1(*b*)

Fig. 1 A bilinear hysteretic system: (*a*) elasto-plastic component, (*b*) restoring force-deformation relationship

Contributed by the Applied Mechanics Division of THE AMERICAN SOCIETY OF MECHANICAL ENGINEERS for publication in the JOURNAL OF APPLIED MECHANICS.

Discussion on this paper should be addressed to the Technical Editor, Leon M. Keer, The Technological Institute, Northwestern University, Evanston, IL 60208, and will be accepted until two months after final publication of the paper itself in the JOURNAL OF APPLIED MECHANICS. Manuscript received by the ASME Applied Mechanics Division, May 18, 1988; final revision, January 27, 1989.

Copyright © 1990 by ASME
Downloaded 03 May 2010 to 171.66.16.244. Redistribution subject to ASME license or copyright; see http://www.asme.org/terms/Terms_Use.cfm

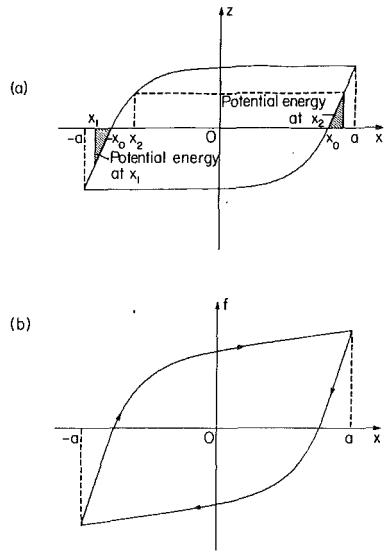


Fig. 2 A smooth hysteretic system: (*a*) hysteretic component, (*b*) restoring force-deformation relationship

For structural reliability estimations, the more detailed knowledge of probability distribution is required. Lutes (1970) obtained an estimate of the response probability density for a bilinear hysteretic system using an equivalent nonhysteretic nonlinear system belonging to Caughey's class of solvable systems (1964). Selection of the equivalent system was based on equal energy dissipation. The applicability of his method requires that the response be a narrow-band random process, since a so-called resonant frequency must be calculated. However, the approximation does not appear to be more accurate than that of the equivalent linearization when values of the mean-square response obtained from the two methods are compared. Subsequently, Lutes and Takemiya (1974) devised a modified power balance method to improve the accuracy of the computed mean-square response, especially for nearly elastoplastic systems.

Roberts (1978) and Zhu and Lei (1987) have used another approach called stochastic averging (Stratonovich, 1963) in the treatment of bilinear hysteretic systems, and obtained the probability densities for the amplitude and the energy envelope, respectively, for the stationary response by solving the so-called Fokker-Planck equations for the respective response variables. Applicability of the stochastic averaging method requires that the energy dissipation must be small. Kobori, Minai, and Suzuki (1976) computed the statistical moments of the displacement and velocity using the Fokker-Planck equation for these variables and assumed forms for approximate probability densities.

The abrupt change of slope in the deformation-restoring force relationship in a bilinear model is obviously not realistic. To remedy this deficiency Iwan (1966) has proposed a distributed hysteretic model, composed of a number of Jenkin's elements in parallel, each of which consists of a linear spring in series with a Coulomb damper. This smooth hysteresis model was used by Takemiya and Lutes (1977) in conjunction with the power balance method, and by Spanos (1979) in conjunction with stochastic averaging and equivalent linearization in the investigation of system response.

Another smooth hysteresis model proposed initially by Bouc (1967), and extended later by Wen (1976, 1980), is described by

$$\dot{z} = -\gamma |\dot{x}| z |z|^{n-1} - \beta \dot{x} |z|^n + A\dot{x}. \tag{5}$$

Sketches of z versus x and the restoring force f versus x are shown in Figs. 2(*a*) and 2(*b*), respectively. By choosing different sets of values for γ, β, n, and A, the behaviors of real hysteretic systems can be approximated closely (Baber and Wen, 1980). This model has recently become more widely used, since it is more amenable to analytical treatments. Further refinements of the model were proposed by Baber and Noori (1985) and by Casciati (1987). The Galerkin method (Wen 1976), Gaussian closure (Iyenger and Dash 1978), equivalent lineraization (Wen 1980), and stochastic averaging (Roberts 1987) have all been applied to the analysis of this model with various degrees of success and limitations.

The references quoted in the previous paragraph were limited to additive random excitations, namely excitations appearing as inhomogeneous terms in the equation of motion. One exception was the work by Shih and Lin (1982) in which a multiplicative random excitation, appearing in a coefficient in the governing equation, was also included in the analysis. In this case, the multiplicative excitation arose due to vertical ground motions during an earthquake. The Gaussian closure technique was employed to compute the statistics of the structural response.

In this paper, a new approximate procedure, developed recently by the authors (1988b) for computing the probability density of the response of a nonlinear oscillator to Gaussian white-noise excitations, is extended for application to hysteretic systems. The excitations can be either additive, or multiplicative, or both. Key issues related particularly to hysteresis models are explained and resolved. The approximation is also based on balancing the statistical averages of energy dissipation, but the approach is more direct, and most importantly, it can be applied without the restrictions of small dissipated energy or being a narrow-band random process.

Method of Energy Dissipation Balancing

Consider a general single degree-of-freedom nonlinear system

$$\ddot{x} + h(x,\dot{x}) = f_i(x,\dot{x}) W_i(\tau) \tag{6}$$

where $W_i(\tau)$ are Gaussian white noises with delta-type correlation functions

$$E[W_i(\tau) W_j(\tau+u)] = 2\pi K_{ij}\delta(u). \tag{7}$$

It has been shown (Cai and Lin, 1988a) that the response of the stochastic system (6) has an exact stationary probability density

$$p_s(x,\dot{x}) = C\exp[-\phi(\lambda)] = \rho(\lambda) \tag{8}$$

where

$$\lambda = \frac{1}{2}\dot{x}^2 + \int_0^x g(u)du = \frac{1}{2}\dot{x}^2 + G(x) \tag{9}$$

if function $h(x,\dot{x})$ in (6) can be expressed in the form of

$$h(x,\dot{x}) = \pi\dot{x}K_{ij} f_i(x,\dot{x}) f_j(x,\dot{x})\phi'(\lambda) - \pi K_{ij} f_i(x,\dot{x})\frac{\partial}{\partial\dot{x}} f_j(x,\dot{x}) + g(x) \tag{10}$$

in which case the system is said to belong to the class of generalized stationary potential. In (8) and (10), C is a normalization constant, ϕ is an arbitrary function, and a prime denotes one differentiation with respect to the argument. Of course, (8) is a valid probability density only if it is normalizable, namely, integration on x and $\dot{x}$ over the state space is finite.

If the multiplicative random excitations are absent or if they do not appear in the coefficient of $\dot{x}$, then $g(x)$ can be identified as the conservative spring force of the system; otherwise, it is the effective spring force (Cai and Lin 1988a) which may include the well-known correction term of Wong and Zakai (1965). Therefore, λ given in equation (9) is either the total kinetic and potential energy or the effective total energy. It is

Downloaded 03 May 2010 to 171.66.16.244. Redistribution subject to ASME license or copyright; see http://www.asme.org/terms/Terms_Use.cfm

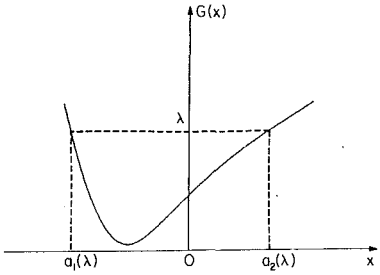


Fig. 3 Potential energy function G(x)

of interest to note that within the class of generalized stationary potential, the system behavior is manifested in the behavior of λ alone.

In many practical cases, equation (10) imposes severe restrictions which cannot be satisfied exactly. However, a substituting system can be found within the class of generalized stationary potential which is closest to the original system in some statistical sense. The criterion we propose to select such a substituting system is that the ensemble average of the dissipated energy remains the same for the substituting and the substituted systems. Application of this criterion yields

$$E\left[\dot{x}h(x,\dot{x}) - \pi\dot{x}^2 K_{ij}\, f_i\, f_j \phi'(\lambda) + \pi\dot{x} K_{ij}\, f_i \frac{\partial f_j}{\partial \dot{x}}\right] = 0 \tag{11}$$

where $E[\ ]$ denotes ensemble averaging. It follows upon using the approximate probability density (8) to evaluate the above ensemble average (Cai and Lin, 1988b),

$$\int_0^\infty \rho(\lambda)d\lambda \int_{a_1(\lambda)}^{a_2(\lambda)} \left\{\left[h + \pi K_{ij}\, f_i \frac{\partial f_j}{\partial \dot{x}} - \pi\dot{x} K_{ij}\, f_i\, f_j \phi'(\lambda)\right]_{\dot{x}=\sqrt{2\lambda - 2G(x)}} - \left[h + \pi K_{ij}\, f_i \frac{\partial f_j}{\partial \dot{x}} - \pi\dot{x} K_{ij}\, f_i\, f_j \phi'(\lambda)\right]_{\dot{x}=-\sqrt{2\lambda-2G(x)}}\right\} dx = 0 \tag{12}$$

where $a_1(\lambda)$ and $a_2(\lambda)$ are the two roots of the equation $G(x) = \lambda$; they are the minimum and the maximum values of x, respectively, corresponding to a given energy level λ, as depicted in Fig. 3.

Equation (12) is satisfied if

$$\phi'(\lambda) = \frac{\displaystyle\int_{a_1(\lambda)}^{a_2(\lambda)} \left\{\left[h + \pi K_{ij}\, f_i \frac{\partial f_j}{\partial \dot{x}}\right]_{\dot{x}=\sqrt{2\lambda-2G(x)}} - \left[h + \pi K_{ij}\, f_i \frac{\partial f_j}{\partial \dot{x}}\right]_{\dot{x}=-\sqrt{2\lambda-2G(x)}}\right\} dx}{\displaystyle \pi \int_{a_1(\lambda)}^{a_2(\lambda)} \left\{\left[\dot{x} K_{ij}\, f_i\, f_j\right]_{\dot{x}=\sqrt{2\lambda-2G(x)}} - \left[\dot{x} K_{ij}\, f_i\, f_j\right]_{\dot{x}=-\sqrt{2\lambda-2G(x)}}\right\} dx} \tag{13}$$

which is a stronger sufficient condition. It requires that the energy dissipations in the substituting and the original systems be equal for every energy level λ.

Application to Hysteretic Systems

For a hysteretic system, the h function in equation (11) is given by

$$h = 2\zeta\dot{x} + \alpha x + (1-\alpha)z \tag{14}$$

where the hysteretic component z is described by (4) for a bilinear system, and by (5) for a smooth hysteretic system. It can be shown that integration of (4) or (5) yields

$$z = \begin{cases} g_1(x,\delta) & \dot{x} \geq 0 \\ g_2(x,\delta) & \dot{x} \leq 0 \end{cases} \tag{15}$$

where δ is an integration constant. If the excitation were deterministic and cyclic, g_1 would represent one half of the hysteresis loop for increasing x, and g_2 would represent the other half for decreasing x, and each value of the integration constant δ would correspond to a given size of the hysteresis loop. Clearly, such a loop size would be determined uniquely by the level of the total energy λ. Thus, we can also write, instead of (15),

$$z = \begin{cases} \tilde{g}_1(x,\lambda) & \dot{x} \geq 0 \\ \tilde{g}_2(x,\lambda) & \dot{x} \leq 0. \end{cases} \tag{16}$$

A larger λ is associated with a larger loop and a longer period.

Under random excitations, δ and λ in (15) and (16), respectively, become random processes. It is reasonable, however, to take the point of view that their one-to-one correspondence remains valid. The use of the stronger sufficient condition (13) for dissipation energy balancing is actually an advantage, since it allows the analysis to proceed irrespective of the probability distribution of λ. However, by allowing λ to be randomly varying, the response of the system is generally not a narrow-band process.

By substituting (14) and (16) into (13), we obtain

$$\phi'(\lambda) = \frac{2\zeta}{\pi K} + \frac{A_r(\lambda)}{2\pi K \displaystyle\int_{-a(\lambda)}^{a(\lambda)} \sqrt{2\lambda - 2G(x)}\, dx} \tag{17}$$

where $A_r(\lambda)$ is the area of the hysteresis loop corresponding to a given λ, and K is the spectral density of the additive random excitation, and $a(\lambda) = -a_1(\lambda) = a_2(\lambda)$ on account of the symmetric constitutive laws considered.

Substituting (17) into (8), we obtain an approximate stationary probability density for the hysteretic system

$$p_s(x,\dot{x}) = \rho(\lambda) = C\exp\left\{-\frac{2\zeta}{\pi K}\lambda - \int \frac{A_r(\lambda)}{2\pi K \displaystyle\int_{-a(\lambda)}^{a(\lambda)} \sqrt{2\lambda - 2G(x)}\, dx} d\lambda\right\} \tag{18}$$

which depends only on λ. We hasten to add that this expression is an approximate probability density for x and $\dot{x}$, but not for λ. The mean-square value of the displacement may be computed from

$$E[x^2] = \int\int_{-\infty}^{+\infty} x^2 p_s(x,\dot{x})\, dx d\dot{x} = \int_0^\infty \rho(\lambda)\left[\int_{-a(\lambda)}^{a(\lambda)} \frac{2x^2}{\sqrt{2\lambda - 2G(x)}} dx\right] d\lambda. \tag{19}$$

The probability densities for the energy level λ and the amplitude a, respectively, can be found readily from (18). Specifically,

$$p_s(\lambda) = 2\rho(\lambda) \int_{-a(\lambda)}^{a(\lambda)} \frac{dx}{\sqrt{2\lambda - 2G(x)}} \tag{20}$$

and

Downloaded 03 May 2010 to 171.66.16.244. Redistribution subject to ASME license or copyright; see http://www.asme.org/terms/Terms_Use.cfm

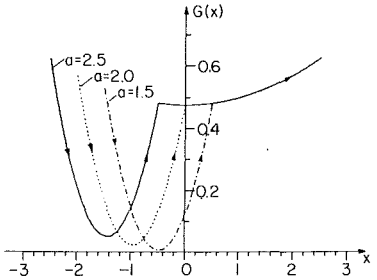


Fig. 4 Potential energy of a bilinear hysteretic system with $\alpha = 1/21$, $\dot{x} \geq 0$

$$p_s(a) = 2\,|g(a)|\,\rho[\lambda(a)] \int_{-a}^{a} \frac{dx}{\sqrt{2\lambda(a) - 2G(x)}}. \tag{21}$$

As indicated, λ must be expressed in terms of the amplitude a in equation (21).

Once the area A_r within a hysteresis loop and the potential energy $G(x)$ are determined, the probability densities (18), (20), and (21) and the mean-square displacement can be evaluated numerically. The area A_r can often be obtained in closed form. However, the physical meaning of the potential energy $G(x)$ of a hysteretic system requires clarification. The potential energy is generally regarded as a measure of the ability of a system to return to its equilibrium configuration. This poses no difficulty if the restoring force is purely elastic; however, if one part of the restoring force is hysteretic, then the equilibrium position is no longer unique, but it drifts continuously. A more general interpretation for potential energy is, therefore, a measure of the ability to return to a local equilibrium. As to be seen in the following specific examples, analytical expressions for potential energies for various hysteretic systems can be obtained with this interpretation.

Bilinear Hysteretic Systems

A bilinear hysteretic system is described mathematically by equations (1), (2), and (4), depicted graphically in Figs. 1(*a*) and 1(*b*). The area of the hysteresis loop A_r, representing the dissipated energy per cycle at amplitude a, which is attributable solely to the hysteretic property can be obtained by inspection:

$$A_r = \begin{cases} 0, & a \leq 1 \\ 4(1-\alpha)\,(a-1), & a \geq 1. \end{cases} \tag{22}$$

The potential energy of the system is the recoverable part of energy if the system is to return to a local equilibrium upon removal of the external force. Its values for different ranges of x can be computed by referring to the shaded areas in Fig. 1(*a*). Specifically,

$$G(x) = \begin{cases} \dfrac{1}{2}x^2, & a \leq 1 \\ \dfrac{1}{2}\alpha x^2 + \dfrac{1}{2}(1-\alpha)(x+a-1)^2; & a \geq 1,\ -a \leq x \leq -a+2 \\ \dfrac{1}{2}\alpha x^2 + \dfrac{1}{2}(1-\alpha); & a \geq 1,\ -a+2 \leq x \leq a. \end{cases} \tag{23}$$

Plots of $G(x)$ versus x for $\alpha = 1/21$ are shown in Fig. 4 for increasing $x(\dot{x} > 0)$. Plots corresponding to decreasing $x(\dot{x} < 0)$ are mirror images of those shown in Fig. 4. The potential energy of a hysteretic system is seen to be a nonunique function of the displacement x, since it also depends on the amplitude a and whether x is increasing or decreasing. Finally, the total energy λ is related to the amplitude as

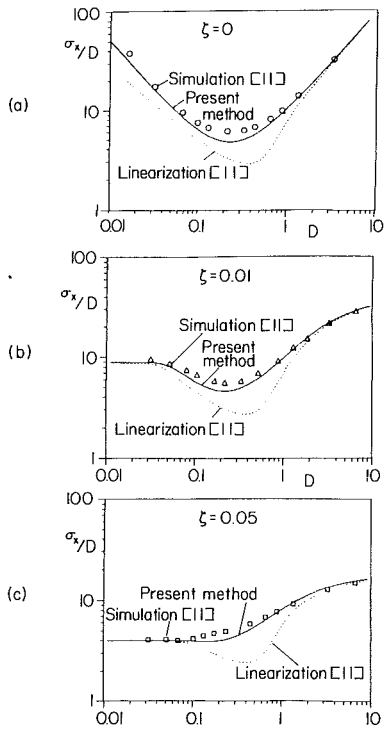


Fig. 5 RMS response of a bilinear hysteretic with $\alpha = 1/21$: (*a*) $\zeta = 0$, (*b*) $\zeta = 0.01$, (*c*) $\zeta = 0.05$. [11] indicates Iwan and Lutes (1968).

$$\lambda = \begin{cases} \dfrac{1}{2}a^2, & a \leq 1 \\ \dfrac{1}{2}(1-\alpha) + \dfrac{1}{2}\alpha a^2, & a > 1. \end{cases} \tag{24}$$

Substituting (22), (23), and (24) into (18) through (21) and integrating with respect to λ numerically, we can obtain the stationary probability density $p_s(\dot{x})$, $p_s(\lambda)$ and $p_s(a)$, as well as the mean-square response $E[x^2]$.

A nearly elastoplastic system ($\alpha = 1/21$) under white-noise excitation was studied numerically. Different values for the viscous damping coefficient ($\zeta = 0$, 0.01, 0.05) were assumed for the investigation. The root-mean-square response σ_x computed for different ζ values, and normalized with respect to $D = \sqrt{2K}$, is shown in Figs. 5(*a*)–(*c*) where D is a measure of the excitation strength. The results appear to be in excellent agreement with known analog simulations (Iwan and Lutes, 1968) at all response levels and for all three values of ζ. Also shown in Figs. 5(*a*)–(*c*) are results obtained from equivalent linearization (Iwan and Lutes, 1968), which do not agree as well with the simulation results, particularly in the range of in-

Downloaded 03 May 2010 to 171.66.16.244. Redistribution subject to ASME license or copyright; see http://www.asme.org/terms/Terms_Use.cfm

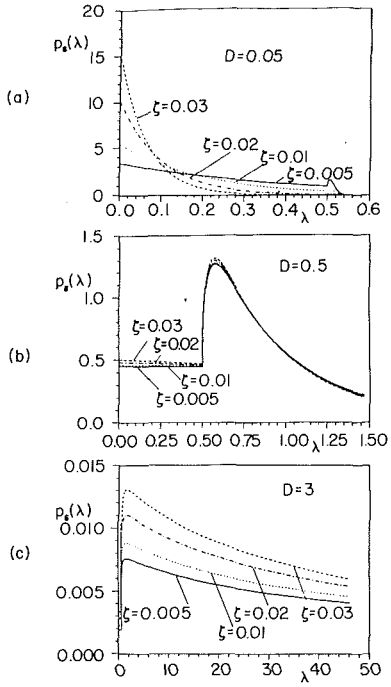


Fig. 6 Stationary probability density of total energy for a bilinear hysteretic system with $\alpha = 1/21$: (a) weak excitation D = 0.05, (b) intermediate excitation D = 0.5, and (c) strong excitation D = 3

termediate excitation levels. Yet, it is in this range that the hysteretic component in the restoring force plays a dominant role. The comparison suggests that the present procedure is much better suited for the analysis of bilinear hysteretic systems.

Figures 6(*a*)-(*c*) depict the computed stationary probability density for the total response energy λ for the same system. It is seen that when the excitation strength is either weak ($D = 0.05$) or strong ($D = 3$), the total energy λ follows approximately an exponential probability distribution, similar to that of a linear system. In such cases, hysteresis effect is unimportant, and the linear viscous effect has a much greater influence on the probabilistic structure of the response. This is also borne out in the computed mean-square properties, shown in Figs. 5(*a*)-(*c*), and explains why linearization technique can lead to somewhat more acceptable results in these ranges. At an intermediate excitation strength ($D = 0.5$), however, the energy dissipated by the hysteresis component is important. Therefore, the probability distribution of the total energy deviates greatly from being exponential, as shown in Fig. 6(*b*).

Smooth Hysteretic Systems

To illustrate how the present procedure can be applied to smooth hysteretic systems, consider the Bouc-Wen model for the hysteretic component governed by equation (5). The area of hysteresis loop corresponding to a given amplitude a is computed from the integral

$$A_r = 2(1-\alpha)\int_{-a}^{a} z(x)dx. \tag{25}$$

The total potential energy again consists of two parts: one stored in the linear element, another in the hysteretic element. The latter may be computed by referring to the shaded areas shown in Fig. 2(*a*) for different values of x. For a specific system, the functional relationship between z and x can be obtained by integrating (5). Then the hysteresis loop area A_r, as a

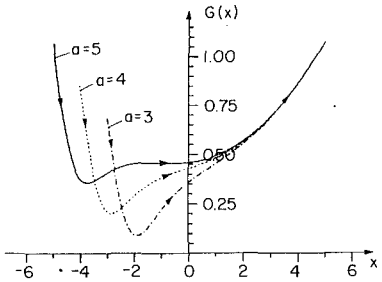


Fig. 7 Potential energy of a smooth hysteretic system with $\alpha = 1/21$ and $\gamma = \beta = 0.05$, $\dot{x} \geq 0$

function of amplitude a, and the total potential energy $G(x)$ can also be obtained in closed forms.

In what follows, the case of $n = 1$, $A = 1$ and $\beta = \gamma$ will be considered in more detail. For this special case, the hysteretic component of the restoring force is found to be

$$z(x) = \begin{cases} x + x_0; & -a \leq x \leq -x_0 \\ \dfrac{1}{2\gamma}[1 - e^{-2\gamma(x+x_0)}]; & -x_0 \leq x \leq a \end{cases} \tag{26}$$

where x_0, shown in Fig. 2(*b*), is uniquely determined for a given amplitude a by solving $z(\pm x_0) = 0$. The area of the hysteresis loop, corresponding to a given amplitude, is given by

$$A_r = -(a - x_0)^2 + \frac{2x_0}{\gamma}, \tag{27}$$

and the potential energy by

$$G(x) = \begin{cases} \dfrac{1}{2}(1-\alpha)(x+x_0)^2 + \dfrac{1}{2}\alpha x^2 & -a \leq x \leq -x_0 \\ \dfrac{1}{8\gamma^2}(1-\alpha)[1 - e^{-2\gamma(x+x_0)}]^2 + \dfrac{1}{2}\alpha x^2 & -x_0 \leq x \leq a. \end{cases} \tag{28}$$

The potential energy of such a smooth hysteretic system is illustrated in Fig. 7 for $\alpha = 1/21$, $\gamma = \beta = 0.5$ and different amplitudes and for increasing x. Plots for decreasing x are mirror images of those shown in Fig. 7. With the aforementioned results, it is rather simple to compute the stationary probability densities for the state variables x and $\dot{x}$, the total energy λ, and the amplitude a, as well as the mean-square response using equations (8)-(21).

A smooth hysteretic system with $\alpha = 1/21$, $\gamma = \beta = 0.5$ was studied numerically in detail. The computed mean-square displacements are shown in Figs. 8(*a*) and (*b*) for $\zeta = 0$ and $\zeta = 0.05$, respectively. Earlier results obtained by Wen (1980) using equivalent linearization and digital simulation, and by Iyenger and Dash (1978) using Gaussian closure, are shown also in the figures for comparison. Results from both equivalent linearization and dissipation energy balancing agree with the simulation results.

The computed probability densities for the response amplitude are shown in Figs. 9(*a*)-(*c*). Under strong ($D > 2$) excitation, the amplitude distribution is closer to Rayleigh, indicating that the linear component of the restoring force has the dominant effect. Under excitations of intermediate range ($0.5 < D < 2$), both the linear and hysteretic components con-

Downloaded 03 May 2010 to 171.66.16.244. Redistribution subject to ASME license or copyright; see http://www.asme.org/terms/Terms_Use.cfm

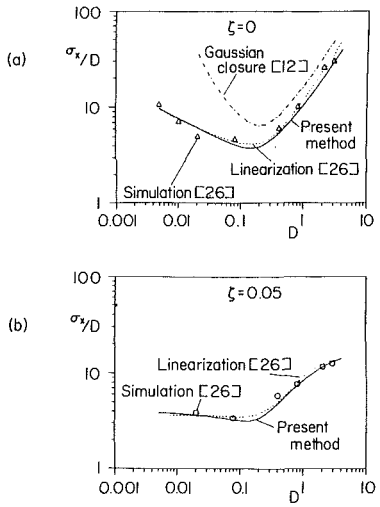


Fig. 8 RMS response of a smooth hysteretic system with $\alpha = 1/21$ and $\gamma = \beta = 0.5$: (*a*) $\zeta = 0$, (*b*) $\zeta = 0.05$. [12] indicates Iyengar and Dash (1978). [26] indicates Wen (1980).

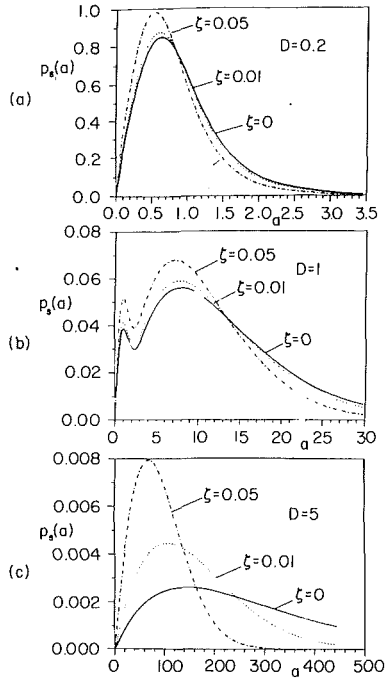


Fig. 9 Stationary probability density of response amplitude of a smooth hysteretic system $\alpha = 1/21$, $\gamma = \beta = 0.5$ and different values of damping: (*a*) weak excitation D = 0.2, (*b*) intermediate excitation D = 1, and (*c*) strong excitation D = 5

tribute importantly, giving rise to two peaks in the amplitude probability density, as shown in Fig. 9(*b*). The added viscous damping does not appear to change the general shape of the distribution. It shifts a peak of the probability density to the left and shortens the tail of the distribution. This effect is greater when the excitation is strong.

Concluding Remarks

Two basic steps are required in the application of the proposed procedure. First, the area of the hysteresis loop must be calculated, and second, expressions for the potential energy stored in the linear spring and the hysteretic elements, representing the ability of the system to return to a local equilibrium, must be obtained for various ranges of deformation. Once these are accomplished, the remaining steps are quite straightforward.

Although attention has been focused on hysteretic systems with a symmetric constitutive law and on purely additive random excitations, the method of analysis is applicable to asymmetric hysteresis and when multiplicative random excitations are also present. Multiplicative excitations can occur, for example, when a column is subjected to vertical seismic motion.

Of course, the present method is applicable only if the system response can indeed approach statistical stationarity. This is not the case for a bilinear system with $\alpha = 0$, nor for a smooth hysteretic system with $\alpha = 0$ and $\gamma + \beta > 0$.

Acknowledgment

The research reported in this paper was supported by subcontract No. NCEER 87-2010 under the auspices of the National Center for Earthquake Engineering Research under NSF Grant ECE-86-07591. Opinions, findings, and conclusions expressed are those of the writers and do not necessarily reflect the views of our sponsors.

References

Baber, T. T., and Noori, M. N., 1985, "Random Vibration of Degrading Pinching System," *Journal of Engineering Mechanics*, ASCE, New York, Vol. 111, EM8, pp. 1010–1026.

Baber, T. T., and Wen, Y. K., 1980, "Stochastic Equivalent Linearization for Hysteretic, Degrading, Multistory Structures," Civil Engineering Studies SRS No. 471, Department of Civil Engineering, University of Illinois, Urbana, Ill.

Bouc, R., 1967, "Forced Vibration of Mechanical System with Hysteresis," Abstract, *Proceedings of 4th Conference on Nonlinear Oscillation*, Prague, Czechoslovakia.

Cai, G. Q., and Lin, Y. K., 1988a, "On Exact Stationary Solutions of Equivalent Nonlinear Stochastic Systems," *International Journal of Nonlinear Mechanics*, Vol. 23, No. 4, pp. 315–325.

Cai, G. Q., and Lin, Y. K., 1988b, "A New Approximate Solution Technique for Randomly Excited Nonlinear Oscillators," *International Journal of Nonlinear Mechanics*, Vol. 23, No. 5-6, pp. 409–420.

Casciati, F., 1987, "Nonlinear Stochastic Dynamics of Large Structural Systems by Equivalent Linearization," *Proceedings of the 5th International Conference on Applications of Statistics and Probability in Soil and Structural Engineering*, Vancouver, Canada, pp. 1165–1172.

Caughey, T. K., 1960, "Random Excitation of a System with Bilinear Hysteresis," ASME JOURNAL OF APPLIED MECHANICS, Vol. 27, pp. 649–652.

Caughey, T. K., 1964, "On the Response of a Class of Nonlinear Oscillators to Stochastic Excitation," *Proc. Colloq. Intern. du Centre National de la Recherche Scientifique*, No. 148, pp. 393–402.

Iwan, W. D., 1966, "A Distributed-Element Model for Hysteresis and its Steady-State Dynamic Response," ASME JOURNAL OF APPLIED MECHANICS, Vol. 33, pp. 393–900.

Iwan, W. D., 1974, "Application of Nonlinear Analysis Techniques," *Applied Mechanics in Earthquake Engineering*, ASME, New York, Vol. 8, pp. 135–162.

Iwan, W. D., and Lutes, L. D., 1968, "Response of the Bilinear Hysteretic System to Stationary Random Excitation," *Journal of the Acoustic Society of America*, Vol. 43, pp. 545–552.

Iyengar, R. N., and Dash, P. K., 1978, "Study of the Random Vibration of Nonlinear Systems by the Gaussian Closure Technique," ASME JOURNAL OF APPLIED MECHANICS, Vol. 45, pp. 393–399.

Kobori, T., Minai, R., and Suzuki, Y., 1976, "Stochastic Seismic Response of Hysteretic Structures," Bulletin of Disaster Prevention Research Institute, Kyoto University, Vol. 26, Part 1, No. 236, pp. 57–70.

Lin, Y. K., and Cai, G. Q., 1988a, "Exact Stationary-Response Solution for Second Order Nonlinear Systems under Parametric and External White-Noise Excitations, Part II," ASME JOURNAL OF APPLIED MECHANICS, Vol. 55, pp. 702–705.

Lin, Y. K., and Cai, G. Q., 1988b, "Energy Dissipation Balancing—An Approximate Solution Technique for Nonlinearly Damped System under Random Excitations," *Developments in Theoretical and Applied Mechanics*, Vol. XIV, Proceedings, 14th Southeastern Conference on Theoretical and Applied Mechanics, pp. 381–388.

Lutes, L. D., 1970, "Approximate Technique for Treating Random Vibration of Hysteretic Systems," *Journal of the Acoustic Society of America*, Vol. 48, pp. 299–306.

Lutes, L. D., and Takemiya, M., 1974, "Random Vibration of Yielding

Downloaded 03 May 2010 to 171.66.16.244. Redistribution subject to ASME license or copyright; see http://www.asme.org/terms/Terms_Use.cfm

Oscillator," *Journal of Engineering Mechanics*, ASCE, New York, Vol. 100, No. EM2, pp. 343-357.

Roberts, J. B., 1978, "The Response of an Oscillator with Bilinear Hysteresis to Stationary Random Excitation," ASME JOURNAL OF APPLIED MECHANICS, Vol. 45, pp. 923-928.

Roberts, J. B., 1987, "Application of Averaging Methods to Randomly Excited Hysteretic Systems," *Proceedings of the IUTAM Symposium on Nonlinear Stochastic Dynamic Engineering Systems*, Springer-Verlag, Berlin, pp. 361-374.

Shih, T. Y., and Lin, Y. K., 1982, "Vertical Seismic Load Effect on Hysteretic Columns," *Journal of Engineering Mechanics*, ASCE, New York, Vol. 88, No. EM2, pp. 242-254.

Sozen, M. A., 1974, "Hysteresis in Structural Elements," *Applied Mechanics in Earthquake Engineering*, ASME, New York, Vol. 8, pp. 63-68.

Spanos, P. D., 1979, "Hysteretic Structural Vibrations under Random Load," *Journal of the Acoustic Society of America*, Vol. 65, pp. 404-410.

Stratonovich, R. L., 1963, *Topics in the Theory of Random Noise*, Vol. 1, Gordon and Breach, New York.

Takemiya, H., and Lutes, L. D., 1977, "Stationary Random Vibration of Hysteretic Systems," *Journal of Engineering Mechanics*, ASCE, New York, Vol. 103, No. EM4, pp. 673-687.

Wen, Y. K., 1976, "Method for Random Vibration of Hysteretic Systems," *Journal of Engineering Mechanics*, ASCE, New York, Vol. 102, No. EM2, pp. 249-263.

Wen, Y. K., 1980, "Equivalent Linearization for Hysteretic Systems under Random Excitation," ASME JOURNAL OF APPLIED MECHANICS, Vol. 47, pp. 150-154.

Wong, E., and Zakai, M., 1965, "On the Relation Between Ordinary and Stochastic Equations," *Int. J. Eng. Sci.*, Vol. 3, No. 2, pp. 213-229.

Zhu, W. Q., and Lei, Y., 1987, "Stochastic Averaging of Energy Envelope of Bilinear Hysteretic Systems," *IUTAM Symposium on Nonlinear Stochastic Dynamics Engineering Systems*, Springer-Verlag, Berlin, pp. 381-391.

Downloaded 03 May 2010 to 171.66.16.244. Redistribution subject to ASME license or copyright; see http://www.asme.org/terms/Terms_Use.cfm

Nonlinear Finite Deformation Response of Open Cell Polyurethane Sponge to Fluid Filtration

Y. Lanir

S. Sauob

P. Maretsky[1]

Department of Biomedical Engineering,
Technion-Israel Institute of Technology,
Haifa 32000, Israel

The nonlinear finite deformation response of open cell polyurethane sponge to fluid filtration was studied, both experimentally and theoretically. The equilibrium uniaxial strain distribution along a sponge cylinder was optically measured while it was supported on its downstream surface by a rigid filter and loaded by fluid pressure of various levels. The strain along the cylinder was found to be highly nonuniform and of sigmoidal pattern—flat near both ends and steep in the middle. The theoretical investigation considers the fluid-filled sponge as an incompressible solid-fluid mixture. The response of the sponge to uniaxial filtration was analyzed in terms of its constitutive properties which were determined experimentally. The model's predictions show good agreement to the measured strain distribution.

1 Introduction

Direct application of fluid pressure on a porous elastic material occurs often when the hydraulic permeability properties are investigated. In such tests the pressure gradient and fluid filtration are typically unidirectional. The permeability is then calculated using Darcy's law as follows:

$$Q/A = -K \cdot \Delta P/\Delta L \tag{1}$$

where Q is the discharge, A the filtration area, ΔP the pressure drop, ΔL the filtration length, and K the permeability.

In tests like these, the filtration length is observed to decrease under the pressure loading, relative to the load-free length. A question then arises as to the reliabilty of the permeability measurement and as to the experimental conditions under which it can be determined most accurately. In some cases it is also important to know the distribution of strain, stress, and fluid pressure across the specimen.

When the solid is deformable, then solid-fluid interaction may give rise to consolidation. This was extensively studied by Biot, for small deformations (Biot, 1955) and for finite deformations (Biot, 1972).

The mixture theory approach was put forward by Truesdell (1962). Specialized mixture theories for solid-fluid systems were developed (e.g., Kenyon (1976) and Bowen (1980)). Mow and Coworkers (e.g., 1980) developed similar theories for the articular cartilage. This was recently generalized to incorporate osmotic effects and microstructural features (Lanir, 1987).

In the present work the response of highly deformable porous specimen to fluid filtration will be studied. The analytic investigation will be based on the mixture theory as applied to the nonlinear finite deformation case.

While conducting the research reported here we learned of a similar study carried out by Parker et al. (1987) and subsequently obtained the corresponding report. Parker et al. used the consolidation approach of Biot and compared predicted to observed effect of ΔP on equilibrium discharge and on the overall shortening of the specimen. In the present study the model validation is carried out in terms of the strain distribution. We chose the strain distribution rather than the overall shortening or the equilibrium discharge to test the theory since the latter are integrals of local events along the fluid pass. Different responses in terms of strain distributions may result in a similar overall shortening or similar discharge. Hence, the strain distribution is likely to be a sensitive indicator to subtle features of the theoretical predictions.

2 The Theoretical Analysis

2.1 Basic Assumptions. The present formulation will be based on several assumptions: (a) both solid and fluid are incompressible, (b) the system is fully saturated with fluid—there are no voids, (c) the fluid stress is represented by its pore hydrostatic pressure P (shear stresses are averaged out), (d) there are negligible inertia and body forces, and (e) fluid filtration is governed by Darcy's law.

A mixture formulation based on these assumptions is summarized in Appendix A. A special version of the aforementioned formulation refers to convective coordinates which move and deform with the solid. This approach is extensively

[1]Deceased, July 28, 1987.

Contributed by the Applied Mechanics Division of The American Society of Mechanical Engineers for publication in the JOURNAL OF APPLIED MECHANICS.

Discussion on this paper should be addressed to the Technical Editor, Leon M. Keer, The Technological Institute, Northwestern University, Evanston, IL 60208, and will be accepted until two months after final publication of the paper itself in the JOURNAL OF APPLIED MECHANICS. Manuscript received by the ASME Applied Mechanics Division, December 1, 1987; final revision, June 25, 1989.

Copyright © 1990 by ASME
Downloaded 03 May 2010 to 171.66.16.244. Redistribution subject to ASME license or copyright; see http://www.asme.org/terms/Terms_Use.cfm

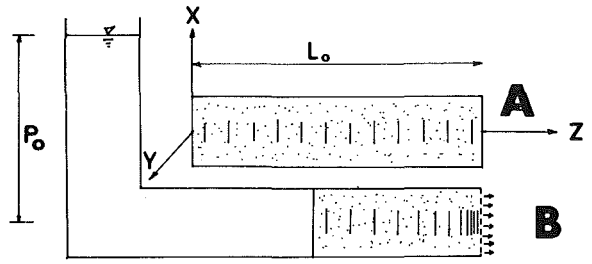


Fig. 1 A scheme of the sponge in the load-free state (A) and during the filtration test (B). The sponge load-free dimensions are: height—8.90 cm, diameter—1.55 cm. The sponge is slightly undersized in this test to minimize friction with the walls. The markings in B show the nonuniform strain distribution.

used by Green and Zerna (1960) for single component solid materials. It is advantageous in the present case of a solid-fluid system as well, since boundary conditions on surfaces which deform or move can be simply prescribed. It will thus be used in the present study. The basic formulation and notation is taken from the previously mentioned source.

2.2 Model Formulation in Convective Coordinates. In a typical permeability test a specimen of unloaded thickness, L_o, is supported on one surface by a rigid, highly permeable filter, while being loaded on the opposite surface by fluid pressure of magnitude, P_o, (Fig. 1).

The kinematics formulation is based on the assumption that both solid and fluid move only in the direction of the specimen length, the Z direction. Hence, a solid particle that was at point (X, Y, Z) in the undeformed state ($t<0$; Fig. 1A) is at the present time t at (X, Y, z) where $z=z(X, Y, Z, t)$. Hence, the relevant components of the metric tensors are:

$$G^{33}=1/\lambda^2; \quad G_{33}=\lambda^2 \tag{2}$$

where $\lambda=\partial z/\partial Z$ and the indices 1, 2, 3 refer to X, Y, Z, respectively. For convenience the coordinate Z is normalized w.r.t., the unloaded thickness (L_o) such that $Z=0$ at the fluid interface and $Z=1$ at the interface with the rigid filter.

The physical component of the particle's velocity is

$$V_s^{(3)}=\lambda V_s^3=\frac{\partial}{\partial t}[z-Z]=\frac{\partial z}{\partial t} \tag{3}$$

since $Z=$ const. V_s^3 is the mathematical component of the solid velocity.

The three mass balance equations (A1) are written in component form as:

$$(q^i+V_s^i)//_i=0 \tag{4}$$

where $//_i$ is a covariant differentiation in the deformed configuration. In the present case the only nontrivial equation is:

$$\frac{\partial}{\partial Z}[\lambda q^3+\lambda V_s^3]=\frac{\partial}{\partial Z}[q^{(3)}+V_s^{(3)}]=0 \tag{5}$$

where $q^{(3)}$ is the physical component of q^3—the filtration flux (equation (A2)).

From equations (3) and (5) we get:

$$-\frac{\partial\lambda}{\partial t}=\frac{\partial q^{(3)}}{\partial t}. \tag{6}$$

The six equations of motion (A4) and (A6), together with (A5), are written in components form as:

$$(\tau^{ij}-PG^{ij})//_j=0 \tag{7}$$

$$K_r^i(-PG^{rj})//_j=q^i \tag{8}$$

where $\mathbf{K}$ is the permeability matrix. It is given by:

$$\mathbf{K}=\mathbf{k}/\mu \tag{9}$$

where $\mathbf{k}$ is the intrinsic permeability and μ is the fluid viscosity. In the present case equations (7) and (8) assume the form

$$\frac{\partial}{\partial Z}(\sigma-P)=0 \tag{10}$$

$$q^{(3)}=\frac{K}{\lambda}\cdot\frac{\partial}{\partial Z}(-P) \tag{11}$$

where $K\equiv K_3^3$ and σ is the physical component of the stress τ^{33}.

By differentiating equation (11) w.r.t. Z and using equations (6) and (10) we get:

$$\frac{\partial\lambda}{\partial t}=\frac{\partial}{\partial Z}\left(\frac{K}{\lambda}\frac{\partial\sigma}{\partial Z}\right). \tag{12}$$

By introducing the engineering strain $e\triangleq\lambda-1$ and expressing $\partial\sigma/\partial Z$ as $(\partial\sigma/\partial e)(\partial e/\partial Z)$, equation (12) can be expressed as:

$$\frac{\partial e}{\partial t}=\frac{\partial}{\partial Z}\left(D(e)\frac{\partial e}{\partial Z}\right) \tag{13}$$

where

$$D(e)=\frac{K(e)}{1+e}\cdot\frac{\partial\sigma}{\partial e}, \tag{14}$$

where $K(e)$ is the strain-dependent permeability and $\sigma(e)$ is the strain dependent stress. Equation (12) is a nonlinear diffusion equation. The boundary conditions in convective coordinate formulation are:

$$Z=0, \quad t>0: \quad P=P_o, \quad e=0 \tag{15}$$

$$Z=1, \quad t>0: \quad P=0, \quad e=\sigma^{-1}(-P_o) \tag{16}$$

where $\sigma^{-1}(-P_o)$ is the strain corresponding to the stress $\sigma=-P_o$ in the $\sigma(e)$ relationship. The initial condition is:

$$e(Z,0)=0 \tag{17}$$

Equation (13) with its boundary and initial conditions requires as inputs the data $\sigma(e)$ and $K(e)$ and the external pressure P_o. The equation was solved numerically by an explicit scheme (Appendix B). The results are presented in Figs. 6–8 for various levels of P_o while using the measured $\sigma(e)$ and $K(e)$ data, which is discussed next and presented in Figs. 4 and 5.

3 The Experimental Investigation

3.1 Materials and Specimen Preparation. The solids used in the present study were cylinders of open-celled polyurethane foams (Fig. 9) cut from rectangular blocks by sharp-edged punches to the desired diameter. It was found that by modifying the cutting technique (e.g. compression, compression while rotating the punch, addition of lubricating fluid), slightly different sized cylinders resulted. The samples used in the present study were cut either by compression or by rotating punch with lubricating fluid to keep the temperature at room level, thus avoiding possible damage to the sponge. Although the foam block was highly uniform, the cut cylinders were at times wider near the edges. These portions were removed to ensure geometrical uniformity.

The foam density was determined by gravimetric technique to be 0.0222 gm/cm^3. Its pore density is 16 per centimeter (a straight line of 1.0-cm length dissects 16 pores in average). The porosity was measured in two different ways: In the gravimetric method, the effective porosity is given by:

$$\phi_f^o=1-\frac{W}{V\cdot\gamma_s} \tag{18}$$

where W is the weight of the moist sponge after it has been strongly squeezed to remove excess of water, V is the cylinder volume, and γ_s is the specific weight of the polyurethane

Downloaded 03 May 2010 to 171.66.16.244. Redistribution subject to ASME license or copyright; see http://www.asme.org/terms/Terms_Use.cfm

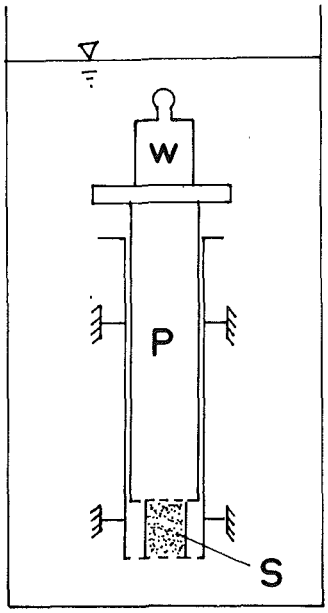


Fig. 2 Scheme of the setup for stress-strain studies. The sponge dimension are: height—2.14 cm; diameter—1.46 cm. W—dead weight; P—plunger; S—sponge specimen.

($\gamma_s = 1.0$ gm/cm^3). In the second method the porosity is evaluated by comparing the free length of the sponge to its length while strongly compressed. Both methods gave a porosity value of 0.96.

Two fluids were used: distilled water and glycerol. The latter has a specific weight of 1.25 gm/cm^3 and viscosity of ca. 50 CPS.

Both fluids were degassed. Glycerol was used in filtration studies to reduce the flow rate such that the Reynolds number be below unity, which is the range of validity of Darcy's law.

3.2 The Experimental Setup. Three types of experiments were performed. Since each required a somewhat different setup, they will be presented separately.

3.2.1 Stress-Strain Relationship σ(e). The setup is schematically presented in Fig. 2. The cylindrical sponge is compressed between two rigid filters: one at the bottom of a fixed Perspex tube of 1.60-cm internal diameter. The other filter is located at the bottom of a Perspex plunger which is loaded by a standard weight. The dimensions of the sponge specimen were chosen so as to avoid any friction with the walls of the outer tube on one hand, and prevent buckling on the other. The length of the sponge was read by a vertical traveling microscope with eyepiece and a scale of 0.02-mm resolution. The engineering strain (equation (13)) is given in the present case by $e = (L - L_o)/L_o$, where L is the length and L_o is the load-free length. The stress is calculated as $\sigma = W/A$ where W is the true (immersed) weight and A is the cross-section area of the sponge. The sponge diameter did not change with loading.

The whole setup was immersed under water for two reasons: First, the stress-strain response that is of interest in filtration is the one of a well-wetted sponge. In addition, since the sponge material was highly compliant, high accuracy of the data at the low strain range can be achieved if the plunger is made buoyant. This was achieved by attaching the required amount of wood chips to the plunger until complete buoyancy is achieved.

Prior to testing, the sponge was preconditioned for several times by repeated compression for a few cycles. This was needed to achieve repeatable response after long rest periods. A similar observation was reported by Parker et al. (1987) and Beavers et al. (1981). Moreover, it was found that under loading, following an initial response, the immersed specimen continued to creep for a few minutes (a period which far exceeds the characteristics filtration time-constant). Hence, this creep is attributed to the properties of the wetted polymer. The data used in the numerical solution is that of the final equilibrium response. This choice was made since all of our filtration data refers to the final equilibrium state when transients have already decayed.

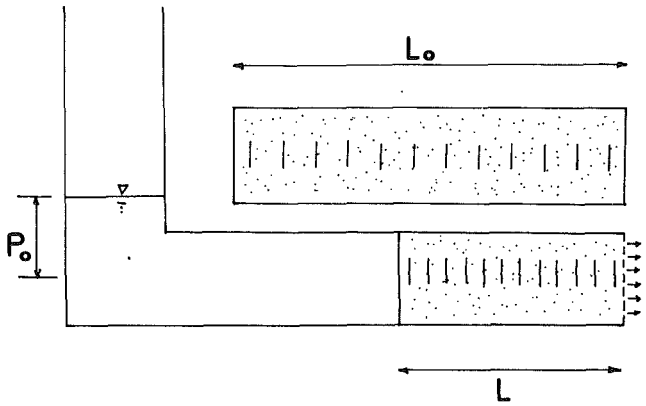


Fig. 3 Scheme of the permeability tests. The sponge dimensions are: height—8.80 cm; diameter—1.62 cm. The sponge is slightly oversized to prevent sideflow of fluid. The equally-spaced markings in this test represent the uniformity of strain distribution.

3.2.2 Permeability-Strain Relationship K(e). A scheme of the setup for permeability studies is shown in Fig. 3. The sponge cylinders were marked by several equidistant lines with a permanent ink. For each strain the sponge was compressed to the desired length. Uniform strain distribution was obtained with the help of a special long flat spatula. After some experience it was possible to obtain uniformly distributed strain (judged by the line markings) throughout the sponge length. A plunger with high friction O-rings was then inserted until contact with the sponge was obtained.

The sponges in these tests were oversized with respect to the outer Perspex tube. This was done for two reasons: First, the friction between the sponge and rigid tube help to maintain its uniform configuration until the plunger was inserted in place. In addition, accuracy in permeability results can be obtained if no gap exists between sponge and outer tube where fluid can flow along and around the sponge.

The water head used in permeability studies was maintained at a low level to avoid any significant filtration-induced strain which would otherwise be added to the preset uniform strain. The low head also ensured low Reynold's numbers where equation (1) applies. The criterion used was that P_o must be very low compared with the stress corresponding to the strain level used, i.e., $P_o << \sigma(e)$.

The lowest level of water head used was 1.5 cm and the highest was 2.5 cm. During the tests, no additional strain was observed due to filtration.

The permeability was calculated from equation (1) using $\Delta P = P_o$, $\Delta L = L$. Discharge was measured using analytic balance and a stop watch.

3.2.3 Response to Fluid Filtration. The experimental setup is shown schematically in Fig. 1 (case B). The cylindrical surface of the sponge was marked by thin black lines at a distance of ca. 5.0 mm. The precise distances were measured by the traveling microscope before testing and compared with the distances between the same lines after the sponge deformation attained a steady state. The equilibrium strain distribution was determined from these sets of readings.

Experimental accuracy is determined by two mutually con-

Downloaded 03 May 2010 to 171.66.16.244. Redistribution subject to ASME license or copyright; see http://www.asme.org/terms/Terms_Use.cfm

flicting requirements. Precise flow data can be obtained if there is no side flow between the sponge and the tube wall, i.e., if the sponge fits perfectly or is slightly oversized. On the other hand, accurate strain distribution data can be measured only if there is no friction in the sponge-wall interface, i.e., if the sponge is slightly undersized. Attempts to reach a perfect fit which could (at least in principle) guarantee high accuracy in both strain and flow measurements, did not meet with success. It was thus decided to concentrate attention on the strain distribution data and use slightly undersized sponges. The motivation behind this choice is outlined in the introduction.

The nonuniformity of strain distribution under fluid filtration is more clearly observable and can be measured more accurately if the deformations are large. This is achieved under high water head, in the range of 0.50 m and up. Under these levels of water heads the measured flow rate was high. Based on the pore size as a characteristic length, the associated Reynold's number was in the range of 50 which is higher and outside the range of validity of Darcy's law. It is possible to reduce the Reynold's number under the same high fluid pressures by using a high viscosity fluid instead of water. In the present study glycerol was used and the resulting flow was associated with Reynold's number of the order of one or less. The use of a different fluid than the one used for permeability studies (water) has the effect of multiplying the permeability by a constant as is evident from equation (9). Hence, although the full solution of equation (13) will be affected by the change from water to glycerol, the equilibrium response will be unaffected by the fluid viscosity, since then, $\partial e/\partial t = 0$.

4 Results and Discussion

Figure 4 shows the stress-strain relationship for the sponge material used (open squares). The strain and stress are negative. The results indicated by + signs are of another sponge material which has porosity of 0.93, density of 0.0275 gm/cm^3 and pore density of 16 per cm. The latter data is

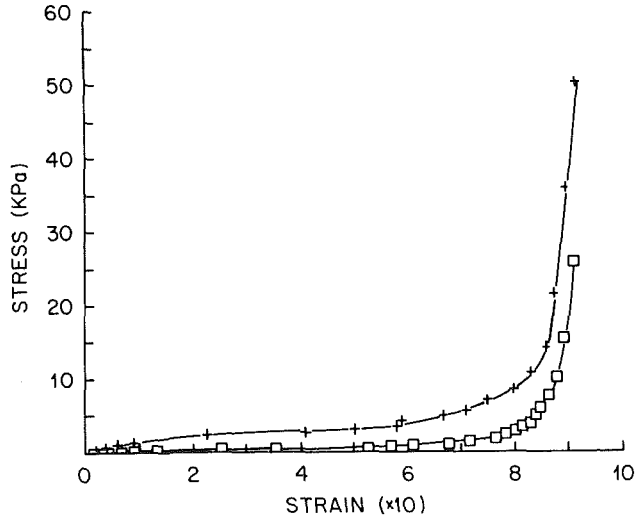


Fig. 4 **Experimental stress-strain data: (□)—sponge used in the present study; (+)—data for a more rigid sponge. The stress and strain are negative.**

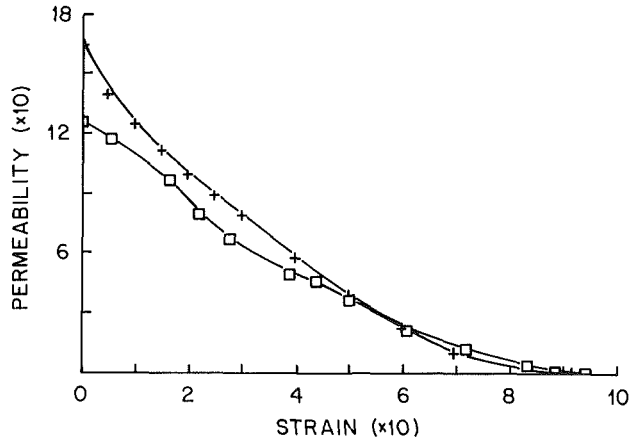


Fig. 5 Experimental permeability-strain data. The data relates to same sponges as in Fig. 4. The strain is negative. Permeability units are cm^4/dyne sec.

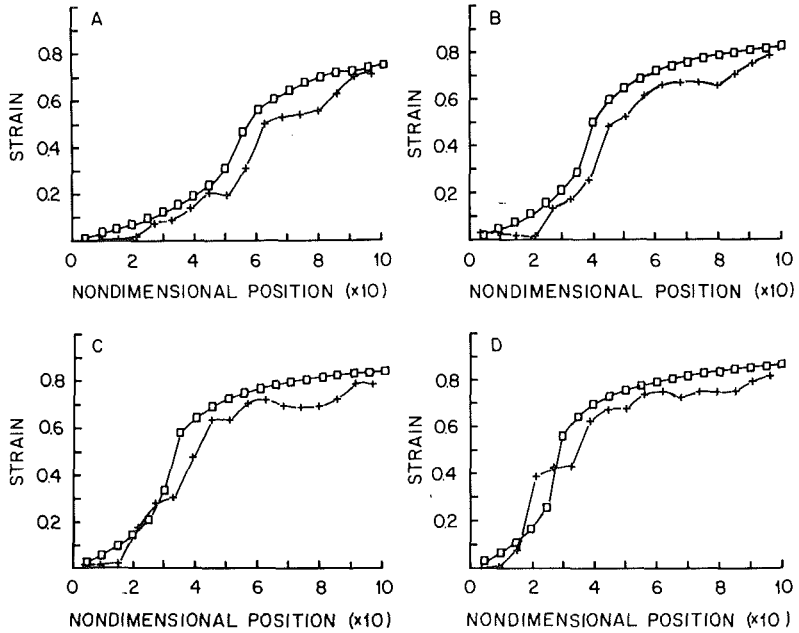


Fig. 6 Equilibrium strain distribution under glycerol filtration. Fluid pressures are: A—2500 Pa; B—5000 Pa; C—7500 Pa; D—10,000 Pa. The strain is negative. (□)—theoretical; (+)—experimental. Position 0—fluid interface; position 1.0—filter interface.

Downloaded 03 May 2010 to 171.66.16.244. Redistribution subject to ASME license or copyright; see http://www.asme.org/terms/Terms_Use.cfm

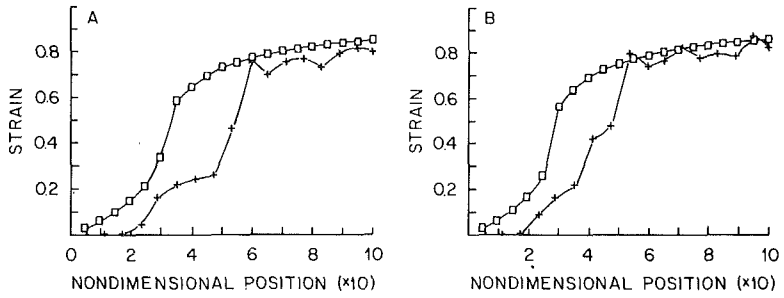


Fig. 7 Equilibrium strain-distribution as in Fig. 6 but under higher water pressure: A—7500 Pa; B—10,000 Pa.; (□)—theoretical; (+)—experimental

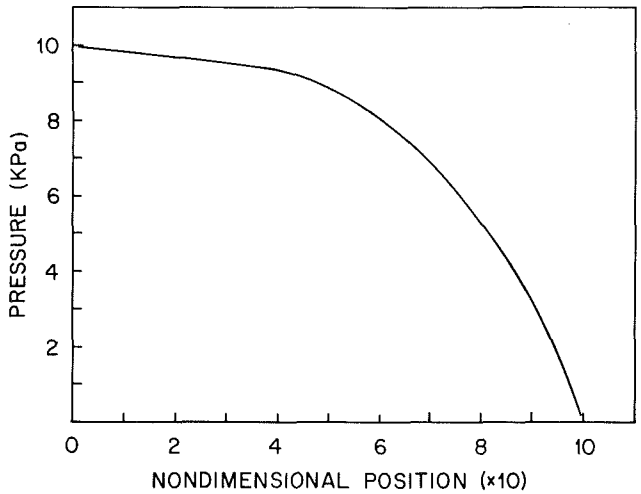


Fig. 8 Predicted equilibrium pressure distribution along the sponge cylinder under a fluid pressure of 10 KPa

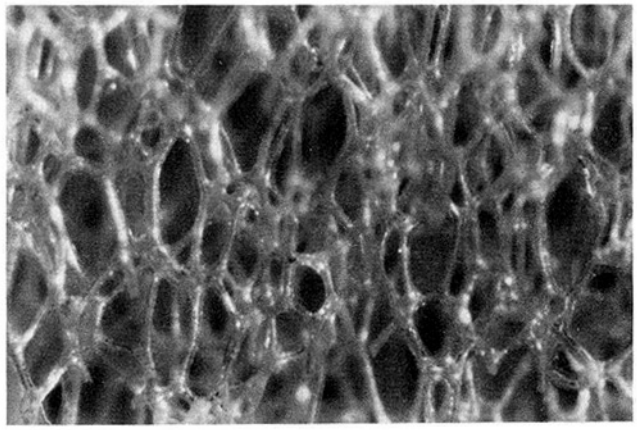


Fig. 9 A photographic view of surface of the polyurethane sponge used in the present study (magnification = X ca. 40)

shown for comparison reasons. As can be seen from the data in Fig. 4, the second sponge is more rigid.

Detailed quantitative comparison of the present stress-strain results to previous data (Parker et al., 1987; Beavers et al., 1981) is difficult since as is seen from Fig. 4, slight differences in density or porosity introduce significant variation in the response. The curves look, however, qualitatively similar to the results in the foregoing sources, especially that of the more rigid sponge.

In Fig. 5 the permeability-strain data for the two sponges is shown. As can be seen, the permeability decays with increasing negative strain and reaches vanishingly low values at a strain level of about -0.9. The permeabilities of the two sponges are quite similar.

The measured equilibrium strain distribution under fluid filtration is shown in Figs. 6 to 7 for tests with glycerol (Fig. 6) and water under high pressure (Fig. 7). Also shown in these figures is the predicted response for each of the fluid pressures used.

The fit between model and data is good for tests with glycerol. On the other hand, in tests with water at high pressures (Fig. 7), there is a gap between model and data at the steep (middle) portion of the curves. This gap is attributed to the high flow rate and the resulting higher Reynold's number, where the law of Darcy (equations (1), (8), and (11)) is not valid. Hence, the numerical solution is not expected to fit the data.

The results in Fig. 6 indicate that the present formulation represents the system adequately well under low Reynolds numbers. Comparison with previous studies shows that the model used by Parker et al. (1987) is different from the present one. This could account for at least some of the discrepancy between predicted and experimental overall shortening of their sponges which, as they indicate, was as high as 35 percent (Fig. 10 in the above study). The underlying theoretical difference between the present model and that of Parker et al. (1987) is difficult to analyze since the details of derivation are not provided in the latter study.

The model predicted equilibrium pressure distribution along the sponge (Fig. 8) indicates a gradual decrease near the fluid interface and a steep one near the filter. This is a direct result of the strain distribution along the sponge: Lower strains and higher permeability near the fluid (and thus lower pressure gradient) while near the filter there is a considerable compaction of the sponge, the permeability is low and the ensuing pressure gradient is steep.

5 Conclusions

The results of the study reconfirm the notion that permeability tests in compliant materials may introduce bias to the permeability results due to the nonuniform distribution of strain along the filtration path. This bias can be reduced by applying as low a fluid pressure drop as possible.

The distribution of strain, stress, and pressure along the sponge indicates that flow limitation is associated mainly with the downstream portions of the matrix due to their high compression and lower permeability.

Comparison between data of different studies must be done with caution since materials of otherwise very similar characteristics may still yield quite a different response, primarily in terms of their stress-strain constitutive behavior.

The nonlinear model based on the mixture theory seems to provide a reliable representation of the present solid-fluid systems.

Downloaded 03 May 2010 to 171.66.16.244. Redistribution subject to ASME license or copyright; see http://www.asme.org/terms/Terms_Use.cfm

Acknowledgement

This research was supported by the fund for the Promotion of Research at the Technion—IIT and by the Technion V.P.R. Fund—Archie Micay Biomedical Research Fund.

References

Beavers, G. S., Wittenberg, K., and Sparrow, E. M., 1981, "Fluid Flow Through a Class of Highly Deformable Porous Media. Part II—Experiments With Water," *ASME Journal of Fluid Engineering*, Vol. 103, pp. 440–444.

Biot, M. A., 1955, "Theory of Elasticity and Consolidation for a Porous, Anisotropic Solid," *Journal of Applied Physics*, Vol. 26, pp. 182–185.

Biot, M. A., 1972, "A Theory of Finite Deformations of Porous Solids," *Indiana University Mathematics Journal*, Vol. 21, pp. 597–620.

Bowen, R. M., 1989, "Incompressible Porous Media Models by Use of the Theory of Mixtures," *International Journal of Engineering Science*, Vol. 18, pp. 1129–1148.

Green, A. E., and Zerna, W., 1960, *Theoretical Elasticity*, Clarendon Press, Oxford, U.K.

Kenyon, D. E., 1976b, "The Theory of Incompressible Solid Fluid Mixture," *Arch. Rational. Mech. Anal.*, Vol. 62, pp. 131–147.

Lanir, Y., 1987, "Biorheology and Fluid Flux in Swelling Tissues. I. Biocomponent Theory for Small Deformations, Including Concentration Effects," *Biorheology*, Vol. 24, pp. 173–187.

Mow, V. C., Kuei, S. C., Lai, W. M., and Armstrong, C. G., 1980, "Biphasic Creep and Stress Relaxation of Articular Cartilage: Theory and Experiments," *ASME Journal of Biomechanical Engineering*, Vol. 102, pp. 73–84.

Parker, K. H., Mehta, R. V., and Caro, C. G., 1987, "Steady Flow in Porous, Elastically Deformable Materials," ASME JOURNAL OF APPLIED MECHANICS, Vol. 54, pp. 794–800.

Truesdell, C., 1962, "Mechanical Basis of Diffusion," *Journal of Chemical Physics*, Vol. 37, pp. 2336–2344.

APPENDIX A

Basic Equations for Solid-Fluid Mixtures

The formulation is based on assumptions (a) to (e) in Section 2.1. Full and detailed derivation is given in several sources (e.g., Kenyon, 1976).

The mass balance equation for incompressible solid-fluid mixtures (assumption (a)) is given by:

$$\nabla \cdot (\mathbf{q} + \mathbf{V}_s) = 0 \tag{A1}$$

where ∇ is the del operator, $\mathbf{V}_s$—the solid velocity and $\mathbf{q}$—the filtration flux given by:

$$\mathbf{q} = \phi_f (\mathbf{V}_f - \mathbf{V}_s) \tag{A2}$$

where $\mathbf{V}_f$ is the fluid velocity and ϕ_f is the porosity—the fluid partial volume. Since there are no voids (assumption (b)), we have:

$$\phi_f + \phi_s = 1.0 \tag{A3}$$

where ϕ_s is the solid partial volume.

In the absence of inertia and body forces (assumption (d)), the equation of motion for the fluid is:

$$-\nabla P + \Psi = 0 \tag{A4}$$

where the hydrostatic pressure P represents the fluid stress (assumption (c)). The term Ψ represents the solid-fluid interaction forces. In the absence of osmotic effects it is solely due to viscous forces associated with the filtration of fluid through the solid. If the filtration flux is low, then assumption (e) is valid and Ψ is given by:

$$\Psi = \mathbf{K}^{-1}\mathbf{q} \tag{A5}$$

where $\mathbf{K}$ is the permeability matrix.

The motion of the whole mixture is governed by:

$$\nabla \cdot \tau - \nabla p = 0 \tag{A6}$$

where τ is the partial stress in the solid skeleton. If the solid is elastic then under isothermal conditions τ is solely a function of the strain.

APPENDIX B

The Numerical Solution of Equation (13)

Using the notation $e_j^n = e(z = j \cdot \Delta z,\ t = n \cdot \Delta t)$, the R.H.S of equation (13) is:

$$\simeq \partial/\partial Z\{D(e)[e^n_{j+1/2} - e^n_{j-1/2}]\}/\Delta Z \tag{B1}$$

and by application of the second differentiation w.r.t. Z, this expression is given by:

$$\simeq (D^n_{j+1/2}(e^n_{j+1} - e^n_j) - D^n_{j-1/2}(e^n_j - e^n_{j-1}))/(\Delta Z)^2 \tag{B2}$$

where $D^n_{j+1} \equiv D(e^n_{j+1/2})$ is acquired from the experimental $D(e)$ data, by interpolation.

The L.H.S. of equation (13) can be approximated as:

$$\partial e/\partial t \simeq (e_j^{n+1} - e_j^n)/\Delta t. \tag{B3}$$

Hence, equation (13) in a difference form is written as:

$$e_j^{n+1} = e_j^n + r(D^n_{j+1/2}(e^n_{j+1} - e^n_j) - D^n_{j-1/2(e^n_j - e^n_{j-1})}) \tag{B4}$$

where $r = \Delta t/(\Delta Z)^2$.

Equation (B4) is to be solved together with the initial and boundary conditions (equations (15)–(17)). This was carried out with $\Delta Z = 1/20$ (Z being the nondimensional distance along the sponge cylinder with a range of 0 to 1) and $\Delta t = 5 * 10^{-5}$ sec.

Downloaded 03 May 2010 to 171.66.16.244. Redistribution subject to ASME license or copyright; see http://www.asme.org/terms/Terms_Use.cfm

Yusuke Fukushima

Norio Hayakawa

Department of Civil Engineering,
Nagaoka University of Technology,
Nagaoka, Niigata, 940-21, Japan

Analysis of Inclined Wall Plume by the k-ϵ Turbulence Model

The similarity solution of inclined wall plume is obtained analytically. The mathematical model used herein consists of the continuity equation of flow, the momentum balance equation in the flow direction, the diffusion equation of concentration, the equation of kinetic energy of turbulence and the equation of viscous dissipation rate of turbulence. It is shown that this set of equations has the similarity solution which can be solved numerically for each angle of the inclined wall. This numerical model is applied to the wide range of the slope angle, which includes the vertical wall plume as the special case and the nearly horizontal wall plume. The velocity and concentration profiles of the inclined wall plume are explained well by the similarity solutions.

1 Introduction

The inclined wall plumes are formed by the fluid flowing in contact with the wall whose density is different from that of the ambient fluid. The heavy fluid near the wall will flow down along the inclined wall. The light fluid near the wall will form the upward flow. These kinds of flow are often observed in nature and are also important from the engineering aspect. The inclined wall plume has been investigated by many researchers. Ellison and Turner (1959) carried out the experiments of an inclined wall plume for the wide range of the slope angle to measure the velocity and density distributions. They have shown that the entrainment coefficient is a strong function of the slope angle. Turner (1973) indicated that the entrainment coefficient of various flows is the function of the overall Richardson number. Komatsu and Tsubaki (1979) carried out the experiments almost the same as Ellison and Turner's (1959) experiments, and proposed a prediction equation of the entrainment coefficient as a function of the overall Richardson number by the layer-integral method, which takes the turbulent structure into consideration. Grella and Faeth (1975)'s experiment have been carried out using the combustion jet of carbon monoxide in air. They have precisely measured the velocity distribution with a hot wire anemometer and the temperature distribution with a thermocouple. Fukuoka et al. (1980, 1980b) carried out experiments of the density underflow as a model of the density current in a reservoir to investigate the characteristics of the velocity and density distributions. Yoshida (1982) measured the turbulent structgure of a vertical wall plume made of saline water by the hydrogen bubble method.

The experimental approach has been taken so far to investigate the inclined wall plumes. The author carried out an analytical study to show that both laminar and turbulent vertical wall plumes have the similarity solutions of the velocity and density distributions (Fukushima, 1982, Fukushima et al., 1983, 1984). In the analysis of the turbulent flow of his work, the eddy viscosity model was used. It is difficult to predict the distribution of eddy viscosity, especially near the wall.

In recent years, turbulence models are applied to the wide variety of flow. Rodi (1980) reviewed the turbulence model and its application to hydrodynamics with special emphasis on the k-ϵ turbulence model in which the kinetic energy of turbulence, k, and viscous dissipation rate, ϵ, were taken as unknown variables. Ljuboja and Rodi (1981) analyzed the vertical wall plumes to compare the experimental results of Grella and Faeth (1975). They used the algebraic stress model which is one of the extensions of the k-ϵ turbulence model. Authors (Fukushima and Fukuda, 1986; Fukushima Fukuda, 1988) applied the k-ϵ turbulence model to the open channel flow with suspended material and showed that the experimental data were represented by the k-ϵ turbulence model.

The objective of this paper is to investigate the characteristics of the inclined wall plume which is a function of the hydraulic conditions. It is shown that the inclined wall plumes have the similarity solution under the k-ϵ turbulence model. Numerical analysis is carried out to the wide range of the slope angle, which includes plumes along the vertical wall as a special case and along the nearly-horizontal wall.

2 Fundamental Equation

Consider the downward (upward) flow of the heavy (light) fluid with density ρ_0 on the inclined wall into the stagnant body of fluid with density ρ as shown in Fig. 1. The flow is two-dimensional and incompressible. Turbulence is thought to be fully developed, and thus the viscous term is negligible. The inflowing fluid mixes with the ambient fluid by the turbulence. The relative density of the two fluids is small enough to adopt the Boussinesq approximation. The flow varies slowly in the

Contributed by the Applied Mechanics Division of THE AMERICAN SOCIETY OF MECHANICAL ENGINEERS for publication in the JOURNAL OF APPLIED MECHANICS.

Discussion on this paper should be addressed to the Technical Editor, Leon M. Keer, The Technological Institute, Northwestern University, Evanston, IL 60208, and will be accepted until two months after final publication of the paper itself in the JOURNAL OF APPLIED MECHANICS. Manuscript received by the ASME Applied Mechanics Division, December 12, 1988; final revision, April 24, 1989.

Copyright © 1990 by ASME
Downloaded 03 May 2010 to 171.66.16.244. Redistribution subject to ASME license or copyright; see http://www.asme.org/terms/Terms_Use.cfm

flow direction so that the boundary layer approximation is adopted.

The equation of continuity, the momentum equations in the x and z direction, and the equation of concentration of salinity (or the other scalar quantity which causes the density difference such as temperature) become, respectively,

$$\frac{\partial u}{\partial x} + \frac{\partial w}{\partial z} = 0 \tag{1}$$

$$u\frac{\partial u}{\partial x} + w\frac{\partial u}{\partial z} = \frac{\rho}{\rho_0} g \sin\theta - g\cos\theta \frac{\partial}{\partial x}\int_z^h Rc\, dz - \frac{\partial}{\partial z}(\overline{u'w'}) \tag{2}$$

$$u\frac{\partial c}{\partial x} + w\frac{\partial c}{\partial z} = -\frac{\partial}{\partial z}(\overline{c'w'}) \tag{3}$$

where u and w are the velocity components in the flow direction x and in the lateral direction z, respectively, g is the gravitational acceleration, θ is the slope angle of the wall, and R is the ratio of the relative density difference to the concentration of salinity (Rc is the relatively density).

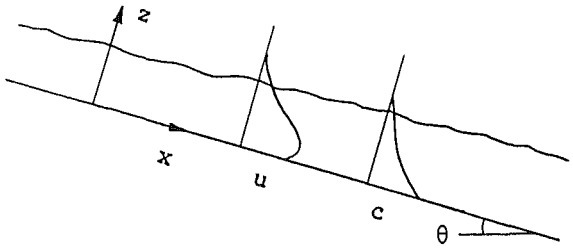


Fig. 1 Definition sketch of inclined wall plume

The eddy viscosity, ν_t, and the turbulent Schmidt number, σ_t, which is the ratio of the eddy viscosity to the eddy diffusivity, are defined as follows:

$$\overline{u'w'} = -\nu_t \frac{\partial u}{\partial z} \tag{4}$$

$$\overline{c'w'} = -\frac{\nu_t}{\sigma_t}\frac{\partial c}{\partial z} \tag{5}$$

where the prime indicates turbulent quantities, and $\overline{u'w'}$ and $\overline{c'w'}$ are Reynolds stress and the correlation of c' and w'. The equation of the kinetic energy of turbulence, k, and the viscous dissipation rate of turbulence, ϵ, are obtained as follows (Rodi, 1980):

$$u\frac{\partial k}{\partial x} + w\frac{\partial k}{\partial z} = \frac{\partial}{\partial z}\left(\frac{\nu_t}{\sigma_k}\frac{\partial k}{\partial z}\right) + \nu_t\left(\frac{\partial u}{\partial z}\right)^2 + Rg\cos\theta\frac{\nu_t}{\sigma_t}\frac{\partial c}{\partial z} - \epsilon \tag{6}$$

$$u\frac{\partial \epsilon}{\partial x} + w\frac{\partial \epsilon}{\partial z} = \frac{\partial}{\partial z}\left(\frac{\nu_t}{\sigma_\epsilon}\frac{\partial \epsilon}{\partial z}\right) + c_{1\epsilon}\frac{\epsilon}{k}\left\{\nu_t\left(\frac{\partial u}{\partial z}\right)^2 + (1-c_{3\epsilon})Rg\cos\theta\frac{\nu_t}{\sigma_t}\frac{\partial c}{\partial z}\right\} - c_{2\epsilon}\frac{\epsilon^2}{k}. \tag{7}$$

The eddy viscosity of the k-ϵ turbulence model is expressed by

$$\nu_t = c_\mu \frac{k^2}{\epsilon}. \tag{8}$$

The coefficients c_μ, σ_k, σ_ϵ, $c_{1\epsilon}$, $c_{2\epsilon}$ included in equations (6),

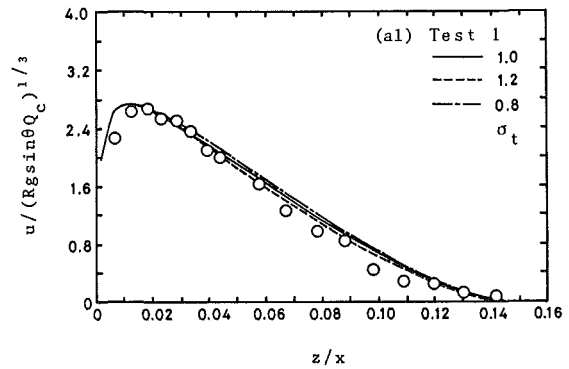


Fig. 2(a1)

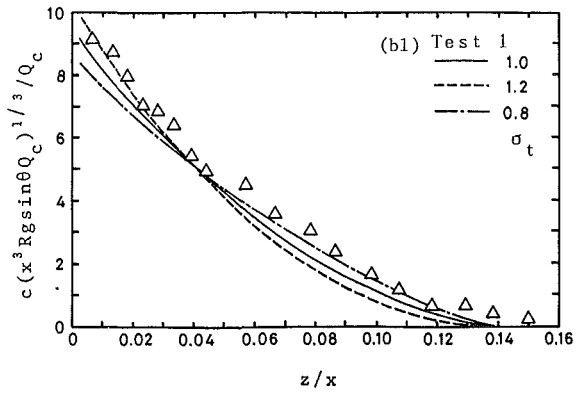


Fig. 2(b1)

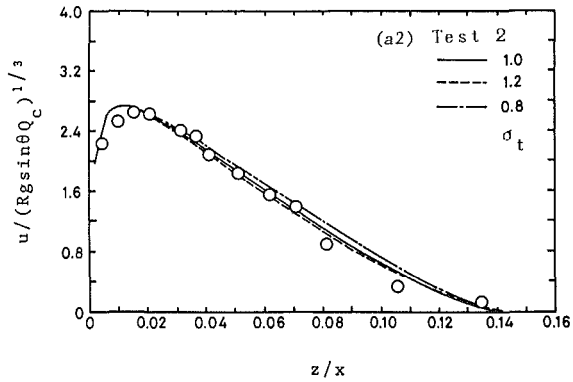


Fig. 2(a2)

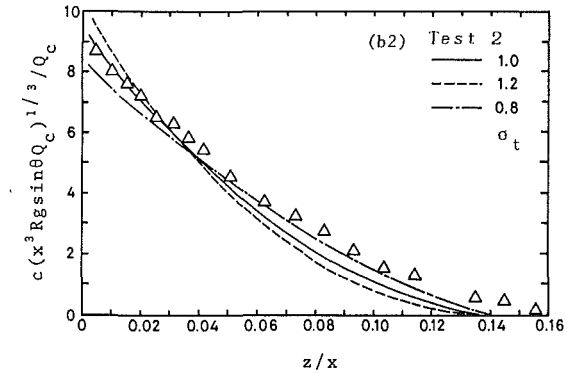


Fig. 2(b2)

Downloaded 03 May 2010 to 171.66.16.244. Redistribution subject to ASME license or copyright; see http://www.asme.org/terms/Terms_Use.cfm

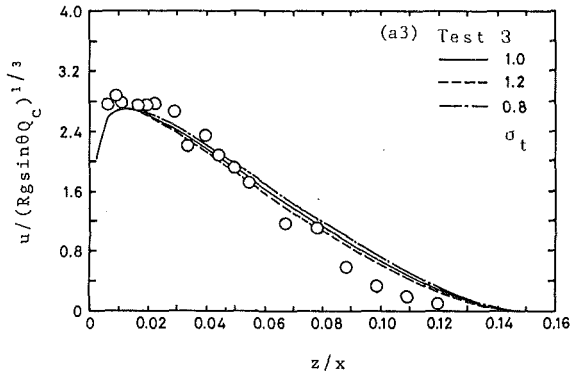


Fig. 2(a3)

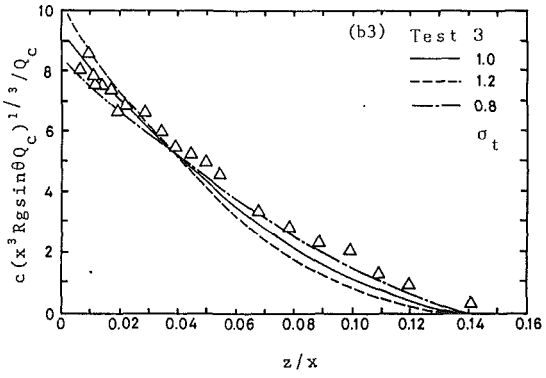


Fig. 2(b3)

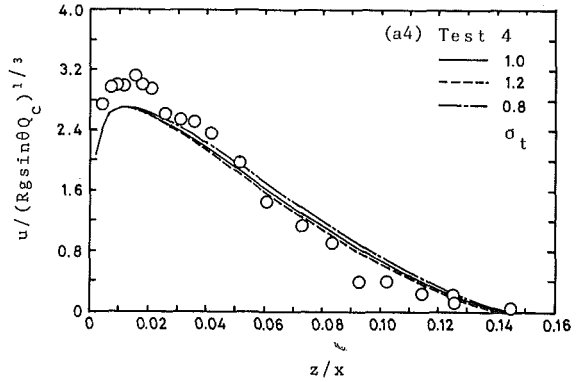


Fig. 2(a4)

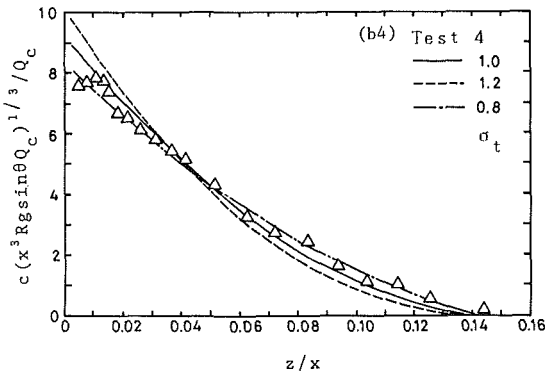


Fig. 2(b4)

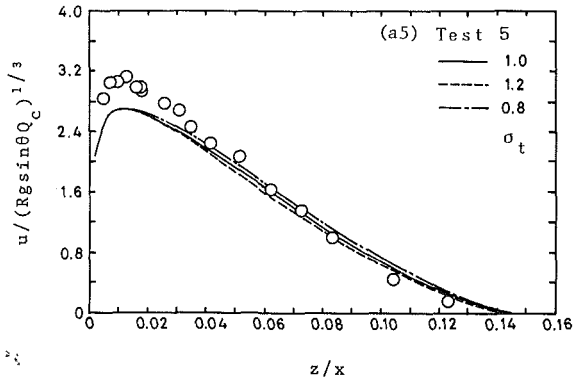


Fig. 2(a5)

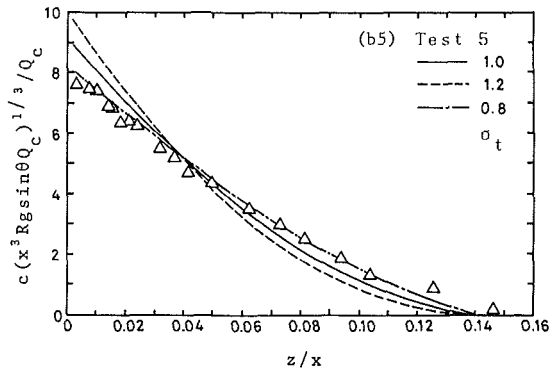


Fig. 2(b5)

Fig. 2 Comparison of numerical solutions with the Grella and Faeth (1975) experimental data of nondimensional velocity and relative density difference ($\theta = 90$ deg); (a1), (b1) Test 1; (a2), (b2) Test 2; (a3), (b3) Test 3; (a4), (b4) Test 4; and (a5), (b5) Test 5

(7), and (8) are estimated by the comparison of various kinds of flow and are given as (Rodi, 1980)

$$c_\mu = 0.09 \quad \sigma_k = 1.0 \quad \sigma_\epsilon = 1.3 \quad c_{1\epsilon} = 1.44 \quad c_{2\epsilon} = 1.92. \tag{9}$$

On the other hand, values of σ_t and $c_{3\epsilon}$ are not known clearly for the flow in which buoyancy effect is dominant.

The stream function ψ is introduced to satisfy equation (2).

$$u = \frac{\partial \psi}{\partial z} \qquad w = -\frac{\partial \psi}{\partial x} \tag{10}$$

In order to find the similarity solutions the variables are written as

$$\eta = azx^{-l} \tag{11a}$$

$$\psi = bx^m F(\eta) \tag{11b}$$

$$c = c_* x^n G(\eta) \tag{11c}$$

$$k = dx^p K(\eta) \tag{11d}$$

$$\epsilon = \epsilon x^q E(\eta) \tag{11e}$$

where η is the similarity variable and F, G, K, and E are the similarity functions. The coefficients a, b, c_*, d, and e and the exponents l, m, n, p, and q are to be determined by equations (2), (3), (6), and (7).

Velocity components u and w are obtained from equation (10).

$$u = \frac{\partial \psi}{\partial z} = \frac{\partial}{\partial z}\{bx^m F(\eta)\} = bx^m \frac{\partial \eta}{\partial z} F' = abx^{m-l} F' \tag{12}$$

Downloaded 03 May 2010 to 171.66.16.244. Redistribution subject to ASME license or copyright; see http://www.asme.org/terms/Terms_Use.cfm

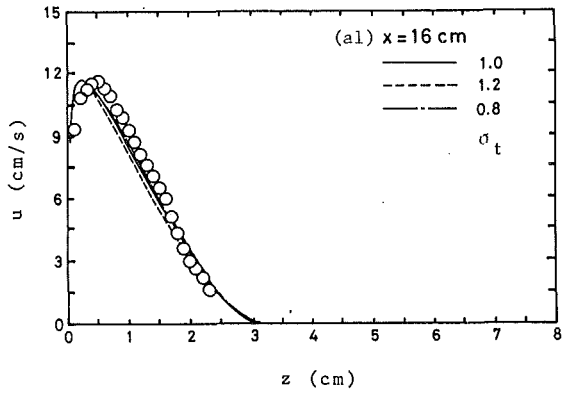


Fig. 3(*a*1)

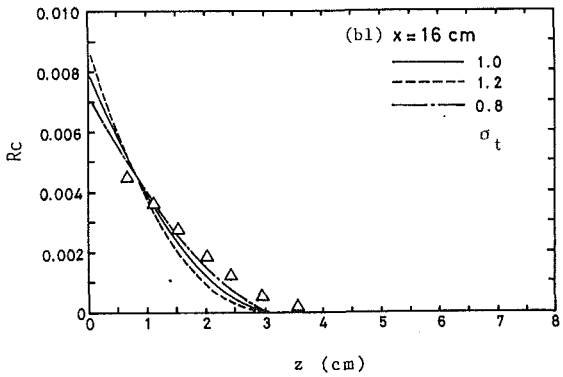


Fig. 3(*b*1)

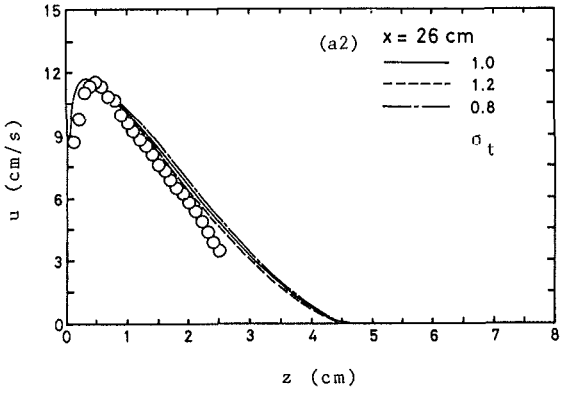


Fig. 3(*a*2)

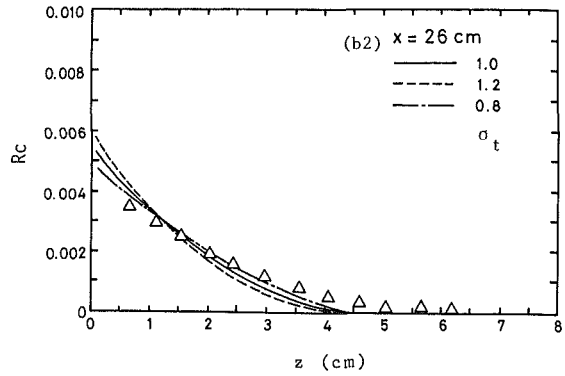


Fig. 3(*b*2)

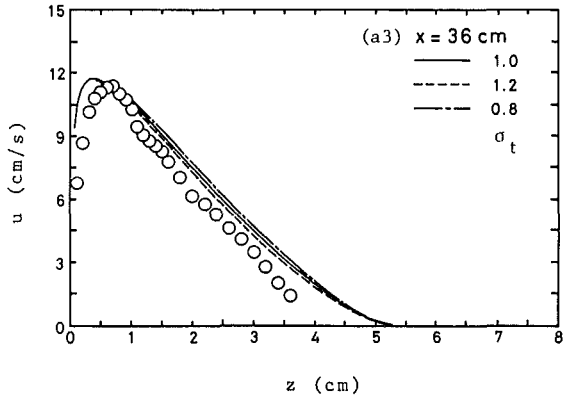


Fig. 3(*a*3)

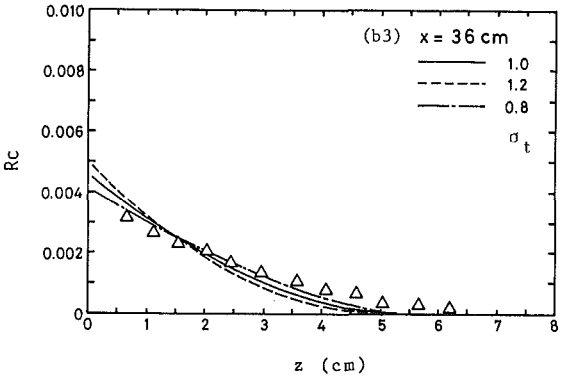


Fig. 3(*b*3)

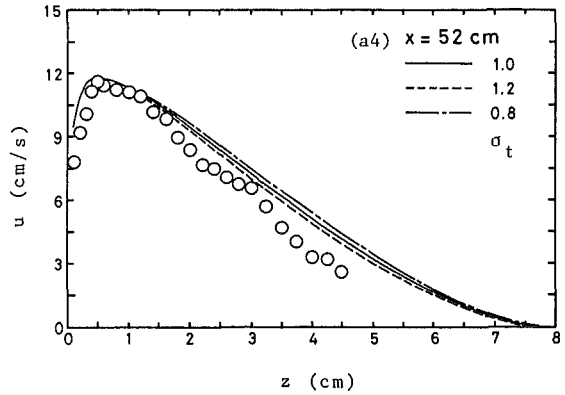


Fig. 3(*a*4)

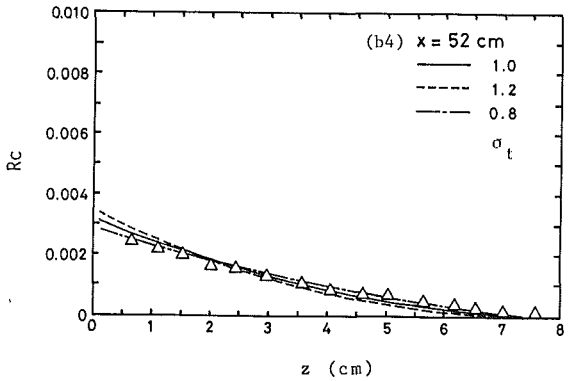


Fig. 3(*b*4)

Fig. 3 Comparison of numerical solutions with the Fukushima et al. (1984) experimental data of velocity and relative density difference ($\theta = 90$ deg). (*a*1), (*b*1) at $x = 0.16$ m; (*a*2), (*b*) at $x = 0.26$ m; (*a*3), (*b*3) at $x = 0.36$ m; (*a*4), (*b*4) at $x = 0.52$ m.

Downloaded 03 May 2010 to 171.66.16.244. Redistribution subject to ASME license or copyright; see http://www.asme.org/terms/Terms_Use.cfm

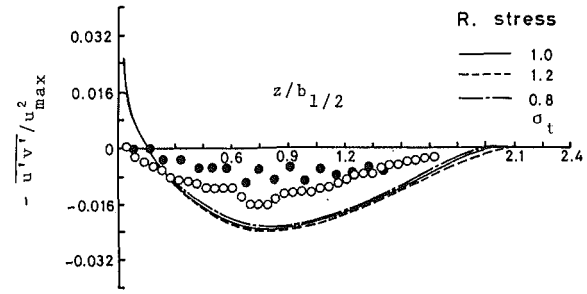


Fig. 4 Distribution of Reynolds stress (open circles indicate the Yoshida (1982) data, close circles indicate the Fukushima et al. (1984) data)

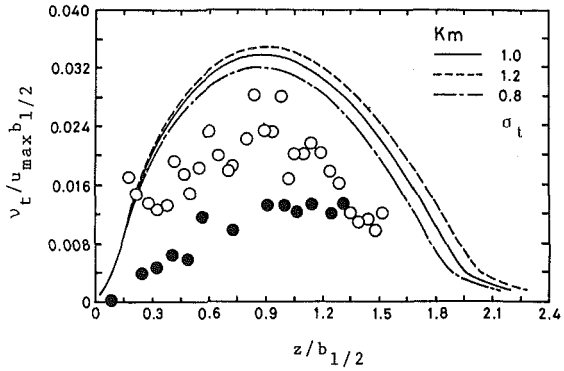


Fig. 5 Distribution of the eddy viscosity (symbols are the same as those of Fig. 4)

$$w = -\frac{\partial \psi}{\partial x} = \frac{\partial}{\partial x}\{bx^m F(\eta)\} = -bx^{m-1}F - bx^m \frac{\partial \eta}{\partial x} F'$$
$$= bx^{m-1}(l\eta F' - mF) \tag{13}$$

Using relations of (11), (12), and (13), equations (2), (3), (6), and (7) become

$$a^2b^2x^{2m-2l-1}\{(m-l)F'^2 - mFF''\} = Rg\sin\theta\, c_* x^n G - \frac{Rc_*}{a} g\cos\theta (n+l)x^{n+l-1}\int_z^h G\, d\eta + c_\mu \frac{a^3bd^2}{e} x^{2p+m-q-3l}\left\{F''\left(\frac{2KK'}{E} - \frac{K^2E'}{E^2}\right) + \frac{K^2}{E}F'''\right\} \tag{14}$$

$$abc_* x^{m+n-l-1}(nF'G - mFG') = \frac{c\mu}{\sigma_t}\frac{a^3c_*d^2}{e} x^{2p-q+n-2l}\left\{G'\left(\frac{2KK'}{E} - \frac{K^2E'}{E^2}\right) + \frac{K^2}{E}G''\right\} \tag{15}$$

$$abdx^{m+p-l-1}(pF'K - mFK') = \frac{c_\mu}{\sigma_k}\frac{a^2d^3}{e} x^{3p-q-2l}\left\{K'\left(\frac{2KK'}{E} - \frac{K^2E''}{E^2}\right) + \frac{K^2}{E}K''\right\} + c_\mu \frac{a^4b^2d^2}{e} x^{2p-q+2m-4l}\frac{K^2}{E}F''^2 + Rg\cos\theta \frac{c_\mu}{\sigma_t}\frac{ac_*d^2}{e} x^{2p-q+n-l}\frac{K^2}{E}G' - ex^qE \tag{16}$$

$$abex^{m+q-l-1}(pF'K - mFK') = \frac{c_\mu}{\sigma_k}\frac{a^2d^3}{e} x^{2p-2l}\left\{E'\left(\frac{2KK'}{E} - \frac{K^2E''}{E^2}\right) + \frac{K^2}{E}E''\right\} + c_{1\epsilon}c_\mu a^4b^2dx^{p+2m-4l}KF''^2 - c_{3\epsilon})Rg\cos\theta \frac{c_\mu}{\sigma_t} ac_*d\, x^{n-l}\frac{K^2}{E}G' - c_{2\epsilon}\frac{e^2}{d}x^{2-p}\frac{E^2}{K}. \tag{17}$$

The buoyancy flux is conserved in the flow direction for the flow considered herein.

$$Q_c = \int_0^\infty uc\, dz = \int_0^\infty abx^{m-l}F'c_*x^nG\frac{\partial z}{\partial \eta}\, d\eta = bc_*x^{m+n}\int_0^\infty F'G\, d\eta \tag{18}$$

The conditions of existence of the similar solutions are that the exponents of x in each equation (14), (15), (16), (17), and (18) are the same. Thus,

$$2m-2l-1 = n = n+l-1 = 2p+m-q-3l \tag{19a}$$
$$m+n-l-1 = 2p-q+n-2l \tag{19b}$$
$$m+p-l-1 = 3p-q-2l$$
$$= 2p-q+2m-4l = 2p-q+n-l = q \tag{19c}$$
$$m+q-l-1 = 2p-2l = p+2m-4l = n-l = 2q-p \tag{19d}$$
$$m+n = 0. \tag{19e}$$

From the equations (19), the values of the exponents of x are derived.

$$l=1,\ m=1,\ n=-1,\ p=0,\ q=-1 \tag{20}$$

The nondimensional eddy viscosity and its derivative are defined as

$$\nu_{t*} = c_\mu \frac{K^2}{E} \tag{21}$$

$$\nu_{t*}' = c_\mu K'\left(\frac{2KK'}{E} - \frac{K^2E'}{E^2}\right). \tag{22}$$

The subscript $(*)$ is omitted hereafter for a simplicity. From the previous expressions of the nondimensional eddy viscosity and its derivative with the values of equation (20), equations (14) to (18) become

$$FF'' + \frac{Rg\sin\theta\, c_*}{a^2b^2}G + \frac{ad^2}{be}(\nu_t'F'' + \nu_tF'''') = 0 \tag{23}$$

$$F'G + FG' + \frac{1}{\sigma_t}\frac{ad^2}{be}(\nu_t'G' + \nu_tG'') = 0 \tag{24}$$

$$FK' + \frac{1}{\sigma_k}\frac{ad^2}{be}(\nu_t'K' + \nu_tK'') + \frac{a^3bd}{e}\nu_tF''^2 + \frac{Rg\cos\theta}{\sigma_t}\frac{c_*d}{be}\nu_tG' - \frac{e}{abd}E \tag{25}$$

$$F'E + FE' + \frac{1}{\sigma_\epsilon}\frac{ad^2}{be}(\nu_t'E' + \nu_tE'') + c_{1\epsilon}\frac{E}{K}\left\{\frac{a^3bd}{e}\nu_tF''^2 + (1-c_{3\epsilon})\frac{Rg\cos\theta}{\sigma_t}\frac{c_*d}{be}\nu_tG'\right\} - c_{2\epsilon}\frac{e}{abd}\frac{E^2}{K} = 0 \tag{26}$$

$$Q_c = bc_*\int_0^\infty F''G\, d\eta = bc_*I \tag{27}$$

Downloaded 03 May 2010 to 171.66.16.244. Redistribution subject to ASME license or copyright; see http://www.asme.org/terms/Terms_Use.cfm

Table 1 Experimental conditions

Case	θ (deg.)	Q_c (cm²/s)	$(\Delta\rho/\rho)_0$	x (m)	Researcher etc.
					Grella & Faeth (1975)
GF1	90.0	5.12	0.0509	0.61	" Test 1
GF2	90.0	11.06	0.0823	0.61	" Test 2
GF3	90.0	4.26	0.0200	1.22	" Test 3
GF4	90.0	10.11	0.0333	1.22	" Test 4
GF5	90.0	24.93	0.0599	1.22	" Test 5
FFH	90.0	0.0804	0.01411	0.16	Fukushima et al. (1984)
				0.26	"
				0.36	"
				0.52	"
Yo	90.0	0.0454	0.0270	0.2	Yoshida (1982)
Na	30.0	0.351	0.01450	0.4	Nakashima (1985)
				0.5	"
Fu1	0.46	0.154	0.00980	4.9	Fukushima Run 1
Fu2	0.46	0.161	0.00919	4.9	" Run 2
Fu3	0.46	0.294	0.01862	4.9	" Run 3

Table 2 Summary of calculational results

θ	F(∞)	F'_{max}	G_{max}	$\eta_{1/2}$	I_1	I_2	I_3	I_4	E_0	R_i	c_f
(deg)	×10²			×10²					×10²		×10³
90.0	6.797	2.72	8.80	7.574	0.968	0.689	0.717	0.551	10.272	0.137	5.204
80.0	6.269	2.79	9.29	7.205	0.942	0.680	0.694	0.535	9.482	0.132	5.245
70.0	5.794	2.87	9.72	6.615	0.943	0.685	0.706	0.542	8.656	0.124	5.607
60.0	5.562	2.94	10.10	5.929	1.007	0.724	0.744	0.569	8.367	0.122	5.636
50.0	5.225	2.99	10.59	5.643	1.000	0.718	0.732	0.561	7.930	0.132	5.677
40.0	4.759	3.07	11.34	5.389	0.960	0.689	0.696	0.534	7.279	0.152	5.700
30.0	3.543	3.34	14.05	3.991	0.986	0.705	0.695	0.534	5.559	0.149	5.955
20.0	3.387	3.38	14.55	4.023	0.940	0.672	0.658	0.505	5.351	0.221	6.000
15.0	2.874	3.56	16.52	3.403	0.954	0.677	0.654	0.499	4.626	0.251	6.186
10.0	2.080	3.83	21.13	2.566	0.963	0.679	0.630	0.482	3.543	0.304	6.288
8.0	1.720	4.01	24.59	2.111	0.999	0.696	0.634	0.480	3.053	0.329	6.292
6.0	1.255	4.25	31.42	1.697	0.968	0.669	0.583	0.442	2.399	0.392	6.300
5.71	1.199	4.30	32.71	1.596	0.991	0.682	0.590	0.446	2.319	0.391	6.377
4.57	0.913	4.53	40.83	1.271	1.005	0.678	0.570	0.425	1.910	0.436	6.310
3.43	0.733	4.90	47.16	1.077	0.948	0.646	0.540	0.402	1.507	0.472	6.847
2.86	0.648	5.15	51.28	0.946	0.947	0.648	0.541	0.401	1.317	0.483	7.104
2.29	0.495	5.60	62.87	0.705	0.981	0.665	0.543	0.403	1.034	0.467	7.777
0.46	0.103	7.94	164.7	0.156	0.834	0.596	0.660	0.480	0.182	0.574	6.970

where the integral I is defined by

$$I=\int_0^\infty F'G\,d\eta. \tag{28}$$

To determine the expressions of a, b, c_*, d, and e, the following coefficients included in (23) to (27) are set to be unity without loss of generality.

$$\frac{Rg\sin\theta\, c_*}{a^2b^2}=1 \tag{29a}$$

$$\frac{ad^2}{be}=1 \tag{29b}$$

$$\frac{a^3bd}{e}=1 \tag{29c}$$

$$\frac{e}{abd}=1 \tag{29d}$$

$$\frac{Q_c/I}{bc_*}=1 \tag{29e}$$

With equations (29), the coefficients a, b, c_*, d, and e are determined as follows:

$$a=1 \tag{30a}$$

$$b=(Rg\sin\theta\, Q_c/I)^{1/3}=U \tag{30b}$$

$$c_*=\frac{(Q_c/I)^{2/3}}{(Rg\sin\theta)^{1/3}} \tag{30c}$$

$$d=(Rg\sin\theta\, Q_c/I)^{2/3}=U^2 \tag{30d}$$

$$e=Rg\sin\theta\, Q_c/I=U^3. \tag{30e}$$

The remaining coefficient included in equations (25) and (26) is obtained from equation (30).

$$\frac{1}{\sigma_t}Rg\cos\theta\frac{c_*d}{be}=\frac{\cot\theta}{\sigma_t}Rg\sin\theta\frac{c_*d}{be}=\frac{\cot\theta}{\sigma_t} \tag{31}$$

With the previous expressions of a, b, c_*, d and e, equations (23) to (27) are written as

$$FF''+G+(\nu_tF''+\nu_tF''')=0 \tag{32}$$

$$F'G+FG'+\frac{1}{\sigma_t}(\nu_t'G'+\nu_tG')=0 \tag{33}$$

$$FK'+\frac{1}{\sigma_k}(\nu_t'K'+\nu_tK')+\nu_tF'^2+\frac{\cot\theta}{\sigma_t}\nu_tG'-E=0 \tag{34}$$

$$F'E+FE'+\frac{1}{\sigma_\epsilon}(\nu_t'E'+\nu_tE'')+c_{1\epsilon}\frac{E}{K}\left\{\nu_tF'^2+(1-c_{3\epsilon})\frac{1}{\sigma_t}\cot\theta\,\nu_tG'\right\}-c_{2\epsilon}\frac{E^2}{K}=0. \tag{35}$$

Equations (31) to (35) are ordinary differential equations

Downloaded 03 May 2010 to 171.66.16.244. Redistribution subject to ASME license or copyright; see http://www.asme.org/terms/Terms_Use.cfm

which the similarity functions of F, G, K, and E should satisfy. Relations between dimensional variables and the similarity variable, η, and the similarity functions F, G, K, and E are derived from equations (11), (20), and (30) as follows:

$$\eta = \frac{z}{x} \tag{36a}$$

$$u = (Rg \sin\theta\ Q_c/I)^{1/3}\ F'(\eta) \tag{36b}$$

$$c = \frac{(Q/I)^{2/3}}{(R \sin\theta)^{1/3}} \frac{1}{x} G(\eta) \tag{36c}$$

$$k = (Rg \sin\theta\ Q_c/I)^{2/3}\ K(\eta) \tag{36d}$$

$$\epsilon = (Rg \sin\theta\ Q_c/I) \frac{1}{x} E(\eta). \tag{36e}$$

3 Boundary Conditions

Consider the boundary conditions for equations (32)–(35). The wall function method (Rodi, 1980) which is widely used in the calculation of turbulence models as boundary conditions for u, k, and ϵ is adopted herein. The lateral component of velocity is zero at the wall. The flux in the z direction of the relative density is set to be zero. Thus, the boundary conditions at the wall, i.e., $z = z_0$, are written as

$$\frac{u_0}{u_*} = \frac{1}{\kappa} \ln\left(\frac{z_0 u_*}{\nu}\right) \tag{37a}$$

$$w = 0 \tag{37b}$$

$$\frac{\partial c}{\partial z} = 0 \tag{37c}$$

$$\frac{k}{u_*^2} = \frac{1}{\sqrt{c_\mu}} \tag{37d}$$

$$\epsilon = \frac{u_*^3}{\kappa z_0} \tag{37e}$$

where κ is the Karman constant. The boundary conditions at the infinity, i.e., $z = \infty$, are

$$u = k = \epsilon = c = 0. \tag{38}$$

Nondimensional expressions of these boundary conditions are derived next. The capital U and U_* indicate nondimensional mean velocity and shear velocity, respectively. Nondimensional form of the log law (37a) is written by

$$\frac{U}{U_*} = \frac{1}{\kappa} \ln(\eta) + A \tag{39}$$

where A for the smooth wall is defined as

$$A = \frac{1}{\kappa} \ln(\mathrm{Re}_*/\eta_{1/2}) + A_s \tag{40a}$$

where

$$\mathrm{Re}_* = u_* b^{1/2\nu} \tag{40b}$$

is the Reynolds number defined by shear velocity and a half-width of plume, and A for the rough wall is defined as

$$A = \frac{1}{\kappa} \ln(b_{1/2}/k_s/\eta_{1/2}) + A_r \tag{41}$$

where k_s is the relative roughness, A_s and A_r are constants, and $\eta_{1/2}$ is the nondimensional half-width of a plume. It is seen from (40a) that boundary conditions vary with the value of the Reynolds number. In a similar way, the value of A in equation (41) is dependent on the plume width, which may increase in the flow direction. The values in both equations (40a) and (41) is a logarithmic function of the Reynolds number, so that the variation of A is very small. For the case of laminar wall plumes, the strict similarity solution can be obtained (Fukushima, 1982; Fukushima et al., 1983). From this point of view, it is concluded that the "weak" similarity solutions exist for the turbulent inclined wall plumes.

Nondimensional expression of equations (37b), (37d), and (37e) become

$$F = 0 \tag{42}$$

$$\frac{K}{U_*^2} = \frac{1}{\sqrt{c_\mu}} \tag{43}$$

$$E = \frac{U_*^3}{\kappa \eta_0}. \tag{44}$$

The boundary conditions at the infinity become

$$F' = G = K = E = 0. \tag{45}$$

Thus, the problem becomes to solve nonlinear ordinary equations (32), (33), (34), and (35) with the boundary conditions (39)–(45). In the numerical calculation, the equations are descretized by the finite difference method and the iteration is carried out to obtain the solutions. The outer edge of calculation is taken about three times the half-width of a plume.

4 Computational Results and Discussions

The numerical model is compared with the experimental results. The experimental conditions used herein are summarized in Table 1. Fukushima's experiments are carried out by using a channel 6 m long and 0.2 m wide with the slope of 1/125. In this experiment, salt water flows down into the body of stagnant water along the bed. The details of the other experiment' are included in the references (Grella and Faeth, 1975; Yoshida, 1982; Fukushima et al., 1984; Nakashima, 1985).

First, the vertical wall plume is discussed as the special case of the inclined wall plumes. In this case $\cot\theta = 0$ and σ_t are included in the equations.

The numerical solutions of velocity and relative density distributions are compared to Grella and Faeth's (1975) experiments shown in Fig. 2. In these figures, the turbulent Schmidt number, σ_t, is varied as a parameter. The Reynolds number, $\mathrm{R_{ex}}$, is widely varied in their experiment. The values of Reynolds number for test 1 to test 5 are 18,300, 23,700, 38,300, 53,200, and 70,000 in this order, where the Reynolds number is defined as $\mathrm{R_{ex}} = U_{\max} x/\nu$. $U_{\max}$ is the maximum velocity, x is the distance from the source, and ν is the molecular viscosity. The effect of the Reynolds number is considered in the calculations. It is seen from Fig. 2 that the influence of the Reynolds number on the velocity and relative density differences distributions is quite small. It is also found the optimum values of σ_t to be 0.8 to 1.0.

In Fig. 3, the calculated and measured velocity and relative density difference distributions are compared in the dimensional form. Also, σ_t is a parameter in figures. The longitudinal variation of velocity and relative density difference distributions are investigated in this experiment. The numerical model explains the longitudinal variation of the vertical wall plume. For this case, the values of σ_t also take the value between 0.8 to 1.0.

The distribution of the Reynolds stress of the vertical wall plume is illustrated in Fig. 4. The distribution of eddy viscosity is shown in Fig. 5. The corresponding experimental data of Yoshida (1982) and Fukushima et al. (1984) are plotted in the figures. In the experiment by Fukushima et al., the Reynolds

Downloaded 03 May 2010 to 171.66.16.244. Redistribution subject to ASME license or copyright; see http://www.asme.org/terms/Terms_Use.cfm

stress was measured at $x = 0.36$ m. The Reynolds stress is nondimensionalized by the square of the maximum velocity. The eddy viscosity is nondimensionalized by the maximum velocity and the half-width of the plume. For each figure, experimental data is small compared with the numerical solutions. The reason is that the Reynolds number of these experiments are not large enough to produce well-developed turbulence.

As discussed previously, the numerical model reproduces the characteristics of the vertical wall plume. Especially, σ_t is estimated as 0.8 to 1.0. The value of $\sigma_t = 1.0$ is adapted by the following calculation. Now the value of $c_{3\epsilon}$ is discussed next.

The similarity solutions in the nondimensional form are shown in Fig. 6 with the slope angle as a parameter. In this case, $c_{3\epsilon}$ is set to be 0.6. As the slope angle decreases the width of the plume decreases, and the maximum velocity and the maximum relative density difference increase. The kinetic energy of turbulence, the viscous dissipation rate of turbulence, and the eddy viscosity are dependent on the slope angle.

Comparison of measured and calculated velocity and relative density difference for $\theta = 30$ deg (Nakashima, 1985) is carried out as shown in Fig. 7. In this case, changing the value of $c_{3\epsilon}$ from 0.0 to 1.0, the value of 0.6–1.0 is found to give good agreement between the experiment and the numerical calculation.

In Fig. 8, the results of calculation and experiments are car-

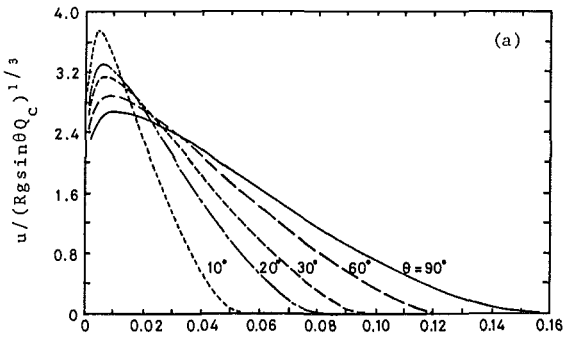


Fig. 6(a)

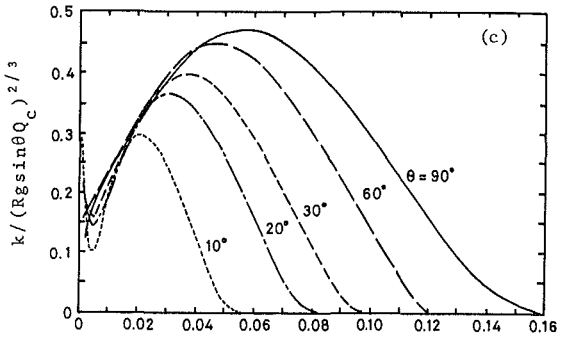


Fig. 6(c)

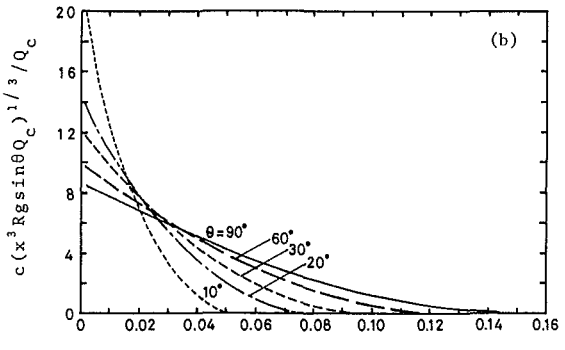


Fig. 6(b)

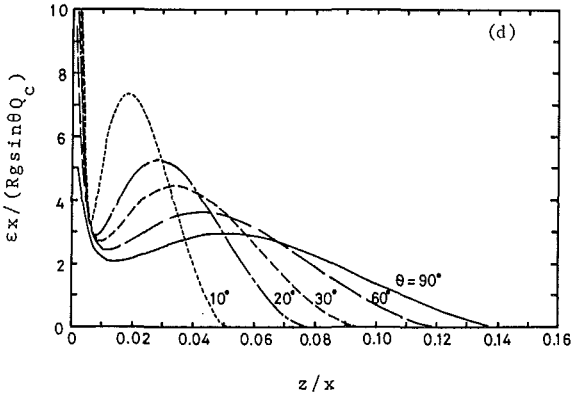


Fig. 6(d)

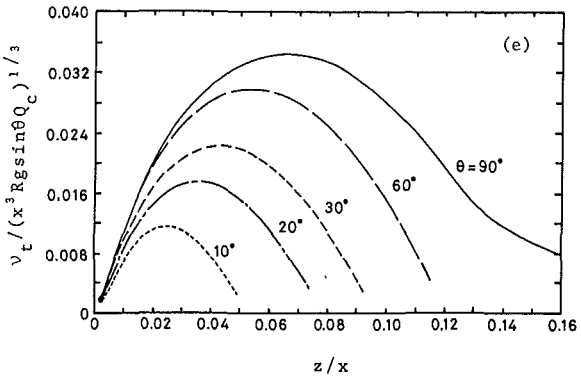


Fig. 6(e)

Fig. 6 Similarity solutions of wall plume with the slope angle as the parameter (a) nondimensional velocity, (b) relative density difference, (c) kinetic energy of turbulence, (d) viscous dissipation rate of turbulence, and (e) eddy viscosity

Downloaded 03 May 2010 to 171.66.16.244. Redistribution subject to ASME license or copyright; see http://www.asme.org/terms/Terms_Use.cfm

ried out by Fukushima in which the slope angle is 0.46 deg are compared. Also, $c_{3\epsilon}$ is chosen as a parameter. Although the value of $c_{3\epsilon}$ is widely changing from 0.0 to 1.0, distributions of velocity and relative density difference changes little. Measured velocity distributions in Run 1 and Run 2 become flat near the maximum velocity. The same tendency is seen from measured relative density difference distributions. This is because the distance from the source is not large enough for the boundary layer to develop for both Run 1 and Run 2. For the case of Run 3, the numerical solution of $c_{3\epsilon} = 1.0$ explains satisfactorily the measured distributions of velocity and relative density difference.

In Fig. 7 and 8, the sensitivity of the parameter $c_{3\epsilon}$ is tested. The values of 0.6–1.0 are optimized to explain the experimental data. Rodi (1980) has reported that the values of $c_{3\epsilon}$ are close to unity for horizontal jets. Thus, the value of $c_{3\epsilon}$ obtained herein is considered to be adequate.

Some properties of an inclined wall plume are investigated by the numerical model. The velocity and concentration distributions are expressed using the maximum velocity $u_{\max}$, the maximum concentration $c_{\max}$, and the half-width of plume $b_{1/2}$ as

$$u = U_{\max} f(\zeta) \tag{46a}$$

$$c = c_{\max} g(\zeta) \tag{46b}$$

where $\zeta = z/b_{1/2}$. The layer integral of the inclined wall plume is defined by

$$\bar{u}\, b = u_{\max} b_{1/2} \int_0^\infty f\, d\zeta = u_{\max} b_{1/2} I_1 \tag{47}$$

$$\overline{u^2 b} = u_{\max}^2 b_{1/2} \int_0^\infty f^2\, d\zeta = u_{\max}^2 b_{1/2} I_2 \tag{48}$$

$$\bar{c}\, b = c_{\max} b_{1/2} \int_0^\infty g\, d\zeta = c_{\max} b_{1/2} I_3 \tag{49}$$

$$\bar{c}\, \bar{u}\, b = c_{\max} u_{\max} b_{1/2} \int_0^\infty fg\, d\zeta = c_{\max} u_{\max} b_{1/2} I_4. \tag{50}$$

From equations (47)–(50), the layer average of velocity, concentration, and the layer depth are obtained by

$$\bar{u} = \frac{I_2}{I_1} u_{\max} \tag{51a}$$

$$b = \frac{I_1^2}{I_2} b_{1/2} \tag{51b}$$

$$\bar{c} = \frac{I_4}{I_1} c_{\max}. \tag{51c}$$

The entrainment coefficient of the plume defined by the layer average velocity is expressed by

$$E_0 = -\frac{w_e}{\bar{u}} = \frac{I_1 F(\infty)}{I_2 F'_{\max}}. \tag{52}$$

In order to obtain equation (52), equations (12), (13), and (51*a*) are used. The overall Richardson number, R_i, can be derived from equations (36) and (51) as follows:

$$R_i = \frac{Rg\bar{c}b}{\bar{u}^2} = \frac{I_1^3 I_4 G_{\max} \eta_{1/2}}{I_1^3 \sin\theta\, F'_{\max}}. \tag{53}$$

The values of integrals of (47)–(50) and the entrainment coefficient, E_0, and the overall Richardson number, R_i, defined by equations (52) and (53), are sumarized in Table 2. In the table, c_f is the friction factor of the all defined by

$$c_f = u_*^2 / u_{\max}^2 \tag{54}$$

The entrainment coefficients calculated by the model are plotted against the overall Richardson number as shown in

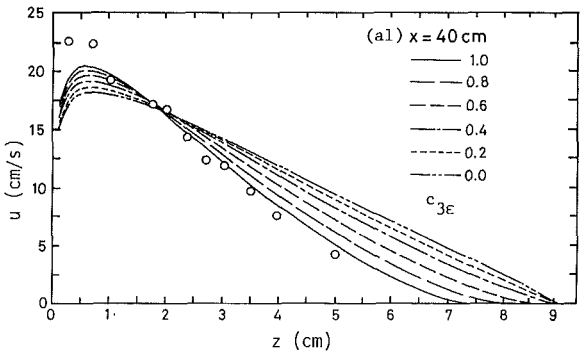


Fig. 7(*a*1)

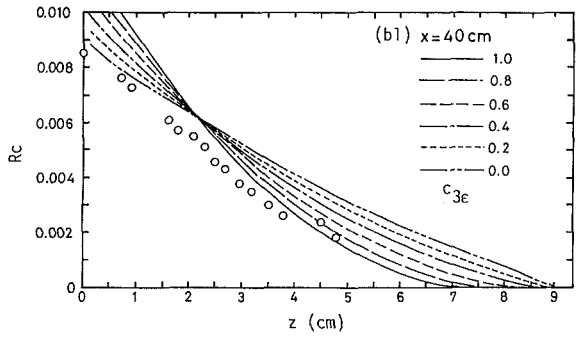


Fig. 7(*b*1)

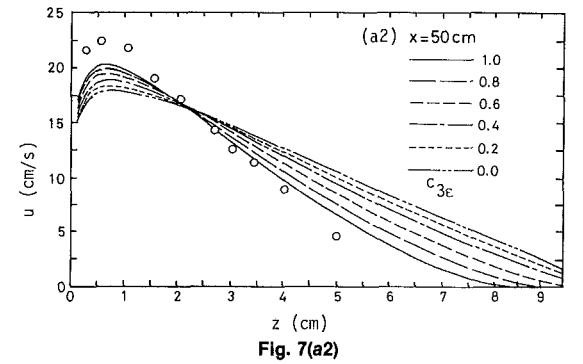


Fig. 7(*a*2)

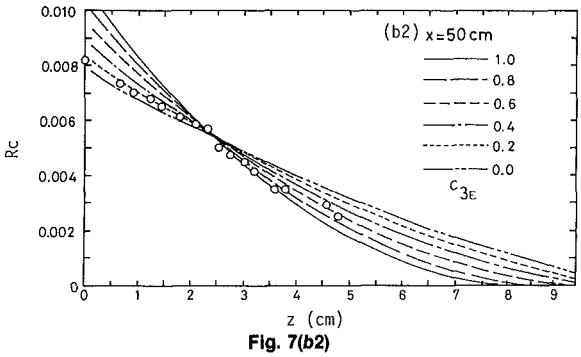


Fig. 7(*b*2)

Fig. 7 Comparison of numerical solutions with the Nakashima (1985) data of velocity and relative density difference ($\theta = 30$ deg) with $c_{3\epsilon}$ as the parameter; (a1), (*b*1) at $x = 0.4$ m; (a2), (*b*2) at $x = 0.5$ m

Downloaded 03 May 2010 to 171.66.16.244. Redistribution subject to ASME license or copyright; see http://www.asme.org/terms/Terms_Use.cfm

Fig. 9. Experimental data which were obtained from the density underflow (Ellison and Turner, 1959; Lofquist, 1961; Egashira, 1980; Fukuoka et al., 1980) are also plotted in the figure. The results of numerical solution tend to be on the larger side of the experimental data, but within an experimental error. Thus, the similarity solution using the k-ϵ turbulence model described well the characteristics of the inclined wall plume; the velocity and the relative density difference profiles, the growth of the plume, and the relationship between the entrainment coefficients and the overall Richardson number.

5 Conclusions

The characteristics of the inclined wall plume are investigated by the k-ϵ turbulence model. It is shown that the "weak" similarity solution is derivable from the fundamental equations which include the equation of kinetic energy of turbulence and the equation of viscous dissipation rate of turbulence. The numerical calculations are carried out for the wide range of the slope angle, from the vertical wall to the nearly horizontal wall. It is shown that the agreement between the numerical solutions and the experimental results is quite satisfying. The proposed model is applicable to the fully developed, inclined wall plume, although it is necessary to take its limitation into consideration.

References

Ellison, T. H., and Turner, J. S., 1959, "Turbulent Entrainment in Stratified Flows," *J. Fluid Mech.*, Vol. 6, pp. 423–448.

Fukuoka, S., Fukushima, Y., Murata, M., and Arai, K., 1980, "Experimental Study of Density Currents Advancing into a Two-Dimensional Stratified Reservoir," *Proc. Japan Society of Civil Engineers*, No. 293, pp. 65–77.

Fukuoka, S., Fukushima, Y., and Nakamura, K., 1980, "Study on the

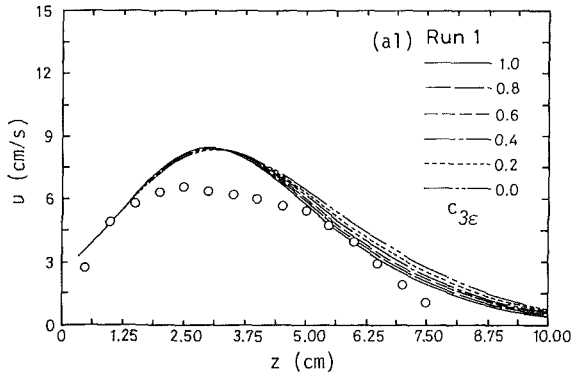


Fig. 8(a1)

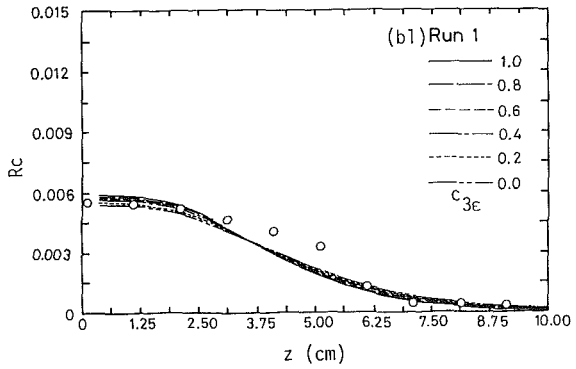


Fig. 8(b1)

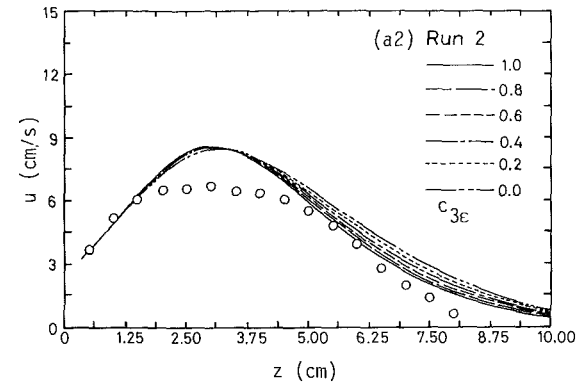


Fig. 8(a2)

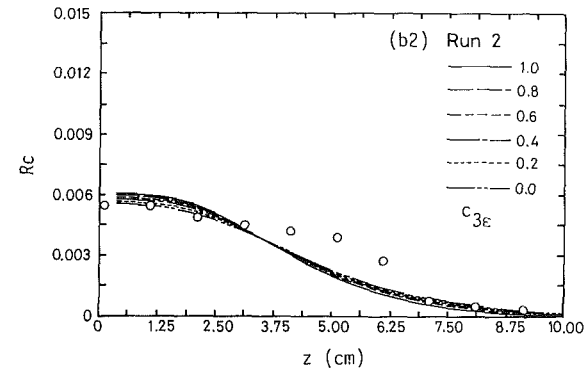


Fig. 8(b2)

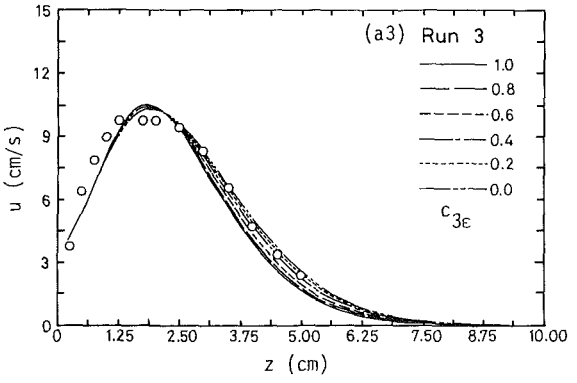


Fig. 8(a3)

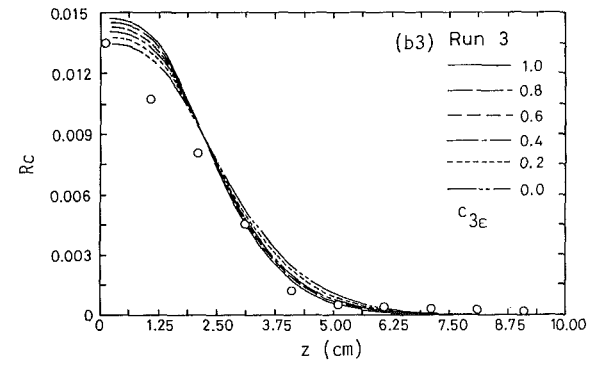


Fig. 8(b3)

Fig. 8 Comparison of numerical solutions with Fukushima's experimental data of velocity and relative density difference ($\tan\theta = 0.008$) with $c_{3\epsilon}$ as the parameter; (a1), (b1) Run 1; (a2), (b2) Run 2; (a3), (b3) Run 3

Downloaded 03 May 2010 to 171.66.16.244. Redistribution subject to ASME license or copyright; see http://www.asme.org/terms/Terms_Use.cfm

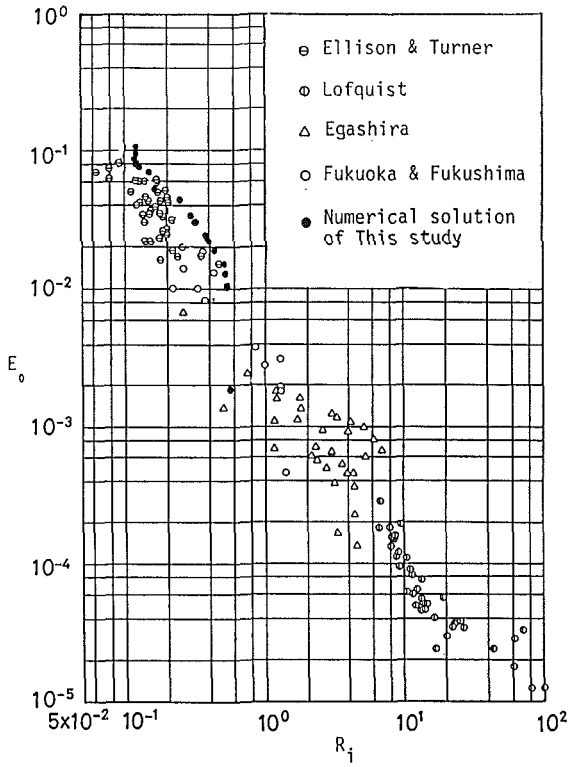


Fig. 9 Entrainment coefficients versus the overall Richardson number

Plunge Depth and Interface Form of Density Currents in a Two-Dimensional Reservoir," *Proc. Japan Society of Civil Engineers*, No. 302, pp. 55–65.

Fukushima, Y., 1982, "Numerical Solution of Velocity and Density Distributions of Laminar Vertical Wall Plume," Trans. 37th Anniversary Meeting of the JSCE, II-188.

Fukushima, Y., Hayakawa, N., and Fukunaga, K., 1983, "Analytical Study of Wall Plume," Technical Report of Nagaoka University of Technology, No. 5, pp. 53–59.

Fukushima, Y., Fukunaga, K., and Hayakawa, N., 1984, "Study on Vertical Turbulent Buoyant Wall Jets," *28th Japanese Conference on Hydraulics*, JSCE, pp. 303–310.

Fukushima, Y., and Fukuda M., 1986, "Analysis of Turbulent Structure of Open-Channel Flow with Suspended Sediments," *J. Hydrosci. and Hydraul. Eng.*, JSCE, Vol. 4, No. 2, pp. 47–54.

Fukushima, Y., and Fukuda, M., 1988, "Numerical Analysis of Non-Uniform Suspension Flow by Turbulence Model," *32nd Japanese Conference on Hydraulics*, JSCE, pp. 413–418.

Grella, J. J., and Faeth, G. M., 1975, "Measurements in a Two-Dimensional Thermal Plume along a Vertical Adiabatic Wall," *J. Fluid Mech.*, Vol. 71, Part 4, pp. 701–710.

Ljuboja, M., and Rodi, W., 1981, "Prediction of Horizontal and Vertical Turbulent Buoyant Wall Jet," ASME *Journal of Heat Transfer*, Vol. 103, pp. 343–349.

Lofquist, K., 1960, "Flow and Stress near an Interface between Stratified Liquids," *Phys. Fluids*, Vol. 3, pp. 158–175.

Nakashima, T., 1985, "Study on Buoyant Wall Plume," Masters Thesis, Nagaoka Univ. of Technology.

Rodi, W., 1980, "Turbulence Models and Their Application in Hydraulics," State of the Arts Paper, IAHR.

Tsubaki, T., and Komatsu, T., 1979, "Flow Properties and Turbulent Entrainment of Stratified Inclined Plume," *23rd Japanese Conference on Hydraulics*, JSCE, pp. 415–422.

Turner, J. S., 1973, *Buoyancy Effects in Fluids*, Cambridge Univ. Press, pp. 178–187.

Yoshida, J., 1982, "On the Velocity Fields and Their Variations in the Two-Dimensional Forced Plumes and the Behavior of the Two-Dimensional Plumes," Doctoral Thesis, Univ. of Tokyo.

Downloaded 03 May 2010 to 171.66.16.244. Redistribution subject to ASME license or copyright; see http://www.asme.org/terms/Terms_Use.cfm

Journal of Applied Mechanics

Brief Notes

A Brief Note is a short paper that presents a specific solution of technical interest in mechanics but which does not necessarily contain new general methods or results. A Brief Note should not exceed 1500 words *or equivalent* (a typical one-column figure or table is equivalent to 250 words; a one line equation to 30 words). Brief Notes will be subject to the usual review procedures prior to publication. After approval such Notes will be published as soon as possible. The Notes should be submitted to the Technical Editor of the JOURNAL OF APPLIED MECHANICS. Discussions on the Brief Notes should be addressed to the Editorial Department, ASME, United Engineering Center, 345 East 47th Street, New York, N. Y. 10017, or to the Technical Editor of the JOURNAL OF APPLIED MECHANICS. Discussions on Brief Notes appearing in this issue will be accepted until two months after publication. Readers who need more time to prepare a Discussion should request an extension of the deadline from the Editorial Department.

Flow Along a Cylinder With Periodic Suction

C. Y. Wang[1]

Introduction

Suction along a solid boundary is extremely important in boundary layer control, suppression of turbulence, and reduction in drag. (See, e.g., Schlichting (1979)). The asymptotic profile for the flow along a flat plate with uniform suction is a well-known exact solution of the Navier-Stokes equations. The solution for the corresponding flow along a circular cylinder with uniform suction was found by Wuest (1955) and Lew (1956). Since, in practice, suction through holes or slots cannot be entirely uniform, Gersten and Gross (1974) investigated the effects of a periodic perturbation of the suction velocity on a flat plate. The present note is to study these effects in the case of a long circular cylinder in a flow parallel to its axis.

Perturbation Solution

Let (u', v', w') be velocity components in the cylindrical directions (θ, r', z'), respectively. On the circular cylinder $(r'=a)$, the normal velocity is given as $v' = -V + V_1 \cos n\theta$, $u' = w' = 0$, where n is integer and V, V_1 are constants. At infinity we have uniform parallel flow $v' = u' = 0$, $w' = W$. Normalize all lengths by a, all velocities by V, the stresses by ρV^2 where ρ is density and drop primes. In the asymptotic state $\partial/\partial z = 0$, and the Navier-Stokes and continuity equations become

$$vv_r + \frac{u}{r}v_\theta - \frac{u^2}{r} = -p_r + \frac{1}{\lambda}\left(\nabla^2 v - \frac{v}{r^2} - \frac{2}{r^2}u_\theta\right) \tag{1}$$

$$vu_r + \frac{u}{r}u_\theta + \frac{uv}{r} = -\frac{1}{r^2}p_\theta + \frac{1}{\lambda}\left(\nabla^2 u + \frac{2}{r^2}v_\theta - \frac{u}{r^2}\right) \tag{2}$$

$$vw_r + \frac{u}{r}w_\theta = \frac{1}{\lambda}\nabla^2 w \tag{3}$$

$$(rv)_r + u_\theta = 0. \tag{4}$$

Here, $\lambda \equiv Va/\text{viscosity}$ is the suction Reynolds number. Let $\gamma \equiv W/V$ and assume $\epsilon \equiv V_1/V << 1$. The boundary conditions become

$$\text{on } r=1,\ v = -1 + \epsilon\cos n\theta,\ u = w = 0 \tag{4a}$$

$$\text{as } r \to \infty,\ u = v = 0,\ w = \gamma. \tag{5}$$

Since ϵ is small, we perturb about the exact solution for uniform suction:

$$v = -\frac{1}{r} + \epsilon v_1(r,\theta),\ u = \epsilon u_1 \tag{6}$$

$$w = \gamma(1 - r^{-\lambda}) + \epsilon w_1,\ p = p_\infty - \frac{1}{2r^2} + \epsilon p_1 \tag{7}$$

Equations (1)–(3) yield, for the first order,

$$-\frac{1}{r}u_{1r} - \frac{1}{r^2}u_1 = -\frac{1}{r}p_{1\theta} + \frac{1}{\lambda}\left(\nabla^2 u_1 + \frac{2}{r^2}v_{1\theta} - \frac{u_1}{r^2}\right) \tag{8}$$

$$-\frac{1}{r}v_{1r} + \frac{v_1}{r^2} = -p_{1r} + \frac{1}{\lambda}\left(\nabla^2 v_1 - \frac{v_1}{r^2} - \frac{2}{r^2}u_{1\theta}\right) \tag{9}$$

$$-\frac{1}{r}w_{1r} + \frac{\gamma\lambda}{r^{\lambda+1}}v_1 = \frac{1}{\lambda}\nabla^2 w_1. \tag{10}$$

The boundary conditions, the homogeneity of equations (8)–(9), and the continuity equation suggest a trial solution

$$v_1 = r^m \cos n\theta,\ u_1 = \frac{-\sin n\theta}{n}(1+m)r^m. \tag{11}$$

Substitution into equations (8)–(9) and elimination of the pressure yield, after some work, presents the algebraic equation:

$$m^4 - 2(n^2+1)m^2 + (n^2-1)^2 + \lambda[m^3 + m^2 - (n^2+1)m + n^2 - 1] = 0. \tag{12}$$

The two negative roots of m are

$$m = -1-n,\ m = 1 - \frac{1}{2}\left(\lambda + \sqrt{\lambda^2 + 4n^2}\right) \equiv -\alpha. \tag{13}$$

Using the boundary conditions

$$v_1(1,\theta) = \cos n\theta \quad u_1(1,\theta) = 0 \tag{14}$$

we find, for $\alpha \neq 1+n$,

$$v_1 = \frac{\cos n\theta}{1-\alpha+n}[(1-\alpha)r^{-n-1} + nr^{-\alpha}] \tag{15}$$

[1]Professor, Michigan State University, East Lansing, MI 48824. Mem. ASME. Manuscript received by the ASME Applied Mechanics Division, January 7, 1988; final revision, April 11, 1988.

Copyright © 1990 by ASME
Downloaded 03 May 2010 to 171.66.16.244. Redistribution subject to ASME license or copyright; see http://www.asme.org/terms/Terms_Use.cfm

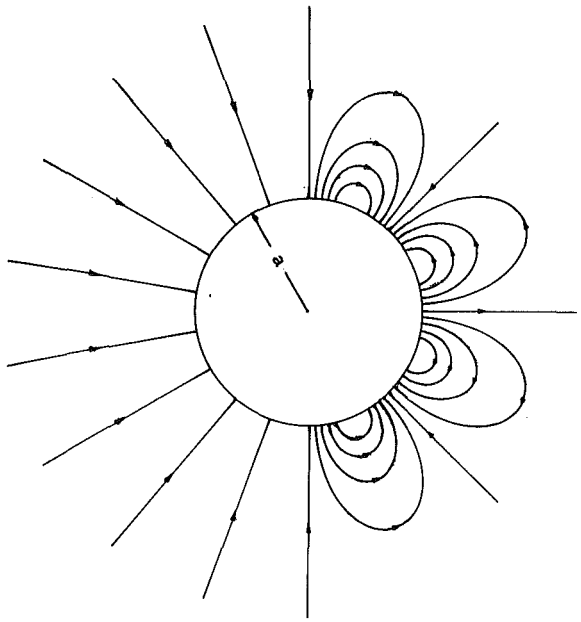


Fig. 1 The cross-flow streamlines; left half: primary suction flow; right half: streamlines due to periodic suction, $n=4$, $\lambda=4$

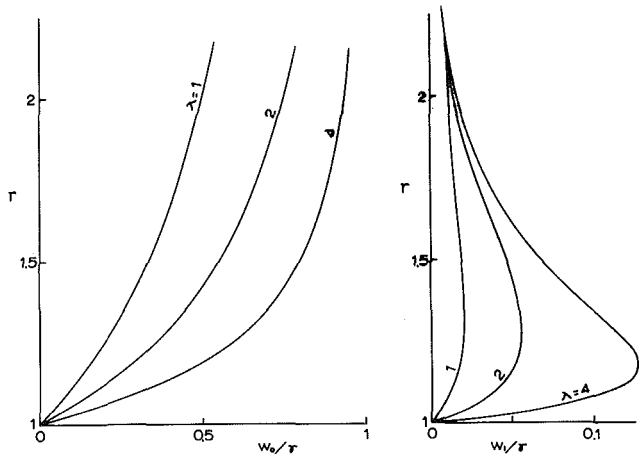


Fig. 2 Longitudinal velocity profiles; left: primary flow $\omega_0/\gamma = 1 - r^{-\lambda}$; right: secondary flow ω_1/γ, $n=4$

$$u_1 = \frac{(1-\alpha)\sin n\theta}{1-\alpha+n}(r^{-n-1} - r^{-\alpha}). \tag{16}$$

Solving equation (10) with equation (15) gives the perturbed axial flow

$$w_1 = \frac{\cos n\theta}{1-\alpha+n}\gamma\lambda^2\left\{\frac{(1-\alpha)}{\lambda n}(r^{-n-\lambda} - r^{-\alpha-1}) + \frac{n}{(\alpha-1)^2+\lambda(\alpha-1)-n^2}(r^{-\lambda-\alpha+1} - r^{-\alpha-1})\right\}. \tag{17}$$

From equation (9) the pressure is obtained

$$p_1 = \frac{\cos n\theta}{1-\alpha+n}\left[(1-\alpha)r^{-n-2} + \frac{4n\alpha}{\lambda(\alpha+1)}r^{-\alpha-1}\right]. \tag{18}$$

If $\alpha = 1+n$ or $\lambda = 4(1+n)/(2+n)$, m has multiple roots and the solution is

$$v_1 = \cos n\theta r^{-n-1}(1 + n\ln r) \tag{19}$$

$$u_1 = \sin n\theta r^{-n-1} n\ln r \tag{20}$$

$$w_1 = \gamma\cos n\theta\left[\lambda r^{-n-\lambda}\ln r + 2\left(\frac{\lambda}{n}+1\right)(r^{-n-\lambda} - r^{-2-n})\right] \tag{21}$$

$$p_1 = \cos n\theta r^{-n-2}\left[n\ln r + \frac{n^2+2n+2}{2(n+1)}\right]. \tag{22}$$

Figure 1 shows the primary and secondary cross-flow streamlines for $n=4$. The longitudinal velocity is shown in Fig. 2. As λ or suction increases, the boundary layer becomes thinner.

Surface Stress and Net Force

The shear stresses on the surface, normalized by ρV^2, are

$$\tau_{r\theta} = \frac{1}{\lambda}\left(u_r - \frac{u}{r} + \frac{1}{r}v_\theta\right) = \epsilon\sin n\theta\left(\frac{\alpha-1-n}{\lambda}\right) + 0(\epsilon^2) \tag{23}$$

$$\tau_{rz} = \frac{1}{\lambda}w_r = \gamma + \epsilon\gamma\frac{\cos n\theta}{1-\alpha+n} \times\left[\frac{(1-\alpha)}{n}(1+\alpha-n-\lambda) + \frac{\lambda n(2-\lambda)}{(\alpha-1)^2+\lambda(\alpha-1)-n^2}\right] + 0(\epsilon^2). \tag{24}$$

In the case of $\alpha = 1+n$, the stresses are

$$\tau_{r\theta} = 0(\epsilon^2) \tag{25}$$

$$\tau_{rz} = \gamma - \epsilon\gamma\cos n\theta\frac{(2+3n)}{(1+n)(2+n)} + 0(\epsilon^2). \tag{26}$$

The surface stress pattern, in general, shows a herring-bone structure, which is similar to the flat-plate case (Gersten and Gross 1974). We note, however, when $\alpha = 1+n$ or $\lambda = 4(1+n)/(2+n)$, the shear stress in the θ direction, to the order considered, becomes zero. In these cases the shear is longitudinal but nonuniform. The total lateral force normalized by $\pi\rho V^2 a^2$ on the cylinder is

$$F = \frac{1}{\pi}\int_0^{2\pi}(\tau_{r\theta}\sin\theta + p\cos\theta)\,d\theta. \tag{27}$$

It is evident that F is zero for all n other than unity. If $n=1$, the side force is

$$F = \epsilon\frac{\lambda(1-\alpha^2)+4\alpha-(2-\alpha)^2(1+\alpha)}{\lambda(2-\alpha)(1+\alpha)} \qquad \alpha \neq 2$$

$$F = \frac{5}{4}\epsilon + (\epsilon^2) \qquad \alpha = 2. \tag{28}$$

Discussion

The effect of longitudinal periodic suction on the asymptotic profile is now clear. The nonuniformity causes both longitudinal and lateral secondary flows. For a circular cylinder the problem depends on the suction Reynolds number, λ, the number of periods, n, the ratio of parallel flow velocity to suction velocity, γ, and the relative amplitude of periodic suction, ϵ. The parameters γ and ϵ appear in both flat-plate and cylinder problems. The parameter n, equivalent to the wave number in the flat-plate problem, is now discrete instead of continuous. The parameter λ has no equivalent for the flat plate.

There are some restrictions on the parameters. Equation (7) shows for uniform flow at infinity, $\lambda > 0$, or suction must be applied. Since n is a positive integer, α is always positive. Equation (17) imposes the extra condition that $\lambda + \alpha > 1$.

Although transverse flow u is not zero, it is interesting that transverse shear can be made zero if $\lambda = 4(1+n)/(2+n)$. For $n=1$, a side force exists. Usually a side force is undesirable, but in certain cases it may be utilized.

Downloaded 03 May 2010 to 171.66.16.244. Redistribution subject to ASME license or copyright; see http://www.asme.org/terms/Terms_Use.cfm

References

Gersten, K., and Gross, J. F., 1974, "Flow and Heat Transfer Along a Plane Wall With Periodic Suction," *Journal of Applied Mathematics and Physics*, Vol. 25, pp. 399–408.

Lew, H. G., 1956, "Asymptotic Suction Characteristics of the Boundary Layer Over a Circular Cylinder," *Journal of the Aeronautical Sciences*, Vol. 23, pp. 895–897.

Schlichting, H., 1979, *Boundary Layer Theory*, McGraw-Hill, New York, Chapter 14.

Wuest, W., 1955, "Asymptotische Absaugegrenzschichten an Längsangeströmten Zylindrischen Körpern," *Ingenieur Archiv*, Vol. 23, pp. 198–205.

Orthogonal Curvilinear Coordinates and Angular Velocity

Thomas R. Kane[2] and David A. Levinson[3]

Introduction

A certain orthonormal triad of vectors can be associated with every orthogonal curvilinear coordinate system. In this Note, a general method is presented for the determination of the angular velocity of this triad in a reference frame.

Curvilinear Coordinates

Let A be a reference frame, $\mathbf{a}_1$, $\mathbf{a}_2$, $\mathbf{a}_3$ mutually perpendicular unit vectors fixed in A, O a point fixed in A, P a point moving in A, and $\mathbf{p}$ the position vector from O to P. Then, if $\mathbf{p}$ is expressed as

$$\mathbf{p} = x_1\mathbf{a}_1 + x_2\mathbf{a}_2 + x_3\mathbf{a}_3, \tag{1}$$

the quantities x_r $(r = 1, 2, 3)$ are Cartesian coordinates of P in A; and if each of these is regarded as a function of three functions of time t, say q_r $(r = 1, 2, 3)$, then q_r $(r = 1, 2, 3)$ are *curvilinear* coordinates of P in A.

Orthogonal Curvilinear Coordinates

The vector $\mathbf{p}$ can be regarded as a function of q_1, q_2, and q_3 in A, and the partial derivative of $\mathbf{p}$ with respect to q_r in A always can be expressed as the product of a unit vector $\mathbf{b}_r$ and a function f_r of q_1, q_2, and q_3:

$$\frac{\partial \mathbf{p}}{\partial q_r} = f_r\mathbf{b}_r \qquad (r = 1,2,3). \tag{2}$$

The unit vectors $\mathbf{b}_r$ $(r = 1,2,3)$ are not necessarily mutually orthogonal; if they are, then q_1, q_2, and q_3 are called *orthogonal* curvilinear coordinates of P in A; and, in any event, one can find a value of f_r $(r = 1,2,3)$ satisfying equation (2) by equating the square of the left-hand member of the equation to that of the right-hand member and then taking the positive square root of each member of the resulting equation, obtaining

$$f_r = \left(\frac{\partial \mathbf{p}}{\partial q_r} \cdot \frac{\partial \mathbf{p}}{\partial q_r}\right)^{1/2} \qquad (r = 1,2,3). \tag{3}$$

Angular Velocity

When q_1, q_2, and q_3 are orthogonal curvilinear coordinates, one can introduce a rigid body B in which the triad of unit vectors $\mathbf{b}_r$ $(r = 1,2,3)$ is fixed (indeed, there exist infinitely many such rigid bodies); B possesses a unique angular velocity ω in reference frame A; and, by definition, the angular velocity of the triad $\mathbf{b}_r$ $(r = 1,2,3)$ in A is precisely ω. Now, ω can be expressed as

$$\omega = \omega_1\mathbf{b}_1 + \omega_2\mathbf{b}_2 + \omega_3\mathbf{b}_3 \tag{4}$$

where ω_r $(r = 1,2,3)$ are functions of the coordinates q_r $(r = 1,2,3)$ and their time derivatives $\dot{q}_r$ $(r = 1,2,3)$. What will be shown in the sequel is that ω_r $(r = 1,2,3)$ are given by

$$\omega_1 = \frac{1}{f_2 f_3}\left(\frac{d}{dt}\frac{\partial \mathbf{p}}{\partial q_2}\right) \cdot \frac{\partial \mathbf{p}}{\partial q_3} \tag{5}$$

$$\omega_2 = \frac{1}{f_3 f_1}\left(\frac{d}{dt}\frac{\partial \mathbf{p}}{\partial q_3}\right) \cdot \frac{\partial \mathbf{p}}{\partial q_1} \tag{6}$$

$$\omega_3 = \frac{1}{f_1 f_2}\left(\frac{d}{dt}\frac{\partial \mathbf{p}}{\partial q_1}\right) \cdot \frac{\partial \mathbf{p}}{\partial q_2} \tag{7}$$

where d/dt denotes differentiation with respect to t in A. Together, equations (4)–(7) furnish a general method for the determination of the angular velocity of the triad $\mathbf{b}_r$ $(r = 1,2,3)$ in A.

Example

Suppose that x_r $(r = 1,2,3)$ are given as

$$x_1 = q_1 q_2 \cos q_3 \tag{8}$$

$$x_2 = q_1 q_2 \sin q_3 \tag{9}$$

$$x_3 = (q_1^2 - q_2^2)/2. \tag{10}$$

Then[4],

$$\frac{\partial \mathbf{p}}{\partial q_r} \underset{(1)}{=} \frac{\partial x_1}{\partial q_r}\mathbf{a}_1 + \frac{\partial x_2}{\partial q_r}\mathbf{a}_2 + \frac{\partial x_3}{\partial q_r}\mathbf{a}_3, \ (r = 1, 2, 3), \tag{11}$$

so that

$$\frac{\partial \mathbf{p}}{\partial q_1} \underset{(11)}{=} q_2 \underset{(8)}{\cos}\ q_3\mathbf{a}_1 + q_2 \underset{(9)}{\sin}\ q_3\mathbf{a}_2 + \underset{(10)}{q_1}\mathbf{a}_3 \tag{12}$$

$$\frac{\partial \mathbf{p}}{\partial q_2} \underset{(11)}{=} q_1 \underset{(8)}{\cos}\ q_3\mathbf{a}_1 + q_1 \underset{(9)}{\sin}\ q_3\mathbf{a}_2 - \underset{(10)}{q_2}\mathbf{a}_3 \tag{13}$$

and

$$\frac{\partial \mathbf{p}}{\partial q_3} \underset{(11)}{=} -q_1 q_2 \underset{(8)}{\sin}\ q_3\mathbf{a}_1 + q_1 q_2 \underset{(9)}{\cos}\ q_3\mathbf{a}_2. \tag{14}$$

Substitution from equations (12)–(14) into equations (3) then gives

$$f_1 \underset{(3,12)}{=} (q_1^2 + q_2^2)^{1/2} \tag{15}$$

$$f_2 \underset{(3,13)}{=} (q_1^2 + q_2^2)^{1/2} \tag{16}$$

$$f_3 \underset{(3,14)}{=} q_1 q_2. \tag{17}$$

The time derivatives of $\partial \mathbf{p}/\partial q_r$ $(r = 1,2,3)$ in A are

$$\frac{d}{dt}\frac{\partial \mathbf{p}}{\partial q_1} \underset{(12)}{=} (\dot{q}_2 \cos q_3 - q_2\dot{q}_3 \sin q_3)\mathbf{a}_1 + (\dot{q}_2 \sin q_3 + q_2\dot{q}_3 \cos q_3)\mathbf{a}_2 + \dot{q}_1\mathbf{a}_3 \tag{18}$$

[2]Professor of Applied Mechanics, Stanford University, Stanford, CA, Fellow ASME.

[3]Research Scientist, Lockheed Palo Alto Research Laboratory, Palo Alto, CA, Mem. ASME.

Manuscript received by the ASME Applied Mechanics Division, December 16, 1988; final revision, April 24, 1989.

[4]Numbers beneath equations refer to equations numbered correspondingly.

Downloaded 03 May 2010 to 171.66.16.244. Redistribution subject to ASME license or copyright; see http://www.asme.org/terms/Terms_Use.cfm

References

Gersten, K., and Gross, J. F., 1974, "Flow and Heat Transfer Along a Plane Wall With Periodic Suction," *Journal of Applied Mathematics and Physics*, Vol. 25, pp. 399–408.

Lew, H. G., 1956, "Asymptotic Suction Characteristics of the Boundary Layer Over a Circular Cylinder," *Journal of the Aeronautical Sciences*, Vol. 23, pp. 895–897.

Schlichting, H., 1979, *Boundary Layer Theory*, McGraw-Hill, New York, Chapter 14.

Wuest, W., 1955, "Asymptotische Absaugegrenzschichten an Längsangeströmten Zylindrischen Körpern," *Ingenieur Archiv*, Vol. 23, pp. 198–205.

Orthogonal Curvilinear Coordinates and Angular Velocity

Thomas R. Kane[2] and David A. Levinson[3]

Introduction

A certain orthonormal triad of vectors can be associated with every orthogonal curvilinear coordinate system. In this Note, a general method is presented for the determination of the angular velocity of this triad in a reference frame.

Curvilinear Coordinates

Let A be a reference frame, $\mathbf{a}_1$, $\mathbf{a}_2$, $\mathbf{a}_3$ mutually perpendicular unit vectors fixed in A, O a point fixed in A, P a point moving in A, and $\mathbf{p}$ the position vector from O to P. Then, if $\mathbf{p}$ is expressed as

$$\mathbf{p} = x_1\mathbf{a}_1 + x_2\mathbf{a}_2 + x_3\mathbf{a}_3, \tag{1}$$

the quantities x_r $(r = 1, 2, 3)$ are Cartesian coordinates of P in A; and if each of these is regarded as a function of three functions of time t, say q_r $(r = 1, 2, 3)$, then q_r $(r = 1, 2, 3)$ are *curvilinear* coordinates of P in A.

Orthogonal Curvilinear Coordinates

The vector $\mathbf{p}$ can be regarded as a function of q_1, q_2, and q_3 in A, and the partial derivative of $\mathbf{p}$ with respect to q_r in A always can be expressed as the product of a unit vector $\mathbf{b}_r$ and a function f_r of q_1, q_2, and q_3:

$$\frac{\partial \mathbf{p}}{\partial q_r} = f_r\mathbf{b}_r \qquad (r = 1,2,3). \tag{2}$$

The unit vectors $\mathbf{b}_r$ $(r = 1,2,3)$ are not necessarily mutually orthogonal; if they are, then q_1, q_2, and q_3 are called *orthogonal* curvilinear coordinates of P in A; and, in any event, one can find a value of f_r $(r = 1,2,3)$ satisfying equation (2) by equating the square of the left-hand member of the equation to that of the right-hand member and then taking the positive square root of each member of the resulting equation, obtaining

$$f_r = \left(\frac{\partial \mathbf{p}}{\partial q_r} \cdot \frac{\partial \mathbf{p}}{\partial q_r}\right)^{1/2} \qquad (r = 1,2,3). \tag{3}$$

Angular Velocity

When q_1, q_2, and q_3 are orthogonal curvilinear coordinates, one can introduce a rigid body B in which the triad of unit vectors $\mathbf{b}_r$ $(r = 1,2,3)$ is fixed (indeed, there exist infinitely many such rigid bodies); B possesses a unique angular velocity ω in reference frame A; and, by definition, the angular velocity of the triad $\mathbf{b}_r$ $(r = 1,2,3)$ in A is precisely ω. Now, ω can be expressed as

$$\omega = \omega_1\mathbf{b}_1 + \omega_2\mathbf{b}_2 + \omega_3\mathbf{b}_3 \tag{4}$$

where ω_r $(r = 1,2,3)$ are functions of the coordinates q_r $(r = 1,2,3)$ and their time derivatives $\dot{q}_r$ $(r = 1,2,3)$. What will be shown in the sequel is that ω_r $(r = 1,2,3)$ are given by

$$\omega_1 = \frac{1}{f_2 f_3}\left(\frac{d}{dt}\frac{\partial \mathbf{p}}{\partial q_2}\right) \cdot \frac{\partial \mathbf{p}}{\partial q_3} \tag{5}$$

$$\omega_2 = \frac{1}{f_3 f_1}\left(\frac{d}{dt}\frac{\partial \mathbf{p}}{\partial q_3}\right) \cdot \frac{\partial \mathbf{p}}{\partial q_1} \tag{6}$$

$$\omega_3 = \frac{1}{f_1 f_2}\left(\frac{d}{dt}\frac{\partial \mathbf{p}}{\partial q_1}\right) \cdot \frac{\partial \mathbf{p}}{\partial q_2} \tag{7}$$

where d/dt denotes differentiation with respect to t in A. Together, equations (4)–(7) furnish a general method for the determination of the angular velocity of the triad $\mathbf{b}_r$ $(r = 1,2,3)$ in A.

Example

Suppose that x_r $(r = 1,2,3)$ are given as

$$x_1 = q_1 q_2 \cos q_3 \tag{8}$$

$$x_2 = q_1 q_2 \sin q_3 \tag{9}$$

$$x_3 = (q_1^2 - q_2^2)/2. \tag{10}$$

Then[4],

$$\frac{\partial \mathbf{p}}{\partial q_r} \underset{(1)}{=} \frac{\partial x_1}{\partial q_r}\mathbf{a}_1 + \frac{\partial x_2}{\partial q_r}\mathbf{a}_2 + \frac{\partial x_3}{\partial q_r}\mathbf{a}_3, \ (r = 1, 2, 3), \tag{11}$$

so that

$$\frac{\partial \mathbf{p}}{\partial q_1} \underset{(11)}{=} q_2 \underset{(8)}{\cos}\ q_3\mathbf{a}_1 + q_2 \underset{(9)}{\sin}\ q_3\mathbf{a}_2 + \underset{(10)}{q_1}\mathbf{a}_3 \tag{12}$$

$$\frac{\partial \mathbf{p}}{\partial q_2} \underset{(11)}{=} q_1 \underset{(8)}{\cos}\ q_3\mathbf{a}_1 + q_1 \underset{(9)}{\sin}\ q_3\mathbf{a}_2 - \underset{(10)}{q_2}\mathbf{a}_3 \tag{13}$$

and

$$\frac{\partial \mathbf{p}}{\partial q_3} \underset{(11)}{=} -q_1 q_2 \underset{(8)}{\sin}\ q_3\mathbf{a}_1 + q_1 q_2 \underset{(9)}{\cos}\ q_3\mathbf{a}_2. \tag{14}$$

Substitution from equations (12)–(14) into equations (3) then gives

$$f_1 \underset{(3,12)}{=} (q_1^2 + q_2^2)^{1/2} \tag{15}$$

$$f_2 \underset{(3,13)}{=} (q_1^2 + q_2^2)^{1/2} \tag{16}$$

$$f_3 \underset{(3,14)}{=} q_1 q_2. \tag{17}$$

The time derivatives of $\partial \mathbf{p}/\partial q_r$ $(r = 1,2,3)$ in A are

$$\frac{d}{dt}\frac{\partial \mathbf{p}}{\partial q_1} \underset{(12)}{=} (\dot{q}_2 \cos q_3 - q_2\dot{q}_3 \sin q_3)\mathbf{a}_1 + (\dot{q}_2 \sin q_3 + q_2\dot{q}_3 \cos q_3)\mathbf{a}_2 + \dot{q}_1\mathbf{a}_3 \tag{18}$$

[2]Professor of Applied Mechanics, Stanford University, Stanford, CA, Fellow ASME.

[3]Research Scientist, Lockheed Palo Alto Research Laboratory, Palo Alto, CA, Mem. ASME.

Manuscript received by the ASME Applied Mechanics Division, December 16, 1988; final revision, April 24, 1989.

[4]Numbers beneath equations refer to equations numbered correspondingly.

Copyright © 1990 by ASME
Downloaded 03 May 2010 to 171.66.16.244. Redistribution subject to ASME license or copyright; see http://www.asme.org/terms/Terms_Use.cfm

Table 1

Common Name for q_1, q_2, q_3	Coordinate Surfaces	Cartesian Coordinates	Angular Velocity Measure Numbers
Parabolic coordinates	Paraboloid	$x_1 = q_1 q_2 \cos q_3$	$\omega_1 = \dfrac{\dot{q}_3 q_1}{(q_1^2 + q_2^2)^{1/2}}$
	Paraboloid	$x_2 = q_1 q_2 \sin q_3$	$\omega_2 = -\dfrac{\dot{q}_3 q_2}{(q_1^2 + q_2^2)^{1/2}}$
	Plane	$x_3 = (q_1^2 - q_2^2)/2$	$\omega_3 = \dfrac{-\dot{q}_1 q_2 + \dot{q}_2 q_1}{q_1^2 + q_2^2}$
Parabolic cylinder coordinates	Parabolic cylinder	$x_1 = (q_1^2 - q_2^2)/2$	$\omega_1 = 0$
	Parabolic cylinder	$x_2 = q_1 q_2$	$\omega_2 = 0$
	Plane	$x_3 = q_3$	$\omega_3 = \dfrac{-\dot{q}_1 q_2 + \dot{q}_2 q_1}{q_1^2 + q_2^2}$
Elliptic cylinder coordinates	Elliptic cylinder	$x_1 = a \cosh q_1 \cos q_2$	$\omega_1 = 0$
	Hyperbolic cylinder	$x_2 = a \sinh q_1 \sin q_2$	$\omega_2 = 0$
	Plane	$x_3 = q_3$	$\omega_3 = \dfrac{-\dot{q}_1 \sin q_2 \cos q_2 + \dot{q}_2 \sinh q_1 \cosh q_1}{\sinh^2 q_1 + \sin^2 q_2}$
Prolate spheroidal coordinates	Prolate spheroid	$x_1 = a \sinh q_1 \sin q_2 \cos q_3$	$\omega_1 = \dfrac{\dot{q}_3 \sinh q_1 \cos q_2}{(\sinh^2 q_1 + \sin^2 q_2)^{1/2}}$
	Hyperboloid	$x_2 = a \sinh q_1 \sin q_2 \sin q_3$	$\omega_2 = \dfrac{-\dot{q}_3 \cosh q_1 \sin q_2}{(\sinh^2 q_1 + \sin^2 q_2)^{1/2}}$
	Plane	$x_3 = a \cosh q_1 \cos q_2$	$\omega_3 = \dfrac{-\dot{q}_1 \sin q_2 \cos q_2 + \dot{q}_2 \sinh q_1 \cosh q_1}{\sinh^2 q_1 + \sin^2 q_2}$
Oblate spheroidal coordinates	Oblate spheroid	$x_1 = a \cosh q_1 \sin q_2 \cos q_3$	$\omega_1 = \dfrac{\dot{q}_3 \cosh q_1 \cos q_2}{(\cosh^2 q_1 - \sin^2 q_2)^{1/2}}$
	Hyperboloid	$x_2 = a \cosh q_1 \sin q_2 \sin q_3$	$\omega_2 = \dfrac{-\dot{q}_3 \sinh q_1 \sin q_2}{(\cosh^2 q_1 - \sin^2 q_2)^{1/2}}$
	Plane	$x_3 = a \sinh q_1 \cos q_2$	$\omega_3 = \dfrac{\dot{q}_1 \sin q_2 \cos q_2 + \dot{q}_2 \sinh q_1 \cosh q_1}{\cosh^2 q_1 - \sin^2 q_2}$
Spherical coordinates	Sphere	$x_1 = q_1 \sin q_2 \cos q_3$	$\omega_1 = \dot{q}_3 \cos q_2$
	Cone	$x_2 = q_1 \sin q_2 \sin q_3$	$\omega_2 = -\dot{q}_3 \sin q_2$
	Plane	$x_3 = q_1 \cos q_2$	$\omega_3 = \dot{q}_2$

$$\frac{d}{dt}\frac{\partial \mathbf{p}}{\partial q_2} \underset{(13)}{=} (\dot{q}_1 \cos q_3 - q_1 \dot{q}_3 \sin q_3)\mathbf{a}_1 + (\dot{q}_1 \sin q_3 + q_1 \dot{q}_3 \cos q_3)\mathbf{a}_2 - \dot{q}_2 \mathbf{a}_3 \tag{19}$$

$$\frac{d}{dt}\frac{\partial \mathbf{p}}{\partial q_3} \underset{(14)}{=} -(\dot{q}_1 q_2 \sin q_3 + q_1 \dot{q}_2 \sin q_3 + q_1 q_2 \dot{q}_3 \cos q_3)\mathbf{a}_1 + (\dot{q}_1 q_2 \cos q_3 + q_1 \dot{q}_2 \cos q_3 - q_1 q_2 \dot{q}_3 \sin q_3)\mathbf{a}_2, \tag{20}$$

Downloaded 03 May 2010 to 171.66.16.244. Redistribution subject to ASME license or copyright; see http://www.asme.org/terms/Terms_Use.cfm

and equations (5)–(7) thus yield (after simplification)

$$\omega_1 \underset{(5,16,17,19,14)}{=} q_1\dot{q}_3/(q_1^2+q_2^2)^{1/2} \tag{21}$$

$$\omega_2 \underset{(6,17,15,20,12)}{=} -q_2\dot{q}_3/(q_1^2+q_2^2)^{1/2} \tag{22}$$

$$\omega_3 \underset{(7,15,16,18,13)}{=} (q_1\dot{q}_2-q_2\dot{q}_1)/(q_1^2+q_2^2). \tag{23}$$

Hence,

$$\omega \underset{(3)}{=} \frac{q_1\dot{q}_3}{(q_1^2+q_2^2)^{1/2}}\mathbf{a}_1 - \frac{q_2\dot{q}_3}{(q_1^2+q_2^2)^{1/2}}\mathbf{a}_2 + \frac{q_1\dot{q}_2-q_2\dot{q}_1}{q_1^2+q_2^2}\mathbf{a}_3. \tag{24}$$

The results just obtained, as well as corresponding results for five more sets of orthogonal curvilinear coordinates, are recorded in Table 1, where the common name of each coordinate system is listed, as are those of associated coordinate surfaces. Note, however, that knowledge of these names played no role in the determination of ω.

Derivation

In Kane and Levinson (1985) ω is defined as

$$\omega = \frac{d\mathbf{b}_2}{dt}\cdot\mathbf{b}_3\mathbf{b}_1 + \frac{d\mathbf{b}_3}{dt}\cdot\mathbf{b}_1\mathbf{b}_2 + \frac{d\mathbf{b}_1}{dt}\cdot\mathbf{b}_2\mathbf{b}_3 \tag{25}$$

where d/dt denotes time differentiation in A. Comparison of this equation with equation (4) shows that

$$\omega_1 = \frac{d\mathbf{b}_2}{dt}\cdot\mathbf{b}_3 \tag{26}$$

$$\omega_2 = \frac{d\mathbf{b}_3}{dt}\cdot\mathbf{b}_1 \tag{27}$$

$$\omega_3 = \frac{d\mathbf{b}_1}{dt}\cdot\mathbf{b}_2 \tag{28}$$

while differentiation of equation (2) with respect to t in A gives

$$\frac{d}{dt}\frac{\partial\mathbf{p}}{\partial q_r} \underset{(2)}{=} \dot{f}_r\mathbf{b}_r + f_r\frac{d\mathbf{b}_r}{dt} \qquad (r=1,\,2,\,3) \tag{29}$$

from which it follows that

$$\frac{d\mathbf{b}_r}{dt} = \frac{1}{f_2}\left(\frac{d}{dt}\frac{\partial\mathbf{p}}{\partial q_r} - \dot{f}_r\mathbf{b}_r\right) \quad (r=1,2,3). \tag{30}$$

Hence,

$$\omega_1 \underset{(26,30)}{=} \frac{1}{f_r}\left(\frac{d}{dt}\frac{\partial\mathbf{p}}{\partial q_2} - \dot{f}_2\mathbf{b}_2\right)\cdot\mathbf{b}_3 \tag{31}$$

But, since $\mathbf{b}_r$ $(r=1,2,3)$ are mutually orthogonal,

$$\mathbf{b}_2\cdot\mathbf{b}_3 = 0. \tag{32}$$

Moreover,

$$\mathbf{b}_3 \underset{(2)}{=} \frac{1}{f_3}\frac{\partial\mathbf{p}}{\partial q_3}. \tag{33}$$

Therefore,

$$\omega_1 \underset{(31-33)}{=} \frac{1}{f_2f_3}\left(\frac{d}{dt}\frac{\partial\mathbf{p}}{\partial q_2}\right)\cdot\frac{\partial\mathbf{p}}{\partial q_3} \tag{34}$$

in agreement with equation (5). To establish the validity of equations (6) and (7), one can proceed similarly, writing in place of equation (31) an equation based on equation (27) or (28) rather than on equation (26).

Conclusion

The method presented here permits one to determine the angular velocity of the orthonormal triad of vectors associated with *any* set of orthogonal curvilinear coordinates whenever one has an expression for each of three rectangular coordinates of a generic point as a function of the curvilinear coordinates under consideration. Geometric considerations play no role in this determination. Of course, when the geometry in question is sufficiently simple, as, for example, in the case of spherical coordinates (see the last entry in Table 1), one can determine the desired angular velocity easily by other means.

Reference

Kane, Thomas R., and Levinson, David A., 1985, *Dynamics: Theory and Applications*, McGraw-Hill, New York, p. 16.

Unified Iso-Deflection Curves for Orthotropic Plates Under Lateral Pressure Pulse

Judah Ari-Gur[4] and M. Jerry Kenig[4]

Introduction

The dynamic response of rectangular plates to lateral pressure pulse depends on the stiffness, mass density, size and boundary conditions of the structure, as well as the loading parameters. Dobyns (1981) presented the elastic analysis of thick orthotropic plates under various static and dynamic loadings. The primary objective of the present study is to propose similarities in the dynamic response of orthotropic rectangular plates under a lateral pressure pulse. It will be shown that, with appropriate nondimensional parameters, the peak deflection for any combination of orthotropy, density, size, and pulse duration is represented by a single general curve. This is an iso-deflection curve, which is a plot of the peak pressure versus total impulse that result in a similar peak deflection of the plate. The iso-response concept dates back to the 1950s. A detailed description for various load shapes together with a brief history of the method were published by Abrahamson and Lindberg (1972).

Iso-Response Plots

The iso-response analysis will be presented here for orthotropic flat rectangular plates, loaded by a lateral pressure pulse $p(x, y, t)$, which is nonzero in the time interval $T \geq t \geq 0$. Its applicability for different pressure distributions and histories of loading results will be presented for the following three different loading cases:

Load Case 1 $\quad p = P\sin(\pi t/T)$ (1)

Load Case 2 $\quad p = P\sin(\pi x/a)\sin(\pi y/b)\sin(\pi t/T)$ (2)

Load Case 3 $\quad p = Pt/T$ (3)

where a, b are the plate dimensions in the x, y directions. Note that $p(t>T)=0$.

Assuming that either P or T or both are sufficiently small

[4]Department of Mechanical Engineering, Western Michigan University, Kalamazoo, MI 49008-5065. Mem. ASME.

Manuscript received by the ASME Applied Mechanics Division, June 8, 1988; final revision, July 26, 1989.

Downloaded 03 May 2010 to 171.66.16.244. Redistribution subject to ASME license or copyright; see http://www.asme.org/terms/Terms_Use.cfm

and equations (5)–(7) thus yield (after simplification)

$$\omega_1 \underset{(5,16,17,19,14)}{=} q_1\dot{q}_3/(q_1^2+q_2^2)^{1/2} \tag{21}$$

$$\omega_2 \underset{(6,17,15,20,12)}{=} -q_2\dot{q}_3/(q_1^2+q_2^2)^{1/2} \tag{22}$$

$$\omega_3 \underset{(7,15,16,18,13)}{=} (q_1\dot{q}_2-q_2\dot{q}_1)/(q_1^2+q_2^2). \tag{23}$$

Hence,

$$\omega \underset{(3)}{=} \frac{q_1\dot{q}_3}{(q_1^2+q_2^2)^{1/2}}\mathbf{a}_1 - \frac{q_2\dot{q}_3}{(q_1^2+q_2^2)^{1/2}}\mathbf{a}_2 + \frac{q_1\dot{q}_2-q_2\dot{q}_1}{q_1^2+q_2^2}\mathbf{a}_3. \tag{24}$$

The results just obtained, as well as corresponding results for five more sets of orthogonal curvilinear coordinates, are recorded in Table 1, where the common name of each coordinate system is listed, as are those of associated coordinate surfaces. Note, however, that knowledge of these names played no role in the determination of ω.

Derivation

In Kane and Levinson (1985) ω is defined as

$$\omega = \frac{d\mathbf{b}_2}{dt}\cdot\mathbf{b}_3\mathbf{b}_1 + \frac{d\mathbf{b}_3}{dt}\cdot\mathbf{b}_1\mathbf{b}_2 + \frac{d\mathbf{b}_1}{dt}\cdot\mathbf{b}_2\mathbf{b}_3 \tag{25}$$

where d/dt denotes time differentiation in A. Comparison of this equation with equation (4) shows that

$$\omega_1 = \frac{d\mathbf{b}_2}{dt}\cdot\mathbf{b}_3 \tag{26}$$

$$\omega_2 = \frac{d\mathbf{b}_3}{dt}\cdot\mathbf{b}_1 \tag{27}$$

$$\omega_3 = \frac{d\mathbf{b}_1}{dt}\cdot\mathbf{b}_2 \tag{28}$$

while differentiation of equation (2) with respect to t in A gives

$$\frac{d}{dt}\frac{\partial\mathbf{p}}{\partial q_r} \underset{(2)}{=} \dot{f}_r\mathbf{b}_r + f_r\frac{d\mathbf{b}_r}{dt} \qquad (r=1,\,2,\,3) \tag{29}$$

from which it follows that

$$\frac{d\mathbf{b}_r}{dt} = \frac{1}{f_2}\left(\frac{d}{dt}\frac{\partial\mathbf{p}}{\partial q_r} - \dot{f}_r\mathbf{b}_r\right) \quad (r=1,2,3). \tag{30}$$

Hence,

$$\omega_1 \underset{(26,30)}{=} \frac{1}{f_r}\left(\frac{d}{dt}\frac{\partial\mathbf{p}}{\partial q_2} - \dot{f}_2\mathbf{b}_2\right)\cdot\mathbf{b}_3 \tag{31}$$

But, since $\mathbf{b}_r$ $(r=1,2,3)$ are mutually orthogonal,

$$\mathbf{b}_2\cdot\mathbf{b}_3 = 0. \tag{32}$$

Moreover,

$$\mathbf{b}_3 \underset{(2)}{=} \frac{1}{f_3}\frac{\partial\mathbf{p}}{\partial q_3}. \tag{33}$$

Therefore,

$$\omega_1 \underset{(31-33)}{=} \frac{1}{f_2 f_3}\left(\frac{d}{dt}\frac{\partial\mathbf{p}}{\partial q_2}\right)\cdot\frac{\partial\mathbf{p}}{\partial q_3} \tag{34}$$

in agreement with equation (5). To establish the validity of equations (6) and (7), one can proceed similarly, writing in place of equation (31) an equation based on equation (27) or (28) rather than on equation (26).

Conclusion

The method presented here permits one to determine the angular velocity of the orthonormal triad of vectors associated with *any* set of orthogonal curvilinear coordinates whenever one has an expression for each of three rectangular coordinates of a generic point as a function of the curvilinear coordinates under consideration. Geometric considerations play no role in this determination. Of course, when the geometry in question is sufficiently simple, as, for example, in the case of spherical coordinates (see the last entry in Table 1), one can determine the desired angular velocity easily by other means.

Reference

Kane, Thomas R., and Levinson, David A., 1985, *Dynamics: Theory and Applications*, McGraw-Hill, New York, p. 16.

Unified Iso-Deflection Curves for Orthotropic Plates Under Lateral Pressure Pulse

Judah Ari-Gur[4] and M. Jerry Kenig[4]

Introduction

The dynamic response of rectangular plates to lateral pressure pulse depends on the stiffness, mass density, size and boundary conditions of the structure, as well as the loading parameters. Dobyns (1981) presented the elastic analysis of thick orthotropic plates under various static and dynamic loadings. The primary objective of the present study is to propose similarities in the dynamic response of orthotropic rectangular plates under a lateral pressure pulse. It will be shown that, with appropriate nondimensional parameters, the peak deflection for any combination of orthotropy, density, size, and pulse duration is represented by a single general curve. This is an iso-deflection curve, which is a plot of the peak pressure versus total impulse that result in a similar peak deflection of the plate. The iso-response concept dates back to the 1950s. A detailed description for various load shapes together with a brief history of the method were published by Abrahamson and Lindberg (1972).

Iso-Response Plots

The iso-response analysis will be presented here for orthotropic flat rectangular plates, loaded by a lateral pressure pulse $p(x, y, t)$, which is nonzero in the time interval $T \geq t \geq 0$. Its applicability for different pressure distributions and histories of loading results will be presented for the following three different loading cases:

Load Case 1 $\quad p = P\sin(\pi t/T)$ (1)

Load Case 2 $\quad p = P\sin(\pi x/a)\sin(\pi y/b)\sin(\pi t/T)$ (2)

Load Case 3 $\quad p = Pt/T$ (3)

where a, b are the plate dimensions in the x, y directions. Note that $p(t>T)=0$.

Assuming that either P or T or both are sufficiently small

[4]Department of Mechanical Engineering, Western Michigan University, Kalamazoo, MI 49008-5065. Mem. ASME.

Manuscript received by the ASME Applied Mechanics Division, June 8, 1988; final revision, July 26, 1989.

Copyright © 1990 by ASME
Downloaded 03 May 2010 to 171.66.16.244. Redistribution subject to ASME license or copyright; see http://www.asme.org/terms/Terms_Use.cfm

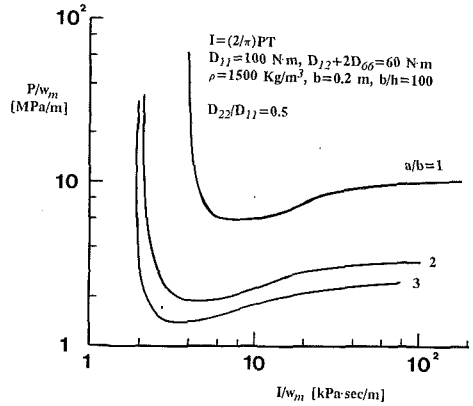


Fig. 1(a)

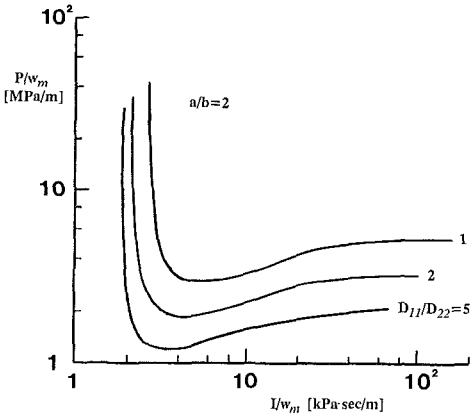


Fig. 1(b)

Fig. 1 Iso-deflection plots for uniform pressure half-sine pulse; (a) various aspect ratios, (b) various orthotropy ratios

such that small deflections are obtained and extensional forces may be neglected, the dynamic deflection $w_c(t)$ at the center $(x=a/2,\ y=b/2)$ of a rectangular simply-supported plate is given by:

$$\frac{\mu w_c}{P}=\frac{16}{\pi^2}\sum_{m=1,3}^{\infty}\sum_{n=1,3}\frac{(-1)^{(m+n-2)/2}}{mn\,\omega_{mn}{}^2(\beta_{mn}{}^2-1)}F_{mn}(t) \tag{4}$$

$$\frac{\mu w_c}{P}=\frac{1}{\omega_{11}{}^2(\beta_{11}{}^2-1)}F_{11}(t) \tag{5}$$

$$\frac{\mu w_c}{P}=\frac{16}{\pi^2}\sum_{m=1,3}^{\infty}\sum_{n=1,3}\frac{(-1)^{(m+n-2)/2}}{\pi mn\omega_{mn}{}^2}G_{mn}(t) \tag{6}$$

for the three load cases, respectively, where

$$F_{mn}(t)=\begin{cases}\beta_{mn}\sin(\omega_{mn}t)-\sin(\Omega t) & ,T\geq t\geq 0\\ 2\beta_{mn}\cos(\omega_{mn}T/2)\sin[\omega_{mn}(t-T/2)] & ,t\geq T\end{cases} \tag{7}$$

$$G_{mn}(t)=\begin{cases}\Omega t-\beta_{mn}\sin(\omega_{mn}t) & ,T\geq t\geq 0\\ \pi\cos[\omega_{mn}(t-T)]-2\beta_{mn}\sin(\omega_{mn}T/2)\cos[\omega_{mn}(t-T/2)] & ,t\geq T\end{cases} \tag{8}$$

Here, μ is the uniform mass per area of the plate, ω_{mn} are the natural frequencies (see, for example, Vinson and Sierakowski (1987)), $\Omega=\pi/T$ is the frequency of the pulse, and $\beta_{mn}=\Omega/\omega_{mn}$ is the frequency ratio. The solution procedure to obtain the solutions is simple, as outlined by Dobyns (1981).

Pressure-impulse iso-deflection curves are presented in Figs. 1-2. Due to the linearity of the solution the peak deflection, for a given loading duration, is proportional to the peak pressure. Hence, the iso-response plots are presented as P/w_m versus I/w_m, with a single curve for a given plate. Note that if large deflections occur and nonlinearity due to extensional forces becomes significant, every plate will have a family of different iso-deflection curves for different values of w_m.

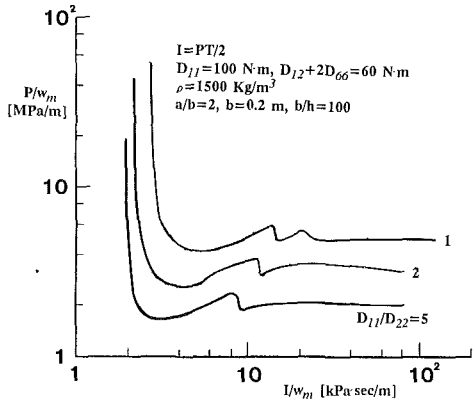


Fig. 2 Iso-deflection plots for uniform pressure triangular pulse

Figure 1 is for the first load case. Results for different plate densities were also plotted, but, for brevity, they are not presented here. The iso-deflection plots for load case 2 are not presented either, since, except for different values, they look like those of Fig. 1. The plots for load case 3 (Fig. 2) exhibit a different iso-deflection shape. Note that the peak deflection w_c is the absolute value, since sometimes, and especially after the abrupt pressure release of load case 3, the largest deflection is negative.

Unified Iso-Deflections

Nondimensional pressure and impulse are defined as follows:

$$\bar{I}=I/I_o\ ;\ \bar{P}=P/P_o \tag{9}$$

where I and P are the applied impulse and pressure that result in a peak deflection w_m, $I_o=I(T\to 0)$ is the minimum impulse and $P_o=P(T\to\infty)$ is the static pressure which are required to cause the deflection w_m.

The peak static $(T\to\infty)$ deflection and the static stiffness P_o/w_m are obtained through equations (4)-(5) for $t=T/2$ and equation (6) for $t=T$.

I_o is obtained by a simple energy analysis. Assuming that the impulse I_o exerts a lateral initial velocity $v=I_o/\mu$, and the kinetic energy is transformed into elastic energy of the plate, then:

$$I_o=C\cdot\sqrt{\mu\cdot w_m\cdot P_o} \tag{10}$$

from which I_o/w_m is obtained. The coefficient C depends on the pressure distribution and the resulting deflection shape when the peak deflection is attained. Assuming a biaxial half-sine bending shape, $C=2/\pi$ for load cases 1 and 3 (uniform pressure) and $C=1$ for load case 2.

Downloaded 03 May 2010 to 171.66.16.244. Redistribution subject to ASME license or copyright; see http://www.asme.org/terms/Terms_Use.cfm

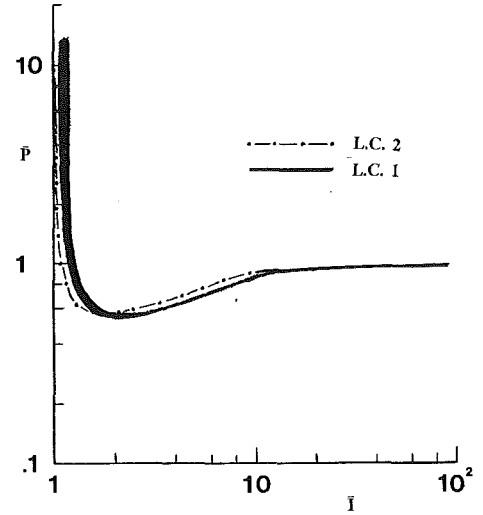


Fig. 3(a)

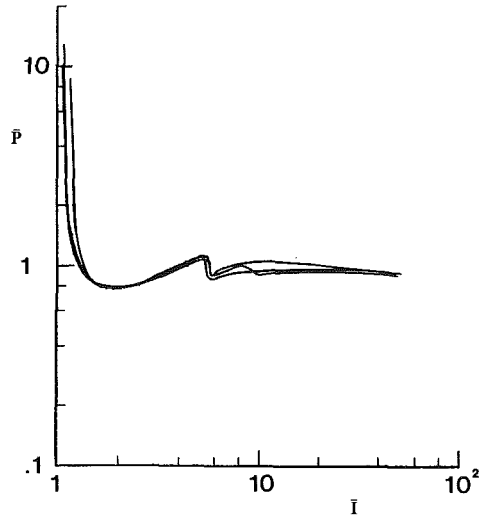


Fig. 3(b)

Fig. 3 Unified nondimensional iso-deflection plots; (*a*) uniform and non-uniform half-sine pulse, (*b*) triangular pulse

The iso-deflection plots of Figs. 1-2 are unified in Fig. 3, using the nondimensional pressure and impulse. It appears that, with a small scatter, all the plots of each load case converge into a single curve.

Concluding Remarks

The development of the iso-deflection curves can be done for isotropic plates, and with the nondimensional pressure and impulse, the curves can then be used also for orthotropic plates. Moreover, knowledge of the coefficient C in equation (10) is not required. If C is omitted, then the lower bound of $\bar{I}$ will not be $\bar{I}=1$ as in Fig. 3, but $\bar{I}=C$.

The expressions for P_o and I_o include only material properties and static stiffness. Hence, to predict the peak dynamic deflection of a plate to a given pulse, only the static ratio P_o/w_m should be calculated before the iso-deflection curve is employed [using: $\bar{P}/\bar{I}=\sqrt{\mu\cdot(w_m/P_o)}/T$]. Thus, evaluation of dynamic deflections may be performed without dynamic calculations, even when not of natural frequencies.

Acknowledgment

This work was supported by the Engineering Foundation, grant RI-A-87-5 and by the WMU Faculty Research Fund 87-037.

References

Abrahamson, G. R., and Lindberg, H. E., 1972, "Peak-load—Impulse Characterization of Critical Pulse Loads in Structural Dynamics," *Dynamic Response of Structures*, G. Herrmann and N. Perrone, eds., Pergamon Press, pp.31-53.

Dobyns, A. L., 1981, "Analysis of Simply-Supported Orthotropic Plates Subject to Static and Dynamic Loads," *AIAA J.*, Vol. 19, pp. 642-650.

Vinson, J. R., and Sierakowski, R. L., 1987, *The Behavior of Structures Composed of Composite Materials*, Martinus Nijhoff Publishers, Chapter 3.

Axisymmetric Upheaval Buckling of a Heavy Sheet

R. E. Hobbs[5]

A large elastic sheet with a significant self-weight subject to biaxial in-plane compression while lying on a rigid horizontal plane may buckle. The buckles, circular areas which lift away from the rigid subgrade, are essentially a plate phenomenon, an axisymmetric analogue to the widely discussed upheaval buckling of beams. It is found that plate upheaval is relatively insensitive to subgrade friction, a fact which may simplify design against such buckling.

Introduction

The present note addresses the possibility of axisymmetric upheaval in a thermally loaded heavy plate or sheet resting on a rigid subgrade. This problem is, in many respects, a natural extension of the analysis of the buckling of axially loaded beams with a significant self-weight lying on a rigid subgrade (Hobbs, 1984). It suggested itself to the author when, in his home town, two large floors consisting of many small, closely jointed timber tiles ("parquet") resting on rigid concrete subgrades buckled on a particularly warm and humid day which marked the end of a much cooler and drier spell. The buckles were clearly upheaval, and even more clearly a plate response, rather than the behavior of a beam.

Analysis

By analogy with the established analysis of the upheaval of beams, then, a circular buckle might be expected (on grounds of symmetry) whose behavior could be treated by the theory for a plate under simultaneous in-plane and transverse load. For a finite friction coefficient between plate and subgrade, an annular region might be expected to slide in towards the buckle, and a displacement compatibility condition might again be expected to play a central role.

Following Timoshenko and Woinowsky-Krieger (1959), the deflection, $w(r)$, (positive downwards) of a uniform circular plate of radius, a, and stiffness, D, under a uniform load, q, is given by

$$w=\frac{qa^4[J_o(kr/a)-J_o(k)]}{2Dk^3J_1(k)}-\frac{qa^2(a^2-r^2)}{4Dk^2} \tag{1}$$

where $k^2=Na^2/D$, with N the uniform compression in the middle plane of the plate, r the radius, and J_o and J_1 are Bessel functions of order zero and one, respectively.

As usual, $D=Et^3/(12(1-\nu)^2)$ where E is Young's modulus,

[5]Reader, Civil Engineering Department, Imperial College, London, SW7 2BU, U.K.

Manuscript received by the ASME Applied Mechanics Division, July 13, 1988; final revision, July 1, 1989.

Downloaded 03 May 2010 to 171.66.16.244. Redistribution subject to ASME license or copyright; see http://www.asme.org/terms/Terms_Use.cfm

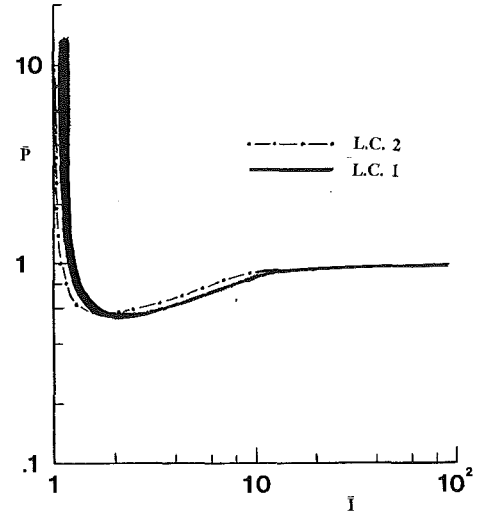


Fig. 3(a)

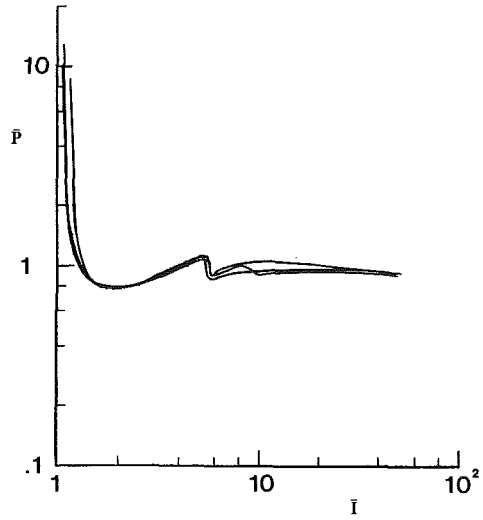


Fig. 3(b)

Fig. 3 Unified nondimensional iso-deflection plots; (a) uniform and non-uniform half-sine pulse, (b) triangular pulse

The iso-deflection plots of Figs. 1-2 are unified in Fig. 3, using the nondimensional pressure and impulse. It appears that, with a small scatter, all the plots of each load case converge into a single curve.

Concluding Remarks

The development of the iso-deflection curves can be done for isotropic plates, and with the nondimensional pressure and impulse, the curves can then be used also for orthotropic plates. Moreover, knowledge of the coefficient C in equation (10) is not required. If C is omitted, then the lower bound of $\bar{I}$ will not be $\bar{I}=1$ as in Fig. 3, but $\bar{I}=C$.

The expressions for P_o and I_o include only material properties and static stiffness. Hence, to predict the peak dynamic deflection of a plate to a given pulse, only the static ratio P_o/w_m should be calculated before the iso-deflection curve is employed [using: $\bar{P}/\bar{I}=\sqrt{\mu\cdot(w_m/P_o)}/T$]. Thus, evaluation of dynamic deflections may be performed without dynamic calculations, even when not of natural frequencies.

Acknowledgment

This work was supported by the Engineering Foundation, grant RI-A-87-5 and by the WMU Faculty Research Fund 87-037.

References

Abrahamson, G. R., and Lindberg, H. E., 1972, "Peak-load—Impulse Characterization of Critical Pulse Loads in Structural Dynamics," *Dynamic Response of Structures*, G. Herrmann and N. Perrone, eds., Pergamon Press, pp.31-53.

Dobyns, A. L., 1981, "Analysis of Simply-Supported Orthotropic Plates Subject to Static and Dynamic Loads," *AIAA J.*, Vol. 19, pp. 642-650.

Vinson, J. R., and Sierakowski, R. L., 1987, *The Behavior of Structures Composed of Composite Materials*, Martinus Nijhoff Publishers, Chapter 3.

Axisymmetric Upheaval Buckling of a Heavy Sheet

R. E. Hobbs[5]

A large elastic sheet with a significant self-weight subject to biaxial in-plane compression while lying on a rigid horizontal plane may buckle. The buckles, circular areas which lift away from the rigid subgrade, are essentially a plate phenomenon, an axisymmetric analogue to the widely discussed upheaval buckling of beams. It is found that plate upheaval is relatively insensitive to subgrade friction, a fact which may simplify design against such buckling.

Introduction

The present note addresses the possibility of axisymmetric upheaval in a thermally loaded heavy plate or sheet resting on a rigid subgrade. This problem is, in many respects, a natural extension of the analysis of the buckling of axially loaded beams with a significant self-weight lying on a rigid subgrade (Hobbs, 1984). It suggested itself to the author when, in his home town, two large floors consisting of many small, closely jointed timber tiles ("parquet") resting on rigid concrete subgrades buckled on a particularly warm and humid day which marked the end of a much cooler and drier spell. The buckles were clearly upheaval, and even more clearly a plate response, rather than the behavior of a beam.

Analysis

By analogy with the established analysis of the upheaval of beams, then, a circular buckle might be expected (on grounds of symmetry) whose behavior could be treated by the theory for a plate under simultaneous in-plane and transverse load. For a finite friction coefficient between plate and subgrade, an annular region might be expected to slide in towards the buckle, and a displacement compatibility condition might again be expected to play a central role.

Following Timoshenko and Woinowsky-Krieger (1959), the deflection, $w(r)$, (positive downwards) of a uniform circular plate of radius, a, and stiffness, D, under a uniform load, q, is given by

$$w=\frac{qa^4[J_o(kr/a)-J_o(k)]}{2Dk^3J_1(k)}-\frac{qa^2(a^2-r^2)}{4Dk^2} \tag{1}$$

where $k^2=Na^2/D$, with N the uniform compression in the middle plane of the plate, r the radius, and J_o and J_1 are Bessel functions of order zero and one, respectively.

As usual, $D=Et^3/(12(1-\nu)^2)$ where E is Young's modulus,

[5]Reader, Civil Engineering Department, Imperial College, London, SW7 2BU, U.K.

Manuscript received by the ASME Applied Mechanics Division, July 13, 1988; final revision, July 1, 1989.

Copyright © 1990 by ASME
Downloaded 03 May 2010 to 171.66.16.244. Redistribution subject to ASME license or copyright; see http://www.asme.org/terms/Terms_Use.cfm

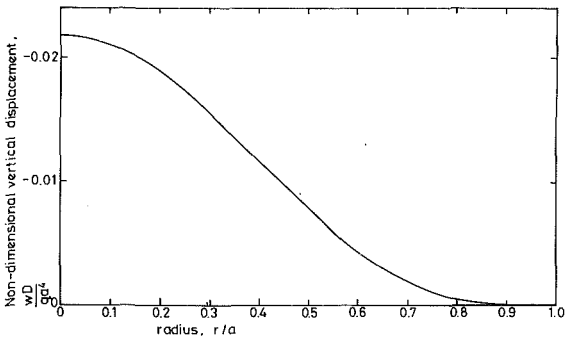


Fig. 1 Plate upheaval—first mode

t the plate thickness, and ν Poisson's ratio. Equation (1) holds for any clamped circular plate, i.e., plates with zero edge displacements and slope. In the present case, the outer radius a has yet to be determined: It is found via the third boundary condition—that of zero radial moment (or, equivalently, zero radial curvature since the tangential curvature is clearly also zero at the edge of the buckle).

Differentiating equation (1) twice with respect to r, the curvature φ' is given by

$$\varphi' = -\frac{d^2w}{dr^2} = \frac{qa^2}{2Dk^2}\left[\frac{k}{J_1(k)}\left(J_o(kr/a) - \frac{a}{kr}J_1(kr/a)\right) - 1\right]. \tag{2}$$

Setting the expression for the curvature equal to zero when $r=a$, the following condition for k is obtained:

$$k\frac{J_o(k)}{J_1(k)} - 2 = 0. \tag{3}$$

The first zero of equation (3) is $k=5.1356223$. The deflected shape for this value of k is plotted in Fig. 1, and clearly meets the unilateral constraint requirement.

The arclength change between the two edges of the buckle is

$$e_1 = 2\int_o^a \frac{1}{2}\left(\frac{dw}{dr}\right)^2 dr = \frac{q^2a^4}{4D^2k^4}\int_o^a \left[\frac{aJ_1(kr/a)}{J_1(k)} - r\right]^2 dr. \tag{4}$$

Using numerical methods,

$$e_1 = 6.5937128\times10^{-4}\, q^2a^7/D^2 = c\, q^2a^7/D^2, \text{ say.} \tag{5}$$

The expansion of the buckle diameter due to the change of in-plane force from N_o to N is the response to a uniform, isotropic stress change (Timoshenko and Goodier, 1951) of

$$\sigma_r = \sigma_\theta = \frac{N_o - N}{t} = \frac{\Delta N}{t}, \text{ say} \tag{6}$$

and the diametral expansion in-plane

$$e_2 = 2a\epsilon_r = 2a\frac{(1-\nu)}{Et}\Delta N. \tag{7}$$

Solution for High Friction. The net inward movement in the buckle is $e_1 - e_2$, and in the absence of any adjacent slipping zone, i.e., for high enough friction, the compatibility condition is

$$e_1 - e_2 = 0 \tag{8}$$

or

$$c\frac{q^2a^7}{D^2} - \frac{2a(1-\nu)}{Et}\Delta N = 0. \tag{9}$$

Rearranging this as an equation for N_o leads to

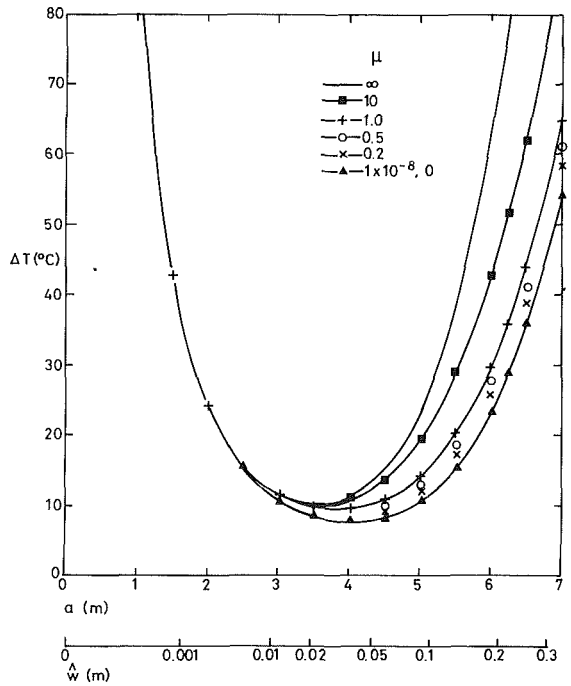


Fig. 2 Plate upheaval for various friction coefficients

$$N_o = \frac{Dk^2}{a^2} + \frac{cEtq^2a^6}{2(1-\nu)D^2}. \tag{10}$$

It is noted that N_o has a minimum value (analogous to the high friction minimum found in a beam (Hobbs 1984)) when $a=\bar{a}$, say, where

$$\bar{a} = \left(\frac{2k^2}{3c}\cdot\frac{D^3(1-\nu)}{q^2Et}\right)^{0.125}. \tag{11}$$

If N_o is generated by restrained thermal expansion, the temperature change necessary is

$$\Delta T = \frac{(1-\nu)}{E\alpha t}N_o \tag{12}$$

where α is the coefficient of linear thermal expansion.

Solution for Zero Friction. Because of the development of hoop stresses in the annular slipping region which forms around the buckle, the inward displacement of the edge of the slipping zone, u_a, is finite even when the friction coefficient, μ, is zero. The results for this case form a useful lower-bound check on the finite friction case. A plane stress analysis shows that

$$u_a = a\,\Delta N(1+\nu)/(Et) \tag{13}$$

so that the compatibility equation (9) becomes

$$c\frac{q^2a^7}{D^2} - \frac{2a(1-\nu)}{Et}\Delta N = \frac{2a(1+\nu)}{Et}\Delta N \tag{14}$$

so that

$$N_o = \frac{Dk^2}{a^2} + \frac{cEtq^2a^6}{4D^2}. \tag{15}$$

Comparing equations (15) and (10), a minimum value is again expected, at say $\breve{a}$ now, where

$$\breve{a} = \left(\frac{4k^2}{3c}\cdot\frac{D^3}{q^2Et}\right)^{0.125} \tag{16}$$

or

$$\breve{a} = (2/(1-\nu))^{0.125}\bar{a}. \tag{17}$$

Downloaded 03 May 2010 to 171.66.16.244. Redistribution subject to ASME license or copyright; see http://www.asme.org/terms/Terms_Use.cfm

Example and Discussion

Figure 2 presents initial force (expressed as the equivalent temperature rise) against buckle radius data for a 25-mm thick steel plate with the following properties:

$E = 205000\ \text{N/mm}^2 \qquad \nu = 0.3$

$q = 1.912 \times 10^{-3}\ \text{N/mm}^2 \qquad \alpha = 11 \times 10^{-6}/°\text{C}.$

Some results for finite subgrade friction values are also included.

The major difference between beam and plate upheaval is the different behaviors for small friction coefficients. Beam upheaval for $\mu = 0$ does not have a rising branch. Plate upheaval for $\mu = 0$, on the other hand, shows a strong rising branch reflecting the ability of the slipping annulus to reach equilibrium by generating internal hoop stresses. The modest separation between the rising paths for $\mu = 0$ and $\mu = \infty$ means that the effect of μ is, in general, much less marked in plate upheaval than in beam upheaval.

The plate upheaval $\mu = 0$ curve is so easy to generate, and so close to the equally easily obtained $\mu = \infty$ curve that these curves (and their minima in particular) may form a useful design aid as an alternative to the more complex calculations for finite friction, particularly as the actual friction coefficient is often unknown in practice. For example, in the case presented in Fig. 2, the minimum of the $\mu = \infty$ curve occurs at $\bar{a} = 3.549$ m and $\Delta T = 10.17°\text{C}$, while for $\mu = 0$ the corresponding figures are $\check{a} = 4.046$ m and $\Delta T = 7.82°\text{C}$ (the ratio of the two temperature increments is, of course, $(\check{a}/\bar{a})^2$ or $(2/(1-\nu))^{0.25}$). The close proximity of these curves would mean, in many practical cases, that a "safe temperature" approach based on the smaller value of ΔT might suffice in a design check against plate upheaval.

Conclusions

The axisymmetric upheaval buckling of heavy plates in unilateral contact with a rigid subgrade has been treated in an analysis which draws on the insights obtained in the familiar one-dimensional upheaval buckling of beams.

It is shown, in contrast to the results found in the beam case, that the behavior of the plate buckle is relatively insensitive to subgrade friction to the point that the easily computed, zero friction buckling case may suffice for design purposes.

References

Hobbs, R. E., 1984, "In-service buckling of heated pipelines," *ASCE Journal of Transportation Engineering*, Vol. 110, pp. 175–189.

Timoshenko, S. P., and Goodier, J. N., 1951, *Theory of Elasticity*, 2nd ed. McGraw-Hill, New York, pp. 58, 66–70.

Timoshenko, S. P., and Woinowsky-Kreiger, S., 1959, *Theory of Plates and Shells*, 2nd ed. McGraw-Hill, New York, pp. 51, 53, 391.

Some Remarks on Three Micromechanical Models in Composite Media

Y. Benveniste[6]

Introduction

The present note establishes an equivalence between the predictions of three micromechanics models in relation to the effective stiffness tensor of two-phase composites. The three theories are: Levin's model (Levin (1975, 1976)); Willis's model of closure approximation (Willis (1978, 1981, 1984)); and Mori-Tanaka's model, (Mori and Tanaka (1973)), in its implementation in composite media, see Benveniste (1987) and references cited therein.

It is shown here that the prediction of these three models coincide in the case of two-phase particulate media consisting of aligned anisotropic ellipsoidal inclusions of the same shape, which are embedded in an anisotropic matrix. Levin's model is also shown to coincide with Mori-Tanaka's predictions for the case of a composite with nonoriented isotropic ellipsoidal inclusions.

It is only natural that this short note will not deal with the detailed derivations of these theories as the reader can find them in the original works. It will suffice here to provide only the essential features of the models and then proceed to establish the equivalence of the final results.

General Framework

Consider a two-phase composite under homogeneous boundary conditions

$$\mathbf{u}(S) = \epsilon^0 \mathbf{x}, \tag{1}$$

where $\mathbf{u}$ denotes the displacement field, S is the outside boundary of the composite, ϵ^0 is a constant strain tensor, and $\mathbf{x}$ denotes a Cartesian coordinate system. The effective stiffness tensor $\mathbf{L}^*$ can be shown to be given by (see Walpole (1969) for example)

$$\mathbf{L}^* = \mathbf{L}_1 + c_2\{(\mathbf{L}_2 - \mathbf{L}_1)\mathbf{A}\}, \tag{2}$$

where $\mathbf{L}_1$ and $\mathbf{L}_2$ denote the stiffness tensors of the matrix and particulate phase, respectively, c_2 is the volume fraction of the particulate phase, and $\mathbf{A}$ is the so-called concentration fractor defined by

$$\bar{\epsilon}^{(2)} = \mathbf{A}\epsilon^0 \tag{3}$$

where $\bar{\epsilon}^{(2)}$ is the orientation-dependent average strain in a typical individual inclusion and the curly brackets $\{\ \}$ in (2) denote an average over all possible orientation. A knowledge of $\mathbf{A}$ is thus sufficient to determine the effective stiffness tensor $\mathbf{L}^*$. This being a tremendously difficult task, different models have been proposed in the literature which approximate $\mathbf{A}$.

An alternative basis for the computation of the effective stiffness tensor can be given in terms of the so-called polarization tensor. Let the composite possess a tensor of moduli $\mathbf{L}$ which varies with position, the stress-strain relation being denoted by $\sigma = \mathbf{L}\epsilon$. Define a homogeneous comparison material with moduli $\mathbf{L}_0$, and the stress polarization tensor τ given by

$$\tau = (\mathbf{L} - \mathbf{L}_0)\epsilon, \tag{4}$$

so that

$$\sigma = \mathbf{L}_0\epsilon + \tau. \tag{5}$$

Choosing the matrix as the comparison medium and taking an ensemble average of (5) provides

$$<\sigma> = \mathbf{L}_1 <\epsilon> + <\tau>. \tag{6}$$

As it is known, for statistically uniform composites under boundary conditions of the type (1), ensemble averages may be expected to agree with some suitably defined, local representative volume average.

Since the effective stiffness tensor $\mathbf{L}^*$ is given by $<\sigma> = \mathbf{L}^* <\epsilon>$, it follows that if $<\tau>$ is assumed to be related to $<\epsilon>$ through

$$<\tau> = \mathbf{t} <\mathbf{e}>, \tag{7}$$

[6]Department of Solid Mechanics, Materials, and Structures, Faculty of Engineering, Tel-Aviv University, Ramat-Aviv, Israel.

Manuscript received by the ASME Applied Mechanics Division, January 6, 1989; final revision, April 24, 1989.

Downloaded 03 May 2010 to 171.66.16.244. Redistribution subject to ASME license or copyright; see http://www.asme.org/terms/Terms_Use.cfm

Example and Discussion

Figure 2 presents initial force (expressed as the equivalent temperature rise) against buckle radius data for a 25-mm thick steel plate with the following properties:

$E = 205000\ \text{N/mm}^2$ $\quad \nu = 0.3$

$q = 1.912 \times 10^{-3}\ \text{N/mm}^2$ $\quad \alpha = 11 \times 10^{-6}/°\text{C}.$

Some results for finite subgrade friction values are also included.

The major difference between beam and plate upheaval is the different behaviors for small friction coefficients. Beam upheaval for $\mu = 0$ does not have a rising branch. Plate upheaval for $\mu = 0$, on the other hand, shows a strong rising branch reflecting the ability of the slipping annulus to reach equilibrium by generating internal hoop stresses. The modest separation between the rising paths for $\mu = 0$ and $\mu = \infty$ means that the effect of μ is, in general, much less marked in plate upheaval than in beam upheaval.

The plate upheaval $\mu = 0$ curve is so easy to generate, and so close to the equally easily obtained $\mu = \infty$ curve that these curves (and their minima in particular) may form a useful design aid as an alternative to the more complex calculations for finite friction, particularly as the actual friction coefficient is often unknown in practice. For example, in the case presented in Fig. 2, the minimum of the $\mu = \infty$ curve occurs at $\bar{a} = 3.549$ m and $\Delta T = 10.17°\text{C}$, while for $\mu = 0$ the corresponding figures are $\check{a} = 4.046$ m and $\Delta T = 7.82°\text{C}$ (the ratio of the two temperature increments is, of course, $(\check{a}/\bar{a})^2$ or $(2/(1-\nu))^{0.25}$). The close proximity of these curves would mean, in many practical cases, that a "safe temperature" approach based on the smaller value of ΔT might suffice in a design check against plate upheaval.

Conclusions

The axisymmetric upheaval buckling of heavy plates in unilateral contact with a rigid subgrade has been treated in an analysis which draws on the insights obtained in the familiar one-dimensional upheaval buckling of beams.

It is shown, in contrast to the results found in the beam case, that the behavior of the plate buckle is relatively insensitive to subgrade friction to the point that the easily computed, zero friction buckling case may suffice for design purposes.

References

Hobbs, R. E., 1984, "In-service buckling of heated pipelines," *ASCE Journal of Transportation Engineering*, Vol. 110, pp. 175–189.

Timoshenko, S. P., and Goodier, J. N., 1951, *Theory of Elasticity*, 2nd ed. McGraw-Hill, New York, pp. 58, 66–70.

Timoshenko, S. P., and Woinowsky-Kreiger, S., 1959, *Theory of Plates and Shells*, 2nd ed. McGraw-Hill, New York, pp. 51, 53, 391.

Some Remarks on Three Micromechanical Models in Composite Media

Y. Benveniste[6]

Introduction

The present note establishes an equivalence between the predictions of three micromechanics models in relation to the effective stiffness tensor of two-phase composites. The three theories are: Levin's model (Levin (1975, 1976)); Willis's model of closure approximation (Willis (1978, 1981, 1984)); and Mori-Tanaka's model, (Mori and Tanaka (1973)), in its implementation in composite media, see Benveniste (1987) and references cited therein.

It is shown here that the prediction of these three models coincide in the case of two-phase particulate media consisting of aligned anisotropic ellipsoidal inclusions of the same shape, which are embedded in an anisotropic matrix. Levin's model is also shown to coincide with Mori-Tanaka's predictions for the case of a composite with nonoriented isotropic ellipsoidal inclusions.

It is only natural that this short note will not deal with the detailed derivations of these theories as the reader can find them in the original works. It will suffice here to provide only the essential features of the models and then proceed to establish the equivalence of the final results.

General Framework

Consider a two-phase composite under homogeneous boundary conditions

$$\mathbf{u}(S) = \epsilon^0 \mathbf{x}, \tag{1}$$

where $\mathbf{u}$ denotes the displacement field, S is the outside boundary of the composite, ϵ^0 is a constant strain tensor, and $\mathbf{x}$ denotes a Cartesian coordinate system. The effective stiffness tensor $\mathbf{L}^*$ can be shown to be given by (see Walpole (1969) for example)

$$\mathbf{L}^* = \mathbf{L}_1 + c_2\{(\mathbf{L}_2 - \mathbf{L}_1)\mathbf{A}\}, \tag{2}$$

where $\mathbf{L}_1$ and $\mathbf{L}_2$ denote the stiffness tensors of the matrix and particulate phase, respectively, c_2 is the volume fraction of the particulate phase, and $\mathbf{A}$ is the so-called concentration fractor defined by

$$\bar{\epsilon}^{(2)} = \mathbf{A}\epsilon^0 \tag{3}$$

where $\bar{\epsilon}^{(2)}$ is the orientation-dependent average strain in a typical individual inclusion and the curly brackets $\{\ \}$ in (2) denote an average over all possible orientation. A knowledge of $\mathbf{A}$ is thus sufficient to determine the effective stiffness tensor $\mathbf{L}^*$. This being a tremendously difficult task, different models have been proposed in the literature which approximate $\mathbf{A}$.

An alternative basis for the computation of the effective stiffness tensor can be given in terms of the so-called polarization tensor. Let the composite possess a tensor of moduli $\mathbf{L}$ which varies with position, the stress-strain relation being denoted by $\sigma = \mathbf{L}\epsilon$. Define a homogeneous comparison material with moduli $\mathbf{L}_0$, and the stress polarization tensor τ given by

$$\tau = (\mathbf{L} - \mathbf{L}_0)\epsilon, \tag{4}$$

so that

$$\sigma = \mathbf{L}_0\epsilon + \tau. \tag{5}$$

Choosing the matrix as the comparison medium and taking an ensemble average of (5) provides

$$<\sigma> = \mathbf{L}_1 <\epsilon> + <\tau>. \tag{6}$$

As it is known, for statistically uniform composites under boundary conditions of the type (1), ensemble averages may be expected to agree with some suitably defined, local representative volume average.

Since the effective stiffness tensor $\mathbf{L}^*$ is given by $<\sigma> = \mathbf{L}^* <\epsilon>$, it follows that if $<\tau>$ is assumed to be related to $<\epsilon>$ through

$$<\tau> = \mathbf{t} <\mathbf{e}>, \tag{7}$$

[6]Department of Solid Mechanics, Materials, and Structures, Faculty of Engineering, Tel-Aviv University, Ramat-Aviv, Israel.

Manuscript received by the ASME Applied Mechanics Division, January 6, 1989; final revision, April 24, 1989.

Copyright © 1990 by ASME
Downloaded 03 May 2010 to 171.66.16.244. Redistribution subject to ASME license or copyright; see http://www.asme.org/terms/Terms_Use.cfm

then $\mathbf{L}^*$ results as

$$\mathbf{L}^* = \mathbf{L}_1 + \mathbf{t}, \tag{8}$$

so that determination of $\mathbf{L}^*$ hinges upon a knowledge of $\mathbf{t}$.

Levin's Model

The starting point of this model, as well as Willis's closure approximation, is the representation of the strain field in the composite by means of an integral equation. Suppose the composite is subjected to boundary conditions $\mathbf{u}(S) = \mathbf{u}^0(\mathbf{x})$. The strain field can then be shown to be given by

$$\boldsymbol{\epsilon}(\mathbf{x}) = \boldsymbol{\epsilon}^0(\mathbf{x}) - \int_V \boldsymbol{\Gamma}(\mathbf{x},\mathbf{x}')(\mathbf{L}-\mathbf{L}_0)\boldsymbol{\epsilon}(\mathbf{x}')d\mathbf{x}', \tag{9}$$

where $\boldsymbol{\epsilon}^0(\mathbf{x})$ denotes the strain field that would exist in the homogeneous comparison medium under the same boundary conditions, and $\boldsymbol{\Gamma}$ is defined by

$$\Gamma_{ijpq}(\mathbf{x},\mathbf{x}') = \frac{\partial^2 G_{ip}}{\partial x_j \partial x'_q}\bigg|_{(ij)\,(pq)}, \tag{10}$$

the suffix (ij) implying symmetrization on these indices; G_{ip} is the Green's function in the homogeneous medium, and satisfies

$$(L_0)_{ijkl} G_{kp,lj}(\mathbf{x},\mathbf{x}') + \delta_{ip}\delta(\mathbf{x}-\mathbf{x}') = 0 \qquad x \epsilon V \tag{11}$$

with $G_{ip}(\mathbf{x},\mathbf{x}') = 0$ for $\mathbf{x} \epsilon \partial V$, where V is the volume of the composite and of the comparison medium, δ_{ip} is the Kronecker delta, and $\delta(x-x')$ is the Dirac's delta function.

In Levin's derivation $\mathbf{L}_0$ is chosen as $\mathbf{L}_1$, so that under (1) equation (9) becomes

$$\boldsymbol{\epsilon}(\mathbf{x}) = \boldsymbol{\epsilon}^0 - \sum_{j=1}^{N} \int_{V_j} \boldsymbol{\Gamma}(\mathbf{x},\mathbf{x}')(\mathbf{L}_2 - \mathbf{L}_1)\boldsymbol{\epsilon}(\mathbf{x}')d\mathbf{x}', \tag{12}$$

where N denotes the number of particles in V, V_j is the volume of each particle, and $\boldsymbol{\epsilon}^0$ denotes now a uniform strain. Taking the point $\mathbf{x}$ in the region V_j of the jth inclusion, it is seen that equation (12) consists of a system of integral equations relating to the N-tensor functions $\boldsymbol{\epsilon}(\mathbf{x})$, with $\mathbf{x} \epsilon V_j (j = 1,\ldots N)$. The system of equations (12) is solved by Levin in an approximate manner for the average strain in a particle. Levin's analysis eventually generates an approximation for the tensor $\mathbf{A}$ defined in (3) which, when substituted in (2), yields the following equation for $\mathbf{L}^*$ for the case of isotropic inclusions

$$\mathbf{L}^* = \mathbf{L}_1 + (\mathbf{L}_2 - \mathbf{L}_1)[\mathbf{I} - \{\mathbf{TP}\}c_2(\mathbf{L}_2 - \mathbf{L}_1)]^{-1}\{\mathbf{T}\}c_2, \tag{13}$$

where $\mathbf{I}$ is fourth-order unit tensor, and $\mathbf{P}$ and $\mathbf{T}$ are given by:

$$\mathbf{P} = \mathbf{S}\mathbf{L}_1^{-1} \quad , \quad \mathbf{T} = [\mathbf{I} + \mathbf{P}(\mathbf{L}_2 - \mathbf{L}_1)]^{-1}, \tag{14}$$

with $\mathbf{S}$ being Eshelby's tensor. Taking into account some difference in our notation, equation (13) is readily identified as equation (2.12) of Levin's 1976 paper.

To make contact with the other two models in the sequel, it is useful now to cast (13) into a different form. We first recall that the tensor $\mathbf{P}$ is related to another tensor $\mathbf{P}_1$ by the relation

$$\mathbf{P}(\mathbf{L}_2 - \mathbf{L}_1)\mathbf{P}_1 = \mathbf{P} - \mathbf{P}_1, \tag{15}$$

where both $\mathbf{P}_1$ and $\mathbf{P}$ can be proved to be symmetric tensors, and the tensor $\mathbf{T}$ can be written as (see Walpole (1969)):

$$\mathbf{T} = [\mathbf{I} + \mathbf{P}_1(\mathbf{L}_1 - \mathbf{L}_2)]. \tag{16}$$

Using (16) in the expression $\{\mathbf{TP}\}$ of (13) and invoking the symmetry property of the $\mathbf{L}_1$, $\mathbf{L}_2$, $\mathbf{P}_1$, and $\mathbf{P}$ tensors, yields $\{\mathbf{TP}\} = \{\mathbf{P}_1\}$. Substituting this last expression in (13) and making use of the identity

$$[\mathbf{I}c_1 + c_2\{\mathbf{T}\}]^{-1}\{\mathbf{T}\} = \{\mathbf{T}\}[\mathbf{I}c_1 + c_2\{\mathbf{T}\}]^{-1}, \tag{17}$$

where $c_1 = 1 - c_2$, finally provides:

$$\mathbf{L}^* = \mathbf{L}_1 + c_2(\mathbf{L}_2 - \mathbf{L}_1)\{\mathbf{T}\}[c_1\mathbf{I} + c_2\{\mathbf{T}\}]^{-1}. \tag{18}$$

It can be readily checked that for the case of anisotropic constituents, but aligned particles of the same shape, the theory predicts the expression for $\mathbf{L}^*$ as that given in equation (18), this time, however, with the brackets { } omitted.

Willis's Closure Model

The integral equation for the strain field (12) forms again a basis for Willis in deriving a wealth of information on the effective behavior of composites. In a series of important contributions Willis derives results pertaining to perturbation theory, variational principles, self-consistent estimates, and closure assumptions (see Willis (1981) for reference). We are concerned in this note with the approximation obtained using what is called the "closure assumption," which is also identified by Willis in this context as Lax's quasi-crystalline approximation (Lax (1951)).

Taking note of the definition of the polarization tensor $\boldsymbol{\tau}$ in (5), under boundary conditions (1) the integral equation (12) can be transformed into (Willis (1981)):

$$(\mathbf{L}_2 - \mathbf{L}_1)^{-1}\boldsymbol{\tau} + \boldsymbol{\Gamma}\boldsymbol{\tau} = \boldsymbol{\epsilon}^0, \tag{19}$$

where $\boldsymbol{\Gamma}$ denotes now the integral operator of (12). Equation (19) is an integral equation for $\boldsymbol{\tau}$ from which an approximation for the tensor $\mathbf{t}$ in (7) can in principle be obtained. For a composite containing oriented ellipsoidal inclusions of identical shape, the analysis of Willis (1981), after invoking certain assumptions on the expectation values of $\boldsymbol{\tau}$, yields the following approximation for the tensor $\mathbf{t}$:

$$\mathbf{t} = c_2[(\mathbf{L}_2 - \mathbf{L}_1)^{-1} + (1 - c_2)\mathbf{P}]^{-1}. \tag{20}$$

Substitution of (20) in (8) yields an approximation for the effective stiffness

$$\mathbf{L}^* = \mathbf{L}_1 + c_2[(\mathbf{L}_2 - \mathbf{L}_1)^{-1} + (1 - c_2)\mathbf{P}]^{-1} \tag{21}$$

identified as equation (4.54) in Willis (1981). Solving for $\mathbf{P}$ in terms of $\mathbf{T}$ in (14) and substituting in (21) readily provides

$$\mathbf{L}^* = \mathbf{L}_1 + c_2(\mathbf{L}_2 - \mathbf{L}_1)\mathbf{T}[c_1\mathbf{I} + c_2\mathbf{T}]^{-1}, \tag{22}$$

which is identical to equation (18) with the curly brackets being omitted.

Mori-Tanaka's Model

The work of Mori and Tanaka (1973), originally concerned with calculating the average internal stress in the matrix of a material containing precipitates with eigenstrain, has been the starting point of a series of papers in the literature of composite materials (see, for example, Taya and Chou (1981), Taya and Mura (1981), and Weng (1984)). Following a different approach, this theory has been recently reformulated and given an explicit form by the present author (Benveniste, 1987). Further investigation of the theory in the thermomechanical context is given in Benveniste and Dvorak (1988). See also Pedersen (1983) for a discussion of the Mori-Tanaka's model in relation to the mean field theory of Brown and Stobbs (1971).

It is useful to start here with the dilute approximation in which the auxiliary configuration, leading to an estimate of the $\mathbf{A}$ tensor, consists in surrounding one particle by an infinite matrix medium and subjecting it to the boundary conditions (1). In that configuration the average strain in the matrix is simply $\boldsymbol{\epsilon}^0$, since a single particle fails to change the average strain that existed there before the particle was embedded. In the composite, however, the matrix is disturbed due to the presence of other particles, and the average strain in it, $\bar{\boldsymbol{\epsilon}}^{(1)}$, is different than $\boldsymbol{\epsilon}^0$. The Mori-Tanaka model simulates the particle interaction in the composite by the auxiliary configuration of a particle in a large matrix domain in which the average strain is $\bar{\boldsymbol{\epsilon}}^{(1)}$; a situation which would prevail if the outside

Downloaded 03 May 2010 to 171.66.16.244. Redistribution subject to ASME license or copyright; see http://www.asme.org/terms/Terms_Use.cfm

boundary of the matrix in the auxiliary configuration is subjected to $\mathbf{u}(S) = \bar{\epsilon}^{(1)}\mathbf{x}$. The average strain in the particle is therefore approximated by $\bar{\epsilon}^{(2)} = \mathbf{T}\bar{\epsilon}^{(1)}$ where $\mathbf{T}$ is defined in (16). Recalling that the average strain in the composite ϵ^0 is given by:

$$\epsilon^0 = c_1\bar{\epsilon}^{(1)} + c_2\{\bar{\epsilon}^{(2)}\} = [c_1\mathbf{I} + c_2\{\mathbf{T}\}]\bar{\epsilon}^{(1)} \tag{23}$$

provides an estimate for $\bar{\epsilon}^{(1)}$ and therefore for $\bar{\epsilon}^{(2)}$, eventually yielding the following approximation for $\mathbf{L}^*$:

$$\mathbf{L}^* = \mathbf{L}_1 + c_2\{(\mathbf{L}_2 - \mathbf{L}_1)\mathbf{T}\}[c_1\mathbf{I} + c_2\{\mathbf{T}\}]^{-1}. \tag{24}$$

For the case of isotropic inclusions, (24) reduces identically to (18). For oriented inclusions and anisotropic constituents, equations (18), (22), and (24) coincide. An application of (24) for the case of aligned, randomly-oriented isotropic ellipsoidal inclusions can be found in Benveniste (1987).

Finally, it is of interest to dwell on the question of the diagonal symmetry of the $\mathbf{L}^*$ tensor predicted in these theories. Consider first the case of oriented anisotropic inclusions of identical shape. Since $\mathbf{P}$, $\mathbf{L}_1$, and $\mathbf{L}_2$ are symmetric, it follows that $\mathbf{L}^*$ of (21), and thus of (18), (22), and (24), is symmetric. For the case of nonaligned isotropic inclusions, writing first (18) in the form of

$$\mathbf{L}^* = \mathbf{L}_1 + c_2(\mathbf{L}_2 - \mathbf{L}_1)[\{\mathbf{T}\}^{-1}c_1 + c_2\mathbf{I}]^{-1}, \tag{25}$$

and substituting (16) into this expression provides after some manipulations:

$$\mathbf{L}^* = \mathbf{L}_1 + c_2[[(\mathbf{L}_2 - \mathbf{L}_1) - (\mathbf{L}_1 - \mathbf{L}_2)\{\mathbf{P}_1\}(\mathbf{L}_1 - \mathbf{L}_2)]^{-1}c_1 + c_2(\mathbf{L}_2 - \mathbf{L}_1)^{-1}]^{-1} \tag{26}$$

which shows that $\mathbf{L}^*$ is diagonally symmetric. It appears that such a symmetry property does not exist, in general, in (24) for the case of anisotropic inclusions with misaligned axis of symmetry and the use of Mori-Tanaka's model in this situation should be avoided.

References

Benveniste, Y., 1987, "A New Approach to the Application of Mori-Tanaka's Theory in Composite Materials," *Mechanics of Materials*, Vol. 6, pp. 147–157.

Benveniste, Y., and Dvorak, G. J., 1989, "On a Correspondence Between Mechanical and Thermal Effects in Two-Phase Composites," in *Toshio Mura Anniversary Volume*, G. J. Weng, M. Taya, and H. Abe, Springer Verlag, New York.

Brown, L. M., and Stobbs, W. M., 1971, "The work-hardening of Copper Silica I. A Model Based on Internal Stresses, with no Plastic Relaxation," *Phil. Mag.*, Vol. 23, pp. 1185–1199.

Lax, M., 1952, "Multiple Scattering of Waves II. The Effective Field in Dense Systems," *Phys. Rev.*, Vol. 85, pp. 621–629.

Levin, V. M., 1975, "Determination of Effective Elastic Moduli of Composite Materials," *Dokl. Akad. Nauk SSSR*, Vol. 220, pp. 1042–1045, (Translation of *Sov. Phy. Dokl.*, Vol. 20, pp. 147–148, 1975).

Levin, V. M., 1976, "Determination of Composite Material Elastic and Thermoelastic Constants," *Izv. AN SSSR, Mekhaniika Tverdogo Tela*, Vol. 11, pp. 137–145, (Translation: *Mechanics of Solids*, Vol. 11, No. 6, pp. 119–126, 1976).

Mori, T., and Tanaka, K., 1973, "Average Stress in Matrix and Average Elastic Energy of Materials with Misfitting Inclusions," *Acta Metal.*, Vol. 21, pp. 571–574.

Pedersen, O. B., 1983, "Thermoelasticity and Plasticity of Composites — I. Mean Field Theory," *Acta Metal.*, Vol. 31, pp. 1795–1808.

Taya, M., and Chou, T. W., 1981, "On Two Kinds of Ellipsoidal Inhomogeneities in an Infinite Elastic Body: An Application to a Hybrid Composite," *Int. J. Solids and Structures*, Vol. 17, pp. 553–563.

Taya, M., and Mura, T., 1981, "On Stiffness and Strength of an Aligned Short-fiber Reinforced Composites Containing Fiber-End Cracks Under Uniaxial Applied Stress," ASME JOURNAL OF APPLIED MECHANICS, Vol. 48, pp. 361–367.

Walpole, L. J., 1969, "On the Overall Elastic Moduli of Composite Materials," *J. Mech. Phys. Solids*, Vol. 17, pp. 235–251.

Weng, G. J., 1984, "Some Elastic Properties of Reinforced Solids, with Special Reference to Isotropic Ones Containing Special Inclusions," *Int. J. Engng. Sci.*, Vol. 22, pp. 845–856.

Willis, J. R., 1978, "Variational Principles and Bounds for the Overall Properties of Composites," *In Continuum Models of Discrete Systems*, J. W. Provan, ed., University of Waterloo Press, pp. 185–215.

Willis, J. R., 1981, "Variational and Related Methods for the Overall Properties of Composites," *Advances in Applied Mechanics*, Vol. 21, C. S. Yih, ed., Academic Press, New York, pp. 1–78.

Willis, J. R., 1984, "Some Remarks on the Application of the QCA to the Determination of the Overall Elastic Response of a Matrix/Inclusion Composite," *J. Math. Phys.*, Vol. 25, pp. 2116–2120.

Dynamic Stiffness of Cracked Interfaces

Dimitrios A. Sotiropoulos[7]

Quantitative relationships are derived between the dynamic macromechanical stiffness and microparameters of planar interfaces containing distributed cracks. The derivation is based on the solution of the problem of elastic wave reflection by a plane with a continuous distribution of springs to model the cracked interface at the macrolevel. The dynamic spring stiffness is then, through averaging, related to crack-opening volumes and other microparameters. For linear springs and periodic crack distributions, numerical examples are presented for plain strain. The stiffness is shown to strongly depend on frequency.

Introduction

The model of a planar interface containing distributed microcracks can be applied in many areas of materials research and seismology. In composite materials it can represent the weak diffusion bond or adhesion whose strength changes because of the formation of microflaws during manufacture (Thomas et al., 1987; Schramm et al., 1982). Cracking bridging (Rose, 1987) is also a direct application. It is of interest to determine the mechanical properties of partially cracked interfaces for the role they play in the material response and failure under static or dynamic loads. In this paper a quantitative relationship is derived between the dynamic stiffness and microparameters of cracked interfaces. The derivation is based on the solultion of the problem of elastic wave reflection by a plane with a continuous distribution of springs to model the cracked interface at the macrolevel. The dynamic spring stiffness is then, through averaging, related to crack-opening volumes and crack spacing. For linear springs and periodic crack distributions numerical examples are presented for plain strain. Quasi-static elastic wave reflection and static stiffness has been studied (Baik and Thompson, 1984) in connection with the nondestructive evaluation of imperfect interfaces.

Macro-Micro Correlations

A planar interface containing distributed cracks and separating two semi-infinite elastic and isotropic solids is considered. The cracked plane, defined by $y = 0$, acts as an infinite plane of reflection and transmission for incident elastic waves. Here, a longitudinally polarized plane time-harmonic wave is considered as the generic problem. The incident displacement wave is written as

$$u^I = \frac{A}{ik_1} e^{ik_1 y} e^{-i\omega t} \tag{1}$$

where A is its dimensionless amplitude, $k_1 = \omega/c_1$ is the wave number with ω the angular frequency, and with

[7]Department of Civil Engineering, The Technological Institute, Northwestern University Evanston, IL 60208.

Manuscript received by the ASME Applied Mechanics Division, March 30, 1988; final revision, December 6, 1988.

Downloaded 03 May 2010 to 171.66.16.244. Redistribution subject to ASME license or copyright; see http://www.asme.org/terms/Terms_Use.cfm

boundary of the matrix in the auxiliary configuration is subjected to $\mathbf{u}(S) = \bar{\epsilon}^{(1)}\mathbf{x}$. The average strain in the particle is therefore approximated by $\bar{\epsilon}^{(2)} = \mathbf{T}\bar{\epsilon}^{(1)}$ where $\mathbf{T}$ is defined in (16). Recalling that the average strain in the composite ϵ^0 is given by:

$$\epsilon^0 = c_1\bar{\epsilon}^{(1)} + c_2\{\bar{\epsilon}^{(2)}\} = [c_1\mathbf{I} + c_2\{\mathbf{T}\}]\bar{\epsilon}^{(1)} \tag{23}$$

provides an estimate for $\bar{\epsilon}^{(1)}$ and therefore for $\bar{\epsilon}^{(2)}$, eventually yielding the following approximation for $\mathbf{L}^*$:

$$\mathbf{L}^* = \mathbf{L}_1 + c_2\{(\mathbf{L}_2 - \mathbf{L}_1)\mathbf{T}\}[c_1\mathbf{I} + c_2\{\mathbf{T}\}]^{-1}. \tag{24}$$

For the case of isotropic inclusions, (24) reduces identically to (18). For oriented inclusions and anisotropic constituents, equations (18), (22), and (24) coincide. An application of (24) for the case of aligned, randomly-oriented isotropic ellipsoidal inclusions can be found in Benveniste (1987).

Finally, it is of interest to dwell on the question of the diagonal symmetry of the $\mathbf{L}^*$ tensor predicted in these theories. Consider first the case of oriented anisotropic inclusions of identical shape. Since $\mathbf{P}$, $\mathbf{L}_1$, and $\mathbf{L}_2$ are symmetric, it follows that $\mathbf{L}^*$ of (21), and thus of (18), (22), and (24), is symmetric. For the case of nonaligned isotropic inclusions, writing first (18) in the form of

$$\mathbf{L}^* = \mathbf{L}_1 + c_2(\mathbf{L}_2 - \mathbf{L}_1)[\{\mathbf{T}\}^{-1}c_1 + c_2\mathbf{I}]^{-1}, \tag{25}$$

and substituting (16) into this expression provides after some manipulations:

$$\mathbf{L}^* = \mathbf{L}_1 + c_2[[(\mathbf{L}_2 - \mathbf{L}_1) - (\mathbf{L}_1 - \mathbf{L}_2)\{\mathbf{P}_1\}(\mathbf{L}_1 - \mathbf{L}_2)]^{-1}c_1 + c_2(\mathbf{L}_2 - \mathbf{L}_1)^{-1}]^{-1} \tag{26}$$

which shows that $\mathbf{L}^*$ is diagonally symmetric. It appears that such a symmetry property does not exist, in general, in (24) for the case of anisotropic inclusions with misaligned axis of symmetry and the use of Mori-Tanaka's model in this situation should be avoided.

References

Benveniste, Y., 1987, "A New Approach to the Application of Mori-Tanaka's Theory in Composite Materials," *Mechanics of Materials*, Vol. 6, pp. 147–157.

Benveniste, Y., and Dvorak, G. J., 1989, "On a Correspondence Between Mechanical and Thermal Effects in Two-Phase Composites," in *Toshio Mura Anniversary Volume*, G. J. Weng, M. Taya, and H. Abe, Springer Verlag, New York.

Brown, L. M., and Stobbs, W. M., 1971, "The work-hardening of Copper Silica I. A Model Based on Internal Stresses, with no Plastic Relaxation," *Phil. Mag.*, Vol. 23, pp. 1185–1199.

Lax, M., 1952, "Multiple Scattering of Waves II. The Effective Field in Dense Systems," *Phys. Rev.*, Vol. 85, pp. 621–629.

Levin, V. M., 1975, "Determination of Effective Elastic Moduli of Composite Materials," *Dokl. Akad. Nauk SSSR*, Vol. 220, pp. 1042–1045, (Translation of *Sov. Phy. Dokl.*, Vol. 20, pp. 147–148, 1975).

Levin, V. M., 1976, "Determination of Composite Material Elastic and Thermoelastic Constants," *Izv. AN SSSR, Mekhaniika Tverdogo Tela*, Vol. 11, pp. 137–145, (Translation: *Mechanics of Solids*, Vol. 11, No. 6, pp. 119–126, 1976).

Mori, T., and Tanaka, K., 1973, "Average Stress in Matrix and Average Elastic Energy of Materials with Misfitting Inclusions," *Acta Metal.*, Vol. 21, pp. 571–574.

Pedersen, O. B., 1983, "Thermoelasticity and Plasticity of Composites — I. Mean Field Theory," *Acta Metal.*, Vol. 31, pp. 1795–1808.

Taya, M., and Chou, T. W., 1981, "On Two Kinds of Ellipsoidal Inhomogeneities in an Infinite Elastic Body: An Application to a Hybrid Composite," *Int. J. Solids and Structures*, Vol. 17, pp. 553–563.

Taya, M., and Mura, T., 1981, "On Stiffness and Strength of an Aligned Short-fiber Reinforced Composites Containing Fiber-End Cracks Under Uniaxial Applied Stress," ASME JOURNAL OF APPLIED MECHANICS, Vol. 48, pp. 361–367.

Walpole, L. J., 1969, "On the Overall Elastic Moduli of Composite Materials," *J. Mech. Phys. Solids*, Vol. 17, pp. 235–251.

Weng, G. J., 1984, "Some Elastic Properties of Reinforced Solids, with Special Reference to Isotropic Ones Containing Special Inclusions," *Int. J. Engng. Sci.*, Vol. 22, pp. 845–856.

Willis, J. R., 1978, "Variational Principles and Bounds for the Overall Properties of Composites," *In Continuum Models of Discrete Systems*, J. W. Provan, ed., University of Waterloo Press, pp. 185–215.

Willis, J. R., 1981, "Variational and Related Methods for the Overall Properties of Composites," *Advances in Applied Mechanics*, Vol. 21, C. S. Yih, ed., Academic Press, New York, pp. 1–78.

Willis, J. R., 1984, "Some Remarks on the Application of the QCA to the Determination of the Overall Elastic Response of a Matrix/Inclusion Composite," *J. Math. Phys.*, Vol. 25, pp. 2116–2120.

Dynamic Stiffness of Cracked Interfaces

Dimitrios A. Sotiropoulos[7]

Quantitative relationships are derived between the dynamic macromechanical stiffness and microparameters of planar interfaces containing distributed cracks. The derivation is based on the solution of the problem of elastic wave reflection by a plane with a continuous distribution of springs to model the cracked interface at the macrolevel. The dynamic spring stiffness is then, through averaging, related to crack-opening volumes and other microparameters. For linear springs and periodic crack distributions, numerical examples are presented for plain strain. The stiffness is shown to strongly depend on frequency.

Introduction

The model of a planar interface containing distributed microcracks can be applied in many areas of materials research and seismology. In composite materials it can represent the weak diffusion bond or adhesion whose strength changes because of the formation of microflaws during manufacture (Thomas et al., 1987; Schramm et al., 1982). Cracking bridging (Rose, 1987) is also a direct application. It is of interest to determine the mechanical properties of partially cracked interfaces for the role they play in the material response and failure under static or dynamic loads. In this paper a quantitative relationship is derived between the dynamic stiffness and microparameters of cracked interfaces. The derivation is based on the solultion of the problem of elastic wave reflection by a plane with a continuous distribution of springs to model the cracked interface at the macrolevel. The dynamic spring stiffness is then, through averaging, related to crack-opening volumes and crack spacing. For linear springs and periodic crack distributions numerical examples are presented for plain strain. Quasi-static elastic wave reflection and static stiffness has been studied (Baik and Thompson, 1984) in connection with the nondestructive evaluation of imperfect interfaces.

Macro-Micro Correlations

A planar interface containing distributed cracks and separating two semi-infinite elastic and isotropic solids is considered. The cracked plane, defined by $y = 0$, acts as an infinite plane of reflection and transmission for incident elastic waves. Here, a longitudinally polarized plane time-harmonic wave is considered as the generic problem. The incident displacement wave is written as

$$u^I = \frac{A}{ik_1} e^{ik_1 y} e^{-i\omega t} \tag{1}$$

where A is its dimensionless amplitude, $k_1 = \omega/c_1$ is the wave number with ω the angular frequency, and with

[7]Department of Civil Engineering, The Technological Institute, Northwestern University Evanston, IL 60208.

Manuscript received by the ASME Applied Mechanics Division, March 30, 1988; final revision, December 6, 1988.

Copyright © 1990 by ASME
Downloaded 03 May 2010 to 171.66.16.244. Redistribution subject to ASME license or copyright; see http://www.asme.org/terms/Terms_Use.cfm

$c_1^2 = (\lambda_1 + 2\mu_1)/\rho_1$ the wave speed. λ_1, μ_1, ρ_1 are the Lamé constants and density characterizing medium-1 through which the incident wave propagates. In the limit of zero frequency, a nonzero stress is obtained from equation (1). Under the insonification given by (1), the cracked plane gives rise to reflected and transmitted waves which are, respectively, written as

$$u^R = -\frac{AR}{ik_1} e^{-k_1 y} \tag{2}$$

and

$$u^T = \frac{AT}{ik_2} e^{ik_2 y} \tag{3}$$

with R and T the reflection and transmission coefficients, respectively, and k_2 the wave number in medium-2. The factor $e^{-i\omega t}$ has and will be omitted from all field quantities. For up to moderately high frequencies, the reflected and transmitted plane waves are dominant.

The boundary condition of the cracked plane is the usual, i.e., continuity in normal stress. The displacement, however, is discontinuous at the macrolevel. The average displacement jump, Δu, across the partially cracked interface follows from equations (1)–(3) as

$$\Delta u = u(0^+) - u(0^-) = \frac{A}{ik_2}\left[T + \frac{k_2}{k_1}(R-1)\right]. \tag{4}$$

From the continuity of normal stress it also follows that

$$T = (1+R)\left(\frac{\rho_1}{\rho_2}\right)\left(\frac{k_2}{k_1}\right)^2. \tag{5}$$

Substitution of (5) into (4) gives

$$\Delta u = \frac{A}{ik_1}\left[(1+R)\left(\frac{\rho_1}{\rho_2}\right)\left(\frac{k_2}{k_1}\right) + (R-1)\right]. \tag{6}$$

The relationship between Δu and the stress acting on the cracked plane depends on the model one chooses. If one models the cracked plane at the macrolevel as a continuous distribution of linear springs with infinitesimal lengths, i.e.,

$$\sigma(0) = M\Delta u, \tag{7}$$

then the spring constant M may be expressed in terms of Δu through use of equations (5)–(7) together with $\sigma(0) = (\lambda_2 + 2\mu_2)AT$. The result is

$$M = \frac{(\lambda_1 + 2\mu_1)}{1 + \dfrac{\rho_1}{\rho_2}\dfrac{k_2}{k_1}}\left(\frac{2A}{\Delta u} + ik_1\right). \tag{8}$$

To relate the stiffness M to microparameters that characterize the cracked plane from the form of equation (8), it is concluded that there only remains to express the macrolevel displacement jump, Δu, in terms of parameters at the microcrack level. This is achieved through use of an averaging procedure. Let us consider that there exists a large number, N, of microcracks of lengths, $2a_i$, and separation distances, D_i, between consecutive crack centers, that are distributed over the bimaterial interface. Then, the average spring extension, Δu, can be written as

$$\Delta u = \frac{1}{l}\int_0^l u^*(x)dx \tag{9}$$

where $l = \sum_{i=1}^{N} D_i$ is the length of the interface and $u^*(x)$ is the displacement jump at the microlevel. However, at the microlevel only along the crack lengths is the jump nonzero, and is the so-called crack-opening displacement, which is called here u_c. Then equation (9) becomes

$$\Delta u = \frac{\sum_{i=1}^{N} V_i/N}{\sum_{i=1}^{N} D_i/N}, \quad V_i = \int_{-a_i}^{a_i} u_c(x)dx \tag{10a,b}$$

where V_i is the crack-opening volume of the ith crack per unit length in the z-direction for the two-dimensional geometry under consideration. Equation (10a) expresses the spring extension as the ratio of the average microcrack-opening volume to the average microcrack separation distance. Equations (8), (10a,b) express the macro-micro correlation of the partially cracked interface. To obtain the stiffness of a given cracked plane, the dynamic crack-opening volumes have to be calculated first. In the literature, many methods have appeared to calculate crack-opening displacements or volumes when the crack array is periodic and the two materials are similar (e.g., Mikata and Achenbach, 1988), for the dynamic case. For the nonperiodic (deterministic or probabilistic) case, a method was recently (Sotiropoulos and Achenbach, 1988) developed to calculate dynamic crack-opening volumes.

When the substrates are similar, and the partially cracked plane contains infinite periodic crack arrays, the dynamic stiffness of equation (8) becomes

$$M = (\lambda + 2\mu)\left(\frac{AD}{V} + \frac{ik}{2}\right) \tag{11}$$

where it should be noted that the dynamic crack-opening volume, V, is a complex quantity. This simple form of the dynamic stiffness is used next to present numerical examples.

Numerical Examples

We now present some numerical examples to demonstrate the dependence of the stiffness M of (11) on frequency. The crack-opening volume, V, is calculated following the boundary integral equation approach (e.g., Mikata and Achenbach, 1988). The numerical calculations are carried out for similar substrates whose Poisson's ratio is 0.25. In Figs. 1(a,b) the absolute value of the dimensionless stiffness, $S = |M|D/\mu\pi$, is plotted versus the dimensionless frequency, $F = Dk_2/2\pi$, where $k_2 = \omega/c_2$, $c_2^2 = \mu/\rho$. In Fig. 1(a), the separation distance (center to center) beween consecutive cracks is $a/D = 0.25$ while, in Fig. 1(b), is $a/D = 0.40$. It is observed that the stiffness exhibits strong dependence on frequency. Also, as expected, the stiffness is, in general, higher for planes that are cracked less. The results for zero frequency were checked against the closed-form analytical static result, which is derived in the next paragraph.

It should be mentioned that for the static case, $k_1 = 0$, an analytical expression relating explicitly the stiffness M to the geometrical parameter a/D can be derived, as was done by Baik and Thompson (1984) from energy considerations. The result is

$$M = -\frac{\pi\mu/D}{2(1-\upsilon)\ln|\cos\pi a/D|}. \tag{12}$$

This expression can also be derived with the method of the present paper. For $k_1 = 0$, equation (11) becomes

$$M = (\lambda + 2\mu)\frac{AD}{V} \tag{13}$$

which could have alternatively been derived by considering a typical cell for the periodic array, and writing $\sigma = M\Delta u$, $\Delta u = V/D$, and $\sigma = (\lambda + 2\mu)A$ the statically applied external stress at infinity. The crack-opening displacement for this case is known (e.g., Mura, 1982). Its integration in (10b), and subsequent substitution in (13), gives (12).

Downloaded 03 May 2010 to 171.66.16.244. Redistribution subject to ASME license or copyright; see http://www.asme.org/terms/Terms_Use.cfm

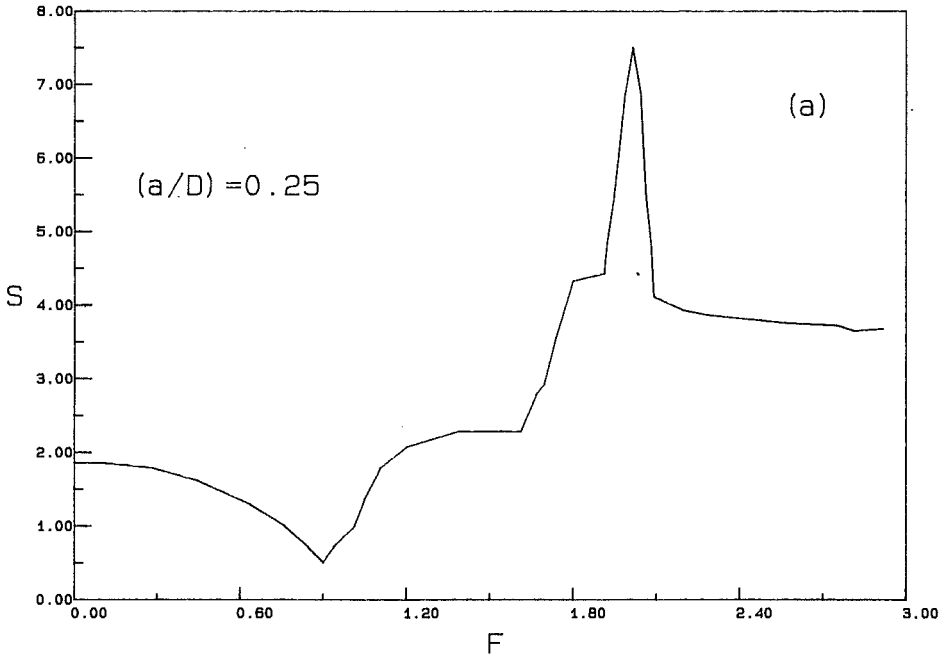


Fig. 1(*a*)

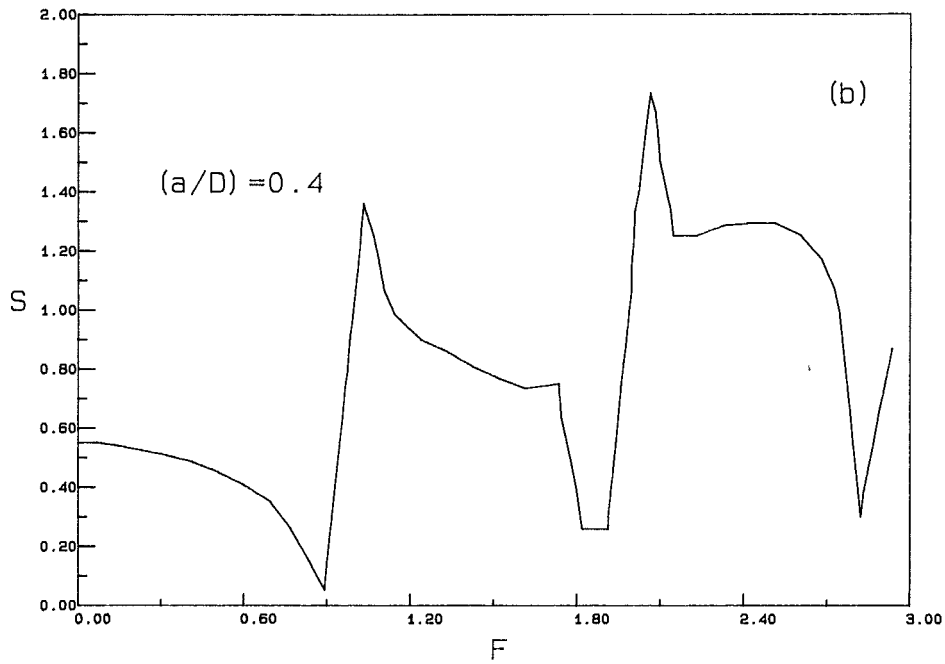


Fig. 1(*b*)

Fig. 1 Dimensionless dynamic stiffness versus dimensionless frequency

References

Baik, J. M., and Thompson, R. B., 1984, "Ultrasonic Scattering from Imperfect Interfaces: A Quasistatic Model," *Journal of Nondestructive Evaluation*, Vol. 4, pp. 177–196.

Mikata, Y., and Achenbach, J. D., 1988, "Interaction of Harmonic Waves With a Periodic Array of Inclined Cracks," *Wave Motion*, Vol. 10, pp. 59–65.

Mura, T., 1982, *Micromechanics of Defects in Solids*, Marthinus Nijhoff, The Hague, The Netherlands.

Rose, J. L., 1987, "Effective Spring Constants for Unbroken Ligaments Between Crack Faces," *International Journal of Fracture*, Vol. 33, pp. 145–152.

Schramm, S. W., Daniel, I. M., and Hamilton, W. G., 1982, "Evaluation of Sensitivity of Ultrasonic Detection of Disbonds in Graphite Epoxy to Metal Joint," *Polymers Plastics Technology Engineering*, Vol. 18, pp. 65–72.

Sotiropoulos, D. A., and Achenbach, J. D., 1988, "Reflection of Elastic Waves by a Coplanar Distribution of Cracks," *Journal of the Acoustical Society of America*, Vol. 84, pp. 752–759.

Thomas, G. H., Springarn, J. R., and Benson, S. E., 1987, "Ultrasonic Evaluation and Image of Tube Closure Welds," *Review of Progress in Quantitative Nondestructive Evaluation*, Vol. 6, pp. 1747–1753.

Downloaded 03 May 2010 to 171.66.16.244. Redistribution subject to ASME license or copyright; see http://www.asme.org/terms/Terms_Use.cfm

Journal of Applied Mechanics

Discussion

The Buckling of Thin-Walled Open-Profile Bars[1]

Raul Rosas e Silva.[2] The paper by Ojalvo has the merit of raising due concern with respect to the calculation of buckling loads using classical thin-walled beam theory. His results differ from the conventional ones for torsional buckling under compression because he used the average longitudinal displacement of the section w_c in equation (4), whereas in equation (6) he introduced a nonlinear term in w_c as a function of the squares of the derivatives of the transverse centroidal displacements u_c and v_c. It can be shown that if a similar averaging process had been used in defining quantities $(u_c')^2$ and $(v_c')^2$, the results would agree with the classical theory.

The average value of the square of a linear function (displacement in the cross-section) is not the same as the square of the average of the same function, except if the function is itself a constant. Therefore, the author's analysis essentially considers the transverse displacements derivatives to be constant in the cross-section; such an approximation fits the case of biaxial bending but contradicts the kinematic assumptions for torsion, which were indeed used in equation (1*a*) and (1*b*). Consequently, the end tractions appear to act through rollers which slide under torsional warping but follow the displacements of the centroid.

This result serves as a reminder that the potential of applied loads is dependent on the particular traction distribution whenever second-order terms are being considered. In other words, modifying quadratic terms in the potential functions may inadvertently introduce unwanted load behavior upon buckling (Silva, 1984).

The writer wishes to suggest that there is a common ground between the conventional and Ojalvo's theories, without resort to the so-called Wagner hypothesis, if the averaging procedure is adopted for the loaded area of the end cross-section. Consider acting over a certain area of the end face of the bar a uniform longitudinal stress traction distribution, its resultant being a force passing through the centroid of the section. If the area of distribution of such tractions is the total cross-section, the conventional theory applies. If the area of traction distribution is infinitesimal (concentrated force applied at the centroid), then the author's theory is to be used. For intermediate cases, replace the ratio between the centroidal polar moment of inertia and the area of the total cross-section (present in the conventional theory) by the same ratio computed for the area of traction distribution. Acting end moments received a different treatment in the paper, but it appears that a similar argument would apply.

Such theories retain the traditional kinematical constraints for thin-walled open-profile bars, with no provision for large displacements, local buckling, distortion of the cross-sections in their planes, or inelastic material behavior. Further refinements would require displacement fields and constitutive relationships of a more complex nature.

Reference

Silva, R. R., 1984, "Effect of Load Behavior and Kinematic Relations on Buckling of Curved Members," *Proceedings of the Annual Technical Session*, Structural Stability Research Council, pp. 83–90.

Author's Closure

We wish to thank the writer for his thoughtful remarks which are much appreciated. We respond as follows:

It is necessary to emphasize that, in mechanics, the object analyzed is never the prototype itself but, rather, a mathematical model of it. The foregoing is true for the simplest of bodies with the simplest of loadings and restraints, and continues to hold whether a technical or an elasticity theory is used.

With this in mind, we defined our model in the section labeled "The Bar." The model conforms to the "classical" representation in all respects and it is this model which dictates, for w_c, the form of equation (6) when the distortions are those which characterize lateral-torsional buckling. If another expression is suggested for w_c, it must conform to another model.

When a model for the bar is chosen it must be adhered to for all stages of the analysis and not solely to vindicate a particular part of the results such as the Wagner hypothesis. Most importantly, it must be possible to use the same model in an equilibrium method analysis and to achieve, in a totally acceptable way, the results of the variational method analysis. This is so because the variational theorem is derived from the virtual work theorem, which in turn is derived from the same concepts of continuity, equilibrium, and material behavior as form the foundation for an equilibrium method analysis (Fung, 1965, pp. 284–288).

The writer states we have considered the transverse displacement derivatives to be constant in a cross-section and that this contradicts the kinematic assumption of torsion. We disagree: The kinematic assumptions referred to are

$$U_g = u + (y_o - y)\,\theta \tag{20a}$$

and

$$V_g = v - (x_o - x)\,\theta \tag{20b}$$

where U_g and V_g are the transverse displacements of a general point in the profile plane parallel to the x and y-axes. Because x and y are centroidal axes for the profile area, the average values of U_g' and V_g' for the bar are

[1] By Morris Ojalvo and published in the September 1989 issue of the ASME Journal of Applied Mechanics, Vol. 56, pp. 633–638.

[2] Associate Professor, Department of Civil Engineering, Pontificia Universidade Catolica do Rio de Janeiro, Rio de Janeiro, RJ 22453, Brazil.

Copyright © 1990 by ASME
Downloaded 03 May 2010 to 171.66.16.244. Redistribution subject to ASME license or copyright; see http://www.asme.org/terms/Terms_Use.cfm

$$\frac{1}{A}\int(U_g')\,dA = u' + y_o\,\theta' = u_c' \qquad (21a)$$

and

$$\frac{1}{A}\int(V_g')\,dA = v' - x_o\,\theta' = v_c'. \qquad (21b)$$

We have used average values for the displacement derivatives of the bar in equation (6), although we obtained them more directly from equation (1).

The writer correctly implies that using $1/A\int(U_g')^2\,dA$ for $(u_c')^2$ and $1/A\int(V_g')^2\,dA$ for $(v_c')^2$ in equation (6) produces the conventional results. But this seemingly innocuous change requires us to deviate from the line model with which the theory is developed. In effect, it would require the adoption of a multifilament representation for the bar. Note how a longitudinal displacement at an end profile is determined from equation (4) for a single-filament representation for the bar. If one followed the conventional approach one would obtain longitudinal displacements by considering the sags of the individual filaments of a multifilament representation of the bar.

The writer suggests there may be room for both theories. Again, we disagree. We have shown that the theory based on our model for the bar results in potentials for the applied loads which are not dependant on a particular distribution of the tractions. There is, therefore, no reason to limit our theory to point loaded columns. The prototype, we believe, is similarly insensitive to the way the tractions are distributed, provided the resultants remain the same (H. Bleich, 1953). On the other hand, the conventional theory suffers from the theoretical deficiencies enumerated and is sensitive to the way tractions are distributed.

Reference

Fung, Y. C., 1965, *Foundations of Solid Mechanics*, Prentice-Hall, Englewood Cliffs, NJ.

Downloaded 03 May 2010 to 171.66.16.244. Redistribution subject to ASME license or copyright; see http://www.asme.org/terms/Terms_Use.cfm

Journal of Applied Mechanics

Book Reviews

Material Instabilities in Continuum Mechanics, and Related Mathematical Problems, edited by J. M. Ball. Oxford Science Publications, 1988. 542 pages.

REVIEWED BY D. D. JOSEPH[1]

This volume contains the proceedings of the symposium year on "Material Instabilities in Continuum Mechanics," which was held during 1985-86 in the Department of Mathematics of Heriot-Watt University, Edinburgh. The majority of the articles concern various aspects of the mathematical theory of phase transitions in solids and fluids, and reflect the revitalization of this area by recent advances in the theory of systems of nonlinear partial differential equations and in the calculus of variations. These advances have led to new insights into the morphology of phase transitions and their dynamic behavior. The remaining articles concern related problems and techniques in solid and fluid mechanics, mathematical physics, and optimization.

There are 31 papers collected into this volume. The titles and authors are as follows: An approximation lemma for $W^{1,p}$ functions, by E. Acerbi and N. Fusco; Homogenization and periodic structure with holes, by E. Acerbi; Thin insulating layers: The optimization point of view, by G. Buttazzo; Lower semicontinuity and relaxation for some problems in optimal design, by E. Cabib; Mathematical models of phase boundaries, by G. Caginalp; Continua with contrained or latent microstructure, by G. Capriz; Elastic behavior of very thin cellular structures, by D. Cioranescu and J. Saint Jan Paulin; A counterexample in the vectorial calculus of variations, by B. Dacorogna and P. Marcellini; Elastic invariants in crystal theory, by C. Davini; Concentrations in solutions to conservative systems, by R. J. DiPerna; Some contrained elastic crystals, by J. L. Ericksen; Some results for a linear, partly hyperbolic model of viscoelastic flow past a plate, by L. E. Fraenkel; Derivation and validity of the Boltzmann equation, by R. Illner; Microstructure and weak convergence, by R. D. James; Standing waves of nonlinear Schrödinger equations: Existence and stability, by C. K. R. T. Jones; Remarks about equilibrium configurations of crystals, by D. Kinderlehrer; Some remarks on uniqueness properties, by J. L. Lions; On a certain variational problem of phase equilibrium, by K. A. Lurie and A. V. Cherkaev; Some remarks on non-convex problems, by E. Mascolo; Experimental and theoretical aspects of cellular and dendritic solidification, by D. G. McCartney and J. D. Hunt; On the viscous Cahn-Hilliard equations, by A. Novick-Cohen; Some asymptotic problems of linear elasticity, by O. A. Oleinik; Phase mixtures in nonlinear viscoelasticity in one dimension, by R. L. Pego; Statistical mechanics and the kinetics of phase separation, by O. Penrose; On 1- and 3-dimensional models in "non-convex" elasticity, by M. Pitteri; An application of the method of compensated compactness to a problem in phase transitions, by V. Roytburd and M. Slemrod; A review of some non-convex problems, by R. Schianchi; Nonlinear geometric optics and conservation laws, by M. E. Schonbek; On the admissibility of shocks and propagating phase boundaries in a van der Waals fluid, by M. Silhavy; Unilateral problems in continuum mechanics, by F. Tomarelli; Surface tension effects in phase transitions, by A. Visintin.

This is a very outstanding and varied collection of topics of current interest to analysts interested in the mathematical aspects of continuum mechanics.

[1]Department of Aerospace and Mechanics, University of Minnesota, Minneapolis, MN 55455.

Copyright © 1990 by ASME
Downloaded 03 May 2010 to 171.66.16.244. Redistribution subject to ASME license or copyright; see http://www.asme.org/terms/Terms_Use.cfm